

A STUDY OF RADIATION-INDUCED EFFECTS IN PHOTONIC DEVICES: ACOUSTOOPTIC MODULATORS AND DEFLECTORS

**Edward W. Taylor, Anthony D. Sanchez, James E. Winter,
Stanley J. McKinney, Alan H. Paxton, Harald Schone,
and Douglas M. Craig**

January 1998

Final Report

19980831 002

APPROVED FOR PUBLIC RELEASE; DISTRIBUTION IS UNLIMITED.

DTIC QUALITY INSPECTED 1



**AIR FORCE RESEARCH LABORATORY
Space Vehicles Directorate
3550 Aberdeen Ave SE
AIR FORCE MATERIEL COMMAND
KIRTLAND AIR FORCE BASE, NM 87117-5776**


Using Government drawings, specifications, or other data included in this document for any purpose other than Government procurement does not in any way obligate the U.S. Government. The fact that the Government formulated or supplied the drawings, specifications, or other data, does not license the holder or any other person or corporation; or convey any rights or permission to manufacture, use, or sell any patented invention that may relate to them.

This report has been reviewed by the Public Affairs Office and is releasable to the National Technical Information Service (NTIS). At NTIS, it will be available to the general public, including foreign nationals.

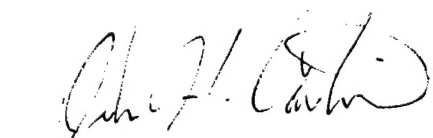
If you change your address, wish to be removed from this mailing list, or your organization no longer employs the addressee, please notify AFRL/VS, 3550 Aberdeen Ave SE, Kirtland AFB, NM 87117-5776.

Do not return copies of this report unless contractual obligations or notice on a specific document requires its return.

This report has been approved for publication.



EDWARD W. TAYLOR, DR-III
Principal Investigator



JOHN H. COMTOIS, Major, USAF
Chief, Space Electronics and Protection
Technologies Branch

FOR THE COMMANDER



CHRISTINE M. ANDERSON, SES
Director, Space Vehicles

REPORT DOCUMENTATION PAGE			Form Approved OMB No. 074-0188	
Public reporting burden for this collection of information is estimated to average 1 hour per response, including the time for reviewing instructions, searching existing data sources, gathering and maintaining the data needed, and completing and reviewing this collection of information. Send comments regarding this burden estimate or any other aspect of this collection of information, including suggestions for reducing this burden to Washington Headquarters Services, Directorate for Information Operations and Reports, 1215 Jefferson Davis Highway, Suite 1204, Arlington, VA 22202-4302, and to the Office of Management and Budget, Paperwork Reduction Project (0704-0188), Washington, DC 20503				
1. AGENCY USE ONLY (Leave blank)	2. REPORT DATE January 1998	3. REPORT TYPE AND DATES COVERED Final Report - 15 Aug 91 through 15 Aug 97		
4. TITLE AND SUBTITLE A Study of Radiation-Induced Effects in Photonic Devices: Acoustooptic Modulators and Deflectors		5. FUNDING NUMBERS PE: PR: DSWA TA: TB WU: 05		
6. AUTHOR(S) Edward W. Taylor, Anthony D. Sanchez, James E. Winter, Stanley J. McKinney, Alan H. Paxton, Harald Schone, and Douglas M. Craig				
7. PERFORMING ORGANIZATION NAME(S) AND ADDRESS(ES) Air Force Research Laboratory/VSSSE 3550 Aberdeen Ave SE Kirtland AFB, NM 87117-5776		8. PERFORMING ORGANIZATION REPORT NUMBER AFRL-VS-PS-TR-1998-1028		
9. SPONSORING / MONITORING AGENCY NAME(S) AND ADDRESS(ES)		10. SPONSORING / MONITORING AGENCY REPORT NUMBER		
11. SUPPLEMENTARY NOTES Preliminary Report: E. W. Taylor et al., A Study of Radiation-Induced Effects in Photonic Devices: Acoustooptic Modulators and Deflectors - Preliminary Results, PL-TR-94-1141, May 1994.				
12a. DISTRIBUTION / AVAILABILITY STATEMENT Approved for Public Release; Distribution is Unlimited			12b. DISTRIBUTION CODE	
13. ABSTRACT (Maximum 200 Words) In a preliminary report acoustooptic devices (AODs) were exposed to flash x-ray, linearly accelerated electrons, and gamma-ray irradiations to determine their sensitivity to radiation and applicability to space and enhanced radiation environments. This final report is a continuation and finalization of those initial studies and details the findings of a comprehensive investigation of radiation induced effects in Lead Molybdate, Gallium Phosphide, Indium Phosphide, Tellurium Dioxide, and Lithium Niobate AO Bragg cell deflectors and modulators. Gamma-ray, X-ray, electrons, proton and neutron irradiations were conducted to bound, delineate, and differentiate radiation induced changes to operational AODs. Instantaneous changes to AOD parameters such as spatial intensities, deflection angles, bandwidth, material absorption, diffraction efficiency and polarization states were determined. A majority of the radiation induced effects observed were determined to evolve from the heating associated with the interaction of radiation with matter. The heating effects were investigated and confirmed using three independent approaches: traditional broad area source, ion microbeam, and CO2 laser irradiations. It was concluded that AO Bragg cell deflectors and modulators are quite insensitive to the long term-low dose radiation environments encountered in the natural space environment. Providing that adequate thermal control is provided, Bragg cells appear very mature for space applications.				
14. SUBJECT TERMS acoustooptic devices, AO deflectors, AO modulators, AO Bragg cells, radiation induced effects, photonic devices.			15. NUMBER OF PAGES 322	
			16. PRICE CODE	
17. SECURITY CLASSIFICATION OF REPORT Unclassified	18. SECURITY CLASSIFICATION OF THIS PAGE Unclassified	19. SECURITY CLASSIFICATION OF ABSTRACT Unclassified	20. LIMITATION OF ABSTRACT Unlimited	

This page intentionally left blank.

ABSTRACT

In a preliminary report acoustooptic devices (AODs) were exposed to flash x-ray, linearly accelerated electrons, and gamma-ray irradiations to determine their sensitivity to radiation and applicability to space and enhanced radiation environments. This final report is a continuation and finalization of those initial studies and details the findings of a comprehensive investigation of radiation induced effects in Lead Molybdate (PbMoO_4), Gallium Phosphide (GaP), Indium Phosphide (InP), Tellurium Dioxide (TeO_2), and Lithium Niobate (LiNbO_3) acoustooptic Bragg cell deflectors and modulators. Gamma-ray, X-ray, electrons, proton and neutron irradiations were conducted to bound, delineate and differentiate radiation induced changes to operational AO Bragg Cells. The majority of the irradiations were performed in situ, wherein the Bragg cells were fully operational during the radiation exposures. Using this approach, instantaneous changes to Bragg cell parameters such as spatial intensities, deflection angles, bandwidth, material absorption, diffraction efficiency and polarization states were determined. A majority of the radiation induced effects observed were determined to evolve from the heating associated with the interaction of radiation with matter, thus resulting in observable thermooptic effects. The effects of heating in AO Bragg crystals were investigated and confirmed using three independent approaches: traditional broad area source irradiations, ion microbeam irradiations, and irradiation by a CO_2 laser. It was concluded that AO Bragg deflectors and modulators are quite insensitive to the long term-low dose radiation environments that would be encountered in the natural space environment. However, under pulsed high dose (or high fluence) irradiations, Bragg cell transient responses could result in disruption of normal operations. Providing that adequate thermal control is implemented, Bragg cells appear very mature for space applications.

This page intentionally left blank.

EXECUTIVE SUMMARY

The responses of Lead Molybdate (PbMoO_4), Gallium Phosphide (GaP), Indium Phosphide (InP), Tellurium Dioxide (TeO_2), and Lithium Niobate (LiNbO_3) acoustooptic modulators and deflectors exposed to various radiation species are reported. In an earlier preliminary report acoustooptic devices (AODs) were exposed to flash x-ray, linearly accelerated electrons, and gamma-ray irradiations to determine their sensitivity to radiation and applicability to space and enhanced radiation environments.

This report is a continuation and finalization of those studies and details the findings of a comprehensive investigation of radiation induced effects in acoustooptic Bragg cell deflectors and modulators composed of PbMoO_4 , TeO_2 , LiNbO_3 , GaP and InP crystals. Gamma-ray, X-ray, electrons, proton and neutron irradiations were conducted to bound, delineate and differentiate radiation induced changes to operational AO Bragg Cells. The majority of the irradiations were performed in situ, wherein the Bragg cells were fully operational during the radiation exposures. Using this approach, instantaneous changes to Bragg cell parameters such as spatial intensities, deflection angles, bandwidth, material absorption, diffraction efficiency and polarization states were determined. Post irradiation recovery of the radiation induced changes were also temporally measured, and several perspicuous models for explaining and predicting the degradation mechanisms and recovery kinetics were published in the open literature.

The contents of this report span the period of performance from 15 August 1991 through 15 August 1997, with emphasis placed on data not reported in the preliminary report. The materials and data in this report are intended to establish a foundation for understanding and predicting the physical processes by which electron, proton, gamma-ray, x-ray and neutron radiation interact with acoustooptic materials and devices.

The basis and justification for the investigation and the focus for the overall program direction was a direct outgrowth of the Photonic Systems Survivability Workshop conducted by

Headquarters Defense Nuclear Agency (HQ DNA / RAES), Washington, DC, in 1991. The conclusions reached at the workshop were that five of eight Transitioning of Optical Processing Systems (TOPS) application areas relied on AO technology and the remaining areas relied on other spatial light modulator technology. While studies of the radiation resistance of optical fibers-a subset of photonics technology-had undergone highly coordinated intensive investigations, this was not true of many related photonic technology areas. One of four areas identified as immediately requiring investigation of radiation induced effects studies were AOMs. This technology area was determined to have experienced extremely limited radiation-induced response research, even though it was a highly mature technology with a dominant role in advanced and state-of-the-art signal processing techniques. These findings led to the investigations reported herein.

The Photonics Research Group (PRG) of the Phillips Laboratory (PL) undertook the investigation of quantifying for the first time, real-time transient and steady state radiation-induced responses of key AOD parameters. Preliminary results were reported to the community on the radiation-induced alteration of Bragg cell AOD characteristics including: diffraction efficiency, deflection angle, spatial intensity distributions, bandwidth responses, and polarization.

Several experimental approaches previously used for measuring radiation-induced effects in integrated optic and optical fiber component technologies were applied to this study which involved observing changes to the refractive index dependent processes. Thus, a portion of the unique transient measurement techniques developed previously were used to study the radiation-induced transient effects in bulk AO modulator devices.

To guide other investigators that may wish to repeat these first measurements, this report delineates many lessons learned in properly choosing and applying the measurement instrumentation and data analysis techniques devised to support this study. Many of the measurement techniques employed during the early stages of this study were found to be inadequate as the researchers' understanding of the radiation-induced response mechanisms

progressed. Therefore, some of the early techniques used for detecting and measuring radiation-induced responses (such as x-ray induced responses in PbMoO_4) were not used in later studies but have been documented for completeness.

A majority of the radiation induced effects observed were determined to evolve from the heating associated with the interaction of radiation with matter, thus resulting in observable thermo-optic effects. In particular, irradiation of AO Bragg cells by 15 MeV protons and electrons caused thermal (refractive index) gradients within the AO cell crystal lattice, which altered the cell diffraction efficiency, spatial intensity distribution, deflection angle, and polarization. Other heating effects affected the cell transducer operation and bandwidth response. The effects of heating in AO Bragg crystals were investigated and confirmed using three independent approaches: traditional broad area source irradiations, ion microbeam irradiations, and irradiation by a CO_2 laser.

It was concluded that AO Bragg deflectors and modulators are quite insensitive to the long term-low dose radiation environments that would be encountered in the natural space environment. However, under pulsed high dose (or high fluence) irradiations, Bragg cell transient responses could result in disruption of normal operations.

Finally, it was concluded, that providing that adequate thermal control is provided, Bragg cells appear very mature for space applications.

This page intentionally left blank.

ACKNOWLEDGEMENTS

The investigations were proposed and funded by Headquarters, Defense Nuclear Agency (HQ DNA/RAES) now known as the Defense Special Weapons Agency (DSWA), Washington, DC, Electronics and Systems Technology Division, and was conducted by the Air Force Materiel Command, Phillips Laboratory (PL) now known as the Space Vehicles Directorate (VS) within the Air Force Research Laboratory (AFRL). The AFRL's Principal Investigator throughout the period of investigation was Mr. Edward W. Taylor, while the HQ DNA/RAES Technical Focal Point and Project Officers for this report were Maj Daniel J. Page and Maj Ronald A. Doby for the interim and Mr. Lewis Cohn (DSWA/ESE) for the remaining period (1995-1997)).

The authors would like to acknowledge former members of the PL/VTET-Photonics Research Group (presently known as the AFRL/VSSE-Photonics Research and Evaluation Team), including Lt Timothy M. Monarski, Capt Richard J. Padden, Dr. Michael Kelly, Mr. Stephen DeWalt, Mr. Scott Chapman, and Capt Nicolas Chamussy of DGA, France, for their many contributions to the experiments. Each of these individuals contributed his knowledge, ingenuity, and energy towards furthering the understanding of radiation effects in acoustooptic technologies.

The authors are also indebted to the many members of the U.S. Army White Sands Missile Range (WSMR), New Mexico, Nuclear Effects Directorate (STEWS-NE-O), for their excellent support in the operation of the WSMR Linear Electron Accelerator facility. In particular, special recognition is due to Dr. John Meason, NE-O Director; Dr. Ralph Dressler; Mr. Tony Ledford and Mr. Andy Langdon for their untiring efforts in supporting the experimental portions of this program. The authors also wish to thank Dr. Barney Doyle of Sandia National Laboratory-Ion Beam Materials Research Laboratory for his support in our ion beam irradiations.

Finally, the authors wish to sincerely thank various members of DSWA for their valuable guidance and sponsorship of this effort. Special recognition is due to Maj Daniel Page for

helping to conceive and advocating the radiation studies on AO devices. His interaction during the early periods of the investigation was inspiring and invaluable. In addition, special thanks are due to Mrs. Joan Ma Pierre, Director of Radiation Sciences, HQ DNA, and Mr. R. C. Webb, Chief, Electronics and Systems Technology Division, HQ DNA, for their foresight and advocacy in support of the research.

CONTENTS

SECTION	PAGE
1.0 INTRODUCTION	1
2.0 ACOUSTOOPTIC INTERACTIONS	7
2.1 ISOTROPIC DIFFRACTION	7
2.2 BRAGG ANGLE DIFFRACTION	9
2.3 ANISOTROPIC DIFFRACTION	14
2.4 ALIGNMENT PROCEDURES-OPTIMIZATION OF BRAGG CELL OPERATION.....	16
3.0 RADIATION INDUCED CHANGES TO POLARIZED AO CELLS	21
3.1 METHODOLOGY FOR MEASURING RADIATION INDUCED DEPOLARIZATION IN PHOTONIC DEVICES	21
3.2 MEASURING DEPOLARIZATION USING PHOTOELASTIC MODULATORS.....	22
3.3 MEASUREMENT OF RADIATION INDUCED CHANGES TO POLARIZATION STATES AND DEGREE OF POLARIZATION.....	24
3.4 EXPERIMENTAL ARRANGEMENT-PROTON IRRADIATION OF AO BRAGG CELLS	25
3.5 EXPERIMENTAL RESULTS - PROTON INDUCED CHANGES TO THE POLARIZATION STATES	27
3.5.1 GaP Bragg Cell Responses	28
3.5.2 TeO ₂ Bragg Cell Responses.....	32
3.6 ANALYSIS-TRANSIENT DEPOLARIZATION OF OPTICAL SIGNALS.....	37
3.7 DISCUSSION OF PROTON IRRADIATION OF AO BRAGG CELL RESULTS.....	41
3.8 ELECTRON INDUCED POLARIZATION CHANGES IN AO BRAGG CELLS	45
3.9 GAMMA-RAY INDUCED POLARIZATION CHANGES IN AO BRAGG CELLS	52
3.9.1 Gamma Exposure of a GaP Acoustooptic Bragg Cell.....	53
3.9.2 Gamma Exposure of a TeO ₂ Acoustooptic Bragg Cell.....	57

CONTENTS (continued)

SECTION	PAGE
4.0 RADIATION INDUCED BANDWIDTH RESPONSES IN ACOUSTOOPTIC BRAGG CELLS	61
4.1 EXPERIMENTAL ARRANGEMENT	61
4.2 AO BANDWIDTH RESPONSES TO PULSED ELECTRON IRRADIATIONS	63
4.3 ANALYSIS OF DIFFRACTION EFFICIENCY - BANDWIDTH RESPONSES	67
4.4 LASER HEATING - SIMULATION OF ELECTRON INDUCED EFFECTS	70
4.5 SUMMARY OF RESULTS	73
5.0 OVERVIEW OF ION BEAM EXPOSURES OF AO BRAGG CELLS	75
5.1 EXTERNAL ION BEAM ANALYSIS	75
5.2 EXPERIMENTAL SETUP OF AO MODULATOR EXPOSURES	77
5.3 GENERAL CONCEPT AND OUTLINE OF DATA REDUCTION	79
5.4 ION BEAM ANALYSIS RESULTS	80
5.4.1 PbMoO ₄ Acoustooptic Bragg Cell	80
5.4.1.1 Discussion of Radiation Induced Effects	83
5.4.2 LiNbO ₃ Acoustooptic Bragg Cell	86
5.4.3 TeO ₂ Acoustooptic Bragg Cell	90
5.4.4 InP Acoustooptic Bragg Cell	95
5.4.5 PbMoO ₄ #2 Acoustooptic Bragg Cell	98
6.0 RESPONSE OF AO DEVICES TO GAMMA AND NEUTRON IRRADIATIONS	103
6.1 DESCRIPTIONS OF EXPOSURES	105
6.1.1 Gamma Exposure of a TeO ₂ Acoustooptic Bragg Cell	105
6.1.2 Gamma Exposure of a GaP Acoustooptic Bragg Cell	108
6.1.3 Neutron Exposure of a TeO ₂ Acoustooptic Bragg Cell	110
6.1.4 Gamma Exposure of a LiNbO ₃ Acoustooptic Bragg Cell #1	113
6.1.5 Gamma Exposure of a LiNbO ₃ Acoustooptic Bragg Cell #2	116
6.1.6 Neutron Exposure of a GaP Acoustooptic Bragg Cell	118
6.1.7 Gamma Exposure of an InP Acoustooptic Bragg Cell	123
6.1.8 Neutron Exposure of a TeO ₂ Acoustooptic Bragg Cell	126

CONTENTS (concluded)

SECTION	PAGE
7.0 PASSIVE NEUTRON EXPOSURE OF LiNbO_3 , GaP, AND InP ACOUSTOOPTIC BRAGG CELLS	131
7.1 GENERAL EXPERIMENT DESCRIPTION	131
7.1.1 Broad Spectral Width Absorption	131
7.1.2 Narrow Spectral Width Absorption	134
7.1.3 Data Analysis of Broad/Narrow Spectral Width Absorption	135
7.1.4 Changes to Diffraction Efficiency at the AOM Center Frequency	135
7.1.5 Changes to AOM Bandwidth	136
7.2 RESULTS OF 1×10^{15} n/cm ² PASSIVE EXPOSURE OF: LiNbO ₃ , GaP, and InP	137
7.2.1 Diffraction Efficiency and Insertion Loss Results	137
7.2.2 Bandwidth Response Results	139
7.2.3 Spectral Characterization Response Results	141
8.0 CONCLUSIONS / RECOMMENDATIONS	147
9.0 REFERENCES	149
APPENDIX A - ION BEAM EXPERIMENTAL RESULTS AND TIMES	155

FIGURES

Figure	page
2-1. Acoustooptic Bragg Deflector.	10
2-2. Conservation of momentum for Bragg angle diffraction.	12
2-3. Vector diagram representing anisotropic Bragg diffraction.	15
2-4. Typical AOD irradiation exposure orientation and alignment geometry.	17
2-5. Typical Bragg angle adjustment and alignment geometry for AOD experiment configurations.	18
3-1. Experimental arrangement for measuring polarization states and depolarization.	23
3-2. Typical arrangement for studying proton induced polarization effects in diffracted beam of acoustooptic devices.	25
3-3. Proton induced changes to the diffracted beam polarization states of a GaP Bragg cell.	29
3-4. Temperature response of a GaP AO Bragg cell under proton irradiation.	30
3-5. Ionization and proton energy in a GaP AO Bragg cell and aluminum heat sink under proton irradiation.	31
3-6. Dose in a GaP AO Bragg cell and aluminum heat sink under proton irradiation.	32
3-7. Proton induced changes to the diffracted beam polarization states of a TeO ₂ Bragg cell.	33
3-8. Temperature response of a TeO ₂ Bragg cell under proton irradiation.	34
3-9. Ionization in a TeO ₂ AO Bragg cell under proton irradiation.	35
3-10. Dose in a TeO ₂ AO Bragg cell under proton irradiation.	36
3-11. Stokes parameter values for a TeO ₂ Bragg deflector under proton irradiation.	39
3-12. Degree of polarization (P) for a TeO ₂ AO Bragg deflector exposed to proton radiation.	41
3-13. Typical arrangement for studying electron induced polarization effects in main beam of acoustooptic devices.	45
3-14. Main beam polarization components response before, during and after electron irradiation exposure.	46
3-15. Dose in pGy per 15.0 MeV electron in TeO ₂	48
3-16. Stokes parameters as a function of time encompassing electron irradiation period.	50
3-17. Diffraction efficiency responses shown for a TeO ₂ AO Bragg cell irradiated to $D_e = 1.05$ Mrad.	51

FIGURES (continued)

Figure	page
3-18. Degree of Polarization response is shown for a TeO ₂ AO Bragg cell irradiated to 1.05 Mrad.	52
3-19. Detector response of the DC1 and DC2 components of the GaP AO cell shown during the irradiation interval and recovery.	53
3-20. Detector response of the diffracted beam of the GaP AO cell during gamma exposure and recovery.	54
3-21. Detector response of the laser reference beam of the GaP AO cell during gamma exposure and recovery.	54
3-22. Horizontal / Vertical polarization of I ₀ ' of the GaP AO cell during gamma exposure and recovery.	55
3-23. +/- 45 degree polarization of I ₀ ' of the GaP AO cell during gamma exposure and recovery.	56
3-24. Circular polarization of I ₀ ' of the GaP AO cell during gamma exposure and recovery.	56
3-25. Experimental arrangement for the TeO ₂ AO cell.	58
3-26. Detector response for Horizontal / Vertical polarization for the PEMS.	59
3-27. Detector response for +/- 45 degree polarization for the PEMS.	60
3-28. Detector response for circular polarization for the PEMS.	60
4-1. Experimental arrangement for measuring AO bandwidth and diffraction efficiency during exposure to pulsed electrons.	61
4-2. Responses of PbMoO ₄ diffracted beam (I _d) is seen in (a) and the responses of the main in (b).	62
4-3. Swept frequency bandwidth responses for PbMoO ₄ AOD.	64
4-4. Temperature responses on and near the PbMoO ₄ AOD.	66
4-5. Swept frequency responses of PbMoO ₄ diffraction efficiency following pulsed electron irradiations.	71
4-6. Effect of the CO ₂ laser heating of a PbMoO ₄ acoustooptic Bragg Deflector.	72
5-1. Sketch of Sandia National Laboratory Ion Beam Research Facility and the ion microbeam line.	76
5-2. Experimental setup for measuring the performance of an AO cell under H ⁺ irradiation.	78
5-3. A conceptual sketch of the PbMoO ₄ #1 acoustooptical modulator.	81
5-4. Contour plot showing the diffraction efficiency as a function of ion beam location on the crystal.	82
5-5. Contour plot showing the diffraction efficiency as a function of ion beam location on the crystal.	82

FIGURES (continued)

Figure	page
5-6. Contour plot showing the diffraction efficiency as a function of ion beam location on the crystal (transducer is at location $y=0$ mm, $t=40$ s, and the ion beam was unblocked at $t=0$ s).	83
5-7. Comparison of experimental diffraction efficiency values with a theoretical curve of the efficiency for scattering from the input beam to the diffracted beam.	85
5-8. A conceptual sketch of the LiNbO_3 acoustooptical modulator.	86
5-9. Two plots showing the measured AO cell response before, during and after an ion beam exposure (upper plot shows the calculated diffraction efficiency and bottom plot shows the ion beam current).	88
5-10. a. Crystal of acoustooptic device. b. Plot shows change in diffraction efficiency, η , as a function of position of incidence of ion beam on crystal face opposite heatsink.	89
5-11. Change of surface temperature during ion beam exposure.	90
5-12. Diagram showing TeO_2 Acoustooptic Deflector.	91
5-13. Plot of diffraction efficiency of TeO_2 AO deflector during and following irradiation of the crystal face opposite the heatsink.	92
5-14. Same as Figure 5-13 except that data were acquired for a 180 s, to show relaxation of the diffraction efficiency to the pre-irradiation value.	93
5-15. A conceptual sketch of the InP acoustooptical modulator.	96
5-16. Top part of figure shows absolute diffraction efficiency of InP modulator (irradiation position is $x=12.5$ mm, $y=0.5$ mm).	97
5-17. A conceptual sketch of the PbMoO_4 acoustooptical modulator.	99
5-18. Change of diffraction efficiency during the proton exposure for time slices starting at 5 s to 40 s after start of the beam exposure.	100
6-1. A drawing of the TeO_2 device under investigation in this exposure.	105
6-2. Experimental configuration for an active TeO_2 AO device bandwidth measurement in a gamma radiation environment.	106
6-3. Overlay of the bandwidth responses of a TeO_2 AO device at a gamma-ray dose of approximately 1 Mrad(Si) and the responses prior to radiation exposure.	107
6-4. Experimental configuration for an active GaP AO device attenuation measurement in a gamma-ray radiation environment.	108
6-5. Pre-irradiation and 420 krad(Si) Co-60 irradiation material attenuation data for an unmodulated GaP AOD.	109

FIGURES (continued)

Figure	page
6-6. TeO ₂ device under investigation in exposure 3.	110
6-7. Initial experimental configuration for performing an active AO device diffraction efficiency measurement in a neutron environment.	111
6-8. Neutron irradiation of TeO ₂ AO device to a 1 MeV equivalent fluence of 1×10^{15} n/cm ² during intermittent operation at 130 MHz.	112
6-9. Laser reference detector response during the neutron irradiation of TeO ₂ AO device to a 1 MeV equivalent fluence of 1×10^{15} n/cm ² during intermittent operation of device.	112
6-10. Drawing of the LiNbO ₃ device under investigation in exposure 4.	113
6-11. Experimental configuration for conducting active LiNbO ₃ AO device bandwidth measurements in a gamma-ray environment.	114
6-12. LiNbO ₃ diffraction efficiencies before, during (peak) and after irradiation.	115
6-13. Comparison of the detector responses of pre-irradiation, end of irradiation, and recovery of the zero order beams for the LiNbO ₃ AOD.	116
6-14. Comparison of the pre-irradiation, end of irradiation, and recovery of the laser reference beams of the LiNbO ₃ AOD.	117
6-15. Comparison of the pre-irradiation, end of irradiation, and recovery of the thermistors on the LiNbO ₃ AOD.	117
6-16. A drawing of the GaP device under investigation in exposure 6.	119
6-17. Experimental set-up for the GaP AO device.	120
6-18. Optical detector response to light ($\lambda = 670$ nm) from an Injection Laser Diode (ILD) through an unmodulated GaP AO device during exposure to neutrons.	121
6-19. Laser reference and dark detector reference response during the course of neutron exposure of an GaP AO device and recovery.	122
6-20. A drawing of the InP device under investigation in exposure 7.	123
6-21. Diffracted beam (I_d) response of InP AO Bragg cell exposed to a 1 Mrad gamma irradiation dose.	124
6-22. HeNe laser reference beam response of InP AO Bragg cell exposed to a 1 Mrad gamma irradiation dose.	124
6-23. Main beam (I_0') response of InP AO Bragg cell exposed to a 1 Mrad gamma irradiation dose.	125

FIGURES (continued)

Figure	page
6-24. Temperature response of InP AO Bragg cell exposed to a 1Mrad gamma irradiation dose.	125
6-25. A drawing of the TeO ₂ device under investigation in exposure 8.	126
6-26. SPR III active irradiation configuration for measuring diffraction efficiency of a TeO ₂ acoustooptic device under an exposure of 1×10^{15} n/cm ²	127
6-27. TeO ₂ zero order beam I ₀ ' response to 1×10^{15} n/cm ² fluence.	128
6-28. TeO ₂ diffracted beam response to 1×10^{15} n/cm ² fluence.	128
6-29. HeNe laser reference beam response to 1×10^{15} n/cm ² fluence.	129
6-30. TeO ₂ AO device temperature response to 1×10^{15} n/cm ² fluence.	129
7-1. LiNbO ₃ device under investigation in this exposure.	132
7-2. GaP device under investigation in this exposure.	133
7-3. InP device under investigation in this exposure.	133
7-4. Typical spectral characterization response configuration used for broad spectral width absorption measurements.	134
7-5. Typical spectral characterization response configuration used for narrow spectral width absorption measurements.	135
7-6. Typical acoustooptic device bandwidth response configuration.	136
7-7. Pre and post irradiation bandwidth diffraction efficiency (GaP).	139
7-8. Pre and post irradiation bandwidth diffraction efficiency (LiNbO ₃).	140
7-9. Pre and post irradiation bandwidth diffraction efficiency (InP).	141
7-10. Spectral output characterization of a ($\lambda=670$ nm) Injection Laser Diode (ILD) for narrow spectral width absorption measurements (Post-Irradiation - Spectral Scan).	142
7-11. Spectral transmission of Gallium Phosphide modulator when illuminated with $\lambda=670$ nm Injection Laser Diode (ILD) after a 1×10^{15} n/cm ² fluence exposure of AO cell.	142
7-12. Spectral output characterization of a Xenon lamp for broad spectral width absorption measurements (Post-Irradiation - Spectral Scan).	143
7-13. Spectral transmission of Gallium Phosphide modulator when illuminated with a Xenon light source after a 1×10^{15} n/cm ² fluence exposure of AO cell.	143

FIGURES (continued)

Figure	page
7-14. Spectral output characterization of a ($\lambda=670$ nm) Injection Laser Diode (ILD) for narrow spectral width absorption measurements (Post-Irradiation - Spectral Scan).	144
7-15. Spectral transmission of Lithium Niobate deflector when illuminated with a $\lambda=670$ nm Injection Laser Diode (ILD) after a 1×10^{15} n/cm ² fluence exposure of AO cell.	144
7-16. Spectral output characterization of a Xenon lamp for broad spectral width absorption measurements (Post Irradiation - Spectral Scan).	145
7-17. Spectral transmission of Lithium Niobate deflector when illuminated with a Xenon light source after a 1×10^{15} n/cm ² fluence exposure of AO cell.	145
A-1. Plots showing calculated diffraction efficiency and ion beam current ($z=unk$, $y=unk$).	158
A-2. Plots showing calculated diffraction efficiency and ion beam current ($z=2.5$ mm, $y=0.5$ mm).	159
A-3. Plots showing calculated diffraction efficiency and ion beam current ($z=4.5$ mm, $y=0.5$ mm).	160
A-4. Plots showing calculated diffraction efficiency and ion beam current ($z=6.5$ mm, $y=0.5$ mm).	161
A-5. Plots showing calculated diffraction efficiency and ion beam current ($z=6.5$ mm, $y=2.5$ mm).	162
A-6. Plots showing calculated diffraction efficiency and ion beam current ($z=4.5$ mm, $y=2.5$ mm).	163
A-7. Plots showing calculated diffraction efficiency and ion beam current ($z=2.5$ mm, $y=2.5$ mm).	164
A-8. Plots showing calculated diffraction efficiency and ion beam current ($z=0.5$ mm, $y=2.5$ mm).	165
A-9. Plots showing calculated diffraction efficiency and ion beam current ($z=0.5$ mm, $y=4.5$ mm).	166
A-10. Plots showing calculated diffraction efficiency and ion beam current ($z=0.5$ mm, $y=4.5$ mm).	167
A-11. Plots showing calculated diffraction efficiency and ion beam current ($z=2.5$ mm, $y=4.5$ mm).	168
A-12. Plots showing calculated diffraction efficiency and ion beam current ($z=4.5$ mm, $y=4.5$ mm).	169
A-13. Plots showing calculated diffraction efficiency and ion beam current ($z=6.5$ mm, $y=4.5$ mm).	170
A-14. Plots showing calculated diffraction efficiency and ion beam current ($z=6.5$ mm, $y=6.0$ mm).	171
A-15. Plots showing calculated diffraction efficiency and ion beam current ($z=4.5$ mm, $y=6.0$ mm).	172
A-16. Plots showing calculated diffraction efficiency and ion beam current ($z=2.5$ mm, $y=6.0$ mm).	173
A-17. Plots showing calculated diffraction efficiency and ion beam current ($z=0.5$ mm, $y=6.0$ mm).	174
A-18. Plots showing calculated diffraction efficiency and ion beam current (RF Transducer).	175

FIGURES (continued)

Figure	page
A-19. Plots showing calculated diffraction efficiency, ion beam current, and temperature of TeO ₂ AO deflector during and following irradiation of the crystal face (z=2.5 mm, y=0.5 mm).	176
A-20. Plots showing calculated diffraction efficiency, ion beam current, and temperature of TeO ₂ AO deflector during and following irradiation of the crystal face (z=4.5 mm, y=0.5 mm).	177
A-21. Plots showing calculated diffraction efficiency, ion beam current, and temperature of TeO ₂ AO deflector during and following irradiation of the crystal face (z=6.5 mm, y=0.5 mm).	178
A-22. Plots showing calculated diffraction efficiency, ion beam current, and temperature of TeO ₂ AO deflector during and following irradiation of the crystal face (z=6.5 mm, y=2.5 mm).	179
A-23. Same as Figure A-22, except that the optical beam was blocked to ensure that neither radiation nor electrical noise substantially affected the detected optical power.	180
A-24. Plots showing calculated diffraction efficiency, ion beam current, and temperature of TeO ₂ AO deflector during and following irradiation of the crystal face (z=4.5 mm, y=2.5 mm).	181
A-25. Plots showing calculated diffraction efficiency, ion beam current, and temperature of TeO ₂ AO deflector during and following irradiation of the crystal face (z=2.5 mm, y=2.5 mm).	182
A-26. Plots showing calculated diffraction efficiency, ion beam current, and temperature of TeO ₂ AO deflector during and following irradiation of the crystal face (z=0.5 mm, y=2.5 mm).	183
A-27. Plots showing calculated diffraction efficiency, ion beam current, and temperature of TeO ₂ AO deflector during and following irradiation of the crystal face (z=1.0 mm, y=0.0 mm @ 45°).	184
A-28. Same as Figure A-27, but the irradiated spot was centered 2.0 mm from the laser-exit facet.	185
A-29. Same as Figure A-27, but the irradiated spot was centered 3.0 mm from the laser-exit facet.	186
A-30. Same as Figure A-27, but the irradiated spot was centered 4.0 mm from the laser-exit facet.	187
A-31. Same as Figure A-27, but the irradiated spot was centered 5.0 mm from the laser-exit facet.	188
A-32. Same as Figure A-27, but the irradiated spot was centered 6.0 mm from the laser-exit facet.	189
A-33. Temperature plots corresponding to the runs shown in Figures A-27 through A-29.	190
A-34. Temperature plots corresponding to the runs shown in Figures A-30 through A-32.	191
A-35. Plots showing absolute diffraction efficiency of InP modulator and the ion beam current as a function of time (irradiation position is x=10.5 mm, y=0.5 mm).	192
A-36. Plots showing absolute diffraction efficiency of InP modulator and the ion beam current as a function of time (irradiation position is x=8.5 mm, y=0.5 mm).	193

FIGURES (continued)

Figure	page
A-37. Plots showing absolute diffraction efficiency of InP modulator and the ion beam current as a function of time (irradiation position is $x=6.5$ mm, $y=0.5$ mm).	194
A-38. Plots showing absolute diffraction efficiency of InP modulator and the ion beam current as a function of time (irradiation position is $x=4.5$ mm, $y=0.5$ mm).	195
A-39. Plots showing absolute diffraction efficiency of InP modulator and the ion beam current as a function of time (irradiation position is $x=2.5$ mm, $y=0.5$ mm).	196
A-40. Plots showing absolute diffraction efficiency of InP modulator and the ion beam current as a function of time (irradiation position is $x=0.5$ mm, $y=0.5$ mm).	197
A-41. Plots showing absolute diffraction efficiency of InP modulator and the ion beam current as a function of time (irradiation position is $x=0.5$ mm, $y=2.5$ mm).	198
A-42. Plots showing absolute diffraction efficiency of InP modulator and the ion beam current as a function of time (irradiation position is $x=2.5$ mm, $y=2.5$ mm).	199
A-43. Plots showing absolute diffraction efficiency of InP modulator and the ion beam current as a function of time (irradiation position is $x=4.5$ mm, $y=2.5$ mm).	200
A-44. Plots showing absolute diffraction efficiency of InP modulator and the ion beam current as a function of time (irradiation position is $x=6.5$ mm, $y=2.5$ mm).	201
A-45. Plots showing absolute diffraction efficiency of InP modulator and the ion beam current as a function of time (irradiation position is $x=8.5$ mm, $y=2.5$ mm).	202
A-46. Plots showing absolute diffraction efficiency of InP modulator and the ion beam current as a function of time (irradiation position is $x=10.5$ mm, $y=2.5$ mm).	203
A-47. Plots showing absolute diffraction efficiency of InP modulator and the ion beam current as a function of time (irradiation position is $x=12.5$ mm, $y=2.5$ mm).	204
A-48. Plots showing absolute diffraction efficiency of InP modulator and the ion beam current as a function of time (irradiation position is $x=12.5$ mm, $y=4.5$ mm).	205
A-49. Plots showing absolute diffraction efficiency of InP modulator and the ion beam current as a function of time (irradiation position is $x=12.5$ mm, $y=4.5$ mm).	206
A-50. Plots showing absolute diffraction efficiency of InP modulator and the ion beam current as a function of time (irradiation position is $x=10.5$ mm, $y=4.5$ mm).	207
A-51. Plots showing absolute diffraction efficiency of InP modulator and the ion beam current as a function of time (irradiation position is $x=8.5$ mm, $y=4.5$ mm).	208
A-52. Plots showing absolute diffraction efficiency of InP modulator and the ion beam current as a function of time (irradiation position is $x=6.5$ mm, $y=4.5$ mm).	209

FIGURES (continued)

Figure	page
A-53. Plots showing absolute diffraction efficiency of InP modulator and the ion beam current as a function of time (irradiation position is $x=4.5$ mm, $y=4.5$ mm).	210
A-54. Plots showing absolute diffraction efficiency of InP modulator and the ion beam current as a function of time (irradiation position is $x=2.5$ mm, $y=4.5$ mm).	211
A-55. Ion beam irradiation of center of transducer.	212
A-56. Summary of diffraction efficiency change as a function of distance from Transducer for position $x=7, 8$ and 9 mm.	213
A-57. Summary of diffraction efficiency change as a function of distance from Transducer for position $x=10, 11$ and 12 mm.	214
A-58. Summary of diffraction efficiency change as a function of distance from Transducer for position $x=13, 14$ and 15 mm.	215
A-59. Summary of diffraction efficiency change as a function of distance from Transducer for position $x=16, 17$ and 18 mm.	216
A-60. Plots showing the measured PbMoO_4 AO-cell response before, during and after an ion beam exposure (irradiation position is $x=1$ mm, $y=2$ mm).	217
A-61. Plots showing the measured PbMoO_4 AO-cell response before, during and after an ion beam exposure (irradiation position is $x=0$ mm, $y=0$ mm).	218
A-62. Plots showing the measured PbMoO_4 AO-cell response before, during and after an ion beam exposure (irradiation position is $x=1$ mm, $y=0$ mm).	219
A-63. Plots showing the measured PbMoO_4 AO-cell response before, during and after an ion beam exposure (irradiation position is $x=2$ mm, $y=0$ mm).	220
A-64. Plots showing the measured PbMoO_4 AO-cell response before, during and after an ion beam exposure (irradiation position is $x=4$ mm, $y=0$ mm).	221
A-65. Plots showing the measured PbMoO_4 AO-cell response before, during and after an ion beam exposure (irradiation position is $x=0$ mm, $y=0$ mm).	222
A-66. Plots showing the measured PbMoO_4 AO-cell response before, during and after an ion beam exposure (irradiation position is $x=1$ mm, $y=0$ mm).	223
A-67. Plots showing the measured PbMoO_4 AO-cell response before, during and after an ion beam exposure (irradiation position is $x=2$ mm, $y=0$ mm).	224
A-68. Plots showing the measured PbMoO_4 AO-cell response before, during and after an ion beam exposure (irradiation position is $x=3$ mm, $y=0$ mm).	225

FIGURES (continued)

Figure	page
A-69. Plots showing the measured PbMoO_4 AO-cell response before, during and after an ion beam exposure (irradiation position is $x=4$ mm, $y=0$ mm).	226
A-70. Plots showing the measured PbMoO_4 AO-cell response before, during and after an ion beam exposure (irradiation position is $x=5$ mm, $y=0$ mm).	227
A-71. Plots showing the measured PbMoO_4 AO-cell response before, during and after an ion beam exposure (irradiation position is $x=6$ mm, $y=0$ mm).	228
A-72. Plots showing the measured PbMoO_4 AO-cell response before, during and after an ion beam exposure (irradiation position is $x=7$ mm, $y=0$ mm).	229
A-73. Plots showing the measured PbMoO_4 AO-cell response before, during and after an ion beam exposure (irradiation position is $x=8$ mm, $y=0$ mm).	230
A-74. Plots showing the measured PbMoO_4 AO-cell response before, during and after an ion beam exposure (irradiation position is $x=9$ mm, $y=0$ mm).	231
A-75. Plots showing the measured PbMoO_4 AO-cell response before, during and after an ion beam exposure (irradiation position is $x=10$ mm, $y=0$ mm).	232
A-76. Plots showing the measured PbMoO_4 AO-cell response before, during and after an ion beam exposure (irradiation position is $x=10$ mm, $y=1$ mm).	233
A-77. Plots showing the measured PbMoO_4 AO-cell response before, during and after an ion beam exposure (irradiation position is $x=9$ mm, $y=1$ mm).	234
A-78. Plots showing the measured PbMoO_4 AO-cell response before, during and after an ion beam exposure (irradiation position is $x=8$ mm, $y=1$ mm).	235
A-79. Plots showing the measured PbMoO_4 AO-cell response before, during and after an ion beam exposure (irradiation position is $x=7$ mm, $y=1$ mm).	236
A-80. Plots showing the measured PbMoO_4 AO-cell response before, during and after an ion beam exposure (irradiation position is $x=6$ mm, $y=1$ mm).	237
A-81. Plots showing the measured PbMoO_4 AO-cell response before, during and after an ion beam exposure (irradiation position is $x=5$ mm, $y=1$ mm).	238
A-82. Plots showing the measured PbMoO_4 AO-cell response before, during and after an ion beam exposure (irradiation position is $x=4$ mm, $y=1$ mm).	239
A-83. Plots showing the measured PbMoO_4 AO-cell response before, during and after an ion beam exposure (irradiation position is $x=3$ mm, $y=1$ mm).	240
A-84. Plots showing the measured PbMoO_4 AO-cell response before, during and after an ion beam exposure (irradiation position is $x=2$ mm, $y=1$ mm).	241

FIGURES (continued)

Figure	page
A-85. Plots showing the measured PbMoO ₄ AO-cell response before, during and after an ion beam exposure (irradiation position is x=1 mm, y=1 mm).	242
A-86. Plots showing the measured PbMoO ₄ AO-cell response before, during and after an ion beam exposure (irradiation position is x=0 mm, y=1 mm).	243
A-87. Plots showing the measured PbMoO ₄ AO-cell response before, during and after an ion beam exposure (irradiation position is x= -1 mm, y=1 mm).	244
A-88. Plots showing the measured PbMoO ₄ AO-cell response before, during and after an ion beam exposure (irradiation position is x= -1 mm, y=2 mm).	245
A-89. Plots showing the measured PbMoO ₄ AO-cell response before, during and after an ion beam exposure (irradiation position is x=0 mm, y=2 mm).	246
A-90. Plots showing the measured PbMoO ₄ AO-cell response before, during and after an ion beam exposure (irradiation position is x=1 mm, y=2 mm).	247
A-91. Plots showing the measured PbMoO ₄ AO-cell response before, during and after an ion beam exposure (irradiation position is x=2 mm, y=2 mm).	248
A-92. Plots showing the measured PbMoO ₄ AO-cell response before, during and after an ion beam exposure (irradiation position is x=3 mm, y=2 mm).	249
A-93. Plots showing the measured PbMoO ₄ AO-cell response before, during and after an ion beam exposure (irradiation position is x=4 mm, y=2 mm).	250
A-94. Plots showing the measured PbMoO ₄ AO-cell response before, during and after an ion beam exposure (irradiation position is x=5 mm, y=2 mm).	251
A-95. Plots showing the measured PbMoO ₄ AO-cell response before, during and after an ion beam exposure (irradiation position is x=6 mm, y=2 mm).	252
A-96. Plots showing the measured PbMoO ₄ AO-cell response before, during and after an ion beam exposure (irradiation position is x=7 mm, y=2 mm).	253
A-97. Plots showing the measured PbMoO ₄ AO-cell response before, during and after an ion beam exposure (irradiation position is x=8 mm, y=2 mm).	254
A-98. Plots showing the measured PbMoO ₄ AO-cell response before, during and after an ion beam exposure (irradiation position is x=9 mm, y=2 mm).	255
A-99. Plots showing the measured PbMoO ₄ AO-cell response before, during and after an ion beam exposure (irradiation position is x=10 mm, y=2 mm).	256

FIGURES (continued)

Figure	page
A-100. Plots showing the measured PbMoO ₄ AO-cell response before, during and after an ion beam exposure (irradiation position is x=10 mm, y=2 mm).	257
A-101. Plots showing the measured PbMoO ₄ AO-cell response before, during and after an ion beam exposure (irradiation position is x=9 mm, y=2 mm).	258
A-102. Plots showing the measured PbMoO ₄ AO-cell response before, during and after an ion beam exposure (irradiation position is x=8 mm, y=2 mm).	259
A-103. Plots showing the measured PbMoO ₄ AO-cell response before, during and after an ion beam exposure (irradiation position is x=7 mm, y=2 mm).	260
A-104. Plots showing the measured PbMoO ₄ AO-cell response before, during and after an ion beam exposure (irradiation position is x=6 mm, y=2 mm).	261
A-105. Plots showing the measured PbMoO ₄ AO-cell response before, during and after an ion beam exposure (irradiation position is x=5 mm, y=2 mm).	262
A-106. Plots showing the measured PbMoO ₄ AO-cell response before, during and after an ion beam exposure (irradiation position is x=4 mm, y=2 mm).	263
A-107. Plots showing the measured PbMoO ₄ AO-cell response before, during and after an ion beam exposure (irradiation position is x=3 mm, y=2 mm).	264
A-108. Plots showing the measured PbMoO ₄ AO-cell response before, during and after an ion beam exposure (irradiation position is x=2 mm, y=2 mm).	265
A-109. Plots showing the measured PbMoO ₄ AO-cell response before, during and after an ion beam exposure (irradiation position is x=0 mm, y=0 mm).	266
A-110. Plots showing the measured PbMoO ₄ AO-cell response before, during and after an ion beam exposure (irradiation position is x=0 mm, y=2 mm).	267
A-111. Plots showing the measured PbMoO ₄ AO-cell response before, during and after an ion beam exposure (irradiation position is x= -1 mm, y=2 mm).	268
A-112. Plots showing the measured PbMoO ₄ AO-cell response before, during and after an ion beam exposure (irradiation position is x= -1 mm, y=3 mm).	269
A-113. Plots showing the measured PbMoO ₄ AO-cell response before, during and after an ion beam exposure (irradiation position is x=0 mm, y=3 mm).	270
A-114. Plots showing the measured PbMoO ₄ AO-cell response before, during and after an ion beam exposure (irradiation position is x=1 mm, y=3 mm).	271

FIGURES (continued)

Figure	page
A-115. Plots showing the measured PbMoO ₄ AO-cell response before, during and after an ion beam exposure (irradiation position is x=2 mm, y=3 mm).	272
A-116. Plots showing the measured PbMoO ₄ AO-cell response before, during and after an ion beam exposure (irradiation position is x=3 mm, y=3 mm).	273
A-117. Plots showing the measured PbMoO ₄ AO-cell response before, during and after an ion beam exposure (irradiation position is x=4 mm, y=3 mm).	274
A-118. Plots showing the measured PbMoO ₄ AO-cell response before, during and after an ion beam exposure (irradiation position is x=5 mm, y=3 mm).	275
A-119. Plots showing the measured PbMoO ₄ AO-cell response before, during and after an ion beam exposure (irradiation position is x=6 mm, y=3 mm).	276
A-120. Plots showing the measured PbMoO ₄ AO-cell response before, during and after an ion beam exposure (irradiation position is x=7 mm, y=3 mm).	277
A-121. Plots showing the measured PbMoO ₄ AO-cell response before, during and after an ion beam exposure (irradiation position is x=8 mm, y=3 mm).	278
A-122. Plots showing the measured PbMoO ₄ AO-cell response before, during and after an ion beam exposure (irradiation position is x=9 mm, y=3 mm).	279
A-123. Plots showing the measured PbMoO ₄ AO-cell response before, during and after an ion beam exposure (irradiation position is x=10 mm, y=3 mm).	280
A-124. Plots showing the measured PbMoO ₄ AO-cell response before, during and after an ion beam exposure (irradiation position is x=10 mm, y=4 mm).	281
A-125. Plots showing the measured PbMoO ₄ AO-cell response before, during and after an ion beam exposure (irradiation position is x=9 mm, y=4 mm).	282
A-126. Plots showing the measured PbMoO ₄ AO-cell response before, during and after an ion beam exposure (irradiation position is x=8 mm, y=4 mm).	283
A-127. Plots showing the measured PbMoO ₄ AO-cell response before, during and after an ion beam exposure (irradiation position is x=7 mm, y=4 mm).	284
A-128. Plots showing the measured PbMoO ₄ AO-cell response before, during and after an ion beam exposure (irradiation position is x=6 mm, y=4 mm).	285
A-129. Plots showing the measured PbMoO ₄ AO-cell response before, during and after an ion beam exposure (irradiation position is x=5 mm, y=4 mm).	286

FIGURES (concluded)

<u>Figure</u>	<u>page</u>
A-130. Plots showing the measured PbMoO_4 AO-cell response before, during and after an ion beam exposure (irradiation position is $x=4$ mm, $y=4$ mm).	287
A-131. Plots showing the measured PbMoO_4 AO-cell response before, during and after an ion beam exposure (irradiation position is $x=3$ mm, $y=4$ mm).	288
A-132. Plots showing the measured PbMoO_4 AO-cell response before, during and after an ion beam exposure (irradiation position is $x=2$ mm, $y=4$ mm).	289
A-133. Plots showing the measured PbMoO_4 AO-cell response before, during and after an ion beam exposure (irradiation position is $x=1$ mm, $y=4$ mm).	290
A-134. Plots showing the measured PbMoO_4 AO-cell response before, during and after an ion beam exposure (irradiation position is $x=0$ mm, $y=4$ mm).	291

TABLES

Table	page
3-1. Tabular data for the Stokes column vector and degree of polarization for proton irradiated TeO ₂	38
4-1. Summary of radiation induced changes to the AODB diffraction efficiencies, frequency response, and bandwidth.	67
5-1. General capability of ion micro-beam facility, dpi refers to the displacements per ion.	77
6-1. Summary of AOD exposures conducted by the Photonics Research Group (FY95-97).	104
7-1. Diffraction efficiency changes as a result of 1×10^{15} n/cm ² fluence on AO devices.	138
7-2. Changes to insertion loss (attenuation) as a result of 1×10^{15} neutron/cm ² exposure.	138
A-1. Ion micro-beam experimental dates and times.	155
A-2. Ion beam location for each exposure shown in Figure 5-9, and Figures A-35 through A-59, where the Exposure number is indicated on Figures.	156
A-3. Ion beam location for each exposure shown in Figures A-60 through A-134, where the Exposure number is indicated on Figure.	157

1.0 INTRODUCTION

The responses of Lead Molybdate (PbMoO_4), Gallium Phosphide (GaP), Indium Phosphide (InP), Tellurium Dioxide (TeO_2), and Lithium Niobate (LiNbO_3) acoustooptic (AO) modulators and deflectors exposed to various radiation species are reported. In an earlier preliminary report acoustooptic devices (AODs) were exposed to flash x-ray, linearly accelerated electrons, and gamma-ray irradiations to determine their sensitivity to radiation and applicability to space and enhanced radiation environments.¹ This report is a continuation and finalization of those studies.

Radiation-induced responses observed in the course of this study included: attenuation of and shifts in the spatial intensities of AODs operated near or at the Bragg angle, changes to polarization states and the degree of polarization, changes to the diffraction efficiency and changes in the operational bandwidth. The experimental data indicate that x-ray, electron, proton and neutron irradiation degrade the performance of AODs. The electron- and proton-induced displacements of spatial intensities are believed to be largely due to radiation-induced temperature gradients within the AO crystal and by temperature-induced changes in the AO transducers. These non-radiation-induced heating effects can alter the sound velocity or transducer efficiency in the AO devices. Radiation-induced refractive index gradients precipitating transient changes to diffraction efficiencies and spatial intensities have also been observed. Other short-lived electron- and proton-induced optical signal attenuations and decreases to AO diffraction efficiencies were determined to be primarily due to the formation of transient color centers, alteration of the crystal refractive index and of phase grating index amplitudes. Both conventional broad area source irradiations and precisely localizing irradiation using a new ion microbeam methodology to investigate and differentiate the effects of radiation on AO modulators and deflectors are presented in this report.

The contents of this report spans the period of performance from 15 August 1991 through 15 August 1997, with emphasis placed on data not reported in the preliminary report. The materials and data in this report are intended to establish a foundation for understanding and predicting the

physical processes by which electron, proton, gamma-ray, x-ray and neutron radiation interact with acoustooptic materials and devices.

First observed radiation-induced phenomena including material absorption, spatial intensity displacements, depolarization of spatial intensities, changes to device bandwidths and diffraction efficiency are reported.

The final results of a theoretical and experimental investigation for differentiating the responses of acoustooptic modulators (AOMs) and deflectors operating under dynamic conditions while exposed to nuclear environments are contained herein. The bulk of the material presented is concerned with experimentation conducted to differentiate the responses of AODs exposed to various radiation sources including electrons, x-ray, gamma-ray, protons, and neutrons. X-ray induced responses were previously presented in the preliminary report and are mentioned only briefly within this report.

The basis and justification for the investigation and the focus for the overall program direction was a direct outgrowth of the Photonic Systems Survivability Workshop conducted by Headquarters Defense Nuclear Agency (HQ DNA / RAES), Washington, DC, in 1991.² The workshop participants concluded that the importance of photonics in commercial and military markets was dramatically increasing, particularly in the application area of optical processing technology. While near-term military applications such as the Transitioning of Optical Processing Systems (TOPS) program of the Advanced Research Project Agency (ARPA), in Washington, DC, were providing demonstrations of prototype optical processing units in military systems, very little if any radiation testing of photonic materials or devices (sources, modulators, detectors and passive elements) key to these applications had been conducted. The conclusions reached at the workshop were that five of eight TOPS application areas relied on AO technology, while the remaining areas relied on spatial light modulators.² From an extensive survey of literature and documentation of photonic programs conducted by various research and development organizations, it was determined that "...the state of radiation effects research on optical materials and components appears quite primitive when compared to the mass of

information compiled on electronic materials and devices," and "One field appears to be a major gap in our knowledge of radiation effects on optical processing systems -- optical modulators. What little information is available appears to concentrate on total dose effects and not transient effects."² These findings led to the investigations reported herein.

While studies of the radiation resistance of optical fibers - a subset of photonics technology - had undergone highly coordinated intensive investigations, this was not true of many related photonic technology areas. Four areas identified as immediately requiring radiation effects studies were: GaAs laser diodes, Si charge-coupled detectors (CCDs) (and related detector technologies), two-dimensional (2D) spatial light modulators, and AOMs. This latter technology area was determined to have experienced extremely limited radiation-induced response research, even though it was a highly mature technology with a dominant role in advanced and state-of-the-art signal processing techniques.

As a result of these findings, the Photonics Research Group (PRG) of the Phillips Laboratory (PL) undertook the detailed investigation of quantifying for the first time, real-time transient and steady-state radiation-induced response measurements of key AOD parameters. Preliminary results were reported to the community³⁻⁵ on the radiation-induced alteration of Bragg cell AOD characteristics including diffraction efficiency, Bragg angle, and spatial intensity distributions.

The investigations centered on five AOD materials: PbMoO₄, TeO₂, GaP, InP, and LiNbO₃. The rationale for studying these materials was based on current, reported radiation responses of materials used in AODs, potential use in optical processing or optical correlators, and to provide a database on AO materials and devices whose radiation sensitivity was largely unknown or nonexistent.⁶⁻⁹

For example, recent radiation response studies of photonic components comprised of LiNbO₃ and Lithium Tantalate (LiTaO₃) indicated that optical directional coupler waveguides composed of these two non-centrosymmetric materials were prone to radiation-induced photorefractive-like

effects. As first reported by Taylor et al.,⁹ crosstalk (asynchronous coupling) effects persisting for many tens of minutes, as well as transient attenuation and polarization changes, could be induced by single and multiple, pulsed electron irradiations. These coupled-wave devices were primarily thin film structures. AODs composed of identical or similar materials were of bulk material technology, thereby raising concerns about different response mechanisms. Related studies of polarization-maintaining optical fibers that were comprised of neither thin film nor bulk materials but composite materials, also displayed widely varying radiation-induced transient changes in transmission and polarization properties when subjected to proton irradiations.¹⁰ Since many photonic technologies with vastly differing material properties or crystal geometries displayed sensitivity to radiation, it was not unreasonable to expect that refractive index changes caused by ionization-induced color centers or other radiation effects such as heating could alter the AO coupling, polarization, and transmission properties of the AODs.

The experimental approach used for measuring radiation-induced effects in integrated optic and optical fiber component technologies was applied to the acoustooptical coupling interactions inherent in Bragg cell modulators and deflectors which again involved observing changes to the refractive index dependent processes. Thus, a portion of the unique transient measurement techniques⁷⁻¹¹ developed previously were used to study the radiation-induced transient effects in bulk AO modulator devices.

Finally, to guide other investigators that may wish to repeat these first measurements, this report delineates many lessons learned in properly choosing and applying the measurement instrumentation and data analysis techniques devised to support this study. Many of the measurement techniques employed during the early stages of this study were found to be inadequate as the researchers' understanding of the radiation-induced response mechanisms progressed. Therefore, some of the early techniques used for detecting and measuring radiation-induced responses (such as x-ray induced responses in PbMoO_4) were not used in later studies but have been documented for completeness.

Physical models are presented within this report which hypothesize the manner by which AO materials respond to ionizing radiation environments. Finally, a hypothesis is advanced to explain the observed deviation of Bragg cell spatial intensities due largely to radiation-induced thermal gradients in and near the acoustooptical interaction regions. This hypothesis was first independently substantiated for PbMoO_4 by simulating the radiation-induced thermal gradients, creating similar gradients through direct laser heating of the PbMoO_4 AOD. The hypothesis was again confirmed using ion microbeam investigations.

This page intentionally left blank.

2.0 ACOUSTOOPTIC INTERACTIONS

2.1 ISOTROPIC DIFFRACTION

The phenomenon of sound waves interacting with light has been the subject of much investigation over the past 72 years¹²⁻⁴¹ following Brillouin's observation of light rays scattering from thermal fluctuations in liquid and solid media.¹² These observations were confirmed and advanced by Debye and Sears and others in 1932.¹³⁻¹⁴ Shortly thereafter, the exhaustive treatments by Raman and Nath to generalize the AO interactions using wave equations for arbitrary cell parameters moved the applications of acoustooptics forward, with many elaborate studies and experimental data being reported.¹⁵ More recently, observations of the interaction of high frequency sound waves with infrared optical beams have been reported.²⁹⁻⁴¹ Thus, the interest in AO technologies has covered in excess of seven decades, resulting in many useful applications.

With this historical introduction, a truncated explanation of the AO interaction process is presented, focusing on those areas relevant to the radiation effects measurements performed. In the paragraphs that follow, a general derivation for the interaction of light and sound in liquids, gases, and solids is presented. Special emphasis is placed on crystalline materials since the focus of this investigation dealt with AODs composed of isotropic and anisotropic crystalline media.

When an ultrasonic wave of frequency f traverses an optically transparent medium, a strain is produced in the medium, altering the medium's refractive index in accordance with the applied modulating waveform. If the strain applied is periodic (i.e., sinusoidal) a periodic grating is formed from which scattering, reflection, or diffraction is possible with the interaction strength depending on the grating amplitude, its quality, and the interaction angle between the sound waves and optical beam. The grating arises from the acoustically induced periodic spatial density variations produced within the medium.

Diffraction from acoustic gratings in an isotropic crystal has been extensively treated.¹⁶⁻³⁴ The refractive index of the medium may be expressed by the sinusoidal relationship

$$n(x,t) = n + \Delta n \sin(ft - Kx) \quad (1)$$

Here, the refractive index (n) of the medium is changed (Δn) due to the acoustic strain introduced along the propagation direction (x) in time (t) for the case of a progressive (traveling) acoustic wave of frequency f . The wave number of the planar traveling wave is given by $K = 2\pi / \Lambda$, where Λ is the acoustic wavelength. The instantaneous strain $s(x,t)$ can be expressed as a function of position and time by the analogous expression

$$s(x,t) = S_0 \sin(ft - Kx) \quad (2)$$

where S_0 is maximum the strain amplitude at $\sin(ft - Kx) = 1$.

The strain-induced refractive index change produced by the acoustic perturbation can also be expressed by relating the photoelastic constant, p , to the index change

$$\Delta n = \frac{-p}{2} n^3 S_0 \quad (3)$$

where p is the photoelastic constant characteristic of the medium for the particular mode of AO interaction. The negative value in Equation (3) indicates that positive strain³⁵ or dilation results in a reduction of the refractive index. Thus, the photoelastic constant couples the acoustically induced strain to the refractive index of the medium. The acoustic intensity (I) that generates the strain in the crystal medium is given²⁸ by the expression

$$I = \frac{\rho}{2} v^3 S_0^2 \quad (4)$$

Where ρ is the density of the crystal medium and V is the acoustic velocity. By combining Equations (3) and (4), it is possible to determine the index of refraction change in an isotropic crystal as

$$\Delta n = \left(\frac{1}{2} \frac{p^2 n^6}{\rho V^3} I \right)^{\frac{1}{2}} \quad (5)$$

On the right-hand side of Equation (5), material parameters determining the quality or strength of the AO interaction can be isolated. The figure of merit (M) for isotropic diffraction due solely to material parameters is given by the expression

$$M = \frac{n^6 p^2}{\rho V^3} \quad (6)$$

Thus the change of refractive index for a fixed acoustic intensity strongly depends on a high intrinsic index, low acoustic velocity and density, and a high photoelastic coefficient. These aspects are more fully described in subsections 2.2 and 2.3 and an expression for the diffraction efficiency is determined from Equation 5.

2.2 BRAGG ANGLE DIFFRACTION

Subsection 2.1 discussed the special case of isotropic diffraction with reference to the geometry involved in an AO interaction. Figure 2-1 is a general representation of an AO interaction occurring in Bragg-angle AODs. The special case of Raman-Nath scattering¹⁵ or diffraction is not covered in this report since only Bragg-angle AODs were investigated. Unlike the multiple diffraction orders resulting from Raman-Nath diffraction, ideal Bragg diffraction results in the diffraction of only one side (diffracted) order, allowing simplified diagnostic measurements. However, several of the Bragg cells studied were observed to have more than one side order.

This condition has been reported by Willard¹⁹ to be incipient or anomalous Bragg scattering, which can be prompted by poor cell design or other M-factors as well as optical beam effects (i.e., focusing).

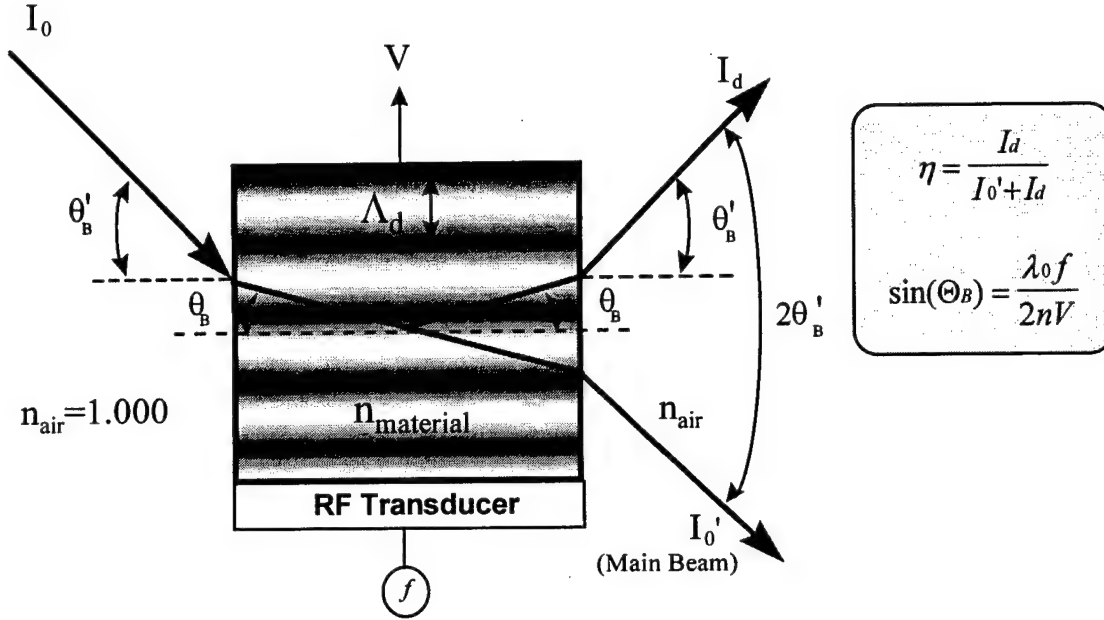


Figure 2-1. Acoustooptic Bragg Deflector. Diffraction of a single side order (I_d) occurs when the input light (I_0) is incident on the AO crystal at the Bragg angle (θ_B). The spacing of the acoustically induced diffraction grating (shaded areas) is indicated by Λ_d and is defined by $\Lambda_d = f/V$, where f and V are the acoustic frequency and acoustic velocity in the crystal, respectively.

As shown in Figure 2-1, an incident optical beam (I_0) enters the Bragg cell at the Bragg angle θ_B (within the medium). The primed notation for θ_B indicates the refractive index adjustment of the Bragg angle when measured in air. Thus, the special condition when the beam I_d is diffracted through an angle $2\theta_B$ (within the medium) with respect to I_0 is known as the Bragg condition. The Bragg angle measured in the acoustic medium is expressed as

$$\theta_B = \sin^{-1} \left(\frac{\lambda_0}{2\Lambda n} \right) \quad (7)$$

Where λ_0 is the optical wavelength in free space and λ_0 / n is the wavelength in the medium. The Bragg angle condition arises when constructive interference is possible. This occurs when the diffraction grating spacing allows a phase shift of 2π between successive reflections so that the diffracted intensities interfere constructively. Both I'_0 and I_d are observed to be bent away from the normal (dotted line) in Figure 2-1, since the refractive index of air is less than the AO medium refractive index. I'_0 is also reduced in amplitude, and under ideal conditions the intensity difference is transferred via the diffraction process to I_d . A straightforward expression for the diffraction efficiency under these conditions is given as

$$\eta = \frac{I_d}{I'_0 + I_d} \quad (8)$$

The diffracted beam is also shifted in frequency by the modulation frequency applied.

A quantum approach for describing the frequency shift is shown in Figure 2-2. Here, a photon with energy $\hbar\omega_i$ and momentum $\hbar K_i$ interacts with a phonon of acoustic frequency $\hbar\Omega_a$ and momentum $\hbar K_a$. Conservation of energy and momentum requires that a photon be generated at frequency $\hbar\omega_d$ with a momentum $\hbar k_d$. These conditions are represented by

$$\hbar\omega_d = \hbar\omega_i \pm \hbar\Omega_a \quad (9)$$

and

$$\hbar k_d = \hbar K_i \pm \hbar K_a \quad (10)$$

The plus or minus sign in Equation 9 is determined by the direction of the incident optical beam. For example, Figure 2-2 shows the incident optical beam traveling against the direction of the acoustic wave. Therefore, the resulting diffracted beam (K_d) is Doppler up-shifted in frequency

and is expressed in Equation 9, where $\omega_d = \omega_i + \Omega_a$. The constant $\hbar = h/2\pi$, where h represents Planck's constant.

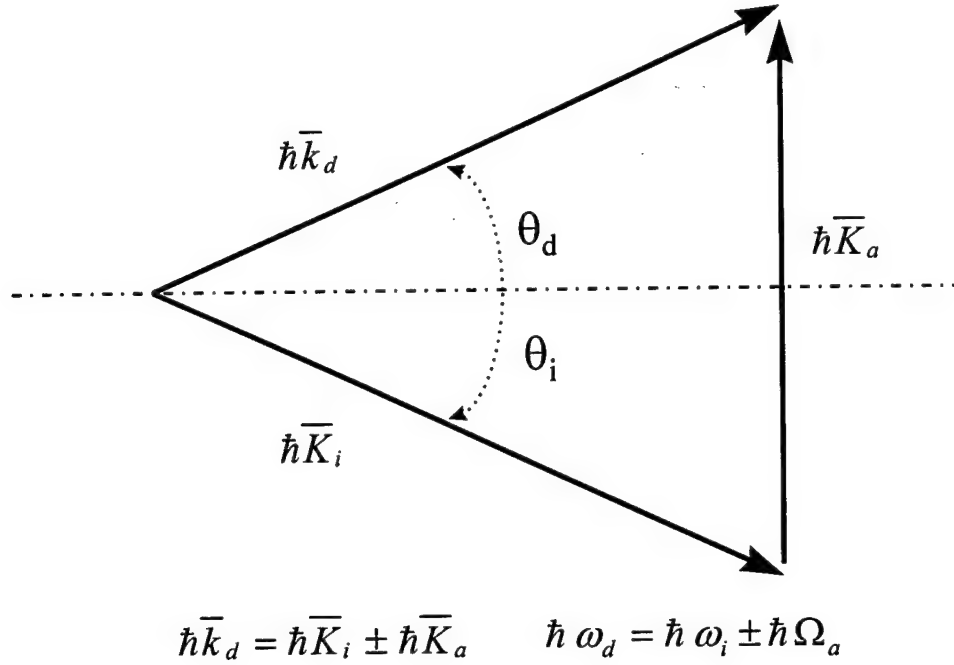


Figure 2-2. Conservation of momentum for Bragg angle diffraction, showing the Doppler up-shift in frequency of the diffracted beam \bar{k}_d .

An expression for the condition of Bragg angle diffraction can be obtained by manipulating Equation 10. Figure 2-2 shows the magnitudes of $|\mathbf{K}_i|$ and $|\mathbf{k}_d|$ in the momentum triangle as approximately equivalent. This arises because the optical frequency (ω) is much greater than the acoustic frequency ($\omega_i \approx 10^{15}$ Hz and 10^6 Hz $\leq \omega_d \leq 10^9$ Hz) and, therefore, $|\mathbf{K}_i| \approx |\mathbf{k}_d|$ and $\theta_d \approx \theta_i$.

Under these approximate conditions, the momentum diagram of Figure 2-2 forms an isosceles triangle wherein the relationship between the incident and diffracted beams is given as

$$\sin \Theta_d = \frac{|\bar{K}_a|}{2 \cdot |\bar{k}_d|} \quad (11)$$

Since $|\mathbf{K}_i| \approx |\mathbf{k}_d|$ and $\Theta_d \approx \Theta_i$ the incident beam angle Θ_B is just $\Theta_B = 2\Theta_d / 2$ in the crystal medium. Substituting the wave number magnitudes $|\mathbf{K}_i| = 2\pi n / \Lambda$ and $|\mathbf{k}_d| = 2\pi n / \lambda_0$, an alternate form for the Bragg angle in the medium (Θ_B) in terms of the acoustic and optical wavelengths, is obtained as

$$\sin \Theta_B = \frac{\lambda_0}{2n\Lambda} \quad (12)$$

The Bragg angle (Θ'_B) measured in air ($n_a = 1.000293$) and shown in Figure 1 is obtained from Snell's law where

$$n_a \sin \Theta'_B = n \sin \Theta_B \quad (13)$$

or,

$$\sin \Theta'_B = \frac{n}{n_a} \sin \Theta_B \quad (n > n_a) \quad (14)$$

The angle of separation between I_d and I'_0 (measured in air), as shown in Figure 1, is twice the Bragg angle

$$2\Theta'_B = \frac{2n}{n_a} \sin^{-1} \left(\frac{\lambda_0}{2n\Lambda} \right) \quad (15)$$

and for small Bragg diffraction angles, Equation 15 may be approximated as

$$2\Theta'_B \cong \frac{\lambda_0}{n_a \Lambda} \quad (16)$$

or, in terms of the applied modulation frequency and Bragg cell sound velocity, the angle of separation in air is expressed as

$$2\Theta'_B \cong \frac{\lambda_0 f}{n_a V} \quad (17)$$

2.3 ANISOTROPIC DIFFRACTION

Several anisotropic AO material devices were studied for their responses to radiation. In the isotropic treatment previously presented, the assumption was made that the refractive index (n) in any direction of the AO material was independent of direction ($n_x = n_y = n_z$). However, in naturally occurring birefringent materials, or in crystalline materials that are stressed, the indices can differ. This gives rise to anisotropic diffraction since the magnitude of the momentum vectors of Figure 2-2 no longer are equivalent, nor are their diffraction angles. Under the condition $|\mathbf{k}_d| \neq |\mathbf{K}_i|$, an anisotropic momentum representation as shown in Figure 2-3 is required. If the index of refraction of the $|\mathbf{K}_d|$ direction is taken as n_d while that of the $|\mathbf{K}_i|$ direction is n_i , the relationship of the diffraction angles of $|\mathbf{K}_i|$ and $|\mathbf{k}_d|$ can be represented by the Dixon equations¹⁶ as

$$\sin \Theta_i = \frac{\lambda_0}{2n_i V} \left[f + \frac{V^2}{\lambda_0^2 f} (n_i^2 - n_d^2) \right] \quad (18)$$

and

$$\sin \Theta_d = \frac{\lambda_0}{2n_d V} \left[f - \frac{V^2}{\lambda_0^2 f} (n_i^2 - n_d^2) \right] \quad (19)$$

Here, the difference in the refractive index terms ($n_i^2 - n_d^2$) is a measure of the birefringence of the AO material. For the case of $n_i = n_d$ or zero birefringence, Equations 18 and 19 reduce to the form of Equation 15.

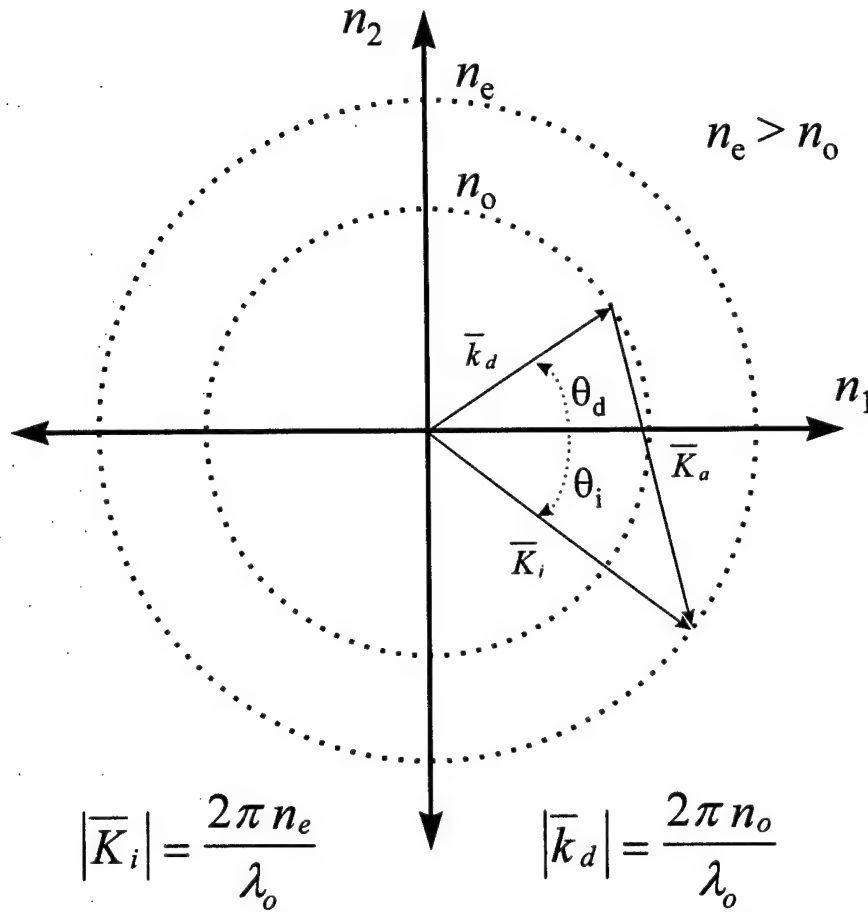


Figure 2-3. Vector diagram representing anisotropic Bragg diffraction. Here, the birefringence of the AO material causes the momentum of light to vary for different light polarization states as determined by the n_o (ordinary) and n_e (extraordinary) indices of refraction.

It is also useful to introduce the undiffracted and diffracted intensities at this point. As discussed by Damon et al.,²⁸ the diffraction efficiency resulting from Bragg angle operation of the AOD is given by

$$\eta = \frac{I_d}{I_0} = \frac{\pi^2}{2} \left[\left(\frac{P_a / LH}{\rho V^3} \right) \left(\frac{n^3 p L}{\lambda_0 \cos \Theta_B} \right)^2 \right] \quad (20)$$

Where $P_a = LHI$ is the power in an acoustic column of intensity (I), width (L), and height (H).

Here, λ_0 is the wavelength of light in air while I_d is defined as the positive first-order (I_{+1}) spatial intensity and I_0 is the input intensity (undiffracted main beam).

These basic relationships of Bragg angle and diffraction efficiency were used throughout the study for determining the effects of radiation on AODs operating at the Bragg angle. Other measurements such as the polarization and bandwidth properties of AODs were also studied. The discussion of these AOD properties and the results of the radiation studies performed to measure changes to the polarization and bandwidth are examined in later sections.

2.4 ALIGNMENT PROCEDURES-OPTIMIZATION OF BRAGG CELL OPERATION

This section is provided to explain protocols involved for the tuning of the AODs. Prior to any radiation exposure, the AO cell was optimized to operate at the Bragg angle, θ_B , and the radio frequency (RF) power was adjusted so that the output light intensity in I_d , the first-order diffracted beam, was maximized (Figure 2-4).

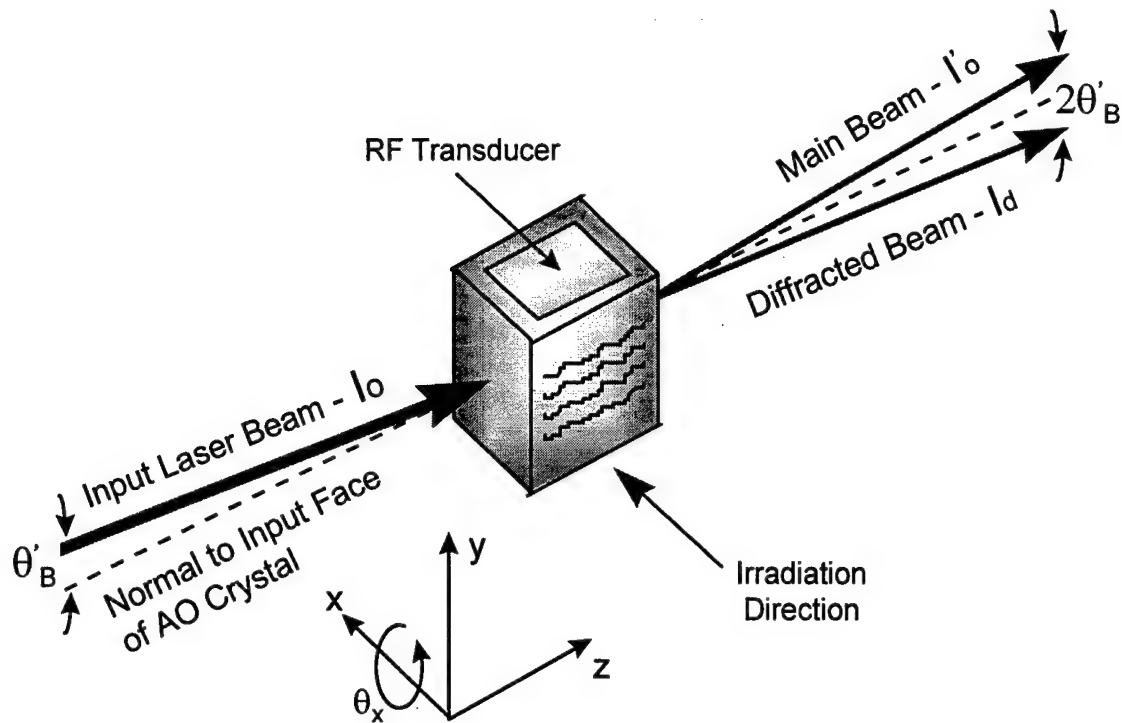


Figure 2-4. Typical AOD irradiation exposure orientation and alignment geometry.

The Bragg angle adjustment was accomplished by directing a collimated laser beam of the proper wavelength, polarization state, and diameter into the center of the AO cell. The AO cell was then rotated slowly about θ_x , as shown in Figure 2-5, aligning the reflected beam approximately colinear with the source beam. This was accomplished by mounting the AO cell on a motor-driven micrometer rotation stage and rotating the cell accordingly. However, care was taken to insure that the laser beam was slightly misaligned about θ_y to prevent reflections of energy back into the laser cavity. This also aided in observing the location of the reflected beam from the AOD first surface on the laser head housing. At this orientation, the input laser beam was observed to be approximately normal to the AO cell input surface and a starting position (or zero angle reference) for further rotational alignment was ascertained.

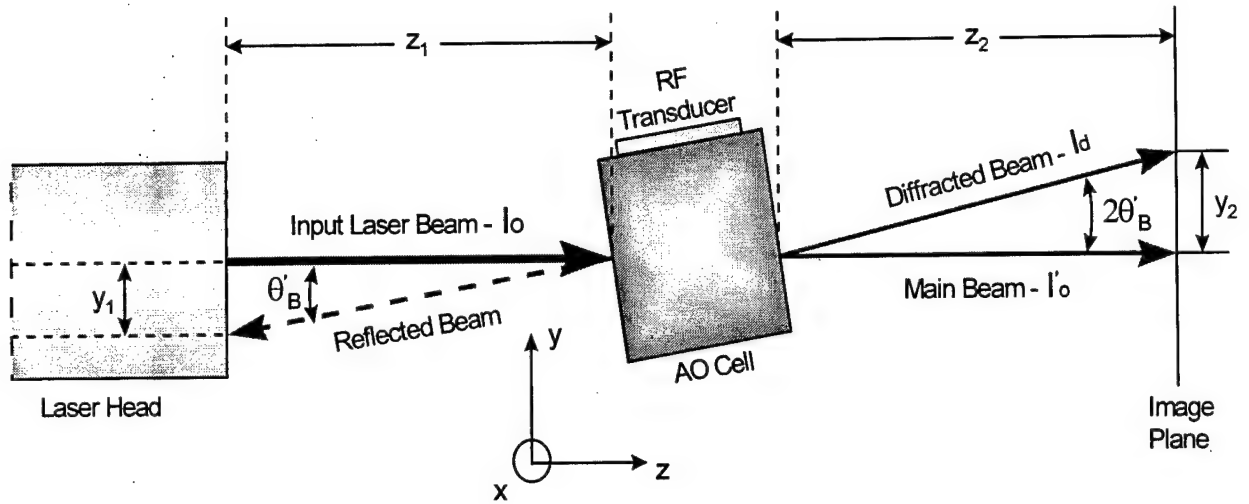


Figure 2-5. Typical Bragg angle adjustment and alignment geometry for AOD experiment configurations.

The RF drive power was then applied to the AO cell at its center frequency and was monitored using an in-line power meter. The device was typically driven at 70 percent of the recommended maximum power in order to align the AO cell and the light beam. An image screen was placed 1 to 2 m from the output side of the AOD, and Raman-Nath diffraction was observed, i.e., multiple-order diffraction. The AO cell was next rotated slowly about θ_x until only the zero and first-order diffracted beams remained on the image screen. The Bragg angle in air was determined by measuring the horizontal distance between the laser head output and the AOD input surface and the vertical distance between the laser source beam and the reflected beam on the exit port of the laser head housing.

The Bragg angle θ'_B in air was then computed using simple trigonometry and compared to the specified value in the device data sheet using the relationship,

$$\theta'_B = \tan^{-1}\left(\frac{y_1}{z_1}\right) \quad (21)$$

where:

θ'_B	=	Bragg angle in air
z_1	=	horizontal distance between laser head output and AOD input
y_1	=	vertical distance between the output beam and reflected beam at the laser head exit port.

A second measurement was also conducted to verify the Bragg angle. This was accomplished by measuring the angle between the main and first order beam, referred to as the deflection angle ($2\theta'_B$), where

$$2\theta'_B = \tan^{-1}\left(\frac{y_2}{z_2}\right) \quad (22)$$

Here,

$2\theta'_B$	=	separation angle between the main and first order diffracted beams
z_2	=	horizontal distance between the AO cell output and image screen
y_2	=	vertical distance on the image screen between main and first-order diffracted beam

Next, a large area optical power meter was placed into the I_d beam path and actively monitored. Fine adjustments to θ_x were made to maximize the first-order diffracted intensity. Final position adjustments were accomplished by translating the AO cell along the x and y axes while monitoring the optical power to maximize the intensity in the diffracted beam. This procedure is designed to probe for the maximum acoustic wave velocity within the AO cell. The RF drive power was then adjusted to 100 percent of the recommended level. Diffraction efficiency of the AOD was next calculated by measuring the diffracted intensities and comparing the resulting diffraction efficiencies to the specified value in the device data sheet. The diffraction efficiency at the Bragg angle is given by Equation 8. Under these procedures, the AO cell was considered optimized for further characterization and studies.

This page intentionally left blank.

3.0 RADIATION INDUCED CHANGES TO POLARIZED AO CELLS

3.1 METHODOLOGY FOR MEASURING RADIATION INDUCED DEPOLARIZATION IN PHOTONIC DEVICES

A methodology for measuring radiation induced changes to polarized light in photonic devices such as spatial light modulators, integrated optic structures, optical fibers and vertical cavity surface emitting laser diodes and other photonic and optical components evolved from the investigations described in this report. Recently, publications⁴²⁻⁴⁵ have appeared describing the methodology and are also discussed within this report. Emerging space-based systems may depend on using polarization sensitive components for high-speed signal processing, synthetic aperture and phased array radar. The response of polarization dependent components and systems in space and other radiation environments was largely unknown and provided the motivation for the investigations described in these sections. Experimental protocols and analytic techniques developed to measure proton and electron induced depolarization in acoustooptic modulators and deflectors are presented. By using a photoelastic modulator system in conjunction with Mueller matrix analysis and Stokes vector calculus, it is shown in the paragraphs to follow that exact solutions for determining the optical analogs of radiation induced effects in photonic components can be determined.

Recently, in-house development of an innovative methodology for accurately measuring radiation induced polarization effects in a variety of photonic materials and components was reported by the Air Force Phillips Laboratory.⁴⁴ The development of the methodology from experimental protocols has progressed to the stage where most photonic devices can be irradiated while changes to the polarized light passing through these devices can be measured in-situ. Thus, a time resolved history of radiation induced changes to polarization states, light intensity and light scattering can be measured under actual operational conditions.

By analyzing the data using Mueller-matrix⁴⁶ and Stokes vector calculus,⁴⁷ a mathematical determination of the exact nature of how radiation affects light propagating in an AO Bragg cell is possible. Thus, an optical analog or transfer function representing the nature of the radiation-induced changes to polarization states can be obtained from the experimental data. The cornerstone of the methodology is the application of a photoelastic modulator (PEM)-analyzer system to detect, analyze and quantify polarization changes. In the next sections, a brief description of the PEM system's operational function is briefly discussed to illustrate the uniqueness and inherent measurement accuracy of the methodology.

3.2 MEASURING DEPOLARIZATION USING PHOTOELASTIC MODULATORS

Laser-heating induced depolarization of optical signals propagating in a photonic device was first reported in 1996.⁴³ Measurement of this phenomena was accomplished by analyzing the changes to polarized light diffracted from an acoustooptic Bragg cell crystal. The diffracted light was passed through a photoelastic modulator system (PEMS) which allowed real-time measurements of polarization changes caused by laser induced heating of an AO Bragg cell lead molybdate crystal. This approach is also appropriate for measuring radiation-induced changes to polarized light as will be shown in the next sections.

Figure 3-1 depicts a typical experimental arrangement successfully used to measure the response of an acoustooptic device exposed to various radiation sources. As shown in Figure 3-1, the PEMS may be comprised of one or more photoelastic crystals, which serve as optical wave retarders. Optical retardation is accomplished by using transducers to mechanically stress the crystals causing an induced birefringence (photoelasticity) in the PEMS crystals. By sinusoidally applying stress, each crystal is amplitude modulated, which, in turn, modulates polarized light passing through the crystal. The varying birefringence, then, causes time varying retardations in the polarization states of the polarized light under study. The PEMS is used to lock onto the

different frequencies ($f_1 = 42 \text{ kHz}$, $f_2 = 47 \text{ kHz}$) of the optical signals to detect, differentiate and measure the relative polarization-intensities. The reader is referred to previous publications for a detailed discussion of the PEMS operation.⁴²⁻⁴⁵

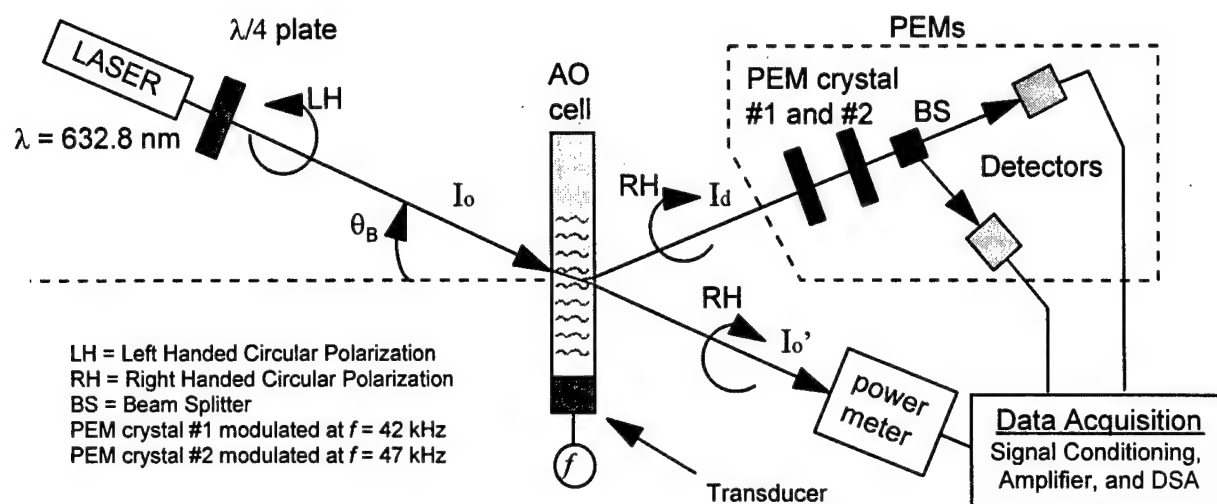


Figure 3-1. Experimental arrangement for measuring polarization states and depolarization. Left handed circular polarization enters the AO cell and is rotated to right-handed circular polarization. A photoelastic modulator system detects, differentiates and measures changes to the polarization states and irradiance of the diffracted beam (I_d).

In general, this measurement method can be used in any radiation environment, which allows shielding of the PEMS and input optics from the radiation environment. In Figure 3-1, either an electron or proton beam can be directed at the frequency (f) driven transducer, or at the crystal volume where an optical beam and acoustic waves interact. Under Bragg angle conditions, I_0 undergoes diffraction by the acoustic wavefronts, and two optical beams emerge: the intensity reduced main beam (I_0') and the diffracted beam, I_d . The beams separated by the deflection angle $2\theta_B$. By analyzing the polarization states of I_d prior to irradiation, during irradiation, and following irradiation, the radiation induced polarization changes can be ascertained and modeled to predict system responses.

In the arrangement shown in Figure 3-1, two photoelastic crystal modulators are aligned at offset angles of 45° with respect to their optical axes. This alignment allows simultaneous measurement of the magnitudes of the modulated polarized light intensities prior to, during and following irradiation. In this manner, the intensity modulated components of the diffracted beam (I_d) are detected and can be compared to the initial polarization states of the input beam (I_0) or to the initial conditions of output beams (I_0' , I_d) prior to radiation exposure. The bandwidth of the individual PEMS components, the lock-in amplifier and the sampling rate of the digitizing signal analyzers (DSAs) limit the speed with which the measurements can be performed. For example, the 100 kHz bandwidth of the lock-in amplifiers potentially allow a maximum time resolution of $\sim 10 \mu\text{s}$. However, the sampling rates of the DSAs were limited to 1.25 Hz or a time resolution of 0.4 s. A slow sampling rate was used in the acquisition of data in order to observe the polarization responses over long periods of time (~ 200 s) determined by the proton or electron dose rates.

3.3 MEASUREMENT OF RADIATION INDUCED CHANGES TO POLARIZATION STATES AND DEGREE OF POLARIZATION

The first observed proton and electron induced responses in thin film and bulk spatial light modulator components (i.e., liquid crystal light valves and acoustooptic deflectors and modulators) subjected to electron and proton radiation were investigated during this study and reported.⁵⁰⁻⁵⁴ For the most part, the radiation induced responses were reported as transient, although permanent attenuation has also been reported in a liquid crystal light valve.⁵¹

Transient changes to the polarization states in Gallium Phosphide (GaP) and Tellurium Dioxide (TeO_2) acoustooptic devices operated in their acoustic shear wave modes and exposed to average proton energies $\bar{E}_{p+} = 63.0$ and 39.9 MeV, respectively. Certain of these results are repeated from previous publications and expanded in the paragraphs that follow.⁴²⁻⁴⁵

3.4 EXPERIMENTAL ARRANGEMENT-PROTON IRRADIATION OF AO BRAGG CELLS

Shown in Figure 3-2 is a typical experimental arrangement⁴⁴ used to determine the radiation-induced effects in a TeO_2 AO device operated at the Bragg angle (Θ_B). The same arrangement was used for conducting the GaP AO studies. The isochronous cyclotron of the Crocker Nuclear Laboratory, University of California (Davis, CA), provided the source of protons. For the data reported in this paper, proton fluxes of $\phi = 1.885 \times 10^{10} \text{ protons} \cdot \text{cm}^{-2} \cdot \text{s}^{-1}$ and $1.897 \times 10^{10} \text{ protons} \cdot \text{cm}^{-2} \cdot \text{s}^{-1}$ were provided for proton energies of $\bar{E}_{p+} = 63.0 \text{ MeV}$ and $\bar{E}_{p+} = 39.9 \text{ MeV}$, respectively.

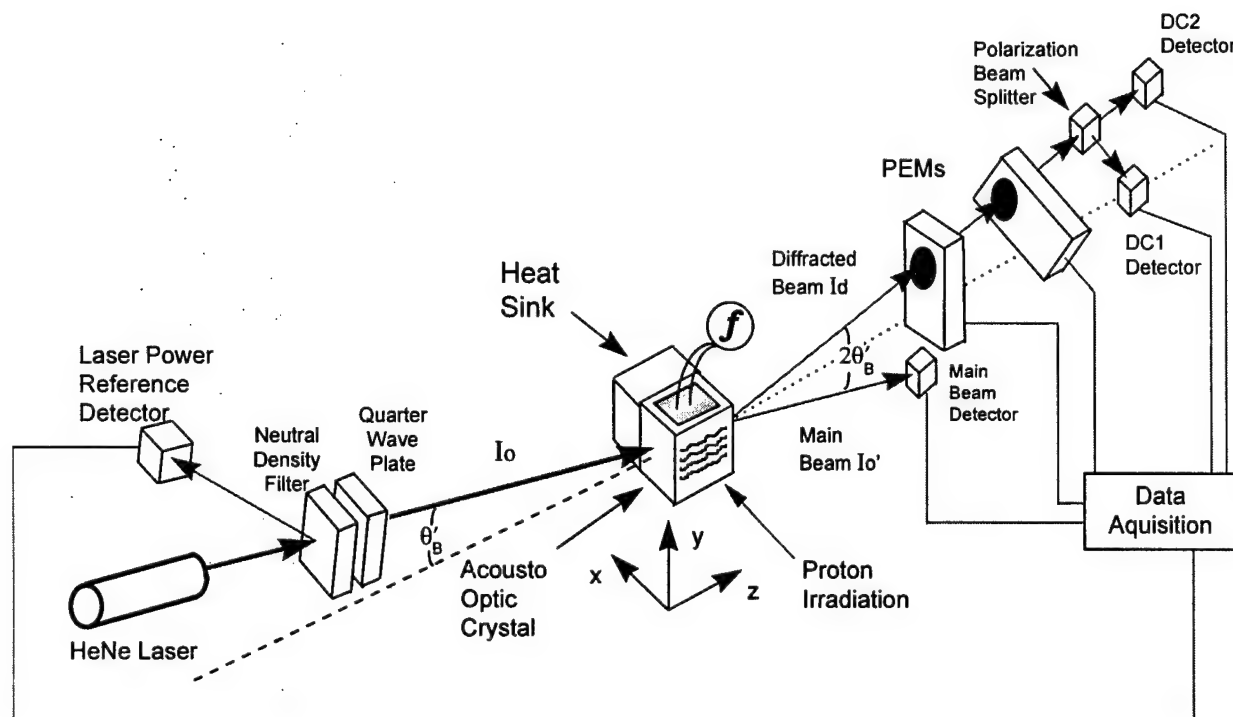


Figure 3-2. Typical arrangement for studying proton induced polarization effects in diffracted beam of acoustooptic devices.

The optical beam from a HeNe laser operating at $\lambda_0 = 0.6328 \mu\text{m}$ (free space wavelength) was incident on the GaP and TeO_2 crystals at the Bragg angle ($\Theta_B = 4.83^\circ$ and $\Theta_B = 2.06^\circ$,

respectively) as shown in Figure 3-2. The spot size of the laser beam was ≈ 1 mm, and the proton beam diameter was 2.3 cm. While the majority of the protons were determined to be confined to the GaP and TeO₂ crystals, some overlap of the proton beam onto other portions of the AO device occurred. Under these conditions the entirety of the AO device was considered to be irradiated by the protons, including the piezoelectric transducer with associated electronics and the heat sink material in contact with the crystal. The remainder of the experiment arrangement was well shielded from the proton irradiation.

The GaP AO modulator was operated at a modulation frequency of $f = 1.125$ GHz and the TeO₂ AO modulator was operated at a modulation frequency of $f = 70.0$ MHz, resulting in the Bragg diffraction of the incident (I_0) optical beam through the deflection angle of $2\Theta_B$. As shown in Figure 3-2, the deflection angle (in air) of the diffracted beam (I_d) from the emerging incident beam (I_0') is given by the relationship:

$$2\Theta'_B = \sin^{-1} \left(\frac{\lambda_0}{V n_a} f \right) \quad (23)$$

Where V represents the velocity of sound in the AO crystal and $n_a \equiv 1$. Diffraction of light occurs when the incident optical beam interacts with the phase grating arising from pressure-induced changes to the refractive index in the acoustic medium. Changes to the phase grating, sound velocity, or other Bragg cell parameters can affect the diffracted light. In this paper, we examine the effects of polarization changes brought about by proton irradiations.

As may be observed in Figure 3-2, four optical detectors were used to monitor the laser output power, main beam (I_0'), and the polarized components of I_d . The latter were quantified using a photoelastic modulation (PEM) detection technique⁴³ (hereafter referred to as the polarimeter). Prior to the proton irradiations, linearly polarized light was introduced into the polarimeter and the polarimeter was calibrated to determine the horizontal/vertical linear, right/left circular, and ± 45 degree linear components of polarized light. Next the AO modulator under assessment

was set in-line and RF voltage was applied. The states of polarization (exiting the crystal) were examined prior to, during, and after the proton irradiations. Changes to the intensity of I_0' were also observed during the irradiation and were used to measure the time dependent proton induced attenuation. A thermistor was placed on the crystal face of both GaP and TeO_2 near the exit points of I_d and I_0' , in order to measure the proton induced heating. In this manner, temperature changes coincident with the changes to the polarization of I_d and the attenuation of I_0' could be studied under irradiation. The operation of the polarimeter and the method for determining the Stokes parameters from the polarimeter-measured responses are given in detail elsewhere.^{42-45,47}

3.5 EXPERIMENTAL RESULTS - PROTON INDUCED CHANGES TO THE POLARIZATION STATES

In general, the polarization states of light interacting with the acoustic waves in GaP and TeO_2 AO crystals were observed to transiently change from their average baseline values at the onset of the radiation event and continued to change throughout the irradiation period. Proton induced transient changes were observed in all polarized components of the diffracted (I_d) and main (I_0') beams. The cell temperature was also observed to increase during the radiation exposures. The AO GaP cell responses discussed in section 4.1 serve to qualitatively illustrate the observation of long term ($t > 400$ s) changes to the polarization states during high proton energy ($\bar{E}_{p+} \approx 63.0$ MeV) and dose ($D_{p+} \approx 2$ kGy(Si)) exposures. The GaP response data are contrasted with the shorter recovery times observed in a TeO_2 deflector exposed to a higher dose $D_{p+} \approx 5$ kGy(Si) but at a lower proton energy, $\bar{E}_{p+} = 39.9$ MeV. The recovery times of the GaP and TeO_2 devices are also compared to the heating each device crystal experienced during irradiation.

3.5.1 GaP Bragg Cell Responses

As may be observed in Figure 3-3, at the onset of proton irradiation, the $+45^\circ$ and horizontal linearly polarized components represented by V_F and V_H respectively, oscillate below the baseline signal during the irradiation time interval and follow an oscillatory increase in voltage at the cessation of the proton irradiation above or near the baseline. The circularly polarized component (V_C) was observed to oscillate above and below the voltage baseline during the proton exposure, followed by a period of oscillation after the end of the proton irradiation. These oscillations are not believed due to the modulated interference effects caused by multiple reflections occurring at the optical surfaces of a polarimeter, which have been extensively discussed by Oakberg.⁴⁸ Since the polarimeter was operated at 42 kHz, 47 kHz and at harmonics of these frequencies, the periods of oscillation observed in Figures 3-3 and 3-4 lie far below those that could arise from any polarimeter modulated signals.

It was determined through calibration, that an increase in detector voltage as shown in Figure 3-3 was indicative of an increase in polarized light intensity (and polarization), while a decrease in voltage resulted from a decrease in the intensity of polarized light (and polarization). At the end of the proton irradiation, the altered polarized signals were observed to begin to revert back to their respective baseline values. However, as may be observed in Figure 3-4, the recovery times of the three polarized signals were neither equivalent nor complete at $t = 470$ s.

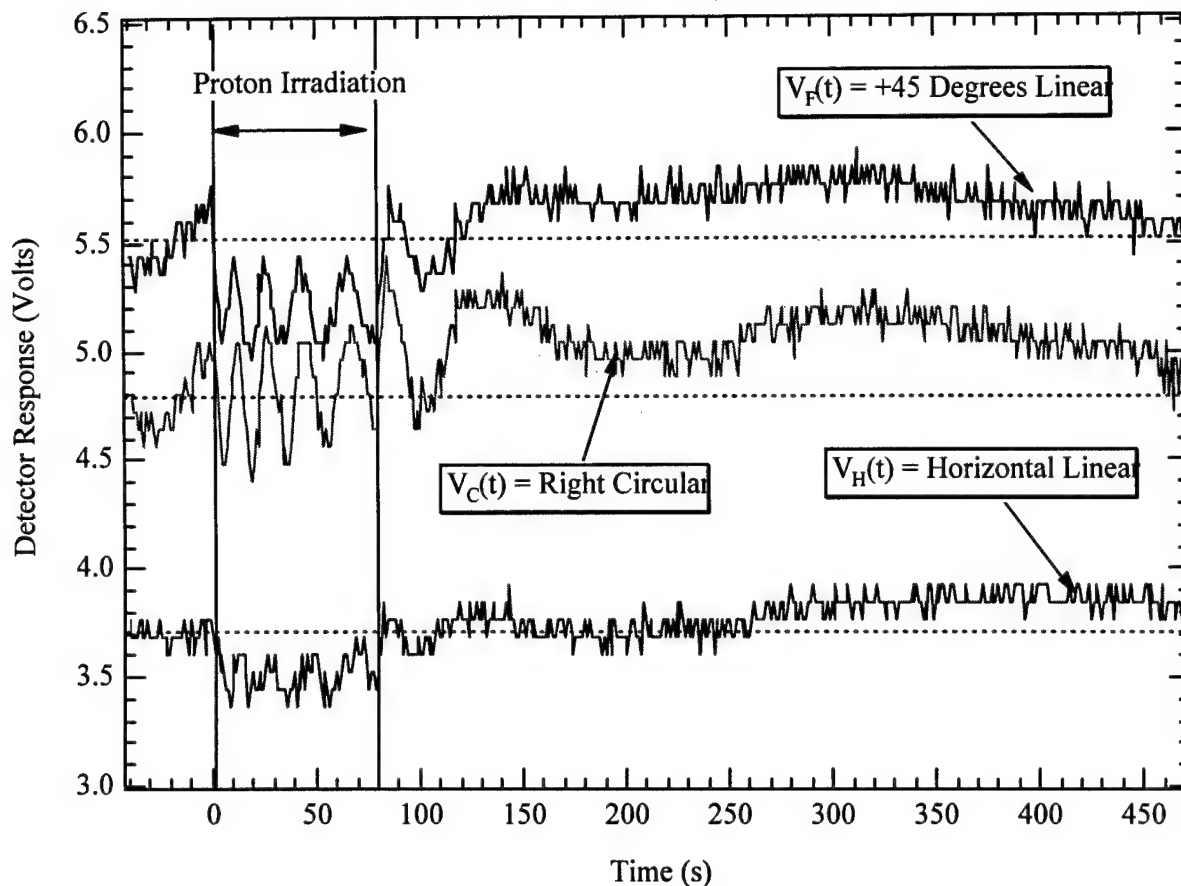


Figure 3-3. Proton induced changes to the diffracted beam polarization states of a GaP Bragg cell. Irradiation conditions: $\bar{E}_{p+} = 63.0$ MeV, flux $\equiv \phi = 1.885 \times 10^{10}$ protons \cdot cm $^{-2}$ \cdot s $^{-1}$, fluence $\equiv \Phi = 1.484 \times 10^{12}$ protons \cdot cm $^{-2}$, irradiation time = 78.71 s (indicated by the vertical dashed lines).

The proton induced heating of the GaP crystal measured by a thermistor is shown in Figure 3-4. As may be observed, the peak crystal heating occurs during the irradiation period with the recovery approximately tracking the recovery of the polarization states from their peak changes. (Note: For higher dose exposures and data (not shown here) the polarization states were restored to their preirradiation baselines, while the cell temperature remained elevated).

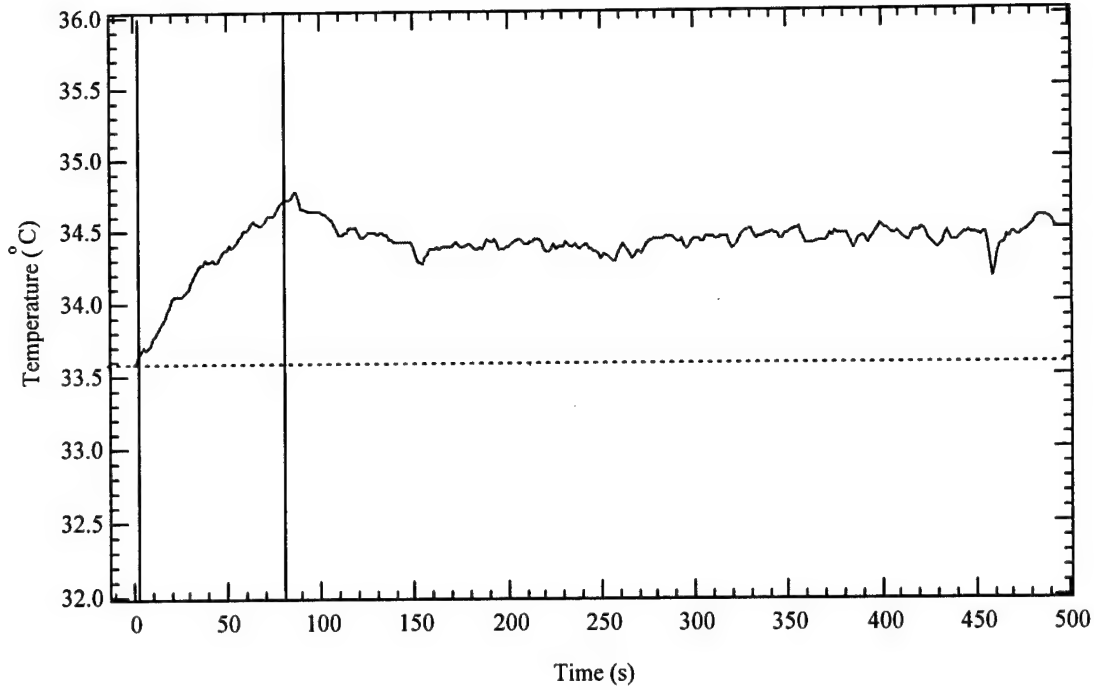


Figure 3-4. Temperature response of a GaP AO Bragg cell under proton irradiation. Irradiation conditions: $\bar{E}_{p+} = 63.0$ MeV, flux $\equiv \phi = 1.885 \times 10^{10}$ protons \cdot cm $^{-2}$ \cdot s $^{-1}$, fluence $\equiv \Phi = 1.484 \times 10^{12}$ protons \cdot cm $^{-2}$, irradiation time = 78.71 s (indicated by the vertical dashed lines).

The ionization produced by protons interacting with the Bragg cell crystal was calculated using the TRIM computer code.⁵⁵ The energy of the protons as well as the energy imparted to the crystal material can be determined from the extent of ionization. Figure 3-5 shows the ionization, proton energy, and proton energy loss in the crystal as a function of depth into the crystal and AO heat sink along the x-axis (see Figure 3-2). The depth of the GaP crystal material extends from 0 to 4.76 mm and an aluminum heat sink some 12.5 mm thick is mounted directly behind the crystal. The abrupt change in the ionization at the GaP and aluminum interface is visible at $x \approx 4.8$ mm. In the proton exposure of GaP, a fluence (Φ) of 1.484×10^{12} protons \cdot cm $^{-2}$ were incident on a thickness (x) of 0.476 cm. The average dose (\bar{D}_{p+}) in Gray (Gy) may be calculated as,

$$\bar{D}_{p+} = 1.602 \times 10^{-10} \frac{\Phi(T_o - T_{ex})}{\rho x} \quad (24)$$

Here, T_0 is the initial proton energy and T_{ex} is the exiting proton energy (MeV) with respect to the GaP thickness (x in cm) and density of $\rho = 4.13 \text{ g}\cdot\text{cm}^{-3}$. The average dose in the GaP crystal was calculated as $\bar{D}_{p+} = 1861.5 \text{ Gy}$. The use of equation 24 for the calculation of \bar{D}_{p+} assumes that the stopping power through the crystal does not change significantly over the crystal depth.⁵⁶ Figure 3-5 shows the dose experienced as a function of depth along the x-axis (mm) for the 63.0 MeV protons incident on the AO Bragg cell.

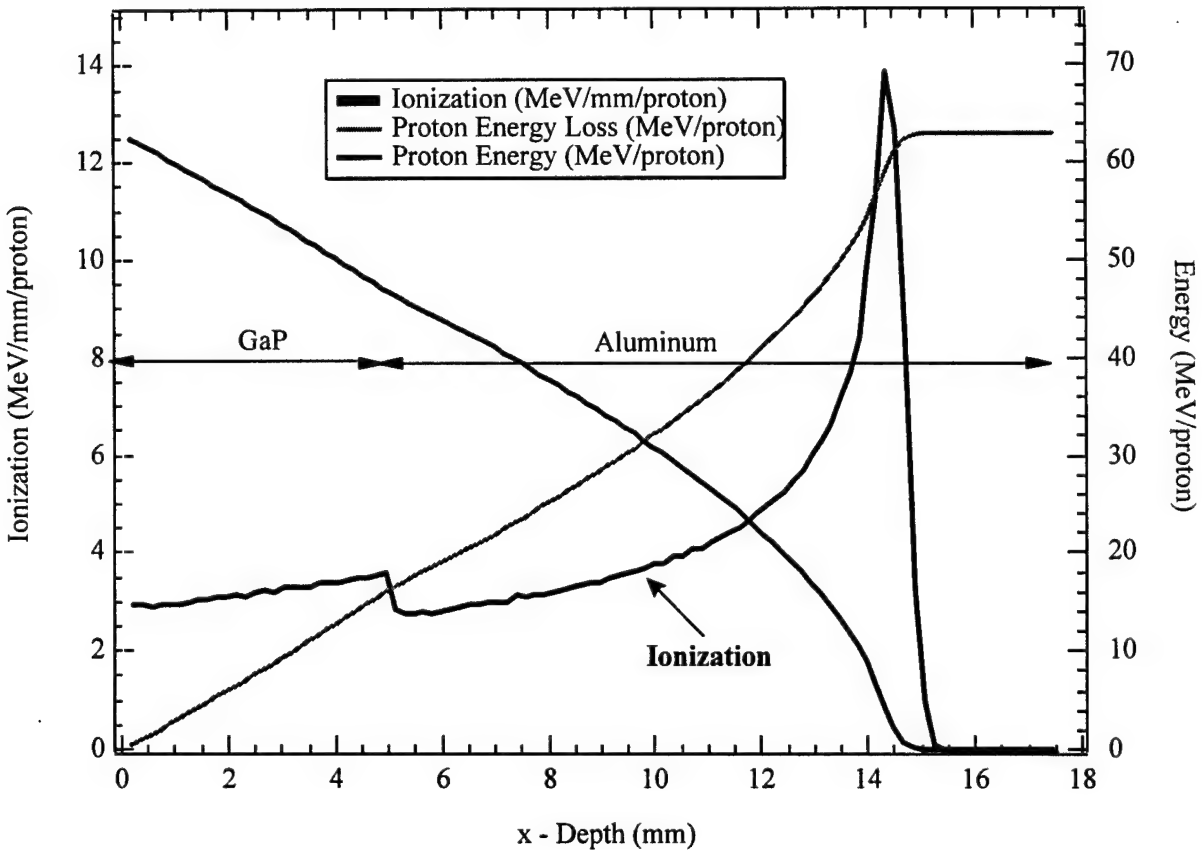


Figure 3-5. Ionization and proton energy in a GaP AO Bragg cell and aluminum heat sink under proton irradiation. The GaP crystal depth extends from 0 to 4.76 mm and the heat sink depth from 4.76 to 17.26 mm. The average dose in the GaP crystal is $\bar{D}_{p+} = 1861.5 \text{ Gy}$. Irradiation conditions: $\bar{E}_{p+} = 63.0 \text{ MeV}$, flux $\equiv \phi = 1.885 \times 10^{10} \text{ protons}\cdot\text{cm}^{-2}\cdot\text{s}^{-1}$, fluence $\equiv \Phi = 1.484 \times 10^{12} \text{ protons}\cdot\text{cm}^{-2}$.

The average dose in the GaP crystal calculated from the numerical method was $\bar{D}_{p+} = 1859.3 \text{ Gy}$ which compares very well with the average dose calculated from equation 24. The majority

of the proton energy is deposited in the aluminum heat sink rather than in the GaP crystal. From Figure 3-6 it is apparent that the aluminum heat sink does receive a significant dose from the protons, $\bar{D}_{p+} = 3.3$ kGy, which constitutes $\approx 75\%$ of the incident proton energy. In this instance, the heat sink may act as a heat source raising the temperature above the value experienced from direct proton heating of the GaP crystal. It is believed that this indirect heating contributes to temperature gradients in the GaP crystal, which distort the acoustic wave fronts.^{1,3-5,11}

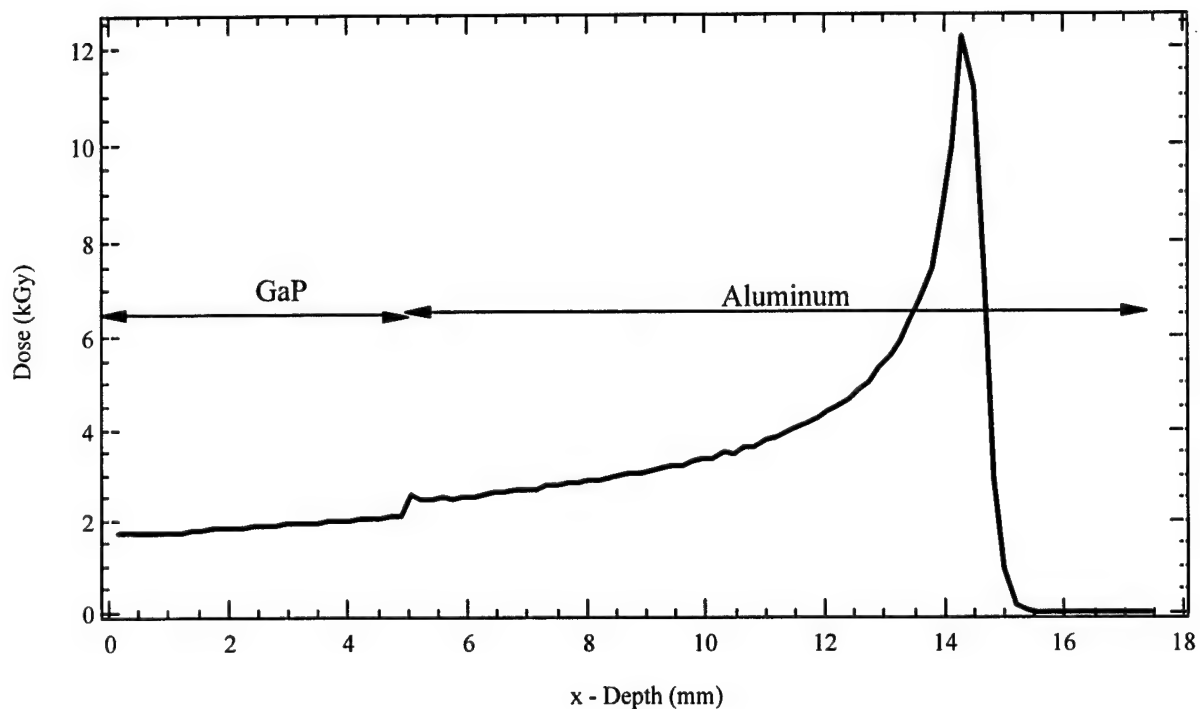


Figure 3-6. Dose in a GaP AO Bragg cell and aluminum heat sink under proton irradiation calculated by numerically solving equation 25. The GaP crystal depth extends from 0 to 4.76 mm and the heat sink depth from 4.76 to 17.26 mm. The average dose in the GaP crystal is $\bar{D}_{p+} = 1859.3$ Gy.

3.5.2 TeO₂ Bragg Cell Responses

The right circular (V_C), horizontal linear (V_H), and + 45 degree linear (V_F) components of the polarized diffracted light propagating in the TeO₂ Bragg cell are represented in Figure 3-7. Left circular polarized light (I_d) was incident on the Bragg cell, which, due to the anisotropy of TeO₂,

was optically rotated to right circular polarization. The right circular component of the diffracted polarized light (I_d) dominates the polarization content of the optical beam exiting the cell.

During the proton exposure, the greatest change in polarization was observed to occur in the right circular polarization component. As shown in Figure 3-7, the extent of right circular polarization component decreases, while the +45 degree linear and horizontal linear polarizations are seen to increase in magnitude. Following the cessation of the proton irradiation ($t = 138.2$ s), the polarization components are nearly restored to their pre-irradiated baseline values although the approximate recovery times vary from $15 \text{ s} \leq t \leq 55 \text{ s}$. V_F does not recover within the time interval shown.

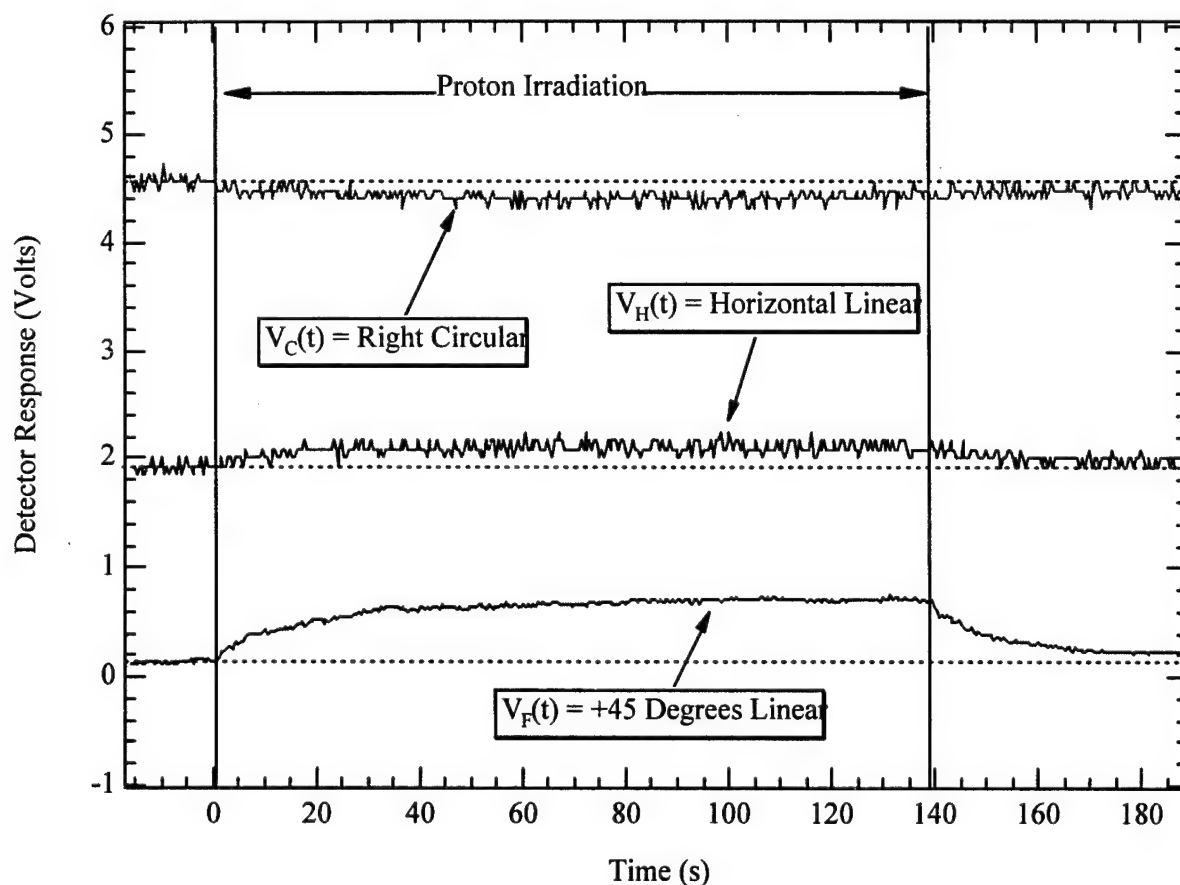


Figure 3-7. Proton induced changes to the diffracted beam polarization states of a TeO_2 Bragg cell. Irradiation conditions: $\bar{E}_{p+} = 39.9 \text{ MeV}$, $\phi = 1.897 \times 10^{10} \text{ protons} \cdot \text{cm}^{-2} \cdot \text{s}^{-1}$, $\Phi = 2.622 \times 10^{12} \text{ protons} \cdot \text{cm}^{-2}$, irradiation time = 138.2 s (indicated by time interval between vertical dashed lines).

Shown in Figure 3-8 is the temperature response of the proton irradiated TeO_2 crystal. As may be observed, the cell temperature increases by $\Delta T \approx 0.8^\circ\text{C}$ during the irradiation and does not recover back to the pre-irradiation baseline within the time span of the measurement window ($\Delta t = 190$ s). The bulk heating and temperature gradients induced by the radiation process contribute to the depolarization and are discussed in the next section.

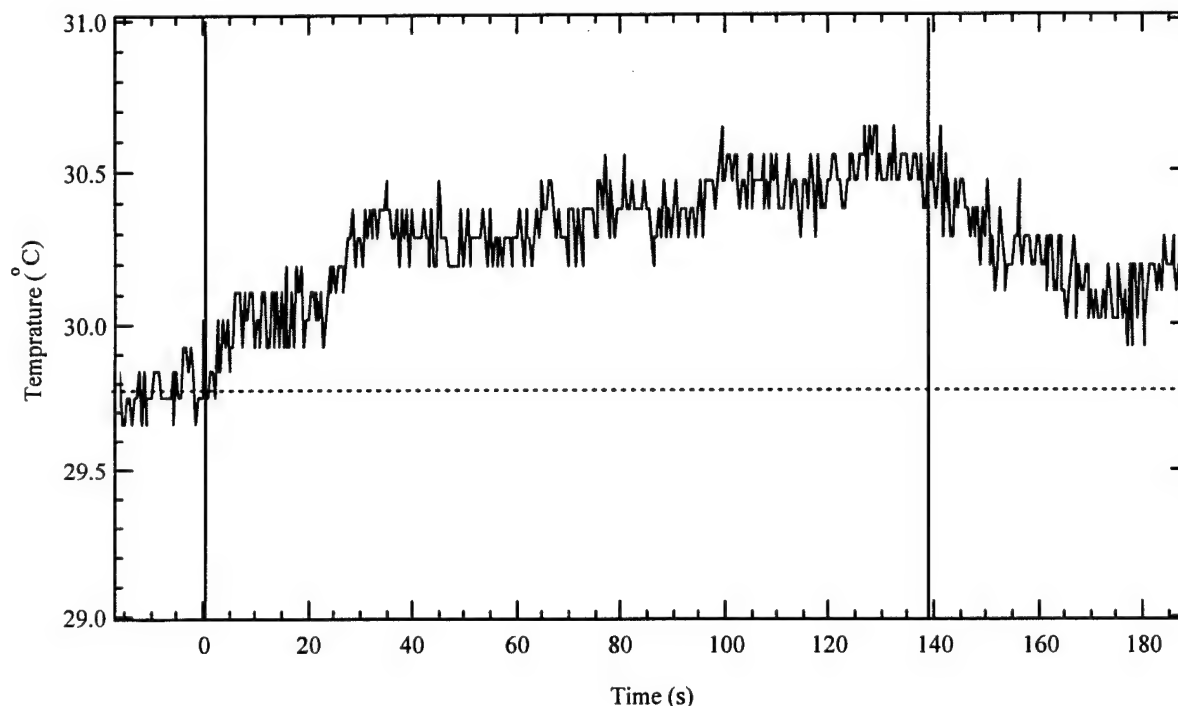


Figure 3-8. Temperature response of a TeO_2 Bragg cell under proton irradiation. Irradiation conditions: $\bar{E}_{p+} = 39.9$ MeV, $\phi = 1.897 \times 10^{10}$ protons $\cdot\text{cm}^{-2}\cdot\text{s}^{-1}$, $\Phi = 2.622 \times 10^{12}$ protons $\cdot\text{cm}^{-2}$, irradiation time = 138.2 s (indicated by time interval between vertical dashed lines).

Figure 3-9 shows the extent of ionization the protons produce as they interact with the TeO_2 crystal volume as predicted by the Transport of Ion in Matter (TRIM) computer code.⁵⁵ Shown are the proton energy and proton energy loss in the crystal as a function of depth along the axis of proton bombardment (x-axis is normal to the crystal face and perpendicular to the laser beam).

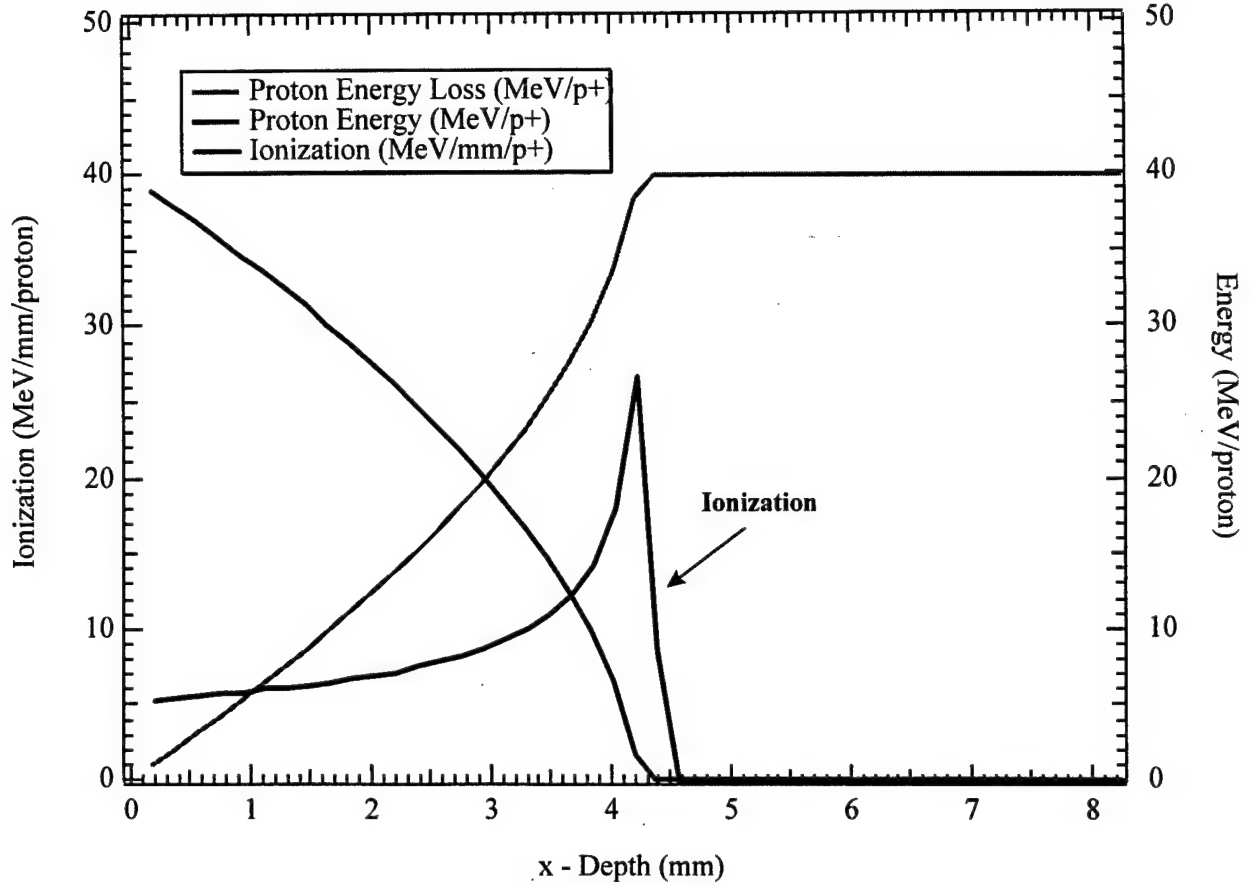


Figure 3-9. Ionization in a TeO_2 AO Bragg cell under proton irradiation. The TeO_2 crystal extends from 0 to 8.25 mm. The average 39.9 MeV proton range in the crystal is 4.38 mm. The average dose in the crystal from $x = 0$ to the maximum proton range is $\bar{D}_{p+} = 6388.79$ Gy. The average dose in the entire crystal is $\bar{D}_{p+} = 3391.87$ Gy. Irradiation conditions: $\bar{E}_{p+} = 39.9$ MeV, $\phi = 1.897 \times 10^{10}$ protons $\cdot\text{cm}^{-2}\cdot\text{s}^{-1}$, $\Phi = 2.622 \times 10^{12}$ protons $\cdot\text{cm}^{-2}$, irradiation time = 138.2 s (indicated by time interval between vertical dashed lines).

The protons expend all of their energy in approximately the first half of the TeO_2 crystal. Since the protons never exit the material ($T_{\text{ex}} = 0$) equation 24 which was used to determine the average dose in GaP can be modified to

$$\bar{D}_{p+} = 1.602 \times 10^{-10} \frac{\Phi T_0}{\rho x} \text{ (Gy)} \quad (25)$$

For $\Phi = 2.622 \times 10^{12}$ protons \cdot cm $^{-2}$, $T_0 = 39.9$ MeV, $x = 0.438$ cm (average range of 39.9 MeV protons in TeO $_2$), and $\rho = 5.99$ gram \cdot cm $^{-3}$ the average dose calculated is $\bar{D}_{p+} = 6388.79$ Gy. The average dose over the entire crystal depth is $\bar{D}_{p+} = 3391.87$ Gy. The average dose from the numerical method is 6390.25 and 3408.13 Gy in the entire crystal and the thickness associated with the average proton range ($0 < x \leq 4.38$ mm) in the TeO $_2$ material respectively, as shown in Figure 3-10 (comparing within 1% of the equation 24 results). As may be observed in Figure 3-10, the majority of the proton energy is deposited in the center of the crystal.

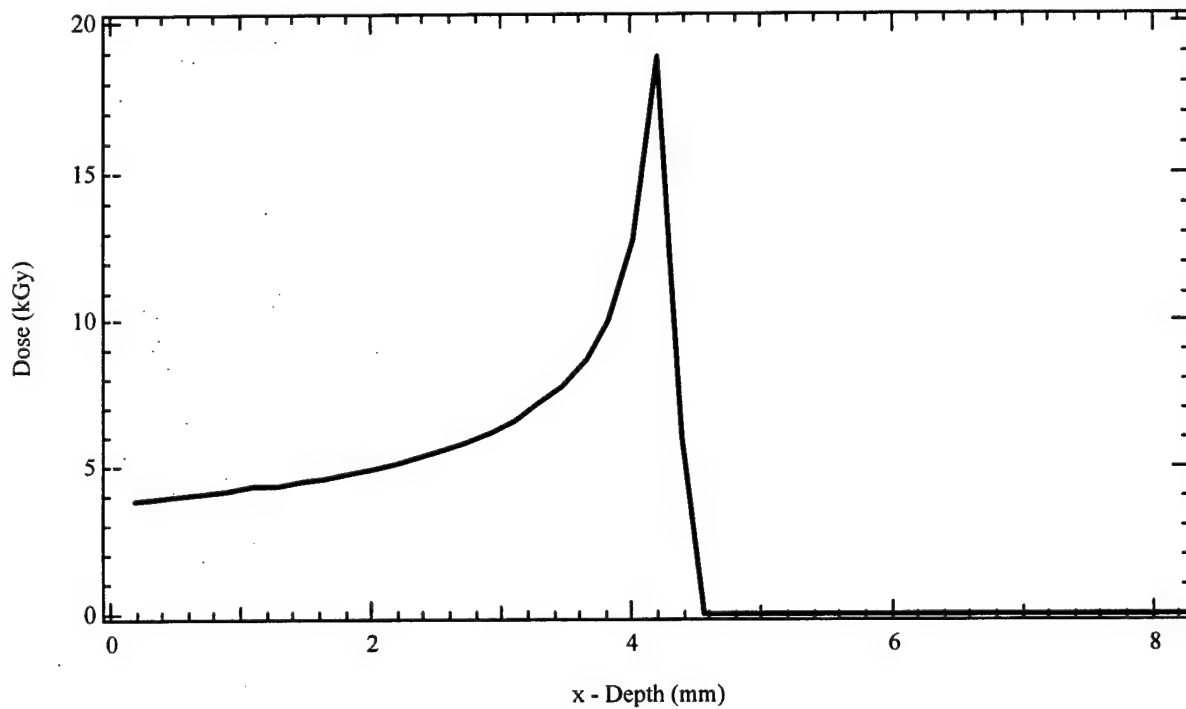


Figure 3-10. Dose in a TeO $_2$ AO Bragg cell under proton irradiation calculated by numerically solving equation 25. The TeO $_2$ crystal depth extends from 0 to 8.25 mm. The average dose in the crystal from the $x = 0$ to $x = 4.38$ mm is $\bar{D}_{p+} = 6390.25$ Gy. The average dose in the entire crystal is $\bar{D}_{p+} = 3408.13$ Gy. Irradiation conditions: $\bar{E}_{p+} = 39.9$ MeV, $\phi = 1.897 \times 10^{10}$ protons \cdot cm $^{-2} \cdot$ s $^{-1}$, $\Phi = 2.622 \times 10^{12}$ protons \cdot cm $^{-2}$, irradiation time = 138.2 s.

3.6 ANALYSIS-TRANSIENT DEPOLARIZATION OF OPTICAL SIGNALS

As an example of the polarization effects arising from the proton exposures, a brief analysis of the TeO_2 deflector responses shown in Figure 3-7 is presented. An example of electron induced depolarization will be presented in a later section. Here, the time dependent voltages V_H , V_C , and V_F , correspond to the horizontal linear, right circular, and +45 degree linear polarization states. The voltages associated with these polarization states may be normalized and readily cast into Stokes⁴⁷ parameters given by the ratios:

$$S_1 = V_H/S_H \quad (26)$$

$$S_2 = V_F/S_F \quad (27)$$

$$S_3 = V_C/S_C \quad (28)$$

Here, S_H , S_F , and S_C are the Stokes calibration factors for the polarimeter system, while S_1 , S_2 , and S_3 represent the normalized Stokes parameters for the polarized components of the light propagating in the AO device. In general, the Stokes representation for determining polarization states is given as:

$$S_0^2 = S_1^2 + S_2^2 + S_3^2 \quad (29)$$

Where S_1 , S_2 and S_3 represent the linear vertical/horizontal, linear +/- 45 and right/left handed circular polarization states, respectively. For the equality to hold in equation 29 the beam of light under study is 100% polarized. Thus, the parameter S_0 is related to the total polarized and unpolarized intensities of the optical beam under study. Both the polarized and unpolarized (S_0) components of the diffracted light exiting the TeO_2 Bragg cell prior to the proton irradiation may be represented in Stokes form as:

$$S = \begin{bmatrix} S_0 \\ S_1 \\ S_2 \\ S_3 \end{bmatrix} = \begin{bmatrix} 0.4208 \\ 0.0730 \\ 0.0042 \\ 0.3995 \end{bmatrix} \quad (30)$$

Where \mathbf{S} is the Stokes column for the light exiting the Bragg cell. An example of the instantaneous change of polarization states and unpolarized light during the irradiation event (e.g., $t = 134$ s) may be represented by the expression:

$$\mathbf{S}' = \begin{bmatrix} S'_0 \\ S'_1 \\ S'_2 \\ S'_3 \end{bmatrix} = \begin{bmatrix} 0.4209 \\ 0.0824 \\ 0.0223 \\ 0.3850 \end{bmatrix} = \mathbf{M} \begin{bmatrix} 0.4208 \\ 0.0730 \\ 0.0042 \\ 0.3995 \end{bmatrix} \quad (31)$$

Here, \mathbf{M} represents the Mueller matrix used in determining the changes to the polarized and unpolarized light at any instant in time. \mathbf{S}' is the Stokes column vector representation of the polarized and unpolarized light following the proton irradiation at a unique time (e.g., data shown in equation 31 is for $t = 134.0$ s, see Table 3-1). \mathbf{M} is a 4 by 4 matrix which can be used to determine the influence of the proton irradiation of the Bragg cell.

Table 3-1. Tabular data for the Stokes column vector and degree of polarization for proton irradiated TeO_2 .

<u>Time(s)</u>	<u>S_1</u>	<u>S_2</u>	<u>S_3</u>	<u>S_0</u>	<u>P</u>
0.0	0.073	0.004	0.399	0.421	0.961
2.0	0.076	0.007	0.392	0.420	0.955
4.0	0.073	0.008	0.399	0.420	0.955
8.0	0.076	0.012	0.392	0.421	0.948
10.0	0.079	0.013	0.385	0.421	0.950
20.0	0.079	0.016	0.392	0.421	0.947
40.0	0.082	0.019	0.385	0.421	0.944
60.0	0.079	0.020	0.378	0.421	0.935
80.0	0.079	0.020	0.385	0.421	0.937
100.0	0.082	0.022	0.385	0.421	0.938
120.0	0.079	0.022	0.385	0.421	0.938
134.0	0.082	0.022	0.385	0.421	0.937
140.0	0.079	0.020	0.385	0.421	0.944
160.0	0.076	0.010	0.392	0.421	0.944
180.0	0.079	0.007	0.392	0.421	0.954

Figure 3-11 shows the S_1 , S_2 , and S_3 Stokes parameters associated with the diffracted beam before, during, and after the irradiation event. Examination of \mathbf{S}' and \mathbf{S} in Figure 3-11, reveals

that the proton irradiation altered the diffracted beam polarization states. For example, the polarization content of the diffracted beam prior to proton irradiation (S) consisted of a mixture of polarization states and unpolarized light. In equation 30, S represents light of highly circular (right handed) polarization. There are also smaller components of horizontal linear polarized light ($S_1 = 0.0730$) and light linearly polarized at $+45^\circ$ ($S_2 = 0.0042$). During and for a period of time following the proton irradiation all polarized components were observed to change, while the irradiance (S_0) appeared nearly invariant ($S_0' \approx S_0$).

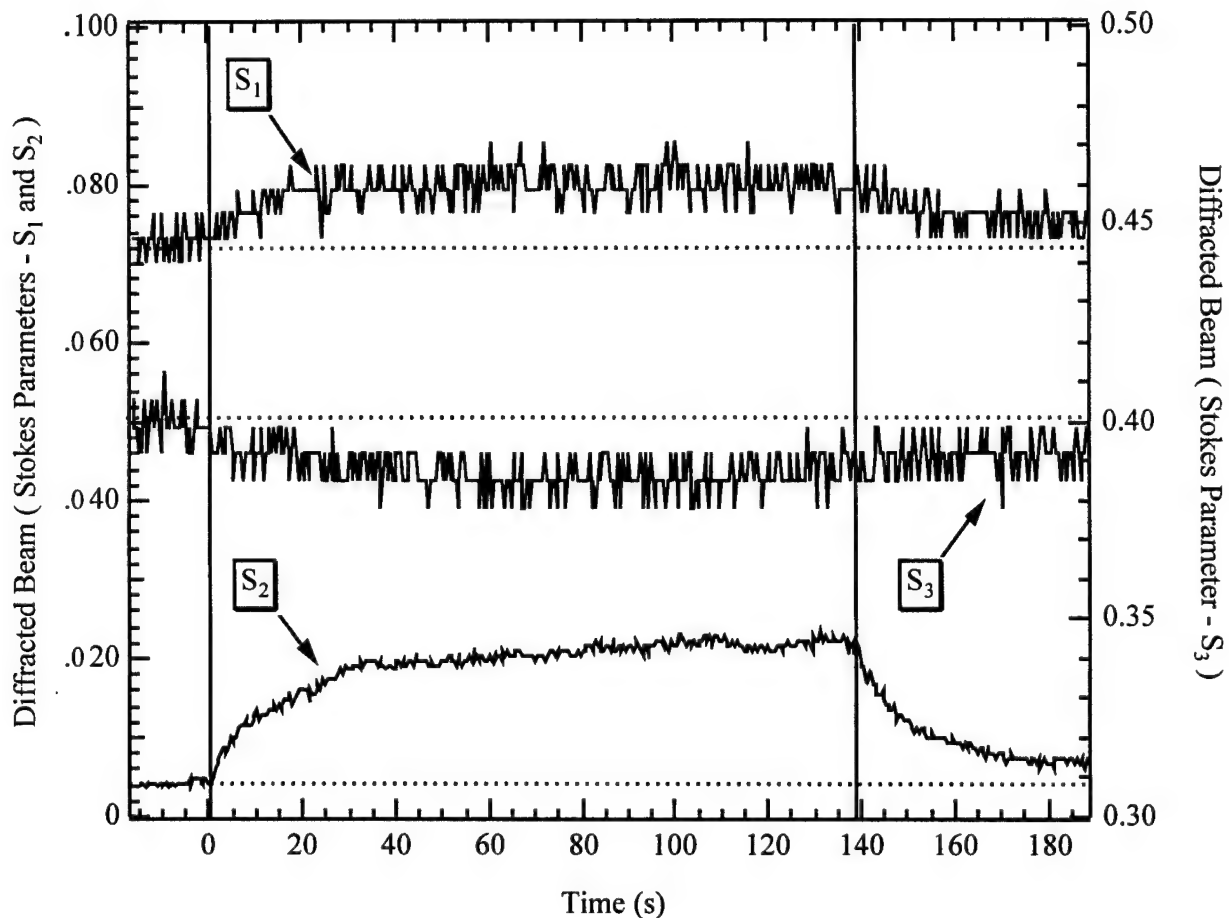


Figure 3-11. Stokes parameter values for a TeO_2 Bragg deflector under proton irradiation. The vertical solid lines show the on ($t=0$ s) and off ($t=138.2$ s) times of the proton beam and the horizontal dotted lines show the pre- irradiation values for the S_1 , S_2 , and S_3 parameters. The diffracted beam (I_d) circular polarization changes dominate and are shown as S_3 (read along the right y - axis).

The effect of the proton irradiations on \mathbf{S} may be observed in the matrix representations of equation 8. Here, $S_0' \approx S_0$, $S_1' > S_1$, $S_2' > S_2$, $S_3' < S_3$. This indicates that under proton irradiation, the diffracted beam became less right circularly polarized while increasing in both horizontal and $+45^\circ$ linear polarization states. In essence, the effect of the radiation was to alter the near circular polarized light to that of elliptically polarized light. Solutions to \mathbf{M} were identified by assuming that the overall effect of the radiation on \mathbf{S} is analogous to a linear retarder with retardation δ and with a fast axis at angle Θ . The fast axis of the hypothetical linear retarder is oriented with respect to the propagation axis of the diffracted beam (I_d). Equation 8 is satisfied within the accuracy of the experiment when a Mueller matrix for an ideal linear retarder with a retardation $\delta = 0.055$ radians and a fast axis angle $\Theta = 164.0^\circ$ are used to determine \mathbf{M} .

While the Stokes formalism allows the analysis of the polarized light, the polarimeter system shown in Figure 3-2 does not allow unpolarized light to be modulated. Therefore, only changes to the polarized components of the light are discussed in this paper. The expression for determining the degree of polarization is given by:

$$P = \sqrt{\frac{S_1^2 + S_2^2 + S_3^2}{S_0^2}} \quad (32)$$

where P is the degree of polarization, and S_0 represents the irradiance of polarized and unpolarized light. For completely polarized light, $P = 1$ (or expressed in percentage as 100%). For the TeO_2 data in Figure 3-7, $\bar{S}_0 = 0.4208$ with a standard deviation of $\sigma = 0.0003$ for the entire experiment ($t = 206$ s). The degree of polarization as a function of time prior to, during, and following the proton irradiation is plotted in Figure 3-12 and tabular data at select times shown in Table 3-1. The average degree of polarization prior to proton irradiation ($t < 0$) was $\bar{P} = 0.9647$ with a standard deviation of $\sigma = 0.0027$. This indicates that the light passing through the TeO_2 Bragg cell prior to the radiation event was 96.47% polarized. Depolarization was observed during the entire radiation event and for a short period following the cessation of proton irradiation. For example, in Figure 3-12, the degree of polarization is observed to

decrease to $P = 0.9369$ at $t = 134.0$ s. Depolarization was also observed to range from 40 s to 120 s following the cessation of proton exposures. None of these effects were permanent.

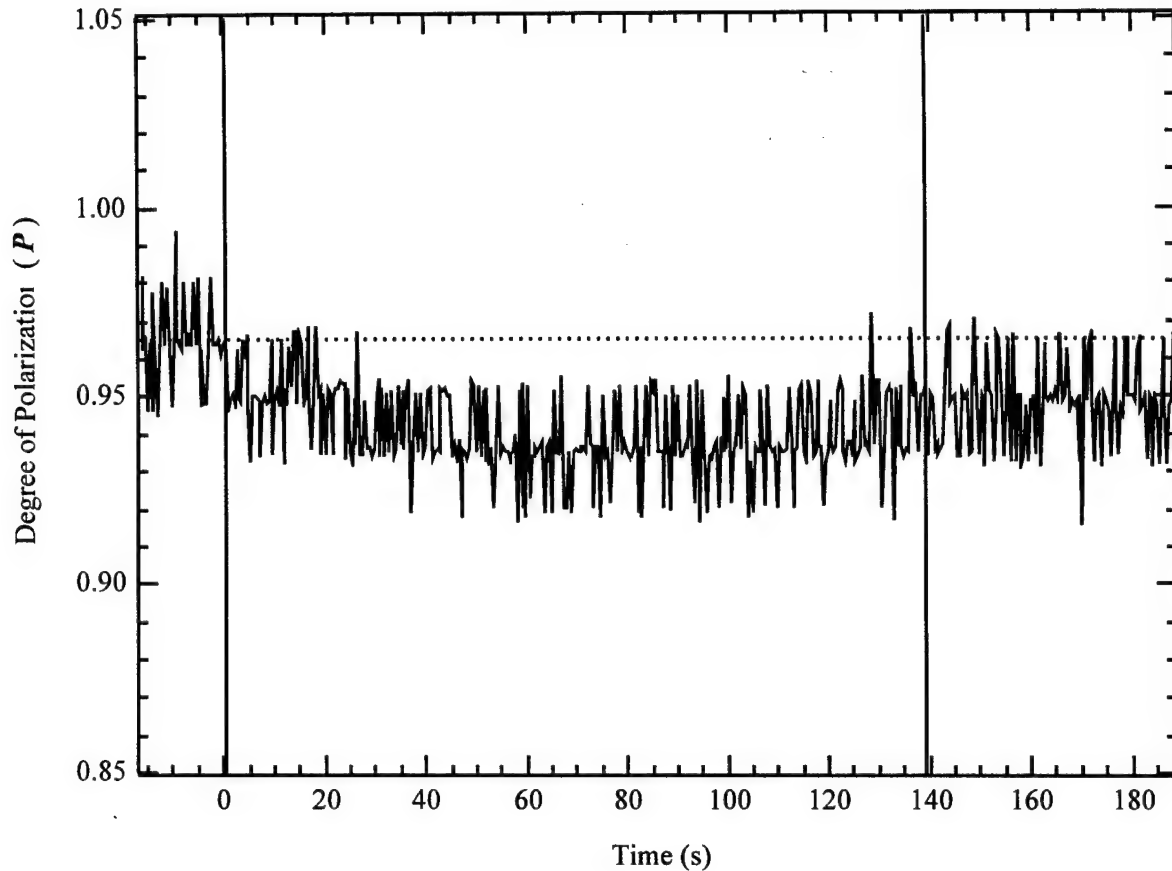


Figure 3-12. Degree of polarization (P) for a TeO_2 AO Bragg deflector exposed to proton radiation. The horizontal dotted line shows the degree of polarization prior to proton irradiation (for all $t < 0$) was $P = 0.9647$ (standard deviation of $\sigma = 0.0027$).

3.7 DISCUSSION OF PROTON IRRADIATION OF AO BRAGG CELL RESULTS

It is important to discuss the responses expected by decreasing the magnitude of circularly polarized light in a TeO_2 Bragg cell optimized to operate with circularly polarized light. TeO_2 is a noncentrosymmetric, optically active, left-handed rotating, positive uniaxial crystal, requiring circularly polarized light for achieving a high diffraction efficiency (η). The direction of the

circular polarized light introduced into the TeO_2 crystal is important since TeO_2 is also anisotropic, and left and right (handed) circular polarized light experience different refractive indices creating a phase difference between the E_x and E_y electric field components of the polarized light. For example, when right circular, polarized light is propagated through an acoustically modulated shear wave TeO_2 crystal (acoustic propagation along $[110]$) it is diffracted as left circularly polarized light. For the data shown in Figure 3-5, left-handed circular light (I_o) was diffracted and detected as right circularly polarized light (I_d) by the polarimeter system shown in Figure 3-2.

Since TeO_2 is anisotropic, the polarization of the incident light influences the degree of coupling between the incident and diffracted optical beams. The nature of the coupling is best understood by considering the changes in the polarization components ($P_{x,y,z}$) which take the form:⁵⁷

$$\Delta P_x \propto \Delta \left(\frac{1}{n^2} \right)_6 E_y \quad (33)$$

$$\Delta P_y \propto \Delta \left(\frac{1}{n^2} \right)_6 E_x \quad (34)$$

$$\Delta P_z = 0 \quad (35)$$

Here E_x and E_y are the electric field components of the circularly polarized light which couple with each other. The subscript (6) for the $(1/n^2)$ term represents the elasto-optic coefficient appropriate for the shear wave propagation in TeO_2 . Equations 33 and 34 show that if the incident light is x-direction polarized, the diffracted light will be y-polarized, and if the incident light is y-direction polarized, the diffracted light will be polarized in the x-direction. Equation 35 indicates that z-polarized light does not couple into either x or y components.

In Figures 3-7 and 3-11, the magnitude of the circular polarization is observed to decrease under proton irradiation. As observed earlier and reported elsewhere, the diffraction efficiency in AO

Bragg deflectors has been observed to decrease for increasing radiation dose, which would indicate that the decrease in diffraction efficiency could be affected in part by depolarization.³

Das⁵⁷ has shown that the diffracted light amplitude is affected by the incident polarization state since different light polarizations will experience different elastooptic contributions to the refractive index change (Δn). The spatial changes to the crystal refractive index caused by the acoustically induced phase grating are responsible for the diffraction of light. The diffraction efficiency (η) at the Bragg angle may be expressed in terms of the acoustically induced phase shift ($\Delta\phi$) as:

$$\eta = \sin^2\left(\frac{\Delta\phi}{2}\right) \quad (36)$$

where,

$$\Delta\phi = -\frac{2\pi}{\lambda_0} \Delta n L \quad (37)$$

Here Δn represents the acoustically induced refractive index change, and L is the interaction path length between the optical and acoustic beams. For the special case of a phase change of $\Delta\phi = \pi$ radians, the diffraction efficiency is maximized, theoretically allowing all of the incident light to be diffracted through the deflection angle $2\Theta_B$. For the data shown in Figure 3-7, the magnitude of the circular polarization in the diffracted beam was observed to decrease during the proton irradiation by approximately 1.6% (volts) which corresponds with a 5.4% decrease in the Stokes parameter value (S_3 , Figure 3-11). However, no decrease in the Bragg cell diffraction efficiency was observed within an experimental accuracy of $\pm 5\%$.

The transient depolarization of optical signals in a TeO_2 Bragg cell has recently been observed and reported for CO_2 laser heating⁴⁹ and for pulsed electron ($\bar{E}_{e^-} = 15 \text{ MeV}$) irradiations.^{1,3,42,45}

The electron-induced depolarization was somewhat more pronounced than for the proton data reported herein. Previous studies have shown that heating induced by electron irradiation causes thermal gradients in AO crystals.¹ Thermal gradients can give rise to displacements of the Bragg cell spatial intensities (I_d, I_o'), while bulk heating of the AO crystal changes the velocity of sound which in turn alters the deflection angle ($2\Theta_B$). Bulk heating and temperature gradients in AO crystals also affect the interaction geometry between the acoustic and optical signals by degrading the planar properties of the acoustic and optical wavefronts. Both of these mechanisms can contribute to increased scattering and depolarization of optical signals.

Due to the broad area electron and proton sources used, irradiation of the crystal transducer and heat sink can also occur which may contribute to the overall responses that have been observed. Ongoing investigations using a precise ion microbeam methodology^{57,58} to confine the proton beam to a ≈ 1 mm spot size will allow individual areas and volumes of the AO device (e.g., transducers, heat sink, crystal areas) to be investigated. In this manner, the responses of the irradiated AO device can be partitioned, identified, and quantified to provide a better understanding of the contributing radiation effects.

The polarization states and degree of polarization of light propagating in TeO_2 and GaP acoustooptic Bragg cells were observed to transiently change as a result of proton irradiations. Radiation induced depolarization in AO devices is believed primarily due to proton induced bulk heating and temperature gradients which affect the crystal refractive index and the phase homogeneity of the acoustic wavefronts. The times required for polarized signals in GaP and TeO_2 devices to recover to their respective pre-irradiation polarized or initial states were observed to significantly differ. These recovery times were also observed to vary with proton energies and the proton dose. When compared to a proton irradiated GaP modulator ($\bar{E}_{p+} = 63$ MeV, $\bar{D}_{p+} \approx 2$ kGy(Si)) shorter recovery times were observed in a TeO_2 deflector exposed to a higher dose $\bar{D}_{p+} \approx 5$ kGy(Si) but at a lower proton energy, $\bar{E}_{p+} = 39.9$ MeV. Proton induced degradation to the AO transducer and transducer circuitry is believed to also contribute to these effects, however the magnitude of the contribution cannot be accurately bounded since a broad

area radiation source was used in the experiment. These issues are being resolved by conducting ion micro beam studies which allow confinement of the proton beam to spot-sized areas on the AO structure with mean breadth ranging from $1\mu\text{m}$ (vacuum) to 1 mm (air). Both TeO_2 and GaP AO devices appear suitable for relatively benign space radiation environments, but may not fare well in rapidly changing temperature or enhanced radiation environments.

3.8 ELECTRON INDUCED POLARIZATION CHANGES IN AO BRAGG CELLS

The previous section dealt with changes to polarized signals resulting from proton irradiation of AO devices. This section reports on similar observed phenomena induced by electron irradiations and recently reported.⁴⁵ The exposure arrangement of a TeO_2 Bragg cell modulator exposed to pulsed electrons is shown in Figure 3-13. The experiment arrangement shows that the PEMS are aligned along the main beam and not the diffracted beam as in the previous section.

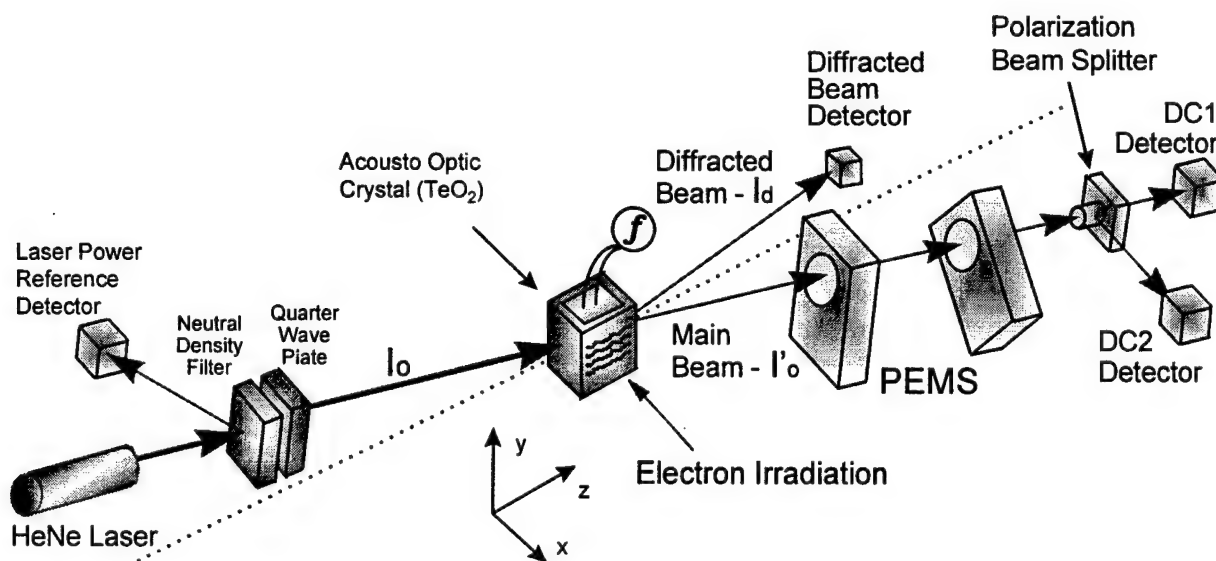


Figure 3-13. Typical arrangement for studying electron induced polarization effects in main beam of acoustooptic devices.

The electron beam was incident normal to both the AO crystal face and an optical beam (I_0) of wavelength $\lambda = 0.6328 \mu\text{m}$. A modulation frequency of $f = 70 \text{ MHz}$ resulted in the first order (I_d) diffraction efficiency of 55.4 %. The exposure of the device consisted of 26 separate exposures of 15.0 MeV electrons at various numbers of total pulses throughout the course of the experiment, ranging from 1 to 700 pulses. The electron pulses from the LINAC had a pulse rate of 30 Hz and a pulse width of 1.0 μs . The dose (as determined from the pin diode detectors used by LINAC operators) was 1.5 krad(Si) per pulse. Figure 3-14 represents a typical set of radiation induced response data observed in polarization sensitive AO devices.

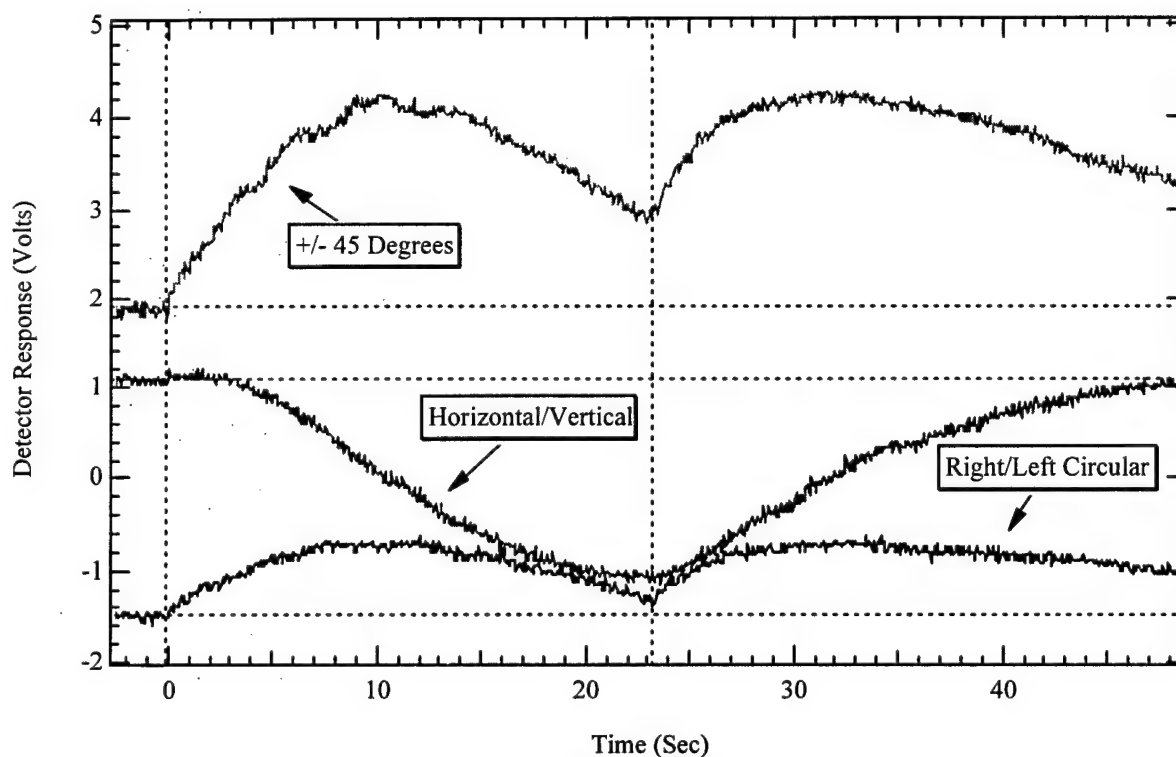


Figure 3-14. Main beam polarization components response before, during and after electron irradiation exposure. The different polarization responses are shown for a TeO_2 AO Bragg cell irradiated to 1.05 Mrad. The horizontal dotted lines show the pre-irradiation polarization state values. The vertical dotted lines depict the 15.0 MeV electron exposure time. The electrons are directed at the Bragg cell in pulses at 30 Hz and each pulse imparts 1.5 krad to the cell. A total dose of 1.05 Mrad achieved with 700 pulses in 23.33 s.

As may be observed, the baseline voltage values for left handed circular, linear horizontal and linear + 45° polarization states exiting the Bragg cell, were established before the application of the electron pulses (denoted by time period between the vertical dotted lines). The maximum transient changes to the polarization components occurred at the end of the applied electron pulses. The linear horizontal, +45° and left circular components recovered to baselines at 16 s, 66 s and 50 s respectively. Measurements of the device front and backside temperatures, before, during and after the electron irradiation show that the AO cell temperature is increased by approximately 10 °C during the electron exposure. This rise in temperature experienced by the Bragg cell was a direct result of electron deposition of heat.

A calculation of the dose rate can be considered in two ways; dose rate during the 1 μs pulse (dose rate) and the dose rate averaged over multiple pulses (integrated dose rate) for 1 μs pulses delivered at 30 Hz. The dose rate is $1.5e^9$ rad(Si)/s and the integrated dose rate is 45,000 rad(Si)/s. As mentioned the total dose in silicon per pulse is determined via a pin diode detector, thus the dose reported must be used and assumed to be correct. The fluence, Φ [electron / cm²], can be determined via equation 38 where the dose in a thin material, where the material thickness is much less than the electron range is given by,

$$D = 1.602e^{-10} \Phi \left(\frac{dT}{\rho dx} \right) \quad (38)$$

where the dose in Gy and the mass collision stopping power is in [MeV cm² / g electron]. For a single pulse the dose is 15 Gy and the mass collision stopping power for 15 MeV electron in silicon is 1.74 [MeV cm² / g electron]. Substitution yields a fluence of $5.38e^{10}$ [electron / cm²] per pulse. Similarly, the fluence, Φ [electron / cm²], can be determined via equation 39 where the average dose for electrons in a thick material where the material thickness is greater than the electron range in that material is given by,

$$\bar{D} = 1.602e^{-10} \frac{\Phi T_0 [1 - Y(T_0)]}{\rho t} \quad (39)$$

where the dose in Gy, T_0 is the initial electron energy perpendicular to the material [MeV], Y is the radiation yield, and ρt is the density times the material thickness. Given a single electron pulse, a ρt equal to 7.992 (continuous slowing-down approximation (CSDA) range of 15.0 MeV electrons in Silicon) [g/cm²], and a Yield of 0.1168 the calculated fluence is $5.65e^{10}$ [electron / cm²]. The calculated fluence values compare quite well, within 5%.

The electron energy loss and energy deposition in the material as a function of position in the TeO₂ crystal along the electron beam propagation axis can be determined. The CPEXS/ONELD code was run with a 15 MeV e-beam incident on a 0.8 cm thick TeO₂, results show the dose maximized at the center of the crystal at depth of 0.4 cm along the irradiation axis. The dose in pGy per 15.0 MeV electron (1 pGy = 0.1 μ rad) in TeO₂ as a function of depth into the AO Bragg cell along the electron beam propagation axis is shown in Figure 3-15.

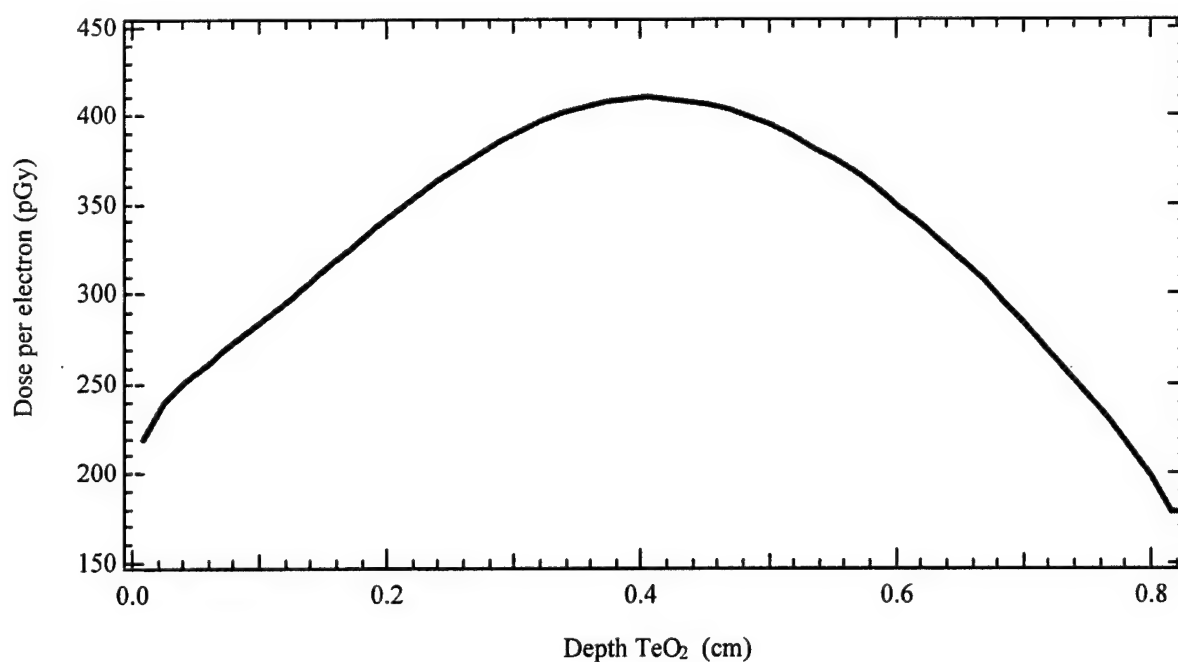


Figure 3-15. Dose in pGy per 15.0 MeV electron (1 pGy = 0.1 μ rad) in TeO₂ as a function of depth into the AO Bragg cell along the electron beam propagation axis (negative x direction in Figure 3-13).

From the plot it is clear that virtually all of the incident electrons were absorbed in the acoustooptic interaction volume (cell thickness = 0.794 cm) causing heating and the generation of thermal gradients. Similarly, results using the Integrated TIGER Series Transport Code,¹ where a 15 MeV Gaussian electron beam incident on a 5 cm thick TeO₂ crystal showed that the stopping power was maximized at 2.5584 MeV-cm²/g-source particle, at a depth of 0.5 cm.¹

As previously reported in detail, the diffraction efficiency and shifts in the image plane location of Bragg cell spatial intensities (I_0' and I_d) can result from electron induced thermal gradients.¹ Additionally, elevation of the cell crystal temperature alters the sonic velocity resulting in changes to the Bragg angle and as will be shown in the sections to follow is believed to alter the AO transducer efficiency. Temperature induced changes to the strain - optic tensor are also believed responsible for depolarizing the Bragg cell light intensities. Transient electron induced changes to the diffraction efficiency and degree of polarization may be determined via methods introduced in earlier sections.

The changes to the polarization states can be evaluated by casting the data shown in Figure 3-14 into Stokes parameter form. The different Stokes parameter responses are calculated using the Stokes Calibration factors and equations 27 through 28. The parameters are shown in Figure 3-16 as a function of time encompassing electron irradiation period to a total dose of 1.05 Mrad via 15.0 MeV electrons. The horizontal dotted lines show the pre-irradiation polarization state values and the vertical dotted depict the exposure time. The Stokes parameters are observed to fully recover to their pre-irradiation baseline values at approximately 500 s. Also, the S_3 parameter recovers faster than the other parameters and is fully recovered at approximately 300 s.

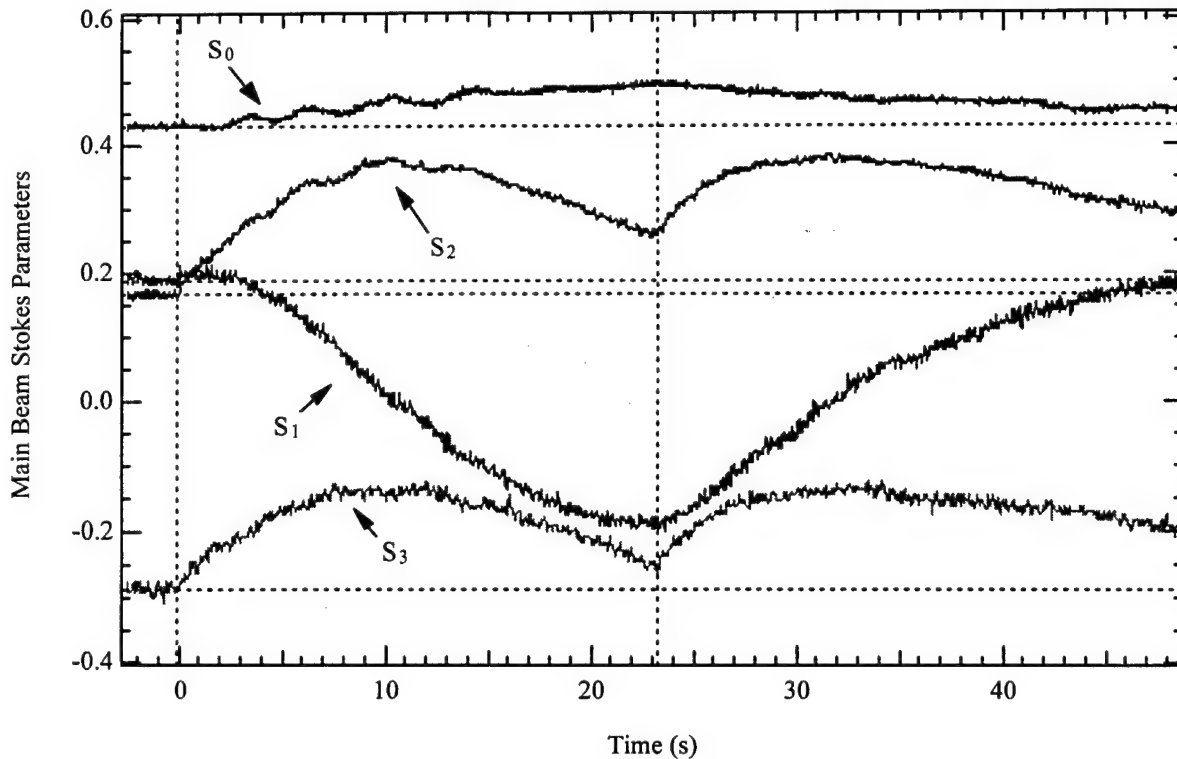


Figure 3-16. Stokes parameters as a function of time encompassing electron irradiation period. The different Stokes parameter responses are shown for a TeO_2 AO Bragg cell irradiated to 1.05 Mrad via 15.0 MeV electrons. The horizontal dotted lines show the pre-irradiation polarization state values. The vertical dotted lines depict the exposure time. The Stokes parameters are observed to fully recover to their pre-irradiation baseline values at approximately 500 s. The S_3 parameter recovers faster than the other parameters and is fully recovered at approximately 300 s.

The changes observed in S_0 indicate a change in the balance of the pre-irradiation proportions of input laser powers between the main and diffracted beams. The S_0 parameter is indicative of the total light - polarized and unpolarized - in the diffracted beam. The main and diffracted beams are observed to recover to approximately pre-irradiation values as early as 200 s after electron irradiation is ended. Since the main beam optical power was monitored before, during and after electron irradiation, the transient electron induced changes to the diffraction efficiency are readily attained using equation 23. The diffraction efficiency responses are shown in Figure 3-17. The horizontal dotted line shows the pre-irradiation values. The diffraction efficiency is observed to decrease during the electron exposure time and begin to recover to baseline

diffraction efficiency values at the cessation of electron irradiation. The diffraction efficiency is observed to recover to approximately pre-irradiation values as early as 200 s after the cessation of the electron irradiation.

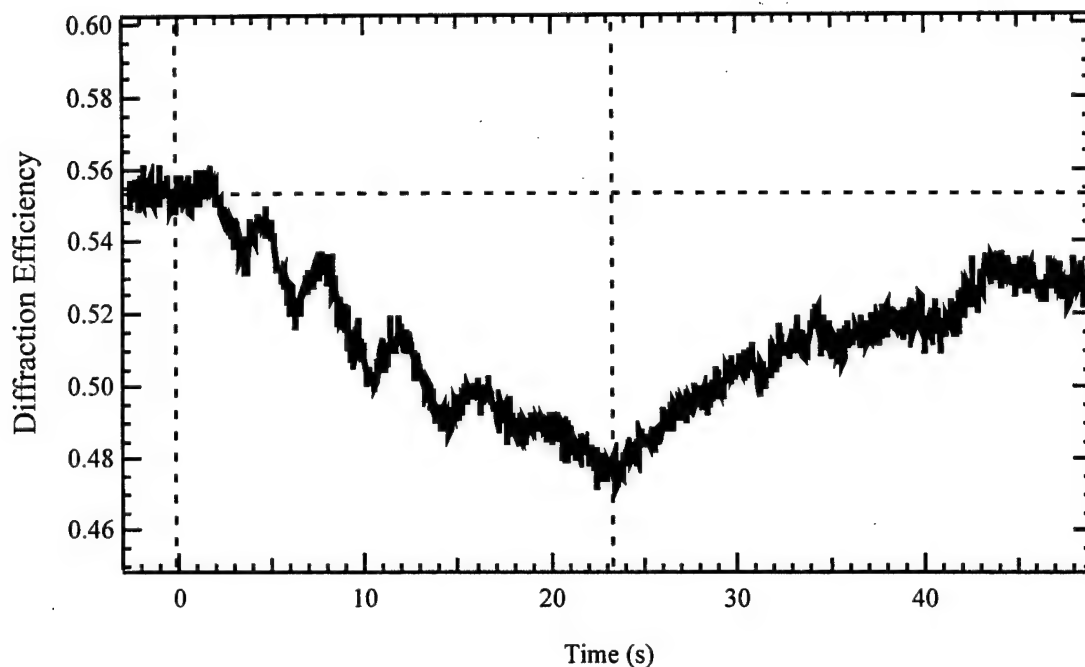


Figure 3-17. Diffraction efficiency responses shown for a TeO_2 AO Bragg cell irradiated to $D_e = 1.05$ Mrad. The horizontal dotted lines show the pre-irradiation diffraction efficiency values. The vertical dotted lines depict the 15.0 MeV electron exposure time. The relative diffraction efficiency is observed to recover to approximately pre-irradiation values as early as 200 s after cessation of the electron irradiation.

Using the data in Figure 3-14 and the Stokes analysis technique utilized in earlier sections the degree of polarization can be determined. Normalization of the polarized components of I_0' results in a value of $S_0 = 0.2481$, establishing the degree of polarization as 100% prior to the onset of electron exposure. From the data in Figure 3-14, the degree of polarization for the duration of the data taken was calculated and is shown in Figure 3-18. The degree of polarization at of I_0' ($t = 6.67$ s) was reduced to $P = 89.3\%$ for an electron

dose of $D_e = 270 \text{ krad(Si)}$. Again, the polarization is observed to recover to its baseline value at the cessation of electron irradiation.

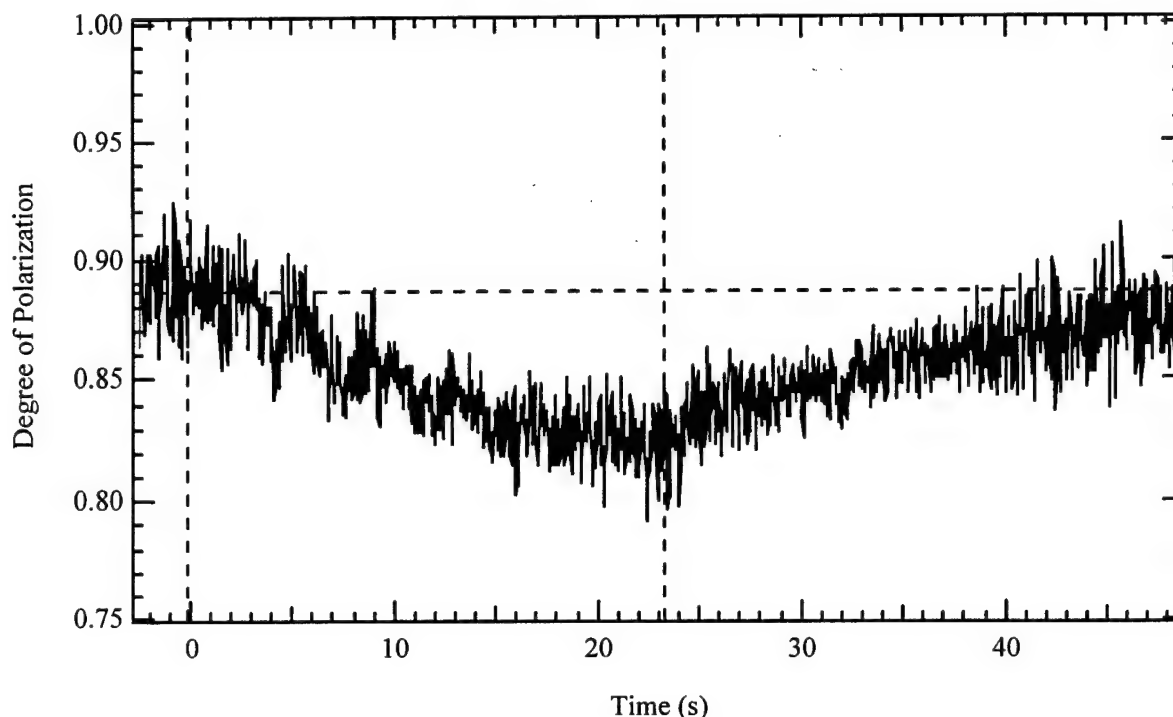


Figure 3-18. Degree of Polarization response is shown for a TeO_2 AO Bragg cell irradiated to 1.05 Mrad. The horizontal dotted lines show the pre-irradiation polarization state values. The vertical dotted lines depict the 15.0 MeV electron exposure time.

3.9 ANALYSIS OF POLARIZATION STATES EXITING AO BRAGG CELLS IN A GAMMA-RAY ENVIRONMENT

The exposure of two AO Bragg cells was accomplished at the AFRL/VSSE Gamma Irradiation Facility. The cells were exposed to the radiation emanating from the Cobalt-60 isotope. The exposure arrangement of a GaP Bragg cell modulator exposed to pulsed electrons is comparable to the arrangement shown in Figure 3-2. The PEMS were aligned such that the polarization states of the diffracted beam were investigated before, during and after gamma-ray exposure. The exposure arrangement of various TeO_2 Bragg cell modulator exposed to pulsed electrons is comparable to the arrangement shown in Figure 3-13, where the PEMS were aligned such that

the polarization states of the main beam were investigated in a gamma-ray environment. In both experiments all of the test equipment shown in Figure 3-2 must be shielded with the exception of the AO cell since the gamma-ray source is a broad area source.

3.9.1 Gamma Exposure of a GaP Acoustooptic Bragg Cell

The objective of this experiment was to actively measure polarization changes to the main beam (I'_0) output while exposing the GaP AO cell to gamma irradiation. In this instance, a Photoelastic Modulator (PEM) system was used to detect and analyze radiation induced polarization state changes, degree of polarization, and the radiation induced attenuation of I'_0 . The GaP device was exposed to a total dose of 1.0 Mrad(Si) without any indication of polarization changes or induced attenuation. This is illustrated in the data that is presented below. First, the DC1 and DC2 detector response voltages represent the total light, both polarized and unpolarized components, in the main beam, shown in Figure 3-19.

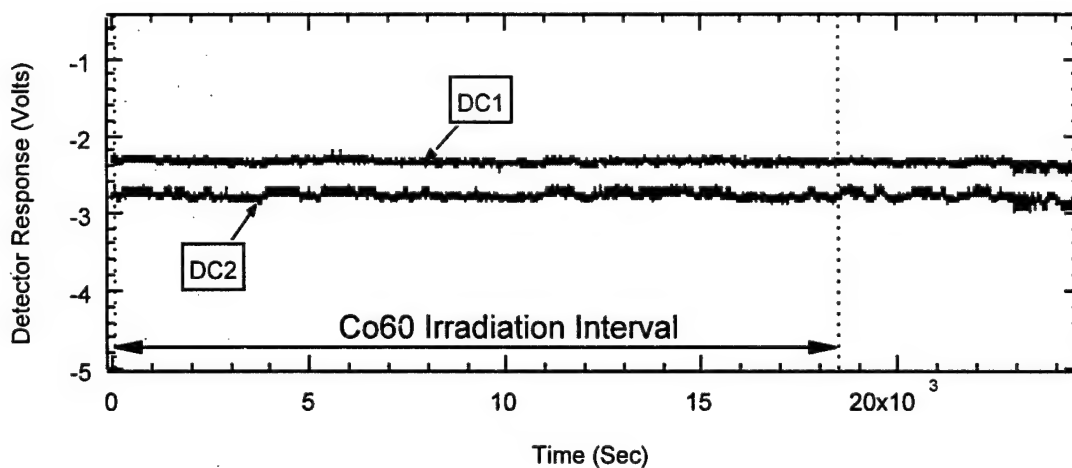


Figure 3-19. Detector response of the DC1 and DC2 components of the GaP AO cell are shown during the irradiation interval and recovery. The absolute values of the sum of the two components represent the total optical power of the main beam and no significant changes to the components are observed.

Note that there are no significant changes to the DC1 and DC2 detector response voltages over the course of the 1 Mrad(Si) gamma irradiation, thus the optical power in main beam is stable for

the duration of the gamma-ray exposure. This is also the case for the optical power in the diffracted and laser reference beams as illustrated in Figures 3-20 and 3-21, respectively

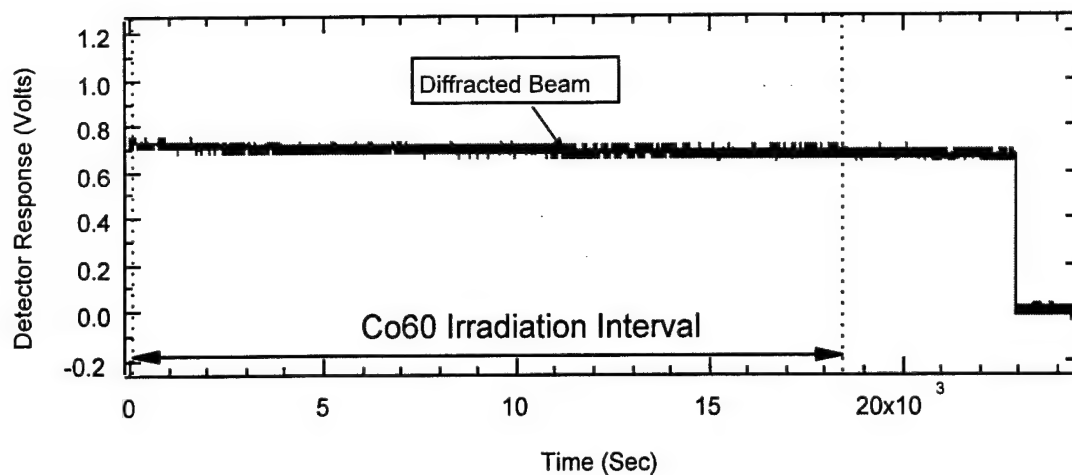


Figure 3-20. Shows the detector response of the diffracted beam of the GaP AO cell during gamma exposure (exposure shown between dotted lines) and recovery ($t > 18.5 \times 10^3$ s). The sharp drop in detector response indicates that the RF power was turned off ($t \geq 22.8 \times 10^3$ s). This detector response for the diffracted beam shows no effect during the irradiation interval.

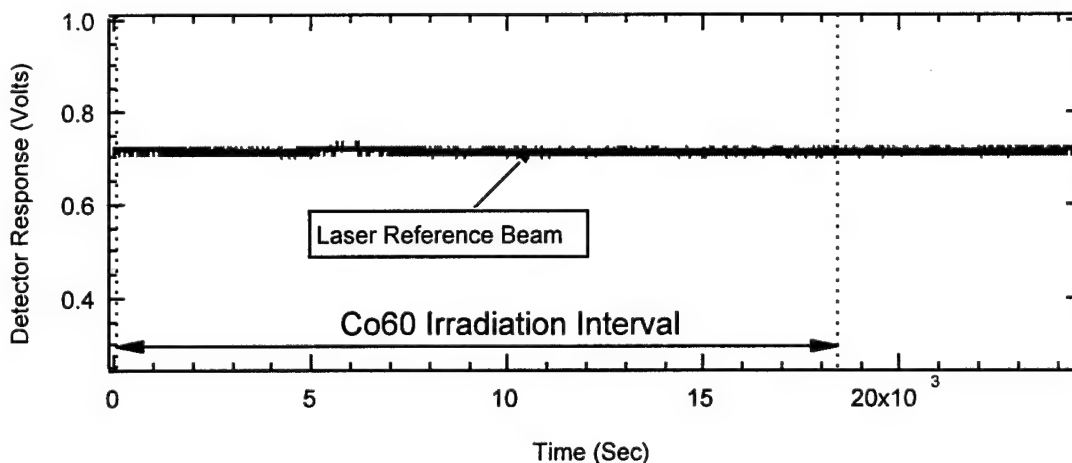


Figure 3-21. The detector response of the laser reference beam of the GaP AO cell during gamma exposure (exposure shown between dotted lines) and recovery is shown. This detector response for the laser reference beam shows no effect during the irradiation interval.

A slight decrease in the detector response voltage for the diffracted beam can be seen in Figure 3-20. The slight decreases in the detector response voltage tracks the slight decreases in the laser reference beam as shown in Figure 3-21. This is caused by a slight increase in the laser temperature, which will decrease the overall laser power output. Since, there are no significant changes to the DC1 and DC2 (optical power in the main beam) and the diffracted beam detector over the course of the 1 Mrad(Si) gamma irradiation, the diffraction efficiency of the AO Cell is stable for the duration of the gamma-ray exposure.

Note the drop in detector response in the diffracted beam optical power which indicates that the RF power was turned off ($t \geq 22.8 \times 10^3$ s) in Figure 3-20. This RF power-off consequence is noticeable in the plots of the polarization components of the main beam, horizontal/vertical linear horizontal, $+45^\circ$ and circular components shown in Figures 3-22, 3-23, and 3-24, respectively. Close examination of the DC1 and DC2 signals reveals the RF power-off as well.

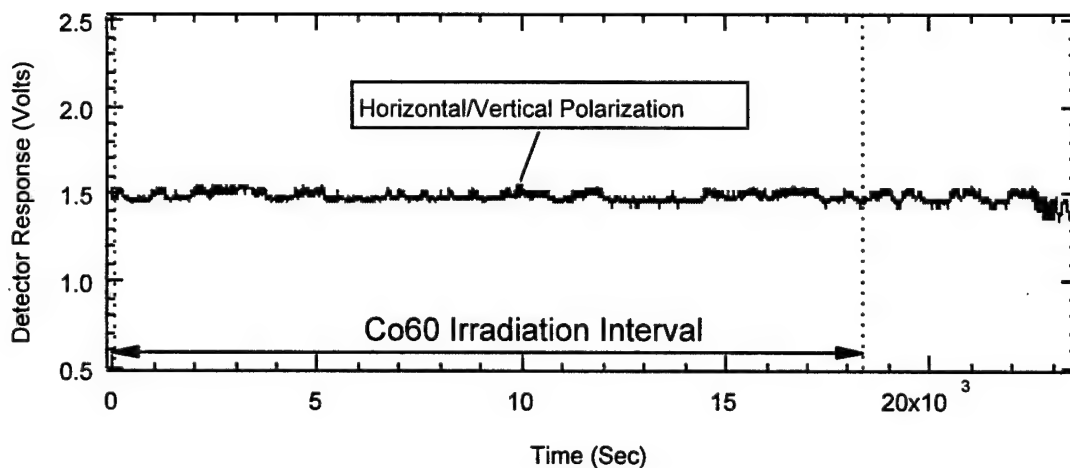


Figure 3-22. Shows the Horizontal/Vertical polarization of I'_0 of the GaP AO cell during (exposure shown between dotted lines) and after gamma exposure. Note that the Stokes parameter is unaffected during the irradiation interval.

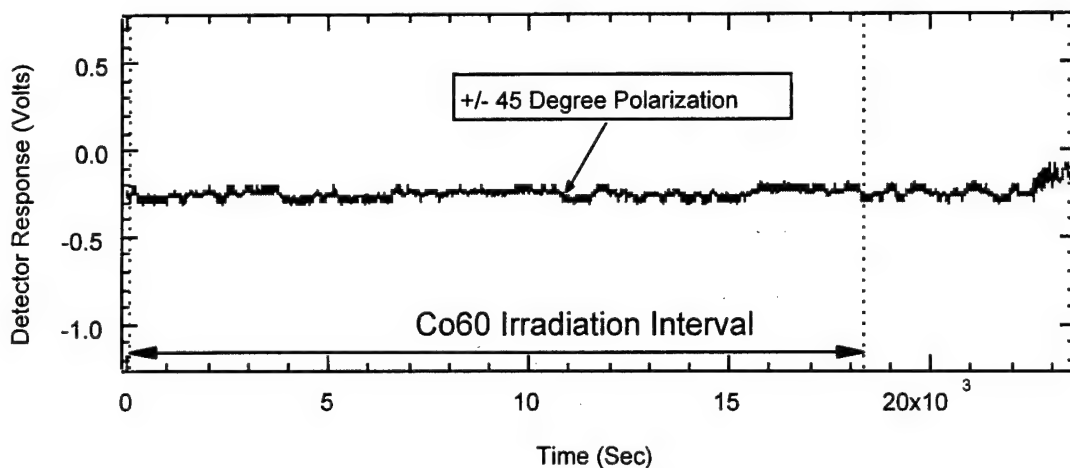


Figure 3-23. Shows the ± 45 degree polarization of I'_0 of the GaP AO cell during (exposure shown between dotted lines) and after gamma exposure. Note that the Stokes parameter is unaffected during the irradiation interval.

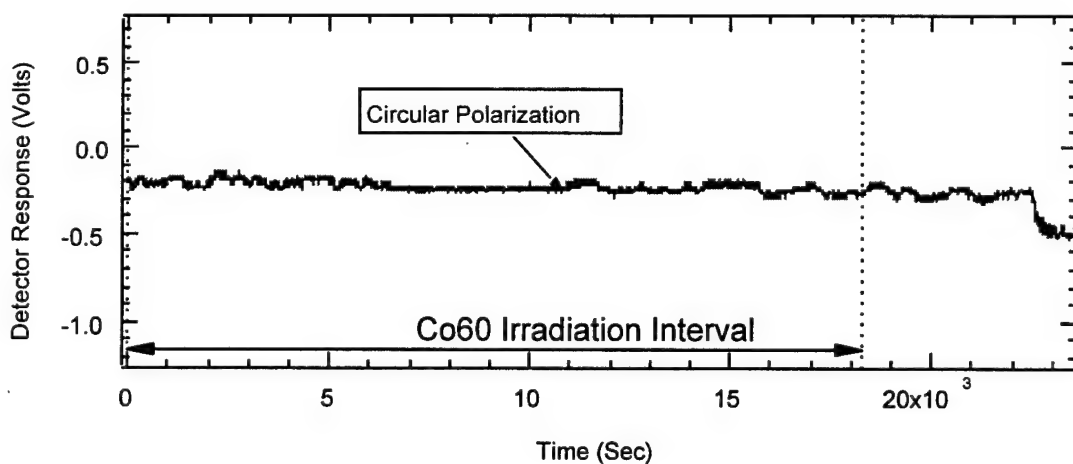


Figure 3-24. Shows the Circular polarization of I'_0 of the GaP AO cell during (exposure shown between dotted lines) and after gamma exposure. Note that the Stokes parameter is unaffected during the irradiation interval.

Figures 3-22, 3-23, and 3-24, show that the polarization states of the main beam are not affected by the gamma-ray irradiation of the AO cell. Thus, the Stokes components, degree of polarization and diffraction efficiency are also unaffected and further analysis is unnecessary.

3.9.2 Gamma Exposure of a TeO₂ Acoustooptic Bragg Cell

The objective of this experiment was to measure changes to the polarization state of the diffracted output beam, I_d , of a TeO₂ AO cell while actively irradiated by gamma rays. One primary challenge in performing this experiment was the calibration of the photoelastic modulator system (PEMS). This calibration is not a problem if the beam being analyzed is the main (undiffracted) beam. The alignment of the Bragg cell is straightforward since the PEMS are aligned and calibrated without the AO cell being in the laser beam. In this instance, the main beam can be easily analyzed when the AOM is inserted into the beam since the input and main beam are both parallel to the table top (Figure 3-25).

This procedure was used in the exposure of a GaP AO cell to gamma irradiation. When analyzing the diffracted beam the procedure is not as simple. There are two configurations options to consider: 1) insert the laser beam parallel to the table top and orient the PEM system with the diffracted beam, 2) tilt the laser such that the AO cell diffracted output is parallel to the table top. In case 1) it is very difficult to align the PEMS to a diffracted output beam which is emerging from the AO cell at $2\theta_B$. Also, the calibration of the PEMS requires a known polarization state into them (done by rotating a quarter wave plate through 360 degrees after a linear polarizer). This necessitates tilting the laser and associated beam conditioning optics into the PEMS at the angle that the diffracted beam would be later positioned. This requires that the laser output (and associated optics) be positioned at the location where the AO cell will later be placed. This condition is physically difficult to accomplish. In case 2) the laser and PEMS are first aligned parallel with respect to the bench top and calibrated. Next, the laser and conditioning optics are positioned at $2\theta_B$ with respect to the bench and the AO cell tilted to $-\theta_B$. Therefore, the emerging AO cell diffracted beam is parallel with respect to the tabletop and is re-injected directly into the PEMS. The important assumption in this case is that the polarization state of the laser and conditioning optics is not changed by repositioning from the parallel to table top to the $2\theta_B$ position. This alignment consideration is extremely important about θ_z ; since this is the orientation that determines the input polarization state injected into the AO cell, and ultimately the diffraction efficiency of the cell under investigation. Based on the above

discussion, case 2 was determined to be the most feasible and was used to perform this assessment. The laser used was a randomly polarized 20mW peak output HeNe.

The laser output was reduced by a neutral density filter (OD=1.0) mounted at approximately 5 degrees with respect to the axis of the laser output (to avoid feedback to the laser). Next, a Glan Thompson polarizer is aligned such that the polarization passed is horizontal linear with respect to the tabletop. The cross port reflection is picked off and used to monitor drift or changes in the laser output power. It is imaged onto a Si photodetector. The through port power (horizontal linear polarization) was routed into a quarter wave plate, which is then rotated through 360° for the purpose of calibrating the PEM system. After the PEM system has been calibrated (without the AO cell in line) the quarter wave plate is removed from the optics train. Therefore, the AO input laser beam polarization state was horizontal with respect to table top. This corresponded to vertical polarization with respect to base of AO cell, i.e., the base of the AO cell was normal to the radial output of the Cobalt 60 source. A representative schematic of the final experiment setup during gamma-ray irradiation is shown in Figure 3-25.

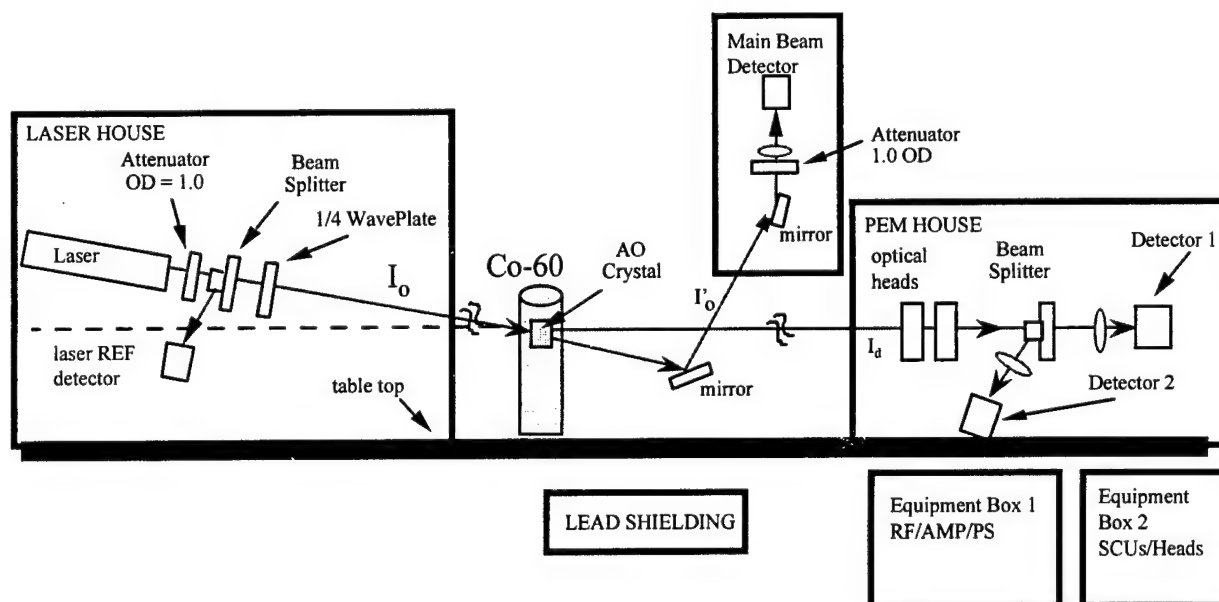


Figure 3-25. Experimental arrangement for gamma-ray exposure of the TeO₂ AO cell. Note that polarization state of the diffracted beam are monitored with the PEMS and the main beam is monitored with an optical detector.

The AO cell was irradiated to a total dose of 1.0 Mrad(Si) with no observable changes to the polarization in the diffracted output beam. The only observable effect was a small decrease in the AO cell temperature, which leads to a slight increase in the overall laser output power.

While no significant changes polarization components of the main beam, horizontal/vertical linear horizontal, +45° and circular components plot of the polarization components are shown in Figures 3-26, 3-27, and 3-28, respectively, for completeness.

The plots show that the polarization states of the main beam are not affected by the gamma-ray irradiation of the AO cell. Thus, the Stokes components, degree of polarization and diffraction efficiency are also unaffected and further analysis is unnecessary

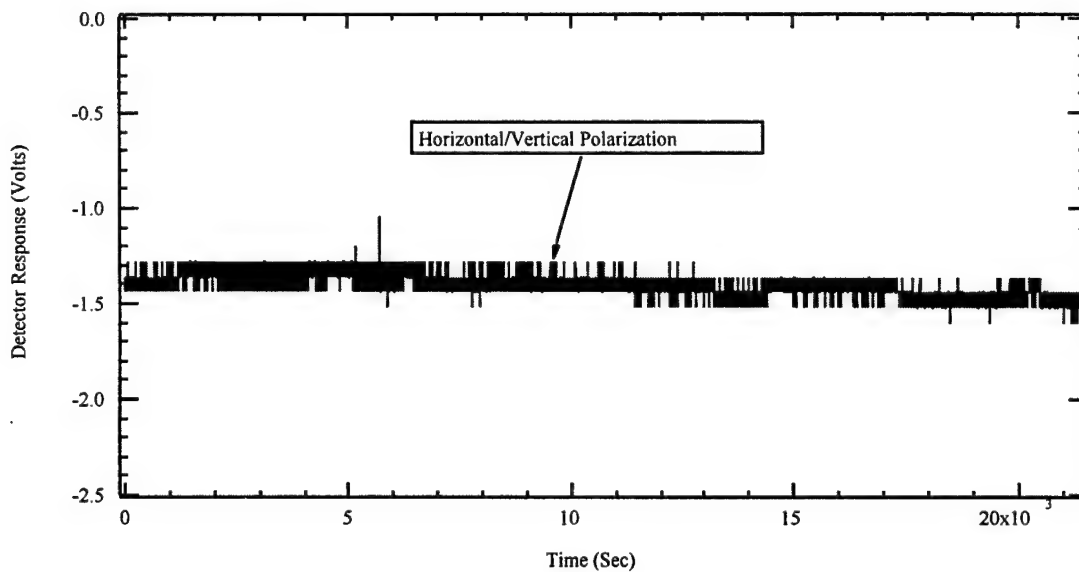


Figure 3-26. Detector response for Horizontal/Vertical polarization for the PEMS while irradiated to 1 Mrad(Si). Note that the Horizontal/Vertical component of the polarization state of the diffracted beam is unaffected during the gamma-ray irradiation.

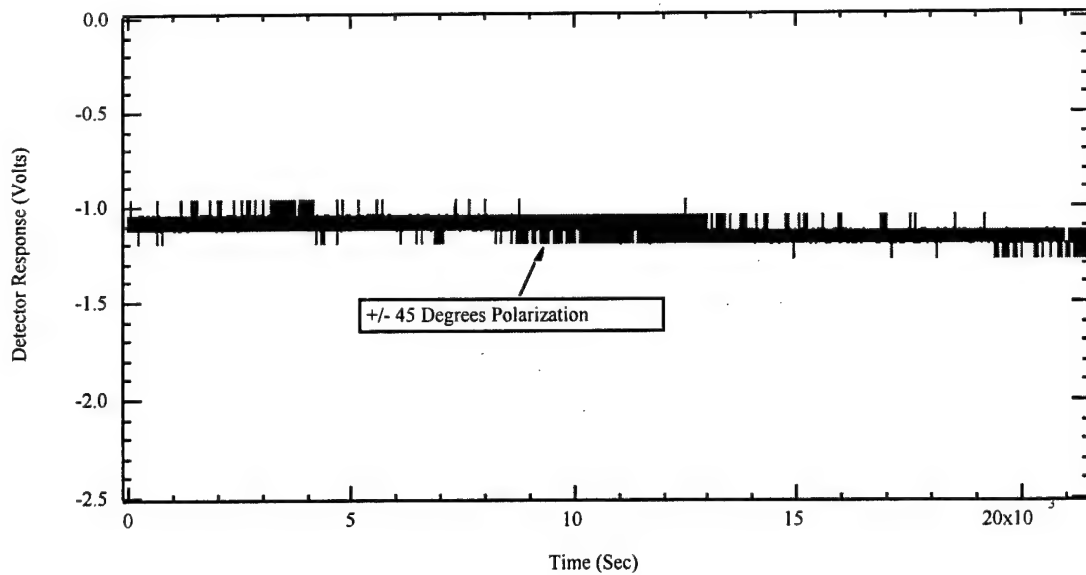


Figure 3-27. Detector response for ± 45 degree polarization for the PEMS while irradiated to 1 Mrad(Si). Note that the ± 45 degree component of the polarization state of the diffracted beam is unaffected during the gamma-ray irradiation.

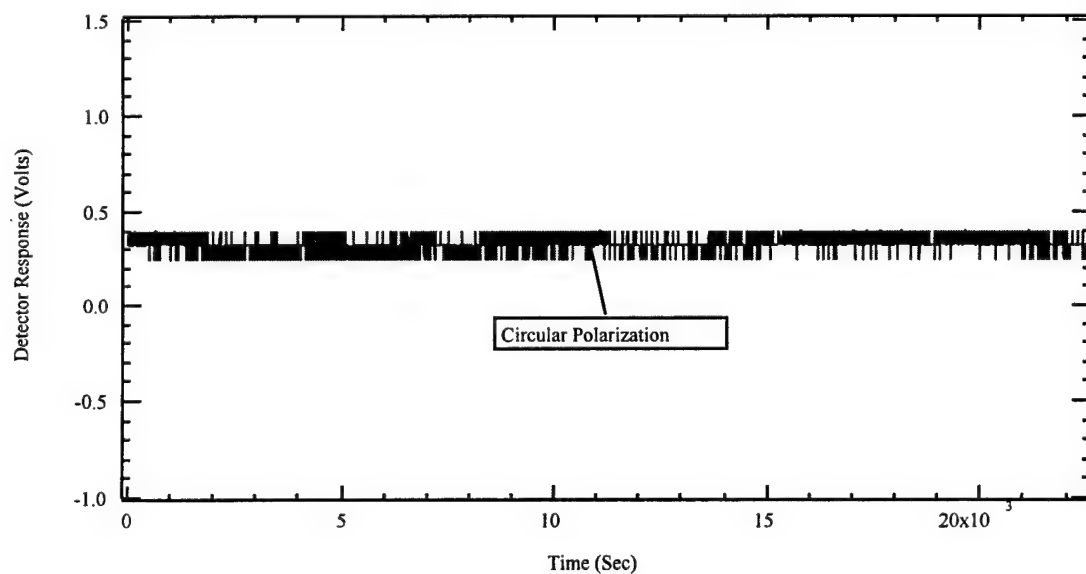


Figure 3-28. Detector response for circular polarization for the PEMS while irradiated to 1 Mrad(Si). Note that the circular component of the polarization state of the diffracted beam is unaffected during the gamma-ray irradiation.

4.0 RADIATION INDUCED BANDWIDTH RESPONSES IN ACOUSTOOPTIC BRAGG CELLS

4.1 EXPERIMENTAL ARRANGEMENT

Show in Figure 4-1, is an experimental arrangement used to measure the bandwidth response of an AO Bragg deflector (AOBD) exposed to pulsed electron irradiations.⁶¹ The PbMoO₄ deflector was operated at a center frequency $f_0 = 80$ MHz, and fixed at the Bragg angle, $\theta_B'(\text{air}) = 0.40^\circ$.

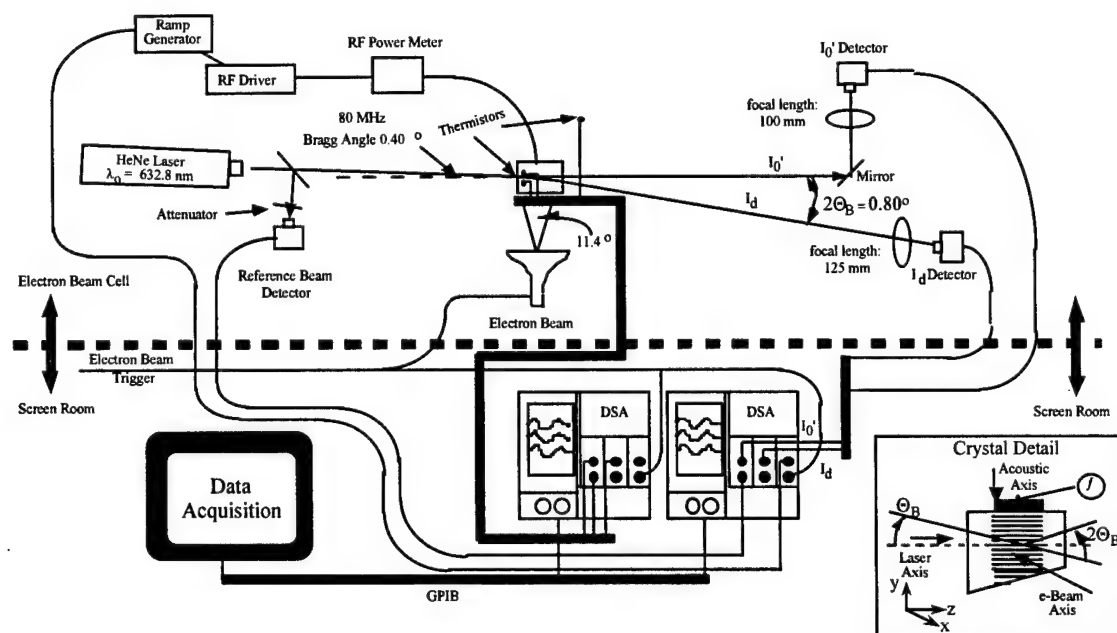


Figure 4-1. Experimental arrangement for measuring AO bandwidth and diffraction efficiency during exposure to pulsed electrons.

A laser of wavelength $\lambda_0 = 0.6328 \text{ } \mu\text{m}$ operating in the continuous mode illuminated the AOBD. The AOBD was exposed to pulsed electrons of 15 MeV average energy using the exposure geometry shown in Figure 4-1. This consisted of directing the electron beam normal to the laser beam and acoustic axes. The AOBD transducer was driven by a swept triangular frequency source ranging from 60 to 100 MHz and back to 60 MHz at a sweep rate of 60 Hz. Timing

between the linear electron accelerator and a pair of digitizing signal analyzers (DSAs) was provided. The device was optimized at f_0 , with an RF power of typically 1.0 ± 0.1 Watts applied across the swept band of frequencies. The non-irradiated AOBD bandwidth responses were measured under these conditions and are shown in Figure 4-2. Radiation induced responses were acquired while operating the AOBD in this manner and are also shown in Figure 4-2.

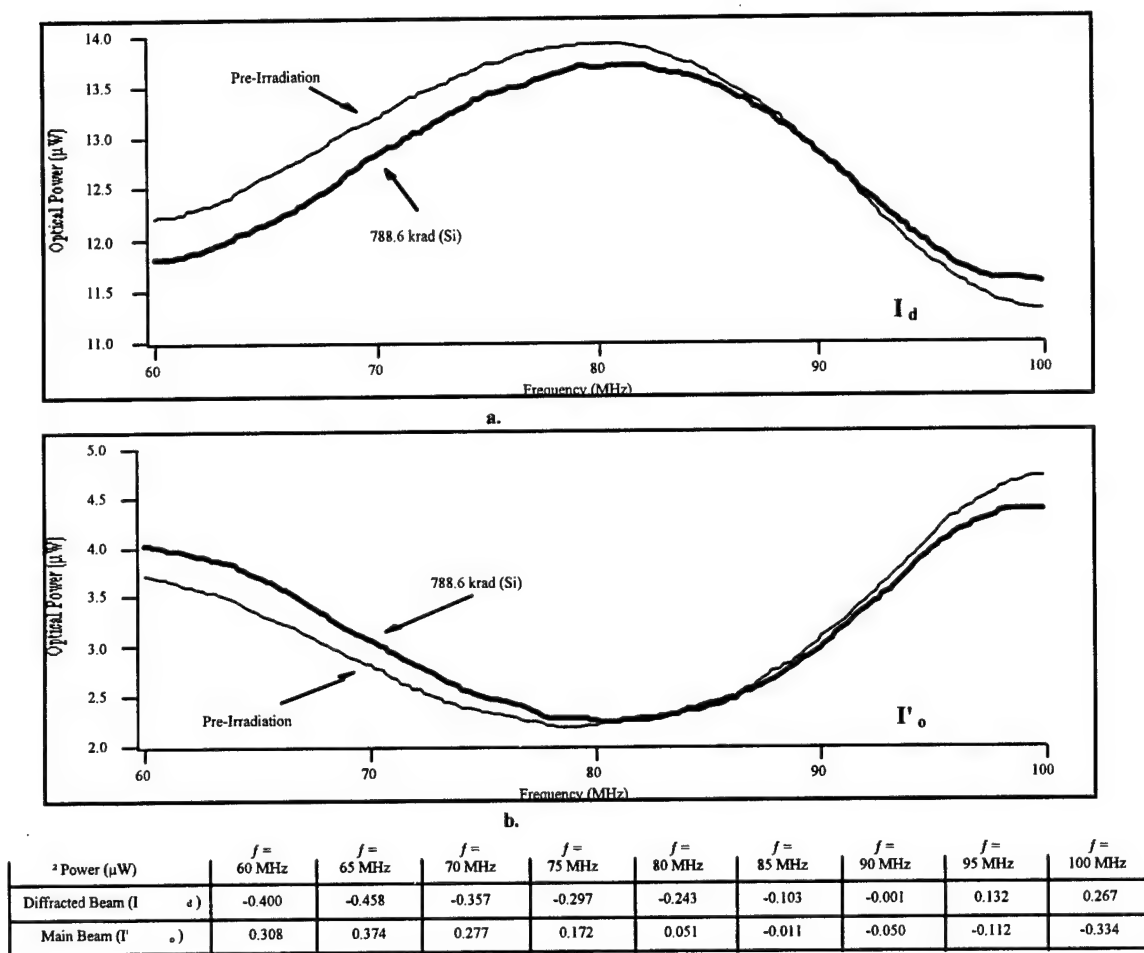


Figure 4-2. Responses of PbMoO₄ diffracted beam (I_d) is seen in (a) and the responses of the main in (b).

As shown in Figure 4-1, the first order diffracted light (I_d) and zero order light (I'_0) intensities were spatially separated and individually focused on different single element detectors (response time = 3 ns) during the frequency sweep. Care was taken to insure that all the light was collected. The resulting temporal traces were then displayed on the pair of DSAs and stored in

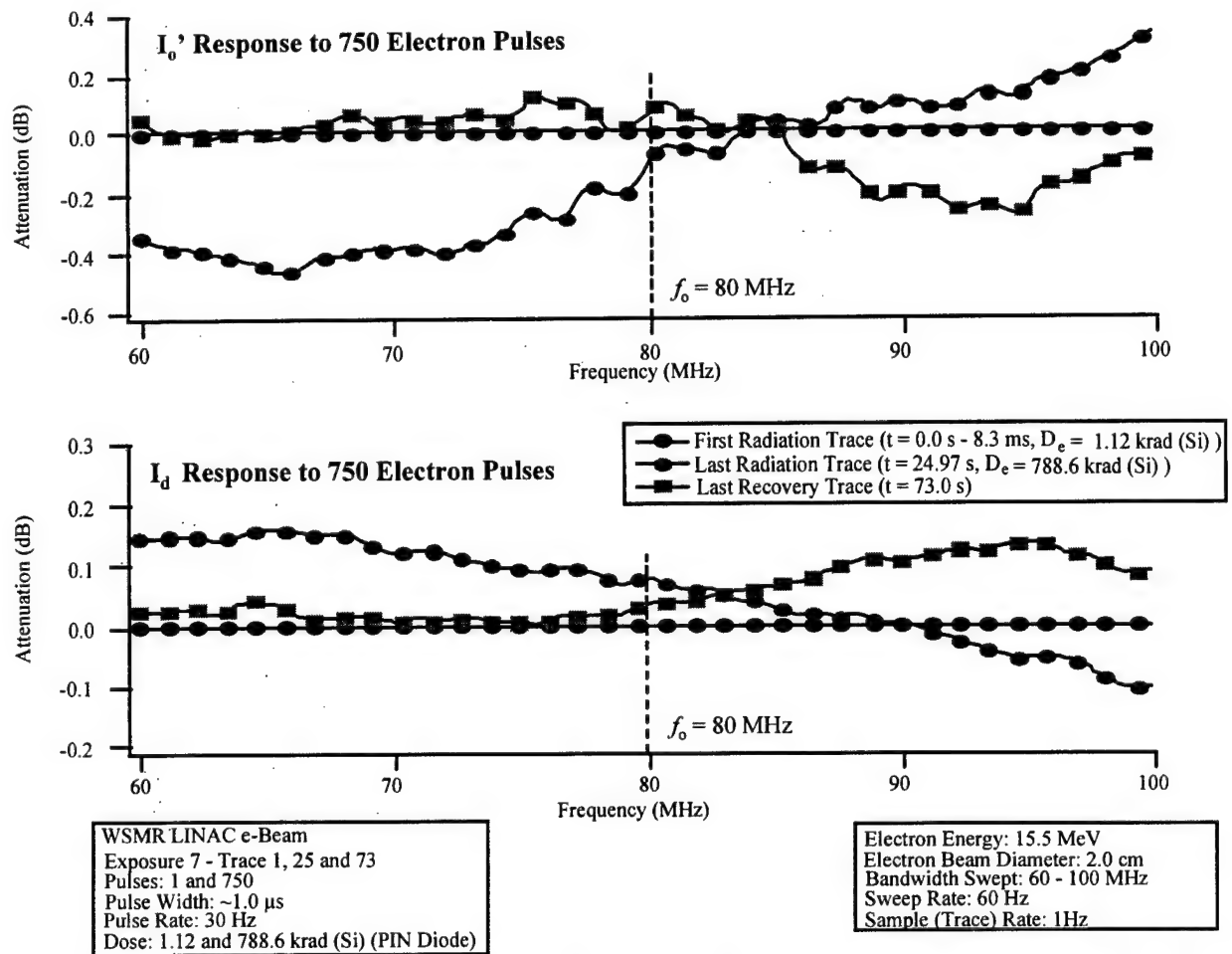
the computer system. These intensities were converted to optical power values for ease in data processing and for analysis.

Thermistors were located on the crystal face nearest the electron beam, on the back of the crystal mount and suspended in air near the back of the crystal mount. Temperature data was acquired for the entire time interval of the electron irradiation and during a portion of the I_d and I_0' recovery times following the cessation of irradiation. Detector voltages were sampled and stored at a frequency of 1 Hz. The data acquisition period included the entire radiation exposure period plus an arbitrary recovery period. The radiation-induced responses were stored to a floppy disk in the DSAs and also transferred to a computer system.

4.2 AO BANDWIDTH RESPONSES TO PULSED ELECTRON IRRADIATIONS

Figure 4-2 shows the pre irradiated responses of I_d and I_0' over the swept frequency range. This bandwidth response trace was acquired at the fixed Bragg angle of $\theta_B' = 0.40^\circ$. Typical swept frequency traces of the PbMoO_4 deflector transient responses for the main (I_0') and the diffracted (I_d) spatial intensities during exposure to a single electron pulse showed no change from the pre irradiation frequency response. Responses of I_d and I_0' were acquired at the end of 750 electron pulses ($t = 24.97$ s) and are also shown in Figure 4-2.

Normally, bandwidth measurements are performed under the reasonable assumption that I_0' remains invariant. However, we report here that this is not a valid assumption for an AO bandwidth measurement performed during pulsed electron irradiations. Both I_d and I_0' are altered due to these irradiations. We report for the first time, that correlated energy exchanges were observed to take place between I_d and I_0' during the pulsed electron irradiations. Generally, the power in the main beam was observed to increase, while the power in the diffracted beam decreased during the irradiations. However, there were exceptions to this behavior at the ends of the frequency range.



Attenuation (dB)	$f = 60 \text{ MHz}$	$f = 65 \text{ MHz}$	$f = 70 \text{ MHz}$	$f = 75 \text{ MHz}$	$f = 80 \text{ MHz}$	$f = 85 \text{ MHz}$	$f = 90 \text{ MHz}$	$f = 95 \text{ MHz}$	$f = 100 \text{ MHz}$
I_d Last Radiation	0.145	0.157	0.119	0.092	0.077	0.030	0.001	-0.056	-0.101
I_d Last Recovery	0.023	0.041	0.007	0.005	0.034	0.063	0.103	0.134	0.087
I_o' Last Radiation	-0.347	-0.455	-0.389	-0.283	-0.100	0.040	0.102	0.134	0.319
I_o' Last Recovery	0.048	-0.011	0.044	0.082	0.066	0.026	-0.201	-0.254	-0.081

Figure 4-3. Swept frequency bandwidth responses for PbMoO_4 AOD. As may be observed, immediately following an electron dose $D_e = 788.6 \text{ krad(Si)}$ I_d is attenuated nearly across the swept frequency range (60-84 MHz), while I_o' is seen to gain over this frequency range. The recovery of both I_d and I_o' signals back to their pre-irradiation baselines is not complete at $t = 73 \text{ s}$.

Figure 4-3 illustrates the recovery ($24.9 \text{ s} \leq t \leq 73 \text{ s}$) of I_d and I_o' following an electron dose of $D_e = 788 \text{ krad(Si)}$ as shown in Figure 4-2. Response curves in Figure 4-3 were also obtained during and following a single ($\approx 1.0 \mu\text{s}$ FWHM) electron pulse which provided a dose $D_e = 1.12 \text{ krad(Si)}$. The shape and magnitude of the I_d and I_o' bandwidth response curves resulting from

the single electron pulse exposure were indistinguishable from the non-irradiated bandwidth responses. These low dose response curves were used as baselines to which the high dose response curves were compared. Here, the frequency swept responses of I_d and I_0' after cessation ($t > 25$ s) of the 750 electron pulses are shown as attenuation (dB) or gain (-dB). As may be observed, complete recovery at high dose exposure was incomplete at $t = 73$ s. This long-term recovery behavior is attributed to radiation induced heating of the AOBD and is discussed in the analysis. The AOBD crystal experienced a peak induced temperature change of $\Delta T = 10.5^\circ\text{C}$ for a dose of $D_e = 788.6$ krad(Si). Figure 4-4 depicts the measured temperature responses on or near the AOBD.

In the high dose data curves of Figure 4-3, there are noticeable changes in I_d and I_0' above and below f_0 and at f_0 . Examining the I_d and I_0' bandwidth regions below $f \sim 90$ MHz, it is observed that I_d is attenuated. Correspondingly, the optical power in I_0' is increased over this frequency range. Examining the bandwidth region above $f \sim 80$ MHz, I_d begins to approach the pre-irradiation signal level (0 dB) at $f \sim 88.9$ MHz, and gains signal for $f > 88.9$ MHz.

Correspondingly, I_0' is observed to also gain power for $f < 84$ MHz and decrease in power for $f \sim 84$ MHz. The exchanges of energy between the diffracted and throughput beams indicate that the diffraction efficiency changed across the bandwidths studied. The mechanisms responsible for these exchanges are discussed in the next section.

Following the cessation of the electron pulses, significant recovery of I_d and I_0' is realized at $t = 73$ s. Due to time limitations imposed by the data acquisition system, longer recovery times could not be studied. The rapid recovery of the diffraction efficiency indicated that the long term ($73 \text{ s} < t < 1000 \text{ s}$) slowly decaying elevated temperature measured in the crystal and the crystal mount did not contribute significantly to the transient changes to the diffraction efficiencies. Permanent attenuation of the intensities over the bandwidth studied was not believed to have occurred, since previous measurements¹⁻³ for the same PbMoO_4 AO device reported the absence of permanent attenuation for comparable electron irradiations.

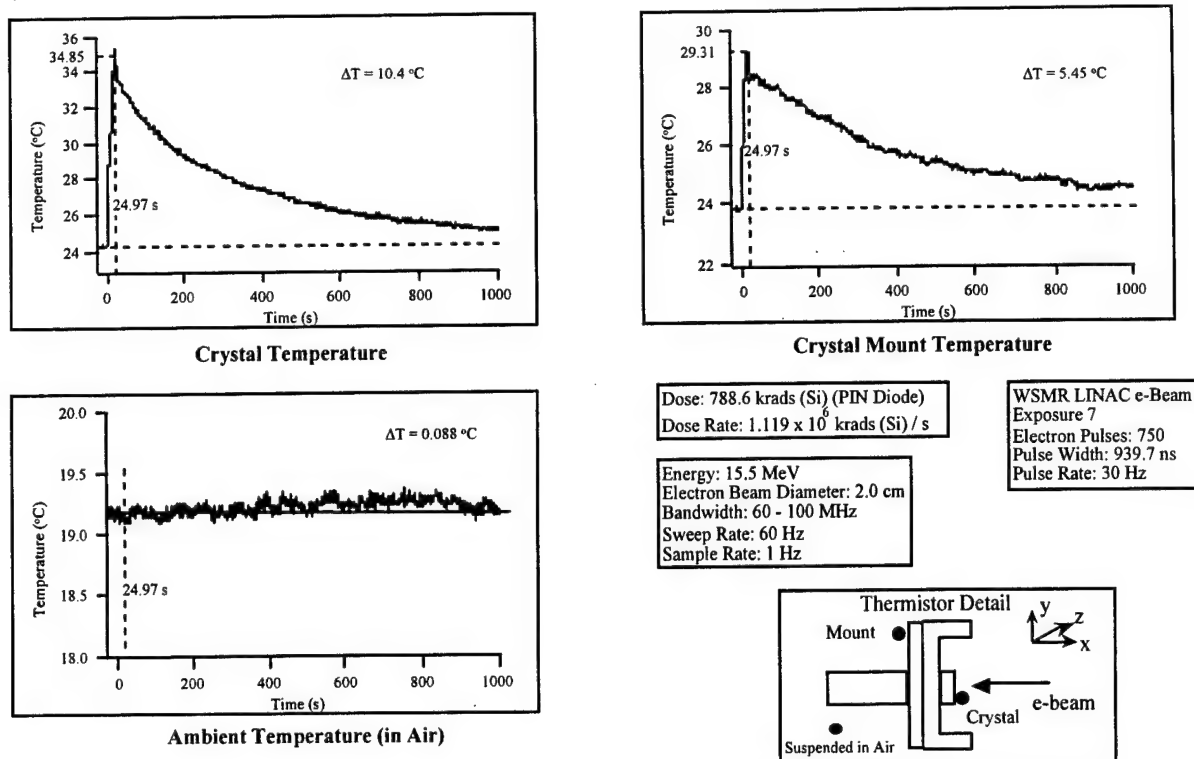


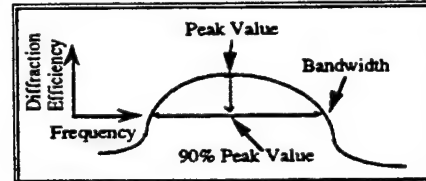
Figure 4-4. Temperature responses on and near the PbMoO_4 AOBD.

Simultaneous with the measurements of I_d and I_0' , electron induced heating of the deflector and the deflector mount were measured. Figure 4-4 illustrates that the maximum temperature rise of the deflector crystal was $\Delta T = 10.4\text{ }^{\circ}\text{C}$ at $t = 25\text{ s}$ for $D_e = 788.6\text{ krad(Si)}$. An exponential decrease in temperature, short of reaching the pre-irradiation level was observed for a period extending to $t < 1000\text{ s}$. Since the recovery of the AO bandwidth responses was nearly complete at $t = 75\text{ s}$, the long-term temperature increase of the AO cell was not believed to be a factor in the recovery process. However, short-term electron induced transient temperature gradients were believed to affect the change in diffraction efficiency, and this aspect is discussed in the analyses. Shown in Table 4-1 is a summary of the radiation-induced changes observed for different electron doses. The bandwidth measured at 90% (peak value) was seen to decrease for increasing D_e , while the diffraction efficiency was changed across the swept bandwidth.

Table 4-1. Summary of radiation induced changes to the AODB diffraction efficiencies, frequency response, and bandwidth.

krad (Si)		60 MHz LF Minimum	80 MHz Center Frequency	100 MHz HF Minimum	Bandwidth*	ΔT Temperature
0	Frequency Shifted to: Diffraction Efficiency	77.26%	79.19 86.46%	69.57%	29.83 MHz	0.0° C
196.6	Frequency Shifted to: Diffraction Efficiency	76.96%	78.636 86.46%	69.47%	28.182 MHz	3.6° C
396	Frequency Shifted to: Diffraction Efficiency	75.09%	79.882 85.77%	71.24%	28.165 MHz	6.0° C
475.6	Frequency Shifted to: Diffraction Efficiency	74.80%	79.653 85.67%	71.57%	26.359 MHz	6.9° C
788.6	Frequency Shifted to: Diffraction Efficiency	74.70%	80.476 85.98%	72.61%	27.62 MHz	10.5° C

*To determine bandwidth, a value that is 90% the peak center frequency value is computed. The curve will achieve this value twice, to either side of the center frequency. The distance, in frequency, between these two points is the bandwidth.



4.3 ANALYSIS OF DIFFRACTION EFFICIENCY - BANDWIDTH RESPONSES

In this analysis, the assumptions are made that the sound velocity of the AOBD is affected solely by the radiation induced heating and not by other radiation induced material processes. This is reasonable since other data^{1,3} have indicated that PbMoO_4 is only transiently affected by electron irradiations. Care was taken not to irradiate the AOBD transducer and it is assumed that the transducer output power was not changed by the irradiation induced heating. An ongoing series of experiments is underway to confirm these assumptions as valid. Under these conditions, the analysis herein provides a good starting point for understanding the experimental data.

The Bragg angle in the AO cell is given as:

$$\Theta_B = \sin^{-1} \left(\frac{\lambda_0}{2n\Lambda} \right) \quad (40)$$

Where n and Λ are the refractive index and acoustic wavelength in the AO crystal. Equation 40 may also be expressed in terms of the sound velocity (V) and frequency (f) of the AOBD as:

$$\Theta_B = \sin^{-1} \left(\frac{\lambda_0 f}{2nV} \right) \quad (41)$$

Radiation induced Bragg angle changes were especially pronounced in the data reported for PbMoO_4 and TeO_2 modulators and deflectors.^{1,3} An hypothesis has been advance that radiation induced heating can occur, causing changes to the sonic velocity of the AO crystal. In this instance the AOBD deflection angle will change in accordance with the temperature coefficient of velocity given as:

$$\frac{1}{V} \frac{dV}{dt} \quad (42)$$

The temperature coefficient of velocity for PbMoO_4 is known to be $-161 \times 10^{-6} \text{°C}^{-1}$ and $175 (\pm 20\%) \times 10^{-6} \text{°C}^{-1}$ for TeO_2 in the longitudinal modes.²⁷ Radiation induced heating can also contribute to the changes of the AOBD crystal refractive index. Depending on the cell geometry, heat sinking, and changes of absorption with temperature, the light propagation can be changed due to induced temperature gradients.

An explanation for the variances observed in the diffraction efficiency may be in part argued from the previous data reported by Taylor et al,^{1,3,42-45} where, radiation induced thermal gradients were shown to be responsible for creating an index of refraction gradient. In PbMoO_4 , the temperature coefficient of index $[(1/n) / (dn / dT)]$ is negative and the index change is given²⁷ as $dn / dT = -71.58 \times 10^{-6} \text{°C}^{-1}$ for the ordinary ray directions. This would indicate that the refractive index of the crystal medium is lowered due to the electron induced volumetric heating. In TeO_2 , $dn/dT = 10.27 \times 10^{-6} \text{°C}^{-1}$ (ordinary ray direction, $n_0 = 2.2597$) and the index change is known to be $dn / dT = 160 \times 10^{-6} \text{°C}^{-1}$ for GaP. Bandshapes for AOBDs comprised of these materials were observed to change under pulsed electron irradiations. While only the analysis of

PbMoO₄ responses will be considered in this section, the same treatment is valid for TeO₂ and GaP.

In addition to the volumetric heating, the presence of a spatially dependent index gradient (or gradients) arising from the electron deposition of heat and the dissipation of heat is possible. This hypothesis has been independently confirmed using CO₂ laser heating to simulate the electron heating.⁴⁹ Thus, radiation induced spatial index gradients introduced across the optical beam - acoustic interaction volume cause gains or losses to the diffraction efficiency. Over a given AO interaction length, the spatial index gradient (ϕ) can be expressed as:

$$\phi = \frac{dn}{dx} \quad (43)$$

Equation 43 expresses a one - dimensional linear refractive index gradient along the path (x-direction) of the incident electron radiation (Figure 4-1). Equation 43 can also be expressed in terms of the index and temperature gradient along x by the expression:

$$\phi = \frac{\frac{dn}{dT}}{\frac{dT}{dx}} \quad (44)$$

By using these relationships, the magnitude of the beam (angular) deflection due to the induced heating can be determined as $\sim 1.13 \times 10^{-3}$ radians for an electron dose of $D_e = 788.6$ krad(Si). Normally, these effects arise from transducer heating or absorption of the optical beam in AO materials with high absorption coefficients at the laser wavelength and are compensated for by transducer design. Radiation induced heating of the AOBD can also cause changes to the sonic velocity and crystal refractive indices. This may result in changes to the Bragg angle and transient attenuation of the diffraction efficiencies. While a linear spatial gradient is assumed, in actuality the deposition of heat by the electron beam may not be linear.

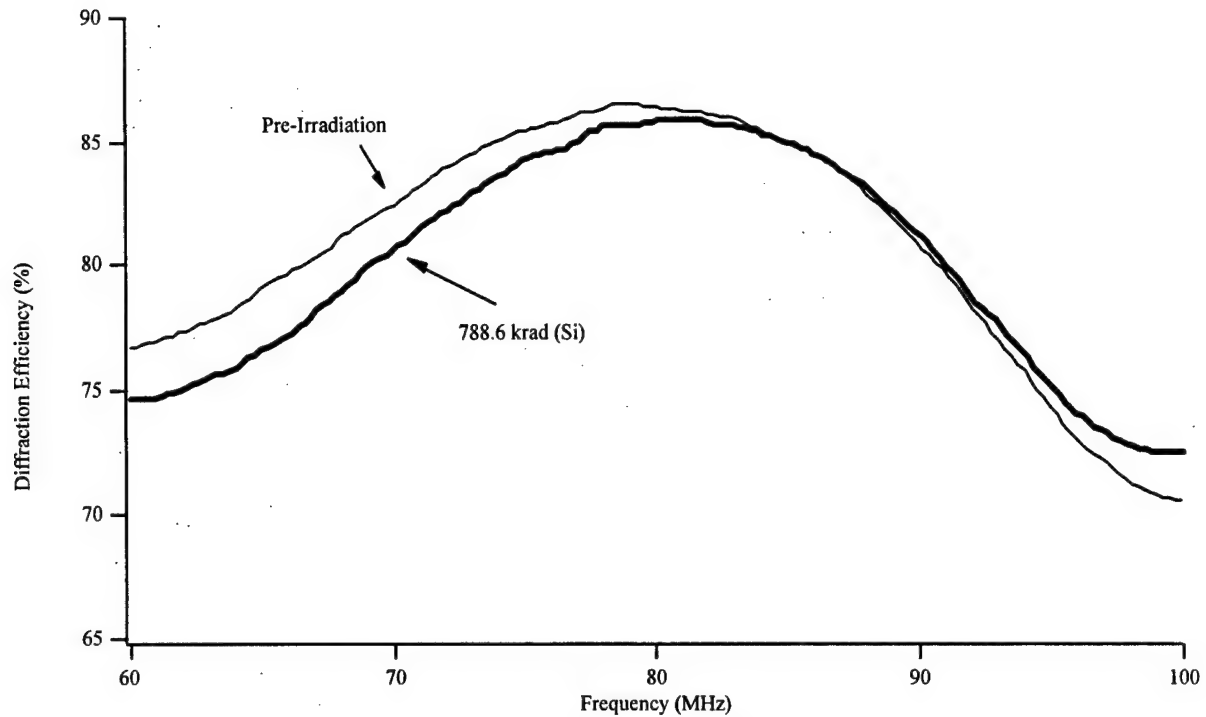
Heating of the crystal and the crystal mount by the electron irradiations are believed to have caused temperature gradients that increased or decreased the diffraction efficiency. Heating of the transducer would also effect the diffraction efficiency (see Section 5.0 - Overview of Ion Beam Exposures of AO Bragg Cells). The diffraction efficiency, η , of the acoustic - optic interaction measured external to the AO medium as shown in Figure 4-1 prior to the onset of electron irradiations is given by the expression,

$$\eta = \sin^2 \left(\frac{\pi \Delta n L}{\lambda_0} \right) \quad (45)$$

Where the Δn is the acoustic perturbation of the AO material refractive index and L is the width of the acoustic column. The diffraction efficiency can also be related to the ratio of the diffracted and main beam spatial intensities via Equation 8 in section 2.2, where I_d and I_0' are directly measured by two photo detectors as illustrated in Figure 4-1. The argument in Equation 45 predicts that η may either decrease or increase depending on the magnitude of Δn . For values of $0 \leq (\pi \Delta n L / \lambda_0) \leq \pi/2$, η increases, while for values of $\pi/2 \leq (\pi \Delta n L / \lambda_0) \leq \pi$, η decreases.

4.4 LASER HEATING - SIMULATION OF ELECTRON INDUCED EFFECTS

As observed in Figure 4-2, the deflector spatial intensities did not remain invariant during or following the electron irradiations. Using Equation 45, the diffraction efficiencies may be calculated from the magnitudes of the spatial intensities over the swept frequencies shown in Figure 4-2, and plotted as shown in Figure 4-5. It has been reported that the recovery from radiation induced color center attenuation for the I_d and I_0' beams is on the order of ~ 20 ms. Therefore, the changes to the diffraction efficiency for times after the cessation of the electron irradiation (as shown in Figures 4-2, 4-3, and 4-5) are believed due to the heating effects discussed above.



Frequency	60 MHz	65 MHz	70 MHz	75 MHz	80 MHz	85 MHz	90 MHz	95 MHz	100 MHz
Diffraction Efficiency (%)	-2.080	-2.462	-1.846	-1.196	-0.483	-0.046	0.225	0.750	1.97

Figure 4-5. Swept frequency responses of PbMoO_4 diffraction efficiency following pulsed electron irradiations.

A CO_2 laser was used to simulate the electron induced heating experienced by the PbMoO_4 AOBD. Figure 4-6 shows the effects on the diffracted intensity of a PbMoO_4 AOBD due to CO_2 heating of the AOBD crystal while the RF input to the AOBD was frequency swept from 60 MHz to 100 MHz. The maximum effect relative to the baseline, can be described qualitatively as follows: (1) The peak intensity decreases, (2) the frequency of the peak intensity shifts up on the order of 1 MHz, (3) the intensity at the higher end of the sweep increases, (4) the intensity at the lower end of the sweep decreases slightly. The intermediate effect, however, is different in three of the four areas: (1) the peak intensity remains the same, (2) the frequency of the peak intensity remains approximately the same, (3) the intensity at the higher end of the sweep increases, and (4) the intensity at the lower end of the sweep increases. In these experiments, the temperature of

the AOBD crystal was measured by a single thermistor in contact with the crystal at the lower edge closest to the optical probe ($\lambda_0 = 0.6328 \mu\text{m}$) input beam. The thermistor indicated a maximum temperature increase of 0.8°C at that point with a CO_2 laser power of 60 mW in a 2 mm diameter beam incident on the middle of the outside face of the crystal.

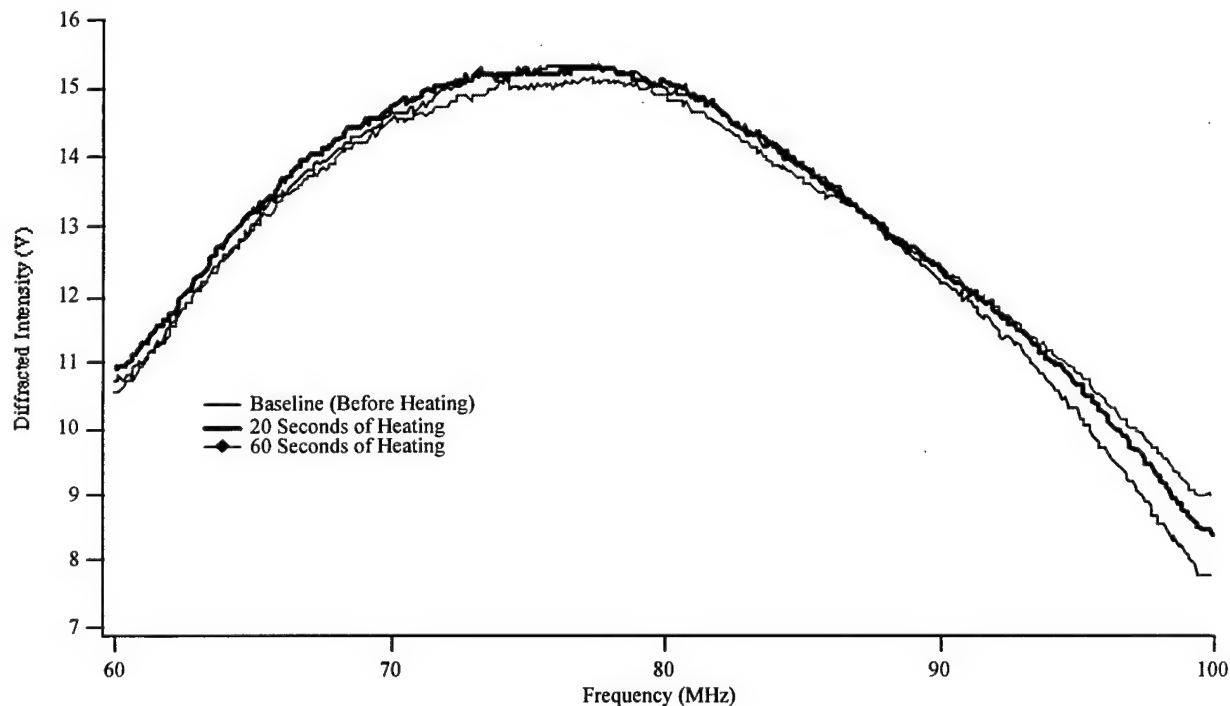


Figure 4-6. Effect of the CO_2 laser heating of a PbMoO_4 acoustooptic Bragg Deflector. Here the diffraction efficiency of the AOBD across the swept frequency range (60 - 100 MHz) is shown to change as the AO crystal is heated. The temperature increase at the edge of the crystal was approximately 0.8°C above the ambient baseline for 60 s of heating.

The qualitative behavior described above for the maximum effect due to the CO_2 laser heating in Figure 4-6 tracks the behavior of the diffracted beam under electron irradiation in Figure 4-2a in all four areas. Although heating of the AOBD crystal by the electrons and laser were not identical, the induced responses correlated very well.

4.5 SUMMARY OF RESULTS

The first observation of the transient bandwidth responses of an acoustooptic Bragg cell exposed to electron irradiation is reported. Pulsed electron exposures of a frequency swept PbMoO_4 deflector resulted in transient changes to the deflector bandwidth, diffraction efficiency and bandshape. Measured at the 10% points, the bandwidth was observed to decrease for increasing electron dose. The peak diffraction efficiency was also measured to decrease from a non-irradiated value of 86.46% to 85.98% at an electron dose of 788.6 krad(Si). The peak diffraction efficiency was also observed to shift from 79.19 MHz (non-irradiated) to 80.476 MHz following an electron dose of 788.6 krad(Si). An explanation of the physical mechanisms responsible for the observed effects has been presented. Radiation induced thermal gradients caused the formation of refractive index gradients. These spatially dependent index gradients altered the index grating formed by the acoustic signal thereby increasing or decreasing the diffraction efficiency. Radiation induced heating responses were independently confirmed using a CO_2 laser and the results were observed to correlate.

This page intentionally left blank.

5.0 OVERVIEW OF ION BEAM EXPOSURES OF AO BRAGG CELLS

This section will report on radiation induced effects in acoustooptic (AO) devices operating under Bragg conditions while exposed to protons from an ion microbeam. These effects include transient changes to: attenuation, bandwidth, diffraction efficiency, deflection angle, and polarization states of the output beams; see "Radiation Induced Bandwidth Responses in Acoustooptic Bragg Cell," by Taylor, et al.⁶¹ and papers cited therein. Various AO Bragg devices composed of PbMoO_4 , TeO_2 , InP , GaP , and LiNbO_3 have been investigated using an ion microbeam. The responses of PbMoO_4 were found to closely parallel those observed earlier using broad area sources as well as a CO_2 laser to simulate radiation-induced thermal effects.⁴⁹ However, use of the ion microbeam allowed very localized regions of the AO devices to be irradiated. Thus we were able to ascertain the effects of radiation induced heating in the transducer regions of the AO device. As a result, thermal changes to the transducer of $\sim 3^\circ\text{C}$ were observed to result in oscillatory perturbations to the AO device diffraction efficiency.

5.1 EXTERNAL ION BEAM ANALYSIS

The proton exposure of the AO devices were performed at the Sandia nuclear microbeam facility. Sandia National Laboratory's nuclear microprobe can deliver ions ranging from protons up to Gold ions with energies ranging from 0.5 MeV to 60 MeV. Figure 5-1 shows a layout of the Ion Beam Material Research Laboratory (IBMRL) and the nuclear ion micro-probe station. The available ion beam spot sizes are about $1\text{ }\mu\text{m}$ or less in vacuum and about 50 to $500\text{ }\mu\text{m}$ in air depending on beam intensity and ion species.⁵⁹ The AO devices under investigation along with the laser source requires a space (~ 3 cubic ft) that is too large to fit in most, if not any, existing microbeam vacuum chamber.

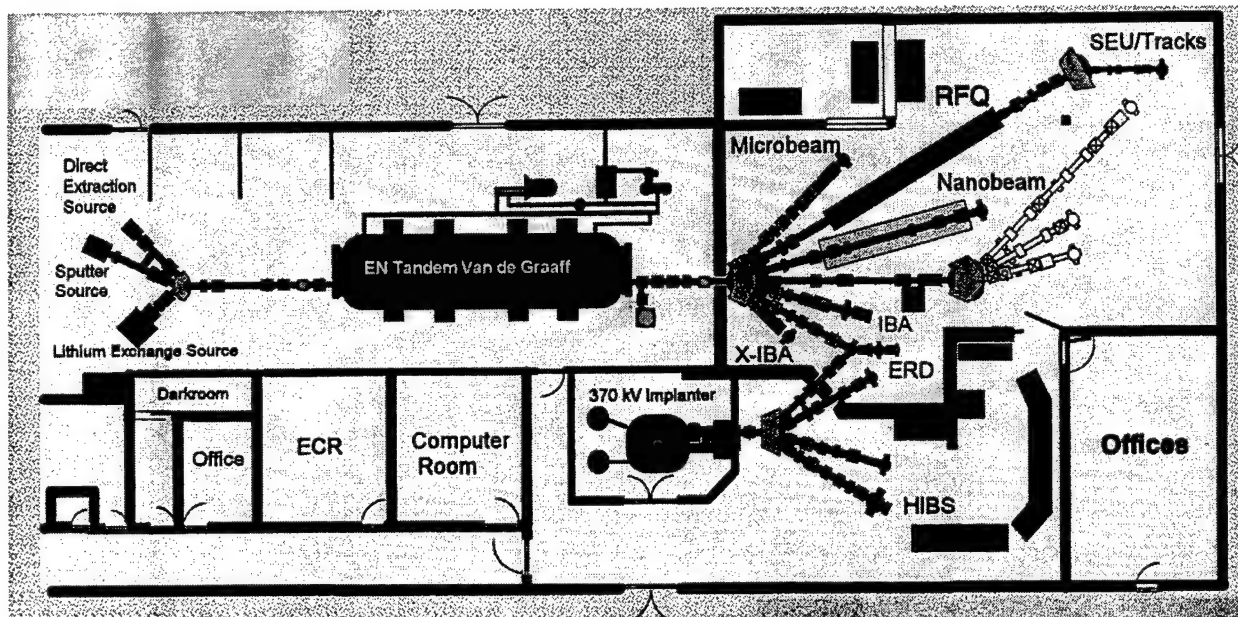


Figure 5-1. Sketch of the Sandia National Laboratory Ion Beam Research Facility and the ion microbeam line.

Sandia has developed an external microbeam analysis setup, that easily can evaluate samples as large as 2 ft x 2 ft. The ion beam is energy analyzed and collimated before entering a 3.5 mm bore magnetic quadrupole lens. The beam is focused onto the sample through a thin ($\sim 15 \mu\text{m}$) Mylar or Al air-to-vacuum window at the end of the chamber. The ion beam current is measured by replacing the sample with a Faraday cup. Additionally, the number of ion induced secondary electrons emitted from the vacuum side of the window are detected and recorded. Subsequently, the beam current on the target is monitored by the electron count rate.

The general capabilities of ion beam facility include: Energy range is limited by practical and usable ion currents (no less than 10% of maximum ion current value); Maximum power/cm² is determined for a focused spot size of $50 \times 50 \mu\text{m}^2$ internally and $100 \times 100 \mu\text{m}^2$ externally; Minimal internal spot size is obtained with ion fluxes of typically $\sim 10^6$ ions/s; Displacements per ion (dpi) is given for maximum energy and divided by ion range (Table 5-1).

Table 5-1. General capability of ion micro-beam facility, dpi refers to the displacements per ion.

General capabilities of ion beam facility								
Ion	energy	range in	max. I	Power [W/cm ²]		min. spot size [μm ²]		dpi/ μm
	[MeV]	GaAs	[A]	internal	external	internal	external	
P	0.5-10	4-400	4x10 ⁻⁷	10,000	8,000	1x1	50x50	0.26
He	0.5-15	1.5-75	5x10 ⁻⁸	6,000	1,500	1x1	100x100	3.9
C	0.5-30	0.7-20	1x10 ⁻⁷	50,000	n.a.	0.3x0.5	n.a.	77
Cu	1-35	0.2-6	5x10 ⁻⁸	25,000	n.a.	0.7x0.7	n.a.	4300

The ion beam current fluctuates rapidly (typically 1 Hz) with RMS variation of about 0.1. However, none of the evaluated AO modulators exhibited responses to the ion beam with time a time constant below 5 s and it is assumed that the rapid beam fluctuation had no significant bearing on the AO device response. The lateral beam uniformity is determined by the inherent aberration of the beam focus and the scatter in the vacuum to air foil. Both effects combined are estimated to result in a beam non-uniformity of less than 10 %. Usually, the slow, long term drift of the average beam current was less than 2% over an exposure of 1000 s.

5.2 EXPERIMENTAL SETUP OF AO MODULATOR EXPOSURES

A 670 nm diode laser, light detectors for the deflected, undeflected and reference laser beam, and the AO device were mounted on a single platform to minimize any misalignment due to size changes of supports with temperature or due to vibration. Figure 5-2 shows a schematic of the experimental setup used for measuring the performance of an AO cell under ion microbeam irradiation. The setup, including all the elements shown in Figure 5-2 except the beam tube, was mounted on a plate which was bolted to a translation stage that allowed it to be moved relative to the ion beam. The setup also allowed the plate to be tilted to change the point of incidence of the microbeam on the AO crystal while the optical alignment was maintained. The photodetector

was a PIN silicon photodiode, the ET4000 Model, manufactured by Electro-Optics Technology, Inc. The AO modulator exposures were performed using 2.0 MeV Helium and 4.0 and 4.5 MeV protons focused to approximately 1mm in air. The beam current ranged from about 40 nA for 2.0 MeV Helium to as much as 140 nA for 4.5 MeV protons. To minimize the amount of X-rays produced by the ion beam traversing in air, a distance of less than 2mm between the sample and the vacuum window was chosen. The X-ray radiation background during a typical proton irradiation was below 0.3 mrad/hr. The diffraction efficiency as a function of ion beam exposure time (dose) was recorded for each exposure location on the AO cell. Subsequently, multiple 2D maps of the device response to the beam radiation as function of beam position on the modulator surface were produced. Each map shows the response for a different exposure time. The following chapters will summarize the observed radiation effects for the various AO cells irradiated. In particular, the next chapter will give a qualitative explanation for the observed spatially dependent diffraction efficiency.⁵⁴

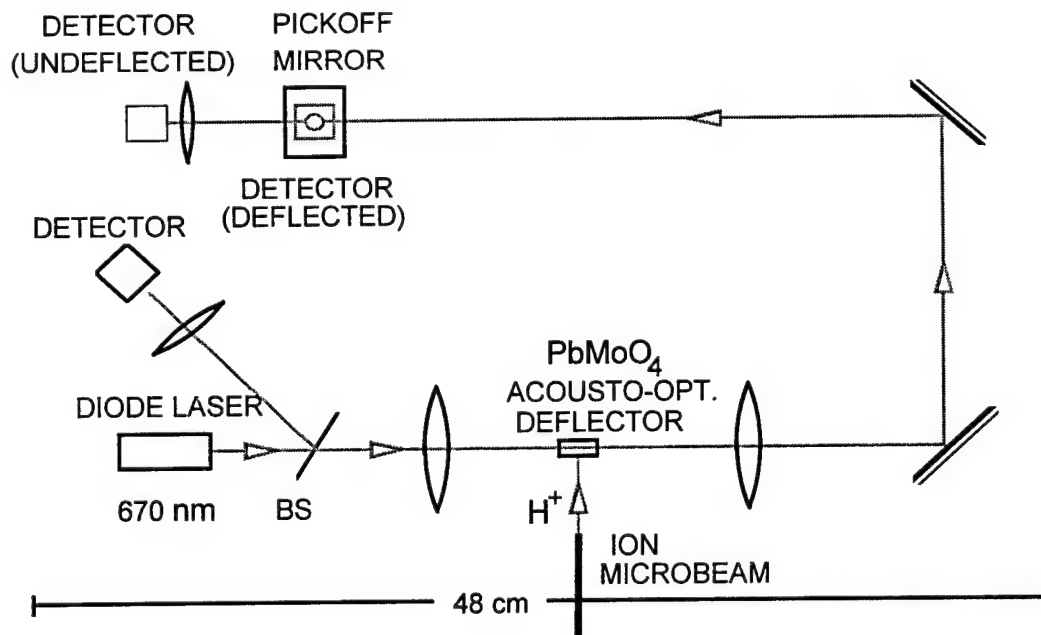


Figure 5-2. Experimental setup for measuring the performance of an AO cell under H^+ irradiation. The setup, including all the elements shown here except the beam tube, was mounted on an aluminum plate which was bolted to a translation stage that allowed it to be moved relative to the H^+ beam.

5.3 GENERAL CONCEPT AND OUTLINE OF DATA REDUCTION

As outlined above, the deflected I_d and undeflected I'_0 laser beam intensity exiting the acoustooptic deflector was recorded. The diffraction efficiency $\eta = I_d / (I_0 + I_d)$, see section 2.2 of this report, was calculated from these quantities for each those exposures. The laser intensities were recorded starting usually 10 to 15 s before the ion beam exposure and continued for 20 to 45 s past the duration of the exposure. The sampling frequency of the laser powers was typically 10 Hz during all the exposures. For all the measurements, care was taken that the AO-cell was tuned for maximum diffraction efficiency at the center RF-frequency with a RF power level at or just below the maximum power level. In addition, the laser beam was aligned to traverse the AO cell as nearly perpendicular to the entrance and exit facets as achievable while avoiding back - reflections from the from the AO cell into the laser.

In addition to recording the individual laser intensities, the ion beam current was monitored during the exposures of PbMoO_4 and LiNbO_3 devices. Recording the ion beam current simultaneous with the deflected and undeflected laser beams allowed us to extract the effect of total dose and dose rate on the diffraction efficiency. Total dose response and dose rate effects for the various acoustooptic devices are discussed in their respective chapters of this section and additional information is contained in several references.^{54,58,59,62,63}

In the case of the PbMoO_4 and LiNbO_3 devices from the diffraction efficiency measurements and beam current, images of diffraction efficiency changes as a function of ion beam position. Typically, 16-20 measurements were taken, establishing an equidistant grid of exposure measurements over the device surface. The diffraction efficiency was normalized to the ion beam current at each surface grid point. This procedure eliminates the effects of relatively small (~10%) dose rate fluctuations on the position dependent diffraction efficiency. Moreover, ion beam intensity drifts that inadvertently occur from one measurement point to the next are eliminated as well. The images assembled from these normalized data reflect the spatial

dependence of the diffraction efficiency on the ion beam position only. Each 2D image created in such a fashion represents the spatial diffraction efficiency at given time of the exposure.

5.4 ION BEAM ANALYSIS RESULTS

The acoustooptic deflectors evaluated included an PbMoO_4 , LiNbO_3 , TeO_2 , InP , and GaP Acoustooptic Bragg Cells. The results from subsequent analysis are outlined in the following sections.

5.4.1 PbMoO_4 Acoustooptic Bragg Cells

An acoustooptic deflector (AOD) composed of PbMoO_4 (see Figure 5-3) was irradiated by ion micro beam 4 MeV protons while operating under Bragg angle conditions. A RF oscillator was used to drive the AO-cell at 110 MHz and at a power level of 0.925 W. The power levels of the deflected and undeflected output light beams were monitored during the H^+ exposure. A 1 mm ion beam propagating in air was directed normal to the crystal face and laser beam. The crystal of the AO device was exposed in a grid of spots with 2.0 mm spacing in both the horizontal (z) and vertical (y) dimensions. The protons ranged out at about 82 μm below the crystal surface. Therefore the temporary degradation of the AO performance was due to thermal effects,^{3,61} since charge creation and crystal defect generation did not take place in the region traversed by the laser beam. The range of the protons was calculated using the SRIM code.⁶⁰ The exposure time was typically 40 s per position, and the (AOD) performance was monitored for 15 s after the microbeam was blocked by the Faraday cup, (AOD) performance was restored to the pre-exposure conditions within 15 s after cessation of the irradiation. Between exposures, the approximately 13 mm \times 8.5 mm AOD was mechanically translated in two dimensions in front of the fixed ion beam. The AOD diffraction efficiency was mapped and was observed to change as a function of ion beam location and dose rate. Figure 5-4 shows an example of 2D maps for a PbMoO_4 AO modulator.

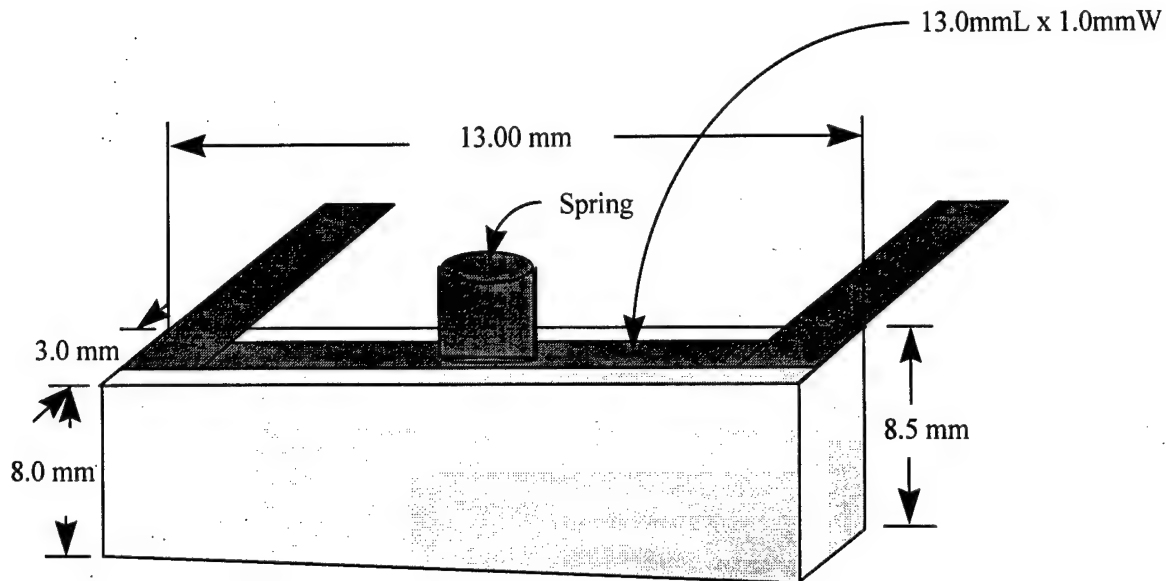


Figure 5-3. A conceptual sketch of the PbMoO_4 #1 acoustooptical modulator. The “x” coordinate is along the horizontal and “y” along the vertical axis of the modulator. “z” is perpendicular to the paper plane. The laser beam entered the AO cell at $x=0$.

The frames in Figure 5-4 represent the diffraction efficiency of the modulator before irradiation and after successively longer ion beam irradiation times. The apparent variation in the diffraction efficiency during the irradiation exhibits areas of high to low radiation sensitivity. These effects are attributed to the induced change in the temperature distribution of the crystal, which changed the sonic velocity and refractive index.^{3,61} Similar effects were observed when the ion beam was directed at the acoustic transducer.

Contour plots of the device diffraction efficiency are shown in Figures 5-4 through 5-6. The y,z coordinate gives the location on the crystal face of the H^+ beam during exposure. The diffraction efficiency is calculated using equation 8 in section 2.2 in terms of: I_d the power of the deflected optical beam, and I'_0 the optical output power in the direction of the incident beam.

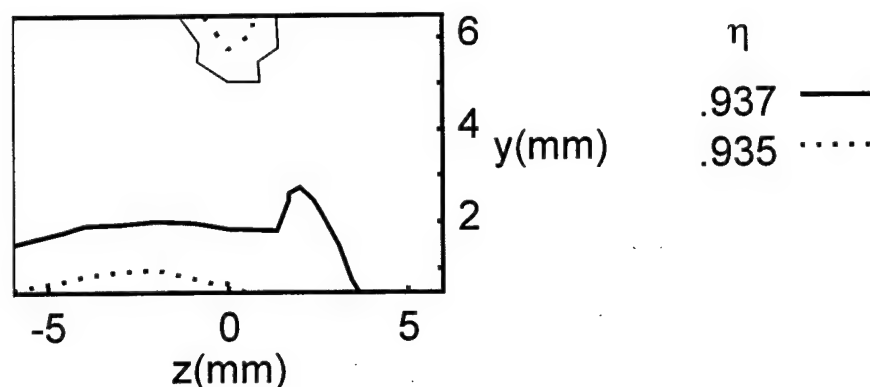


Figure 5-4. Contour plot showing the diffraction efficiency as a function of ion beam location on the crystal. The transducer is at location $y=0$, and the light beam enters the crystal at the face at $z=6.5$. The plot is for time $t=0$ s, just before the ion beam was unblocked.

The H^+ beam was unblocked at time $t=0$, so Figure 5-4 gives the unperturbed diffraction efficiency, and the contours are an indication of the experimental error ($\sim 6.3\%$). Figures 5-5 and 5-6 show the diffraction efficiency as a function of the microbeam location at $t=10$ s and $t=40$ s. There was no significant change from the distribution from $t=30$ s (not shown) to $t=40$ s, so the crystal temperature distribution had reached steady state by this time. The laser beam was located 3.2 ± 0.4 mm from the transducer, and 1.0 ± 0.2 mm from the irradiated crystal face.

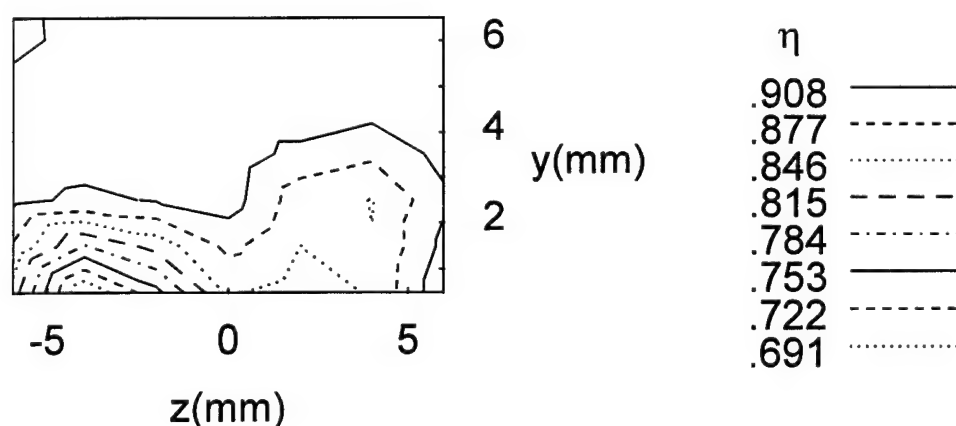


Figure 5-5. Contour plot showing the diffraction efficiency as a function of ion beam location on the crystal. The transducer is at location $y=0$. The plot is for time $t=10$ s, and the ion beam was unblocked at $t=0$.

Very little degradation of the diffraction efficiency occurred for H^+ locations that were not between the laser beam and the transducer, as is seen in Figures 5-5 and 5-6. Another notable feature is the occurrence of the highest diffraction efficiency for beam locations that are centered in the z-dimension. This effect is explained by the theoretical discussion in the next section.

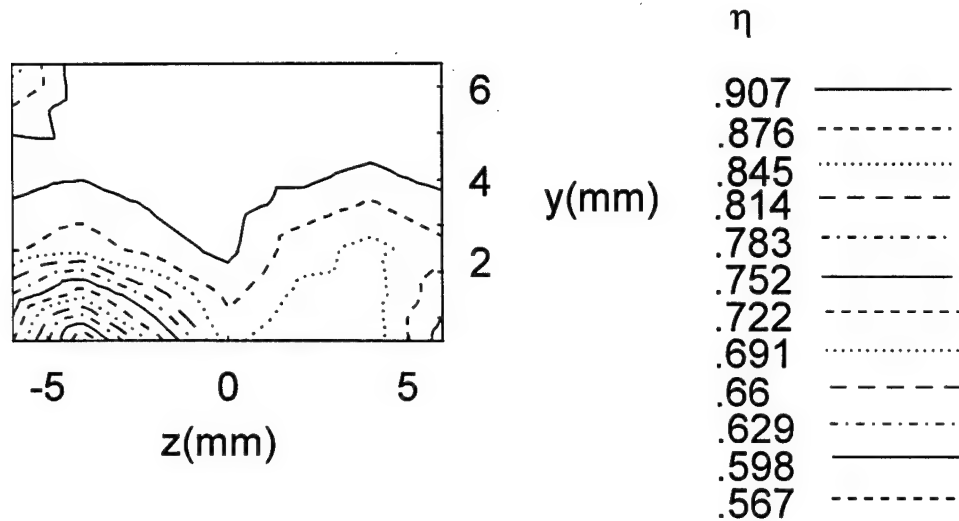


Figure 5-6. Contour plot showing the diffraction efficiency as a function of ion beam location on the crystal. The transducer is at location $y=0$. The plot is for time $t=40$ s, and the ion beam was unblocked at $t=0$.

5.4.1.1 Discussion of Radiation Induced Effects

To understand the thermal effects caused by the microbeam, C_d , the coefficient for scattering of power from the incident light wave into the diffracted wave⁶² for a number of values of z with $y=2.5$ mm was numerically calculated. The diffraction efficiency η is not the same as C_d for this AO device, because the coupling is strong. The diffraction efficiency does vary monotonically with C_d . To calculate C_d , the equilibrium temperature increase in the crystal due to the microbeam was obtained by solving Laplace's equation. Boundary conditions corresponded to constant temperature at the heatsink and a derivative proportional to the beam energy flux at the crystal surface. Heat loss due to thermal radiation and convection was estimated to be less than

1% of the incident power, and these loss mechanisms were ignored. The aberration of the acoustic wave at its intersection with the optical beam was obtained from the temperature distribution, and it was expanded as a spectrum of plane waves. The optical beam only satisfied the condition for Bragg diffraction for the portion of the spectrum very near zero spatial frequency. Therefore C_d was proportional to the square of the zero-frequency component of the acoustic wave.⁶³ The model is described more thoroughly in the next section.

Figure 5-7 shows a comparison of experimental values of diffraction efficiency with a theoretical curve of the efficiency for scattering from the input beam to the diffracted beam. The curves are plotted as a function of the location of the center of the ion beam at the surface of the crystal. When the deposition of the ion-beam energy on the crystal was centered at $z=0$, there was no tilt component to the acoustic wave, and the main lobe of the spatial frequency spectrum was centered at zero. For off-center incidence of the ion beam, the acoustic wave had a tilt component which served to detune it from Bragg resonance with the optical wave.^{30-33,63} This caused a greater decrease in C_d than did the higher order aberrations.⁵⁴ To obtain the overall diffraction efficiency from C_d , a coupled-wave equation would have to be applied, but a consideration of the magnitude of C_d is sufficient to understand the "W" shape of the diffraction efficiency curve.

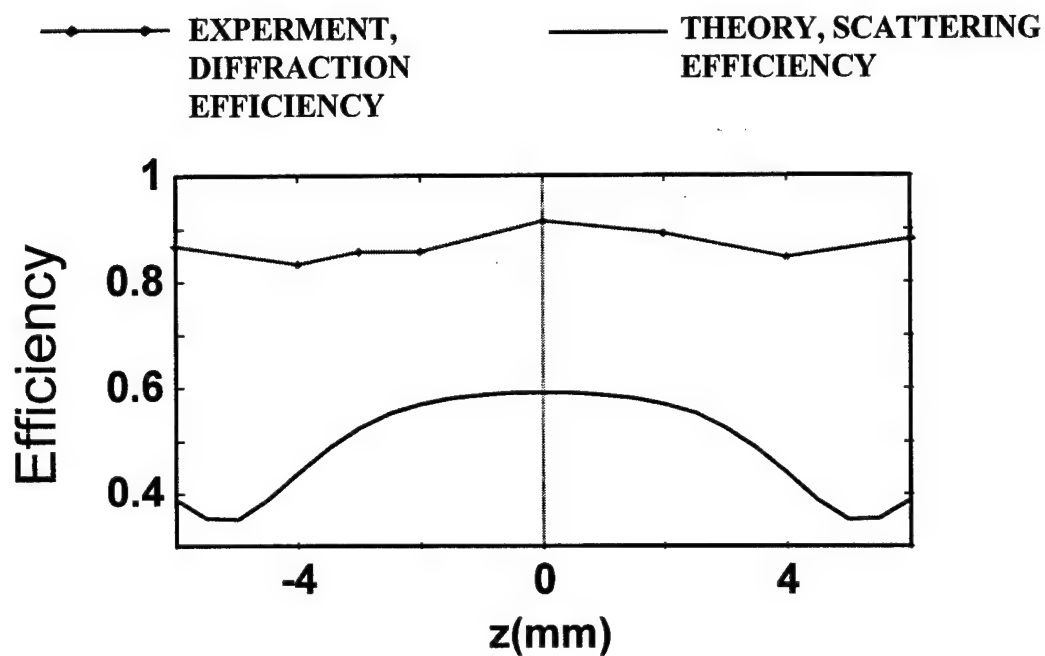


Figure 5-7. Comparison of experimental diffraction efficiency values with a theoretical curve of the efficiency for scattering from the input beam to the diffracted beam. The curves are plotted as a function of the location of the center of the ion beam at the surface of the crystal. The results plotted in this figure were obtained without solving the comprehensive coupled wave equations and reproduce the qualitative structure of the experimental diffraction efficiency.

5.4.2 LiNbO₃ Acoustooptic Bragg Cell

A second Bragg cell, a LiNbO₃ AO modulator (Figure 5-8) was exposed to H⁺ ions, and transient changes to its diffraction efficiency occurred. The 4.0 MeV proton beam current was high (~140 nA) and the beam was focused into a spot that was 0.5 mm x 0.5 mm. The ion beam was directed onto the face of the modulator that was opposite to the heatsink. The range of 4.0 MeV protons in LiNbO₃ is about 89 mm and is therefore outside the range of the laser beam and acoustooptic interaction region. The range of the protons was calculated using the SRIM code.⁶⁰ The diffraction efficiency as a function of time was taken for each of the multiple points on the surface that were irradiated. The points formed a regularly spaced grid.

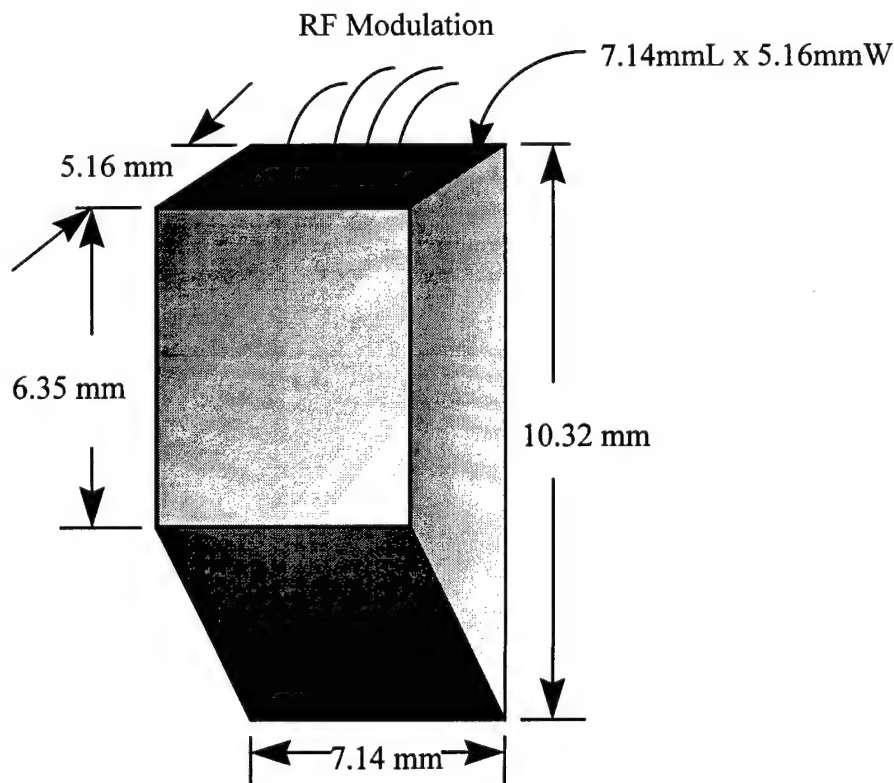


Figure 5-8. A conceptual sketch of the LiNbO₃ acoustooptical modulator. The “x” coordinate is along the horizontal and “y” along the vertical axis of the modulator. “z” is perpendicular to the paper plane. The laser beam entered the AO cell at x=0.

Figure 5-9 shows a diffraction efficiency trace (top) before ($t < 0$ s), during ($0 \leq t \leq 40$ s), and after proton exposure. The location of the ion beam for this example was 0.5 mm from the laser entrance facet and about 1 mm below the laser position. A decrease from 11% to 8% in diffraction efficiency is evident. The bottom trace in Figure 5-9 shows the ion beam current in arbitrary units. Similar traces are shown in Figures A-1 through A-18 (see Appendix A). For an AO cell/laser system that is operated at its rated power level and tuned for optimum Bragg-conditions, one would expect that any external perturbation would decrease the diffraction efficiency. However, in a few cases (Figures A-3, A-6 and A-9 in Appendix A) the diffraction efficiency increased, suggesting that the unperturbed acoustic wave in the modulator was conservatively specified in the data sheets. Heating rather than ionization is believed to have been the dominant cause of the changes observed in the diffraction efficiency of the LiNbO_3 AO modulator because the protons did not sufficiently penetrate the crystal volume to reach the laser beam - acoustooptic interaction region. The diffraction efficiency deteriorated with a time constant of about 4 s, after which the temperature distribution induced by the ion beam had reached equilibrium. The diffraction efficiency returned to pre-exposure values within 8 s after the ion beam had been turned off. This result confirms those reported earlier by Taylor et al.^{3,61} that temperature gradients are the dominant damage mechanism in irradiated AO devices. A representative record of the change in the crystal surface temperature during the ion beam exposure, measured with a thermistor affixed to the same facet surface, is shown in plot 5-11. The temperature at the crystal surface was observed to rise during the entire beam exposure (40 s), maintaining a strong temperature gradient from the crystal surface to the heat sink at the opposite facet. After the beam was removed, the surface temperature decreased rapidly through conductive cooling to the heat sink. However, the entire crystal and heat sink was observed to settle at a new equilibrium temperature some ~ 0.6 °C above the pre-exposure value. The entire crystal and heat sink was cooled predominantly through convective cooling at a much-reduced rate.

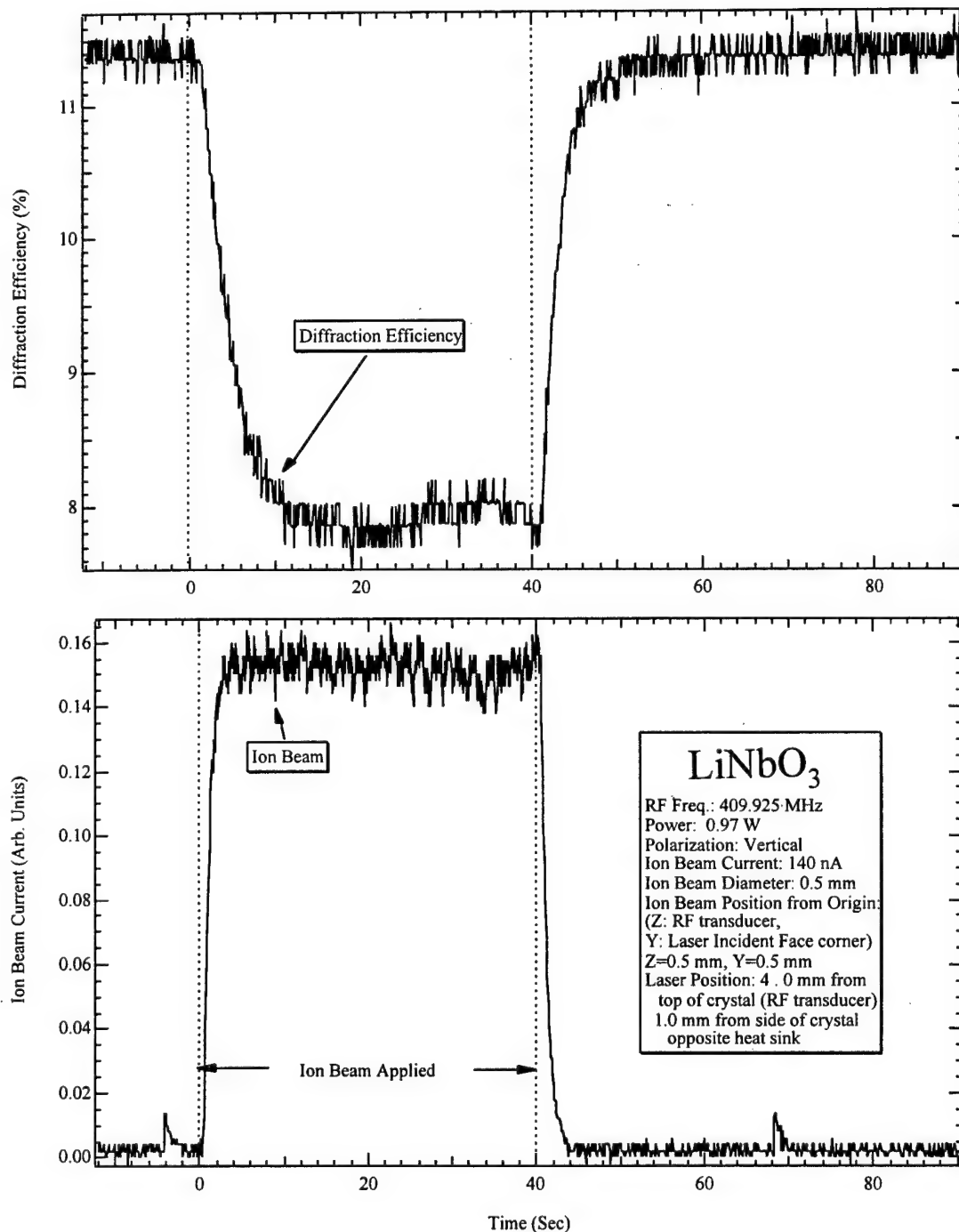


Figure 5-9. Two plots showing the measured AO cell response before, during and after an ion beam exposure. The dashed lines indicate the duration of the ion beam. The upper plot shows the calculated diffraction efficiency and the bottom plot shows the ion beam current in arbitrary units.

A series of 2D maps were generated by plotting the diffraction efficiency as a function of ion beam position for different times after the ion beam was turned on. Figure 5-10 shows a collage of 2D maps for 5 s to 40 s after the start of ion exposure. The spatially dependent diffraction efficiency showed strong variations over the irradiated crystal facet. The maximum change in diffraction efficiency was about 4% and occurred close to the transducer and the laser entrance facet. The variation in the diffraction efficiency was affected by the temperature variation which caused the velocity for acoustic propagation to be inhomogeneous. It was possible to demonstrate this effect due to the small exposure area that could be obtained with the microbeam, in contrast to a broad-area source which would have heated an entire facet almost uniformly. For cases in which the diffraction efficiency increased due to the proton exposure, it was concluded that inherent aberrations of the acoustic wavefronts were probably mitigated by the ion-beam heating.

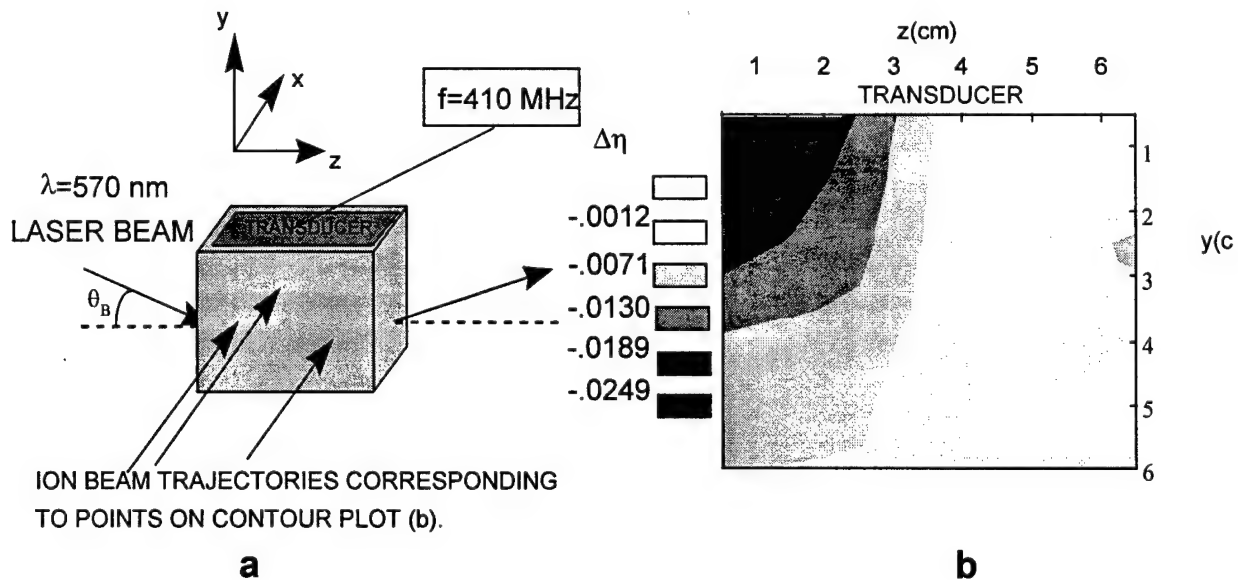


Figure 5-10. a. Crystal of acoustooptic device. b. Plot shows change in diffraction efficiency, η , as a function of position of incidence of ion beam on crystal face opposite heatsink. The material of the acoustooptic cell is LiNbO_3 . The proton energy was 4.0 MeV and the beam current was 130 nA, with a rectangular beam spot approximately 0.5 mm on a side. The unaberrated diffraction efficiency was $\eta = 0.11$.

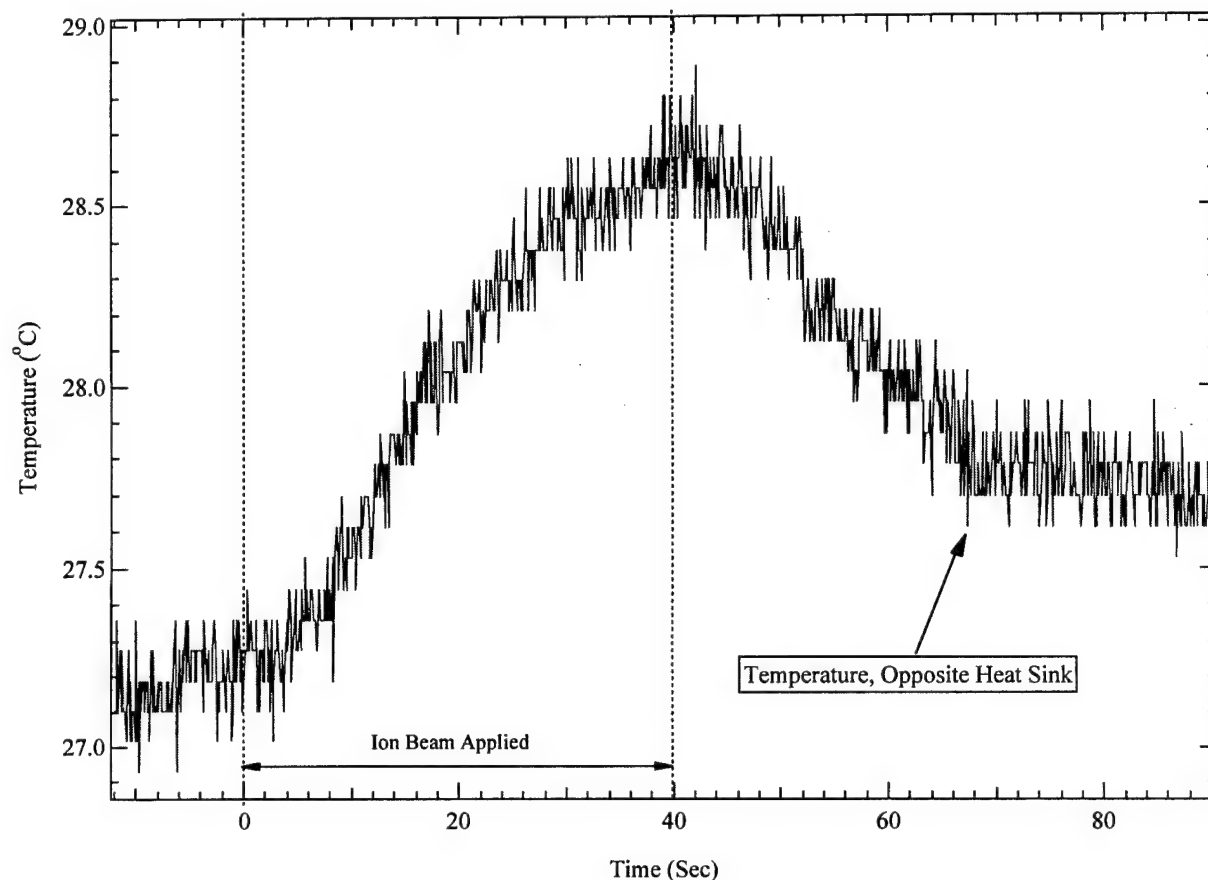


Figure 5-11. Change of surface temperature during ion beam exposure.

5.4.3 TeO₂ Acoustooptic Bragg Cell

A TeO₂ AO beam deflector was evaluated for effects due to exposure by a proton beam focused to a spot (0.5 mm by 0.5 mm) on the device surface. The device, illustrated in Figure 5-12, includes slow shear wave transducers made of LiNbO₃. The 50 MHz bandwidth AOD was specified to be operated at a center frequency 70 MHz. The AOD was operated at 1.0 W at a frequency of $f=70.3$ MHz. Three thermistors were glued to the faces of the crystal. The measured current of the 4.0 MeV proton beam at the beginning of the experiment was $I=130$ nA corresponding to power deposition of 0.52 W. The range of the protons was 85 mm, calculated using the SRIM code.⁶⁰ As with the devices already described, measurements were made for an

array of exposure locations on the facet opposite the heatsink. Spots on the transducer were also irradiated. The laser wavelength was 670 nm. The laser spot size was approximately 1 mm.

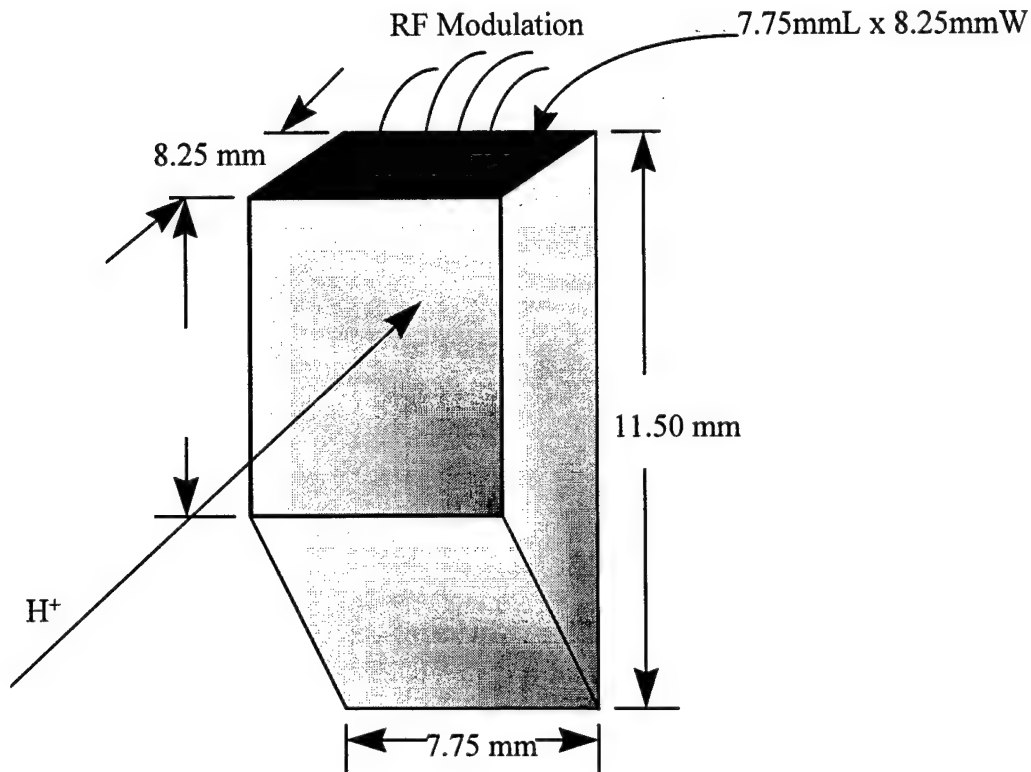


Figure 5-12. Diagram showing TeO₂ Acoustooptic Deflector. A slow shear wave is driven by the LiNbO₃ transducers on the facet at the top of the drawing. The maximum diffraction efficiency is specified at 72%.

The irradiation induced response data always show initially increasing diffraction efficiency (after approximately a 5 s time lag), with slow oscillations following; see Figure 5-13 (similarly Figures A-19 through A-26 found in Appendix A). The oscillatory behavior continues after the cessation of irradiation. A recovery time of 190 s, twice as long as for the other irradiations is shown in Figure 5-14. It is seen that the diffraction efficiency stabilized at the pre-exposure value about 70 s after the proton beam was blocked.

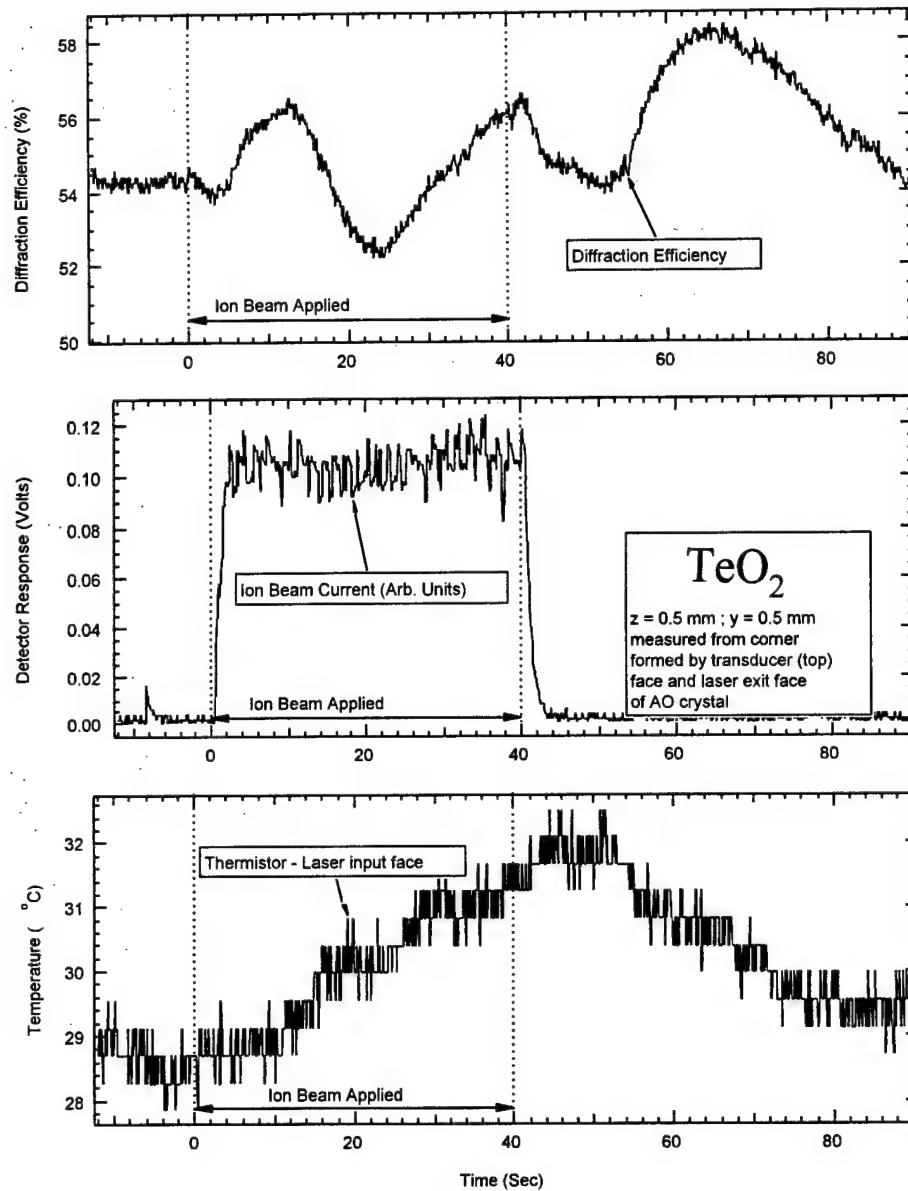


Figure 5-13. Plot of diffraction efficiency of TeO_2 AO deflector during and following irradiation of the crystal face opposite the heatsink. A power of 0.4 W was deposited by the ion beam on the facet opposite the heatsink in a square spot 0.5 mm on a side. The irradiated spot was centered 1 mm from the laser-exit facet and 1 mm from facet on which the transducers are bonded. The irradiation occurred during times between the two vertical dashed lines.

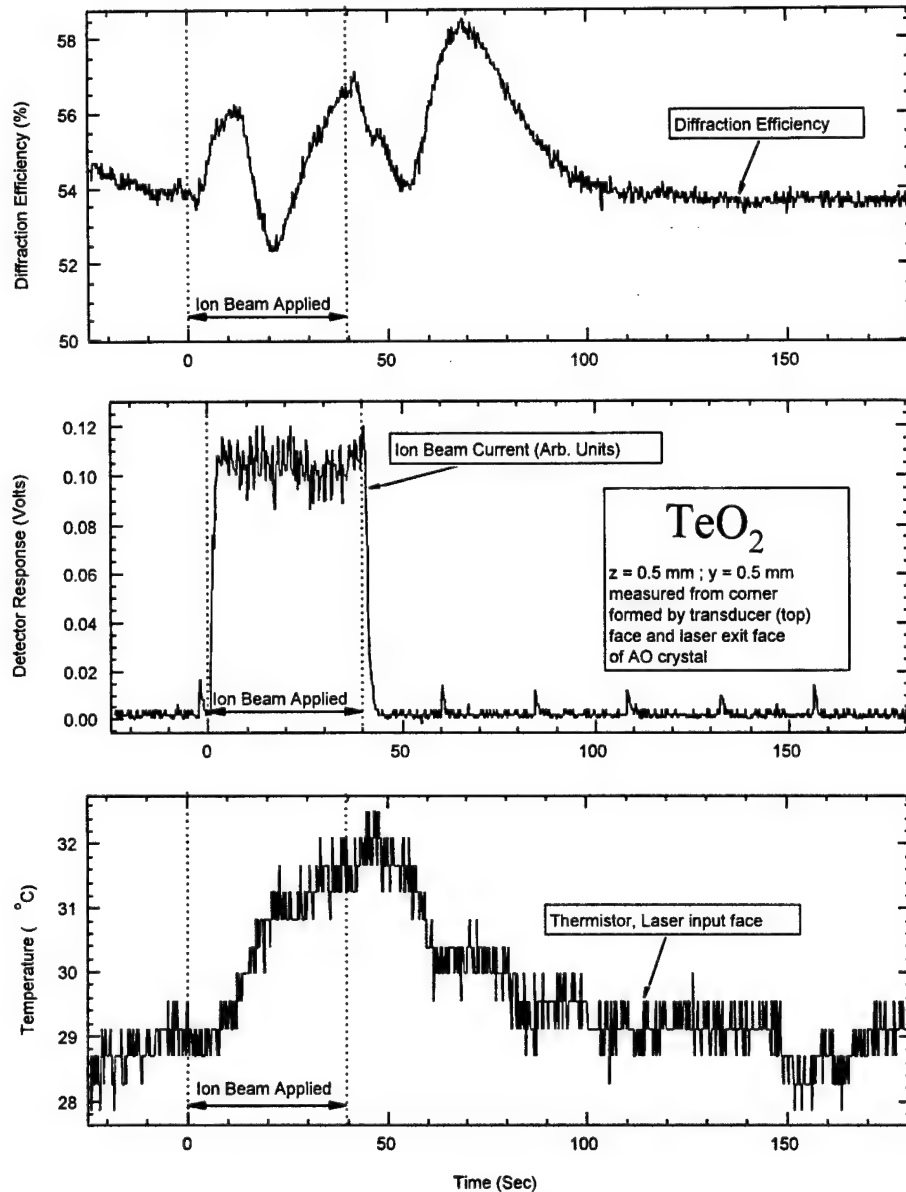


Figure 5-14. Same as Figure 5-13 except that data were acquired for a 180 s, to show relaxation of the diffraction efficiency to the pre-irradiation value. As may be observed in the top graph, large oscillations (η varies by $\pm 2\%$) were observed in the diffraction efficiency during and following proton irradiations.

The cause of the oscillations in the diffraction efficiency is heat deposition by the ion beam and subsequent cooling. Three mechanisms can figure into the oscillatory behavior of the diffraction efficiency: (1) a temperature distribution whose spatial distribution is varying with time, that is added to the equilibrium, unirradiated, temperature distribution caused by the absorption of

acoustic energy; (2) optical interference effects that change because of variation of the average temperature of the crystal; or (3) acoustic effects that accompany variation of the temperature of the transducer that is mounted on the crystal. The relaxation time for a temperature distribution in this crystal is on the order of 1 s, so spatial changes in the temperature distribution with respect to the average temperature are believed to have reached steady-state within a few s. Because the diffraction efficiency is still changing 45 s after the proton beam is shut off, (1) is not the only effect. The temperature increase is only 3 °C, leading to a relative change in the acoustic velocity of 9×10^{-4} . This leads to the same relative change in the deflection angle. Under Bragg conditions at an acoustic frequency of 70 MHz, from Equations 18 and 19, we obtain the deflection angle of the laser beam in air, which is 67 mrad. The change in the deflection angle due to a uniform temperature increase of the crystal by 3 °C would be 60 microrad. The resolvable angle is $\theta_a = \lambda/D = 590$ microrad, where the laser beam diameter is $D = 1$ mm and the laser wavelength is $\lambda = 0.59$ micrometers. Therefore, a uniform temperature increase of 3 °C could not cause a measurable change in the diffraction efficiency.

A change in transmission of the undiffracted beam due to facet reflections cannot account for changes of this magnitude because the facet reflectivity, r , of the AR coating at the 670 nm laser wavelength leads to a peak-to-peak change in the transmitted power of the main beam given by

$$I_0 - I'_0 \approx r^2 I_0 (1 - \eta) \quad (46)$$

for $r \ll 1$. For this device, $r = 0.005$ and $\eta \approx 0.53$, and therefore this effect is negligible.

Having shown that possible causes (1) and (2) can not explain the observed behavior, it seems likely that the properties of the transducers are changed by the heat, causing the changes in the diffraction efficiency. Thermal changes in the acoustic velocity in a transducer can alter its optimum thickness, which is determined by the phase shift of a wave in propagating across it. The maximum change that we measured in the absolute diffraction efficiency was several percent (+5%, -3%).

The transducers of the AO deflector were irradiated to determine radiation induced heating effects. The ion beam was incident on the transducer at a 45° angle to normal. The power flow to the surface of the transducer due to the particle beam was 0.4 W in a rectangular spot 0.5 mm. by 0.7 mm. The performance degradation during the transducer irradiation was qualitatively similar to the degradation when the face opposite the heatsink was irradiated. Figures A-27 to A-32 (see Appendix A) correspond to irradiation spots that move from the laser output end of the crystal to the input end. The spots are about 2/3 of the distance from the heatsink to the opposite face. Figure A-27 shows the performance with the beam incident 1 mm from the laser-exit facet. There are two peaks in the diffraction efficiency during irradiation. As the irradiated spot was moved toward the input facet, the increase in diffraction efficiency at beam turn-on, and the decrease immediately after turn-off became more rapid, as is shown in Figures A-28 to A-32 (see Appendix A). This trend indicates that local heating at the laser-input end had a greater impact on the diffraction efficiency than at the other locations.

Plots of the temperature are shown in Figures A-33 and A-34 (see Appendix A). The data were taken using a thermistor that was glued to the laser-input face of the crystal, as near as possible to the face opposite the heatsink, and centered 2 mm below the transducer facet. The temperature increase was 2 to 3 °C, and was not strongly dependent on the location of the heated spot.

5.4.4 InP Acoustooptic Bragg Cell

The InP AO modulator depicted in Figure 5-15 was exposed to a 4.0 MeV proton beam focused to about 0.5 by 0.5 mm and rastered across the front surface facet of the cell. The average ion beam current during most of the exposures was 140 nA. The range of the protons was 110 mm, calculated using the SRIM code.⁶⁰ For each position, the zero order and the diffracted laser beam ($\lambda=1152$ nm) exiting the AO cell was recorded using the ET3000 PIN-detector . The laser beam entered the crystal facet at $x=0$ mm and approximately $y=1$ mm below the transducer (refer to Figure 5-15). The laser beam entrance angle was tuned to the maximum diffraction efficiency for the RF frequency of $f=200$ MHz at 1.0 W. The device was operated under these conditions

before the first beam exposure, until the system temperature stabilized. Depending on the experimental conditions, the individual exposures were separated by 1 to 5 minutes and the device continued to operate between exposures.

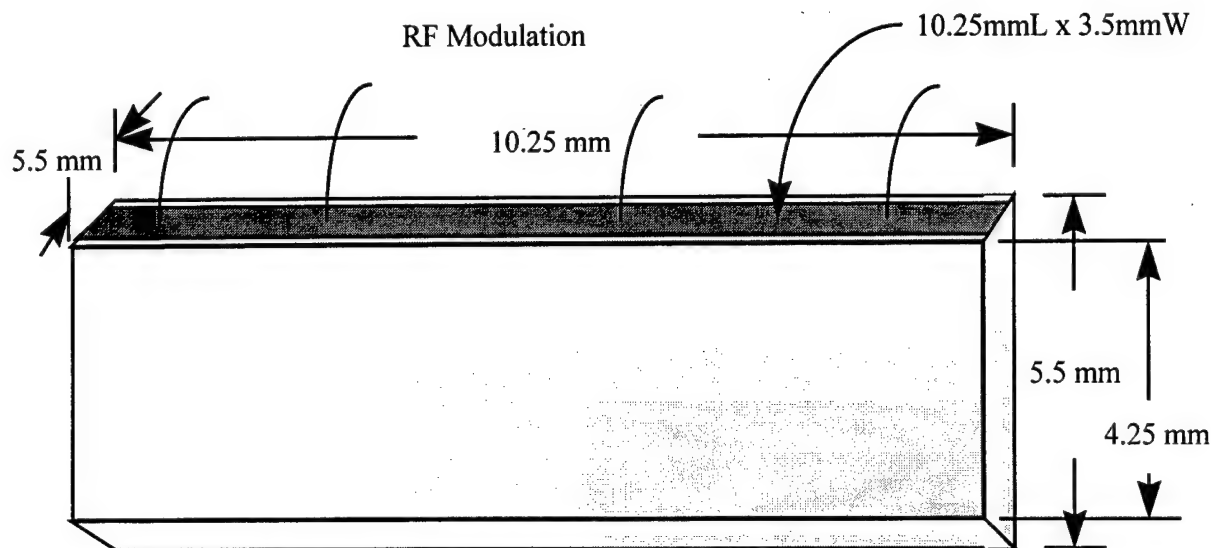


Figure 5-15. A conceptual sketch of the InP acoustooptical modulator. The “x” coordinate is along the horizontal and “y” along the vertical axis of the modulator. “z” is perpendicular to the paper plane. The laser beam entered the AO cell at $x = 0$ and $y \approx 1$ mm.

The device had a specified diffraction efficiency of 40.3%, and we were able to obtain base line efficiencies well above 43% during most of the exposures. Even though the AO cell was operating at the optimum Bragg conditions, for most of the irradiation positions a further enhancement of the diffraction efficiency of up to 1.5% was observed as can be seen in Figure 5-16 and Figures A-35 through A-56, where Figures A-35 through A-56 can be found in Appendix A, without any irradiation-induced deflection of the laser beams. In contrast, for an optimally designed and operating AO cell, we would normally expect that any perturbation would decrease the cell’s performance. The observed improvement was most pronounced for irradiation positions that were close to the transducer. The irradiation positions farthest from the transducer (4.5 mm, Figures A-48 through A-54) are also the farthest from the laser beam position. As stated in the Section 4.1, the 4.0 MeV protons penetrate only 110 μ m into the

sample and any radiation damage other than a transient temperature gradient in the region where the laser beam is propagating is highly unlikely. The additional transverse (z-direction) heat gradient in the AO cell changes the velocity and spatial distribution of the acoustic wave and induces local changes in the refractive index.

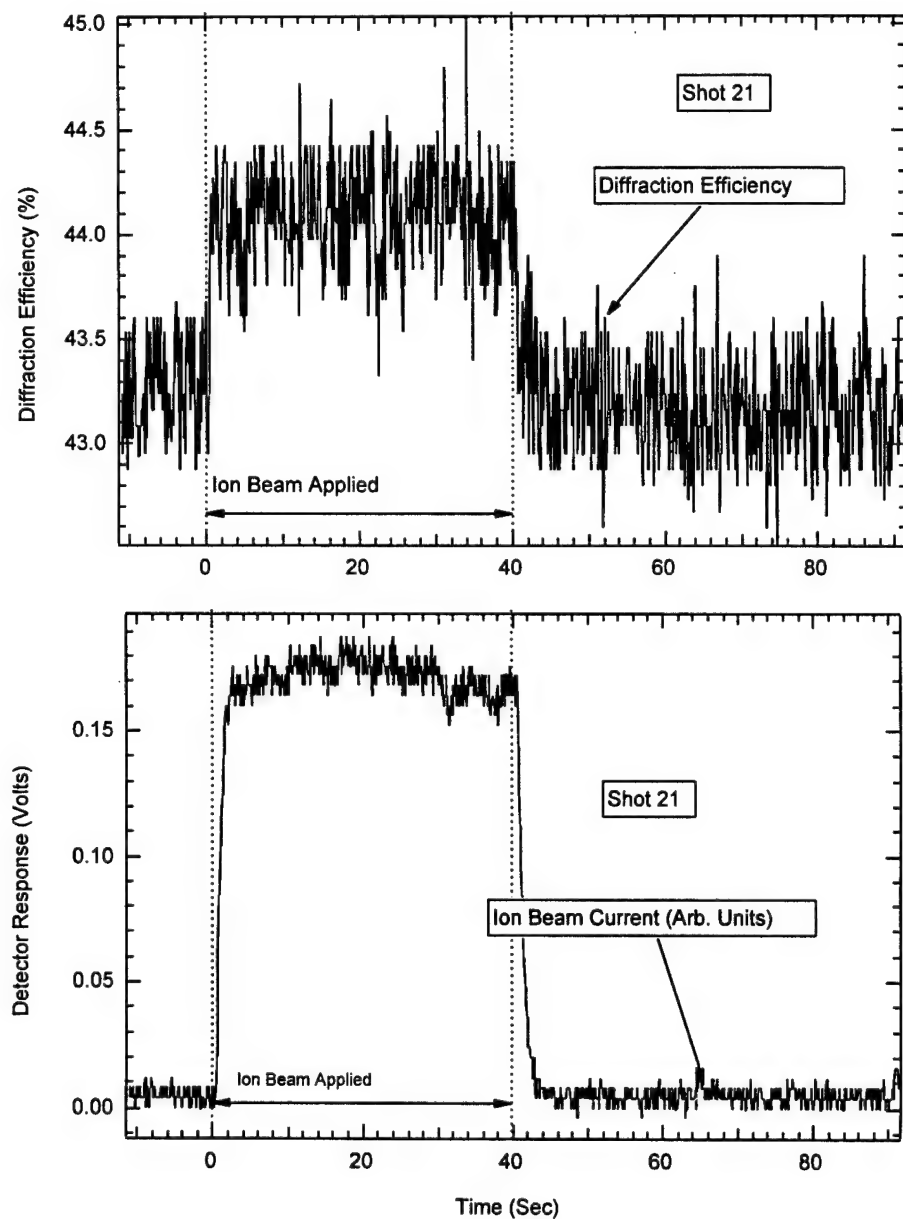


Figure 5-16. Top part of figure shows absolute diffraction efficiency of InP modulator. Lower part of figure shows the ion beam current in arbitrary units as a function of time. Measuring from the top left corner of the modulator the irradiation position is $x=12.5$, $y=0.5$.

In addition to the crystal facet irradiation, the transducer of the AO cell was selectively irradiated under the same operational setup and ion beam conditions. The response of the AO cell was very similar to the response observed when the lower part of the front crystal surface was irradiated. As in the previous observations for the other AO cells irradiated in this manner, this may indicate that the resonance frequency of the electronic RF circuit is shifted by the radiation induced change in the transducer temperature.

5.4.5 PbMoO₄ #2 Acoustooptic Bragg Cell

Very extensive ion beam and broad area exposures have been conducted on this device.^{1,3} For this device, depicted in Figure 5-17, the zero order and first order diffracted laser beams exiting the AO cell were recorded. The laser beam entered the crystal facet at $x=0$ mm (refer to Figure 5-17). The laser beam was tuned to the maximum diffraction efficiency for the RF frequency of $f=82.17$ MHz at 1.0 W. The device was operated under these conditions before the first beam exposure, until the system temperature stabilized. The ion-beam intensity for all the exposures varied between 120 nA and 170 nA. Depending on the experimental conditions, the individual exposures were separated by 1 to 5 minutes and the device continued to operate between exposures.

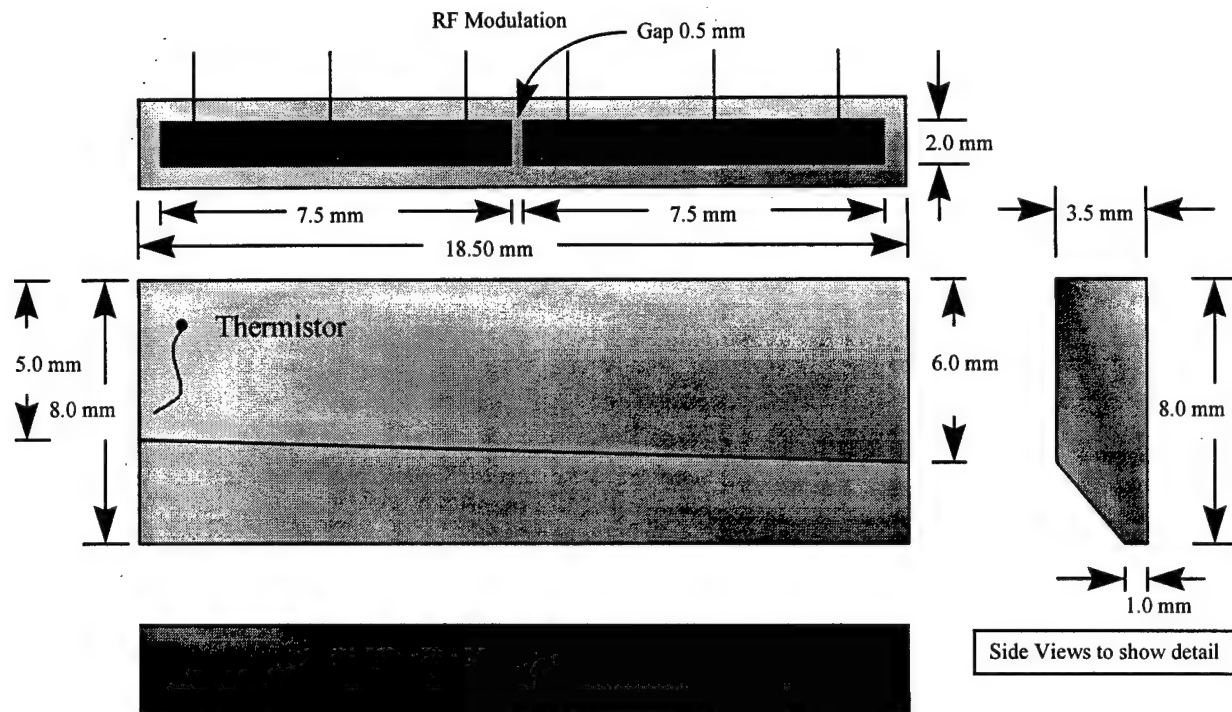


Figure 5-17. A conceptual sketch of the PbMoO_4 acoustooptical modulator. The “x” coordinate is along the horizontal and “y” along the vertical axis of the modulator. “z” is perpendicular to the paper plane. The laser beam entered the AO cell at $x=0$. A thermistor was attached to the front facet at $x=2$ mm and $y=2$ mm and a second was attached to the back of the heatsink.

A series of 2D maps were generated by plotting the diffraction efficiency as a function of ion beam position for different times after the ion beam was turned on. Figure 5-18 shows a collage of 2D diffraction efficiency maps for 10 s to 40 s after the start of ion exposure and a 2D map showing the restoration of the diffraction efficiency 15 s after irradiation. The spatially dependent diffraction efficiency showed strong variations over the irradiated crystal facet. As shown in Figure 5-18, the maximum change in diffraction efficiency was about 30% and occurred close to the transducer and the laser entrance and exit facet. The variation in the diffraction efficiency was affected by the temperature variation, which caused the velocity for acoustic propagation to be inhomogeneous. It was possible to demonstrate this effect due to the small exposure area that could be obtained with the microbeam, in contrast to a broad-area source which would have heated an entire facet almost uniformly. For cases in which the diffraction efficiency increased due to the ion beam exposure, inherent aberrations of the acoustic

wavefronts were probably mitigated by the ion-beam heating, which is consistent with our observations on other AO devices.

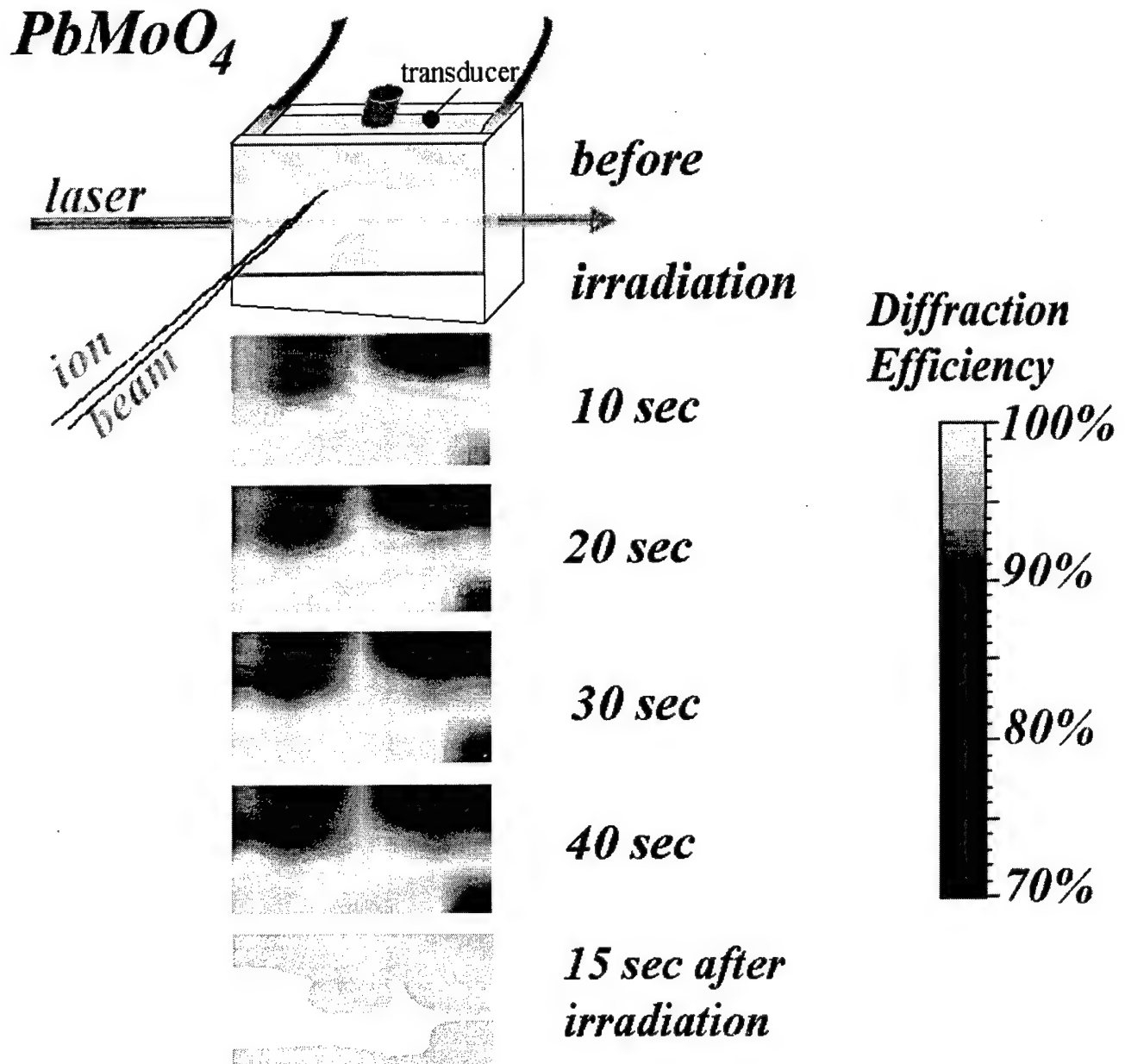


Figure 5-18. Change of diffraction efficiency during the proton exposure for time slices starting at 5 s to 40 s after start of the beam exposure.

During the experiment, measurements were taken of the temperature of the heat sink (at $z=0$ mm) and the temperature of the opposite crystal facet, that was irradiated by the ion beam, using thermistors ($z = \text{max.}$). A typical example of the measurement results is shown in Figure A-75 (see Appendix A). The location of the ion beam on the crystal surface (refer to Table A-3 in Appendix A) was 5.5 mm from the transducer and 8mm from the laser entrance facet. The top graph in Figure A-75 shows the detector responses for the diffracted and undiffracted (zero-order) laser beam exiting the AO cell. The dashed lines at 0 and 50 s indicate the duration of the ion beam exposure. The resulting change in the diffraction efficiency can be seen as a slight enhancement in the zero order power and small drop in the diffracted laser power.

The bottom graph in the same figure calculates the diffraction efficiency η according to equation 8 in section 2.2 of this report. Here, the diffraction efficiency decreases from 64.6% to ~64% within ~5 s and remains at this level until the ion beam is removed. The diffraction efficiency is restored within 10 s to its pre-exposure value, overshoots by ~0.2% and settles close to the preshot value. The overshoot and slight oscillations of the diffraction efficiency are not explained yet. However, one of the possible causes may be the reflection of the ion beam induced temperature wave at the facet walls of the modulator. For all of the exposures of this device, the diffraction efficiency returned within 40 s to the pre-irradiation values.

The graph in the middle of this figure shows the temperature of the heat sink as well as the temperature of the crystal facet exposed to the ion beam. For this exposure, the distance of the ion beam from the center of the thermistor was only 6 mm and a comparatively large temperature rise of 3.2 °C was recorded. The temperature rise resembles an exponential increase with a ~ 4 s delay after the start of the beam exposure. The temperature decreased slowly, again with a 2-4 second delay, after the beam was turned off. The slope of the exponential and the time delay of the temperature rise onset is determined by the heat capacitance and the thermal conductivity, respectively. The median temperature of the heat sink, however, exhibits no change in temperature above RMS noise of the thermistor.

The general ion beam position dependent response of the PbMoO_4 modulator is summarized in the Figures A-56 through A-59 (see Appendix A). The trend of the average change in the diffraction efficiency (normalized) appears to show the greatest changes, when the ion beam is directed close to the transducer. As the beam was directed farther away from the transducer, the diffraction efficiency changed from a positive value to smaller or even negative values. Representative data for changes in the diffraction efficiency are shown in Figures A-75 and A-76. The power from the diffracted beam is directly transferred to the zero order laser beam, with little or no scattering of the laser light in the cell.

Furthermore, the changes in diffraction efficiency were observed to increase as the ion beam was scanned from the laser entrance facet to the exit facet. Additional relevant material can be found in Appendix A.

6.0 RESPONSE OF AO DEVICES TO GAMMA-RAY AND NEUTRON IRRADIATION

Illustrated in Table 6-1, is a summary of the gamma-ray and neutron exposures performed on several Acoustooptic Devices (AODs). In this section, Table 6-1 is essentially discussed one row at a time, followed by a brief description of the experiment and the results. In many of the Cobalt 60 exposures the effect of the gamma irradiation on the AO cell is minimal, or not detectable, and therefore, requires little discussion. In the case of preliminary neutron exposures at the Sandia National Laboratories, SPRIII - reactor (August, November 1995), some experimental equipment was adversely affected by the radiation exposure and the effects induced in the AODs are complex and difficult to deconvolve. To alleviate this problem, the experimental configuration was subsequently modified by removing the radiation sensitive instrumentation from the SPRIII - Kiva (reactor cell). In December 1996, a new instrumentation and exposure configuration was implemented at the SPRIII. All components, except for the AO cell and several front surface mirrors, were removed from the Kiva thus eliminating inadvertent exposure of the light detectors. An active 1×10^{15} neutrons/cm² exposure was performed on a TeO₂ device to study degradation of the AOD's diffraction efficiency. This new experiment configuration yielded improved results.

Table 6-1. Summary of AOD exposures conducted by the Photonics Research Group (FY95-97)

Exposure Number	Material	Center Frequency/ Bandwidth	Bragg Angle (deg)	Mode	Study Performed: *	Notes: Date exposed
1	TeO ₂	130 Mhz 55 MHz	4.00	shear	(γ exposed) BW to 1M rad (active)	8 Aug 95
2	GaP	740Mhz 360 MHz	3.20	shear	(γ exposed) α to 420 krad (active)	29 Aug 95
3	TeO ₂	130 Mhz 62 MHz	4.00	shear	(n exposed) α to 1×10^{15} (active)	29 Aug 95
4	LiNbO ₃	330 Mhz 55 MHz	0.70	long	(γ exposed) BW & η to 1 Mrad (active)	7 Sep95
5	LiNbO ₃	140 MHz 80 MHz	NA	shear	(γ exposed) α to 1 Mrad (active)	15 Sep 95
6	GaP	1.0 Ghz 500 MHz	3.20	long	(n exposed) α to 1×10^{15} (active)	29 Nov 95
7	InP	200 Mhz 50 MHz	2.58	long	(γ exposed) η to 1 M rad (active)	1 Jul 96
8	TeO ₂	133 Mhz 55 MHz	4.00	shear	(n exposed) η to 1×10^{15} (active)	11 Dec 96
9	LiNbO ₃	415 Mhz 50 MHz	1.17	long	(n exposed) η to 1×10^{15} (passive)	Apr 97
9	GaP	1.636 GHz 500MHz	4.47	shear	(n exposed) η to 1×10^{15} (passive)	Apr 97
9	InP	200 MHz 50 MHz	2.58	long	(n exposed) η to 1×10^{15} (passive)	Apr 97

*Where: γ = gamma irradiation, n = neutron irradiation,
 BW = bandwidth measurement, η = diffraction efficiency measurement,
 P = polarization measurement using photoelastic modulator system, α = attenuation measurement,
 I_d = diffracted beam, I_0 = main beam,

6.1 DESCRIPTIONS OF EXPOSURES

6.1.1 Gamma Exposure of a TeO₂ Acoustooptic Bragg Cell

As shown in Table 6-1, exposure 1, gamma exposures were performed with RF modulation swept through a range of frequencies (bandwidth) as specified by the device data sheet. The diffraction efficiency of a TeO₂ AO cell was measured with no observable bandwidth changes for a total gamma dose of 1.0 Mrad(Si).

Shown in Figure 6-2 is the experimental setup used for the irradiation exposure at the Kirtland Air Force Base (KAFB), Air Force Research Lab (AFRL), Space Electronics and Protection Branch (VSSE), Co-60 Irradiation Facility. Figure 6-2, also shows the approximate dimensions between optical components as well as the extent of lead shielding used to protect electronic and photonic equipment used in the experiment. Note that the AO device is positioned as close to the source as possible and that styrofoam was used to prevent unwanted heating from the stainless steel sleeve that encloses the gamma source.

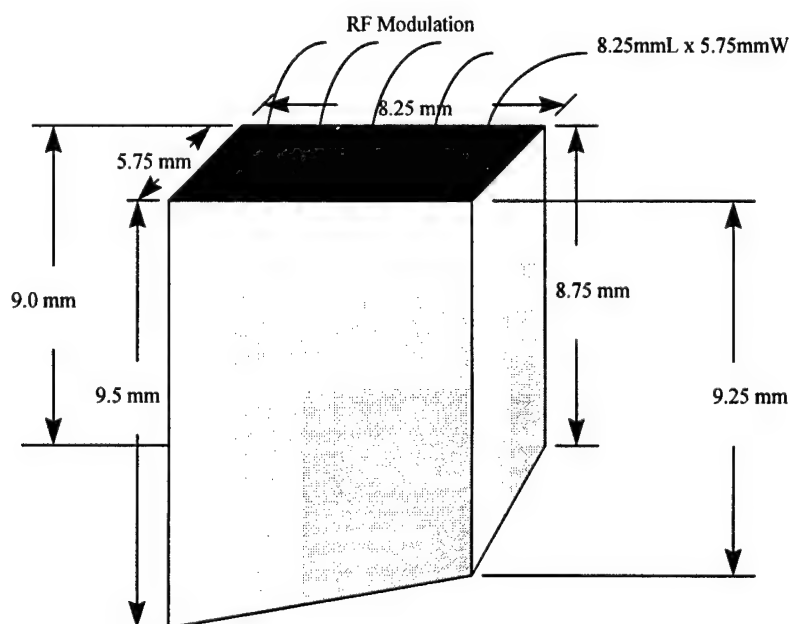


Figure 6-1. A drawing of the TeO₂ device under investigation in this exposure. The direction of the radiation is incident on the front face of the device, i.e., into the plane of the page.

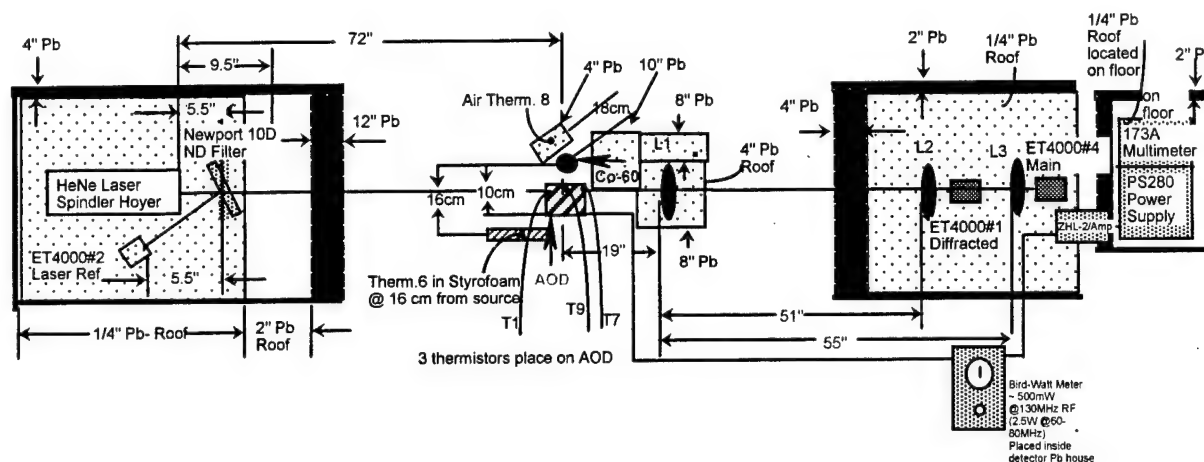


Figure 6-2. Experimental configuration for an active TeO₂ AO device bandwidth measurement in a gamma radiation environment.

The AO device was actively operated while exposed to gamma-ray radiation and exposed to a total dose equivalent of 1 Mrad(Si). The output beams, main and diffracted, are shown in Figure 6-3 as a function of the modulator frequency for a 1 Mrad(Si) total dose. It is evident that irradiation by gamma-rays had no significant effect on the AO beam intensities. This is clearly illustrated when the preirradiation main and diffracted beams are plotted along with the main and diffracted beams after a 1 Mrad(Si) exposure, as shown in Figure 6-3.

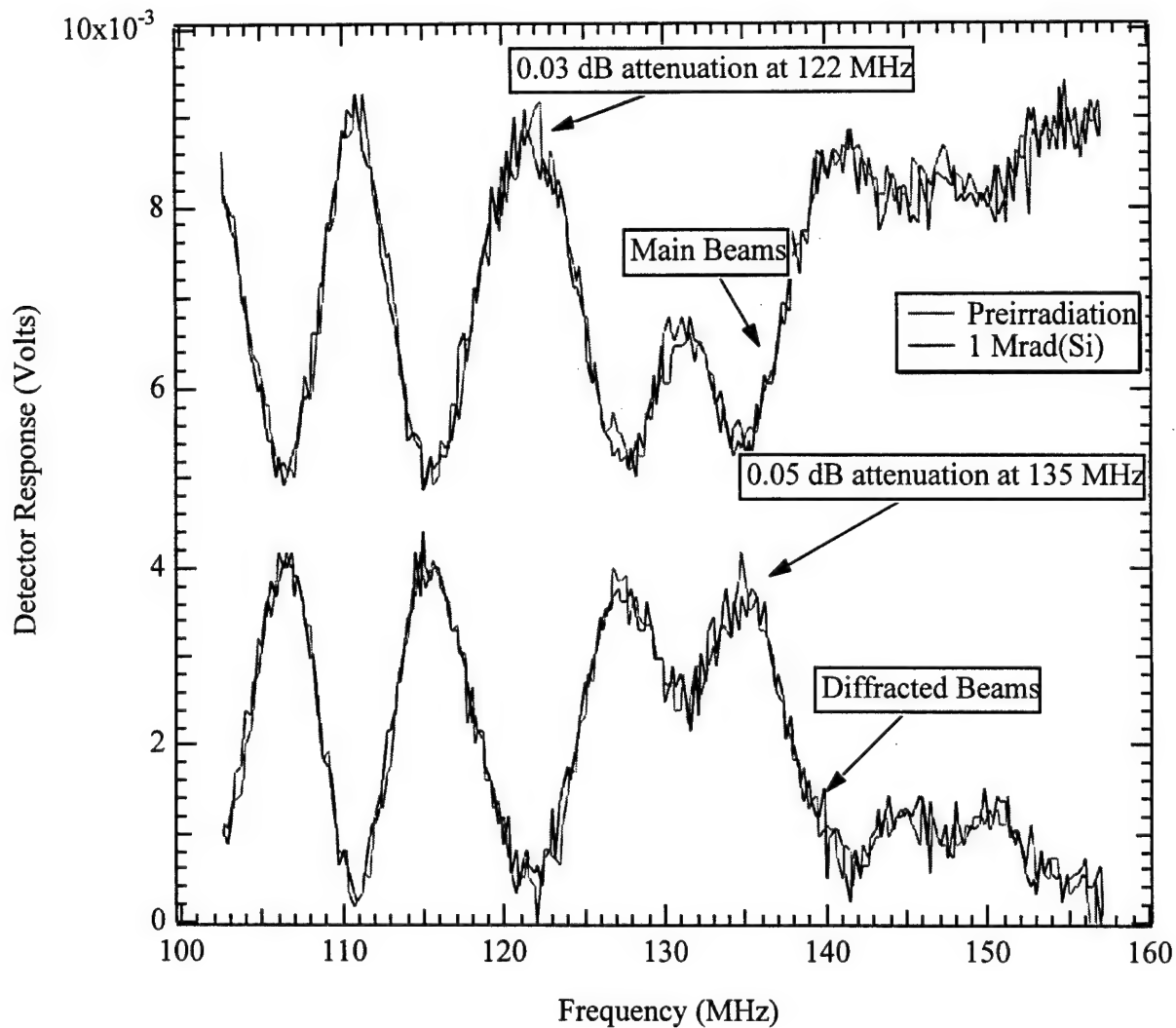
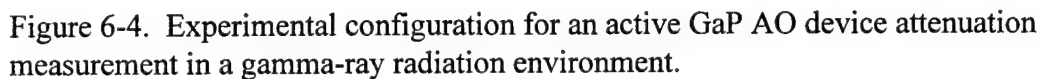


Figure 6-3. Overlay of the bandwidth responses of a TeO₂ AO device prior to radiation exposure and at a gamma-ray dose of approximately 1 Mrad(Si). The photodetector responses for the main and diffracted beams are plotted as a function of the modulation frequency. The bandwidth response, (102.5 MHz to 157.5 MHz) of the device was not affected by a gamma dose from 0 to 1 Mrad(Si), as shown. The device center frequency was 130 MHz with a bandwidth of 55 MHz. The RF input frequency was varied ± 27.5 MHz from the center frequency.

As shown in Table 6-1, exposure 2, the GaP AO cell was irradiated by gamma-rays to a total dose of 420 krad(Si). The experimental setup is shown in Figure 6-4.



108

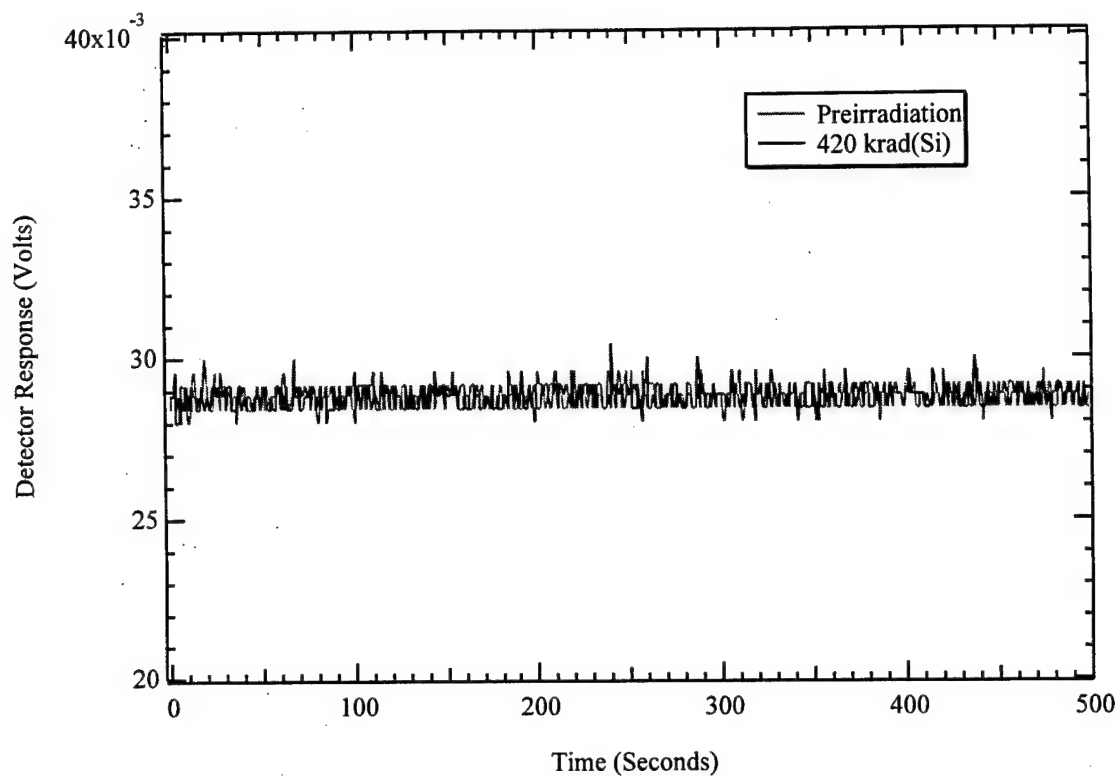


Figure 6-5. Pre-irradiation and 420 krad(Si) Co-60 irradiation material attenuation data for an unmodulated GaP AOD. The HeNe laser throughput detector response voltage is plotted over a period of 500 seconds prior to radiation exposure and during a 500 second period after the deposition of 420 krad(Si) on the device. The pre-irradiation and 420 krad(Si) values are virtually identical indicating the GaP AOD was not affected by gamma-rays.

6.1.3 Neutron Exposure of a TeO_2 Acoustooptic Bragg Cell

In this experiment, a TeO_2 AO Bragg (Figure 6-6) cell was exposed to a total neutron fluence of 1×10^{15} neutrons/cm² (exposure 3, Table 6-1). This was our first attempt to measure neutron induced effects at the Sandia National Laboratory SPRIII reactor. The experimental arrangement used is shown in Figure 6-7. The AOD was adversely affected by the neutron irradiation. The effect of the neutrons and secondary particle species on the experiment apparatus adversely affected the measurements, despite aggressive polyethylene, cadmium, and lead shielding of the light source and detection apparatus.

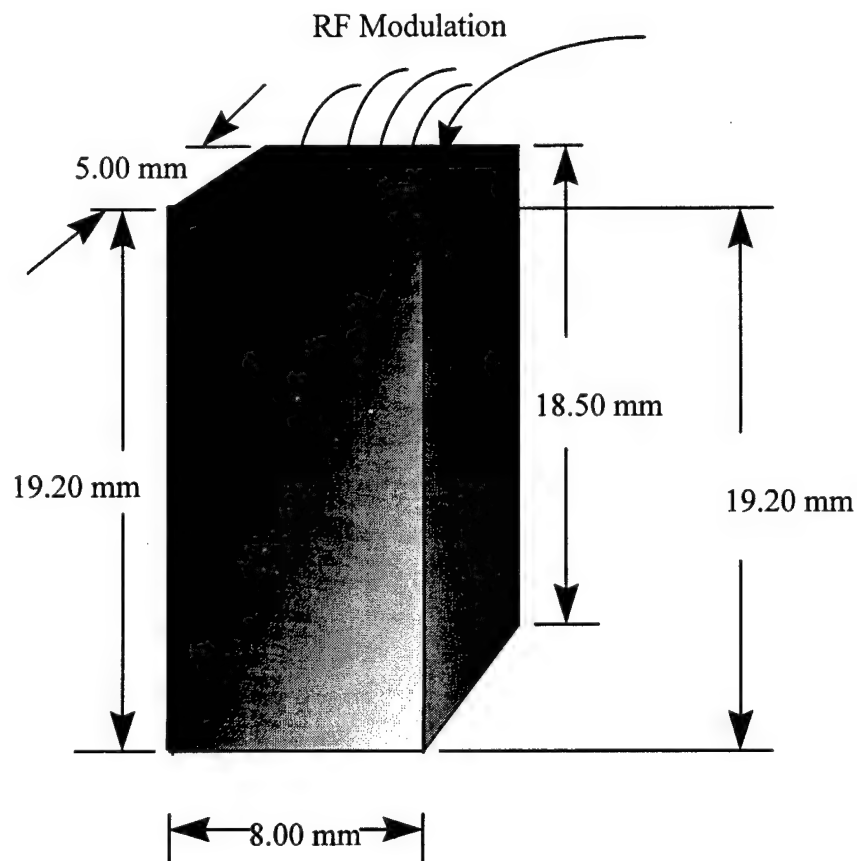


Figure 6-6. The TeO_2 device under investigation in this exposure. The direction of the radiation is incident on the front face of the device, i.e., into the plane of the page.

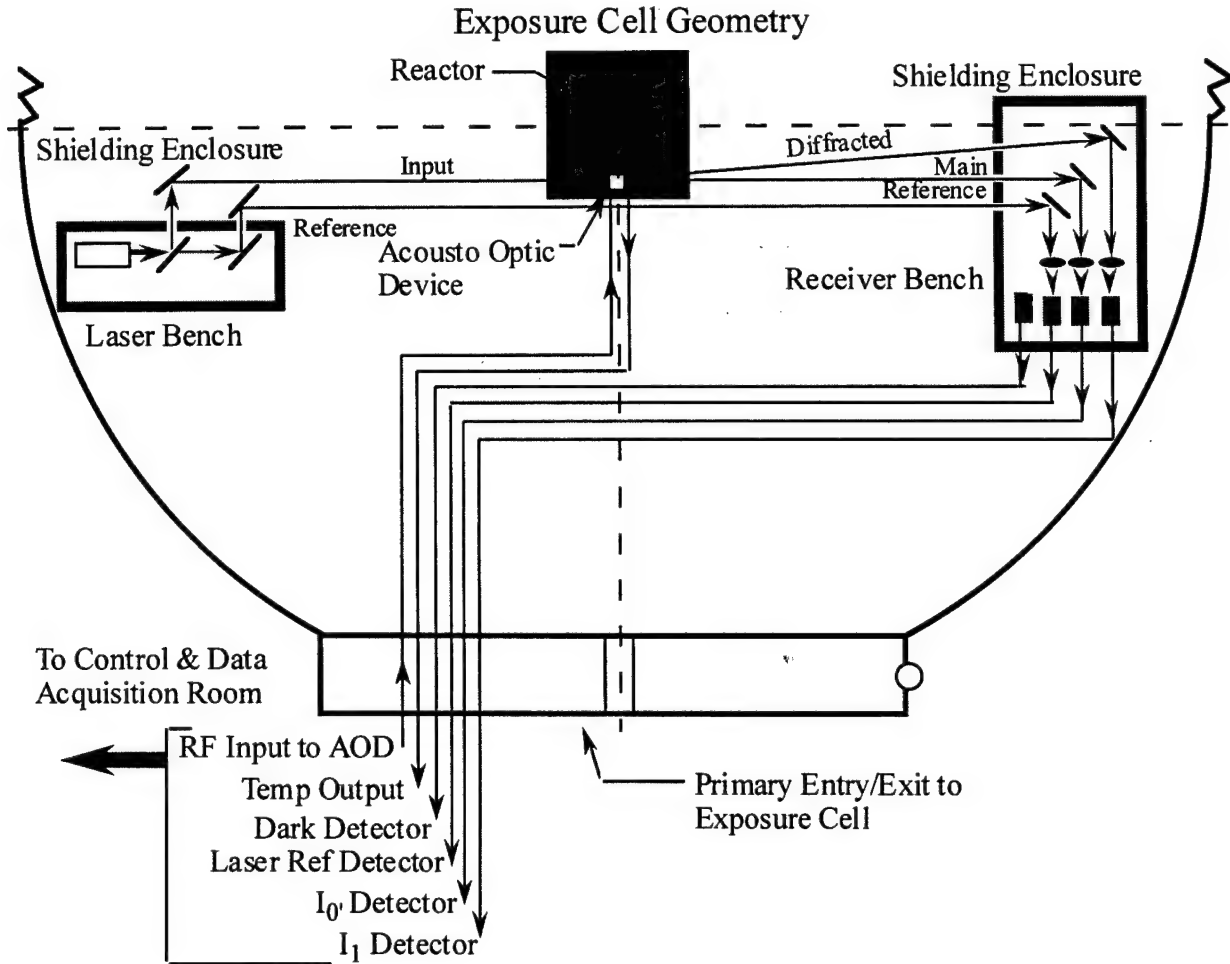


Figure 6-7. Initial experimental configuration for performing an active AO device diffraction efficiency measurement in a neutron environment.

Despite heavy shielding, a combined effect of the radiation exposure on the laser diode source, AO cell, lenses, mirrors and detectors continued to corrupt measurements; since, the voltage signal output from the silicon PIN photodetectors increased proportional to the fluence applied. The lessons learned from this experiment were to remove the detectors and optics from the exposure cell. Figures 6-8 and 6-9, illustrate the main, diffracted and dark detector responses during a 1×10^{15} neutrons/cm² exposure. These plots indicate a generally increasing (corrupted) signal for all channels recorded. Also, it is noted that during the acquisition of this data the RF power was varied from the off state to the on state several times as indicated in Figure 6-8 as intermittent operation of the Bragg cell.

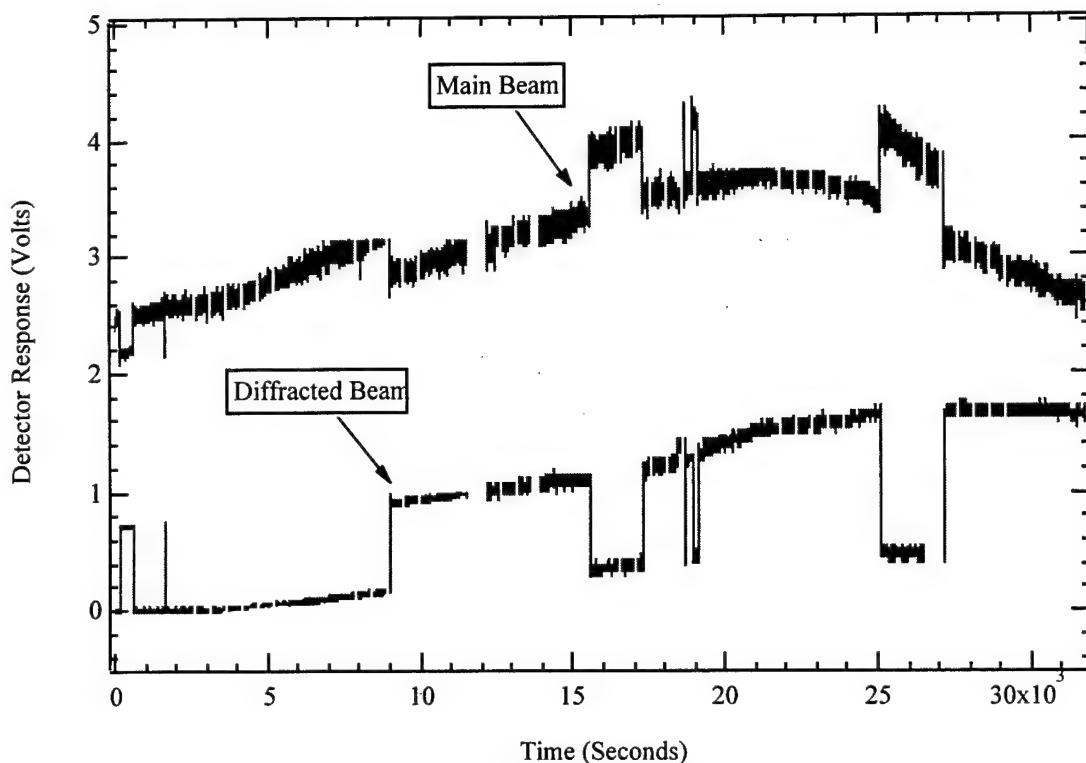


Figure 6-8. Neutron irradiation of TeO_2 AO device to a 1 MeV equivalent fluence of $1 \times 10^{15} \text{ n/cm}^2$ during intermittent operation at 130 MHz. The main and diffracted detector responses are plotted as a function of time and are corrupted (increasing) due to neutron interaction with the experimental apparatus.

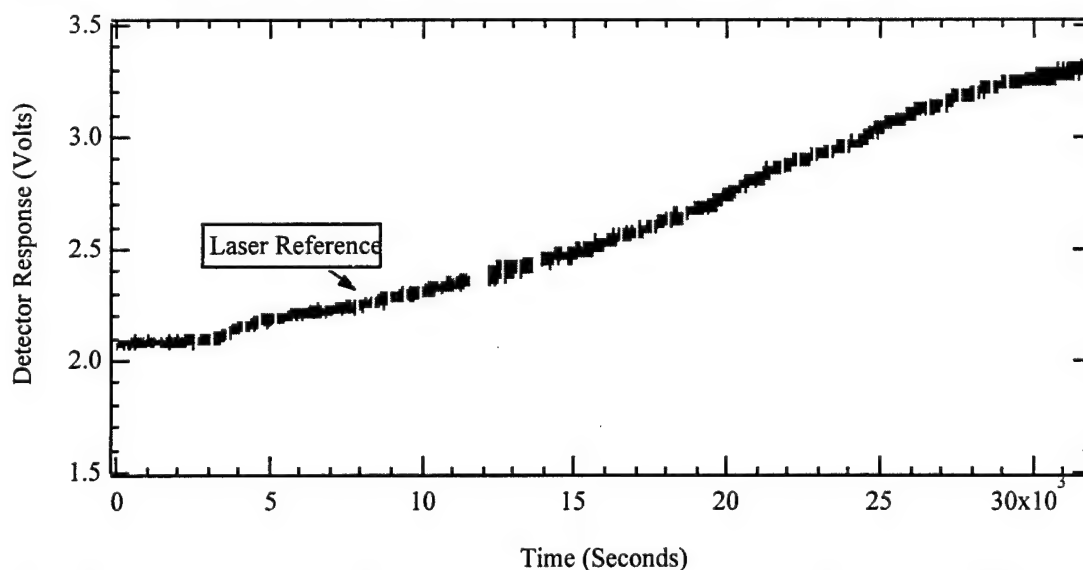


Figure 6-9. Laser reference detector response during the neutron irradiation of a TeO_2 AO device to a 1 MeV equivalent fluence of $1 \times 10^{15} \text{ n/cm}^2$ during intermittent operation of device. This plot indicates that the laser reference output is increasing. In actuality it is not, the increasing signal is due to the photodetector responding to neutrons.

6.1.4 Gamma Exposure of a LiNbO₃ Acoustooptic Bragg Cell #1

Gamma-ray irradiation (exposure 4, Table 6-1) was performed on a LiNbO₃ AO Bragg cell with RF modulation swept through a range of frequency larger than the specified bandwidth of the device. The diffraction efficiency of the bandwidth of the AO cell was measured with no observable changes for a total gamma-ray dose of 1.0 Mrad(Si).

A gamma exposure was performed with the RF modulation applied at a constant frequency and constant RF power. The diffraction efficiency of the AO device was measured up to a total dose of 1.0 Mrad(Si) with little or no change.

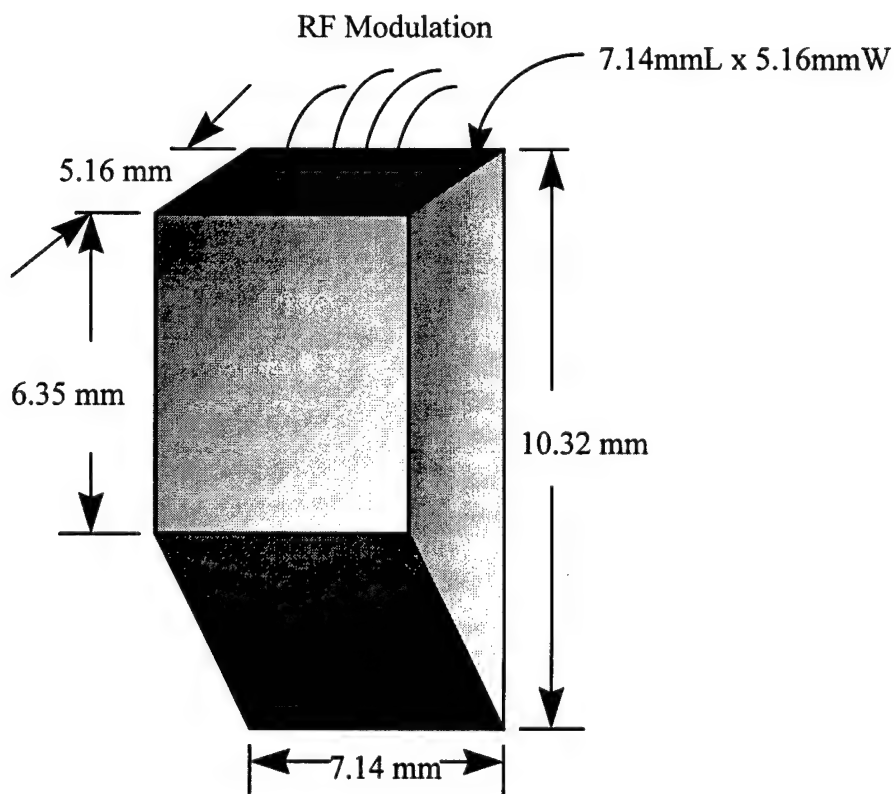


Figure 6-10. A drawing of the LiNbO₃ device under investigation in this exposure. The direction of the radiation is incident on the front face of the device, i.e., into the plane of the page.

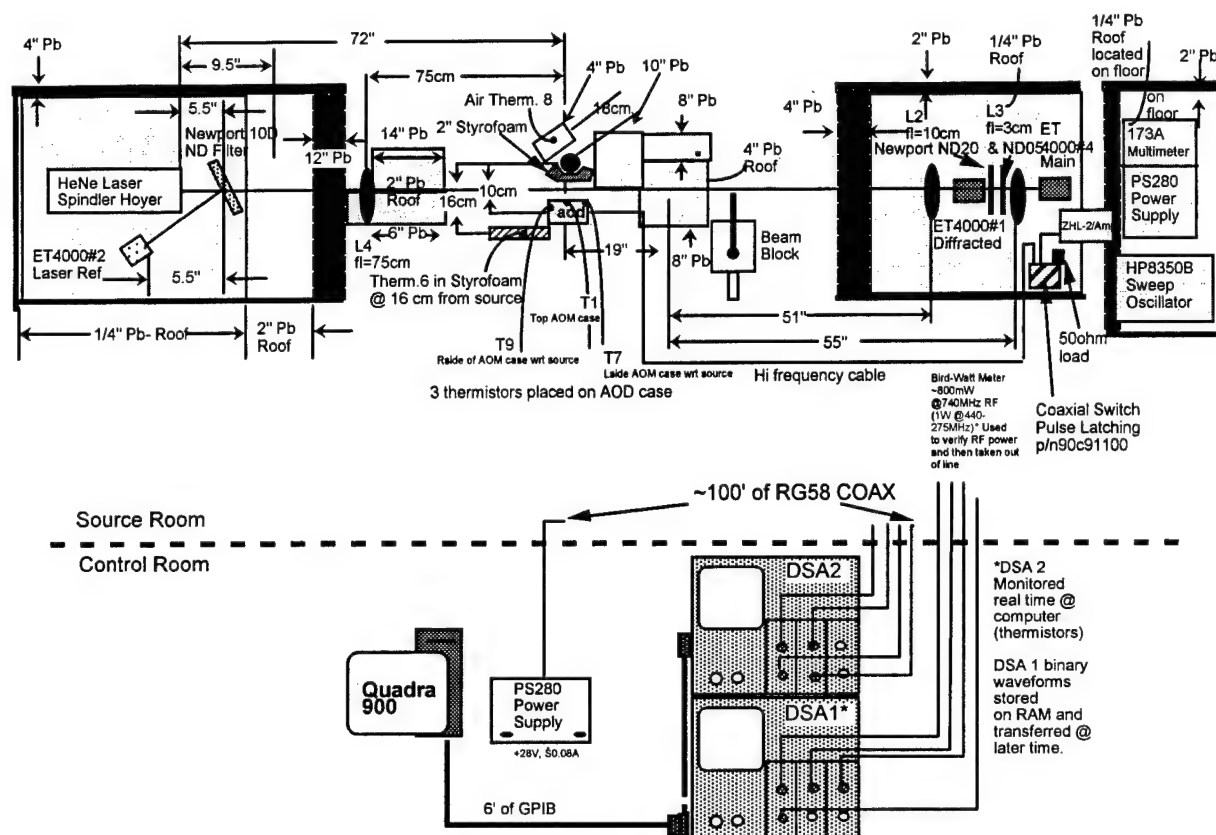


Figure 6-11. Experimental configuration for conducting active LiNbO_3 AO device bandwidth measurements in a gamma-ray environment.

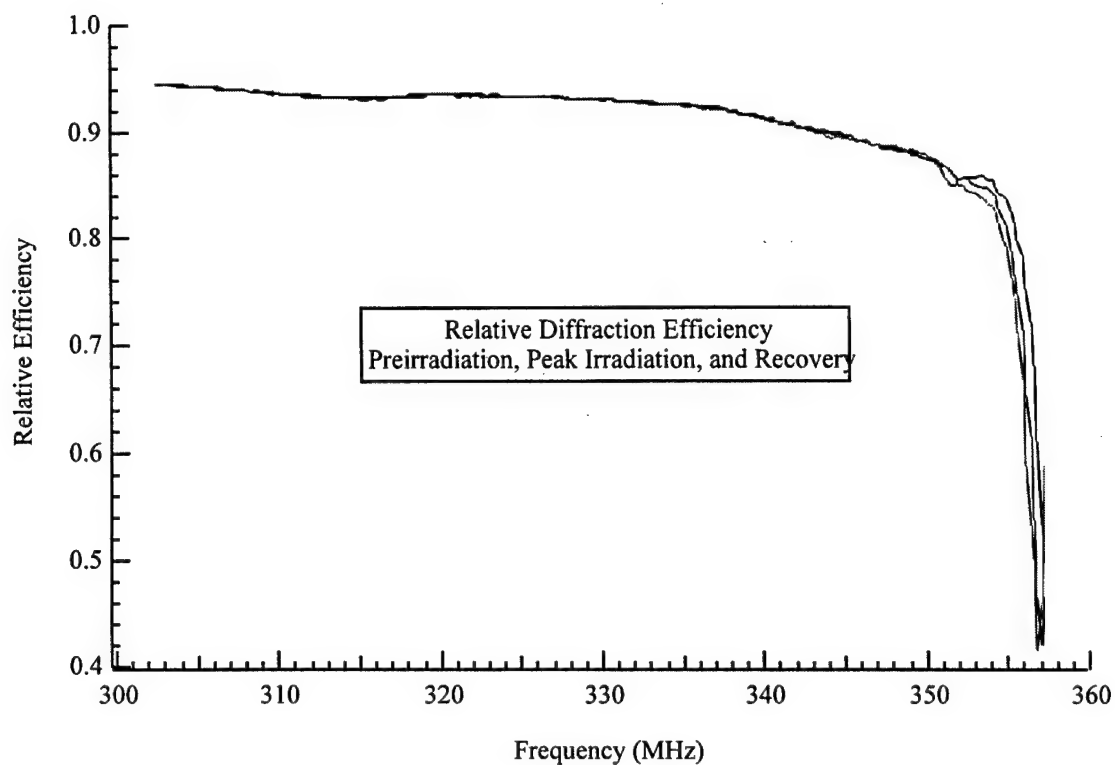


Figure 6-12. LiNbO_3 diffraction efficiencies before, during (peak) and after irradiation. No effect is evidenced by the relative closeness of the three plots. This is particularly true up to about 360 MHz.

6.1.5 Gamma Exposure of a LiNbO_3 Acoustooptic Bragg Cell #2

A gamma-ray exposure was performed on a LiNbO_3 AO Bragg Cell without RF modulation applied (exposure 5, Table 6-1). The radiation induced attenuation (α) was measured on the main beam (I_0') with no observable permanent induced attenuation for a total dose of 1.0 Mrad(Si). The insensitivity of the AOD to gamma-ray exposure is shown in Figure 6-13. The optical power (I_0'), propagating through the LiNbO_3 is reduced by approximately 0.08 dB after a 1.0 Mrad dose. However, the cell recovers to a level very near pre-irradiation levels.

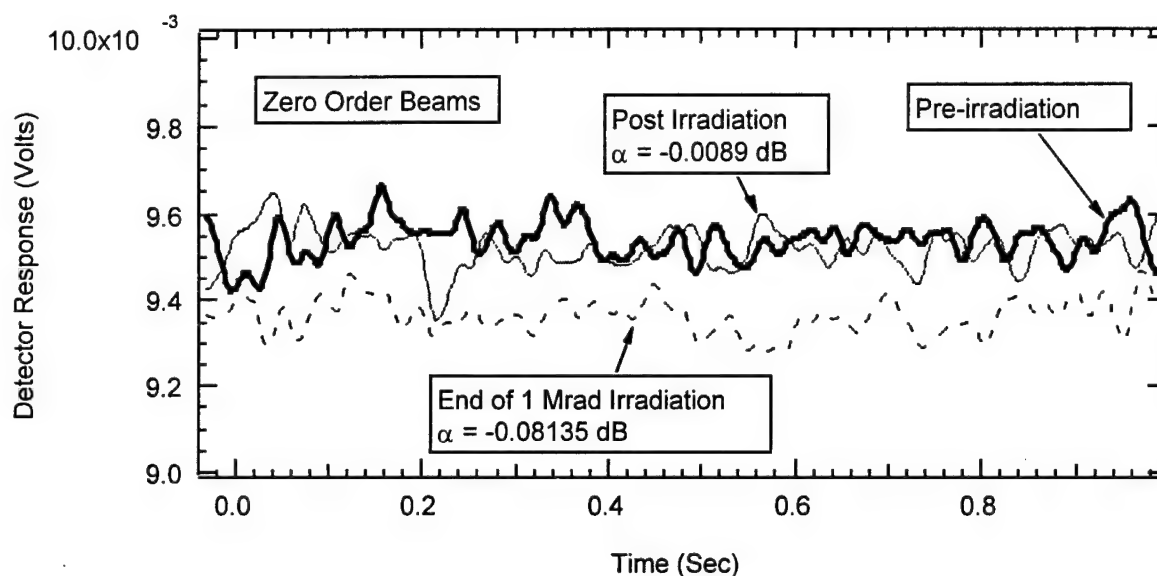


Figure 6-13. Comparison of the detector responses of pre-irradiation, end of irradiation, and recovery of the zero order beam for the LiNbO_3 AOD. Illustrated in this plot are three one second acquisitions of (I_0'), e.g., pre-exposure, end of radiation and end of recovery.

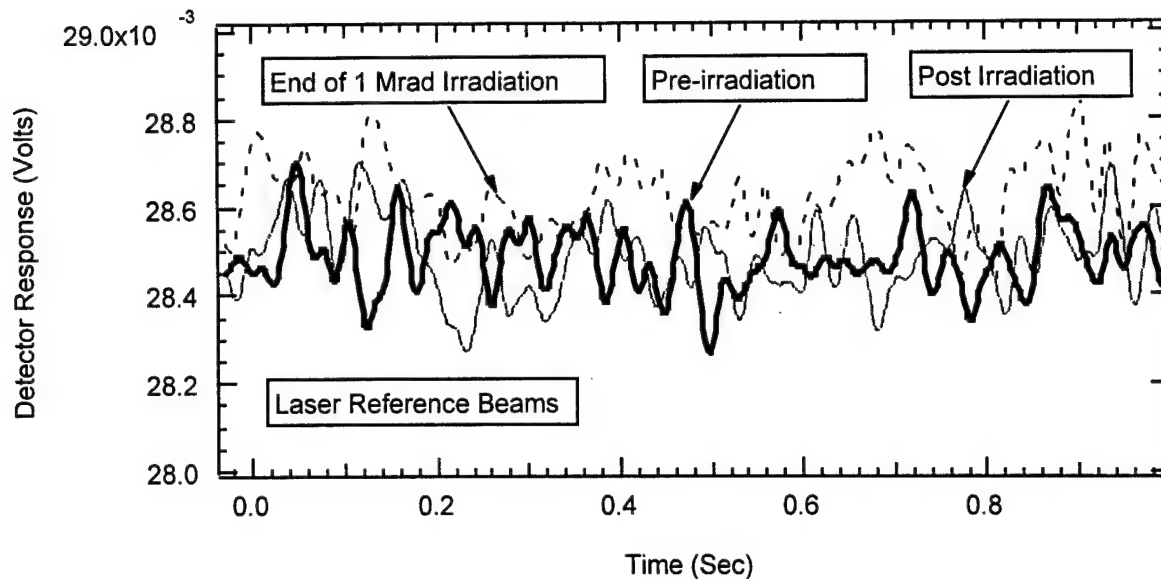


Figure 6-14. Comparison of the pre-irradiation, end of irradiation, and recovery of the laser reference beams of the LiNbO₃ AOD. In this plot, it is confirmed that regardless of the amount of radiation deposited in the AOD, the laser reference signal remains relatively unchanged.

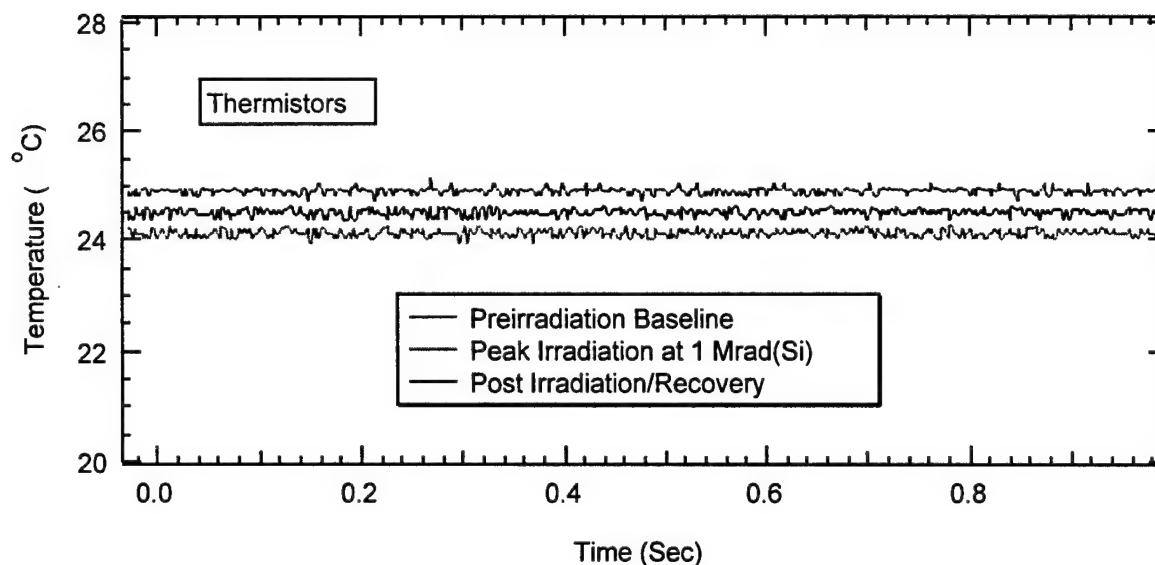


Figure 6-15. Comparison of the pre-irradiation, end of irradiation, and recovery of the thermistors on the LiNbO₃ AOD. This data shows that the temperature of the AO device increased by $\sim 1^\circ\text{C}$ over the course of a 1 Mrad(Si) exposure and cooled by $\sim 0.5^\circ\text{C}$ after the exposure. This is a relatively small temperature change and should not influence the output power of the laser, optical transmission of the LiNbO₃ AOD or response of the detector.

6.1.6 Neutron Exposure of a GaP Acoustooptic Bragg Cell

In this experiment (exposure 6, Table 6-1), a GaP AO cell was exposed to a neutron fluence of 1×10^{15} n/cm². The experimental configuration was modified from the previous neutron exposure, in this case the optical detection portion of the apparatus was located external to the Kiva (exposure cell). This arrangement alleviated the corruption of data observed in earlier measurements (Figure 6-7). The diffraction efficiency of this device was inherently low because of the narrow acoustooptic column (75 μ m). Accurate focusing of the laser diode to this spot size was not possible because of the relatively large distance between the emitter and AO cell; so, only an attenuation measurement of the AO cell was performed. The light source used was a 670 nm laser diode placed inside a polyethylene, cadmium and lead enclosure within the Kiva. This enclosure was constructed in late August 1995 and was also used during the active exposure of a TeO₂ AOM.

As shown in Figure 6-17, the laser diode beam was split by a 30:70 mirror mounted at 45° with respect to the axis of the laser diode output. A portion (30%) of the laser output power was beam split and used to monitor drift or changes in the laser diode output power and the remaining (70%) of the laser beam was routed into the AOM under investigation (referred to as the input beam). The input beam was next reflected off a turret style front surface mirror mounted at 45° with respect to the axis of the laser diode output. In this configuration, the input and reference beams both exited the laser shield enclosure, parallel to each other. Both beams were then reflected off a pair of gold coated mirrors allowing the reference beam to be guided directly through the 4 inch port in the SPRIII Kiva door while the input beam was directed through the AOM. The output from the AOM was subsequently reflected off a front surface coated aluminum mirror and guided through the 4 inch port in the Kiva door. Two additional front surface aluminum mirrors were used outside the Kiva to turn the beams by 90° towards individual optical receivers. Each of the beams were next passed through a neutral density filter and lens and focused onto their respective silicon detectors. Additionally, a “dark detector” was located in proximity to the other silicon detectors, which were illuminated. This “dark detector” was used to determine the radiation effects on a silicon detector alone, independent of the AO

cell or light source. Permanent induced attenuation of the GaP crystal was observed as a result of the neutron irradiation. Visual inspection of the AO crystal before and after the neutron exposure clearly showed that the color had changed from an light yellow to amber, indicating color center damage.

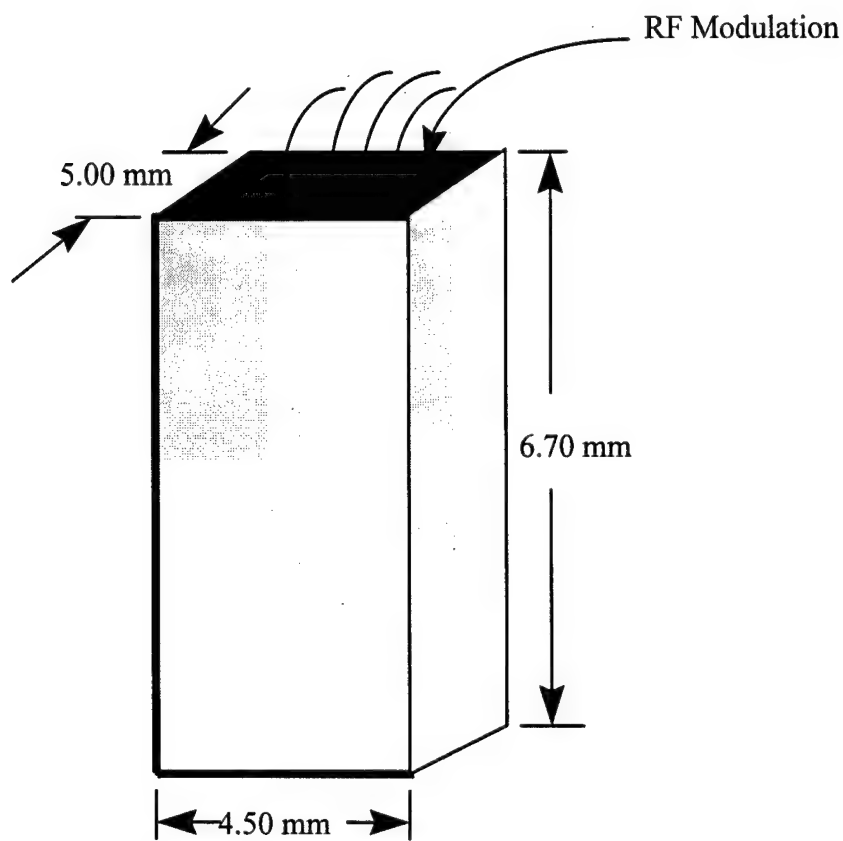


Figure 6-16. GaP device under investigation in exposure 6, Table 6-1. The direction of the radiation is incident on the front face of the device, i.e., into the plane of the page.

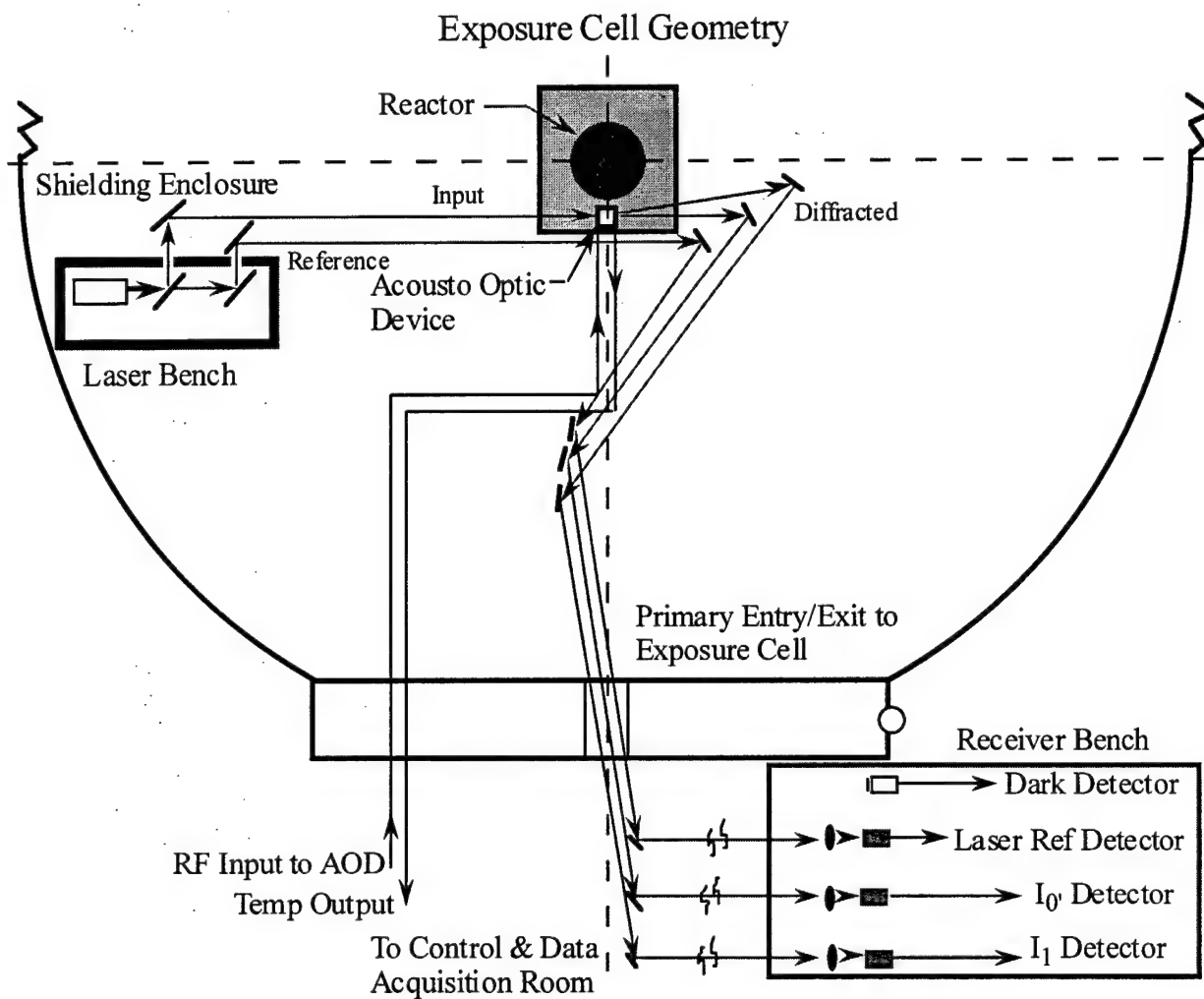


Figure 6-17. Experimental set-up for the GaP AO device (exposure 6, Table 6-1). An improvement over the experimental set-up used in exposure 3, Table 6-1 (see Figure 6-9 for configuration). A reduction of undesired irradiation effects on silicon detectors was realized.

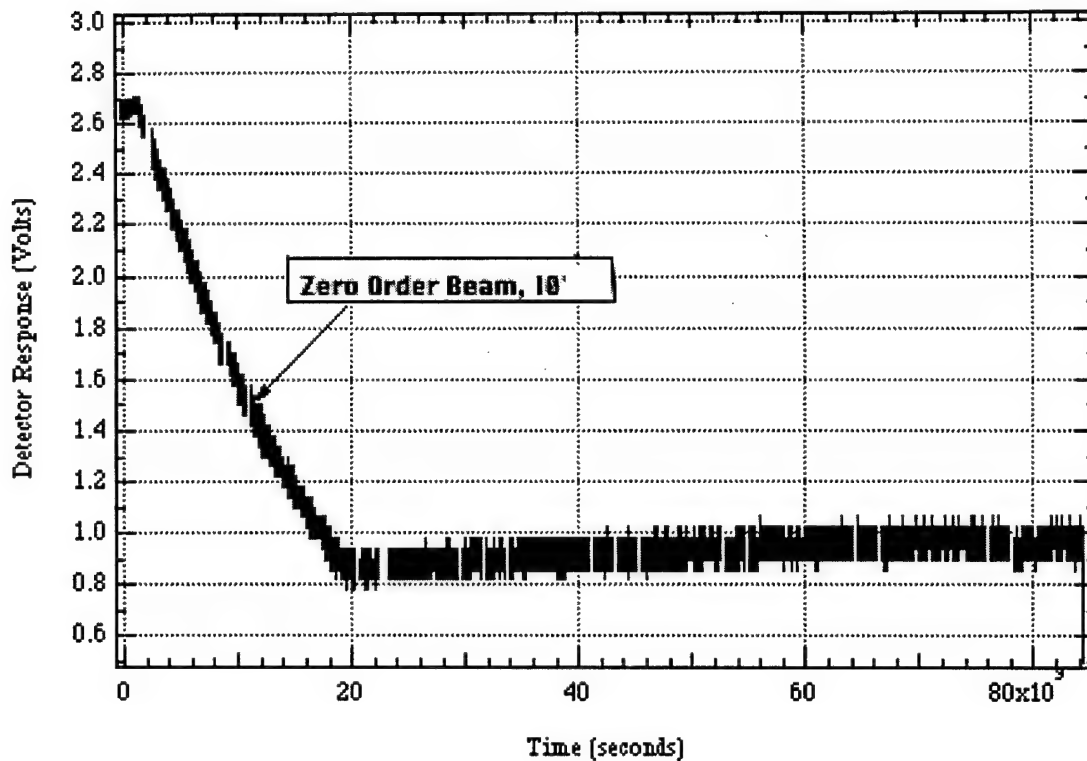


Figure 6-18. Optical detector response to light ($\lambda = 670$ nm) from an Injection Laser Diode (ILD) through an unmodulated GaP AO device during exposure to neutrons. A total neutron fluence of 1×10^{15} n/cm² was applied over a 6 hour period.

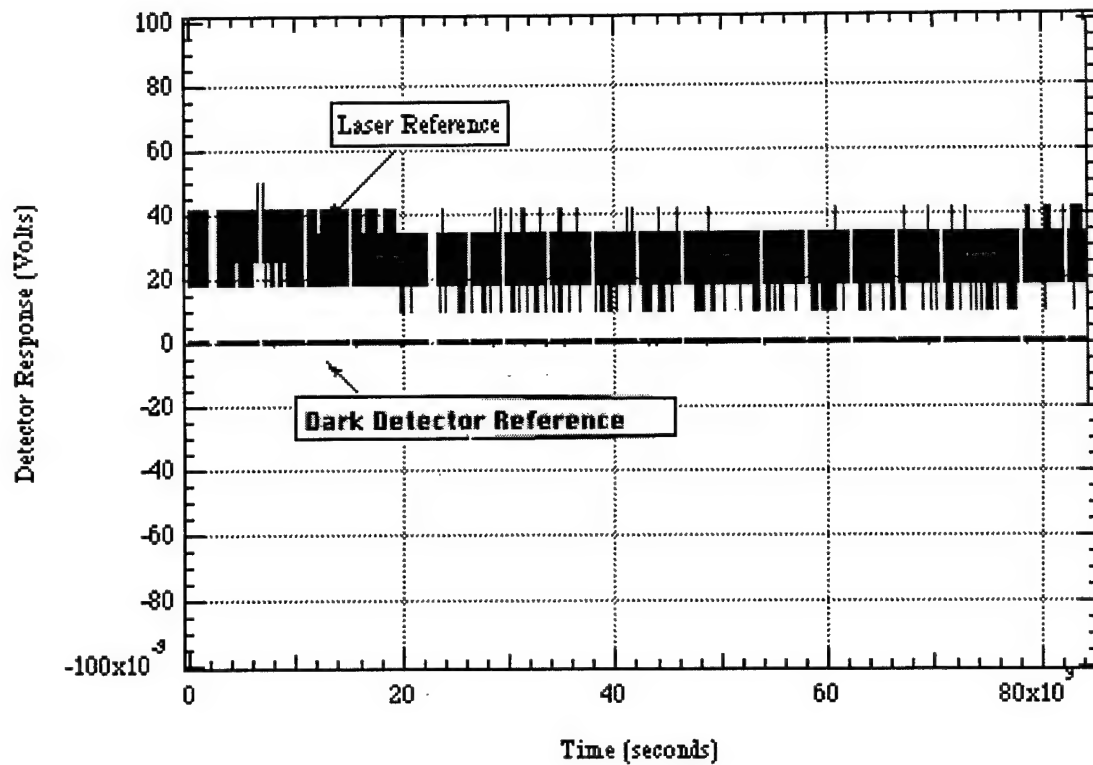


Figure 6-19. Laser reference and dark detector reference response during the course of neutron exposure of a GaP AO device and recovery. This shows that the dark detector and laser source are unaffected by neutron irradiation.

6.1.7 Gamma Exposure of an InP Acoustooptic Bragg Cell

The intent of this exposure was to actively measure the diffraction efficiency of an Indium Phosphide (InP) AO cell to gamma-rays (exposure 7, Table 6-1). This was done by exposing the AO cell to a total dose of 1 Mrad gamma irradiation from a Co-60 source, while monitoring the main beam (I_0) and diffracted beam (I_d) to determine the diffraction efficiency of the cell. A partially reflective mirror was used to monitor a modified HeNe laser ($\lambda = 1152 \text{ nm}$) source beam for drift. The HeNe laser, all detectors, mirrors, lenses, and filters used in the set-up were shielded using lead bricks and sheets. Only the AO cell and its mount were actively irradiated.

The results show little or no transient or permanent damage due to the irradiation. The data dropout and recovery prior to irradiation were due to interference from nearby lightning strikes. Note that the laser reference signal was recorded on a more sensitive scale than the other signals and was observed to change less than 0.1 V.

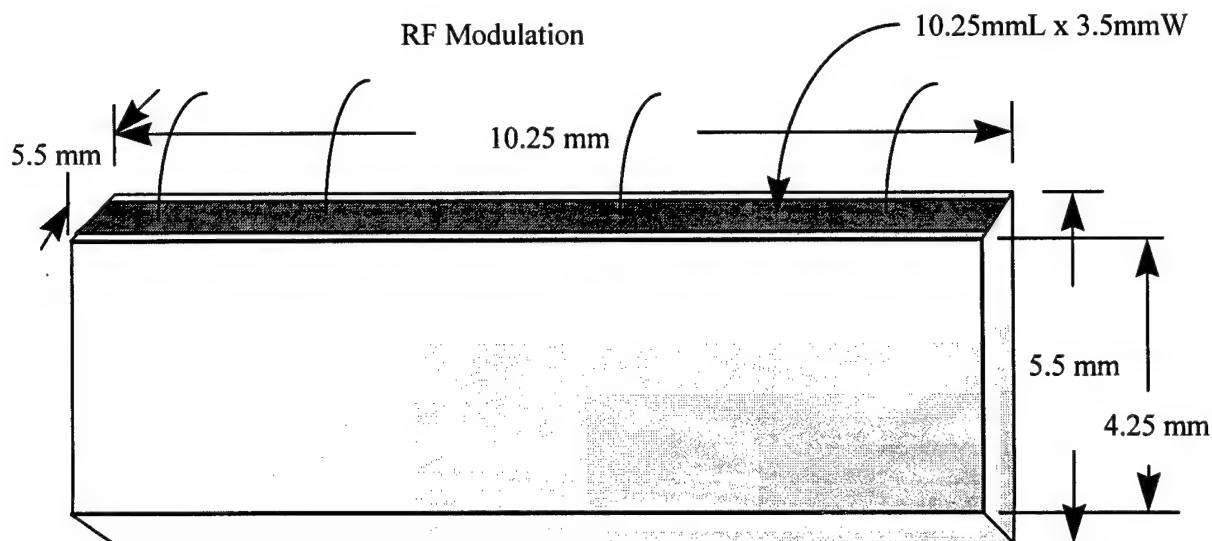


Figure 6-20. A drawing of the InP device under investigation in this exposure.

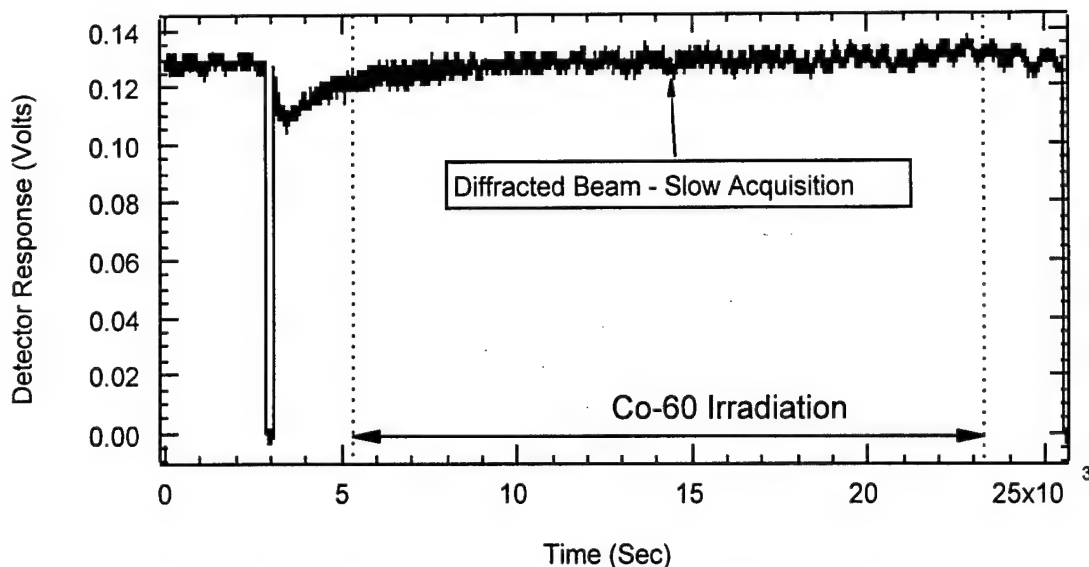


Figure 6-21. Diffracted beam (I_d) response of InP AO Bragg cell exposed to a 1 Mrad gamma irradiation dose. Note: very small change in diffracted beam power over the irradiation period.

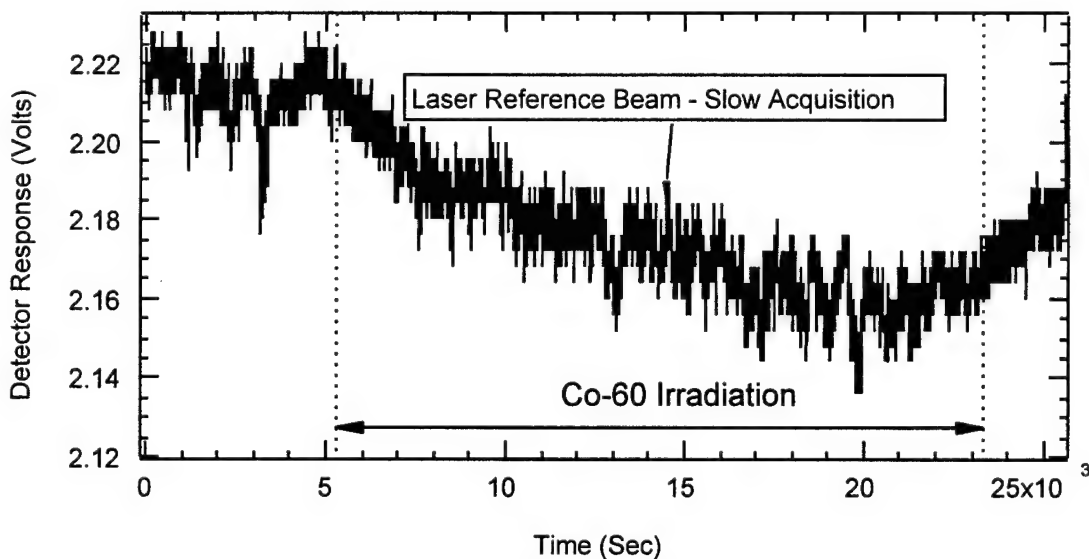


Figure 6-22. HeNe laser reference beam response of InP AO Bragg cell exposed to a 1 Mrad gamma irradiation dose. Note: the scale shown, magnifies the small amount of laser drift. The amount of drift is approximately 5% over the period of investigation (416 min).

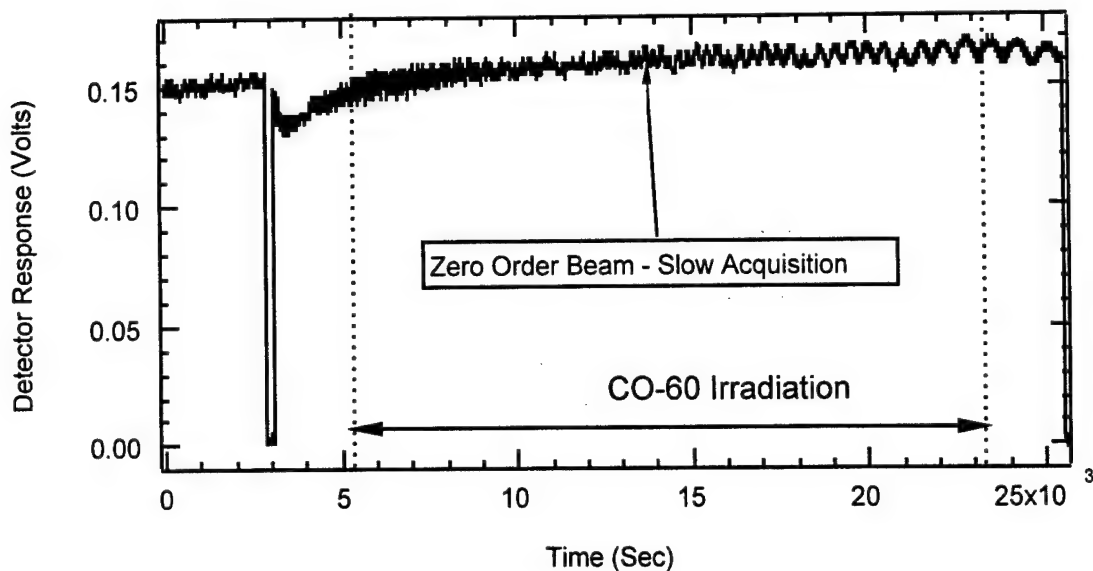


Figure 6-23. Main beam (I_0') response of InP AO Bragg cell exposed to a 1 Mrad gamma irradiation dose.

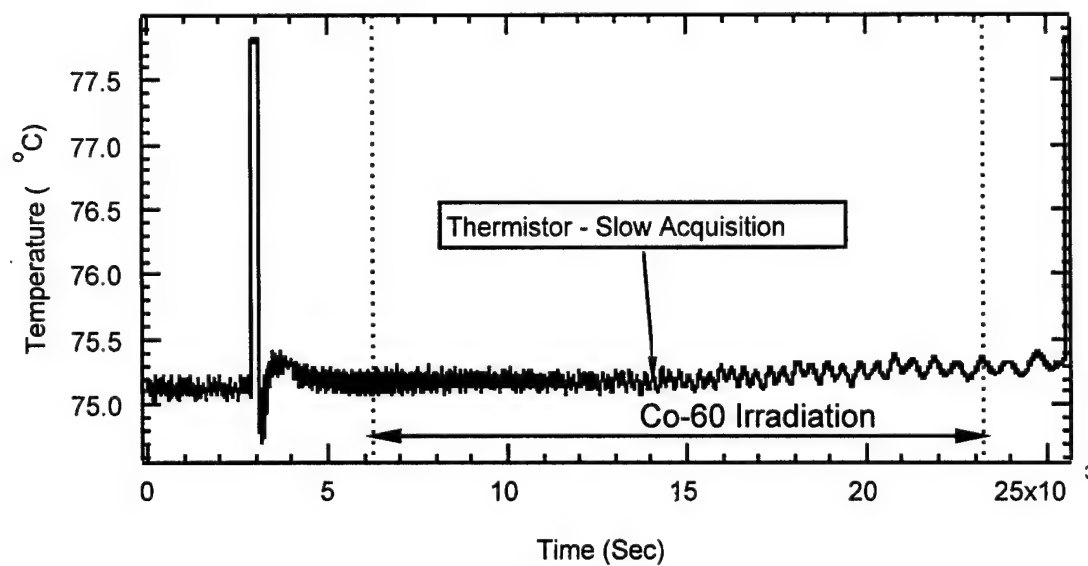


Figure 6-24. Temperature response of InP AO Bragg cell exposed to a 1Mrad gamma irradiation dose.

6.1.8 Neutron Exposure of a TeO_2 Acoustooptic Bragg Cell

Exposure 8, Table 6-1 was performed by actively exposing a Tellurium Dioxide acoustooptic cell at the Sandia National Laboratories Pulsed Reactor III (SPRIII) to a total fluence $1 \times 10^{15} \text{ n/cm}^2$. Based on the results of the in-situ attenuation measurements made in late FY95 and early FY96 at the SNL-SPRIII reactor, it was determined that an alternative method for monitoring optical power adjacent to the reactor was needed, Figure 6-26. This method called for the removal of the optical source and silicon photodetectors from the high radiation area and involved critical alignment of a series of mirrors and lenses. This new arrangement greatly improved our ability to isolate radiation induced effects in the device under irradiation from deleterious effects on the optical source and detectors, Figures 6-27 to 6-30. In this experiment, a HeNe laser emitting at $0.632.8 \mu\text{m}$ was used as a source and PIN detectors were used to monitor the main and diffracted beam optical powers. In summary, no major effects in the TeO_2 were observed as a result of this exposure.

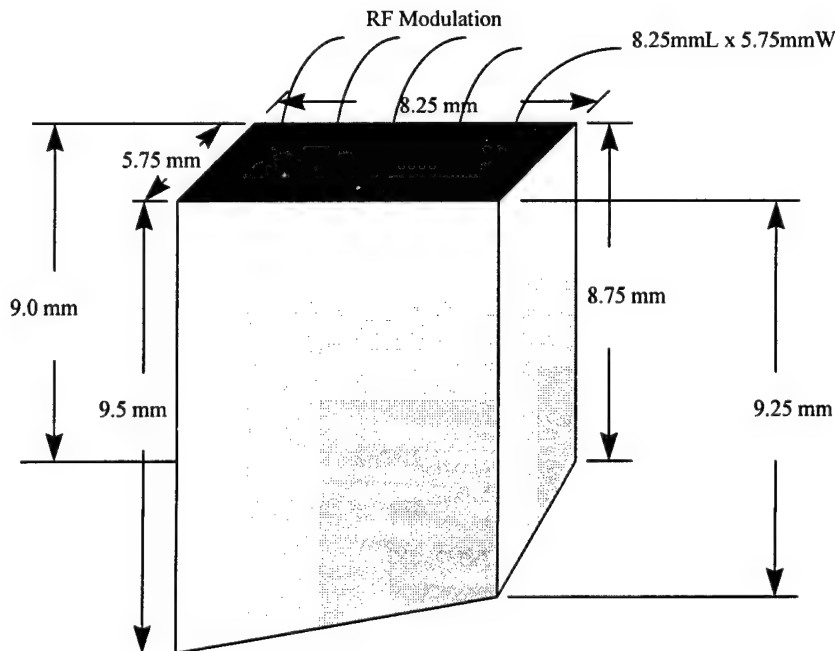


Figure 6-25. A drawing of the TeO_2 device under investigation in this exposure. The direction of the radiation is incident on the front face of the device, i.e., into the plane of the page.

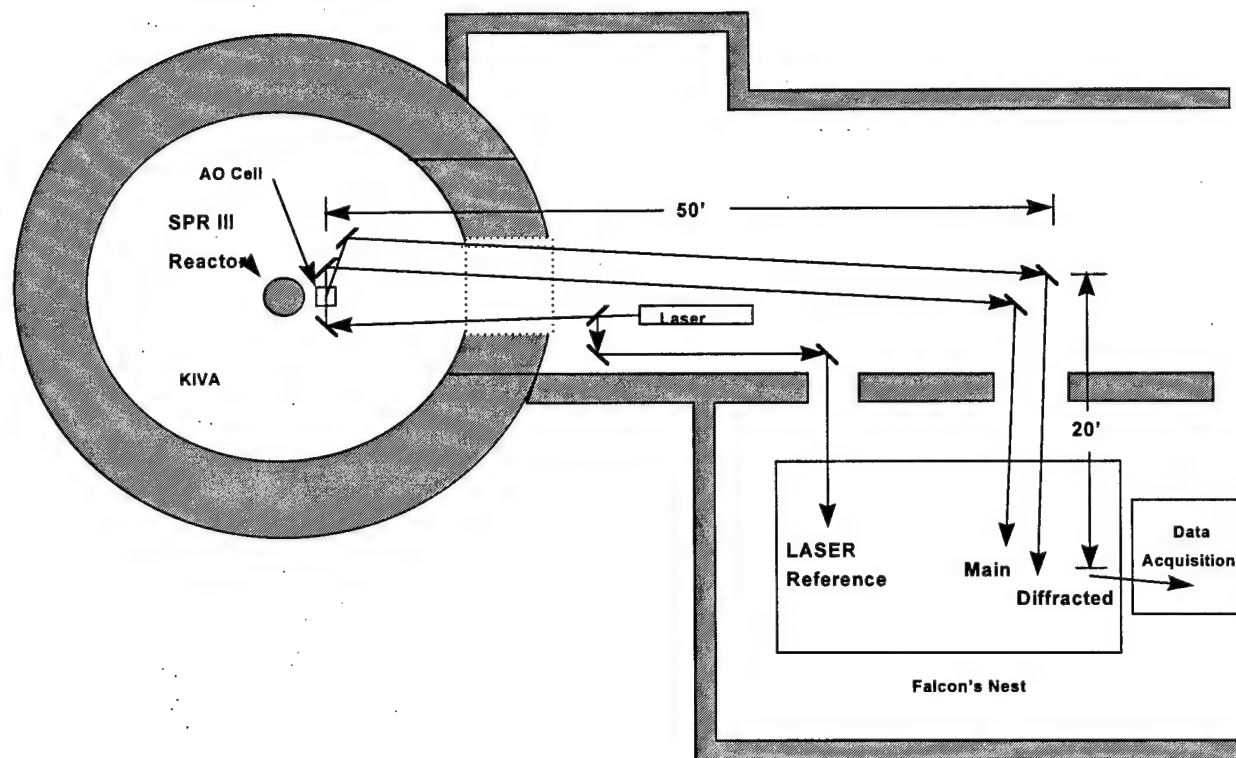


Figure 6-26. SPR III active irradiation configuration for measuring diffraction efficiency of a TeO₂ acoustooptic device under an exposure of 1×10^{15} n/cm². Note: drawing is not to scale, but serves to illustrate the relatively large distance between the AO device and source/detection instrumentation.

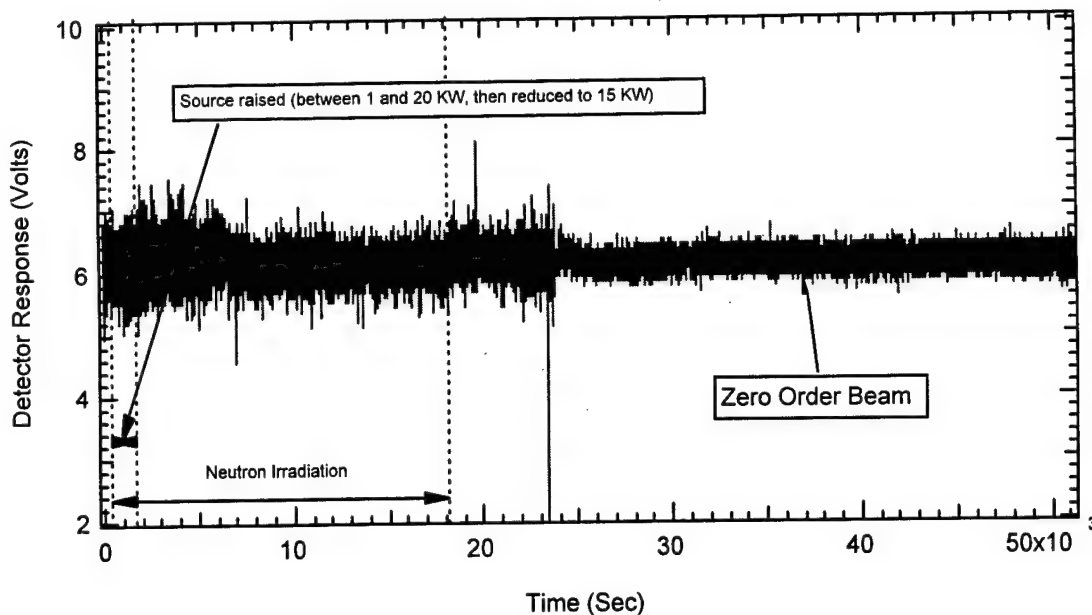


Figure 6-27. TeO₂ zero order beam I₀' response to 1x10¹⁵ n/cm² fluence. Note, no significant degradation to the signal was observed.

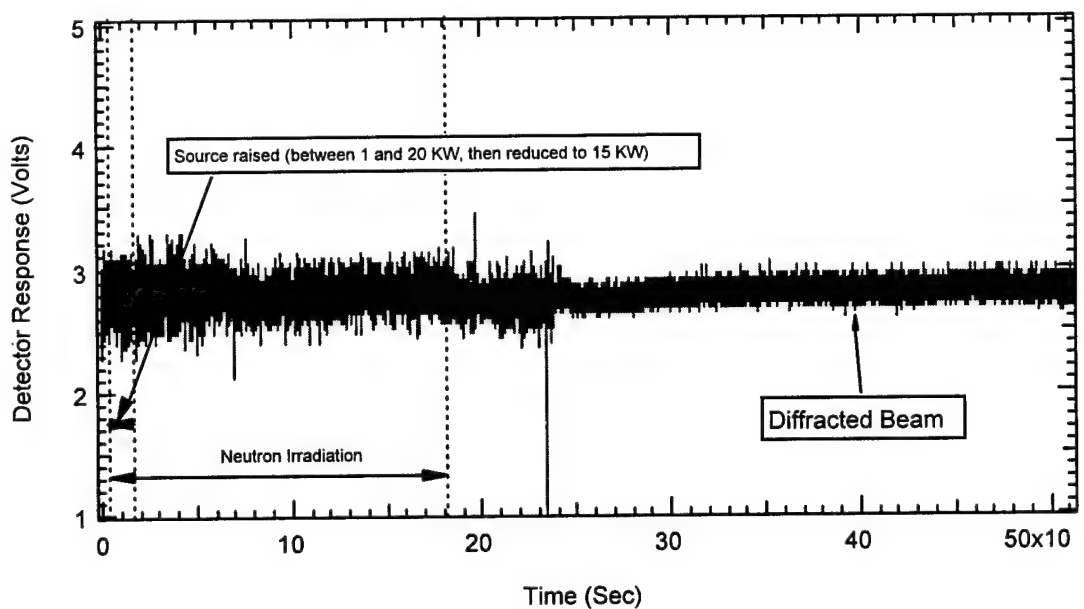


Figure 6-28. TeO₂ diffracted beam response to 1x10¹⁵ n/cm² fluence. Note: no significant degradation to the signal was observed.

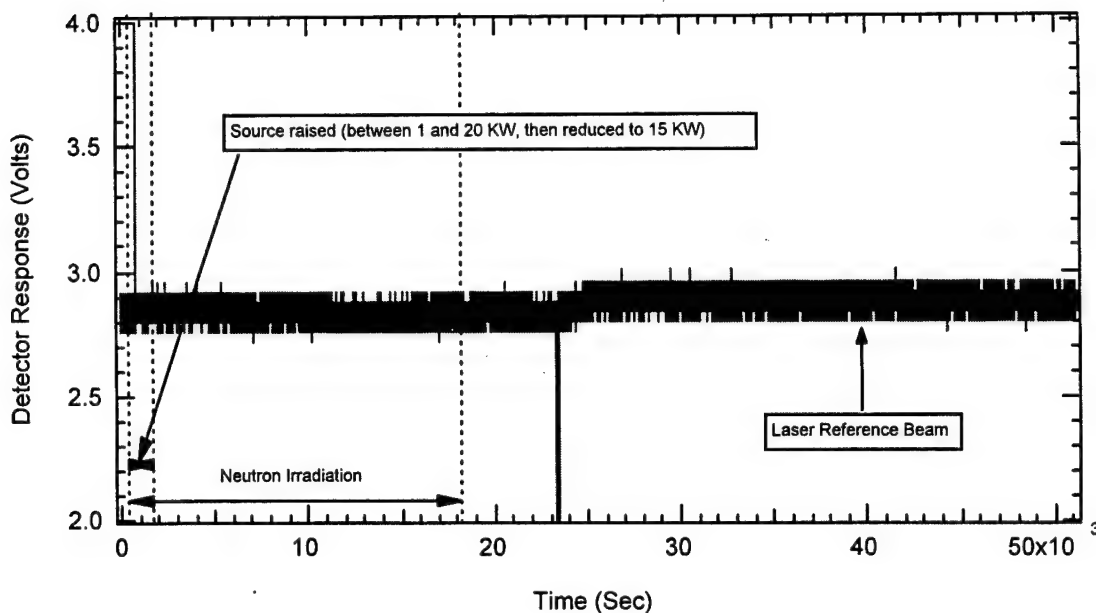


Figure 6-29. HeNe laser reference beam response to 1×10^{15} n/cm² fluence. Note, no significant degradation to the signal was observed.

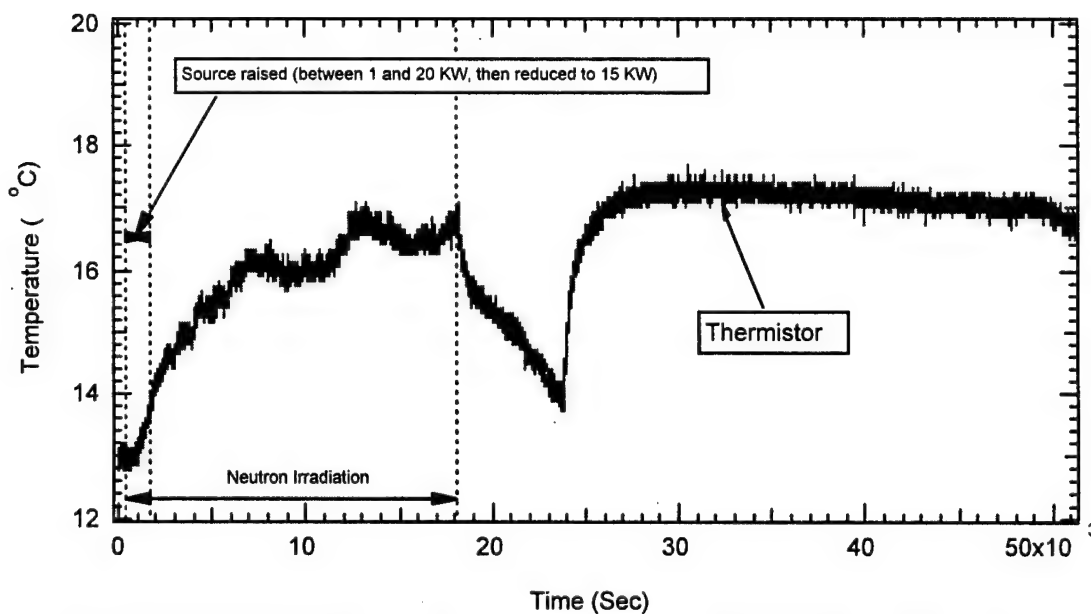


Figure 6-30. TeO₂ AO device temperature response to 1×10^{15} n/cm² fluence. Note temperature variations as a result of reactor operation and position can be seen.

This page intentionally left blank.

7.0 PASSIVE NEUTRON EXPOSURE OF LiNbO₃, GaP, AND InP ACOUSTOOPTIC BRAGG CELLS

Exposure 9, Table 6-1 was performed by passively and simultaneously exposing three acoustooptic cells to the Sandia National Laboratories Pulsed Reactor III (SPRIII). Originally, it was planned that the above listed materials would be monitored actively while being exposed. Unfortunately, circumstances beyond our control would have delayed active exposures into FY98. This delay created a backlog of work for the SPRIII facility, which in turn lead us to perform a passive exposure of the devices. This chapter describes the exposure and findings.

The intent of this investigation was to characterize neutron-induced effects in various acoustooptic devices. It is the fourth in a series conducted during FY95-97 by the Phillips Laboratory - Photonics Research Group at the SNL-SPRIII. This research was a continuation of work targeted at investigating neutron responses of various acoustooptic materials. The experiment methodology and detailed descriptions of the measurements performed are described.

7.1 GENERAL EXPERIMENT DESCRIPTION

Acoustooptic deflectors/modulators, LiNbO₃, GaP, and InP were passively exposed to a total of fluence of 1×10^{15} neutrons/cm² (Figures 7-1 through 7-3) for device dimensions. Pre and post exposure measurements were performed and are subdivided into four categories: broad spectral width absorption, narrow spectral width absorption, diffraction efficiency at the AOM center frequency, and bandwidth responses.

7.1.1 Broad Spectral Width Absorption

Spectral absorption was measured with a scanning monochromometer, Figure 7-4. Light output from a Xenon lamp was UV filtered, apertured, focused and transmitted through the AO material under investigation. This output optical beam from the AO material was then passed through the

scanning monochromator and the light was collected by a silicon photodetector and recorded with a Digital Signal Analyzer (DSA-602). In this case, the monochromator is swept over a relatively large spectral width (~ 150 nm). Initial spectral scans were made absent of any AO material in the light path to obtain spectral characteristics of the lamp and subsequent optical elements. This procedure was repeated before and after the AO device was subjected to neutron irradiation.

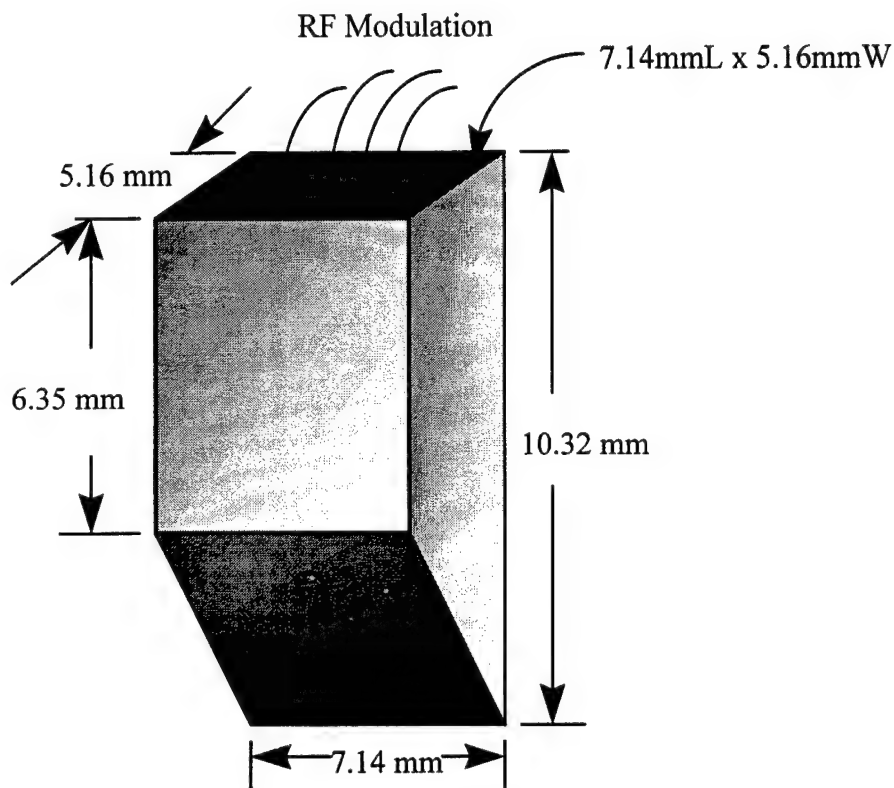


Figure 7-1. LiNbO₃ device under investigation in this exposure. The direction of the radiation is incident on the front face of the device, i.e., into the plane of the page.

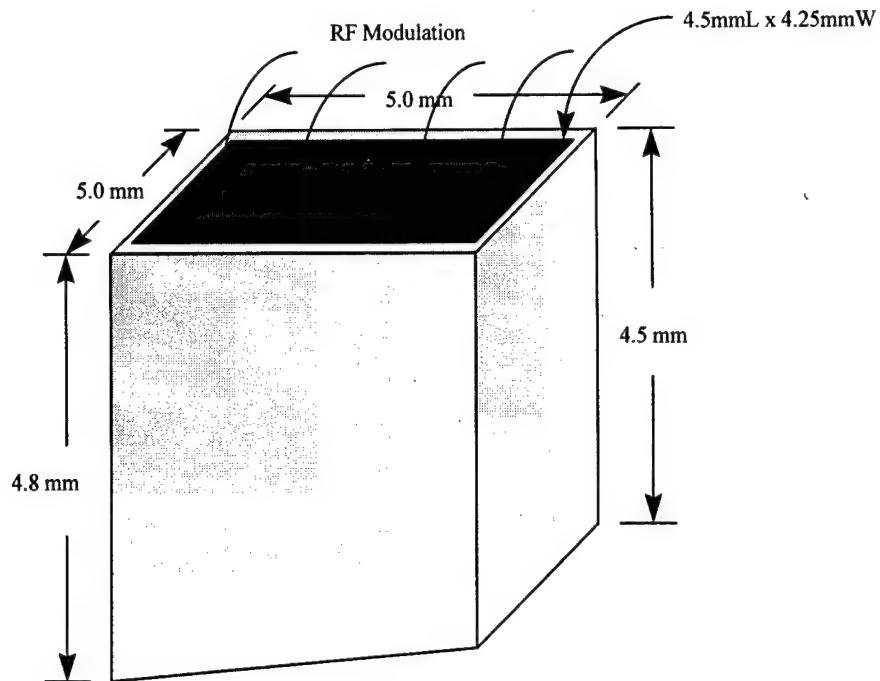


Figure 7-2. GaP device under investigation in this exposure. The direction of the radiation is incident on the front face of the device, i.e., into the plane of the page.

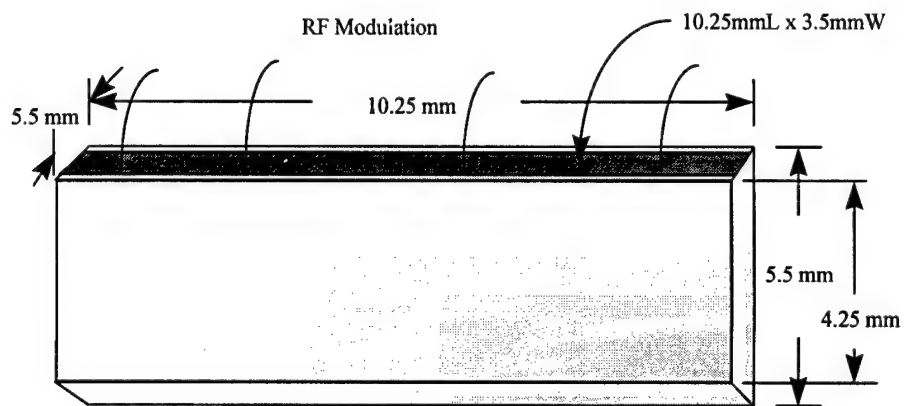


Figure 7-3. InP device under investigation in this exposure. The direction of the radiation is incident on the front face of the device, i.e., into the plane of the page.

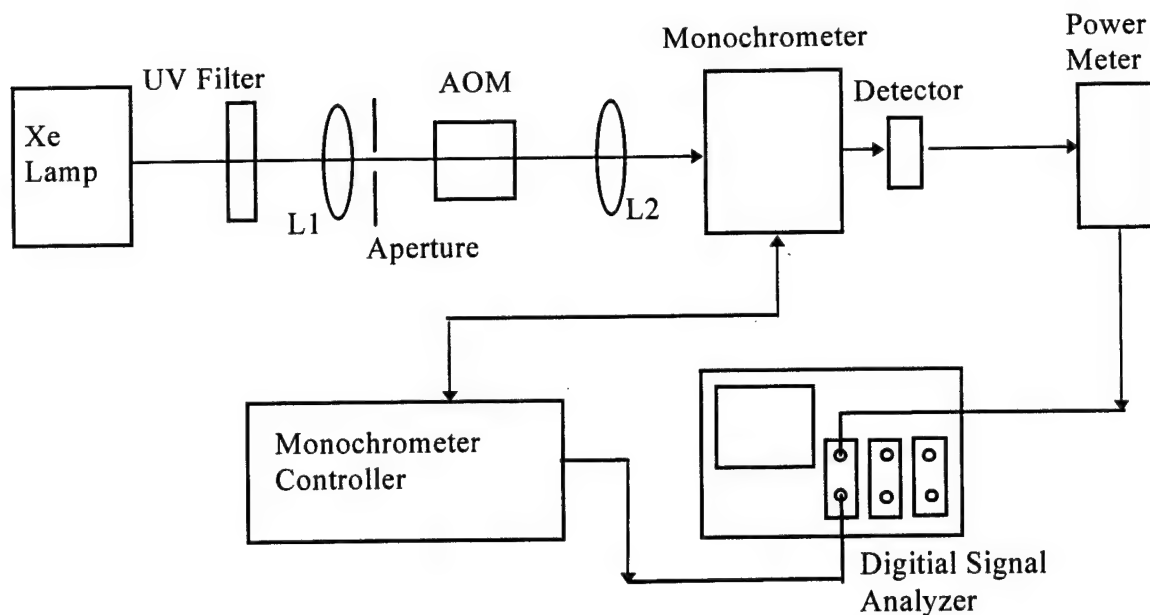


Figure 7-4. Typical spectral characterization response configuration used for broad spectral width absorption measurements.

7.1.2 Narrow Spectral Width Absorption

Light output from a 670 nm laser diode was apertured, focused and transmitted through the AO material under investigation (Figure 7-4). This output optical beam from the AO material was then passed through the scanning monochromator and the light was collected by a silicon photodetector and recorded with a Digital Signal Analyzer (DSA-602). In this case, the monochromator was swept over a relatively narrow spectral width (~10 nm). Initial spectral scans were made absent of any AO material in the light path to obtain spectral characteristics of the laser diode and subsequent optical elements. This procedure was repeated before and after the AO material was subjected to neutron irradiation.

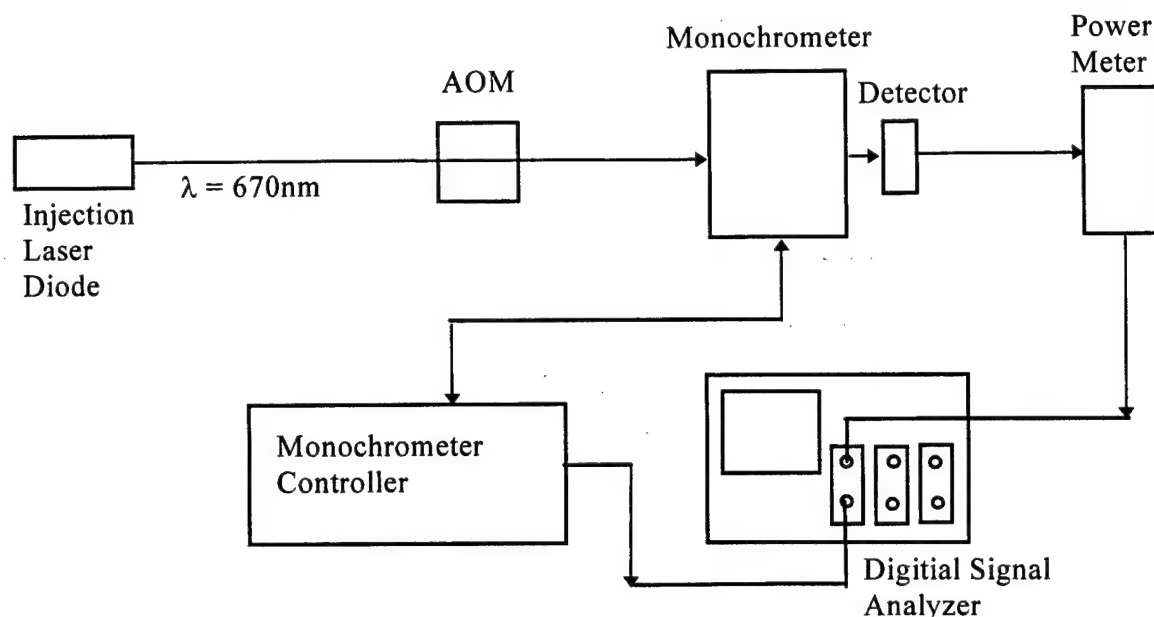


Figure 7-5. Typical spectral characterization response configuration used for narrow spectral width absorption measurements.

7.1.3 Data Analysis of Broad/Narrow Spectral Width Absorption

The intent of performing broad/ narrow spectral absorption measurements was to determine if the radiation exposure changes the material's transmissive properties over the spectral width being scanned. In both cases, the spectral scan signal without the AO material in the light path is subtracted from the scan signal through the AO material. This procedure is performed on the AO sample before and after irradiation exposure. The resultant curves are then compared and analyzed for changes in the transmissivity of the material over the spectral width being scanned.

7.1.4 Changes to Diffraction Efficiency at the AOM Center Frequency

The general procedure for performing a diffraction efficiency measurement to optimize the optical and electrical parameters of the cell is as follows. The optical power in the zero and first order output beams from the AO device are first measured using an optical power meter. Optical optimization includes launching the proper optical polarization, beam size and physical orientation (Bragg angle) of the device. Electrical parameters being input into the AO cell

include: the RF center frequency and power level being delivered to the AO device. Typically, the optical inputs are configured, followed by application of the RF power. The last step was to optimize the cell alignment and measure the optical power in the main and diffracted output beams. In conjunction with this procedure it is convenient to measure the insertion loss of the material. This is simply done by measuring the optical power into and out of the AO material with the RF power in the off state. It is generally performed after the device has been optimized optically and electrically. The advantage to this sequence is that the optical insertion loss is measured through roughly the same path in the material that the light is diffracted through when the RF power is applied.

7.1.5 Changes to AOM Bandwidth

As discussed in the above paragraph, the diffraction efficiency of the cell is optimized at the center frequency. At this stage, the RF frequency input is varied over a range greater than the specified bandwidth. The resulting optical powers in the main and diffracted beams over this frequency range effectively yield the diffraction efficiency of the cell over the useful range of the device. Bandwidth response curves (diffraction efficiency vs. frequency) were measured before and after the AO devices were irradiated.

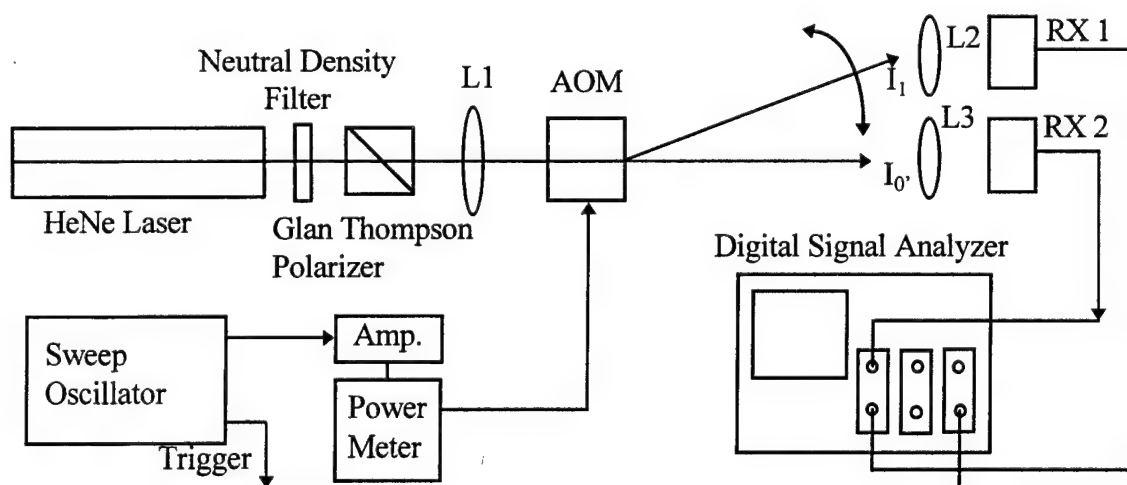


Figure 7-6. Typical acoustooptic device bandwidth response configuration.

Pre-Exposure Measurements:

Spectral scans on AO cell using monochrometer system
Optical power out of laser to be used for actual experiment
Polarization orientation / Extinction into AO cell
Optical power out of AO cell (unmodulated)
Optical power out of AO cell (modulated)
Main Beam
Diffracted beam
Bandwidth response curves
RF power into AO cell at the center frequency
Place dosimetry as required
Distances measured in cm of experiment configuration and other environmental parameters;
temp, time, etc

In-situ Measurements:

TLDs and/or other dosimetry for total dose/dose rate measurement

Post Exposure Measurements:

Spectral scans on AO cell using monochrometer system
Background / device radiation dose rate
Optical power into AOD
Optical power out (modulated)
Main Beam
Diffracted Beam
Optical Power Out (unmodulated)
Main Beam
RF power into AO cell at the center frequency
Bandwidth response curves
Read out total dose from dosimetry.

7.2 RESULTS OF 1×10^{15} n/cm² PASSIVE EXPOSURE OF: GaP, LiNbO₃, and InP**7.2.1 Diffraction Efficiency and Insertion Loss Results**

Summarized in Table 2. are pre and post diffraction efficiency measurements and permanent changes as a result of neutron exposure. The GaP material diffraction efficiency appears to improve slightly after irradiation and the LiNbO₃ and InP degrade by approximately 10%.

Table 7-1. Diffraction efficiency changes as a result of 1×10^{15} n/cm² fluence on AO devices.

Material	η : pre-exposure	η : post-exposure	$\Delta \eta$
GaP	1.03% [1.28%]	1.97% [2.45%]	+0.94% [1.16%]
LiNbO ₃	11.78% [15.12%]	1.01% [11.69%]	-10.77% [-3.43%]
InP	52.13% [50.61%]	41.74% [53.97%]	-10.39% [3.36%]

Note(s): The above measurements are made at the Bragg condition and the device center frequency. For the diffraction efficiency(η), measurements in brackets (i.e. []) represent derived values acquired from silicon photodetectors at the center frequency of the AO cell that were recorded during the bandwidth sweep. The non-bracketed η values represent measurements made with an optical power meter at the center frequency (fixed) prior to the bandwidth sweep.

Summarized in Table 7-2 are pre and post attenuation measurements and permanent changes as a result of neutron exposure. In this case the GaP and InP material show significant increases in their attenuation where LiNbO₃ shows a slight decrease. The measurements were made with an optical power meter without RF power applied to AO cell.

Table 7-2. Changes to insertion loss (attenuation) as a result of 1×10^{15} neutron/cm² exposure.

Material	α : pre-exposure	α : post-exposure	$\Delta \alpha$
GaP	-0.87 dB $\lambda = 632.8$ nm	-7.57 dB $\lambda = 632.8$ nm	-6.70 dB
LiNbO ₃	-0.41 dB $\lambda = 632.8$ nm	-0.32 dB $\lambda = 632.8$ nm	+0.09 dB
InP	-3.08 dB $\lambda = 1152$ nm	-6.08 dB $\lambda = 1152$ nm	-3.00 dB

α is the Insertion loss or bulk attenuation in dB, given by $\alpha = -10 \log_{10}(P_o/P_{in})$, where, P_o is the Optical power out of AO cell (with no RF power) and P_{in} is the Optical power in to AO cell. Note: The above measurements are made at Bragg condition alignment without RF applied.

7.2.2 Bandwidth Response Results

The following plots illustrate the pre and post exposure measurements of bandwidth for the three materials/devices studied.

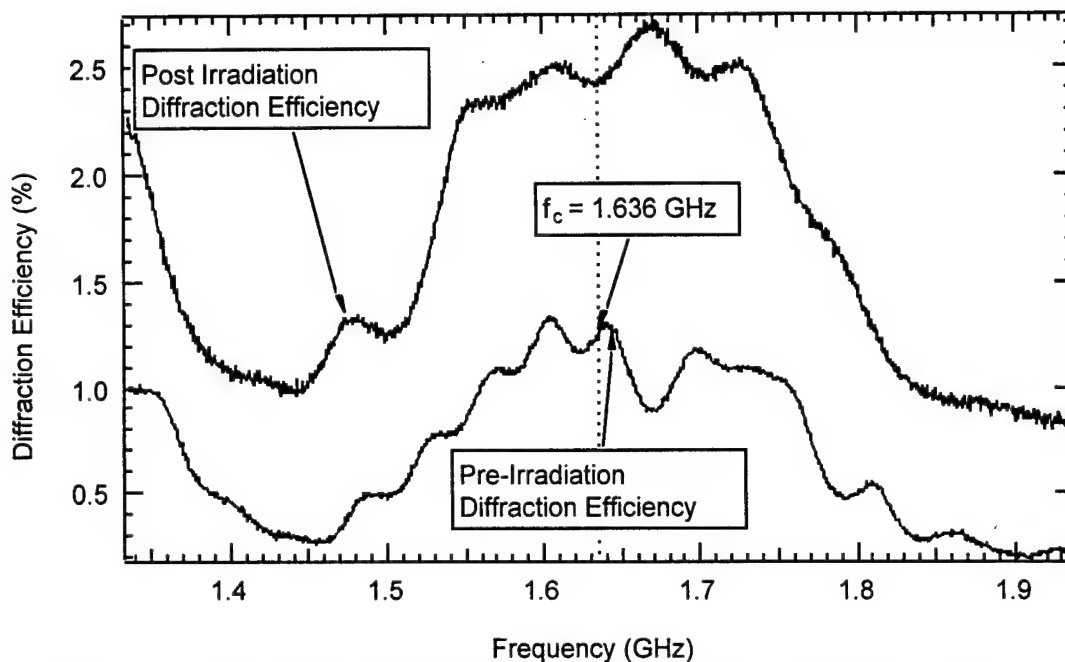


Figure 7-7. Pre and post irradiation bandwidth diffraction efficiency (GaP), where, $\lambda = 632$ nm, $f_c = 1.636$ GHz, BW of Device = 500 MHz, $f_L = 1.336$ GHz, $f_H = 1.936$ GHz, neutron fluence = 1.0×10^{15} neutrons/cm²

For the GaP device, the diffraction efficiency actually improves by 0.94% at the center frequency. Overall, the GaP bandwidth response appears to not be seriously affected by the neutron radiation exposure.

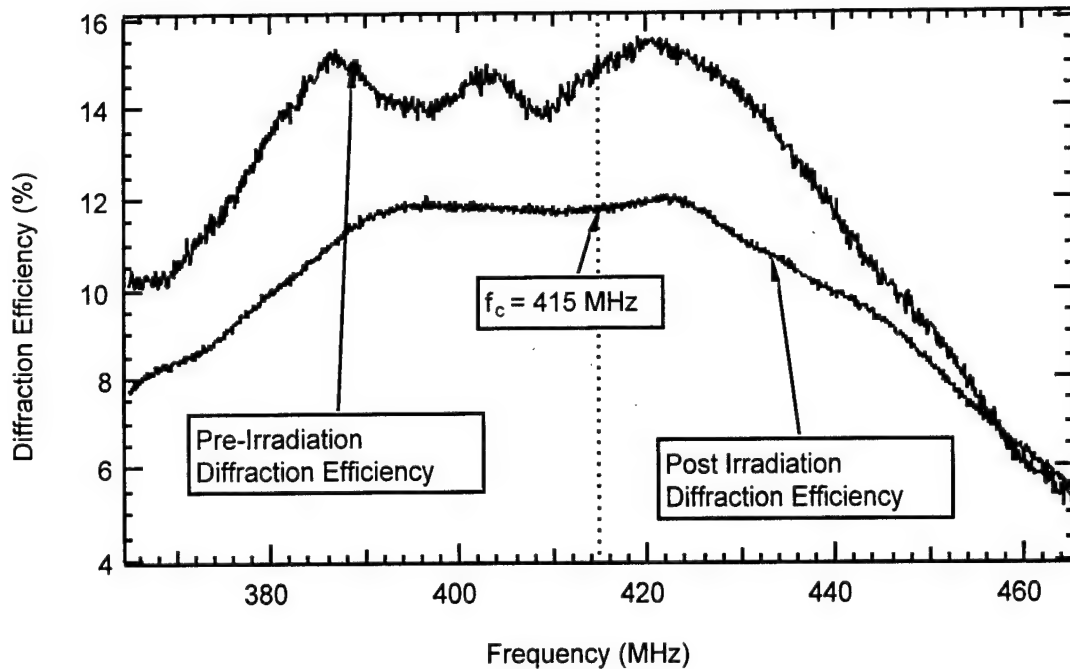


Figure 7-8. Pre and post irradiation bandwidth diffraction efficiency (LiNbO_3), where, $\lambda = 632.8 \text{ nm}$, $f_c = 415 \text{ MHz}$, BW of Device = 50 MHz, $f_L = 365 \text{ MHz}$, $f_H = 465 \text{ MHz}$, neutron fluence = $1.0 \times 10^{15} \text{ neutrons/cm}^2$.

For the LiNbO_3 device, the diffraction efficiency degrades by approximately 2% across the bandwidth of the device studied. However, the overall diffraction efficiency response is flatter across the bandwidth of the device, which appears to not have been altered by the radiation exposure. From a system design standpoint the flat bandwidth response is considered a desirable attribute. In this case, the device does not suffer any permanent insertion loss, but actually improves slightly (0.09 dB). Possible explanations for these improvements were discussed earlier in Chapter 5.0, Overview of Ion Microbeam Exposures of AO Bragg Cells.

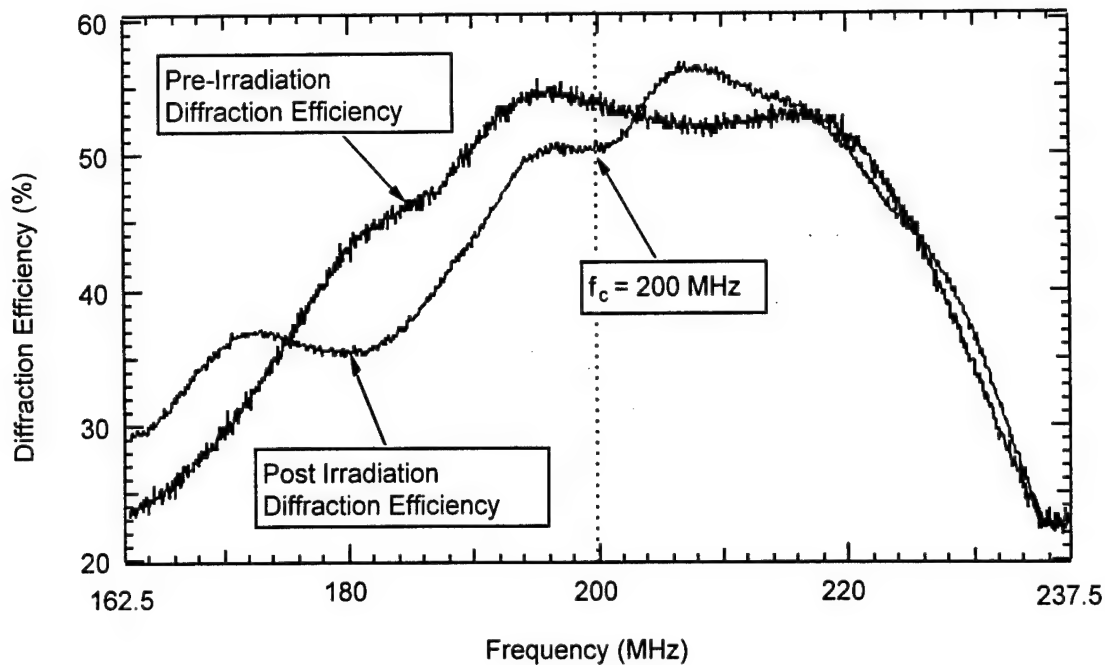


Figure 7-9. Pre and post irradiation bandwidth diffraction efficiency (InP), where, $\lambda = 1152$ nm, $f_c = 200$ MHz, $f_L = 162.5$ MHz, $f_H = 237.5$ MHz, neutron fluence = 1.0×10^{15} Neutrons/cm².

Following irradiation the diffraction efficiency of the InP AOD was degraded by approximately 10% at the center frequency of 200 MHz. The device diffraction efficiency response was also degraded slightly from the mid to low frequencies through the center frequency with little or no effect from the center to high end frequencies.

7.2.3 Spectral Characterization Response Results

The following plots illustrate the pre and post exposure measurements of spectral absorption for the three devices studied.

For the GaP device exposed, the broad spectral width transmission was degraded for the wavelengths scanned between 600 and 750 nm. From direct optical power measurements the device suffered significant permanent attenuation of, -6.7 dB at 632.8 nm as a result of the

neutron exposure. In the case of the narrow spectral width absorption, similar attenuation measurements were recorded at 670 nm.

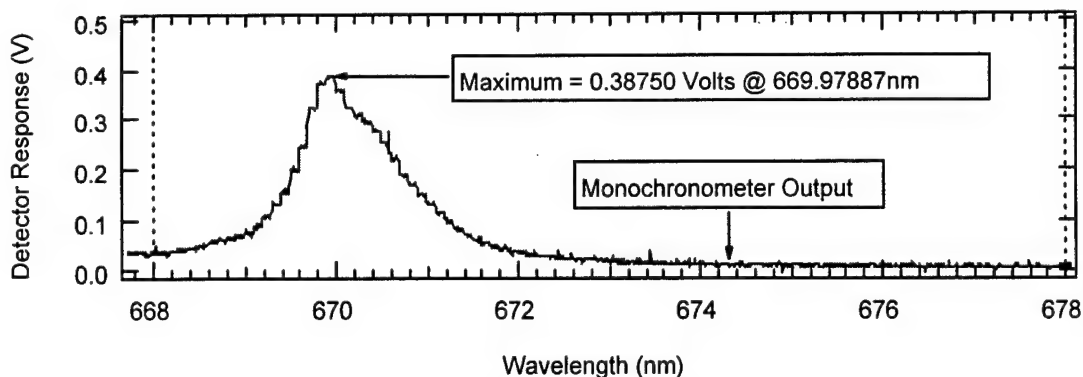


Figure 7-10. Spectral output characterization of a ($\lambda=670$ nm) Injection Laser Diode (ILD) for narrow spectral width absorption measurements, Post-Irradiation - Spectral Scan, Run 4 on 19 August 1997.

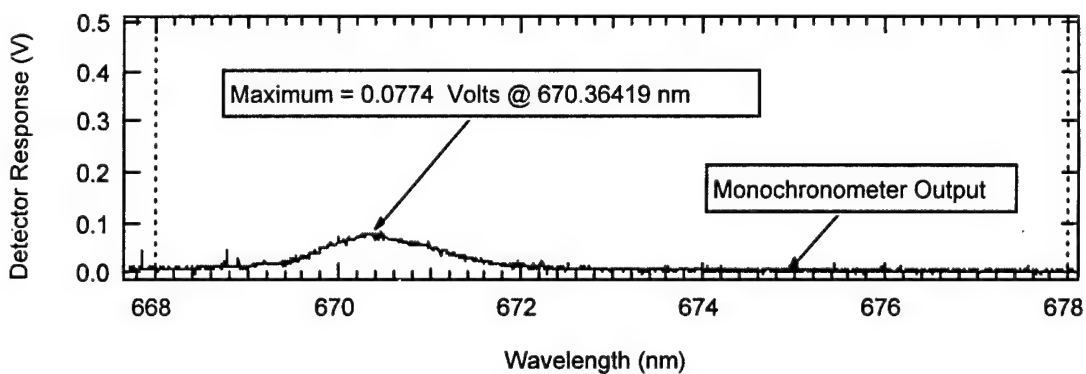


Figure 7-11. Spectral transmission of Gallium Phosphide modulator when illuminated with $\lambda=670$ nm Injection Laser Diode (ILD) (see Figure 7-10 for the input spectrum) after a 1×10^{15} n/cm² fluence exposure of AO cell only (Run 6 on 19 August 1997).

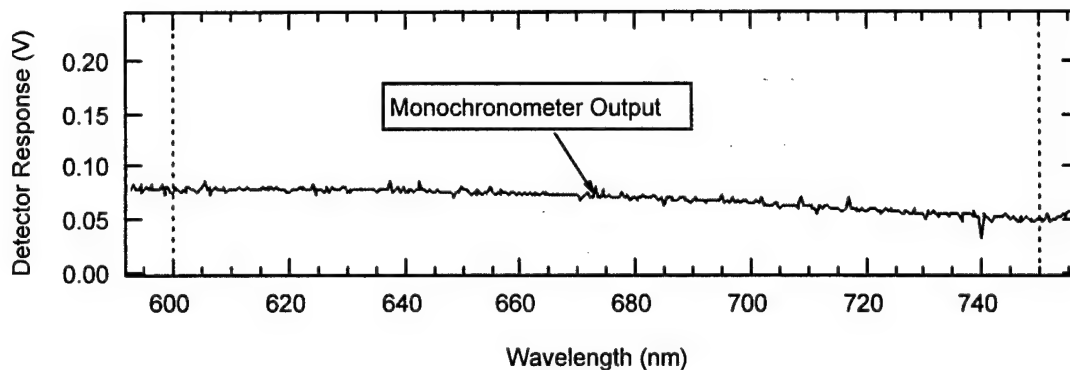


Figure 7-12. Spectral output characterization of a Xenon lamp for broad spectral width absorption measurements, Post-Irradiation - Spectral Scan, Run 1 on 19 August 1997.

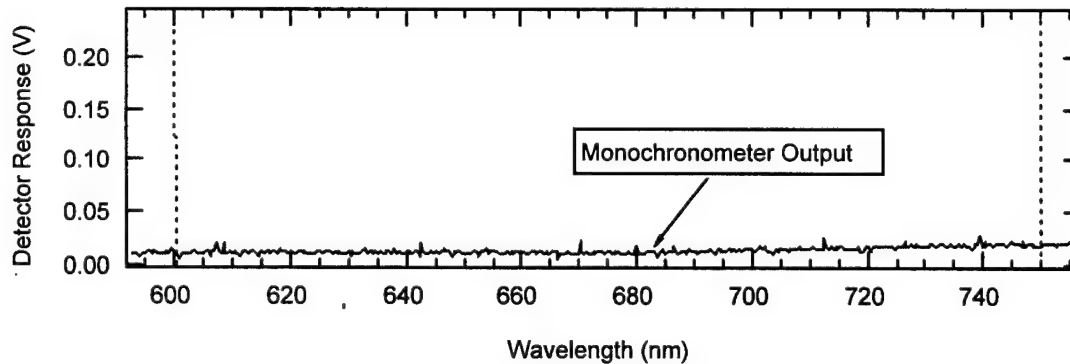


Figure 7-13. Spectral transmission of Gallium Phosphide modulator when illuminated with a Xenon light source, (see Figure 7-12 for the input spectrum) after a 1×10^{15} n/cm² fluence exposure of AO cell only (Run 3 on 19 August 1997).

For the LiNbO_3 device, the broad spectral response is not greatly influenced by the neutron exposure. At, $\lambda = 632.8 \text{ nm}$, the post exposure absorption is slightly less than the pre-exposure value. In the case of narrow spectral response measurements, the LiNbO_3 device appears to not have been altered. While the diffraction efficiency was degraded in this device, as a result of irradiation exposure, it did not affect the spectral characteristics of the material.

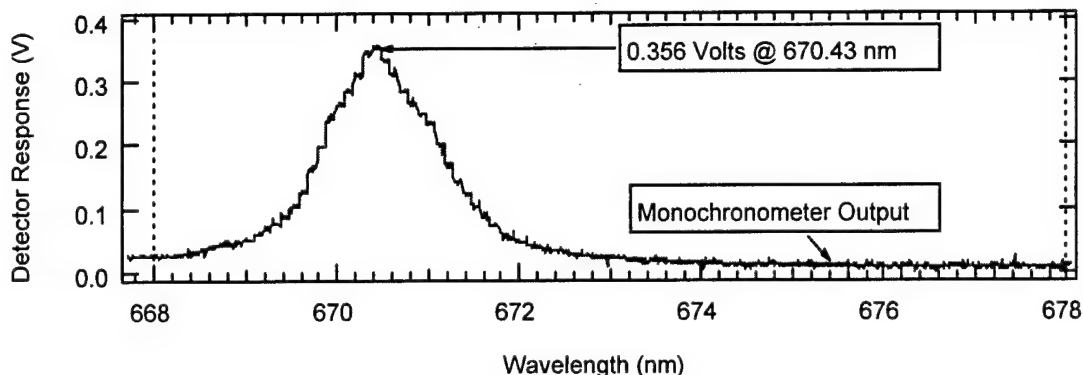


Figure 7-14. Spectral output characterization of a ($\lambda=670 \text{ nm}$) Injection Laser Diode (ILD) for narrow spectral width absorption measurements, Post-Irradiation - Spectral Scan, Run 3 on 19 August 1997.

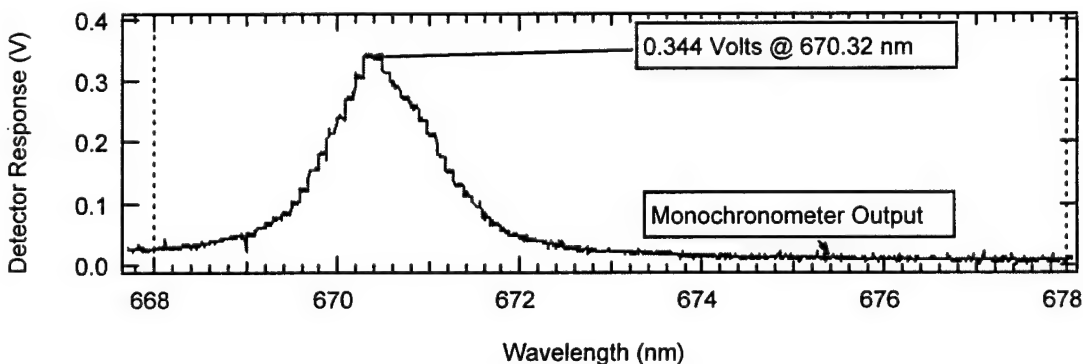


Figure 7-15. Spectral transmission of Lithium Niobate deflector when illuminated with a $\lambda=670 \text{ nm}$ Injection Laser Diode (ILD) (see Figure 7-14 for the input spectrum) after a $1 \times 10^{15} \text{ n/cm}^2$ fluence exposure of AO cell only (Run 3 on 19 August 1997).

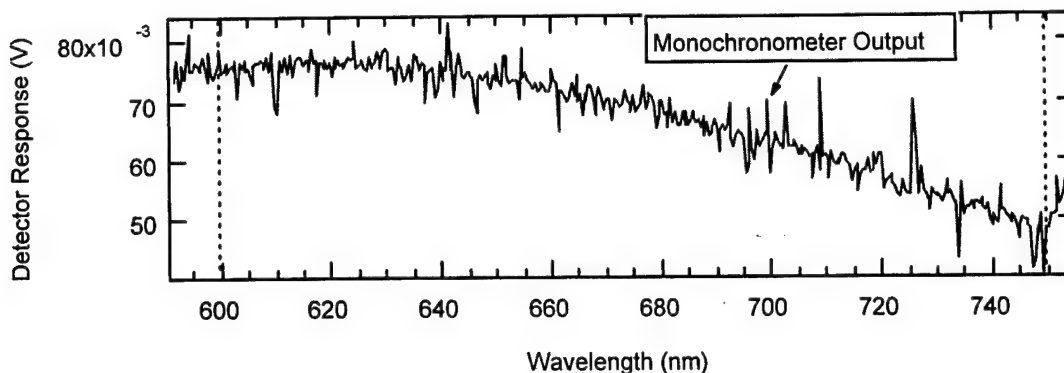


Figure 7-16. Spectral output characterization of a Xenon lamp for broad spectral width absorption measurements. Post Irradiation - Spectral Scan, Run 1 on 19 August 1997.

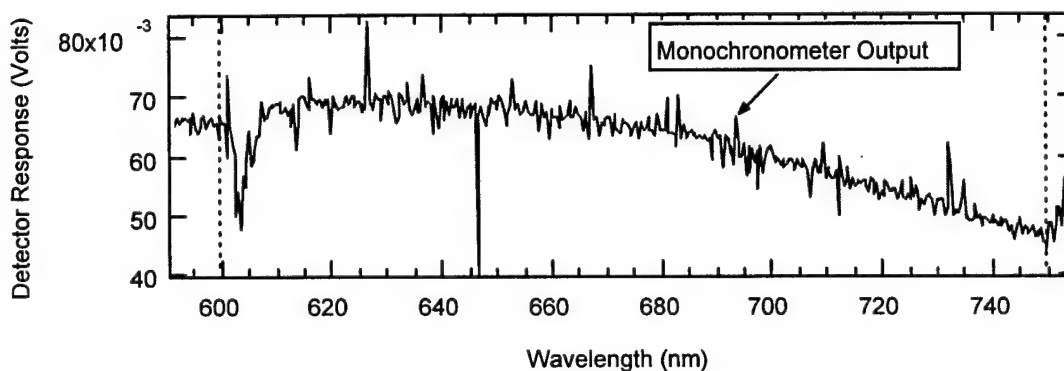


Figure 7-17. Spectral transmission of Lithium Niobate deflector when illuminated with a Xenon light source, (see Figure 7-16 for the input spectrum) after a 1×10^{15} n/cm^2 fluence exposure of AO cell only (Xenon Source, Post Irradiation - Spectral Scan, Run 2 on 19 August 1997).

The InP material is optimized for transmission in the infrared at 1152 nm. A modified HeNe laser emitting at 1152 nm was used for bandwidth and diffraction efficiency measurements. The monochromometer used for measuring the spectral response of the GaP and LiNbO₃ AODs was not optimized for 1152 nm. Therefore, the broad spectral scans in the 600-750 nm region and the narrow scans in the 670 nm region do not reveal much information for the InP. However, for the InP device studied, the spectral transmission at 1152 nm degraded by approximately 3.0 dB. This measurement was performed with an optical power meter before and after the neutron exposure as part of the bandwidth/insertion loss measurement sequence.

This page intentionally left blank.

8.0 CONCLUSIONS / RECOMMENDATIONS

This report details the findings of a comprehensive study of radiation induced effects in acousto optic Bragg cell deflectors and modulators composed of PbMoO_4 , TeO_2 , LiNbO_3 , GaP and InP crystals. Gamma-ray, X-ray, electrons, proton and neutron irradiations were conducted to bound, delineate and differentiate radiation induced changes to operational AO Bragg Cells. The majority of the irradiations were performed in situ, wherein the Bragg cells were fully operational during the radiation exposures. Using this approach, instantaneous changes to Bragg cell parameters such as spatial intensities, deflection angles, bandwidth, material absorption, diffraction efficiency and polarization states were determined. Post irradiation recovery of the radiation induced changes were also temporally measured, and several perspicuous models for explaining and predicting the degradation mechanisms and recovery kinetics were published in the open literature.

A majority of the radiation induced effects observed were coupled with the subsequent heating resulting from the interaction of radiation with matter. Radiation induced thermooptic effects were determined to affect Bragg cell performance. In particular, irradiation of AO Bragg cells by 15 MeV protons and electrons caused thermal gradients within the AO cell crystal lattice, altering the cell refractive index which in turn altered the cell diffraction efficiency, spatial intensity distribution and deflection angle. Other heating effects were shown to affect the cell transducer efficiency and bandwidth responses. The effects of heating and index gradients in AO Bragg crystals were investigated and confirmed using three independent approaches: traditional broad area source irradiations, ion microbeam irradiations, and irradiation by a CO_2 laser.

It was concluded that AO Bragg deflectors and modulators are quite insensitive to the long term-low dose radiation environments that would be encountered in the natural space environment. However, under pulsed - high dose (or high fluence) irradiations, Bragg cell transient responses could result in disruption of normal operations.

The information and data within this report should prove useful to designers concerned with developing hardened Bragg cell systems. Certainly the experimental data has uncovered many phenomena not previously reported for Bragg cell operation in natural and enhanced radiation environments.

Providing that adequate thermal control is possible, Bragg cells appear very mature for space applications.

9.0 REFERENCES

1. E. W. Taylor, A. D. Sanchez, S. A. DeWalt, D. M. Craig, S. P. Chapman, M. A. Kelly, M. F. Mitcham, A Study of Radiation - Induced Effects in Photonic Devices: Acoustooptic Modulators and Deflectors - Preliminary Results, PL-TR-94-1141, May 1994.
2. C. H. Fore III and D. J. Page, Radiation Effects in Optical Processing Systems, A Quick Look Assessment, DASIAC-91-1428, Washington DC, Nov 1991.
3. E. W. Taylor, A. D. Sanchez, S. A. DeWalt, R. J. Padden, S. P. Chapman, T. W. Monarski, D. M. Craig, and D. J. Page, "Radiation-induced Effects in Acoustooptic Devices," *Proc. SPIE*, Vol. 1794, pp. 217-224, Integrated Optical Circuits II, 1992.
4. E. W. Taylor, A. D. Sanchez, S. A. DeWalt, D. M. Craig, M. A. Kelly, S. P. Chapman, and M. F. Mitcham, "Radiation Effects Observed in a Spatial Light Modulator," *Proc. DOD Fiber Optics '94*, pp. 17-20, McLean, VA, 1994.
5. E. W. Taylor, "Radiation Effects in Photonic Technology Devices," *Proc. DOD Fiber Optics Conference '92*, McLean, VA, pp. 29-31, Mar 1992.
6. D. J. Page, E. W. Taylor and K. T. Stalker, "Candidate Experiments for the Microelectronics and Photonics Test Bed Satellite," *Proc. SPIE, Photonics for Space Environments*, Vol. 1953, Apr 1993.
7. E. W. Taylor, "Dual-Use of Photonic Components in Radiation Environments," *Proc. SPIE, Photonics for Space Environments II*, Vol. 2215, Apr 1994.
8. E. W. Taylor, "Ionization-Induced Refractive Index and Polarization Effects in $\text{LiNbO}_3\text{:Ti}$ Directional Coupler Waveguides," *IEEE/OSA J. Lightwave Technology*, Vol. 9, No. 3, pp. 335-340, Mar 1991.
9. R. J. Padden, E. W. Taylor, A. D. Sanchez, S. P. Chapman, J. N. Berry, S. A. DeWalt, and K. K. Wong, " LiTaO_3 and $\text{LiNbO}_3\text{:Ti}$ Responses to Ionizing Radiation," *Proc. SPIE*, Vol. 1474, Apr 1991.
10. E. W. Taylor, V. R. Wilson, M. Vigil, "Ionization-Induced Nonequivalent Absorption in a Birefringent Silica Fiber," *IEEE Photonics Technology Letters*, Vol. 1, No. 8, Aug 1989.
11. E. W. Taylor, "Radiation-Induced Effects in Guided-Wave Devices," *Proc. SPIE*, Vol. 1794, Sep 1992.
12. L. Brillouin, "Diffusion De La Lumiere et Des Rayons X par Un Corps Transparent Homogene, Influence De L'Agitation Thermique," *Annual de Physique*, Vol. 17, pp. 88-122, 1921.

13. P. Debye and F. W. Sears, "On the Scattering of Light By Supersonic Waves," *Proc. Nat. Acad. Of Sciences*, Vol. 18, No. 6, pp. 404-414, Jun 1932.
14. R. Lucas and P. Biquard, "Propriétés Optiques Des Milieux Solides et Liquides Soumis Aux Vibrations Élastiques Ultra Sonores," *Jour. de Physique*, Vol. 71, No. 10, pp. 464-477, 1932.
15. C. V. Raman and N. S. Nagendra Nath, "The Diffraction of Light by Sound Waves of High Frequency: Part II," *Proc. of the Indian Academy of Sciences*, Vol. 2, pp. 413-420, 1935.
16. R. W. Dixon, "Acoustic Diffraction of Light in Anisotropic Media," *IEEE J. Quantum Electronics*, Vol. QE-3, No. 2, 1967.
17. W. R. Klein and B. D. Cook, "Unified Approach to Ultra Sonic Light Diffraction," *IEEE Trans. on Sonics and Ultrasonics*, Vol. SU-14, No. 3, Jul 1967.
18. R. S. Chin and T. Tamir, "Bragg Diffraction by Periodically Modulated Media," *Jour. Opt. Soc. America*, Vol. 66, No. 3, 1976.
19. A. Korpel, "Two Dimensional Plane Wave Theory of Strong Acoustooptic Interaction in Isotropic Media," *Jour. Opt. Soc. America*, Vol. 69, No. 5, 1979.
20. A. Korpel, H. H. Lin and D. J. Medire, "Use of Angular Plane-Wave Spectra in The Analysis of Three-Dimensional Acoustooptic Interactions," *J. Opt. Society of America*, Vol. 4, No. 12, 1987.
21. E. I. Gordon, "A Review of Acoustooptical Deflection and Modulation Devices," *Proc. IEEE*, Vol. 54, 1966.
22. A. Korpel, "Acoustooptics - A Review of Fundamentals," *Proc. IEEE*, Vol. 69, 1981.
23. A. W. Warner, D. L. White and W. A. Bonner, "Acoustooptic Light Deflectors Using Optical Activity in Paratellurite," *Jour. App. Phys.*, Vol. 43, No. 11, Nov 1992.
24. G. A. Coquin, J. P. Griffin and L. K. Anderson, "Wide-Band Acoustooptic Deflectors Using Acoustic Beam Steering," *IEEE Trans. on Science and Ultrasonics*, Vol. SU-17, No. 1, Jan 1970.
25. D. A. Pinnow, "Guidelines for the Selection of Acoustooptic Materials," *IEEE J. of Quantum Electronics*, Vol. QE-6, No. 4, Apr 1970.
26. N. Vchida and N. Niizeki, *Proc. IEEE*, Vol. 61, No. 8, Aug 1973.
27. G. A. Coquin, D. A. Pinnow and A. W. Warner, "Physical Properties of Lead Molybdate Relevant to Acoustooptic Device Applications," *Journ. Appl. Phys.*, Vol. 42, May 1971.

28. R. W. Damon, W. T. Maloney and D. H. McMahon, "Interaction of Light with Ultrasound Phenomena and Applications," *Physical Acoustics*, Vol. 7, pp. 284, W. P. Mason, and R. N. Thurston, Eds; New York Academic Press, NY, 1970.
29. E. W. Taylor and S. S. Alpert, "Temperature Dependence of the Ultrasonic Velocity in Cyclohexane," *J. of the Acoust. Soc. of America*, Vol. 48, No. 5, pp. 1287-1288, Nov 1970.
30. D. A. Benson and E. W. Taylor, Acoustical-Optical Coupling in Gases, AFWL TR-72-167, Air Force Weapons Laboratory, Kirtland AFB, NM, Nov 1972.
31. E. W. Taylor and D. A. Benson, "Interaction of Acoustic Waves and Infrared Radiation in Air," *Bull. American Phys. Soc.*, Vol. 18, No. 3, pp. 477, Mar 1973.
32. E. W. Taylor, "Infrared Probing of a Gaseous Diffraction Grating," *Infrared Physics*, Vol. 16, pp. 403-407, Pergamon Press, Oxford, 1976.
33. E. W. Taylor, Bragg Angle Diffraction of Infrared Radiation in Air, AFWL TR-74-21, Air Force Weapons Laboratory, Kirtland AFB, NM, May 1974.
34. R. Adler, "Interaction Between Light and Sound," *IEEE Spectrum*, Vol. 2, No. 2, May 1967.
35. B. A. Saleh and M. C. Teich, Fundamentals of Photonics, John Wiley & Sons, Inc., ISBN 0-471-83965-5, New York, NY, 1991.
36. A. P. Gontzoulis and D. R. Pape, Design and Fabrication of Acoustooptic Devices, Marcel Debner, Inc., ISBN 0-8247-8930-X, New York, NY, 1994.
37. J. Xu and R. Stroud, Acoustooptic Devices: Principles, Design and Applications, John Wiley & Sons, Inc., ISBN 0-471-61638-9, New York, 1992.
38. R. Waynant and M. Ediger, Electro-Optics Handbook, McGraw Hill, Inc, ISBN 0-07-068663-7, New York, NY, 1993.
39. G. W. Willard, "Criteria for Normal and Abnormal Ultrasonic Light Diffraction Effects," *Journal of the Acoustical Society of America*, Vol. 21, No. 2, pp. 101-108, 1949.
40. N. J. Berg, and John N. Lee, Acoustooptic Signal Processing, Marcel Dekker, Inc., ISBN 0-8247-1667-1, New York, NY, 1983.
41. N. B. Singh and D. J. Todd, Growth and Characterization of Acousto-Optic Materials, Trans Tech Publications Limited, ISBN 0-87849-611-4, Brookfield, VT, 1990.
42. E. W. Taylor, J. E. Winter, A. D. Sanchez, S. J. McKinney, "Electron Induced Depolarization of a Tellurium Dioxide Bragg Cell Modulator," presented at *IEEE Nuclear Science and Radiation Effects on Components*, poster paper, Jul 1996.

43. E. W. Taylor, S. A. DeWalt, J. E. Winter "Application of a Photoelastic Modulator-Analyzer in Photonic Polarization Measurements," *Proc. 42nd ISA International Instrumentation Symposium*, May 1996.
44. E. W. Taylor, J. E. Winter, A. D. Sanchez, S. J. McKinney, "Proton Induced Transient Depolarization in Gallium Phosphide and Tellurium Dioxide Bragg Cells," *Optical Engineering*, **36**(7), pp. 1901-1909, Jul 1997.
45. E. W. Taylor, "Methodology for Measuring Electron and Proton Induced Polarization in Photonic Devices," *Proc. 43rd ISA/IIS*, pp. 299-308, May 1997.
46. H. Mueller, "The Foundations of Optics," *J. Opt. Soc. Am.*, Vol. 38, p. 661, 1948.
47. G. G. Stokes, *Trans. Cambridge Phil. Soc.*, Vol. 9, p. 399, 1852.
48. T. C. Oakberg, "Modulated Interference Effects: Use of Photoelastic Modulators With Lasers", *Optical Engineering*, Vol. 34, No. 6, pp. 1545-1550, Jun 1995.
49. E. W. Taylor, M. A. Kelly, "CO₂ Laser Simulation of Radiation Induced Effects in an Acousto Optic Deflector," *Proc. Int. Soc. for Optical Engineering*, Vol. 2482, pp. 99-108, Apr 1995.
50. E. W. Taylor, "Radiation Effects Observed in Selected Guided Wave Devices," in SPIE CR-45 Integrated Optics and Optoelectronics-Critical Reviews of Optical Science and Technology, K. K. Wong and M. Razaghi, ed., ISBN 08194-1005-5, pp. 299-319, Jan 1993.
51. E. W. Taylor, A. D. Sanchez, S. P. Chapman, S. A. Dewalt, D. M. Craig, M. A. Kelly, M. Mitcham, "Reponses of a Spatial Light Modulator to Pulsed Electron Irradiations," Presented at Optical Society of America Spatial Light Modulators and Applications, Salt Lake City, Utah, *OSA Technical Digest Series*, Vol. 9, pp.152-156, 1995.
52. A. D. Sanchez, S. A. DeWalt, E. W. Taylor, "Photonic Component Characterization Techniques," *Proc. 41st ISA / International Instrumentation Symposium-Photonics*, pp. 53-60, May 1995.
53. E. W. Taylor, J. E. Winter, A. D. Sanchez, S. McKinney, "Radiation Induced Changes in Photonic Devices," *SPIE Photonics for Space Environments IV Conf., Proc. Int. Soc. Opt. Engr.*, Vol. 2811, Aug 96.
54. A. H. Paxton, H. Schone, E. W. Taylor, S. J. McKinney, B. L. Doyle, "Performance of a PbMoO₄ Acousto Optic Bragg Cells Under Ion Microbeam Irradiation," presented at the 5th International Conference on Nuclear Microprobe Technology and Applications, Santa Fe NM, 10-15 November 1996, to be published in *Nuclear Instruments and Methods in Physics Research (B)*.

55. TRIM (The Transport of Ions in Matter) Computer Code, see: J. F. Ziegler, J. P. Biersack, U. Littmark, The Stopping and Range of Ions in Matter, Pergamon Press, New York, 1985 (ISBN 0-08 021603-X).
56. F. H. Attix, Introduction to Radiological Physics and Radiation Dosimetry, John Wiley & Sons, Inc., 1986 (ISBN 0-471-01146-0).
57. P. K. Das and C. M. DeCusatis, Acousto-Optic Signal Processing: Fundamentals & Applications, Artech House, Boston, pp. 53-86, 1991.
58. E. W. Taylor, U. S. Patent No. 5,406,072, Method for Microbeam Ion Testing of Photonic Devices, Apr 1995.
59. B. L. Doyle, N. D. Wing, "The Sandia Microprobe," Sandia Report, SAND 82-2393, 1982.
60. J. F. Ziegler, J. P. Biersack, and U. Littmark, The Stopping Range of Ions in Solids, Pergamon Press, New York, 1985. The SRIM package is available from IBM:
<http://www.research.ibm.com/ionbeams/>
61. E. W. Taylor, S. P. Chapman, M. A. Kelly, A. D. Sanchez, J. Stohs, E. Kinsley, D. M. Craig, "Radiation Induced Bandwidth Responses in Acousto Optic Bragg Cell," presented at SPIE Aerosense-Photonics for Space Environments III Conference, *Proc. Int. Soc. for Optical Engineering*, Vol. 2482, pp.16-27, Apr 1995.
62. A. H. Paxton and E. W. Taylor, "Model for Laser Heating of Acousto-Optic Devices," *Proc. Int. Soc. For Optical Engineering*, Vol. 2811, pp. 38-45, 1996.
63. M. G. Cohen and E. I. Gordon, "Acoustic Beam Probing Using Optical Techniques," *Bell System Tech. J.*, **44**, pp. 693-721, 1965.
64. E. W. Taylor, E. J. Friebele, H. Henschel, et al., "Interlaboratory Comparison of Radiation-Induced Attenuation in Optical Fibers. Part II: Steady State Exposures," *IEEE/OSA Jour. of Lightwave Technology*, Vol. 8, No. 6, pp. 967-976, Jun 1990.
65. E. J. Friebele, P. B. Lyons, E. W. Taylor, et. al., "Interlaboratory Comparison of Radiation-Induced Attenuation in Optical Fibers. Part III: Transient Exposures," *IEEE/OSA Journal of Lightwave Technology*, Vol. 8, No. 6, pp. 977-989, Jun 1990.
66. E.W. Taylor, "On the Measurement of Radiation Induced Crosstalk in Polarization Preserving Optical Fibers and Directional Coupler Waveguides," presented at the RADECS '91 Conference, Le Grande Motte/Montpellier, France, 12 September 1991, *Proc. European Space Agency / IEEE, Radiation Effects on Components and Devices*, Vol. 15, pp. 391-395, Sep 1991.

67. R. J. Padden, E. W. Taylor, A. D. Sanchez, S. P. Chapman, J. N. Berry, S. A. DeWalt, and K. K. Wong, "LiTaO₃ and LiNbO₃:Ti Responses to Ionizing Radiation," *Proc. Int. Soc. for Optical Engineering*, **35**, 1991.
68. E. W. Taylor, "Behavior of Coupled Waveguide Devices in Adverse Environments," *Proc. Int. Soc. for Optical Engineering*, Vol. 1314, pp. 1314-1322, Apr 1990.
69. R. C. Webb, L. Cohn, E. W. Taylor, R. A. Greenwell, "Overview of Radiation Effects Research in Photonics," *Proc. Int. Soc. for Optical Engineering*, Vol. **2482**, pp. 3-15, Apr 1995.
70. R. West and S. Dowling, "Effects in a Lithium Tantalate Waveguide Structure Exposed to Radiation from a Flash X-Ray Source," *IEEE Trans. Nuc. Sci.* **41**(3), pp. 534-537, Sep 1993.
71. E. W. Taylor, S. P. Chapman, A. D. Sanchez, M. A. Kelly, J. Stohs, D. M. Craig, "Radiation Induced Crosstalk in a Proton Exchanged LiNbO₃ Directional Coupler Waveguide," *Proc. Int. Soc. for Optical Engineering*, Vol. 2482, Apr 1995.
72. P. J. Brannon, "Pulsed X-Ray Induced Transient Absorption in LiNbO₃, TiO₂:LiNbO₃ and MgO:LiNbO₃ at 1061 nm," *IEEE Trans. Nuc. Sci.*, **42**(3), pp. 117-120, Jun 1995.
73. D. W. Pentrack, J. M. Hatch, R. A. Greenwell, "Effects of Combined Neutron and Gamma Radiation on a LiNbO₃ Directional Polarization Maintaining Coupler (Passive) and a Large Core Multimode 1 x 2 Coupler," *Proc. Int. Soc. for Optical Engineering*, Vol. 2482, Apr 1995.

APPENDIX A -- ION BEAM EXPERIMENTAL RESULTS AND TIMES

Table A-1. Ion micro-beam experimental dates and times.

Project #	Date	Project	Remarks	Printouts/ disk file	Section
1	2-13-96	AO-Irradiation tests	4.5 MeV Protons	-	n.a.
2	2-15-96	AO-Irradiation tests	4.5 MeV Protons	-	n.a.
3	3-4-96	PbMoO ₄ AO-modulator	4.0 MeV Protons	+	n.a.
4	3-18-96	PbMoO ₄ AO-modulator	4.0 MeV Protons	+	n.a.
5	3-20-96	PbMoO ₄ AO-modulator	4.0 MeV Protons	-	n.a.
6	4-4-96	PbMoO ₄ AO-modulator	4.0 MeV Protons	+	5.4.5
7	4-5-96	PbMoO ₄ AO-modulator	4.0 MeV Protons	+	5.4.5
8	4-18-96	PbMoO ₄ AO-modulator	4.0 MeV Protons	+	5.4.1
9	4-19-96	PbMoO ₄ AO-modulator	4.0 MeV Protons	+	5.4.1
10	5-3-96	TeO ₂ AO-modulator	4.0 MeV Protons	-	n.a.
11	5-16-96	TeO ₂ AO-modulator	4.0 MeV Protons	+	5.4.3
12	5-16-96	LiNbO ₃ AO-modulator	4.0 MeV Protons	+	5.4.2
13	5-29-96	InP		+	5.4.4
14	5-29-96	GaP	4.0 MeV Protons	-	n.a.
15	8-21-96	TeO ₂ AO-modulator	4.0 MeV Protons	+	n.a.

Table A-2. Ion beam location for each exposure shown in Figures 5-9, and Figures A-35 through A-59. Exposure number is indicated on Figures.

<u>Shot¹ #</u>	<u>x-location²</u>	<u>y-location</u>
39	0.5 mm	0.5 mm
40	2.5 mm	0.5 mm
41	4.5 mm	0.5 mm
42	6.5 mm	0.5 mm
43	6.5 mm	2.5 mm
44	4.5 mm	2.5 mm
45	2.5 mm	2.5 mm
46	0.5 mm	2.5 mm
47	0.5 mm	4.5 mm
48	0.5 mm	4.5 mm (detector realignment)
49	2.5 mm	4.5 mm
50	4.5 mm	4.5 mm
51	6.5 mm	4.5 mm
52	6.5 mm	6.0 mm
53	4.5 mm	6.0 mm
54	2.5 mm	6.0 mm
55	0.5 mm	6.0 mm
56	4.0 mm	5.0 mm ³
57	4.0 mm	5.0 mm
58	5.0mm	5.0 mm
59	transducer irradiation, angle 30-35°	

¹ Shot number is indicated on graph

² Locations are in reference to top and right edge of AO-cell crystal.

³ Thermistor calibration, located at 3.0mm and 5.0mm

Table A-3. Ion beam location for each exposure shown in Figures A-60 through A-134.

<u>Shot⁴ #</u>	<u>x-location⁵</u>	<u>y-location</u>	<u>Shot #</u>	<u>x-location</u>	<u>y-location</u>
a1	0 mm	0 mm	a39	8 mm	2 mm
a2	0 mm	0 mm	a40	9 mm	2 mm
a3	1 mm	0 mm	a41	10 mm	2 mm
a4	2 mm	0 mm	a42	10 mm	2 mm
a5	4 mm	0 mm	a43	9 mm	2 mm
a6	0 mm	0 mm	a44	8 mm	2 mm
a7	1 mm	0 mm	a45	7 mm	2 mm
a8	2 mm	0 mm	a46	6 mm	2 mm
a9	3 mm	0 mm	a47	5 mm	2 mm
a10	4 mm	0 mm	a48	4 mm	2 mm
a11	5 mm	0 mm	a49	3 mm	2 mm
a12	6 mm	0 mm	a50	2 mm	2 mm
a13	7 mm	0 mm	1	0 mm	0 mm
a14	8 mm	0 mm	2	0 mm	2 mm
a15	9 mm	0 mm	3	-1 mm	2 mm
a16	10 mm	0 mm	4	-1 mm	3 mm
a17	10 mm	1 mm	5	0 mm	3 mm
a18	9 mm	1 mm	6	1 mm	3 mm
a19	9 mm	1 mm	7	2 mm	3 mm
a20	8 mm	1 mm	8	3 mm	3 mm
a21	7 mm	1 mm	9	4 mm	3 mm
a22	6 mm	1 mm	10	5 mm	3 mm
a23	5 mm	1 mm	11	6 mm	3 mm
a24	4 mm	1 mm	12	7 mm	3 mm
a25	3 mm	1 mm	13	8 mm	3 mm
a26	2 mm	1 mm	14	9 mm	3 mm
a27	1 mm	1 mm	15	10 mm	3 mm
a28	0 mm	1 mm	16	10 mm	4 mm
a29	-1 mm	1 mm	17	9 mm	4 mm
a30	-1 mm	2 mm	18	8 mm	4 mm
a31	0 mm	2 mm	19	7 mm	4 mm
a32	1 mm	2 mm	20	6 mm	4 mm
a33	2 mm	2 mm	21	5 mm	4 mm
a34	3 mm	2 mm	22	4 mm	4 mm
a35	4 mm	2 mm	23	3 mm	4 mm
a36	5 mm	2 mm	24	2 mm	4 mm
a37	6 mm	2 mm	25	1 mm	4 mm
a38	7 mm	2 mm	26	0 mm	4 mm

⁴ Shot number is indicated on graph

⁵ Locations are in reference to first exposure point: ½ mm from bottom and right laser exit facet edge of AO-cell crystal.

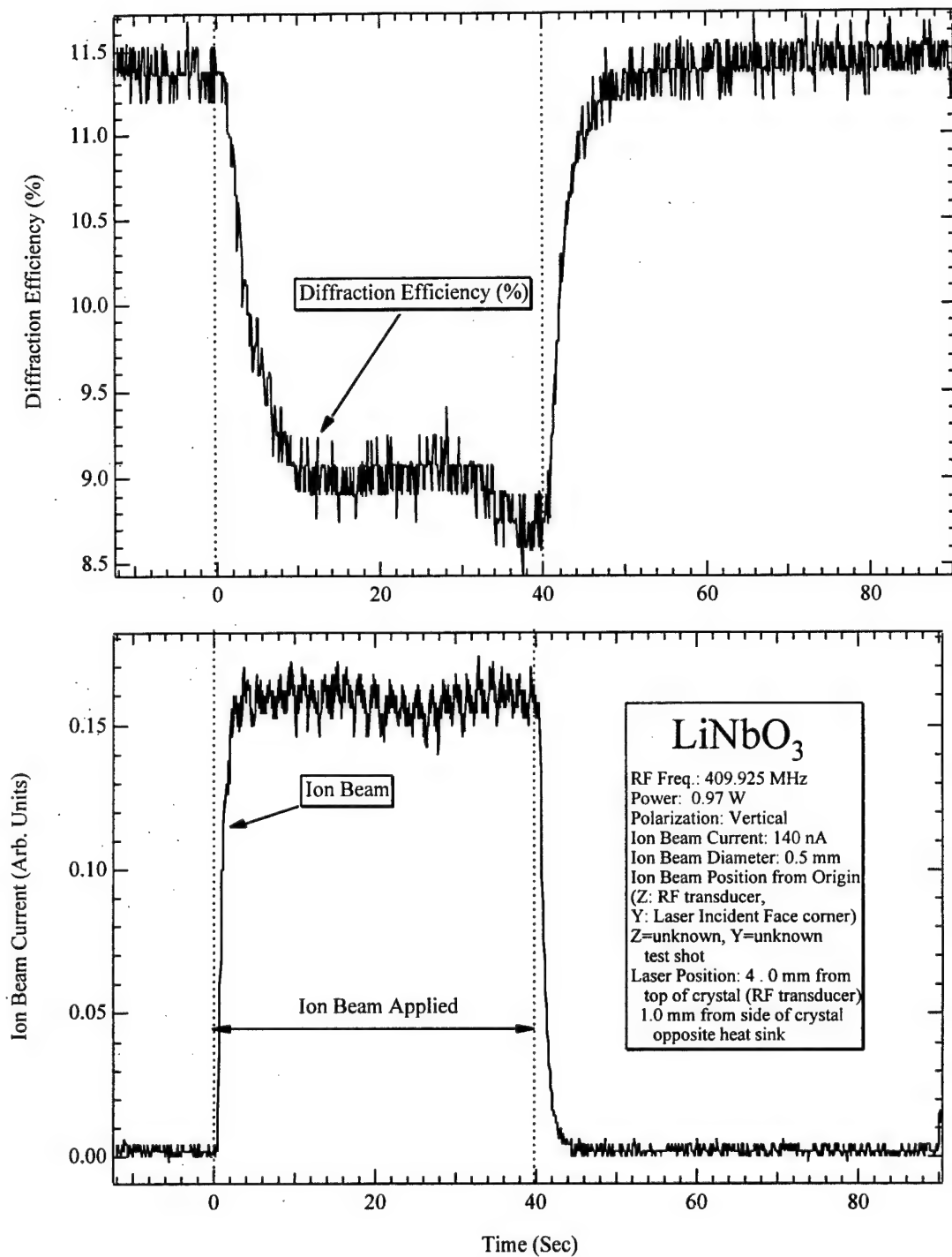


Figure A-1. Two plots showing the measured AO-cell response before, during and after an ion beam exposure. The dashed lines indicate the duration of the ion beam. Refer to Table A-2 for the precise beam location. The upper plot shows the calculated diffraction efficiency. The bottom plot shows the ion beam current in arbitrary units.

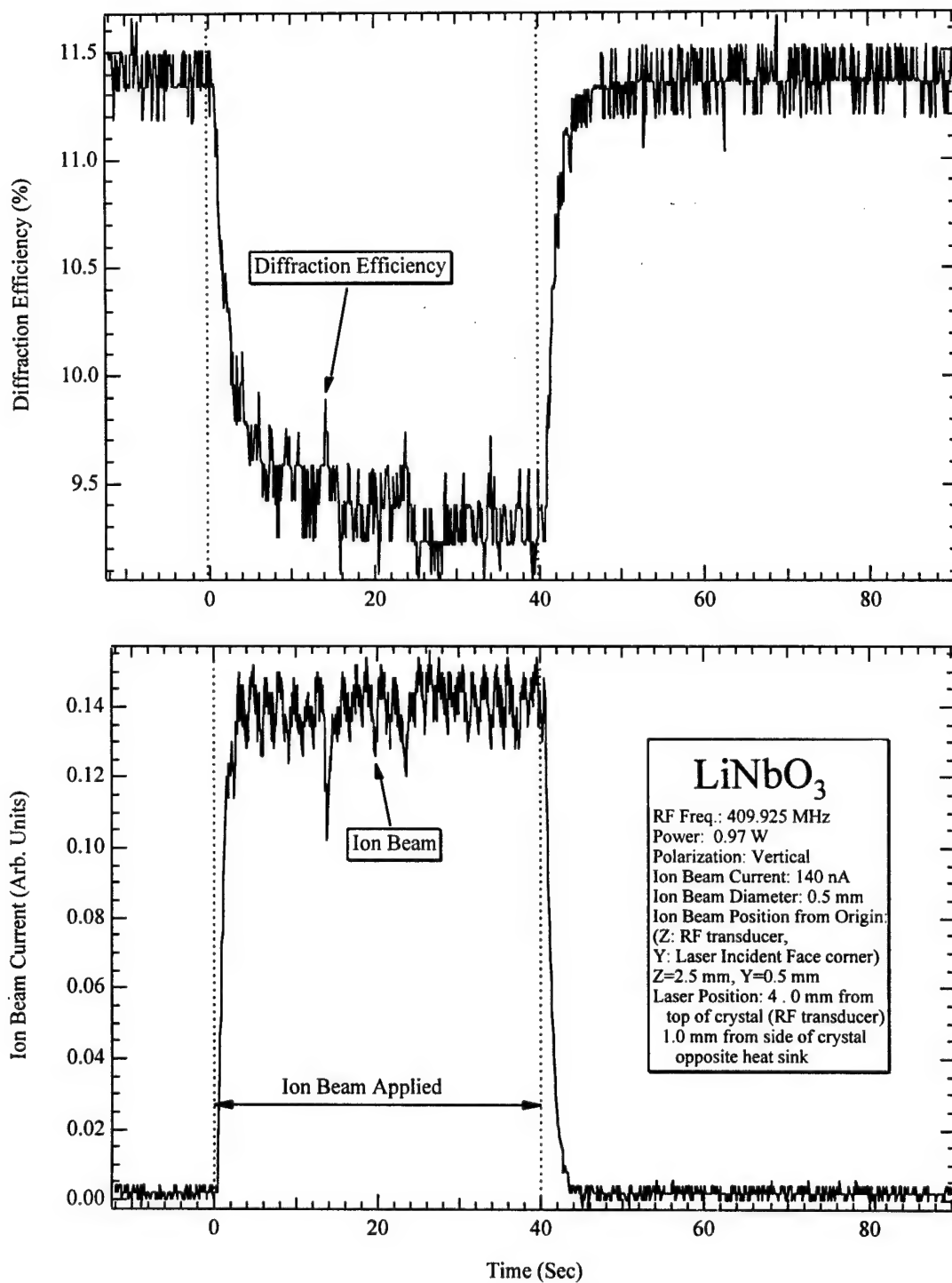


Figure A-2. Two plots showing the measured AO-cell response before, during and after an ion beam exposure. The dashed lines indicate the duration of the ion beam. Refer to Table A-2 for the precise beam location. The upper plot shows the calculated diffraction efficiency. The bottom plot shows the ion beam current in arbitrary units.

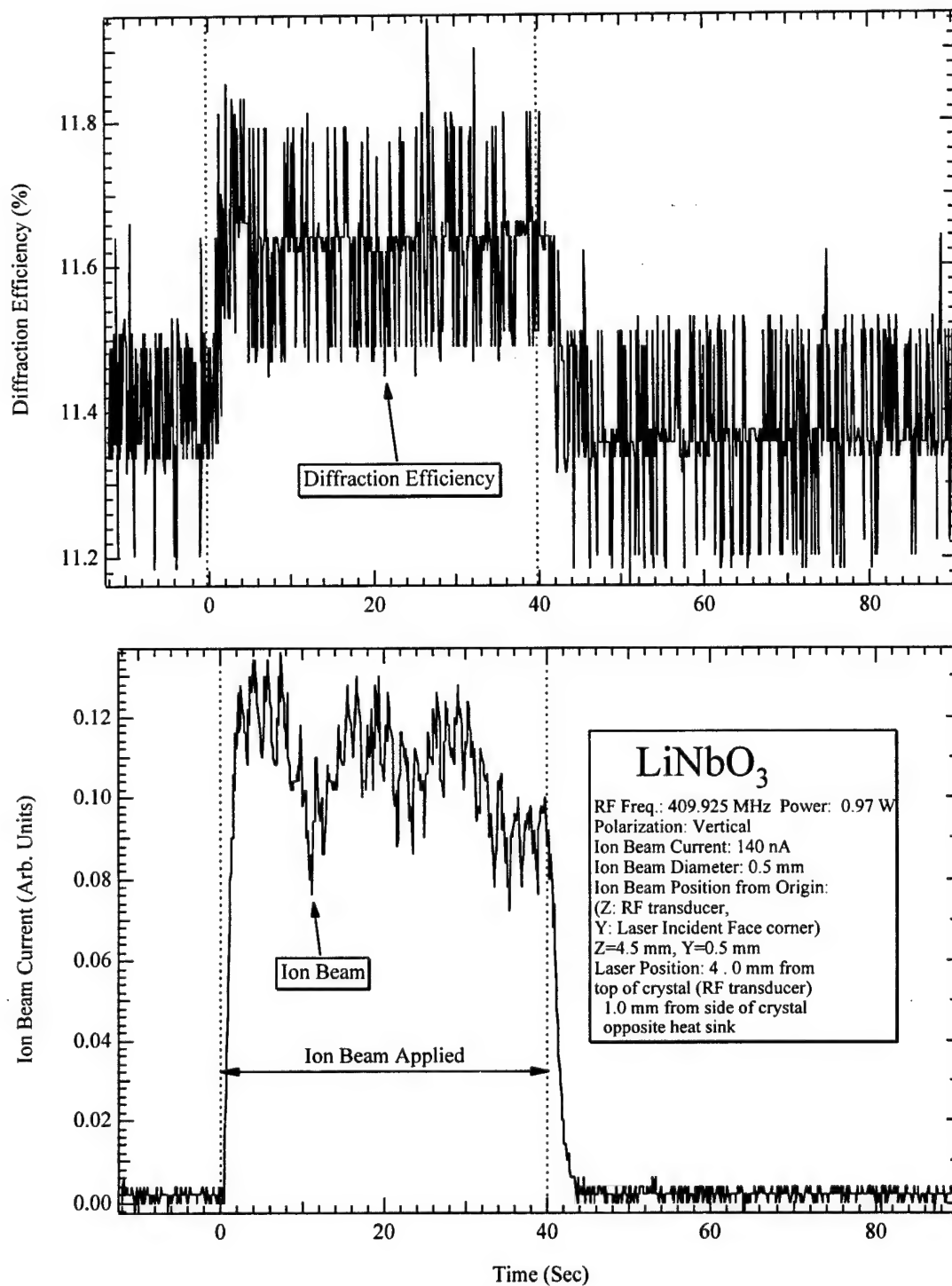


Figure A-3. Two plots showing the measured AO-cell response before, during and after an ion beam exposure. The dashed lines indicate the duration of the ion beam. Refer to Table A-2 for the precise beam location. The upper plot shows the calculated diffraction efficiency. The bottom plot shows the ion beam current in arbitrary units.

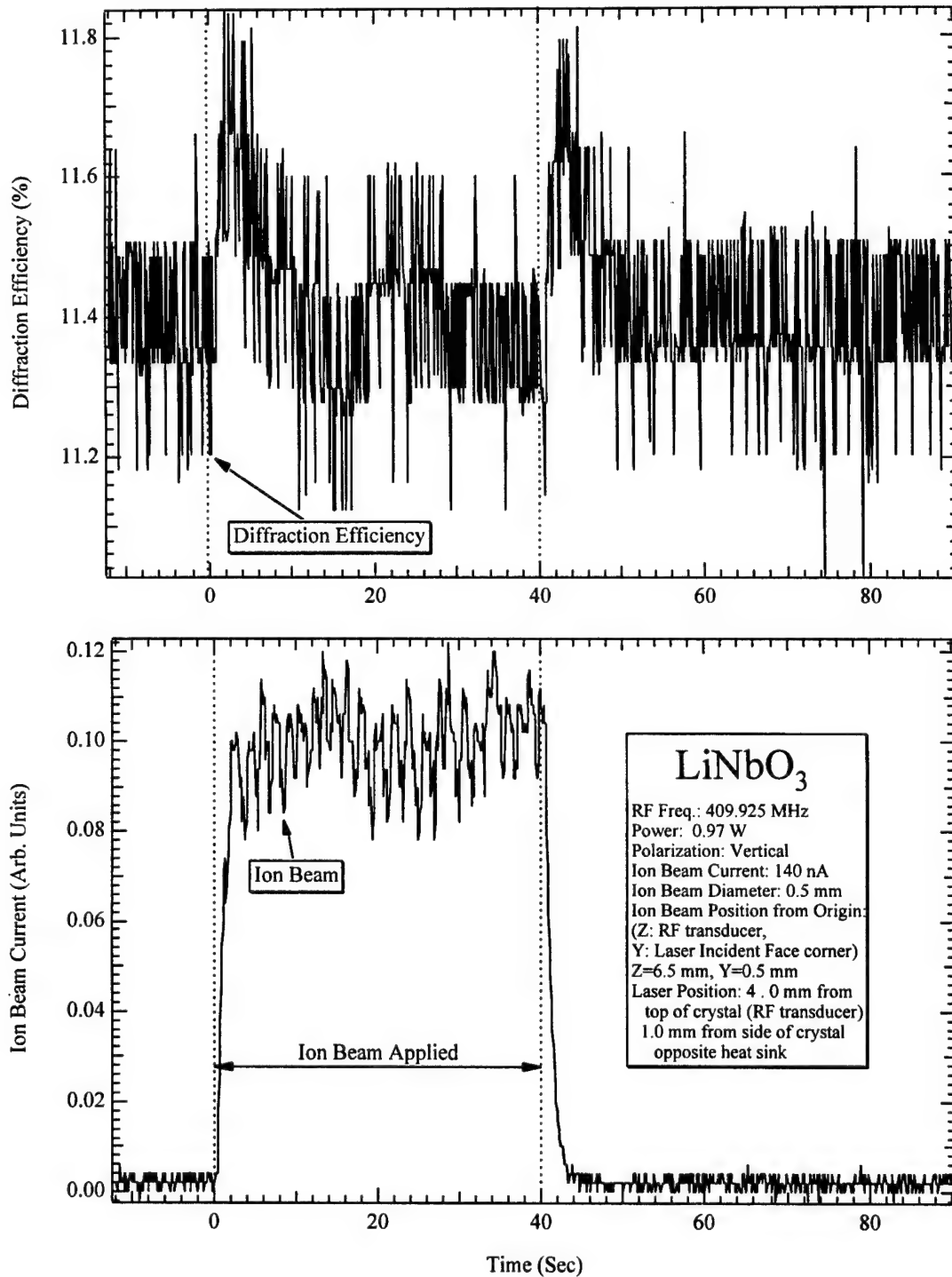


Figure A-4. Two plots showing the measured AO-cell response before, during and after an ion beam exposure. The dashed lines indicate the duration of the ion beam. Refer to Table A-2 for the precise beam location. The upper plot shows the calculated diffraction efficiency. The bottom plot shows the ion beam current in arbitrary units.

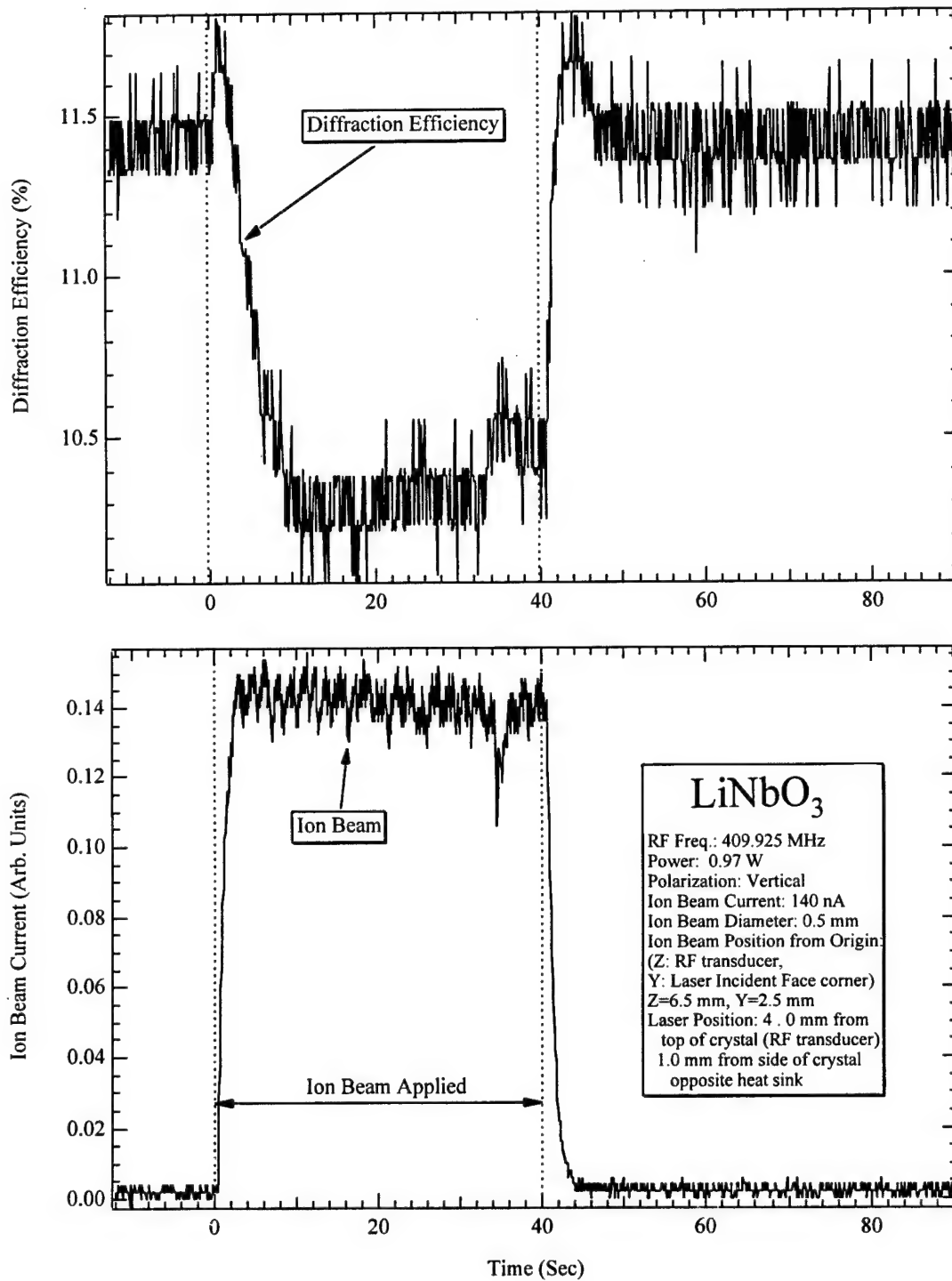


Figure A-5. Two plots showing the measured AO-cell response before, during and after an ion beam exposure. The dashed lines indicate the duration of the ion beam. Refer to Table A-2 for the precise beam location. The upper plot shows the calculated diffraction efficiency. The bottom plot shows the ion beam current in arbitrary units.

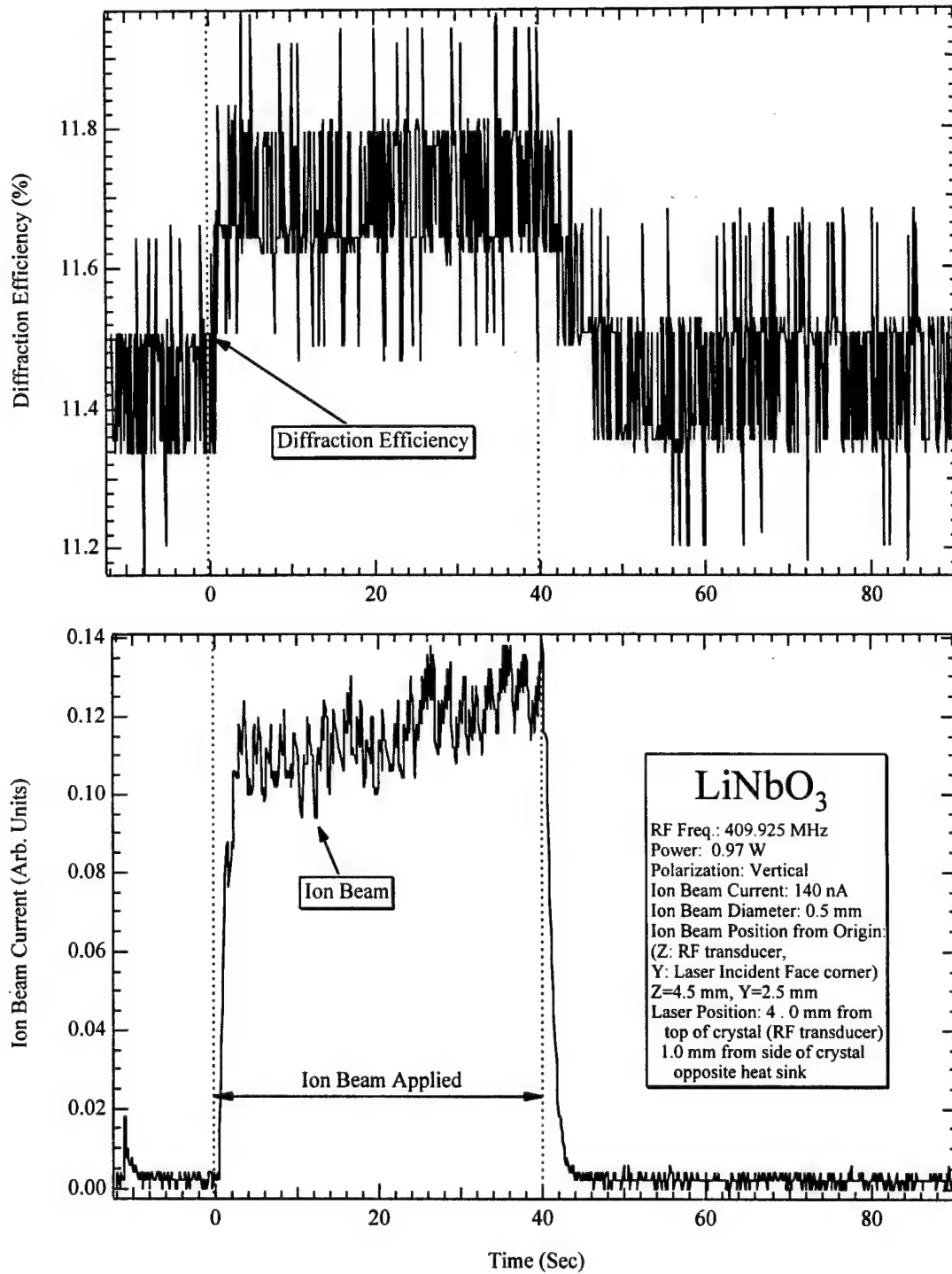


Figure A-6. Two plots showing the measured AO-cell response before, during and after an ion beam exposure. The dashed lines indicate the duration of the ion beam. Refer to Table A-2 for the precise beam location. The upper plot shows the calculated diffraction efficiency. The bottom plot shows the ion beam current in arbitrary units.

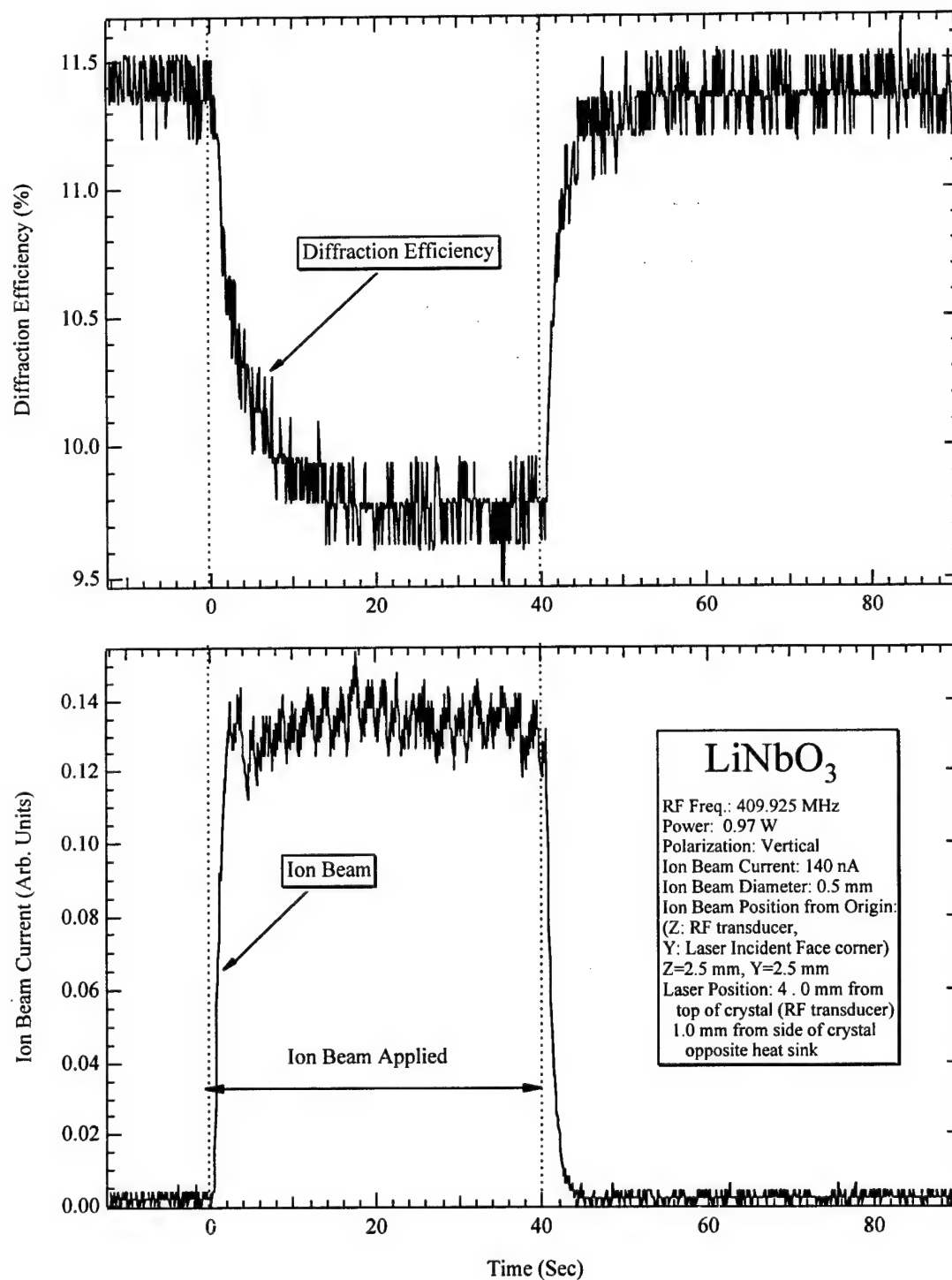


Figure A-7. Two plots showing the measured AO-cell response before, during and after an ion beam exposure. The dashed lines indicate the duration of the ion beam. Refer to Table A-2 for the precise beam location. The upper plot shows the calculated diffraction efficiency. The bottom plot shows the ion beam current in arbitrary units.

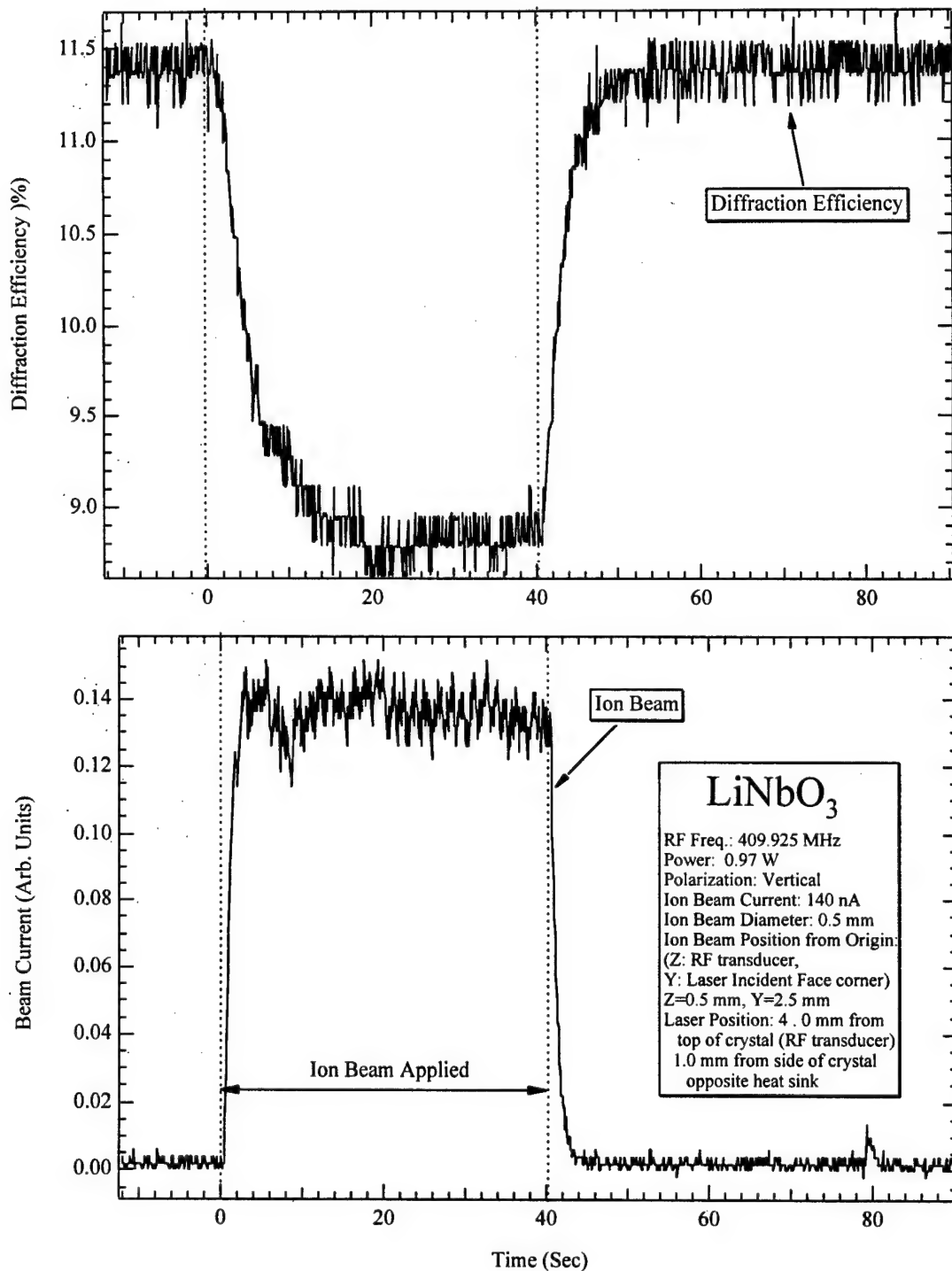


Figure A-8. Two plots showing the measured AO-cell response before, during and after an ion beam exposure. The dashed lines indicate the duration of the ion beam. Refer to Table A-2 for the precise beam location. The upper plot shows the calculated diffraction efficiency. The bottom plot shows the ion beam current in arbitrary units.

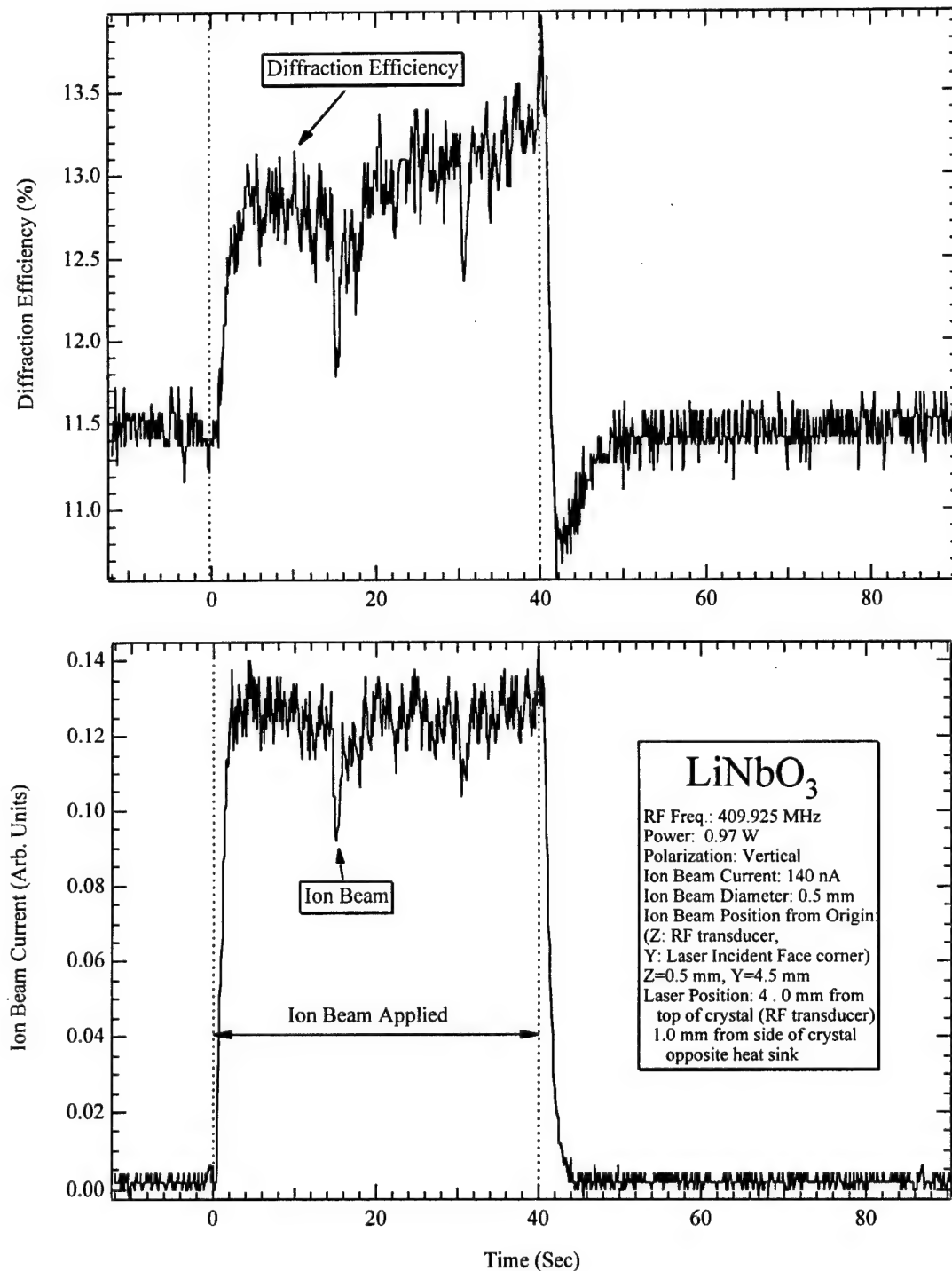


Figure A-9. Two plots showing the measured AO-cell response before, during and after an ion beam exposure. The dashed lines indicate the duration of the ion beam. Refer to Table A-2 for the precise beam location. The upper plot shows the calculated diffraction efficiency. The bottom plot shows the ion beam current in arbitrary units.

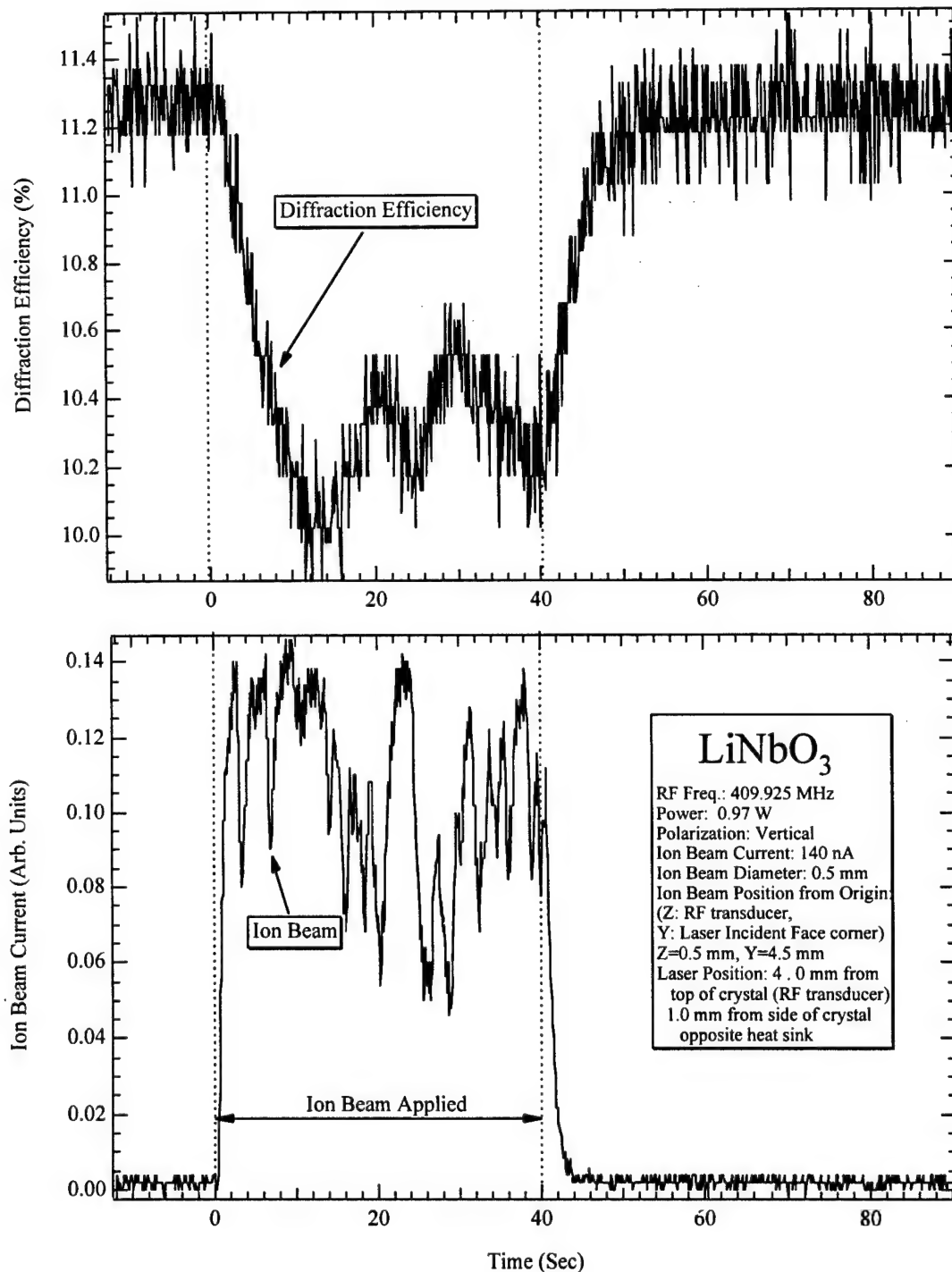


Figure A-10. Two plots showing the measured AO-cell response before, during and after an ion beam exposure. The dashed lines indicate the duration of the ion beam. Refer to Table A-2 for the precise beam location. The upper plot shows the calculated diffraction efficiency. The bottom plot shows the ion beam current in arbitrary units.

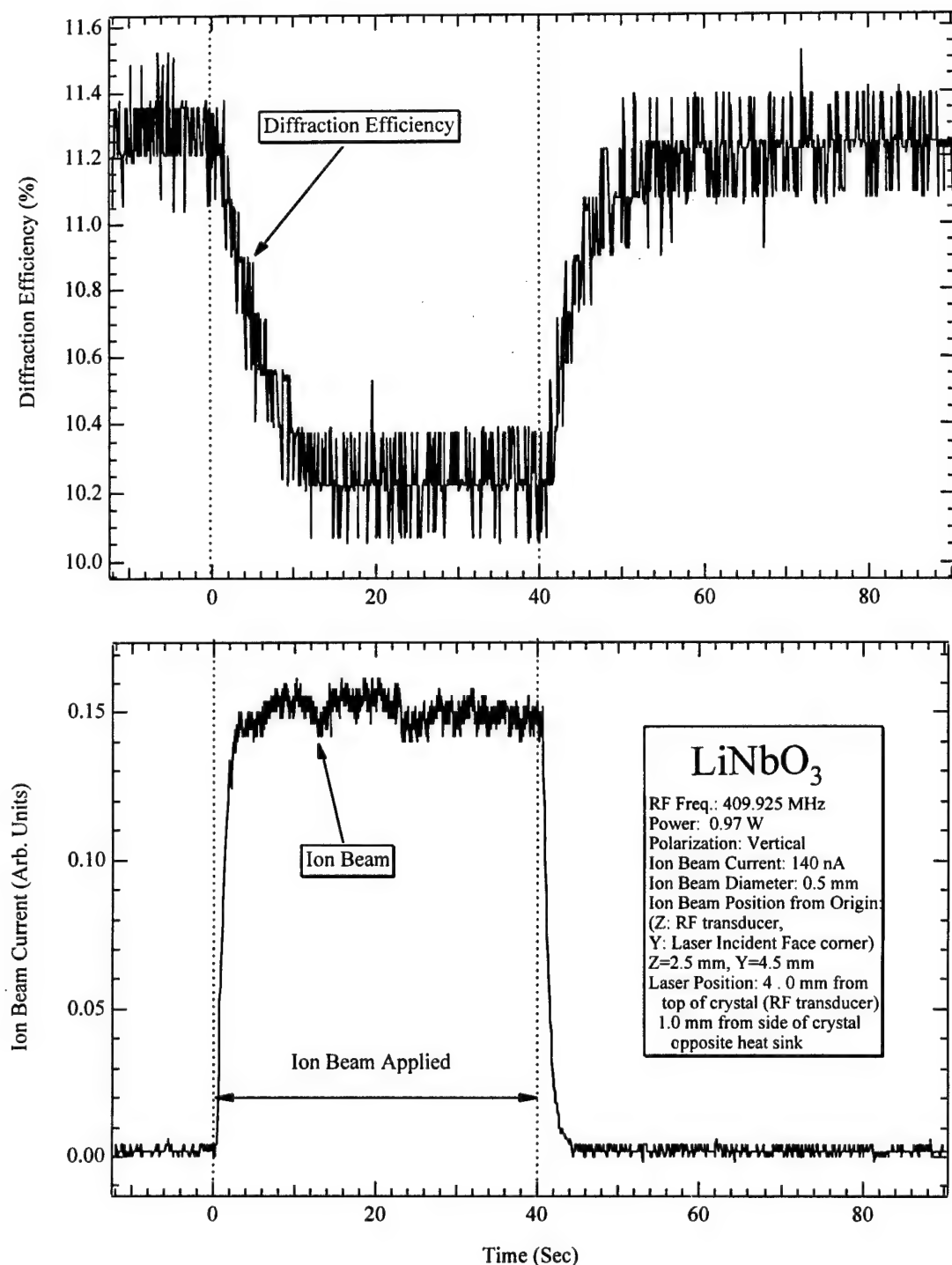


Figure A-11. Two plots showing the measured AO-cell response before, during and after an ion beam exposure. The dashed lines indicate the duration of the ion beam. Refer to Table A-2 for the precise beam location. The upper plot shows the calculated diffraction efficiency. The bottom plot shows the ion beam current in arbitrary units.

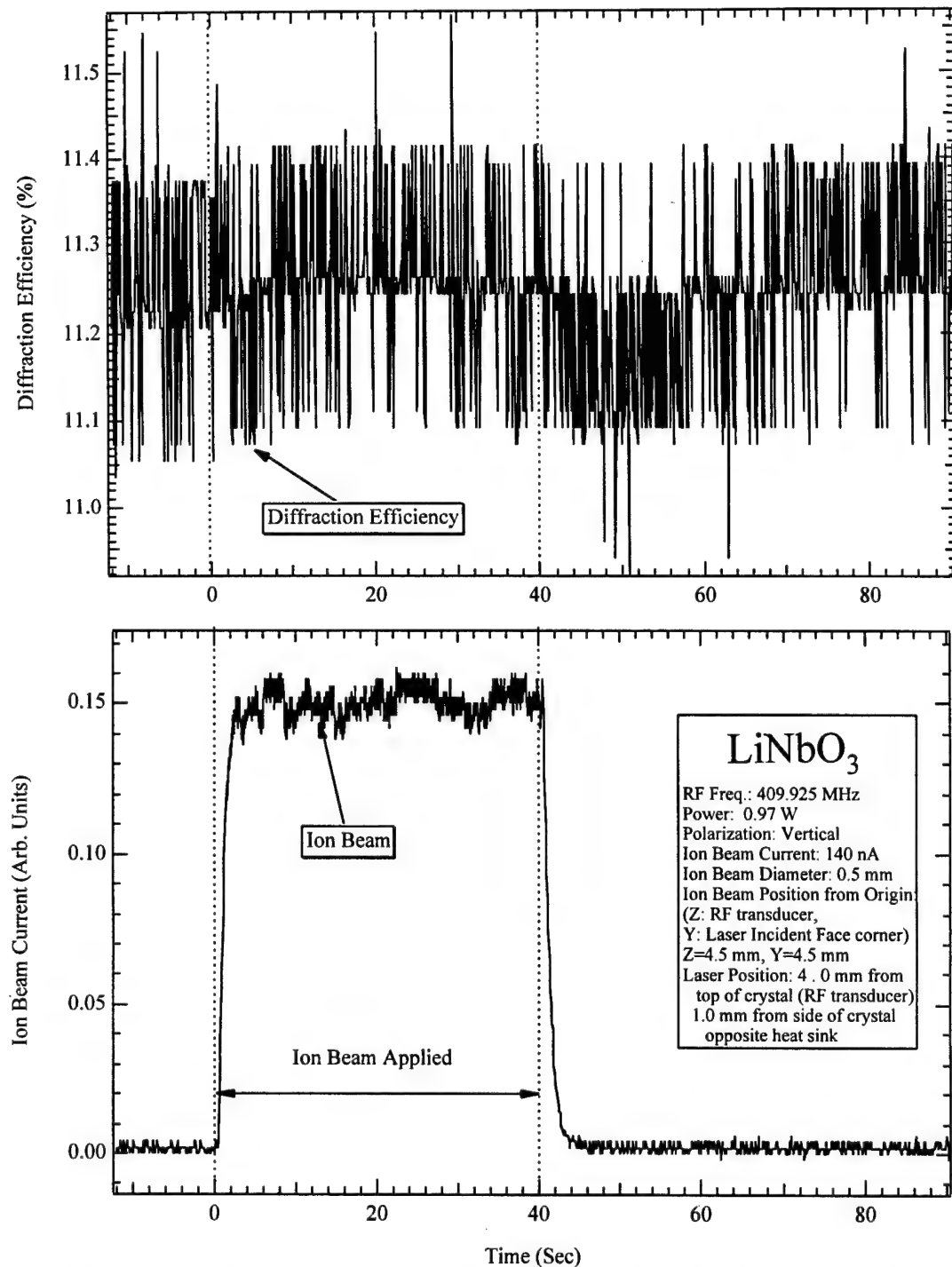


Figure A-12. Two plots showing the measured AO-cell response before, during and after an ion beam exposure. The dashed lines indicate the duration of the ion beam. Refer to Table A-2 for the precise beam location. The upper plot shows the calculated diffraction efficiency. The bottom plot shows the ion beam current in arbitrary units.

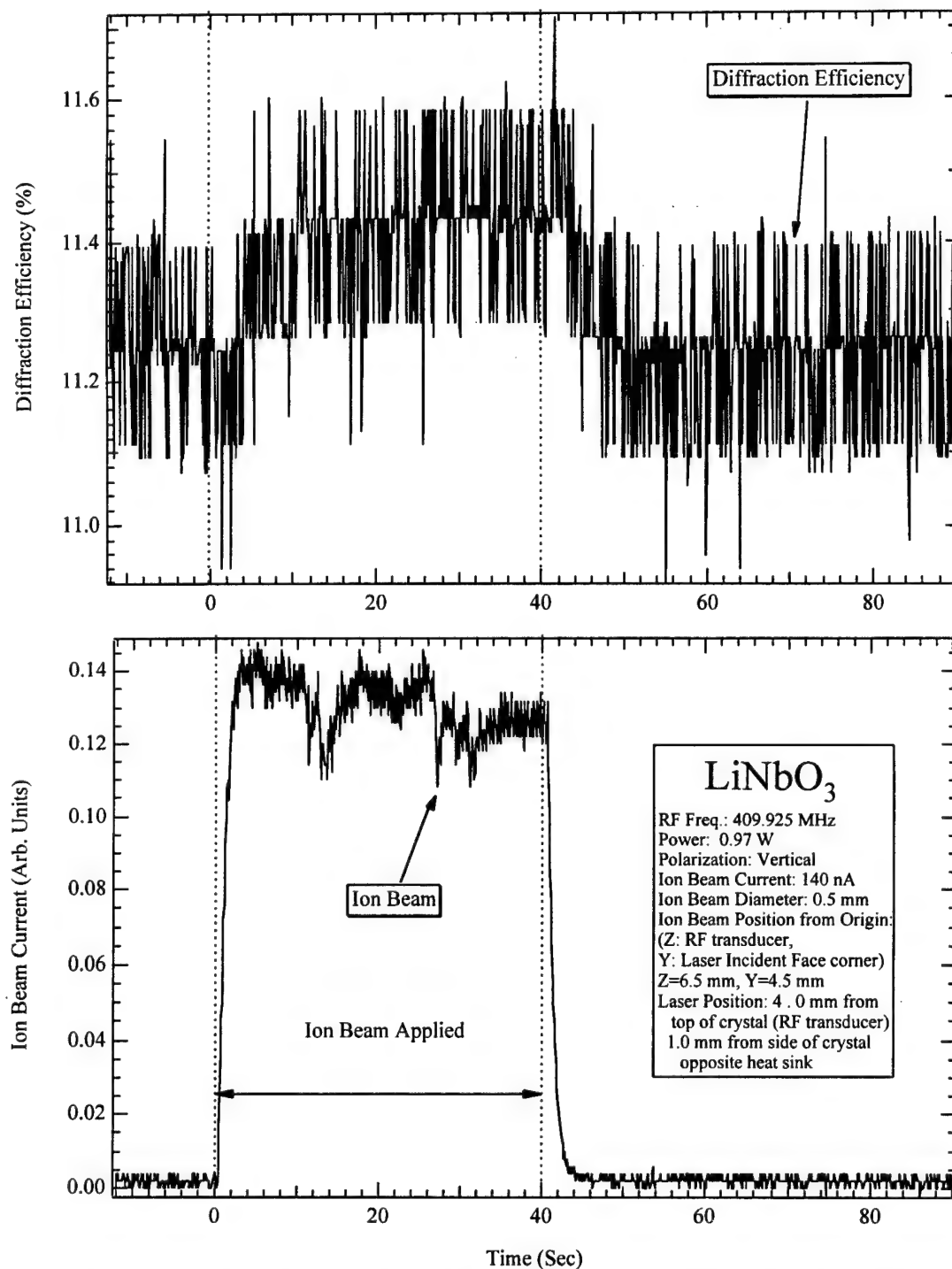


Figure A-13. Two plots showing the measured AO-cell response before, during and after an ion beam exposure. The dashed lines indicate the duration of the ion beam. Refer to Table A-2 for the precise beam location. The upper plot shows the calculated diffraction efficiency. The bottom plot shows the ion beam current in arbitrary units.

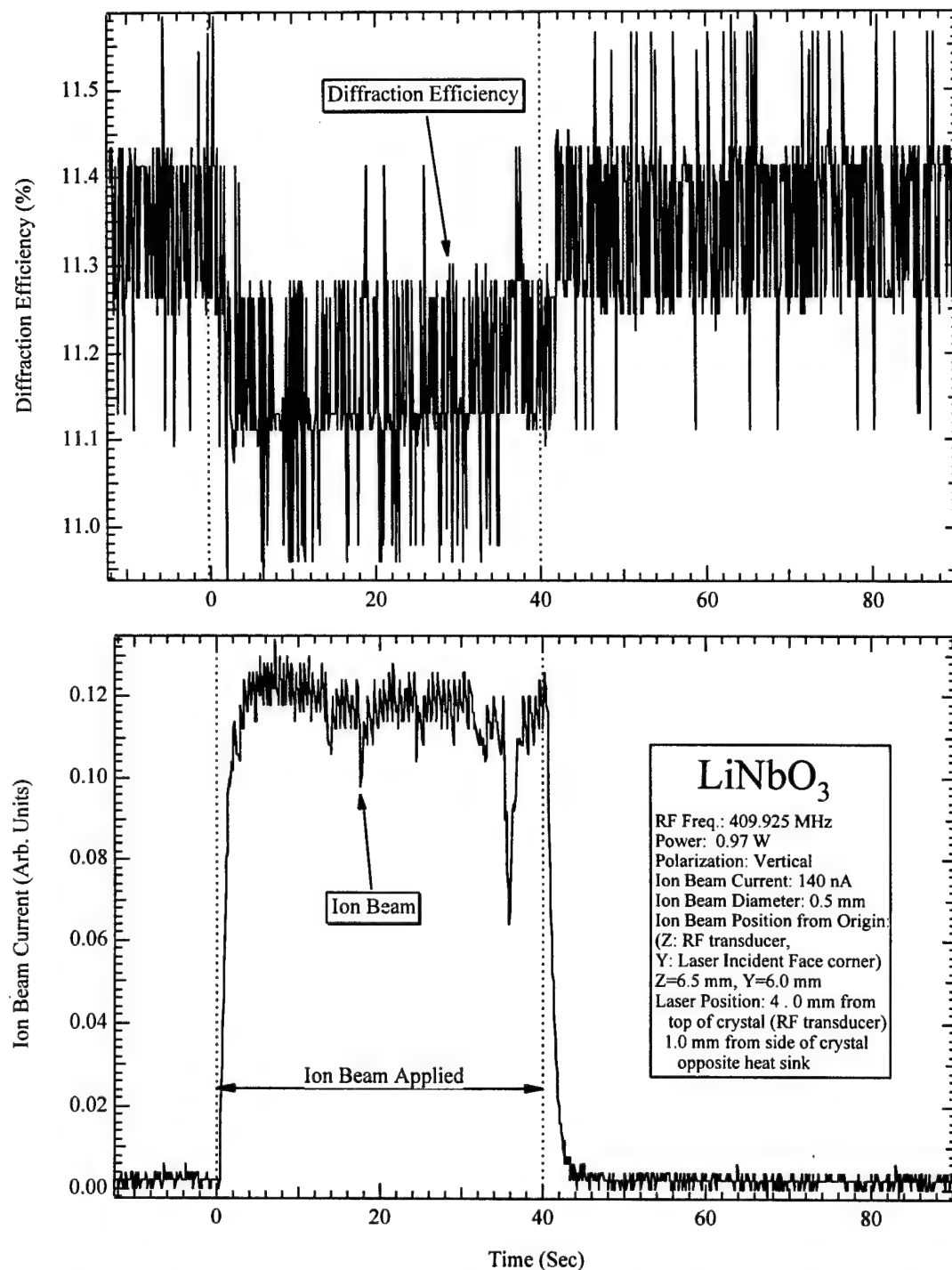


Figure A-14. Two plots showing the measured AO-cell response before, during and after an ion beam exposure. The dashed lines indicate the duration of the ion beam. Refer to Table A-2 for the precise beam location. The upper plot shows the calculated diffraction efficiency. The bottom plot shows the ion beam current in arbitrary units.

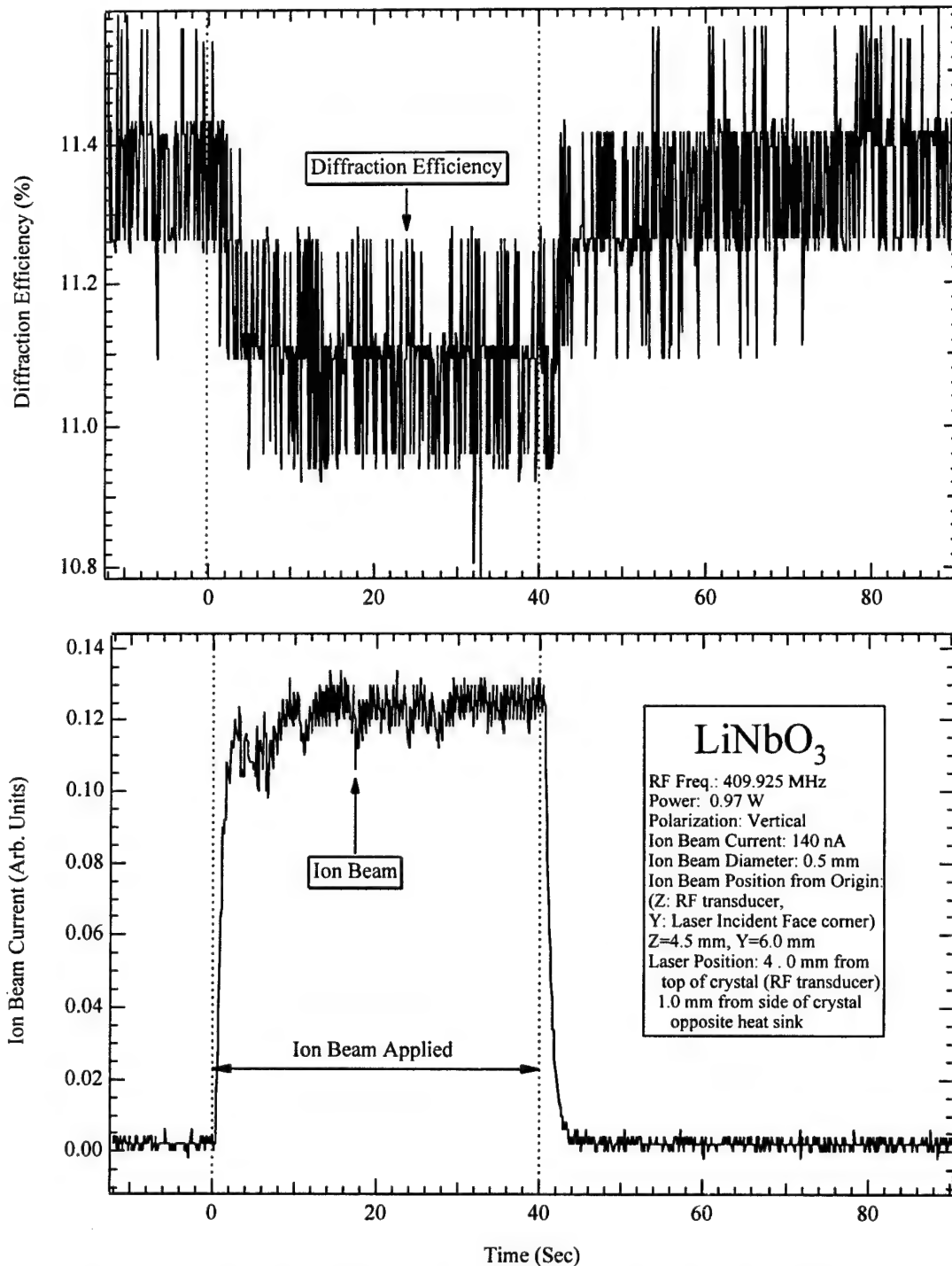


Figure A-15. Two plots showing the measured AO-cell response before, during and after an ion beam exposure. The dashed lines indicate the duration of the ion beam. Refer to Table A-2 for the precise beam location. The upper plot shows the calculated diffraction efficiency. The bottom plot shows the ion beam current in arbitrary units.

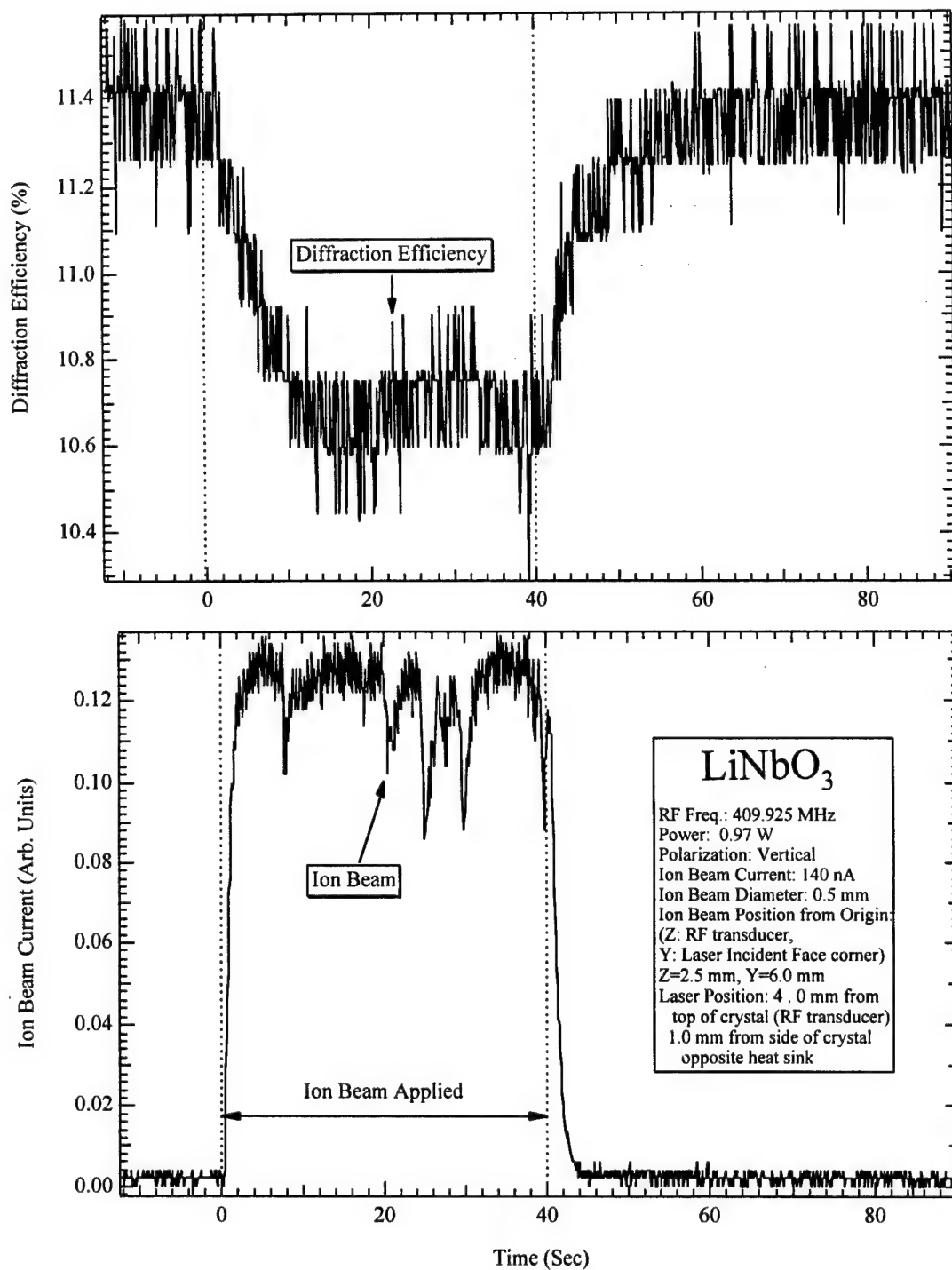


Figure A-16. Two plots showing the measured AO-cell response before, during and after an ion beam exposure. The dashed lines indicate the duration of the ion beam. Refer to Table A-2 for the precise beam location. The upper plot shows the calculated diffraction efficiency. The bottom plot shows the ion beam current in arbitrary units.

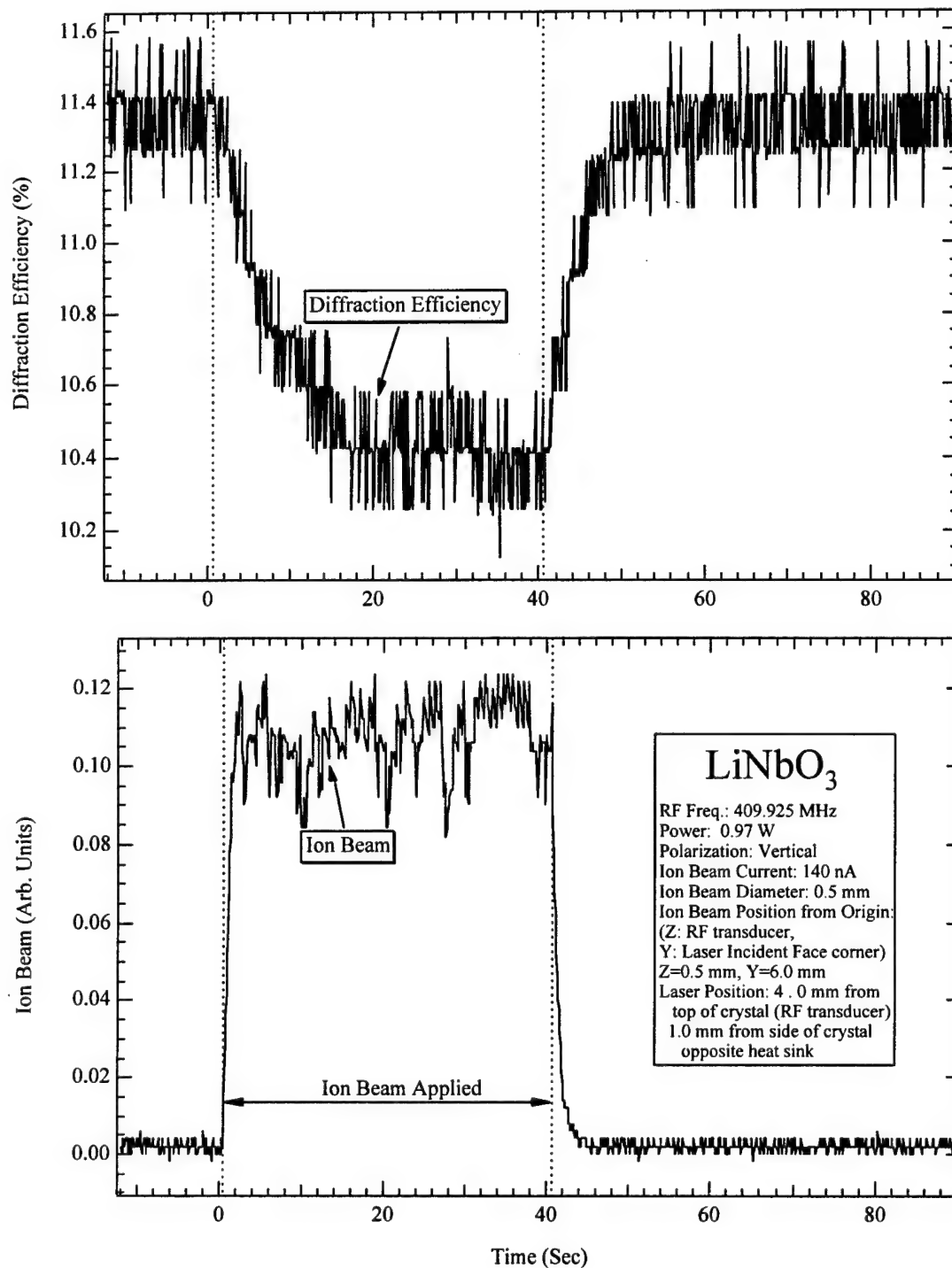


Figure A-17. Two plots showing the measured AO-cell response before, during and after an ion beam exposure. The dashed lines indicate the duration of the ion beam. Refer to Table A-2 for the precise beam location. The upper plot shows the calculated diffraction efficiency. The bottom plot shows the ion beam current in arbitrary units.

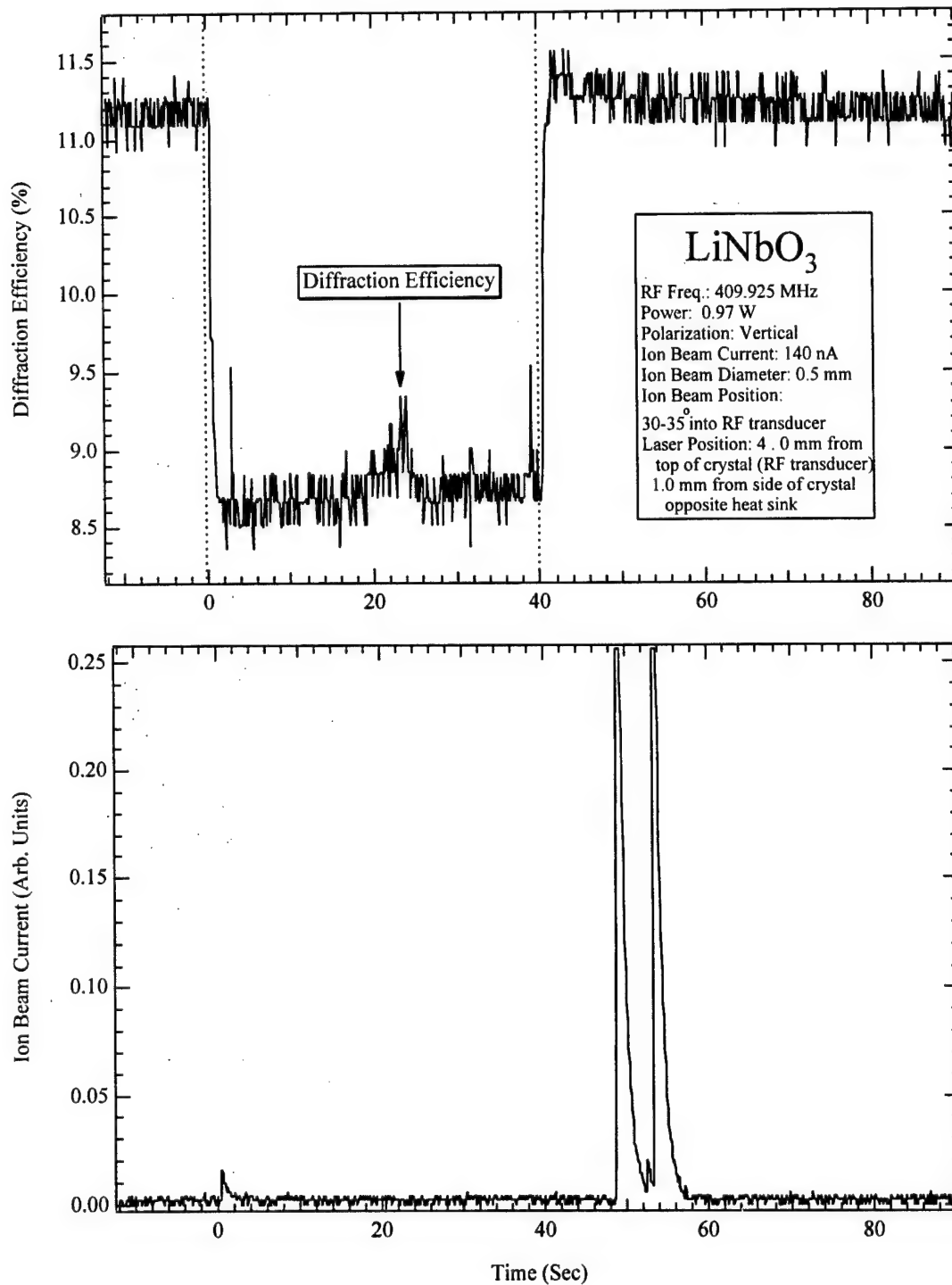


Figure A-18. Two plots showing the measured AO-cell response before, during and after an ion beam exposure. The dashed lines indicate the duration of the ion beam. Refer to Table A-2 for the precise beam location. The upper plot shows the calculated diffraction efficiency. The bottom plot shows the ion beam current in arbitrary units.

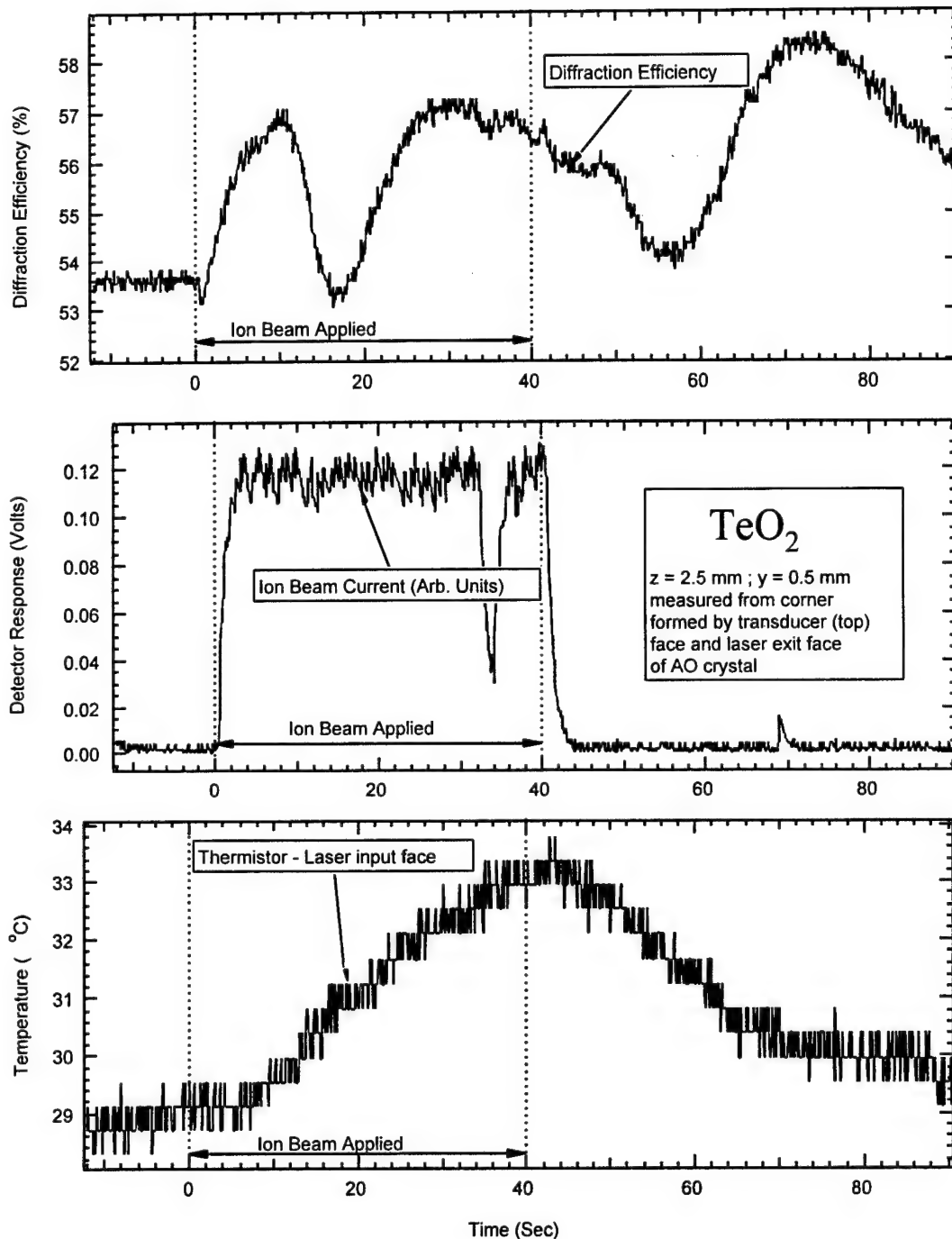


Figure A-19. Plot of diffraction efficiency of TeO_2 AO deflector during and following irradiation of the crystal face opposite the heatsink. A power of 0.4 W was incident on the facet opposite the heatsink in a square spot 0.5 mm on a side. The irradiated spot was centered 3 mm from the laser exit facet and 1 mm from the facet on which the transducers are bonded.

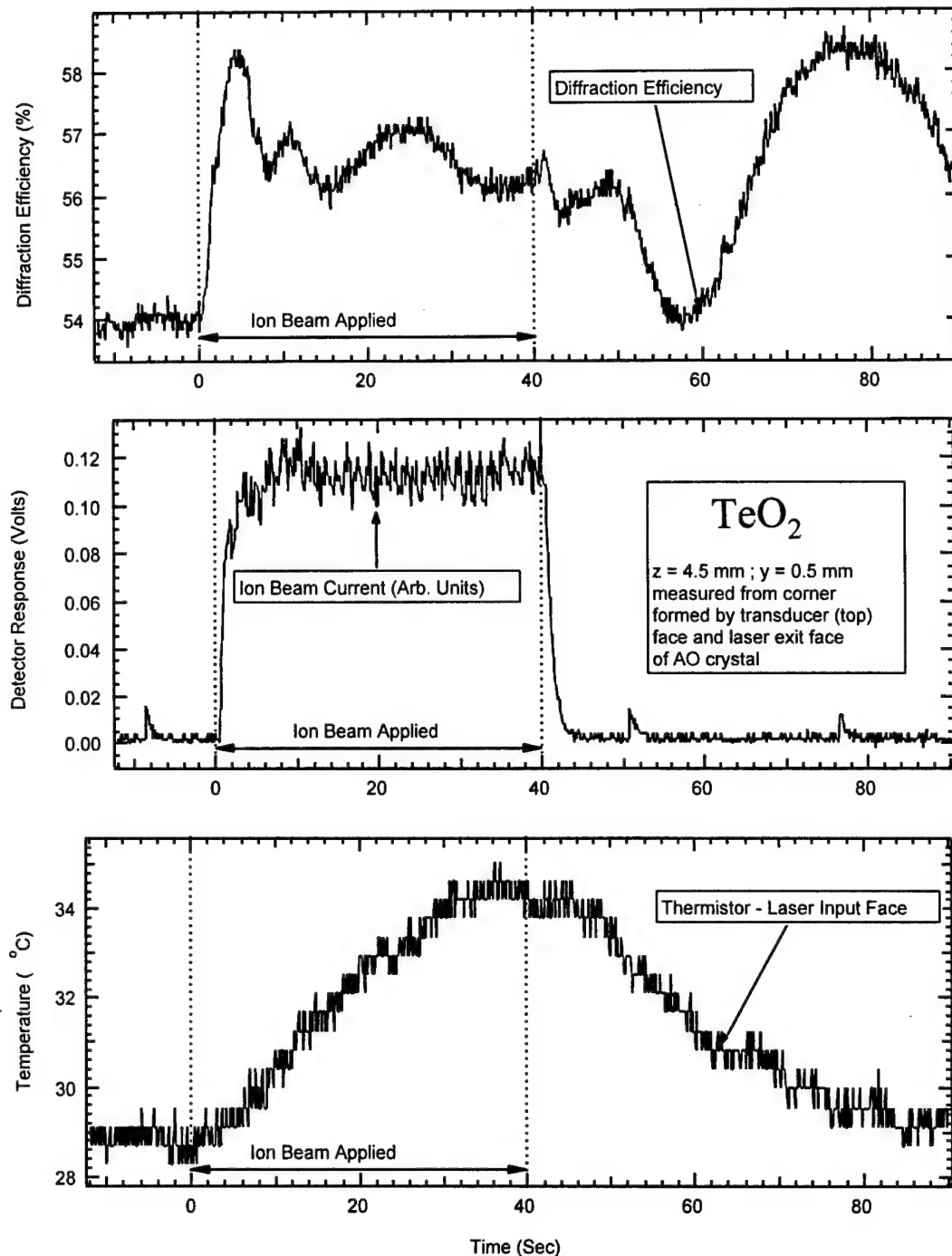


Figure A-20. Plot of diffraction efficiency of TeO_2 AO deflector during and following irradiation of the crystal face opposite the heatsink. A power of 0.4 W was incident on the facet opposite the heatsink in a square spot 0.5 mm on a side. The irradiated spot was centered 5 mm from the laser exit facet and 1 mm from the facet on which the transducers are bonded.

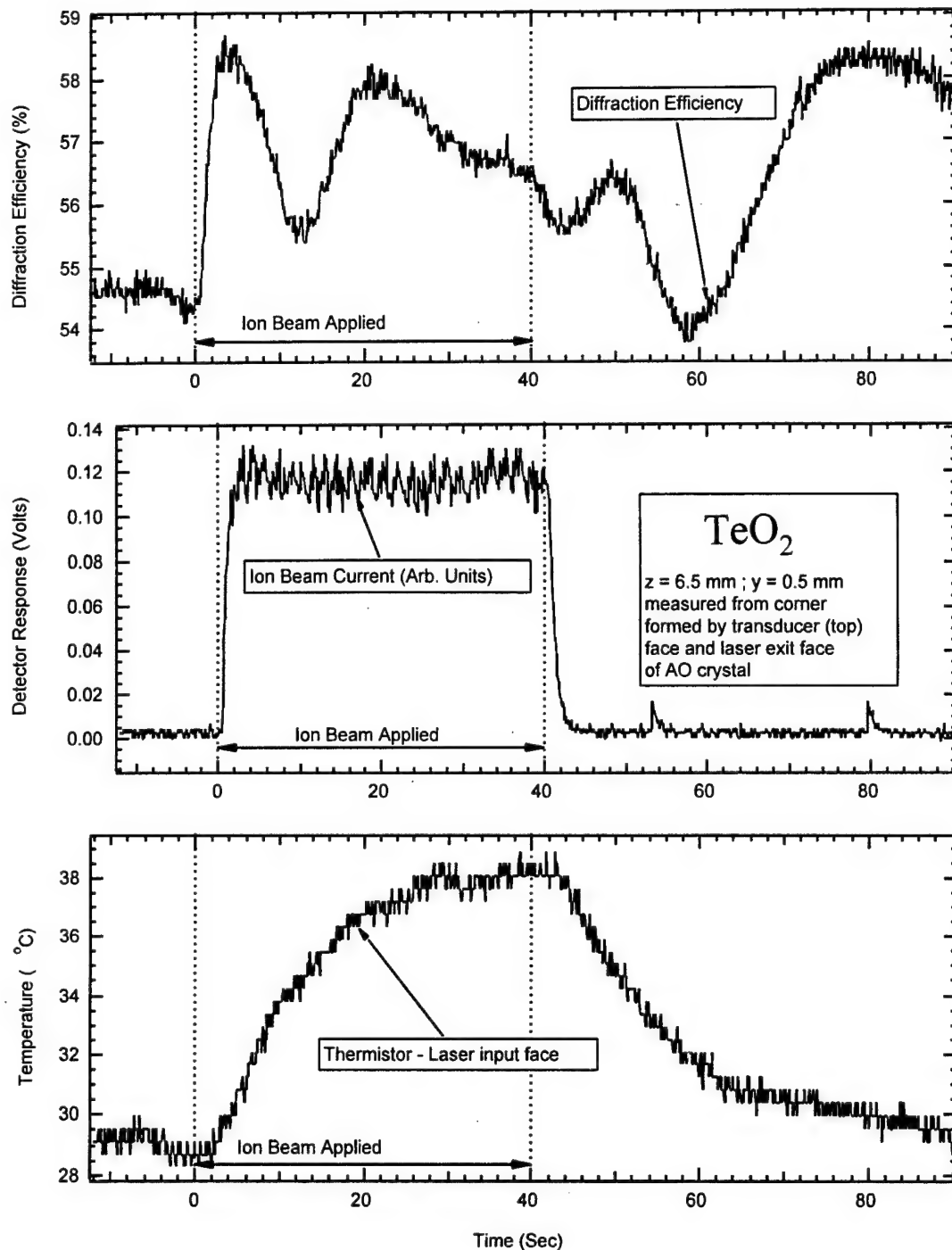


Figure A-21. Plot of diffraction efficiency of TeO_2 AO deflector during and following irradiation of the crystal face opposite the heatsink. A power of 0.4 W was incident on the facet opposite the heatsink in a square spot 0.5 mm on a side. The irradiated spot was centered 7 mm from the laser exit facet and 1 mm from the facet on which the transducers are bonded.

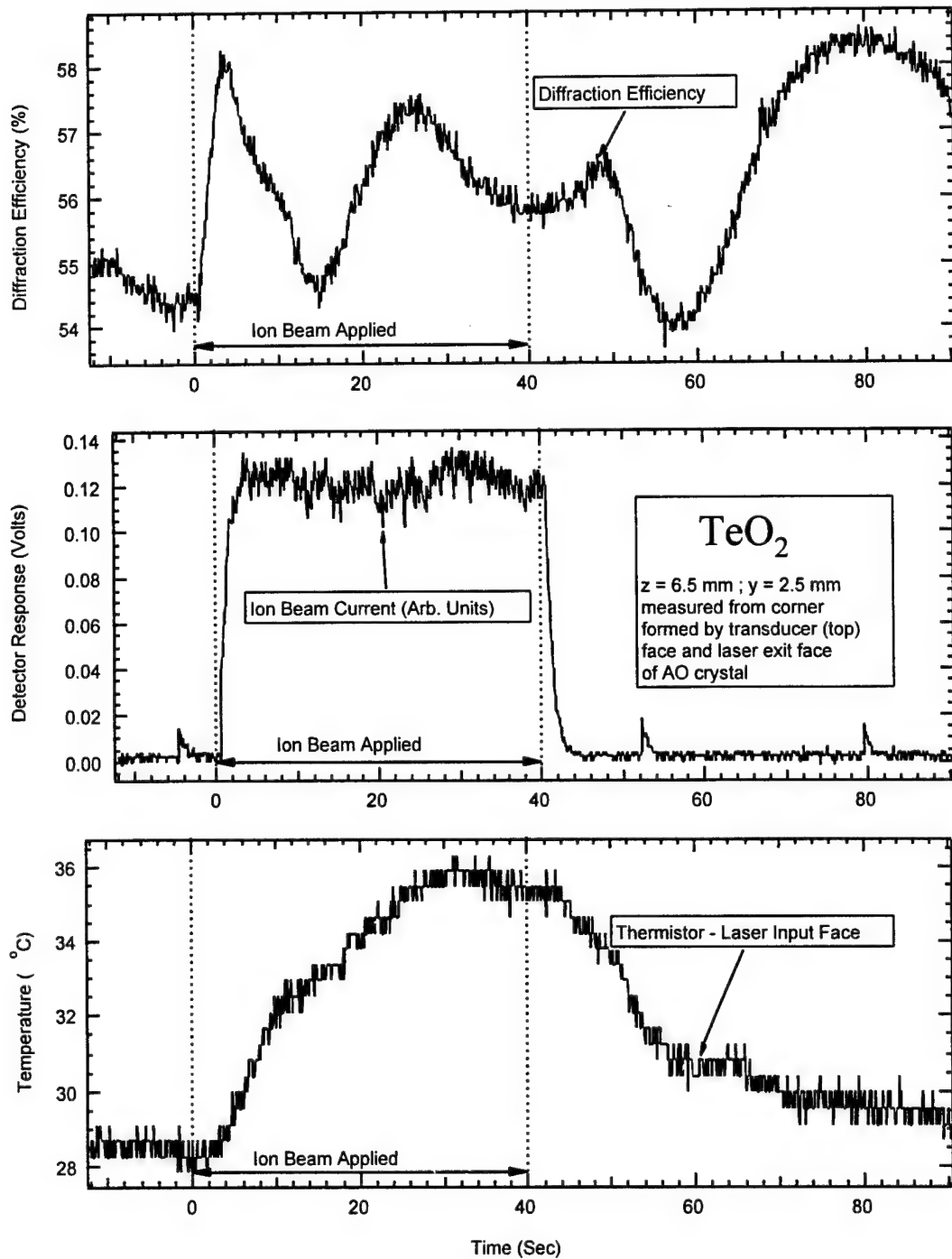


Figure A-22. Plot of diffraction efficiency of TeO_2 AO deflector during and following irradiation of the crystal face opposite the heatsink. A power of 0.4 W was incident on the facet opposite the heatsink in a square spot 0.5 mm on a side. The irradiated spot was centered 7 mm from the laser exit facet and 3 mm from the facet on which the transducers are bonded.

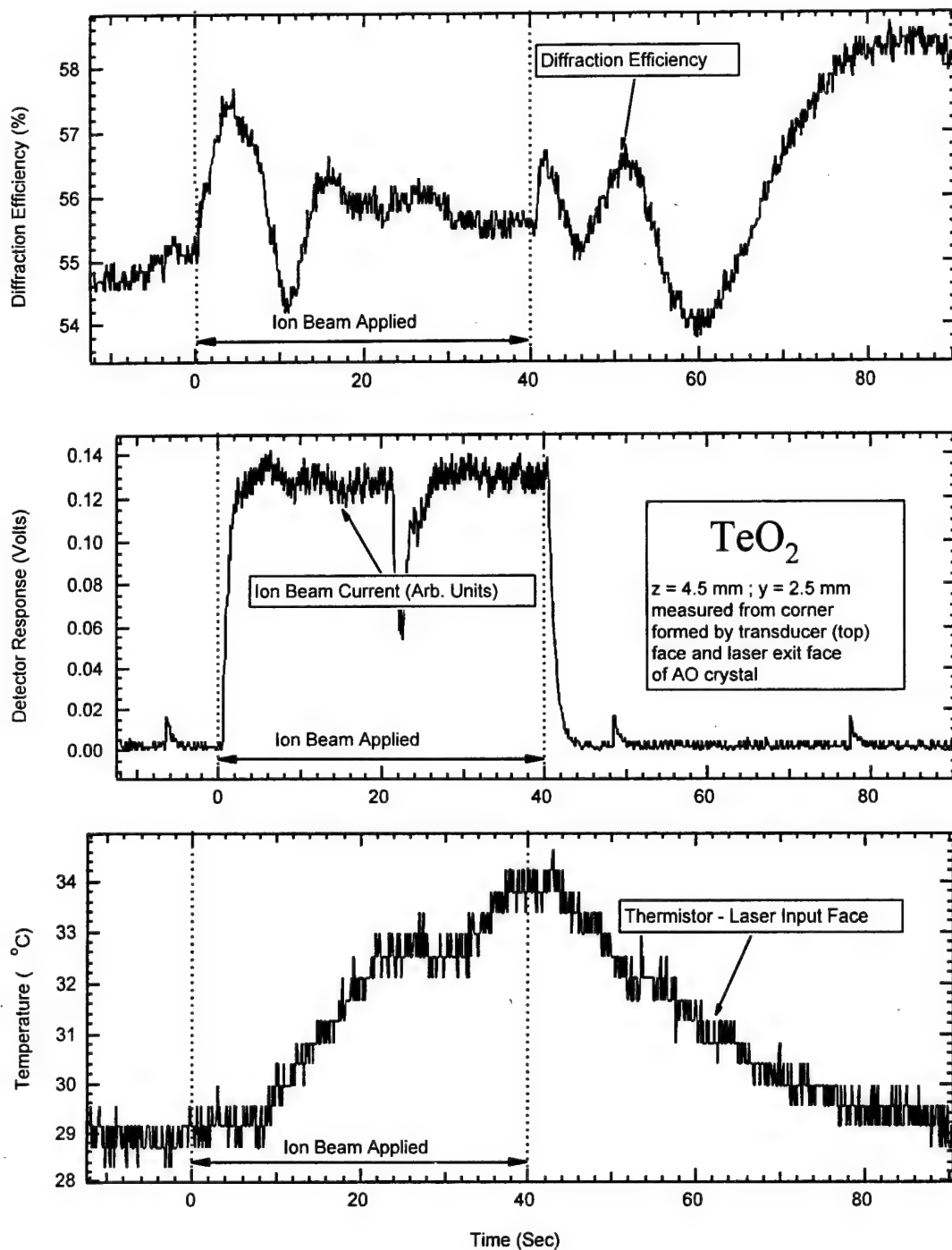


Figure A-23. Same as Figure A-22, except that the optical beam was blocked to ensure that neither radiation nor electrical noise substantially affected the detected optical power.

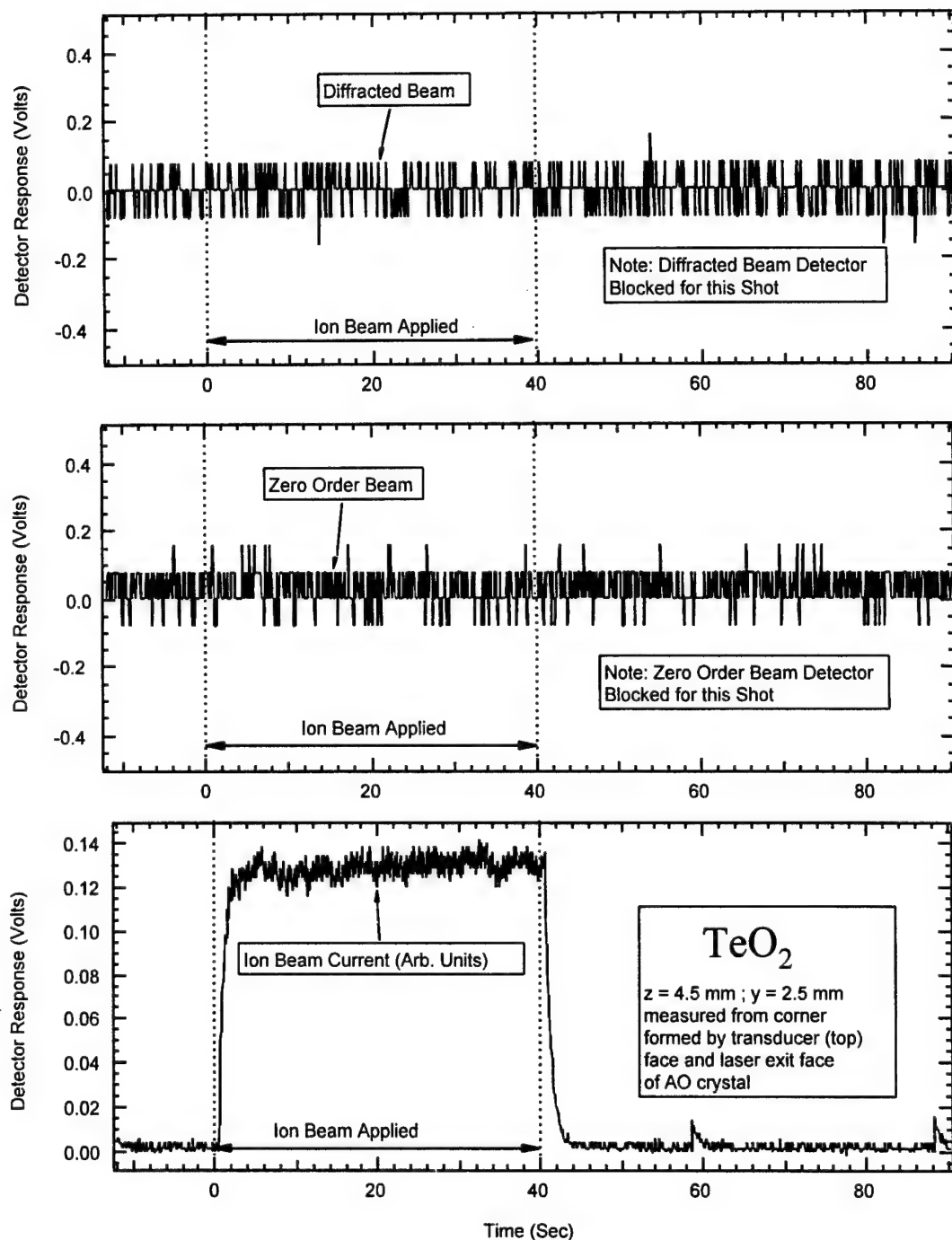


Figure A-24. Plot of diffraction efficiency of TeO₂ AO deflector during and following irradiation of the crystal face opposite the heatsink. A power of 0.4 W was incident on the facet opposite the heatsink in a square spot 0.5 mm on a side. The irradiated spot was centered 5 mm from the laser exit facet and 3 mm from the facet on which the transducers are bonded.

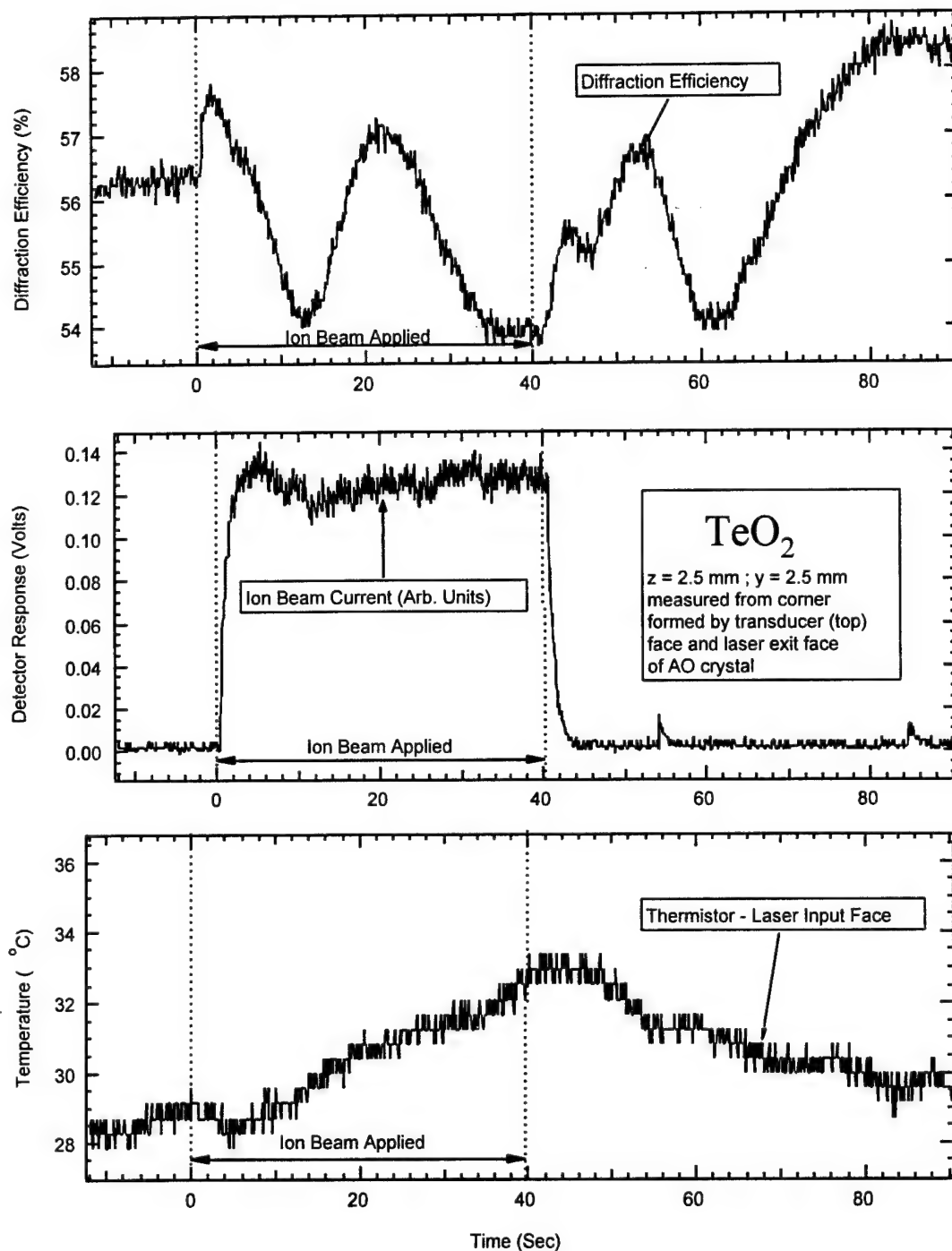


Figure A-25. Plot of diffraction efficiency of TeO_2 AO deflector during and following irradiation of the crystal face opposite the heatsink. A power of 0.4 W was incident on the facet opposite the heatsink in a square spot 0.5 mm on a side. The irradiated spot was centered 3 mm from the laser exit facet and 3 mm from the facet on which the transducers are bonded.

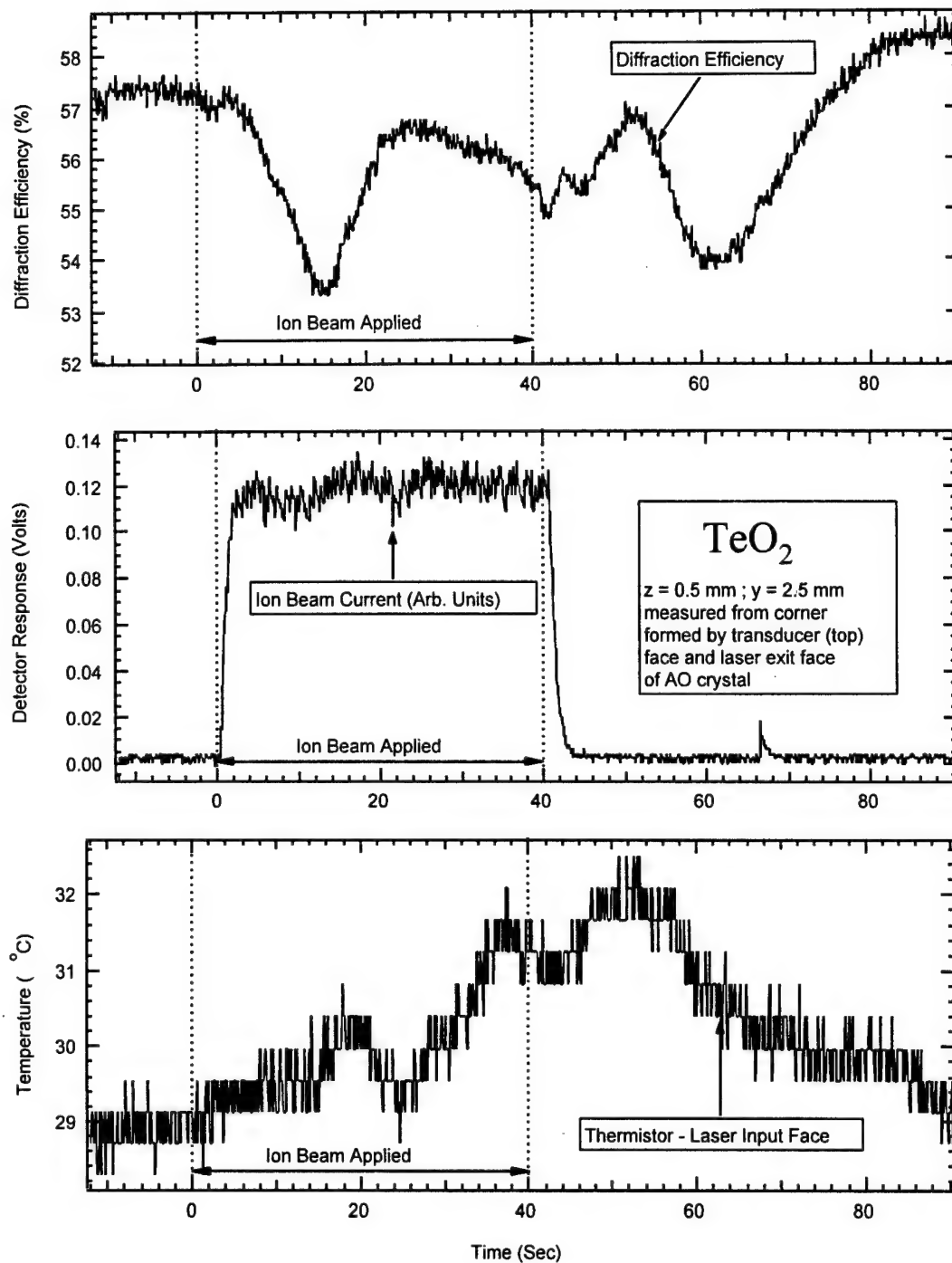


Figure A-26. Plot of diffraction efficiency of TeO_2 AO deflector during and following irradiation of the crystal face opposite the heatsink. A power of 0.4 W was incident on the facet opposite the heatsink in a square spot 0.5 mm on a side. The irradiated spot was centered 1 mm from the laser exit facet and 3 mm from the facet on which the transducers are bonded.

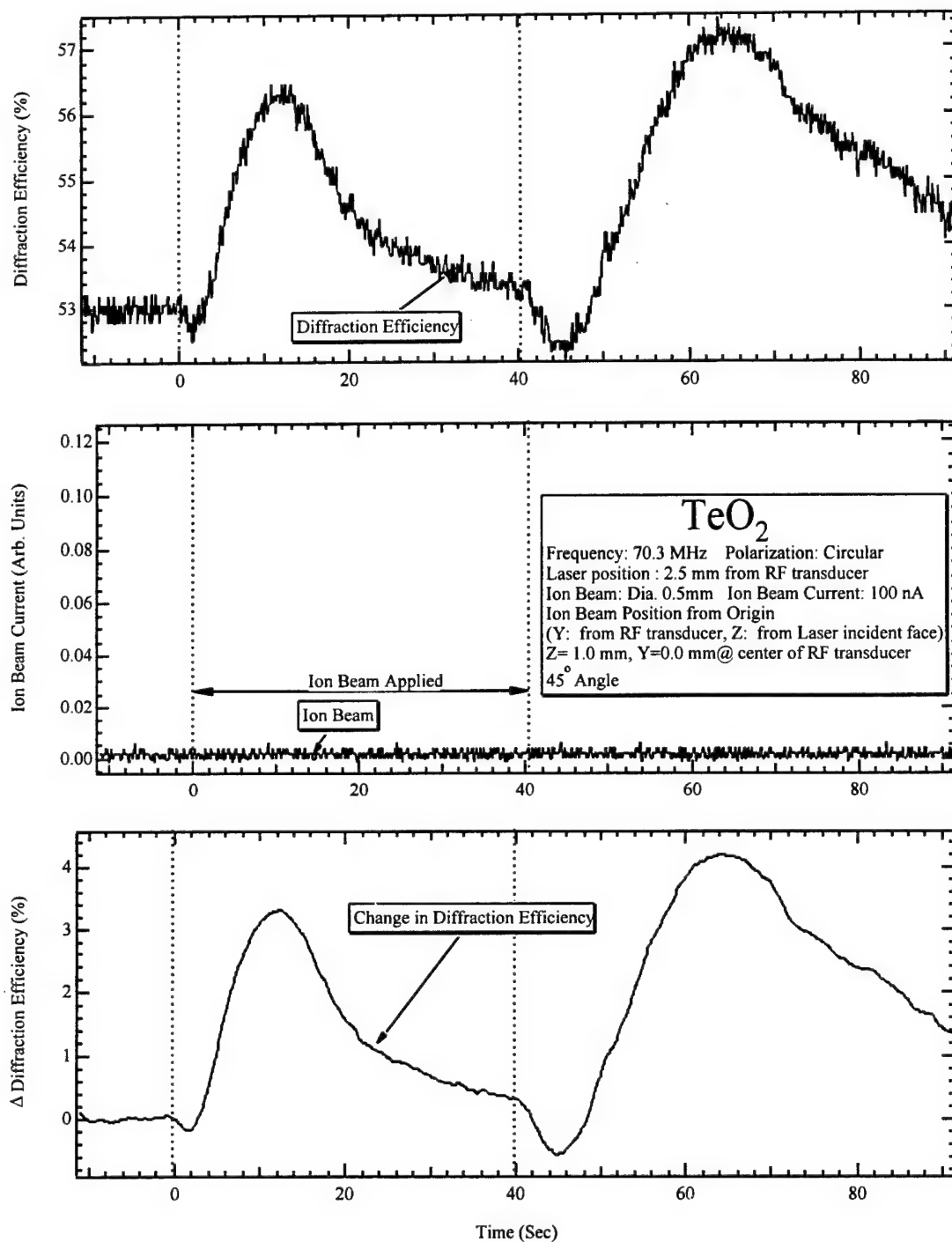


Figure A-27. Plot of diffraction efficiency of TeO₂ AO deflector during and following irradiation of the transducer. A power of 0.4 W was incident at 5.5 mm from the heatsink in a square spot 4.0mm on a side. The irradiated spot was centered 1.0 mm from the laser-exit facet of the crystal. The angle of incidence was 45°. The irradiation occurred during times between the two vertical dashed lines.

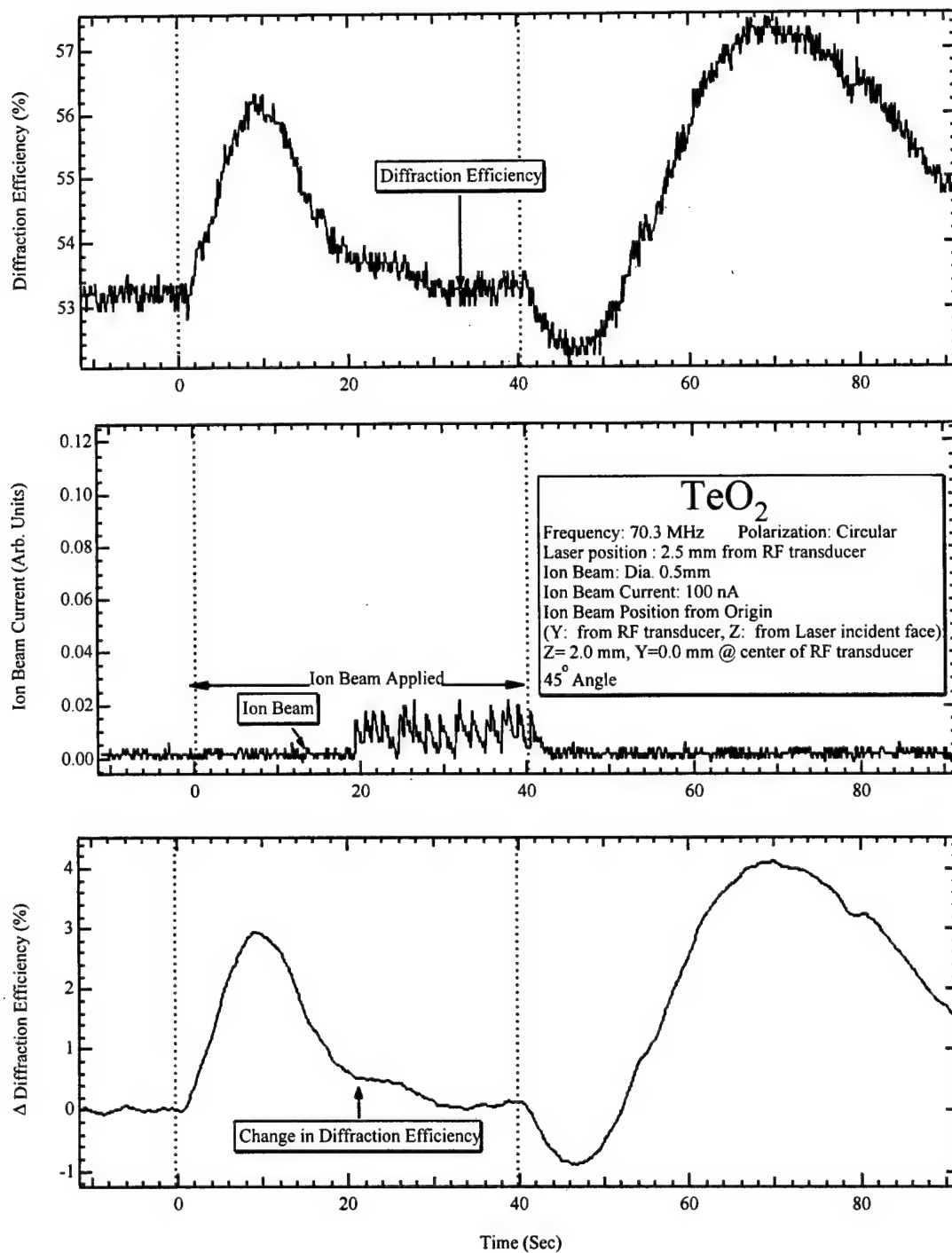


Figure A-28. Same as Figure A-27, but the irradiated spot was centered 2.0 mm from the laser-exit facet.

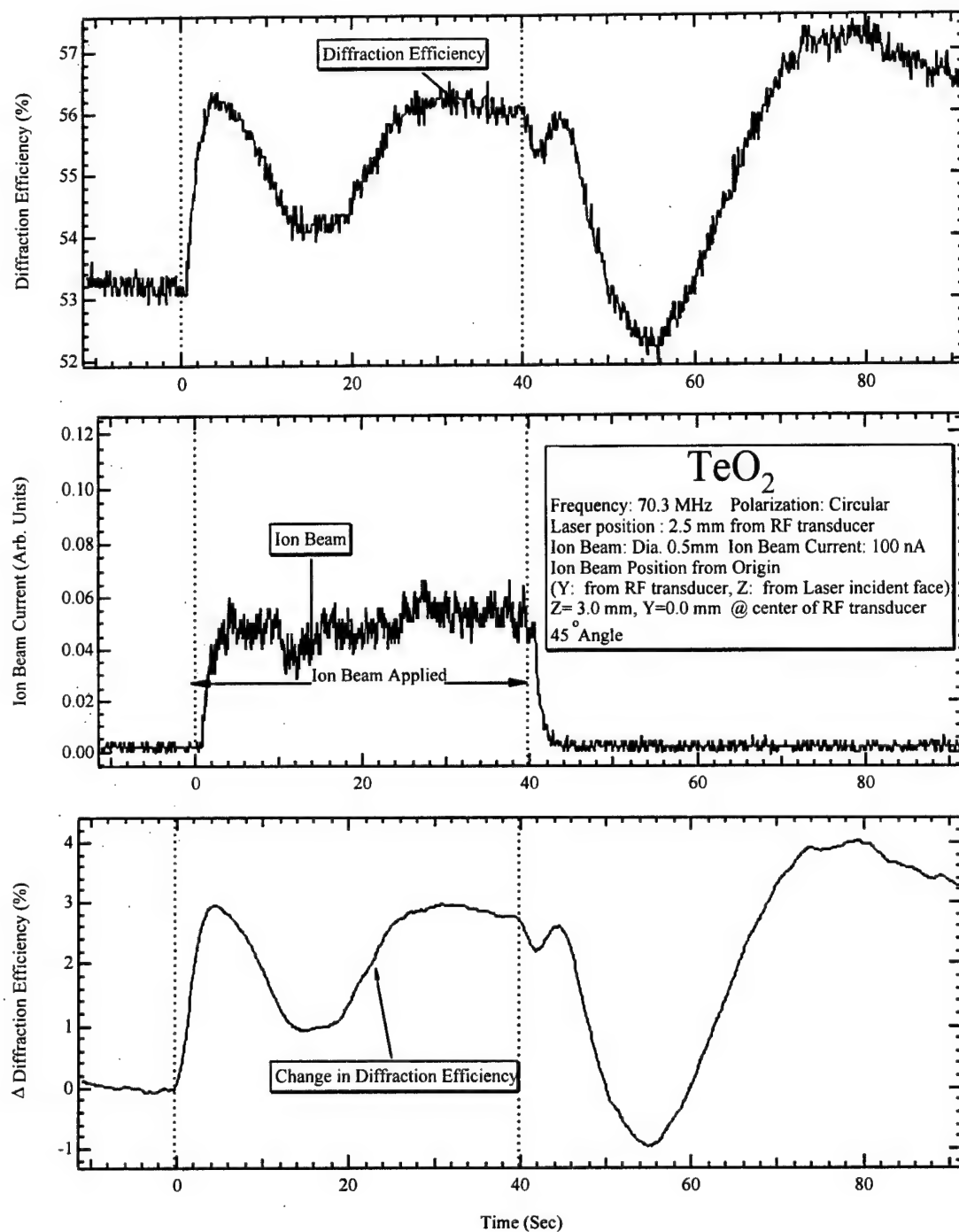


Figure A-29. Same as Figure A-27, but the irradiated spot was centered 3.0 mm from the laser-exit facet.

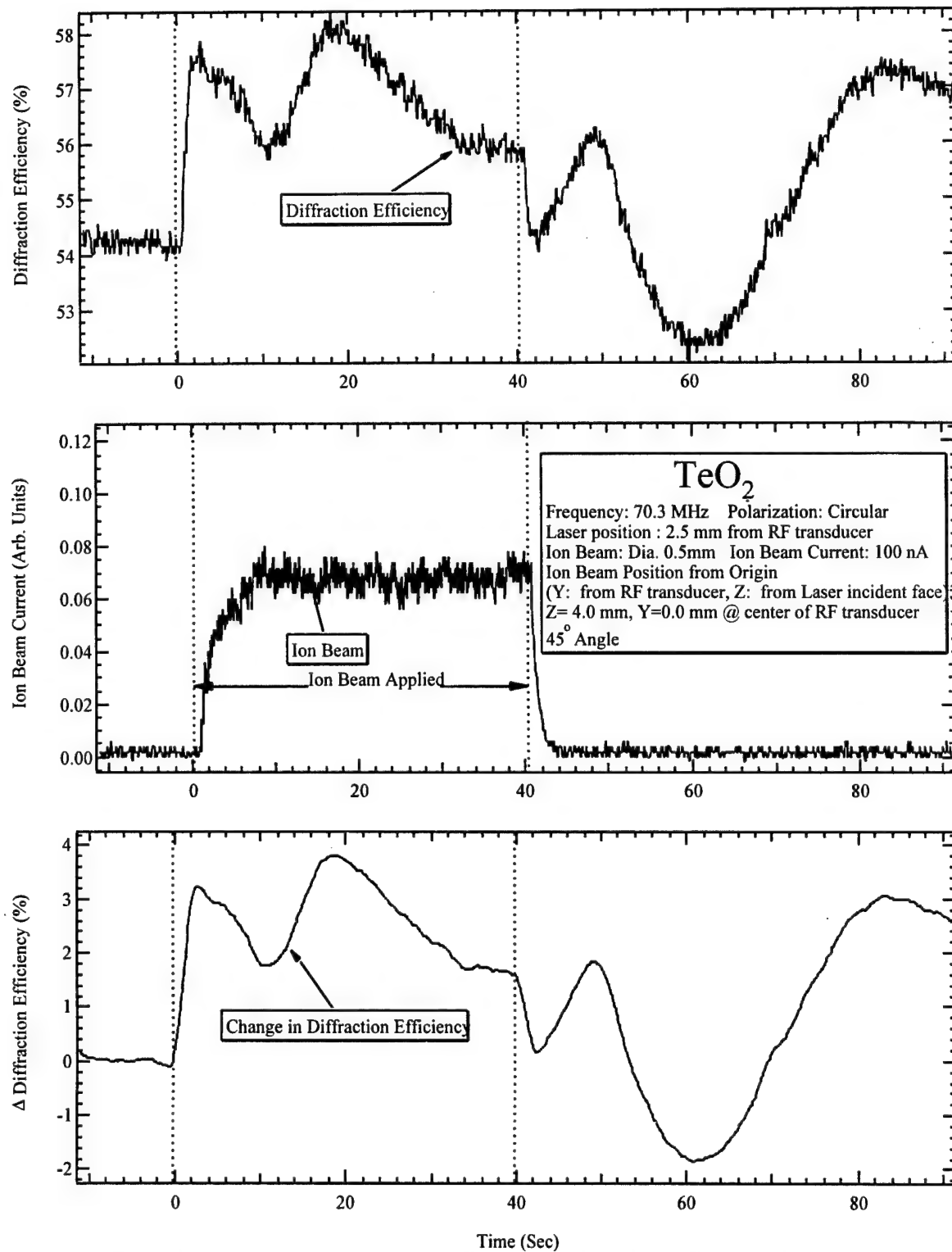


Figure A-30. Same as Figure A-27, but the irradiated spot was centered 4.0 mm from the laser-exit facet.

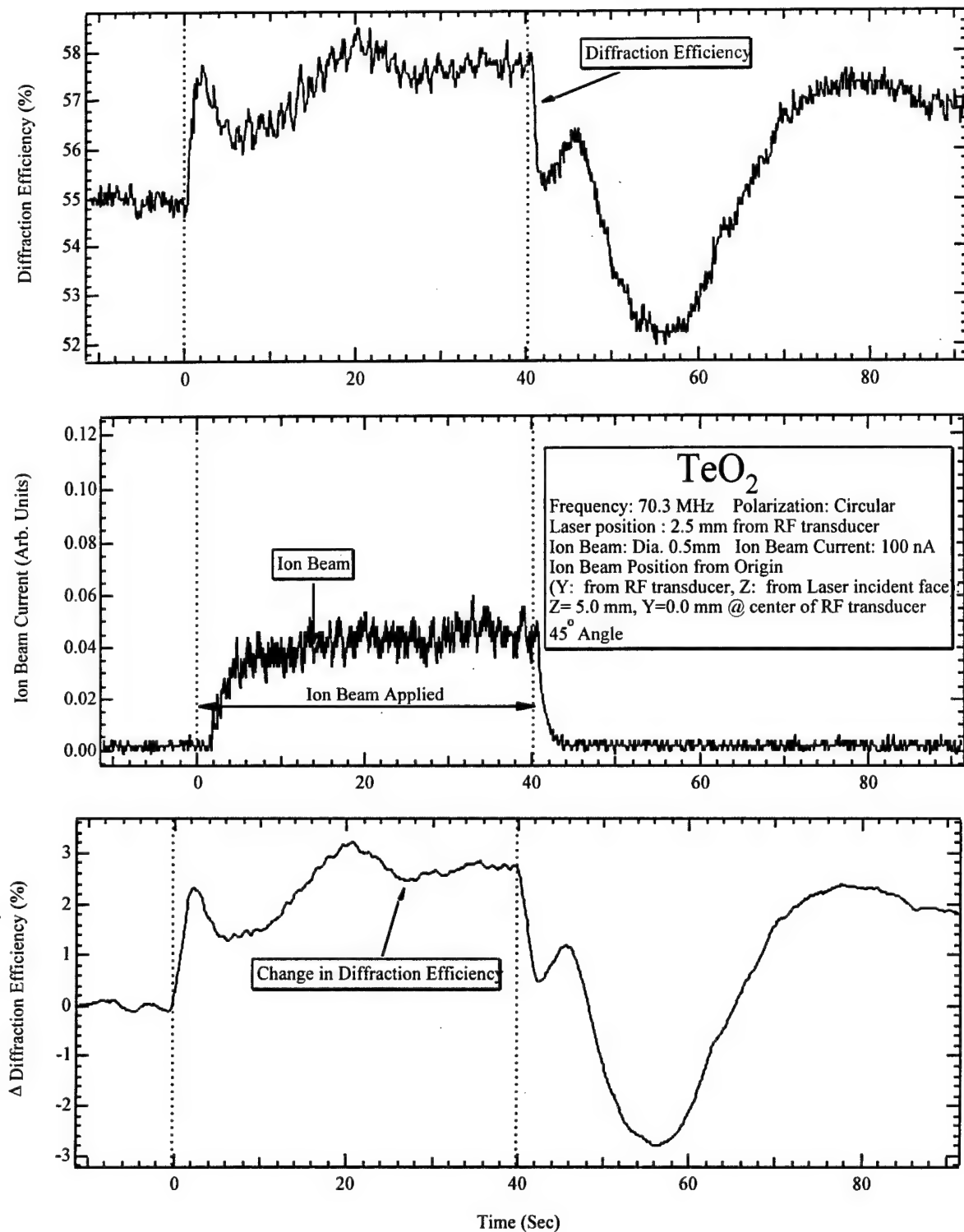


Figure A-31. Same as Figure A-27, but the irradiated spot was centered 5.0 mm from the laser-exit facet.

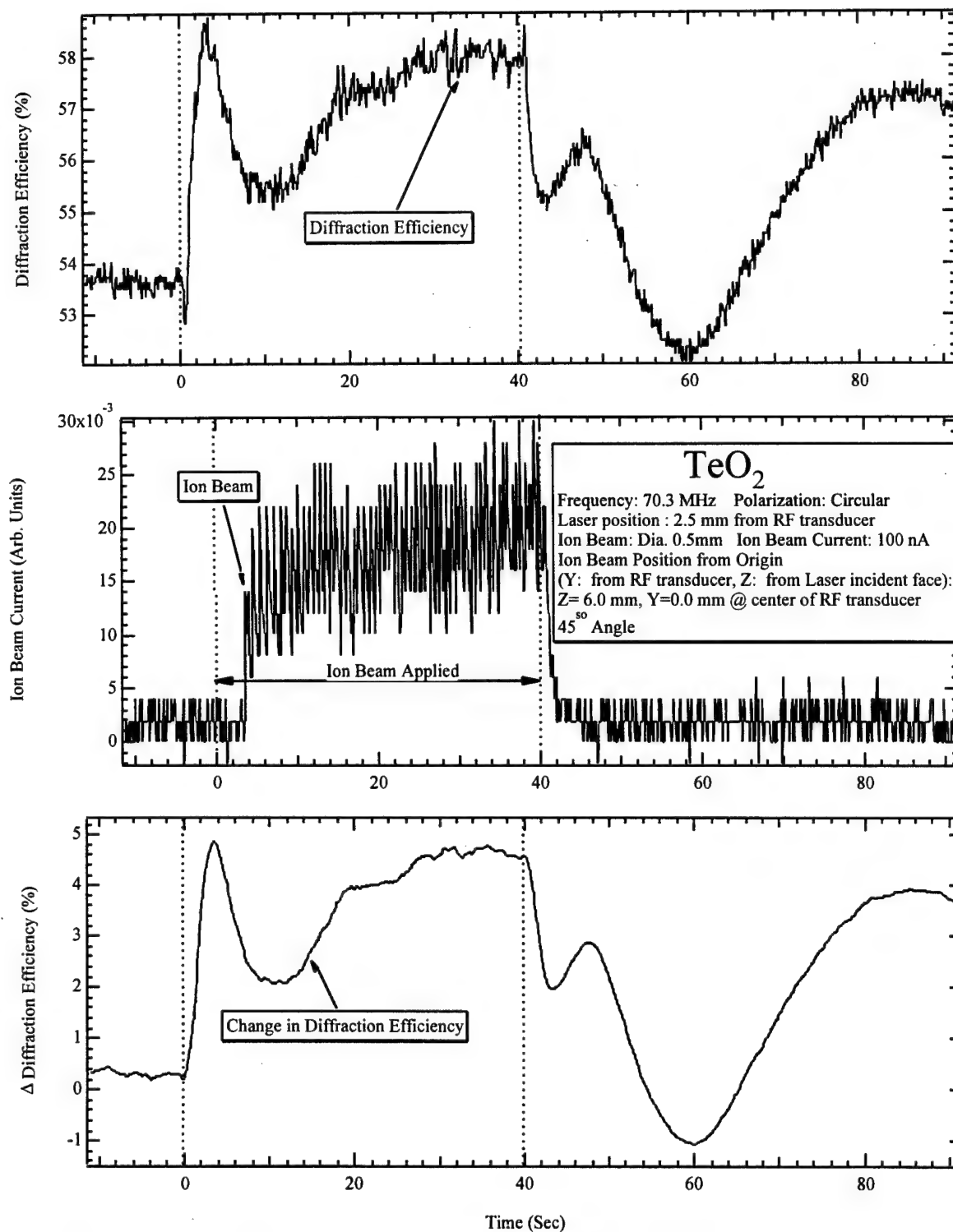


Figure A-32. Same as Figure A-27, but the irradiated spot was centered 6.0 mm from the laser-exit facet.

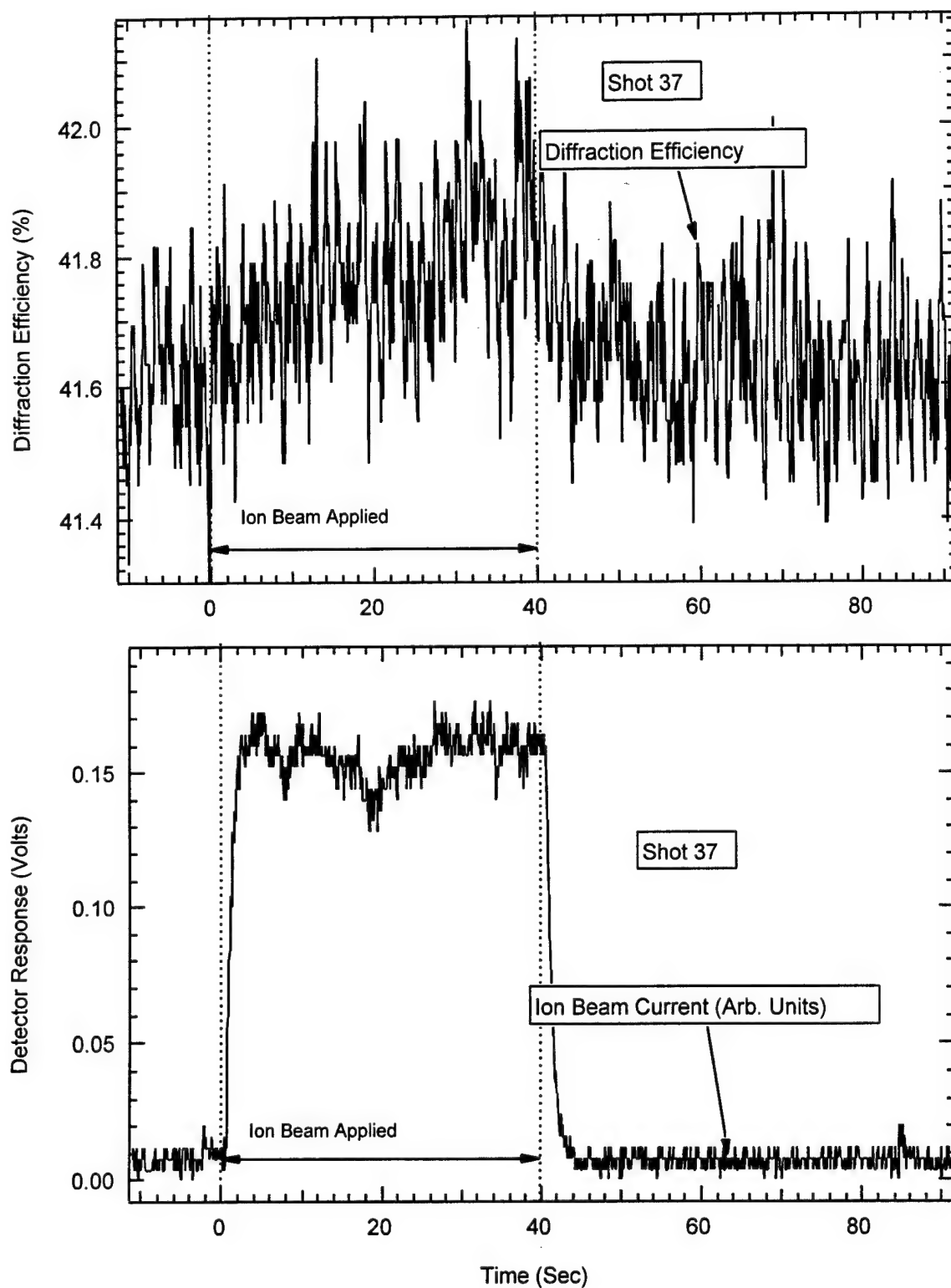


Figure A-33. Temperature plots corresponding to the runs shown in Figures A-27 through A-29. The temperature increased by 2 to 3°C.

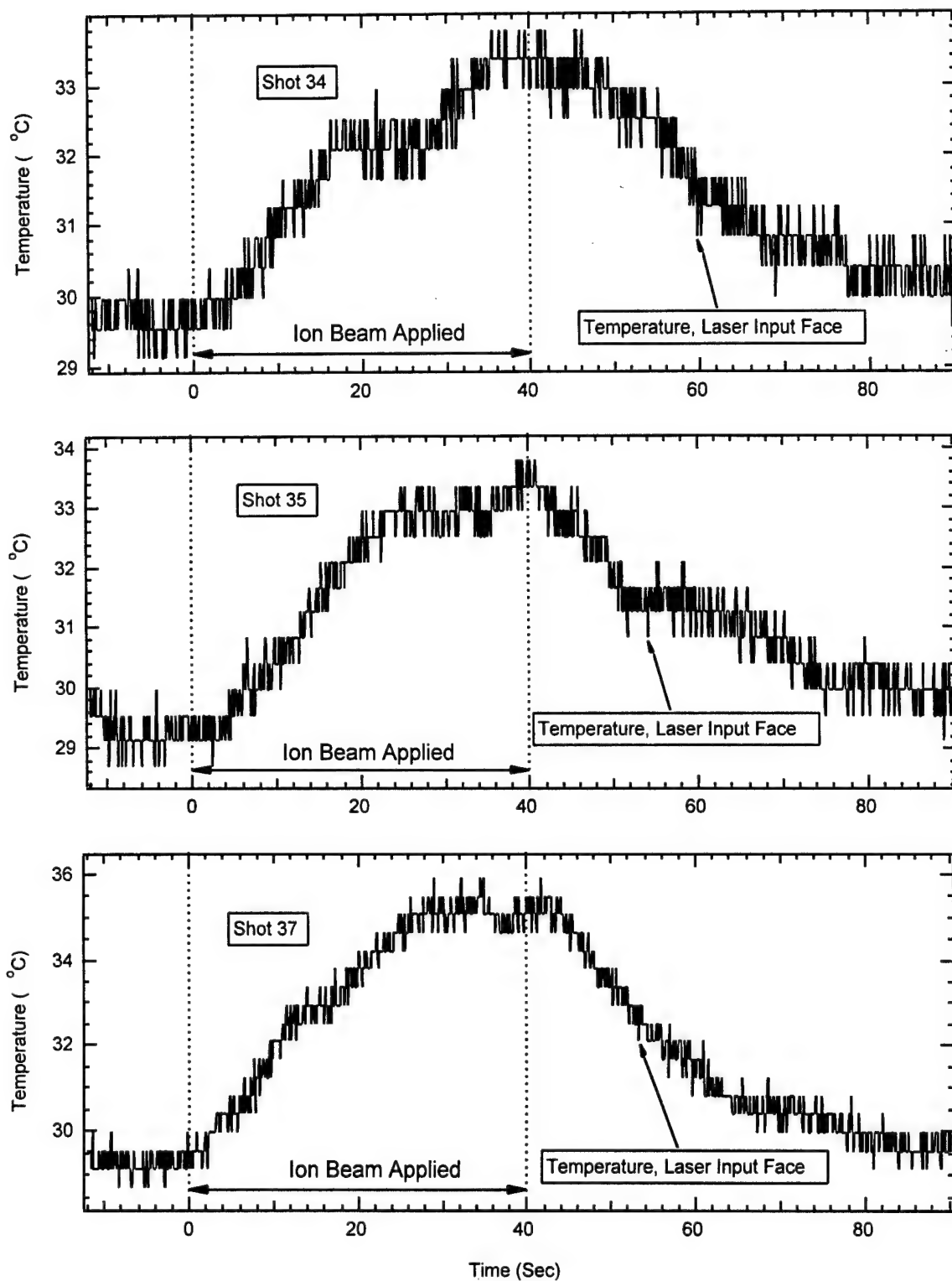


Figure A-34. Temperature plots corresponding to the runs shown in Figures A-30 through A-32. The temperature increased by 2 to 3°C.

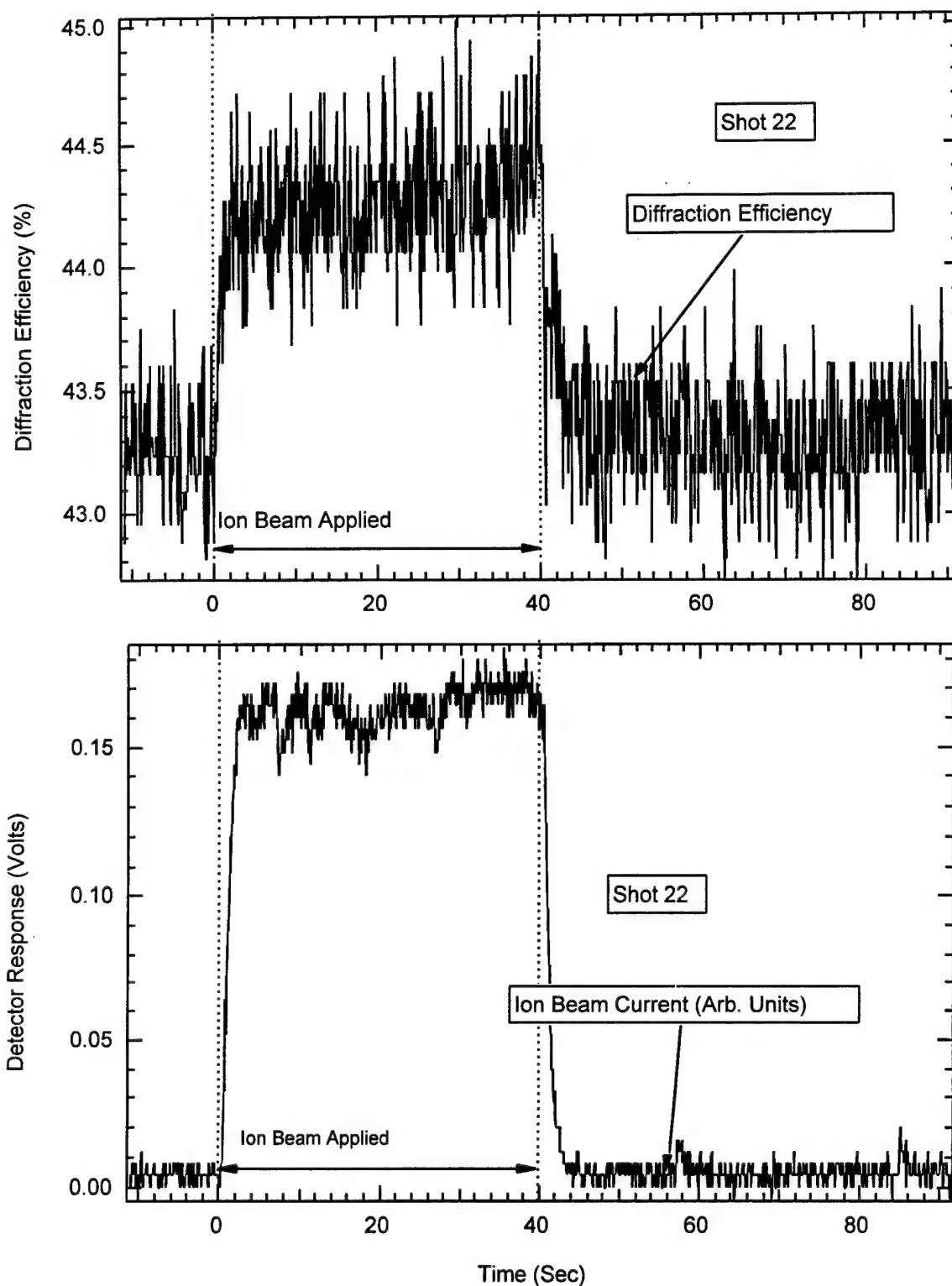


Figure A-35. Top part of figure shows absolute diffraction efficiency of InP modulator. Lower part of figure shows the ion beam current in arbitrary units as a function of time. Measuring from the top left corner of the modulator the irradiation position is $x=10.5$, $y=0.5$.

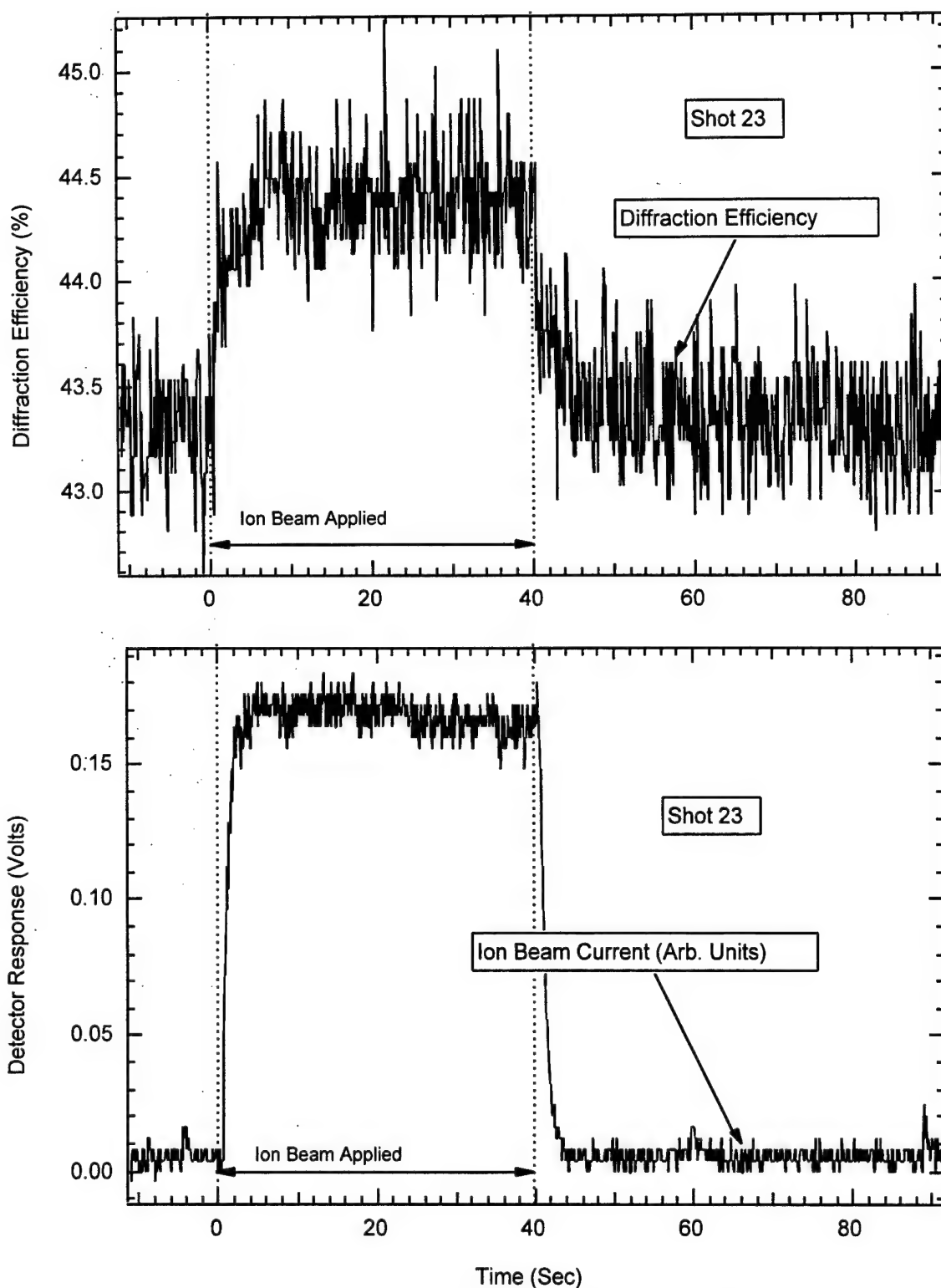


Figure A-36. Top part of figure shows absolute diffraction efficiency of InP modulator. Lower part of figure shows the ion beam current in arbitrary units as a function of time. Measuring from the top left corner of the modulator the irradiation position is $x=8.5$, $y=0.5$.

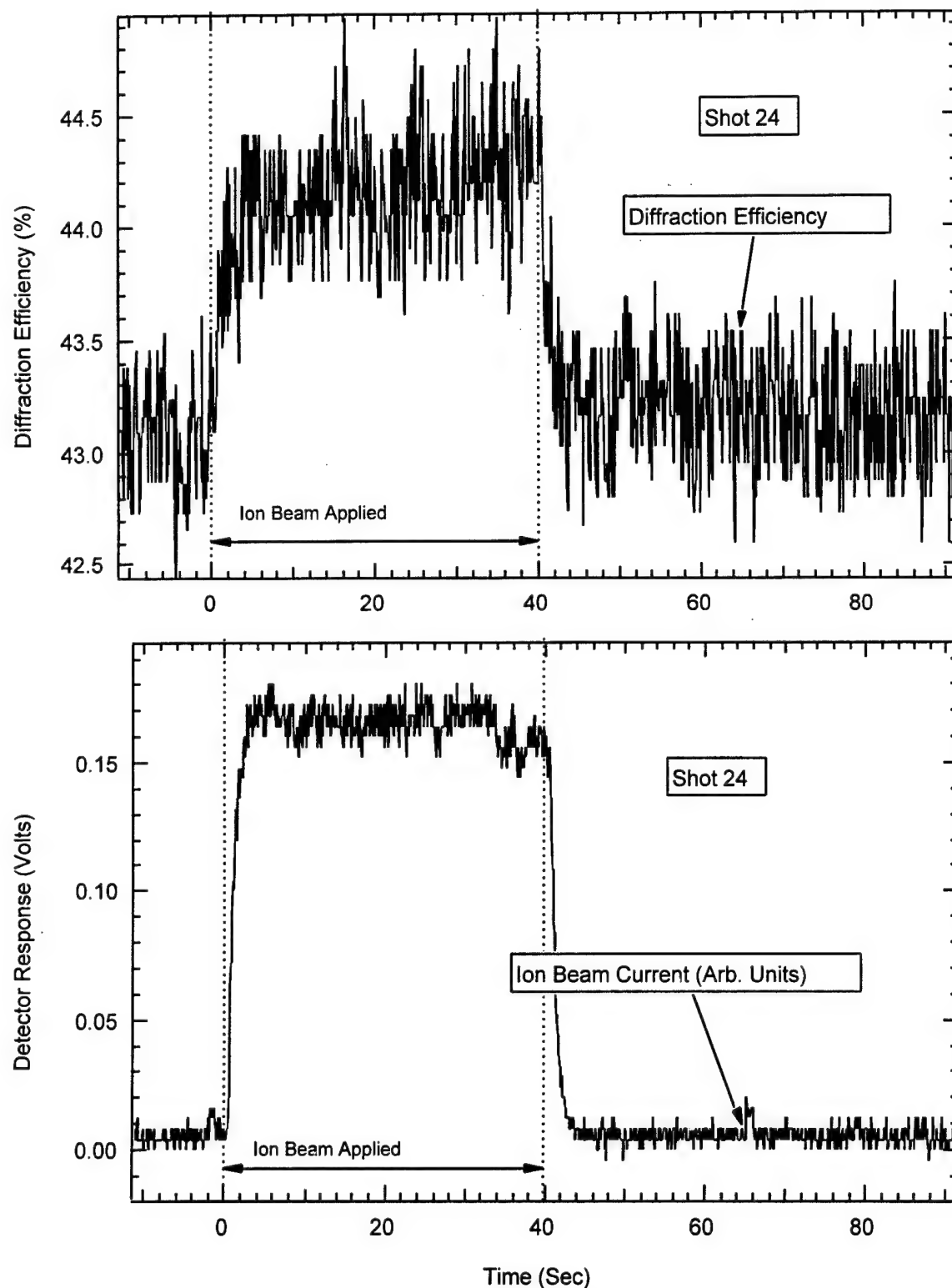


Figure A-37. Top part of figure shows absolute diffraction efficiency of InP modulator. Lower part of figure shows the ion beam current in arbitrary units as a function of time. Measuring from the top left corner of the modulator the irradiation position is $x=6.5$, $y=0.5$.

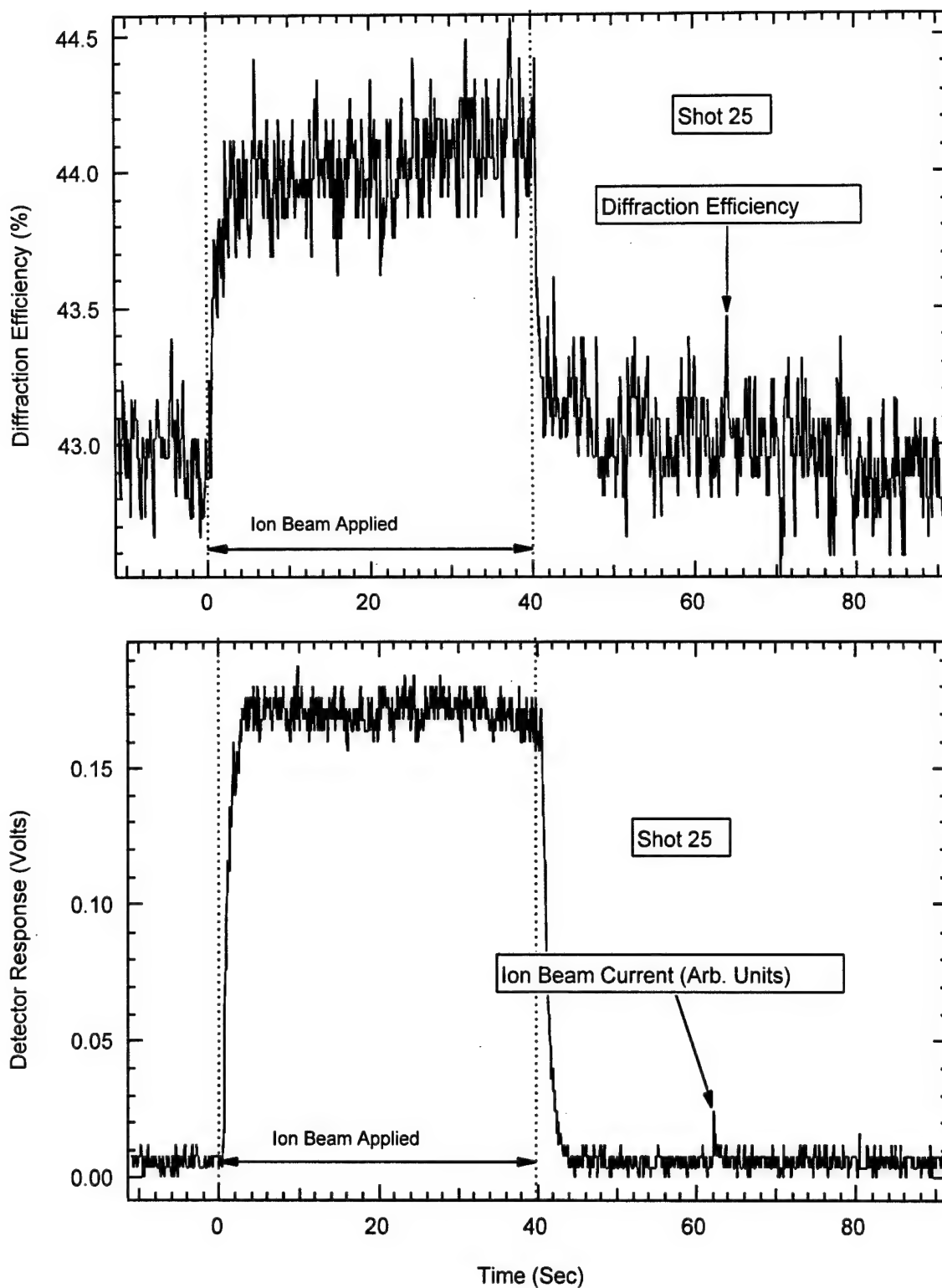


Figure A-38. Top part of figure shows absolute diffraction efficiency of InP modulator. Lower part of figure shows the ion beam current in arbitrary units as a function of time. Measuring from the top left corner of the modulator the irradiation position is $x=4.5$, $y=0.5$.

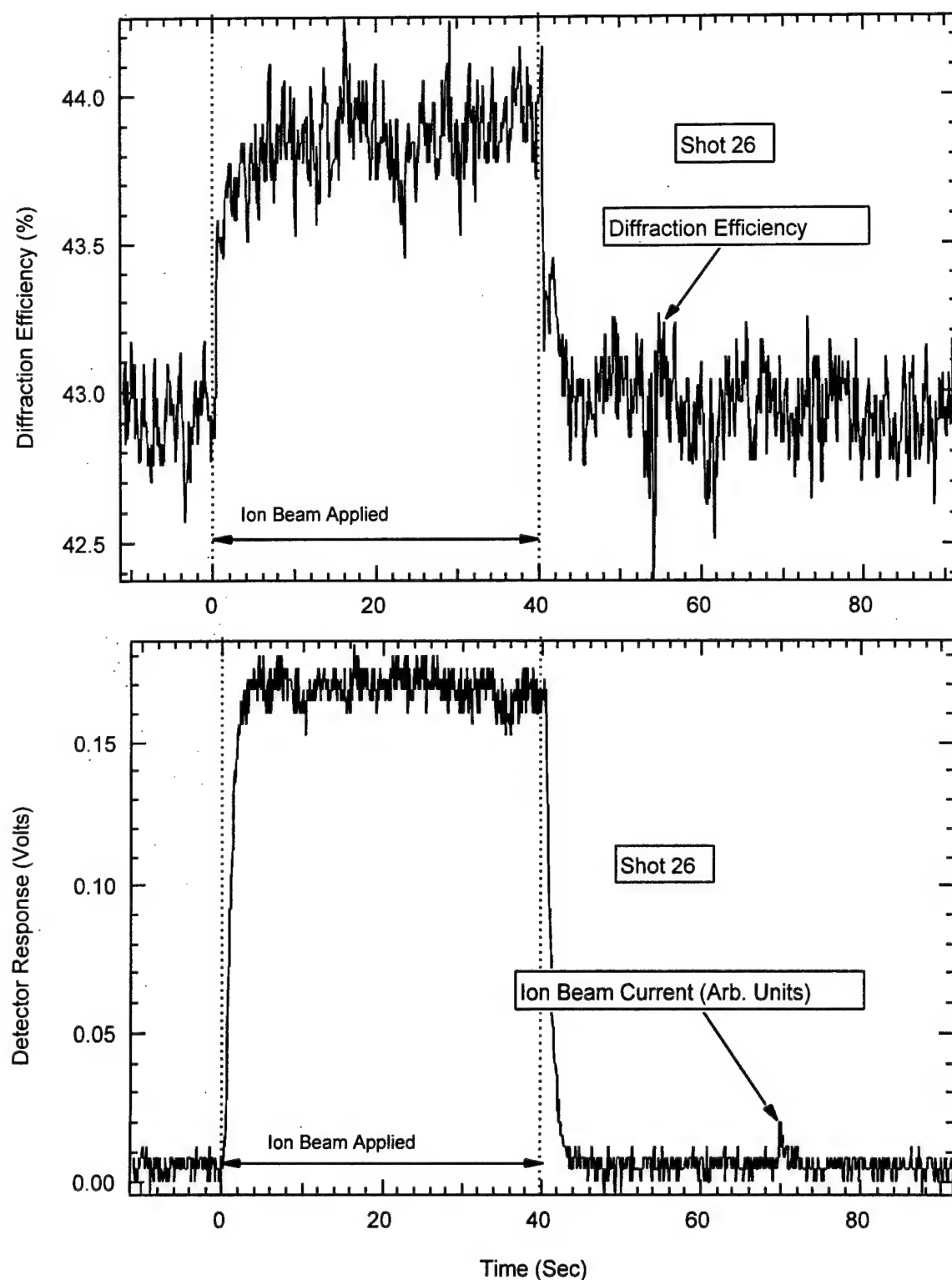


Figure A-39. Top part of figure shows absolute diffraction efficiency of InP modulator. Lower part of figure shows the ion beam current in arbitrary units as a function of time. Measuring from the top left corner of the modulator the irradiation position is $x=2.5$, $y=0.5$.

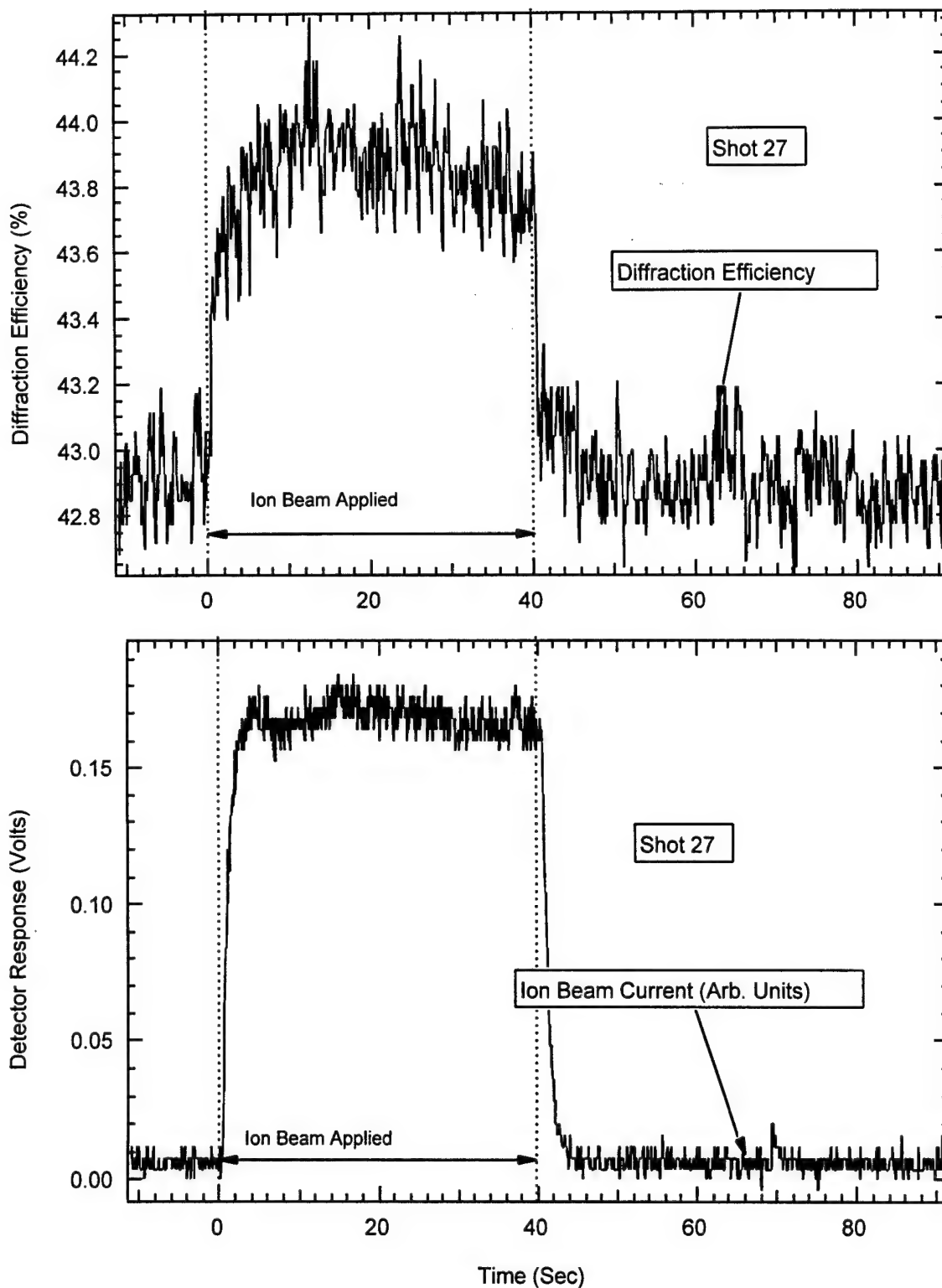


Figure A-40. Top part of figure shows absolute diffraction efficiency of InP modulator. Lower part of figure shows the ion beam current in arbitrary units as a function of time. Measuring from the top left corner of the modulator the irradiation position is $x=0.5$, $y=0.5$.

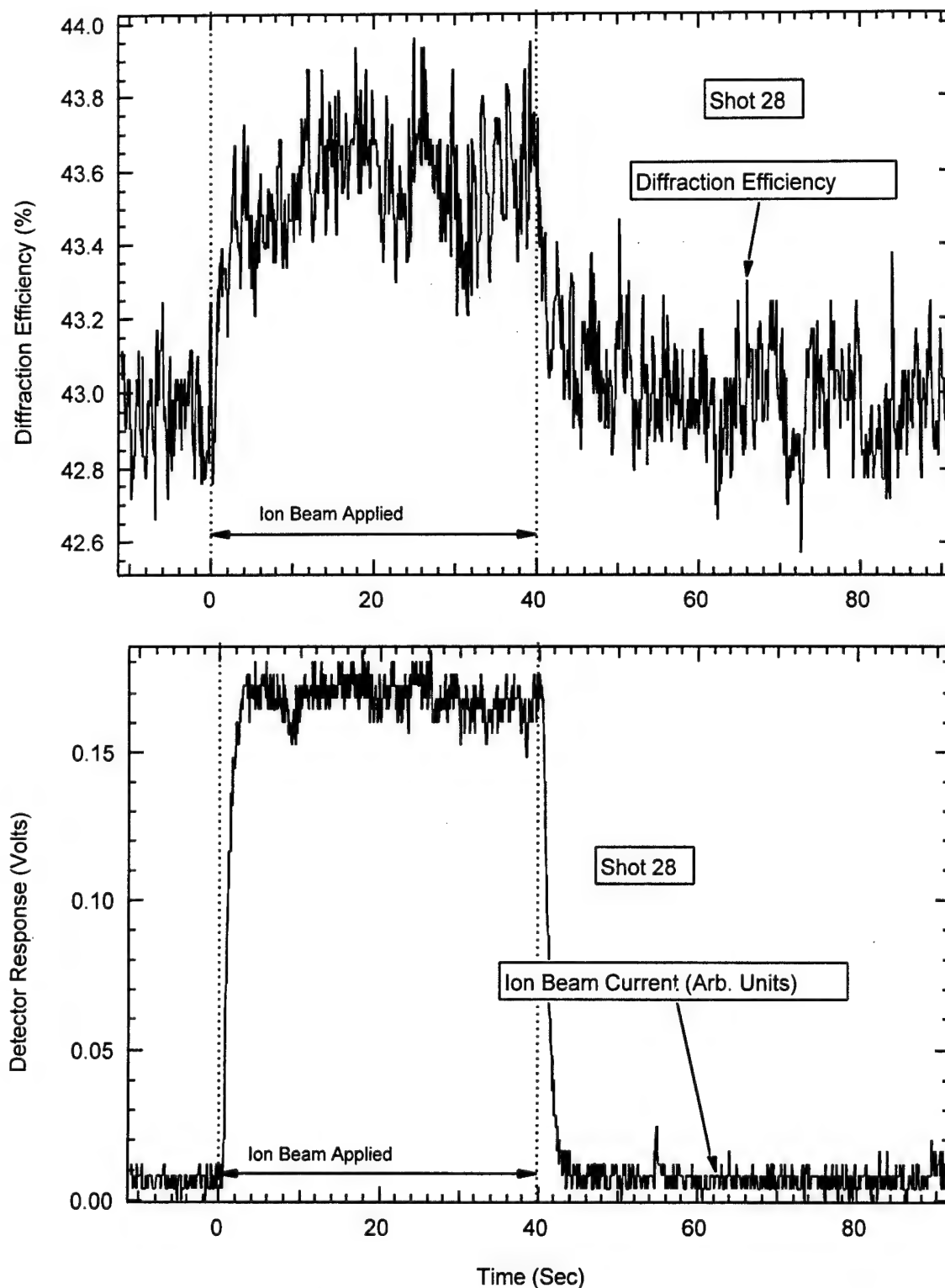


Figure A-41. Top part of figure shows absolute diffraction efficiency of InP modulator. Lower part of figure shows the ion beam current in arbitrary units as a function of time. Measuring from the top left corner of the modulator the irradiation position is $x=0.5$, $y=2.5$.

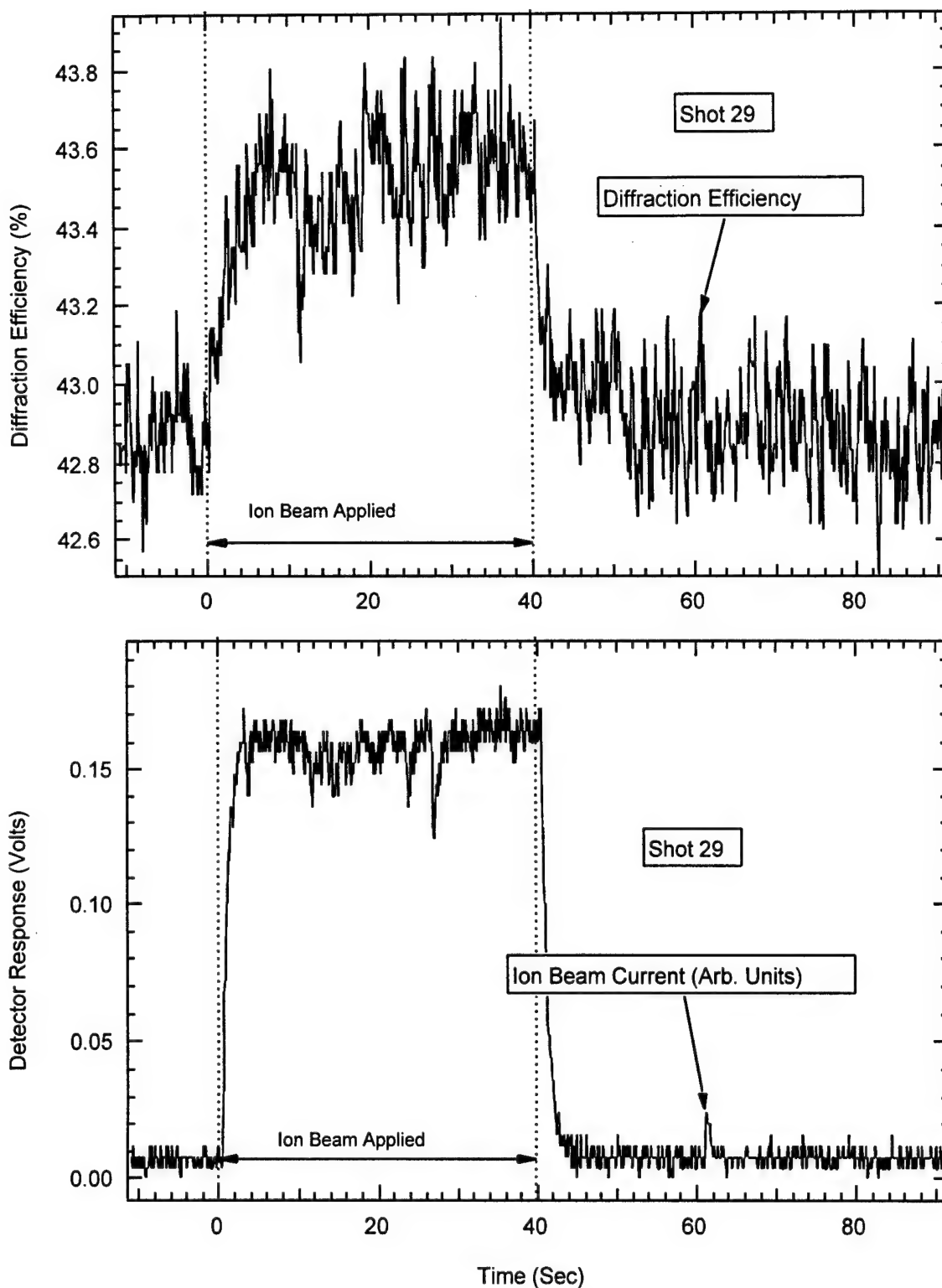


Figure A-42. Top part of figure shows absolute diffraction efficiency of InP modulator. Lower part of figure shows the ion beam current in arbitrary units as a function of time. Measuring from the top left corner of the modulator the irradiation position is $x=2.5$, $y=2.5$.

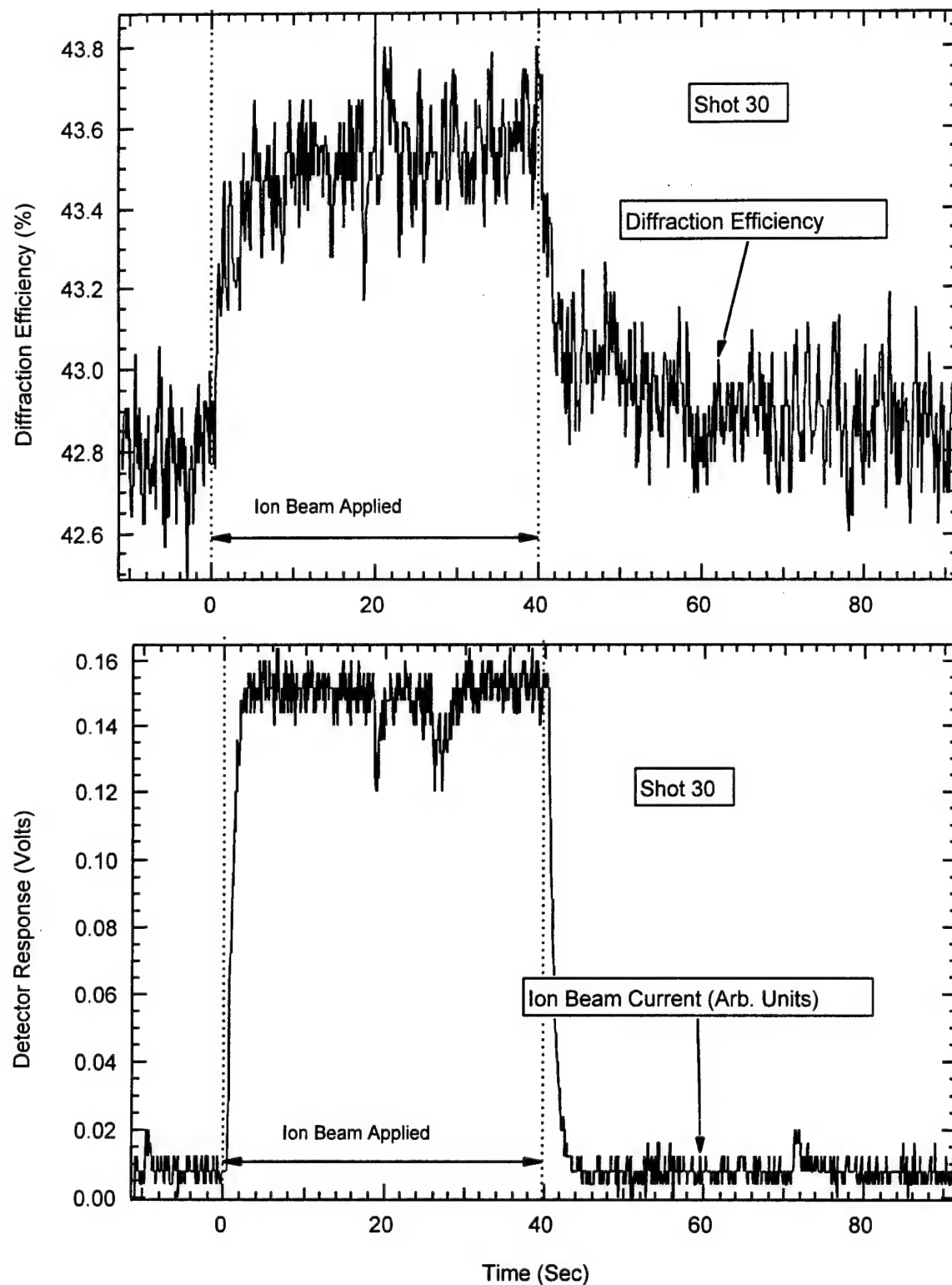


Figure A-43. Top part of figure shows absolute diffraction efficiency of InP modulator. Lower part of figure shows the ion beam current in arbitrary units as a function of time. Measuring from the top left corner of the modulator the irradiation position is $x=4.5$, $y=2.5$.

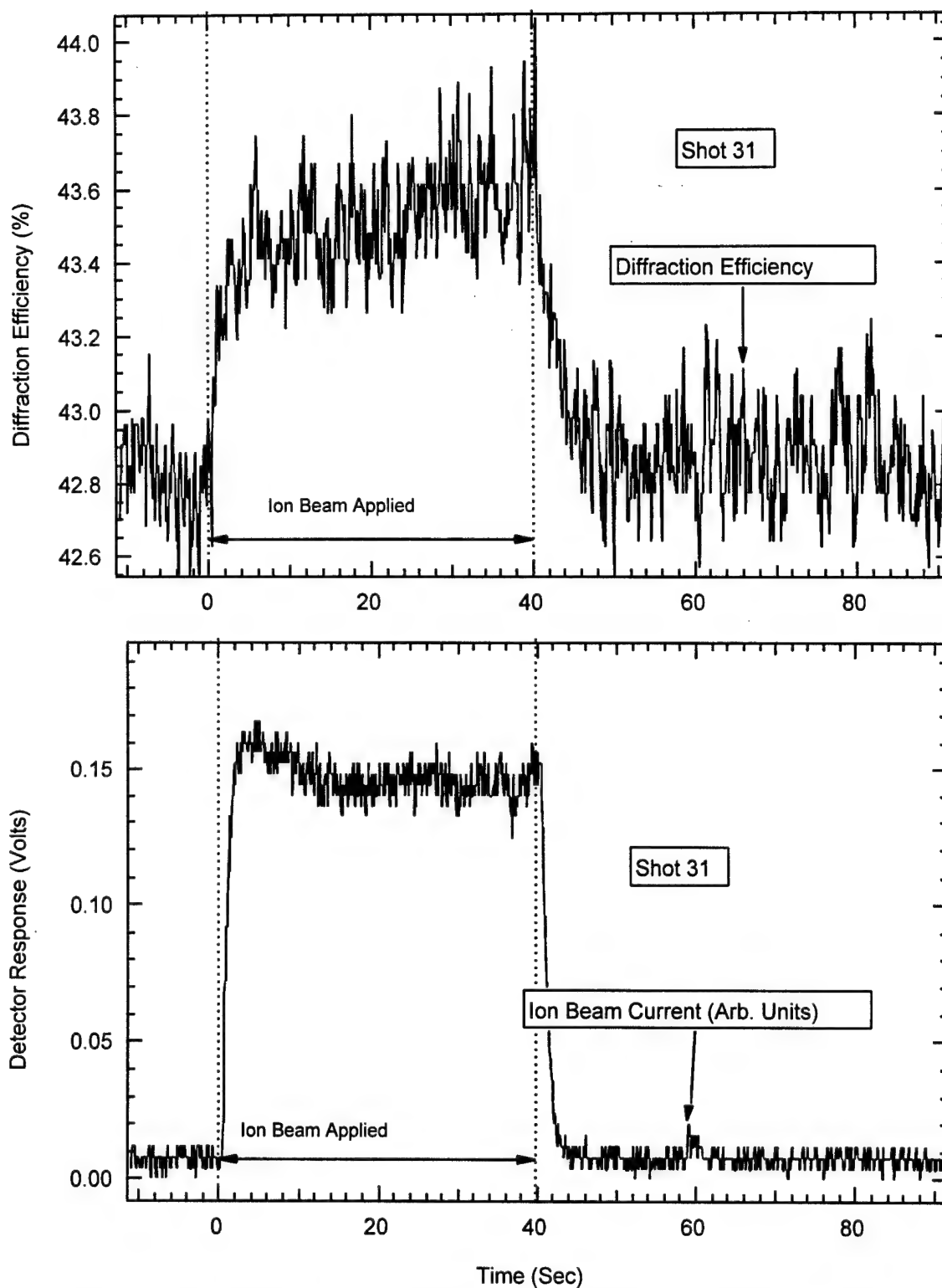


Figure A-44. Top part of figure shows absolute diffraction efficiency of InP modulator. Lower part of figure shows the ion beam current in arbitrary units as a function of time. Measuring from the top left corner of the modulator the irradiation position is $x=6.5$, $y=2.5$.

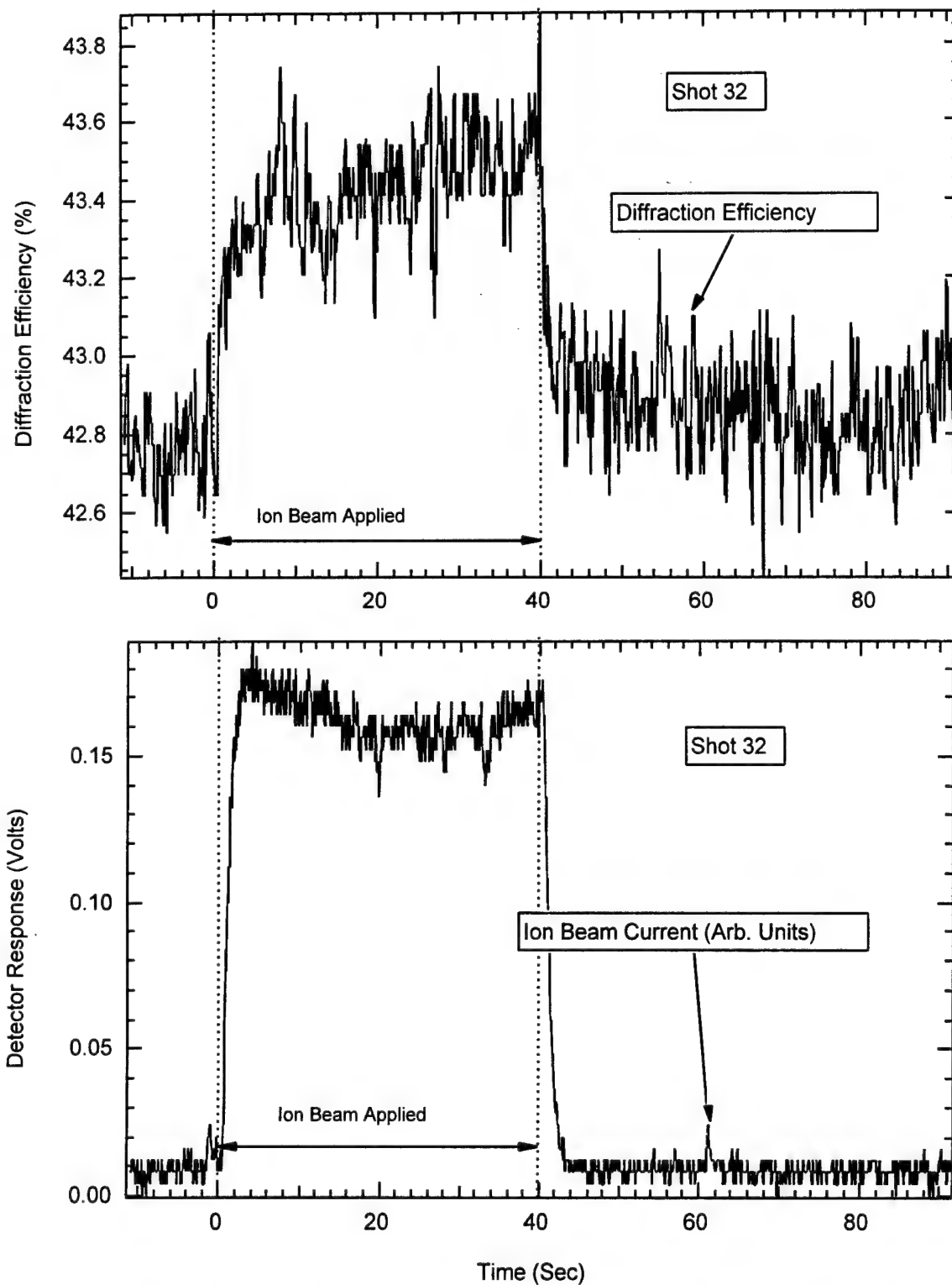


Figure A-45. Top part of figure shows absolute diffraction efficiency of InP modulator. Lower part of figure shows the ion beam current in arbitrary units as a function of time. Measuring from the top left corner of the modulator the irradiation position is $x=8.5$, $y=2.5$.

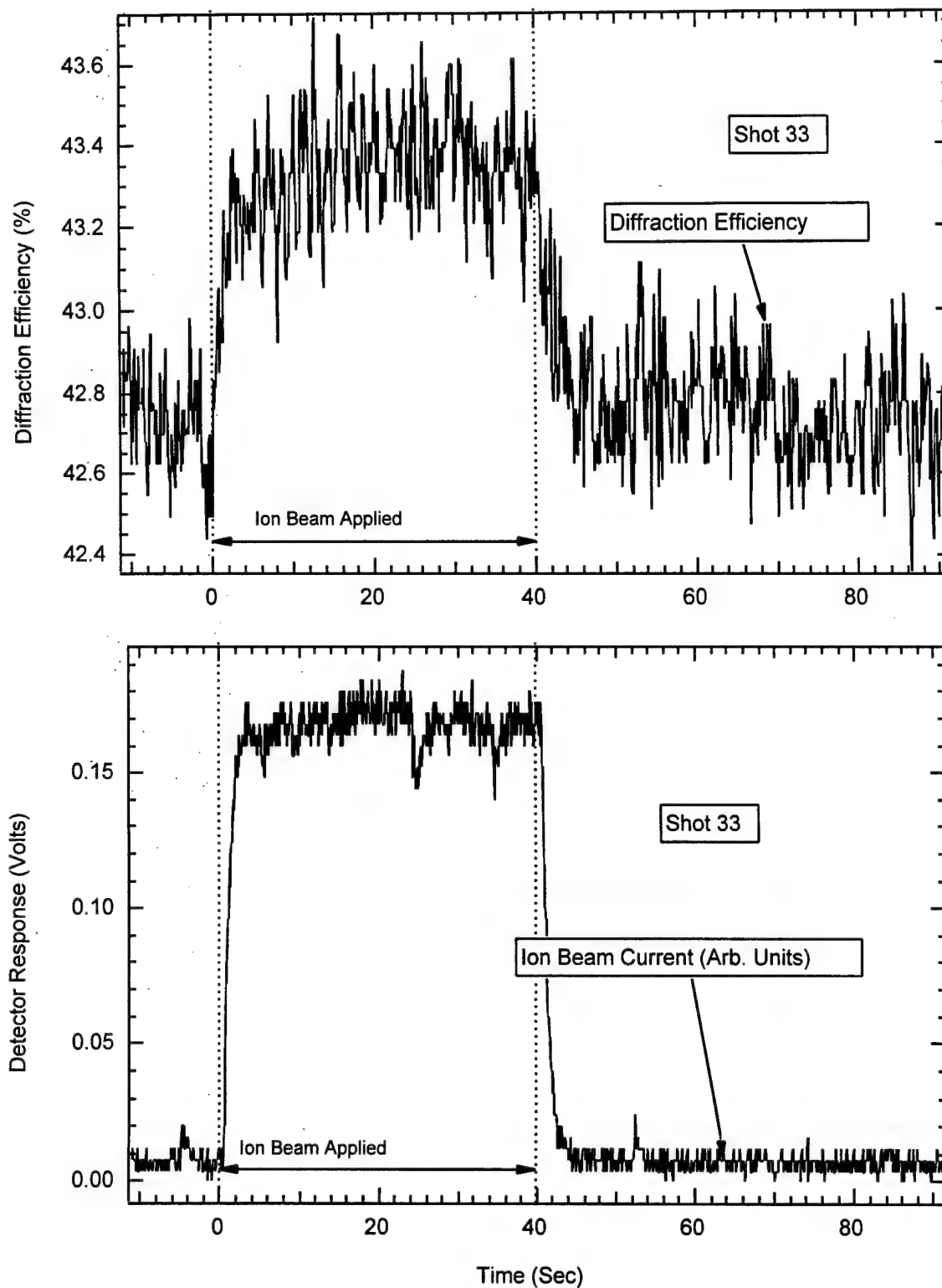


Figure A-46. Top part of figure shows absolute diffraction efficiency of InP modulator. Lower part of figure shows the ion beam current in arbitrary units as a function of time. Measuring from the top left corner of the modulator the irradiation position is $x=10.5$, $y=2.5$.

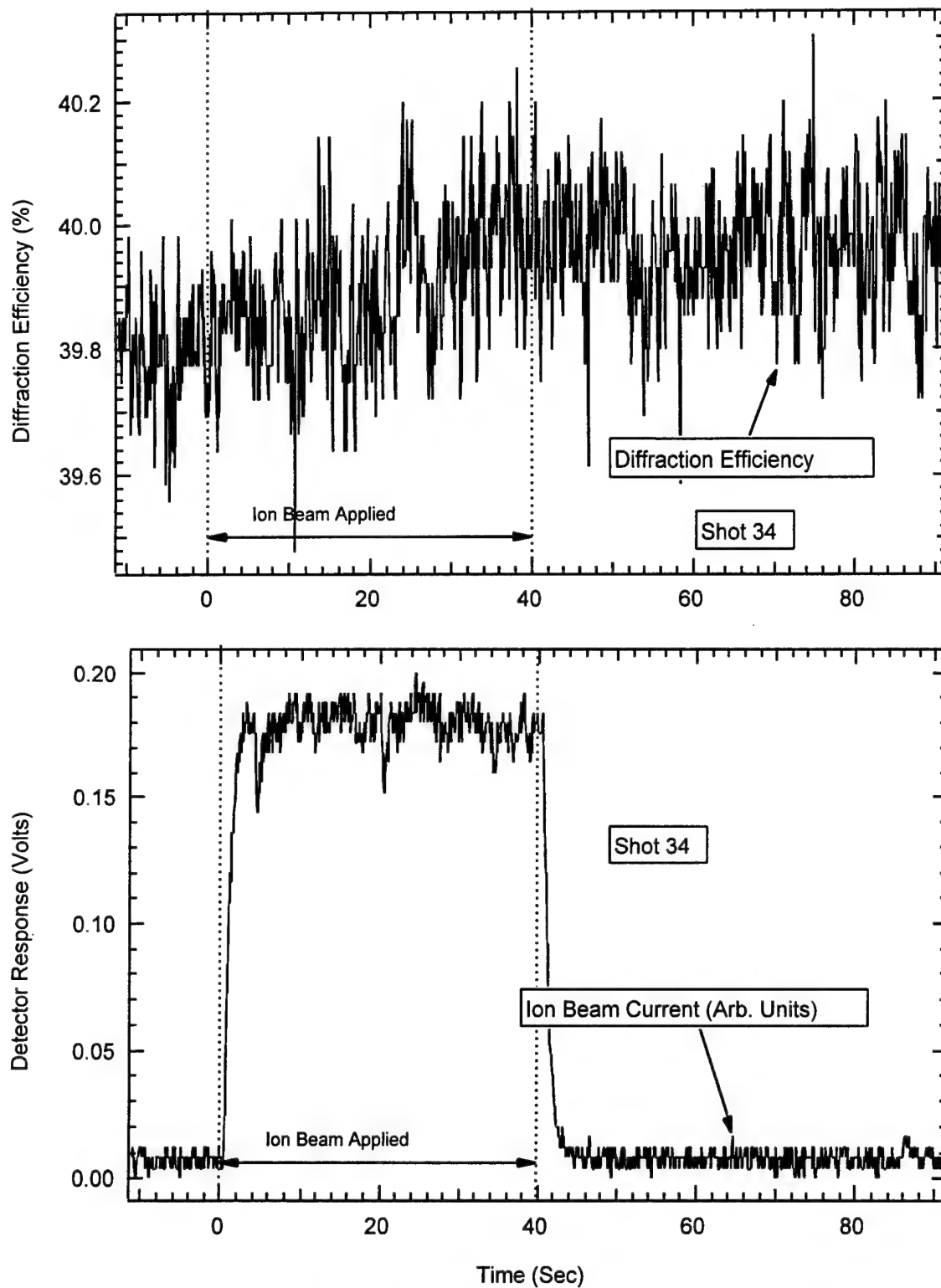


Figure A-47. Top part of figure shows absolute diffraction efficiency of InP modulator. Lower part of figure shows the ion beam current in arbitrary units as a function of time. Measuring from the top left corner of the modulator the irradiation position is $x=12.5$, $y=2.5$.

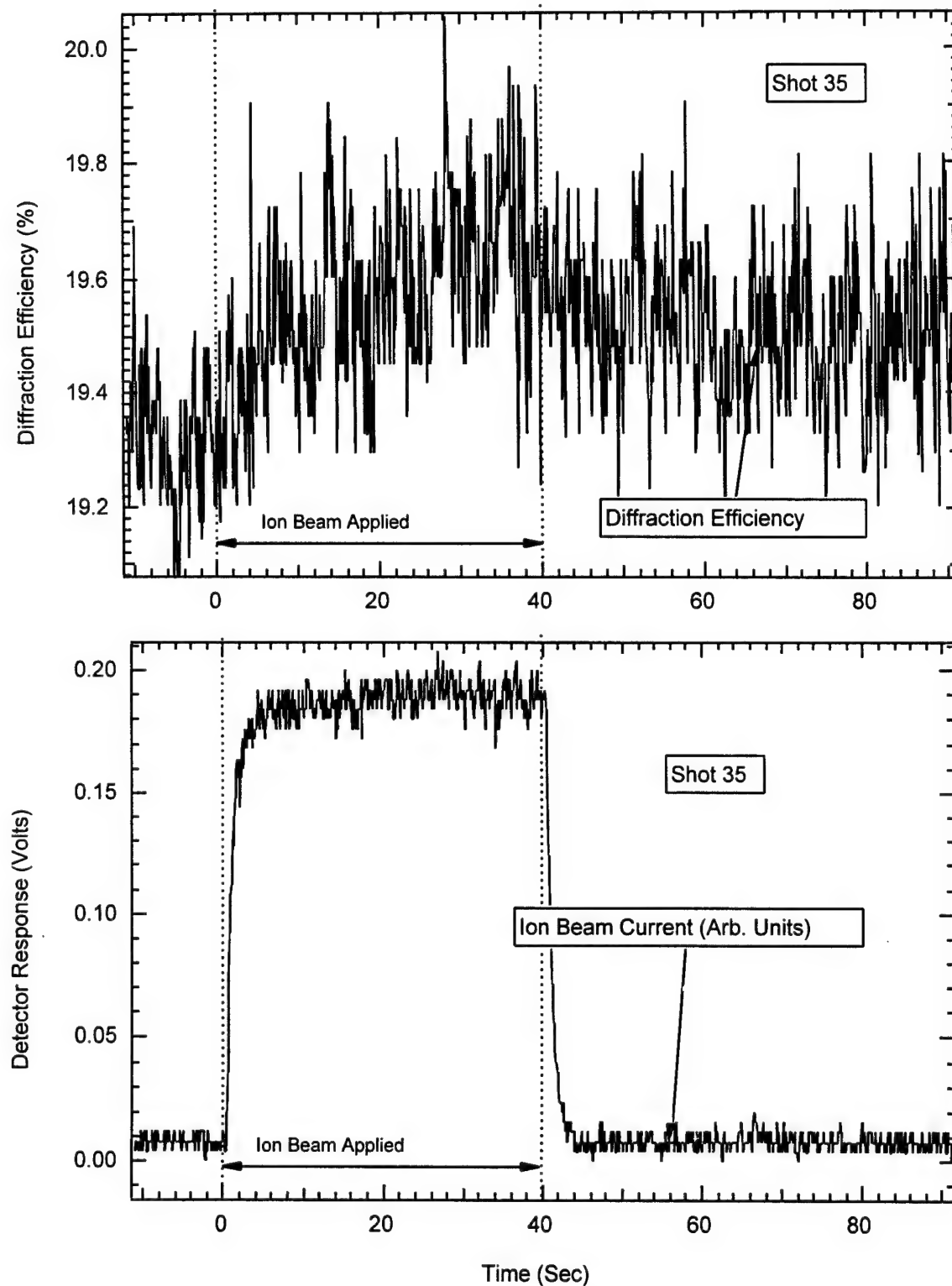


Figure A-48. Top part of figure shows absolute diffraction efficiency of InP modulator. Lower part of figure shows the ion beam current in arbitrary units as a function of time. Measuring from the top left corner of the modulator the irradiation position is $x=12.5$, $y=4.5$.

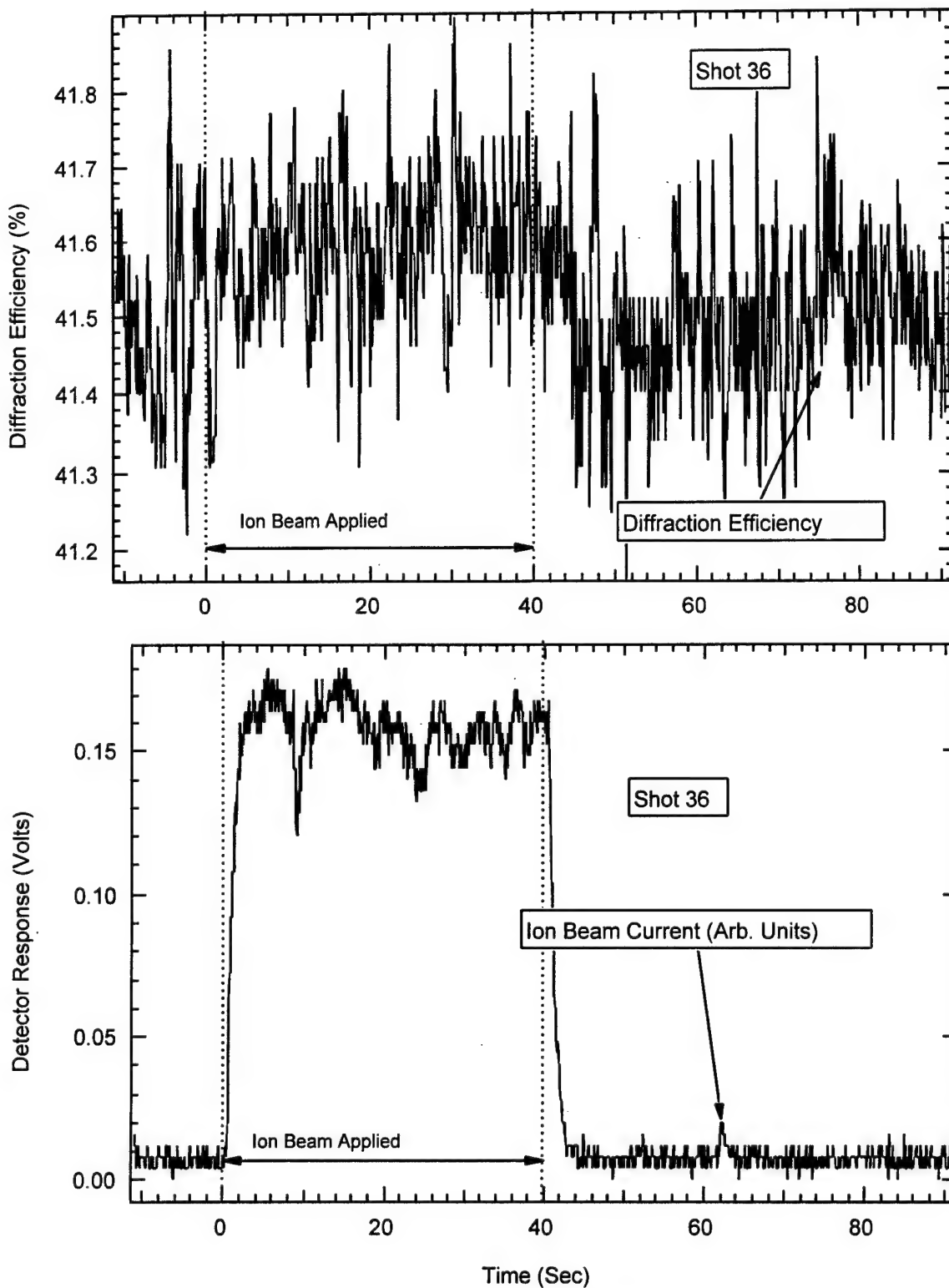


Figure A-49. Top part of figure shows absolute diffraction efficiency of InP modulator. Lower part of figure shows the ion beam current in arbitrary units as a function of time. Measuring from the top left corner of the modulator the irradiation position is $x=12.5$, $y=4.5$.

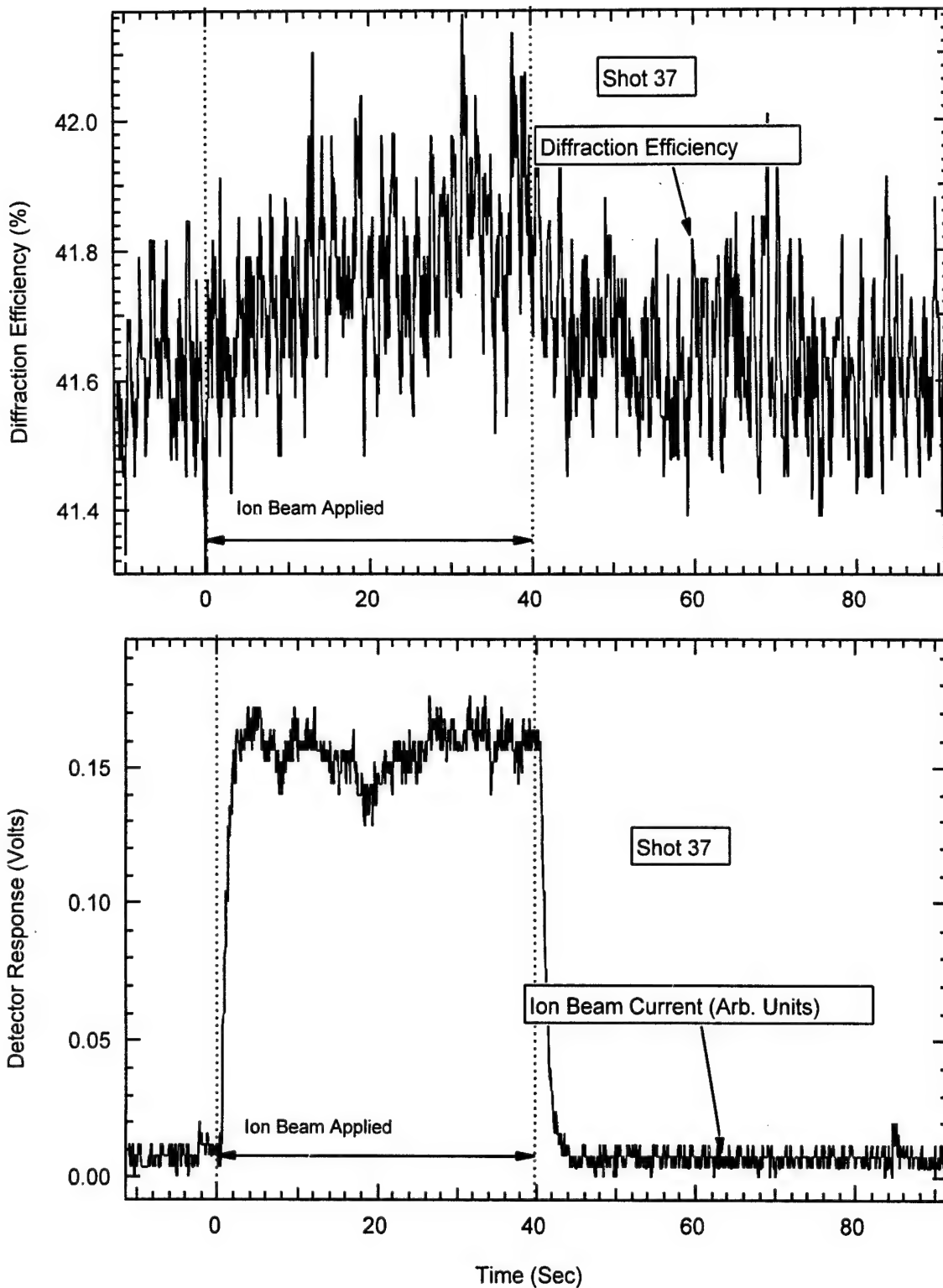


Figure A-50. Top part of figure shows absolute diffraction efficiency of InP modulator. Lower part of figure shows the ion beam current in arbitrary units as a function of time. Measuring from the top left corner of the modulator the irradiation position is $x=10.5$, $y=4.5$.

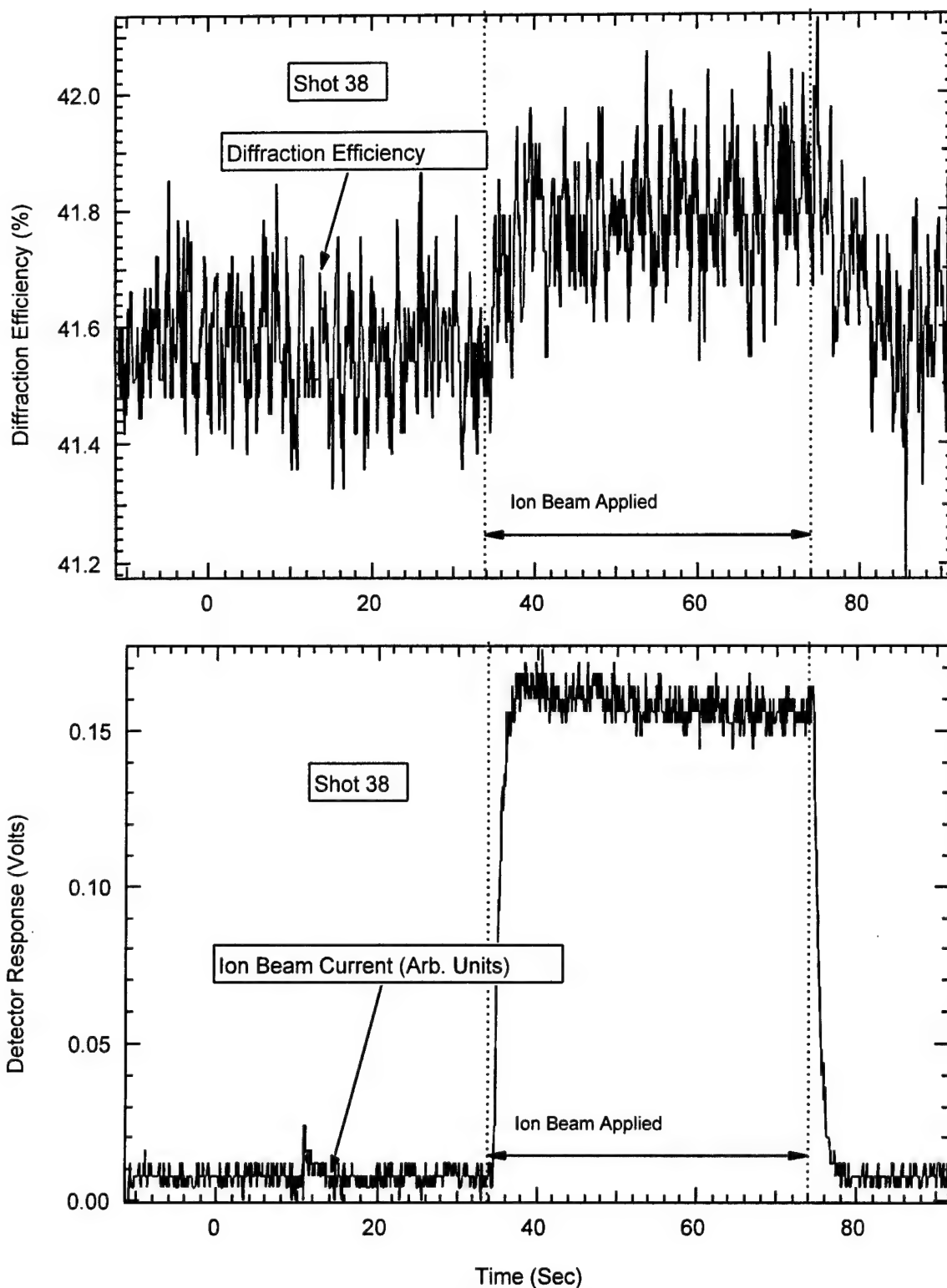


Figure A-51. Top part of figure shows absolute diffraction efficiency of InP modulator. Lower part of figure shows the ion beam current in arbitrary units as a function of time. Measuring from the top left corner of the modulator the irradiation position is $x=8.5$, $y=4.5$.

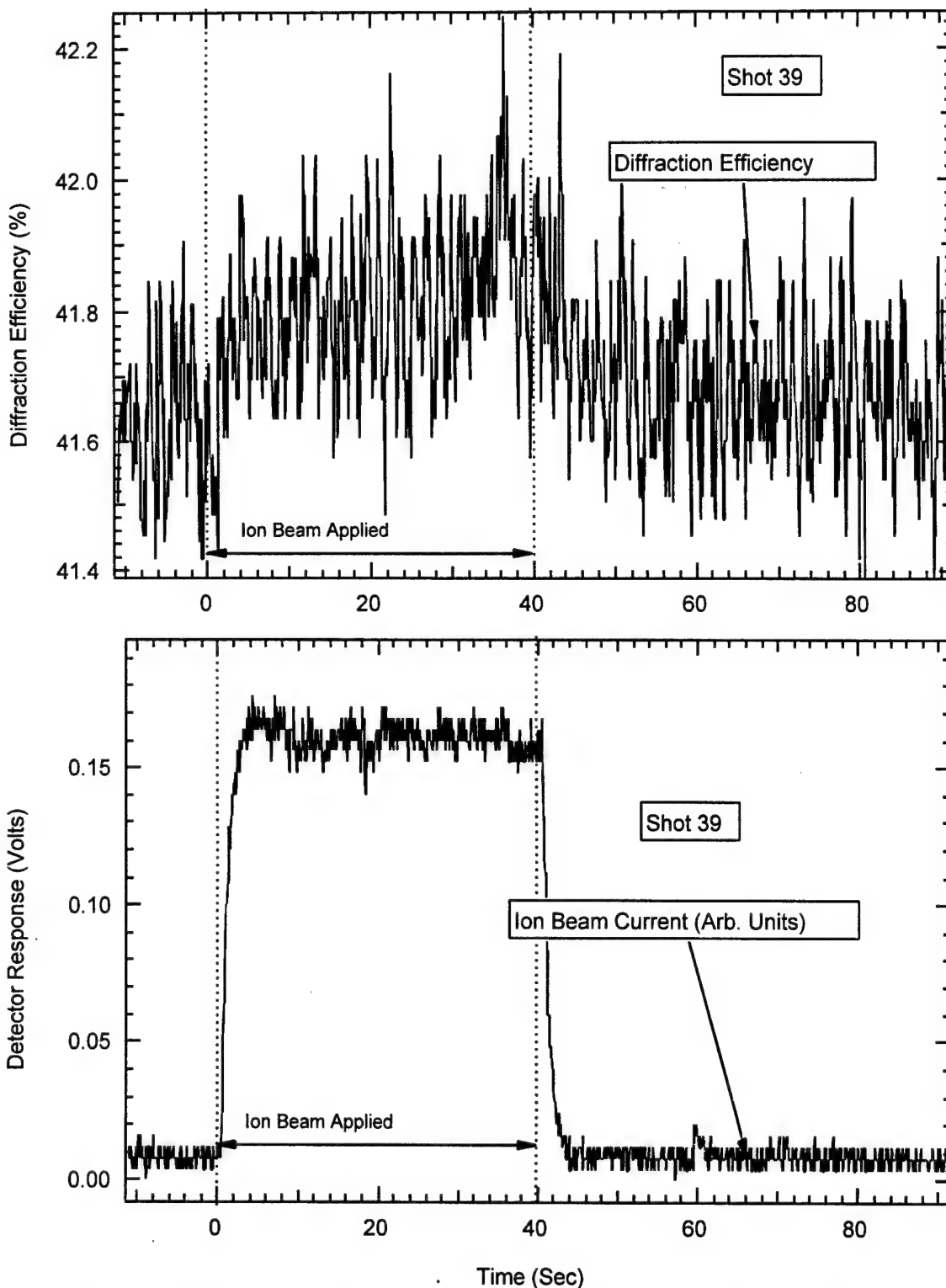


Figure A-52. Top part of figure shows absolute diffraction efficiency of InP modulator. Lower part of figure shows the ion beam current in arbitrary units as a function of time. Measuring from the top left corner of the modulator the irradiation position is $x=6.5$, $y=4.5$.

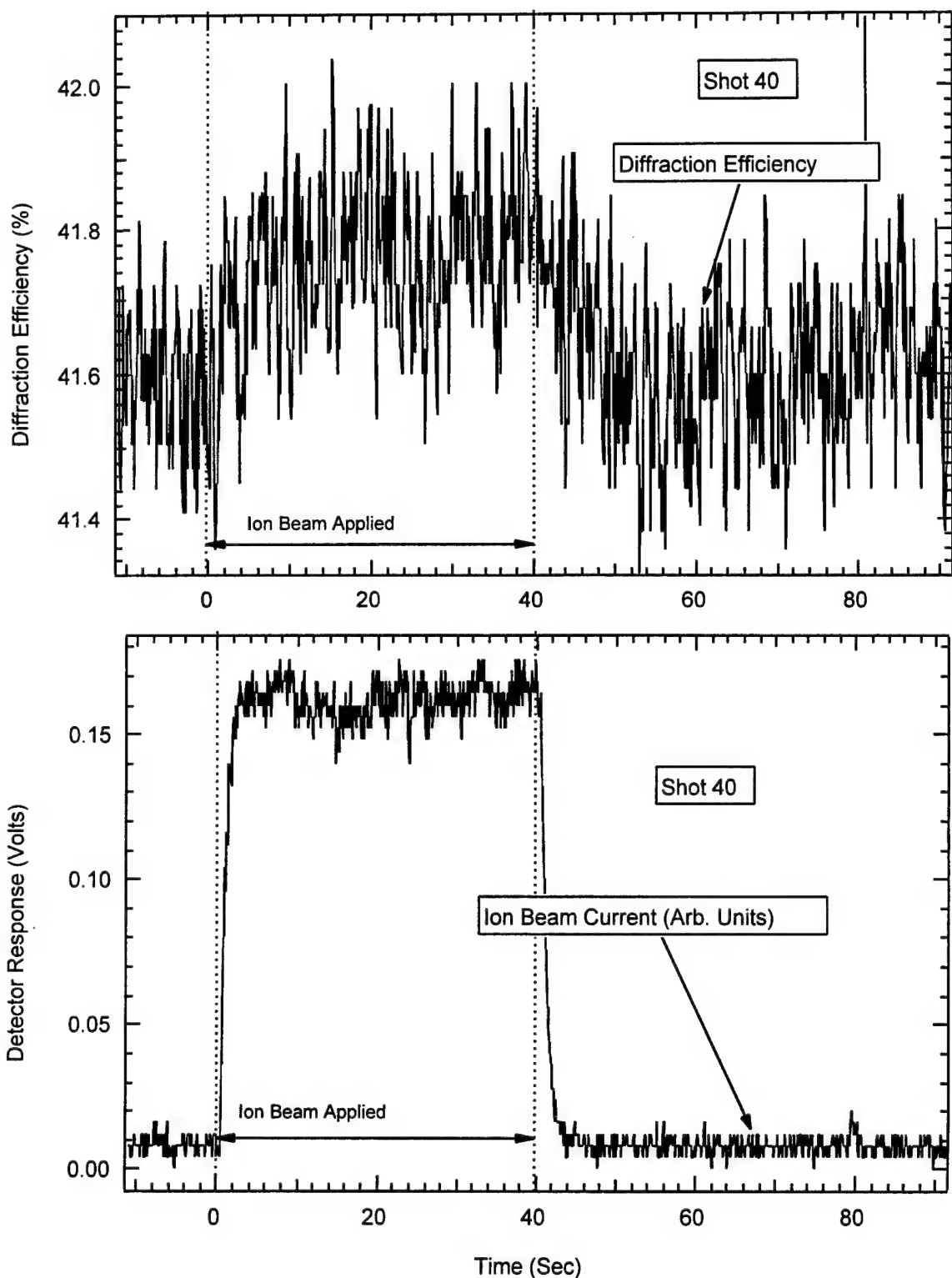


Figure A-53. Top part of figure shows absolute diffraction efficiency of InP modulator. Lower part of figure shows the ion beam current in arbitrary units as a function of time. Measuring from the top left corner of the modulator the irradiation position is $x=4.5$, $y=4.5$.

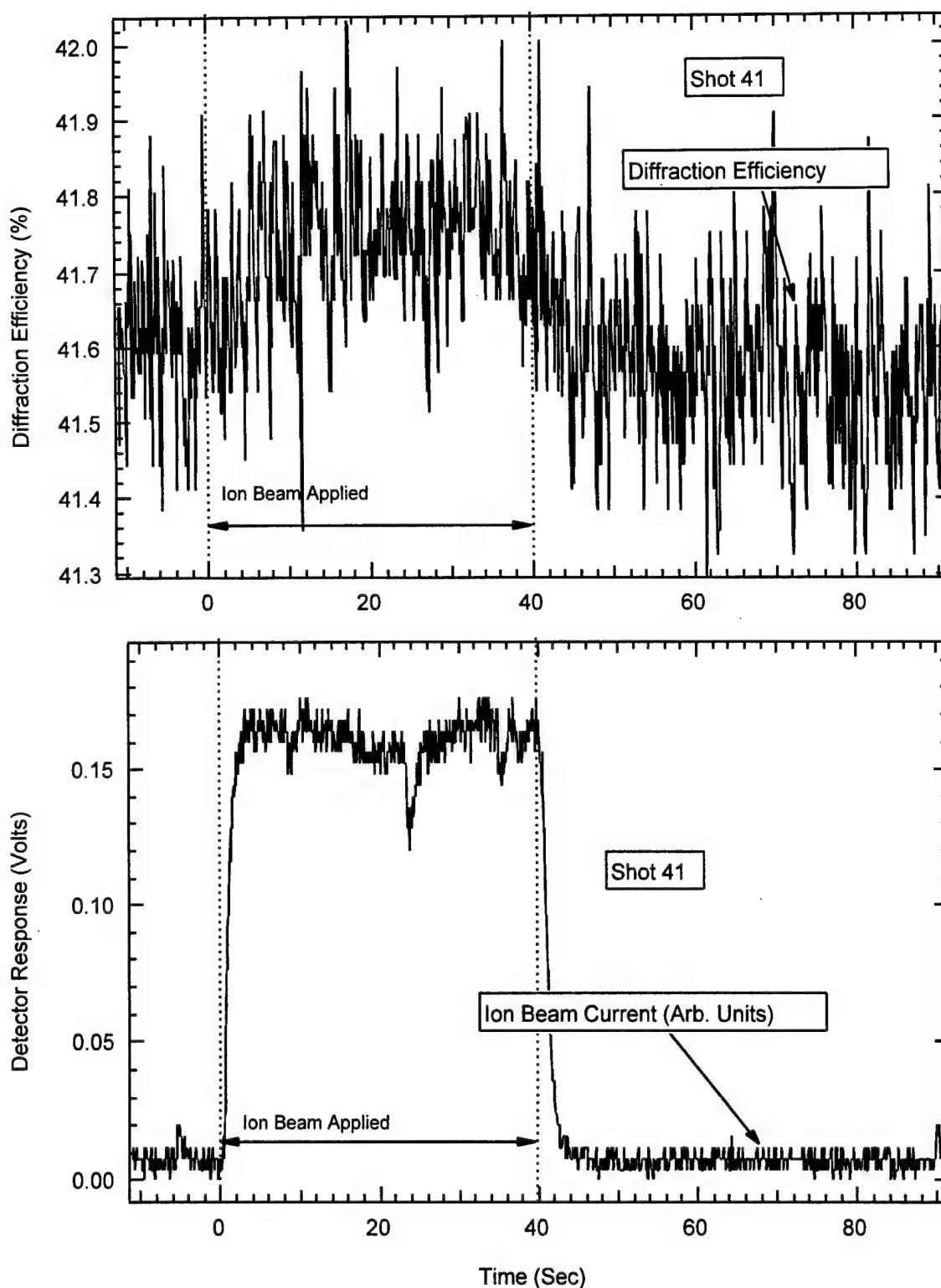


Figure A-54. Top part of figure shows absolute diffraction efficiency of InP modulator. Lower part of figure shows the ion beam current in arbitrary units as a function of time. Measuring from the top left corner of the modulator the irradiation position is $x=2.5$, $y=4.5$.

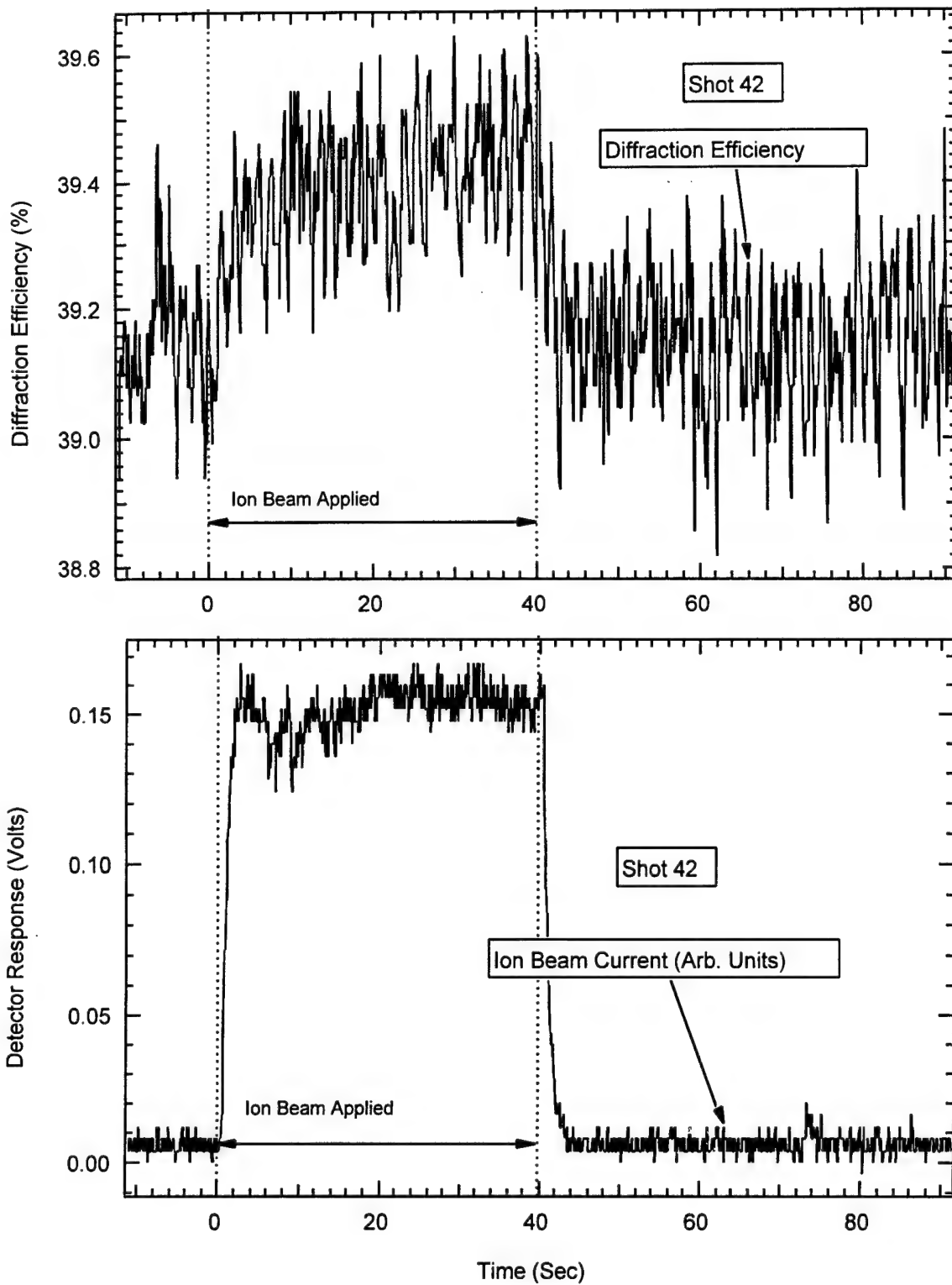


Figure A-55. Ion beam irradiation of center of transducer. AO-cell response similar to ion beam irradiation of crystal facet.

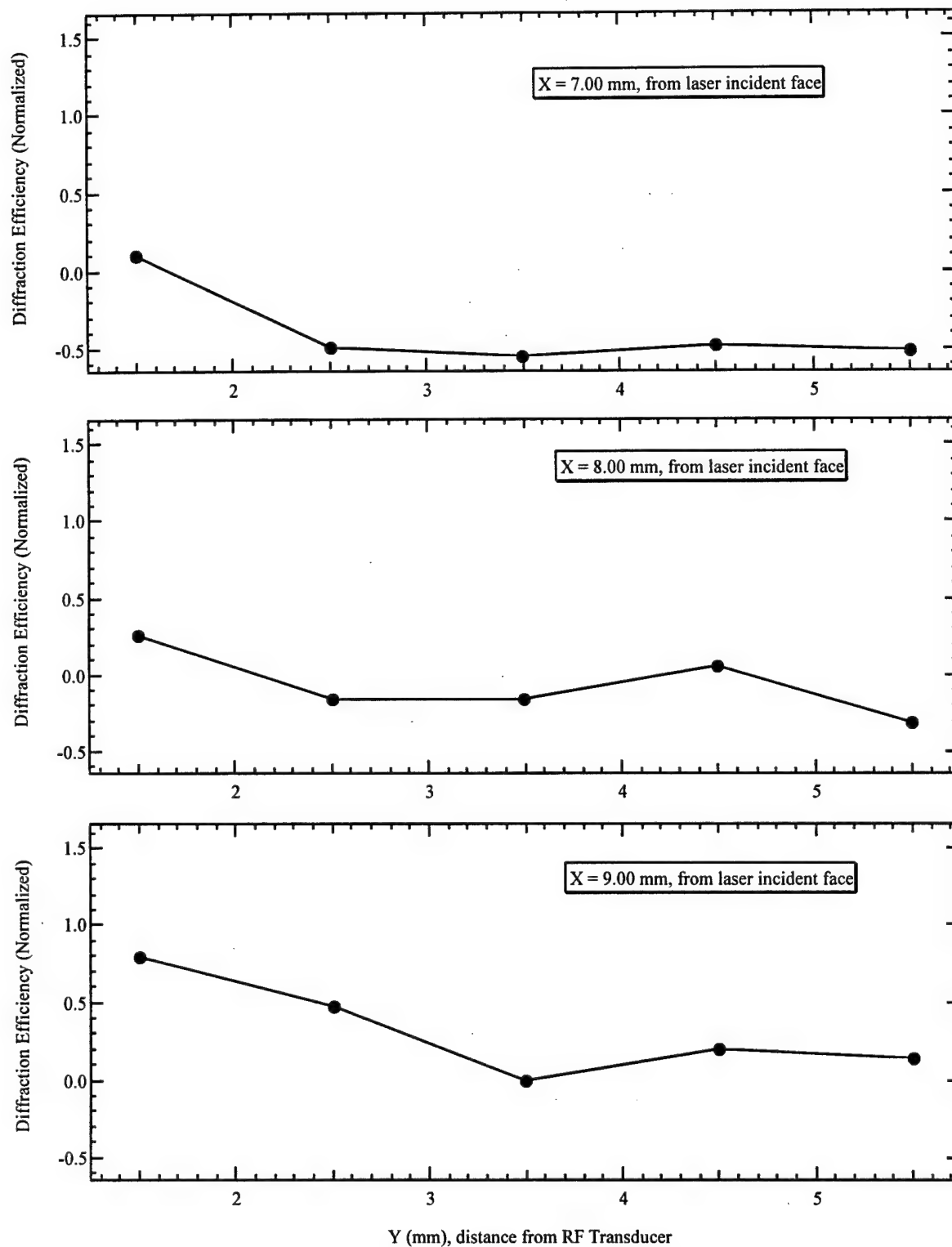


Figure A-56. Summary of diffraction efficiency change as a function of distance from Transducer for position $x=7, 8$ and 9mm .

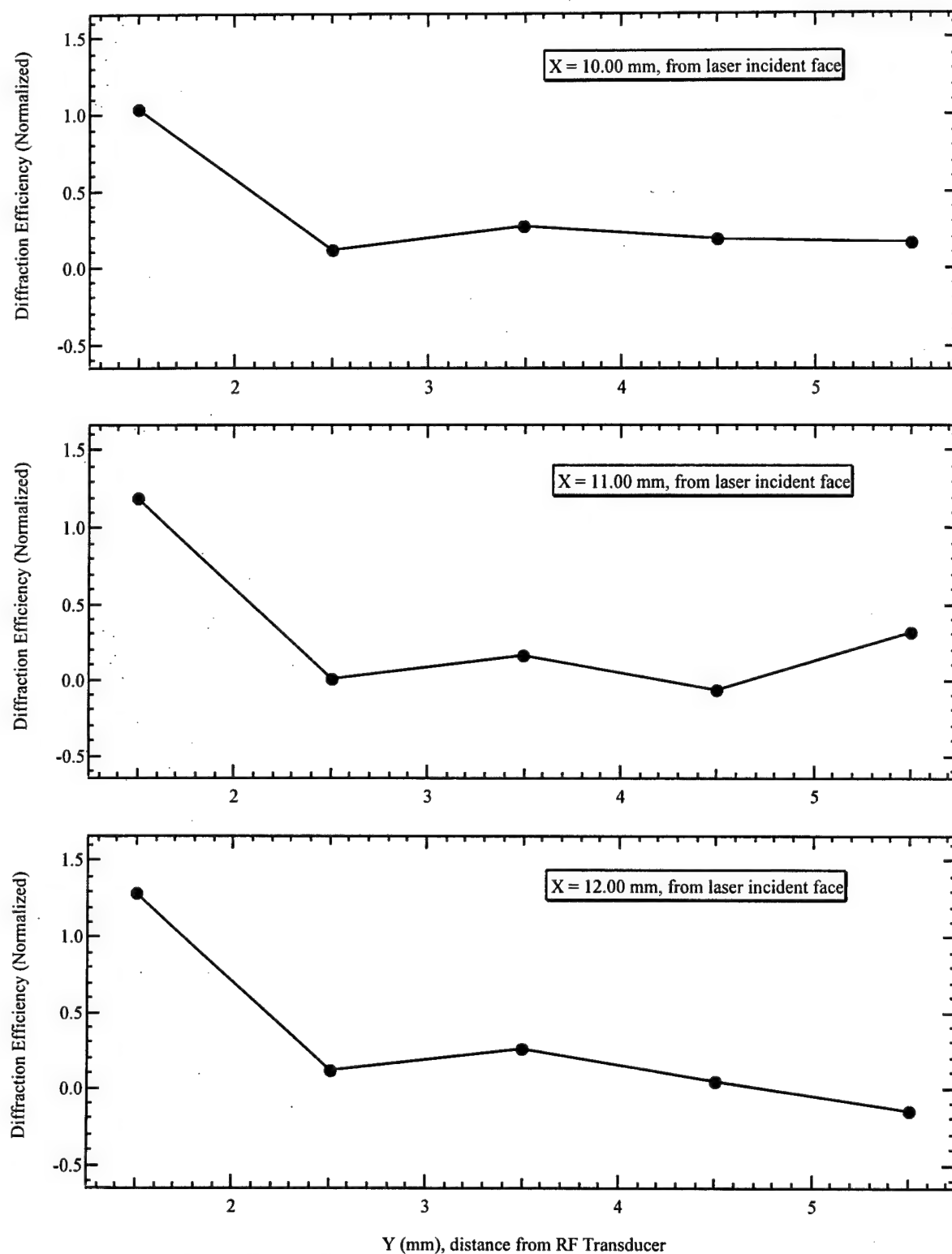


Figure A-57. Summary of diffraction efficiency change as a function of distance from Transducer for position x=10, 11 and 12mm.

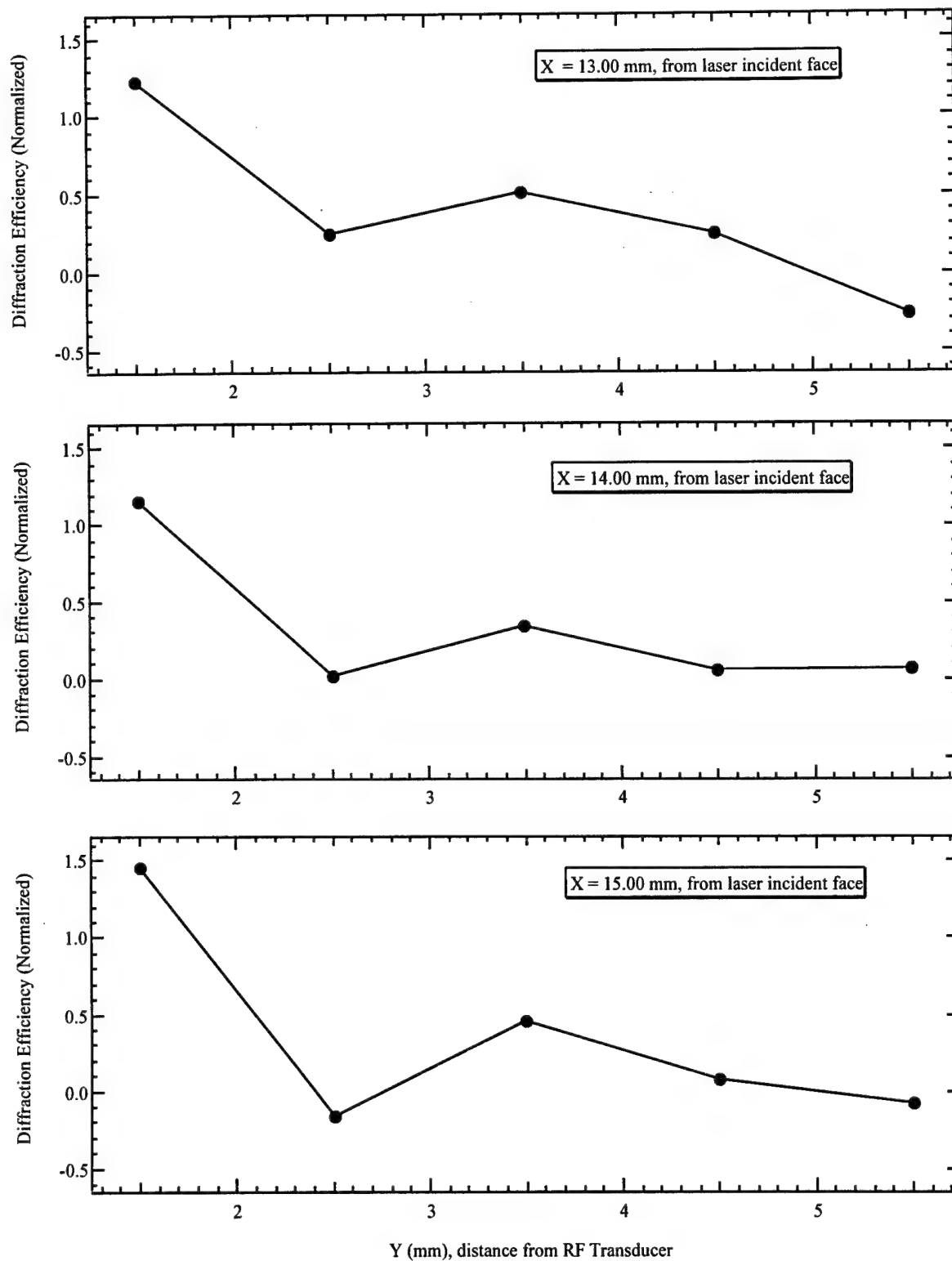


Figure A-58. Summary of diffraction efficiency change as a function of distance from Transducer for position $x=13, 14$ and 15mm .

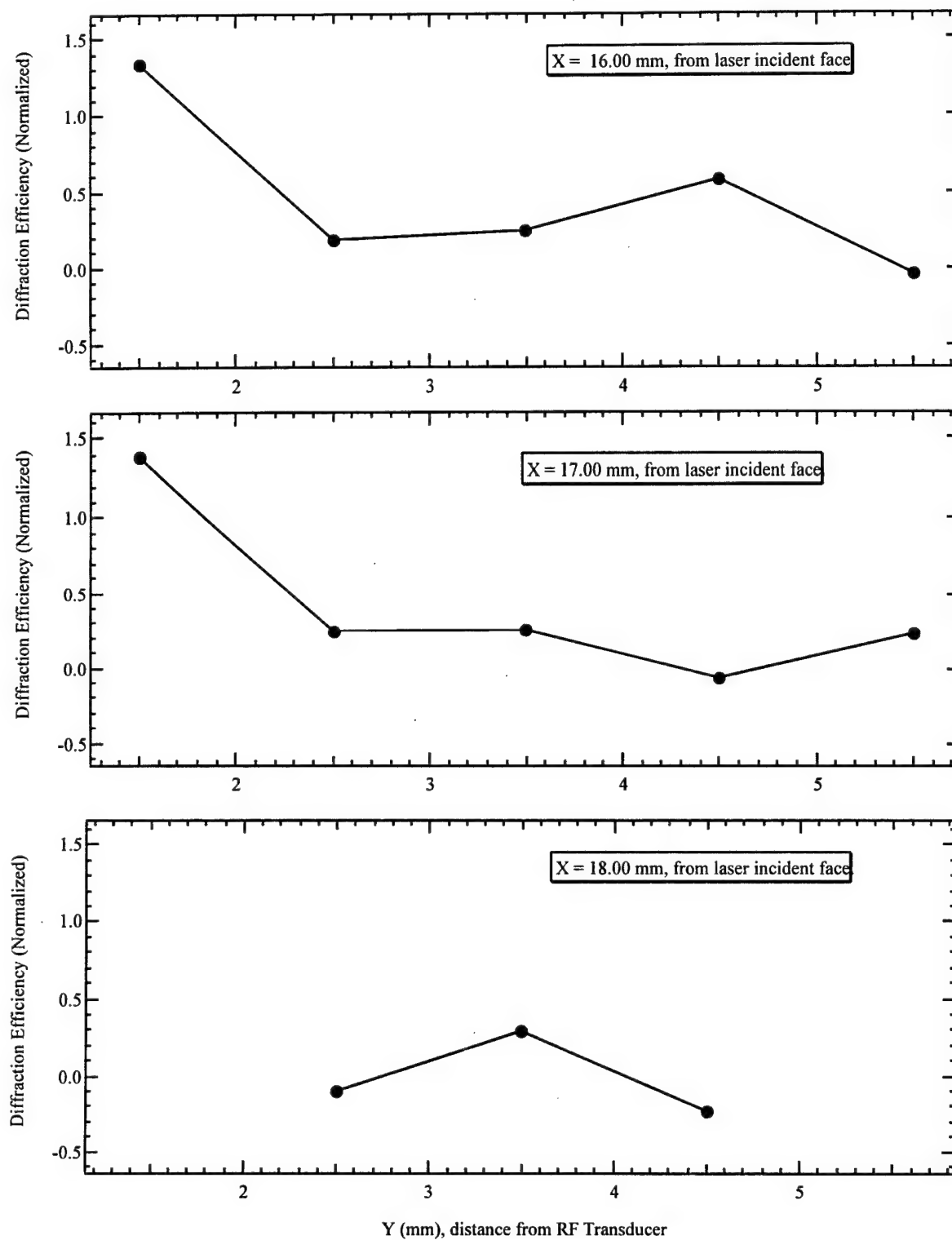


Figure A-59. Summary of diffraction efficiency change as a function of distance from Transducer for position x=16, 17 and 18mm.

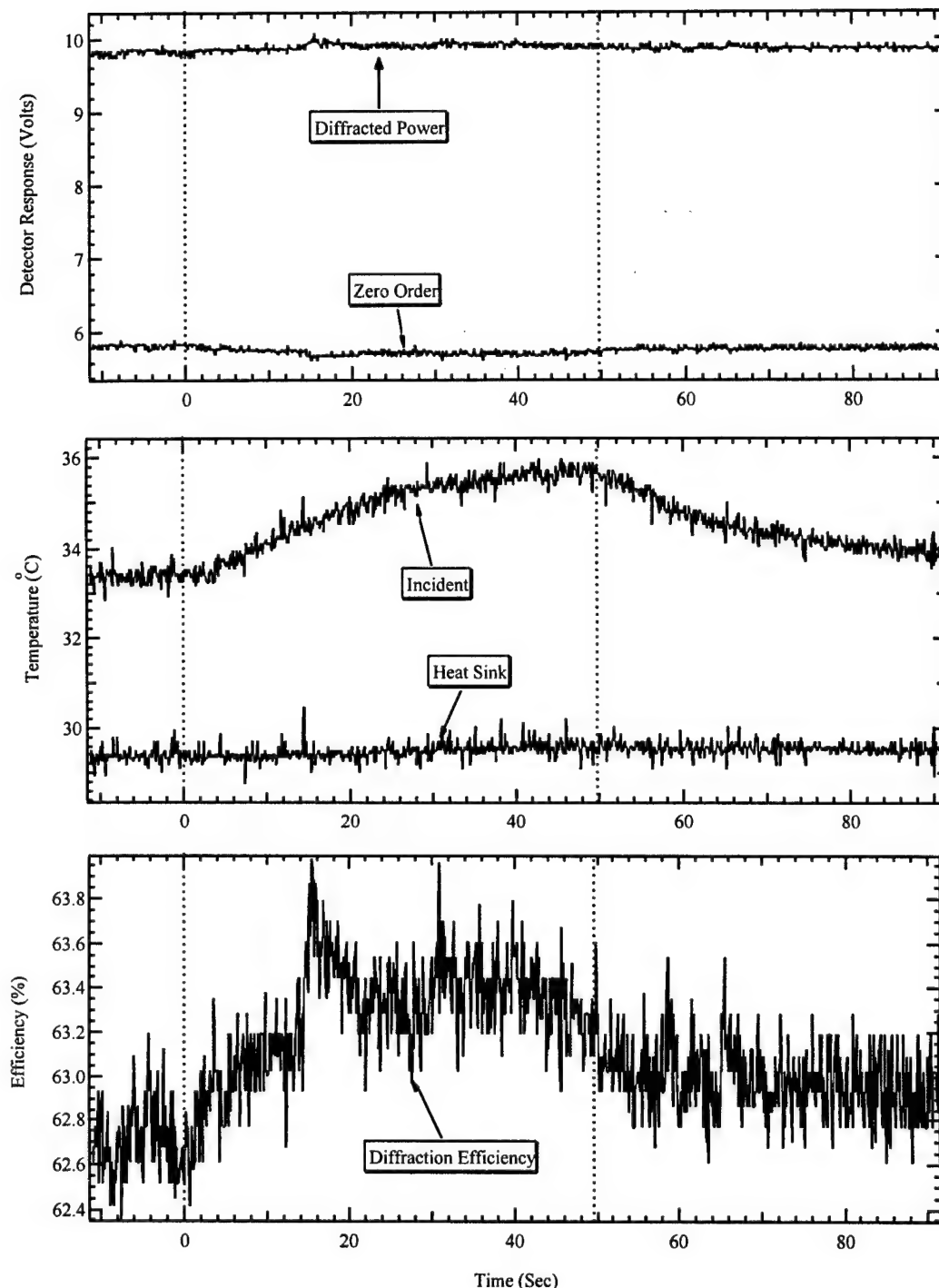


Figure A-60. Three plots showing the measured AO-cell response before, during and after an ion beam exposure #a1. The dashed lines indicate the duration of the ion beam. Refer to Table A-3 for the precise beam location. The upper plot shows the power of the diffracted and zero order laser beam exiting the AO-cell and the center plot shows the temperature of the crystal face being struck by the ion beam as well as the temperature of the heat sink. The bottom plot shows the calculated diffraction efficiency.

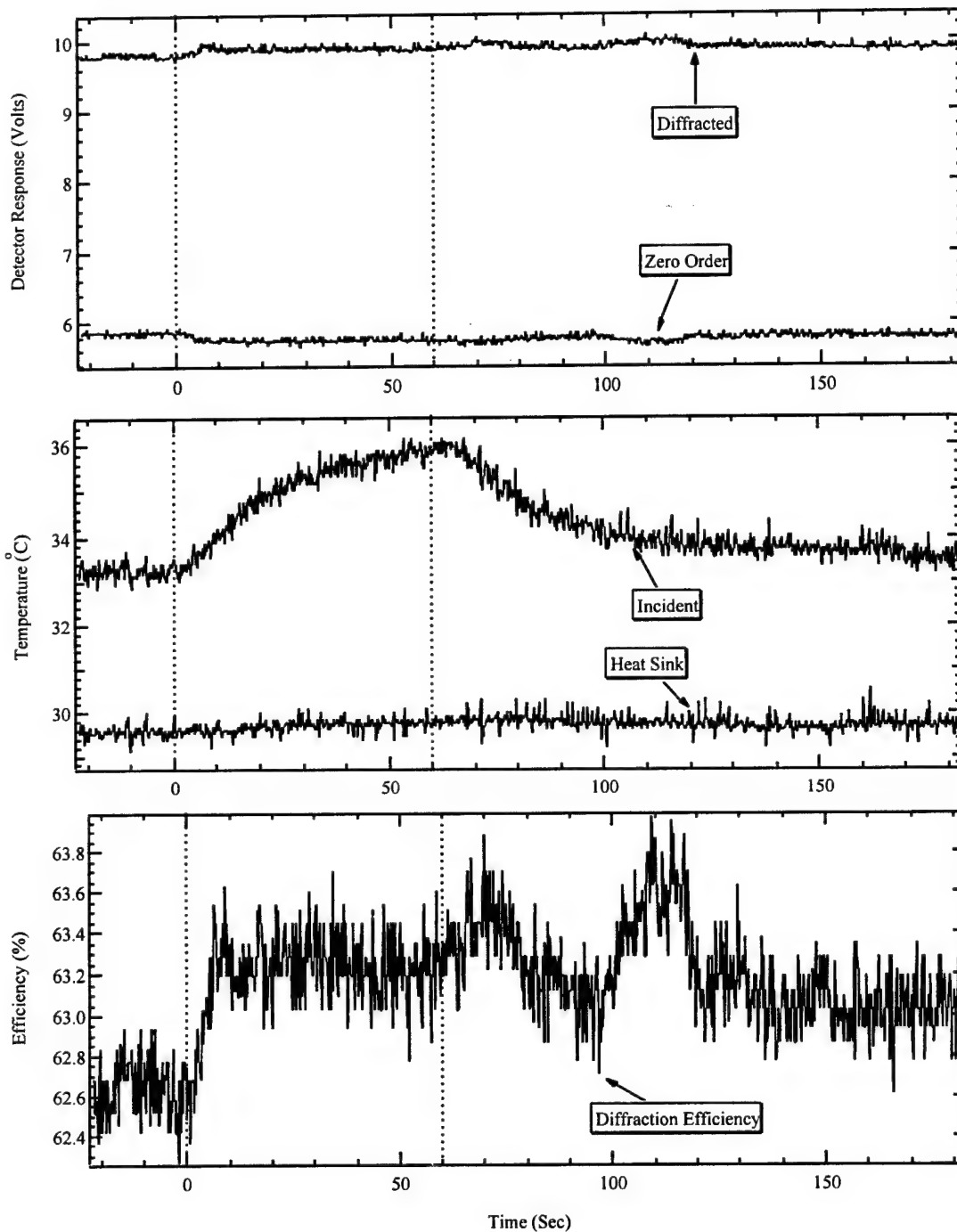


Figure A-61. Three plots showing the measured AO-cell response before, during and after an ion beam exposure #a2. The dashed lines indicate the duration of the ion beam. Refer to Table A-3 for the precise beam location. The upper plot shows the power of the diffracted and zero order laser beam exiting the AO-cell and the center plot shows the temperature of the crystal face being struck by the ion beam as well as the temperature of the heat sink. The bottom plot shows the calculated diffraction efficiency.

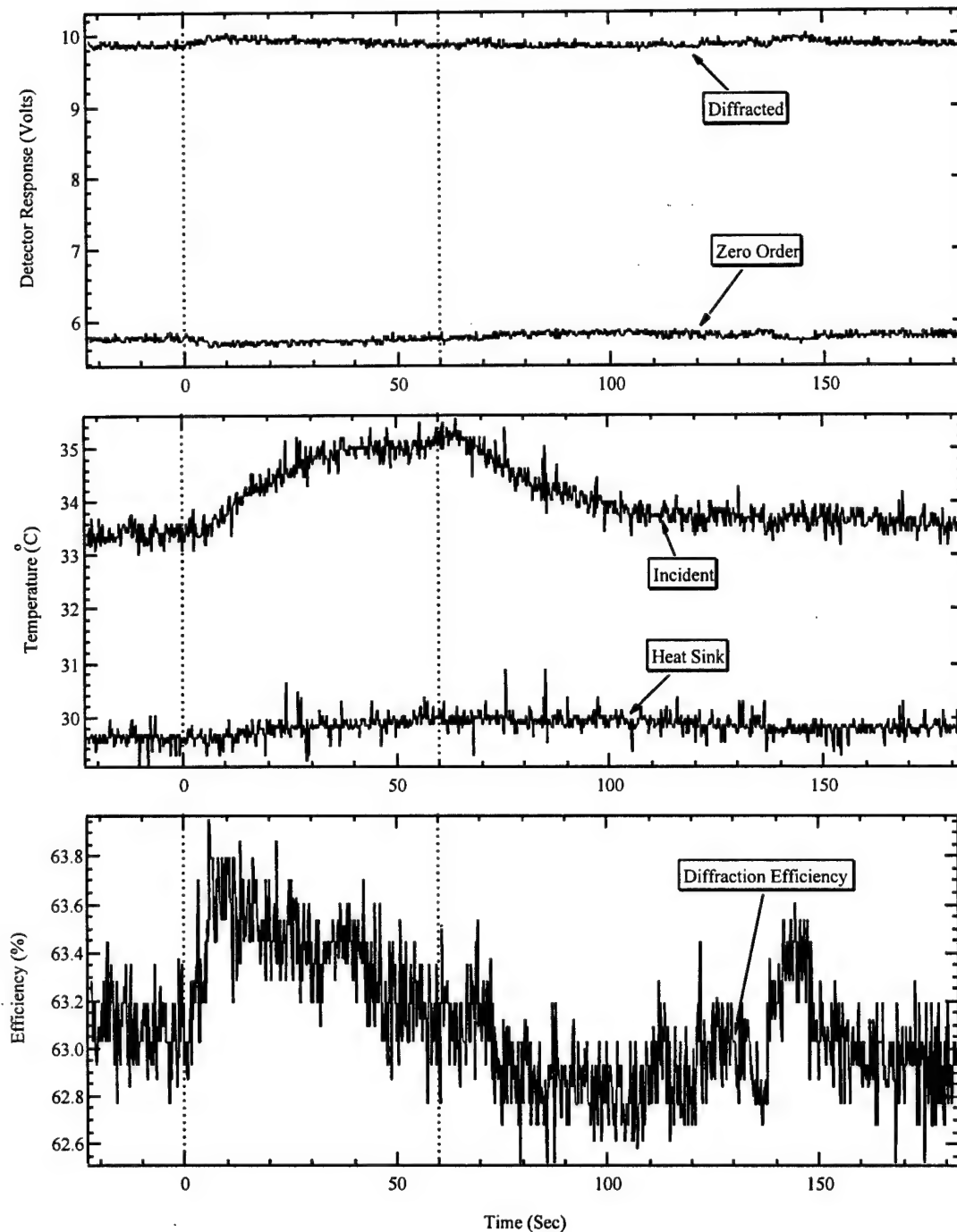


Figure A-62. Three plots showing the measured AO-cell response before, during and after an ion beam exposure #a3. The dashed lines indicate the duration of the ion beam. Refer to Table A-3 for the precise beam location. The upper plot shows the power of the diffracted and zero order laser beam exiting the AO-cell and the center plot shows the temperature of the crystal face being struck by the ion beam as well as the temperature of the heat sink. The bottom plot shows the calculated diffraction efficiency.

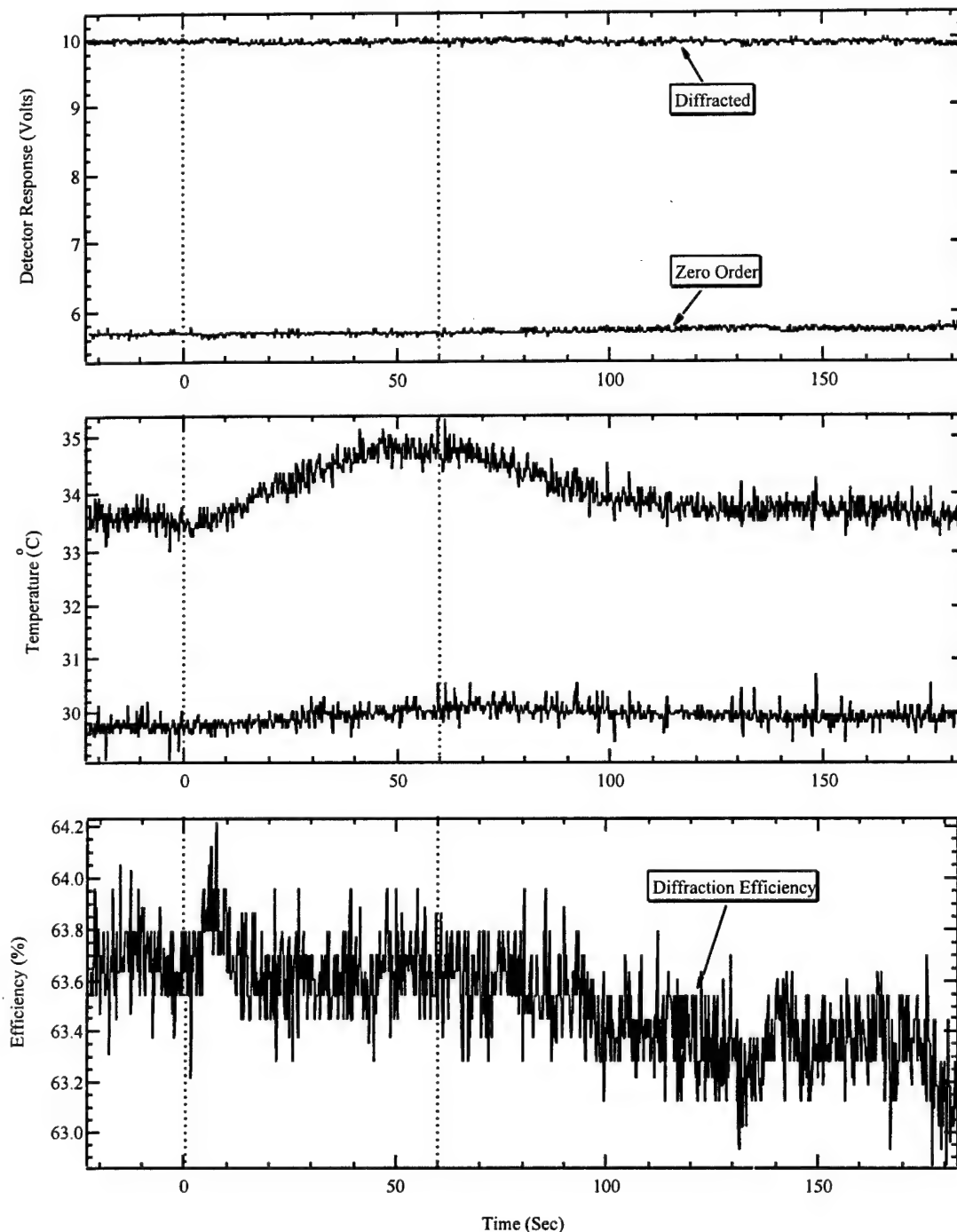


Figure A-63. Three plots showing the measured AO-cell response before, during and after an ion beam exposure #a4. The dashed lines indicate the duration of the ion beam. Refer to Table A-3 for the precise beam location. The upper plot shows the power of the diffracted and zero order laser beam exiting the AO-cell and the center plot shows the temperature of the crystal face being struck by the ion beam as well as the temperature of the heat sink. The bottom plot shows the calculated diffraction efficiency.

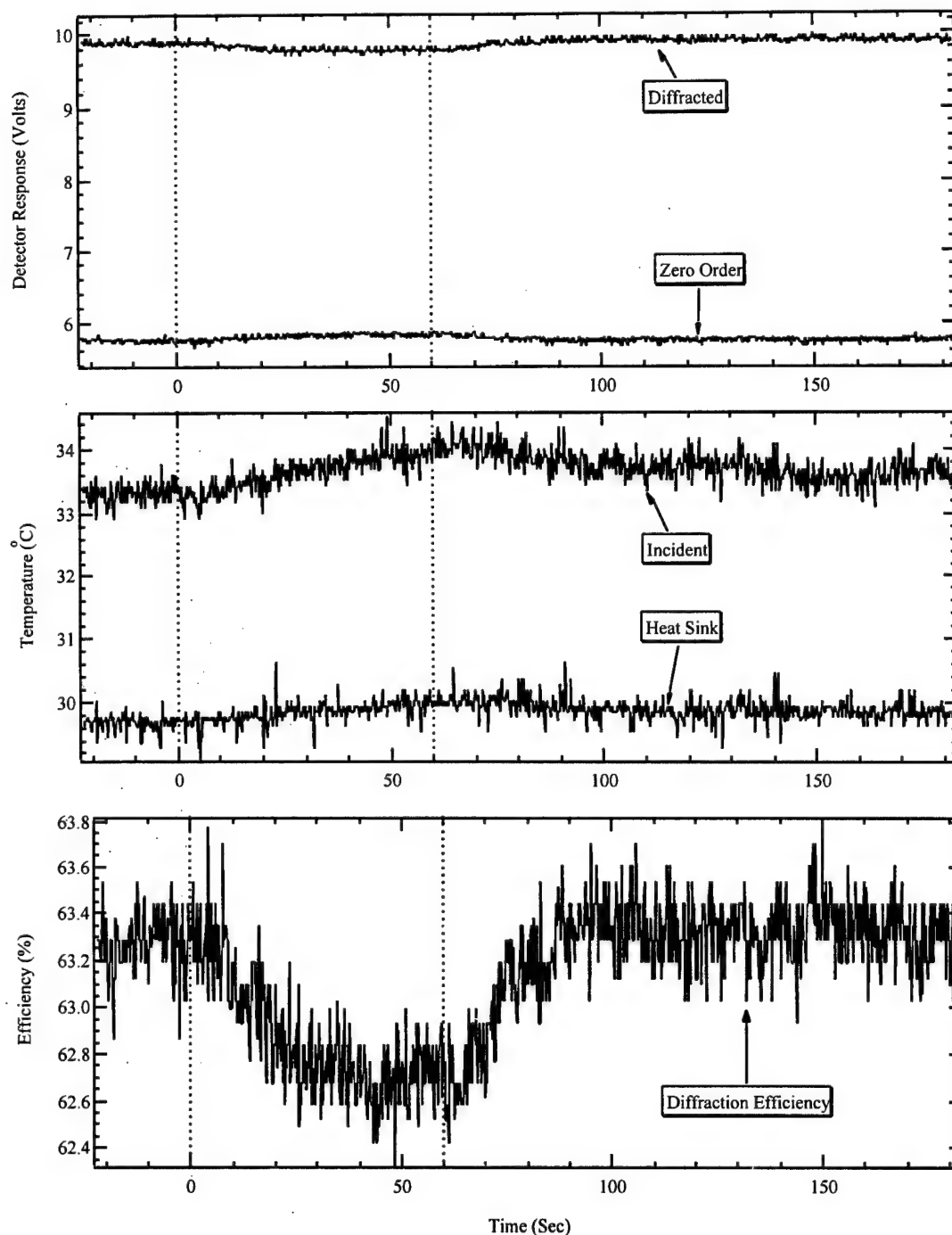


Figure A-64. Three plots showing the measured AO-cell response before, during and after an ion beam exposure #a5. The dashed lines indicate the duration of the ion beam. Refer to Table A-3 for the precise beam location. The upper plot shows the power of the diffracted and zero order laser beam exiting the AO-cell and the center plot shows the temperature of the crystal face being struck by the ion beam as well as the temperature of the heat sink. The bottom plot shows the calculated diffraction efficiency.

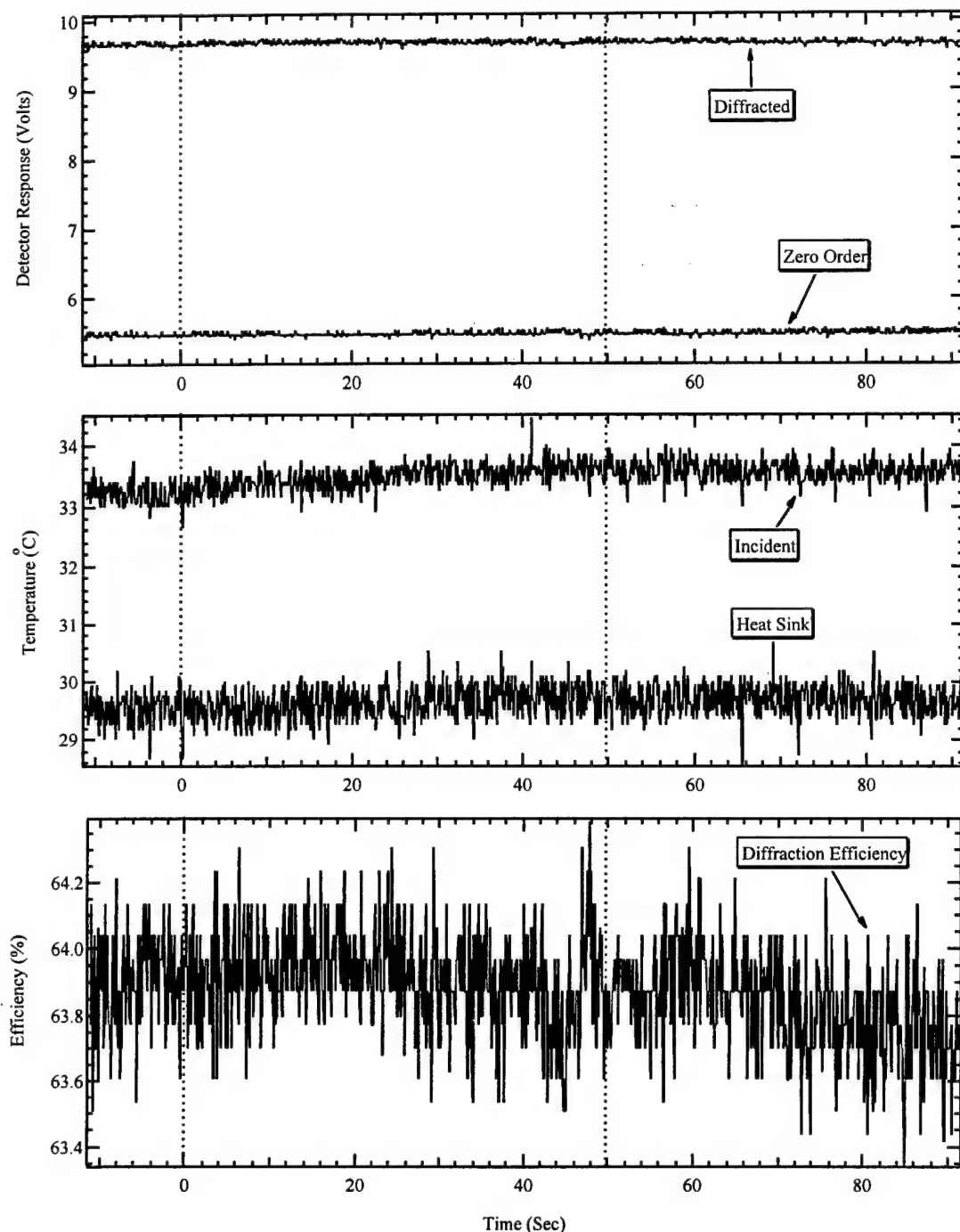


Figure A-65. Three plots showing the measured AO-cell response before, during and after an ion beam exposure #a6. The dashed lines indicate the duration of the ion beam. Refer to Table A-3 for the precise beam location. The upper plot shows the power of the diffracted and zero order laser beam exiting the AO-cell and the center plot shows the temperature of the crystal face being struck by the ion beam as well as the temperature of the heat sink. The bottom plot shows the calculated diffraction efficiency.

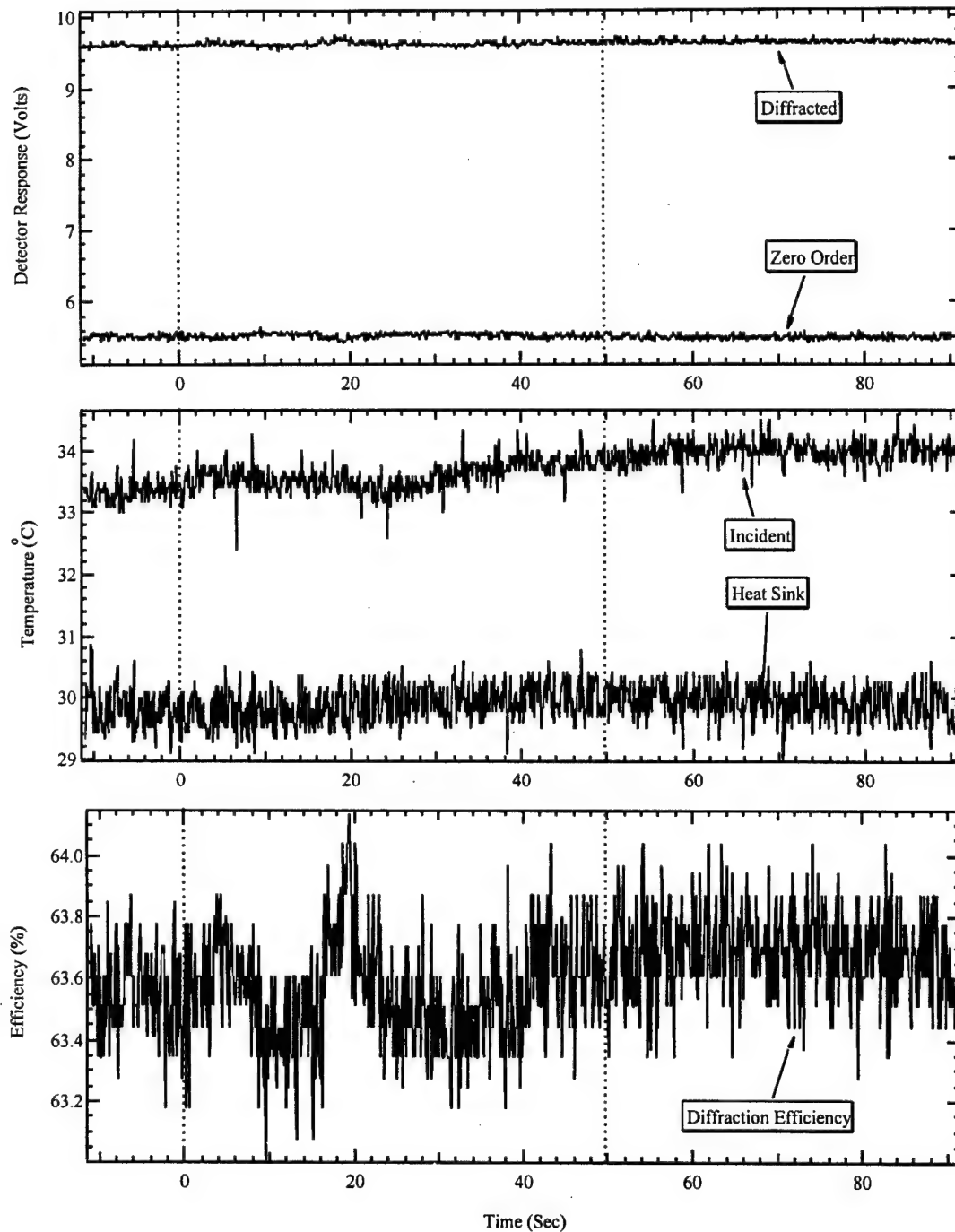


Figure A-66. Three plots showing the measured AO-cell response before, during and after an ion beam exposure #a7. The dashed lines indicate the duration of the ion beam. Refer to Table A-3 for the precise beam location. The upper plot shows the power of the diffracted and zero order laser beam exiting the AO-cell and the center plot shows the temperature of the crystal face being struck by the ion beam as well as the temperature of the heat sink. The bottom plot shows the calculated diffraction efficiency.

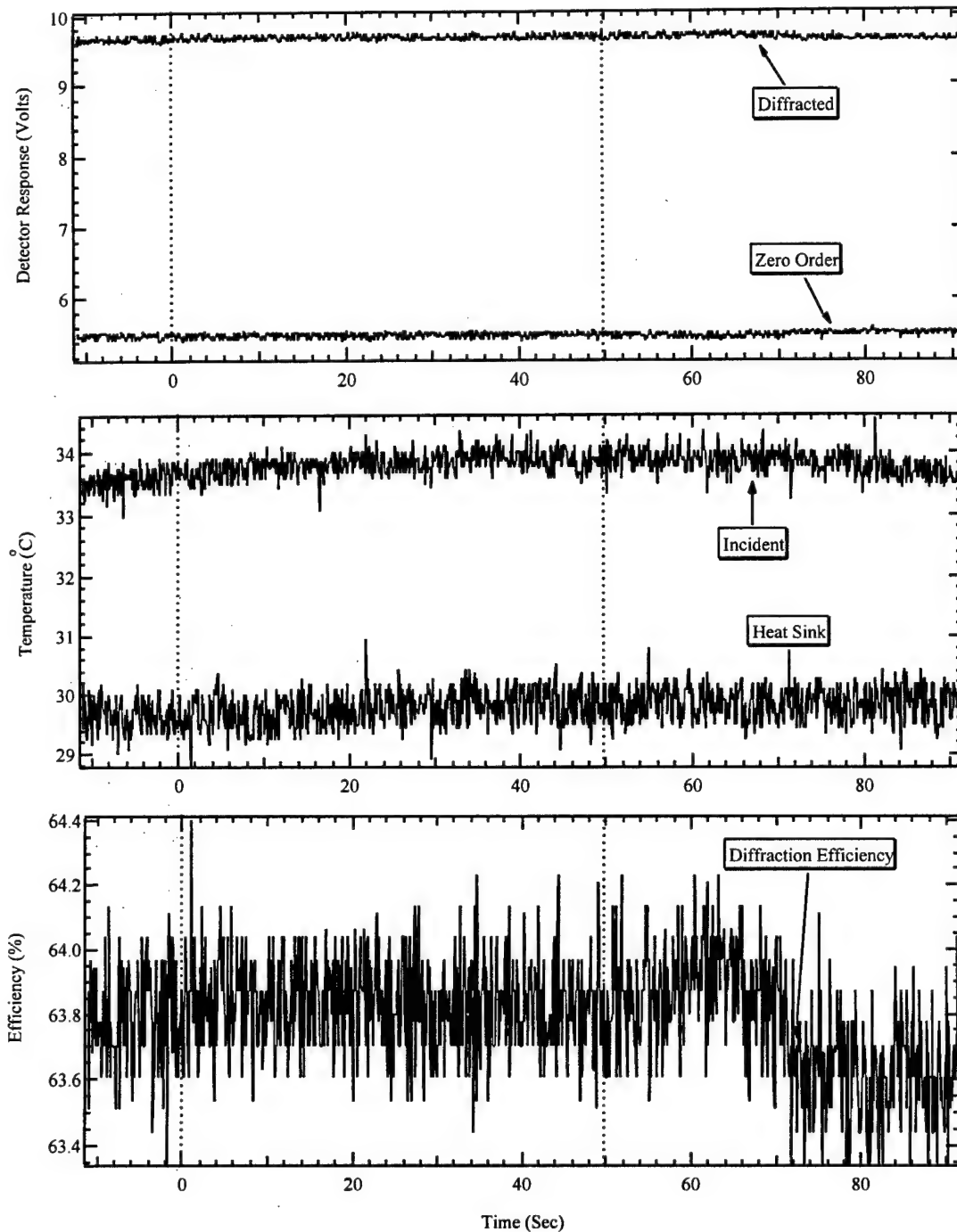


Figure A-67. Three plots showing the measured AO-cell response before, during and after an ion beam exposure #a8. The dashed lines indicate the duration of the ion beam. Refer to Table A-3 for the precise beam location. The upper plot shows the power of the diffracted and zero order laser beam exiting the AO-cell and the center plot shows the temperature of the crystal face being struck by the ion beam as well as the temperature of the heat sink. The bottom plot shows the calculated diffraction efficiency.

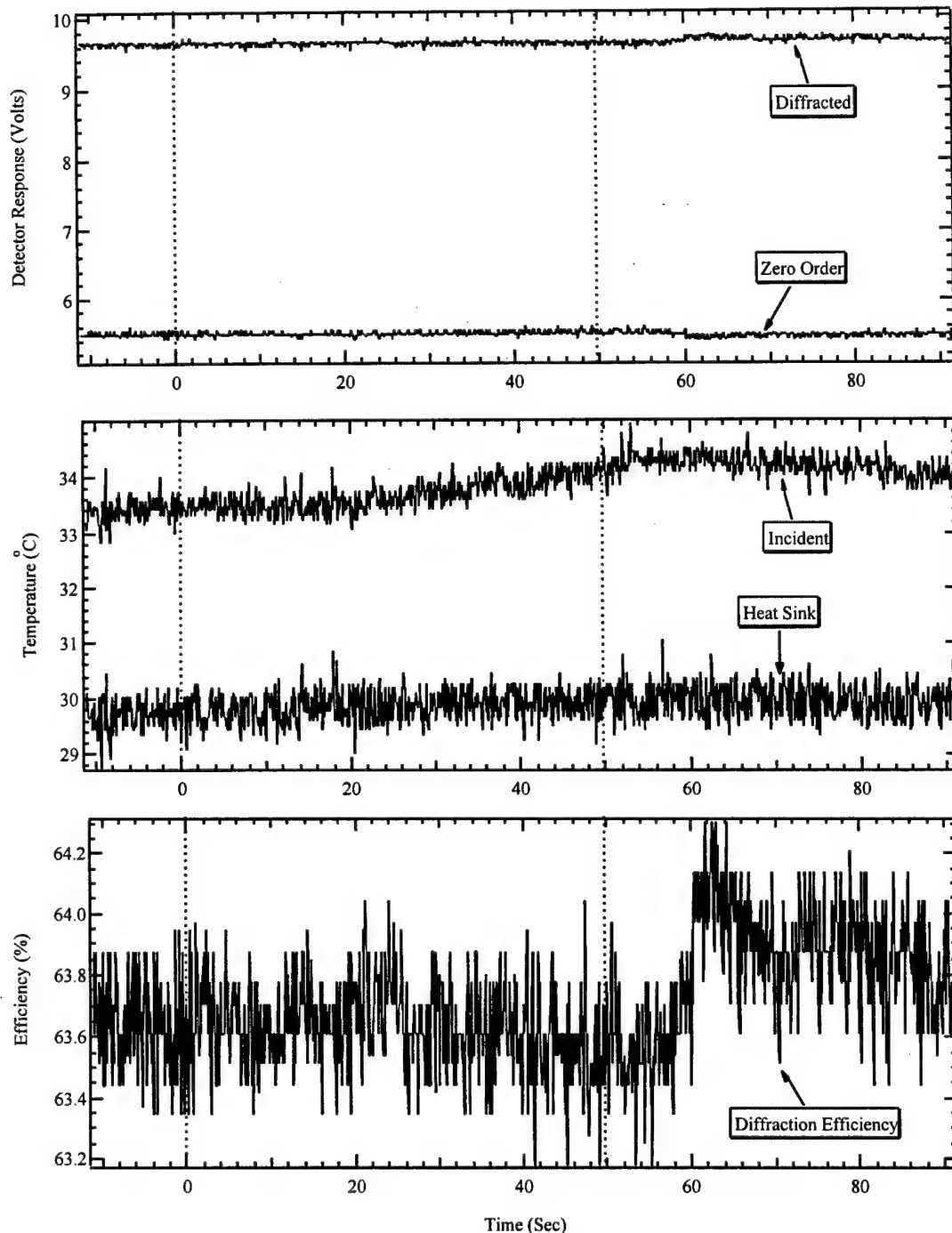


Figure A-68. Three plots showing the measured AO-cell response before, during and after an ion beam exposure #a9. The dashed lines indicate the duration of the ion beam. Refer to Table A-3 for the precise beam location. The upper plot shows the power of the diffracted and zero order laser beam exiting the AO-cell and the center plot shows the temperature of the crystal face being struck by the ion beam as well as the temperature of the heat sink. The bottom plot shows the calculated diffraction efficiency.

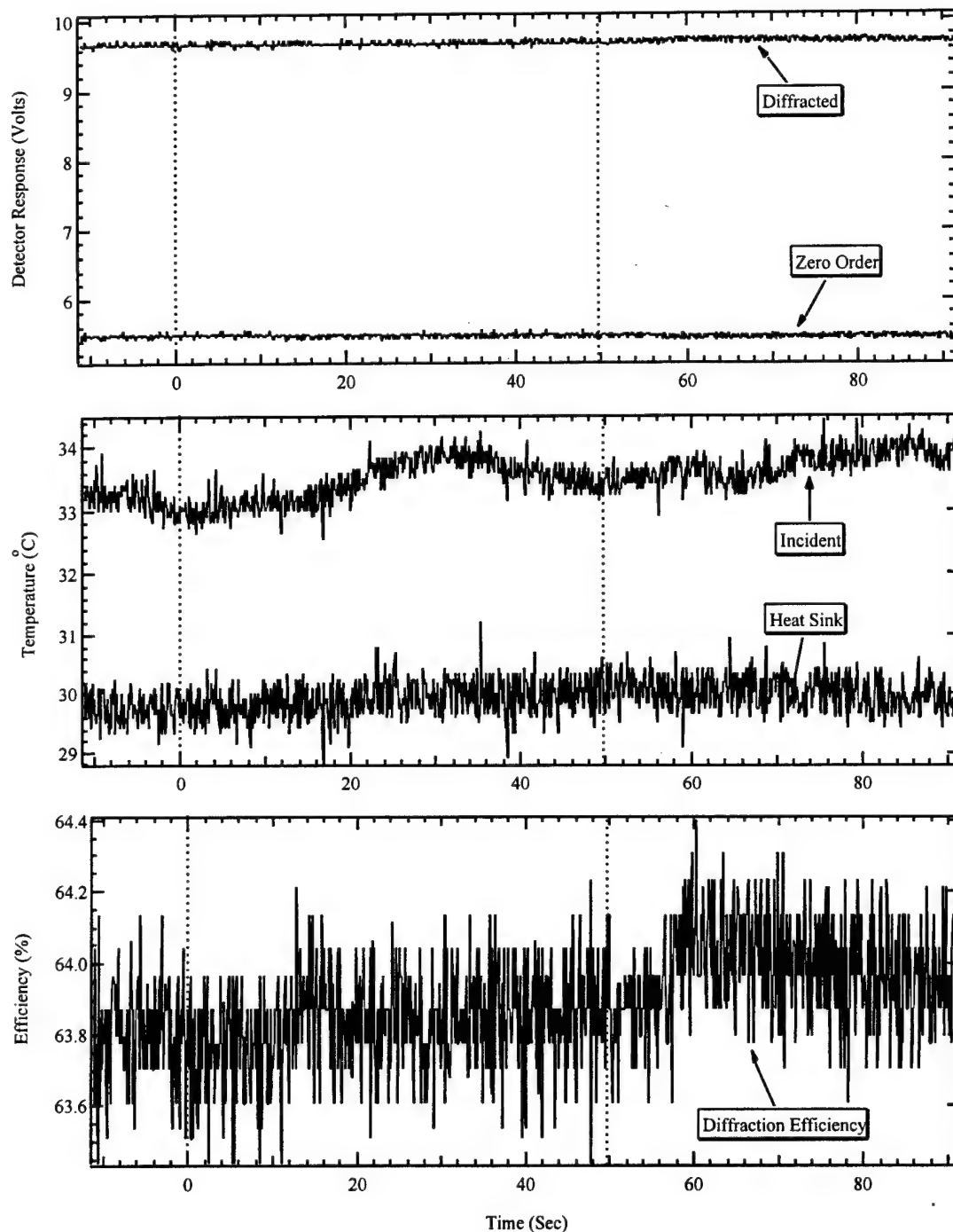


Figure A-69. Three plots showing the measured AO-cell response before, during and after an ion beam exposure #a10. The dashed lines indicate the duration of the ion beam. Refer to Table A-3 for the precise beam location. The upper plot shows the power of the diffracted and zero order laser beam exiting the AO-cell and the center plot shows the temperature of the crystal face being struck by the ion beam as well as the temperature of the heat sink. The bottom plot shows the calculated diffraction efficiency.

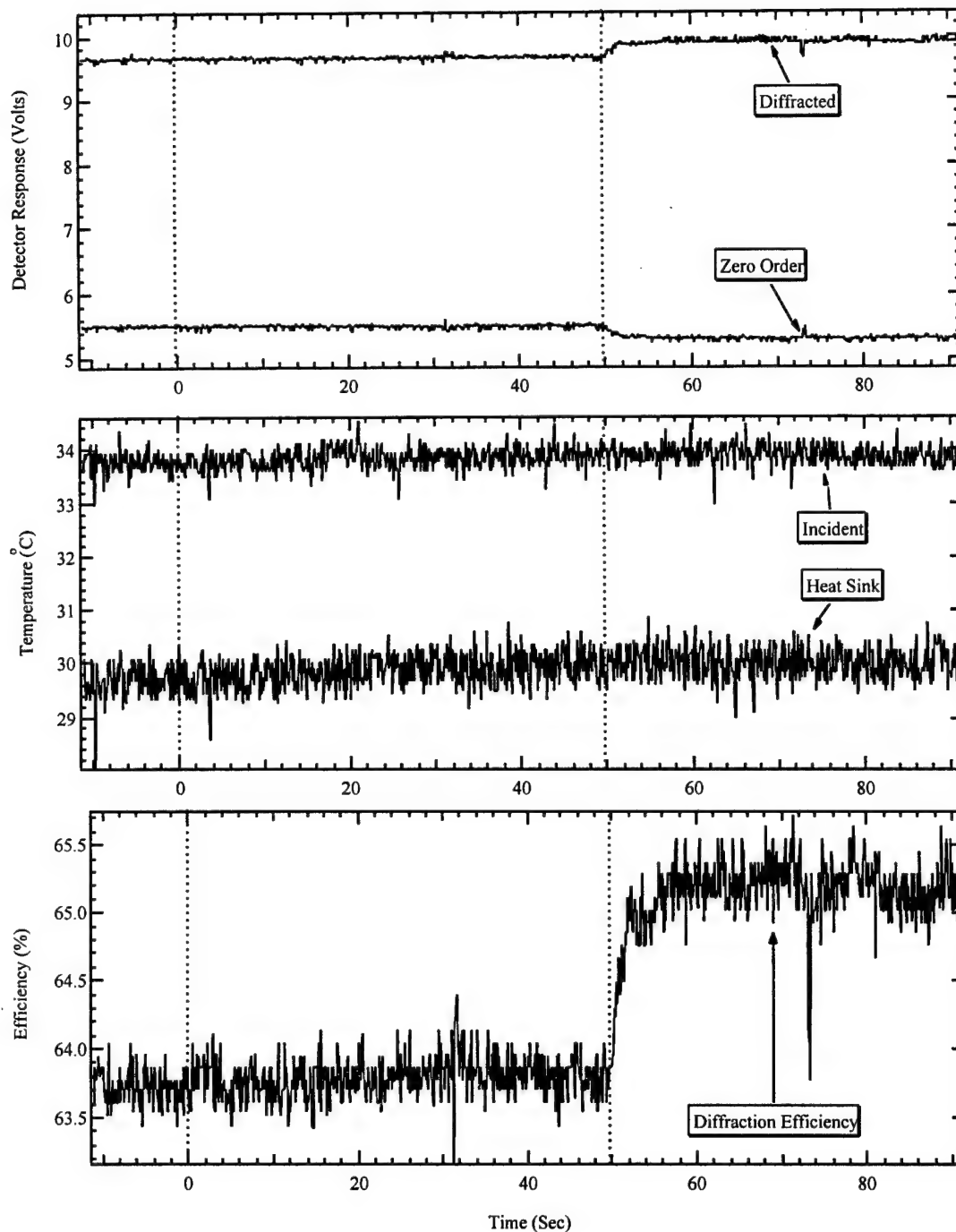


Figure A-70. Three plots showing the measured AO-cell response before, during and after an ion beam exposure #a11. The dashed lines indicate the duration of the ion beam. Refer to Table A-3 for the precise beam location. The upper plot shows the power of the diffracted and zero order laser beam exiting the AO-cell and the center plot shows the temperature of the crystal face being struck by the ion beam as well as the temperature of the heat sink. The bottom plot shows the calculated diffraction efficiency.

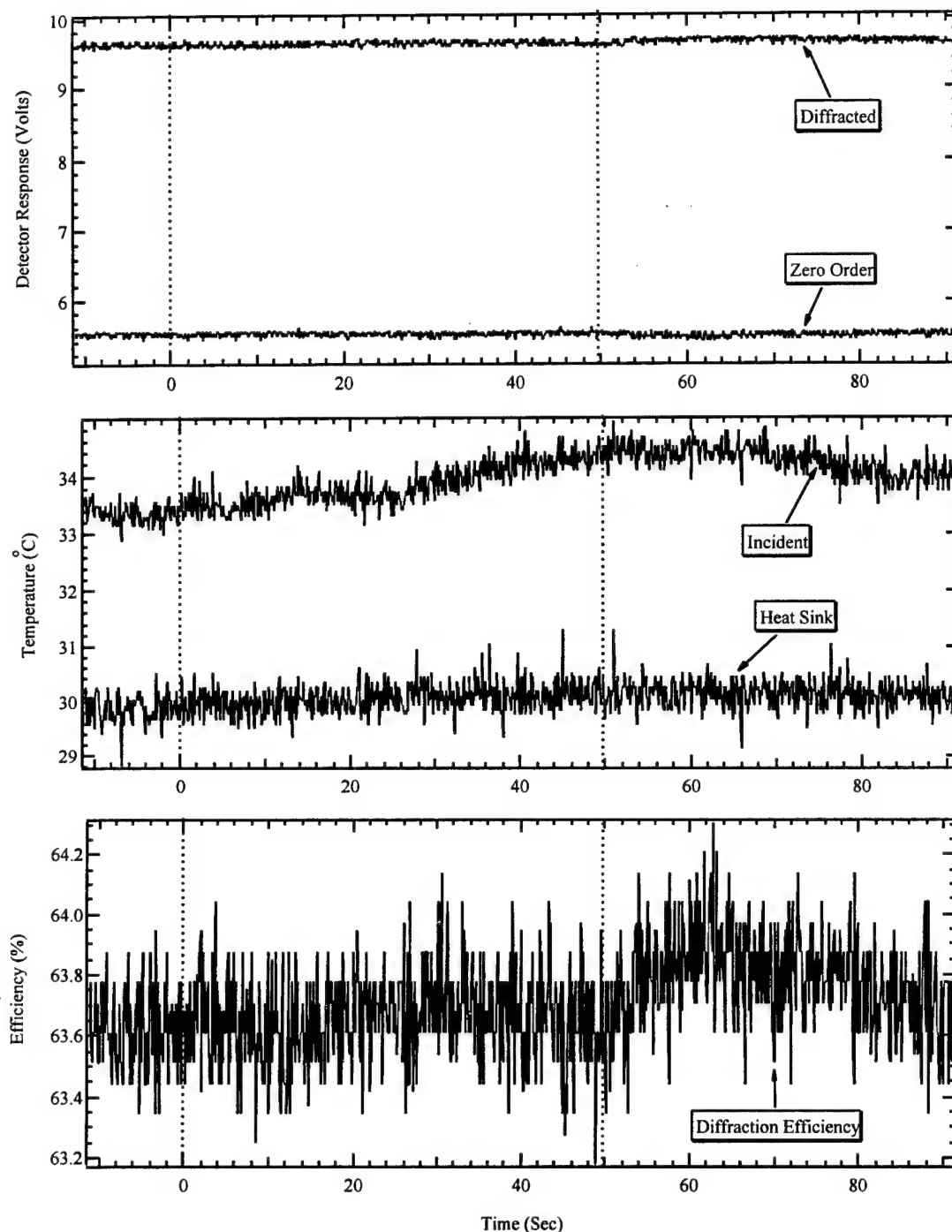


Figure A-71. Three plots showing the measured AO-cell response before, during and after an ion beam exposure #a12. The dashed lines indicate the duration of the ion beam. Refer to Table A-3 for the precise beam location. The upper plot shows the power of the diffracted and zero order laser beam exiting the AO-cell and the center plot shows the temperature of the crystal face being struck by the ion beam as well as the temperature of the heat sink. The bottom plot shows the calculated diffraction efficiency.

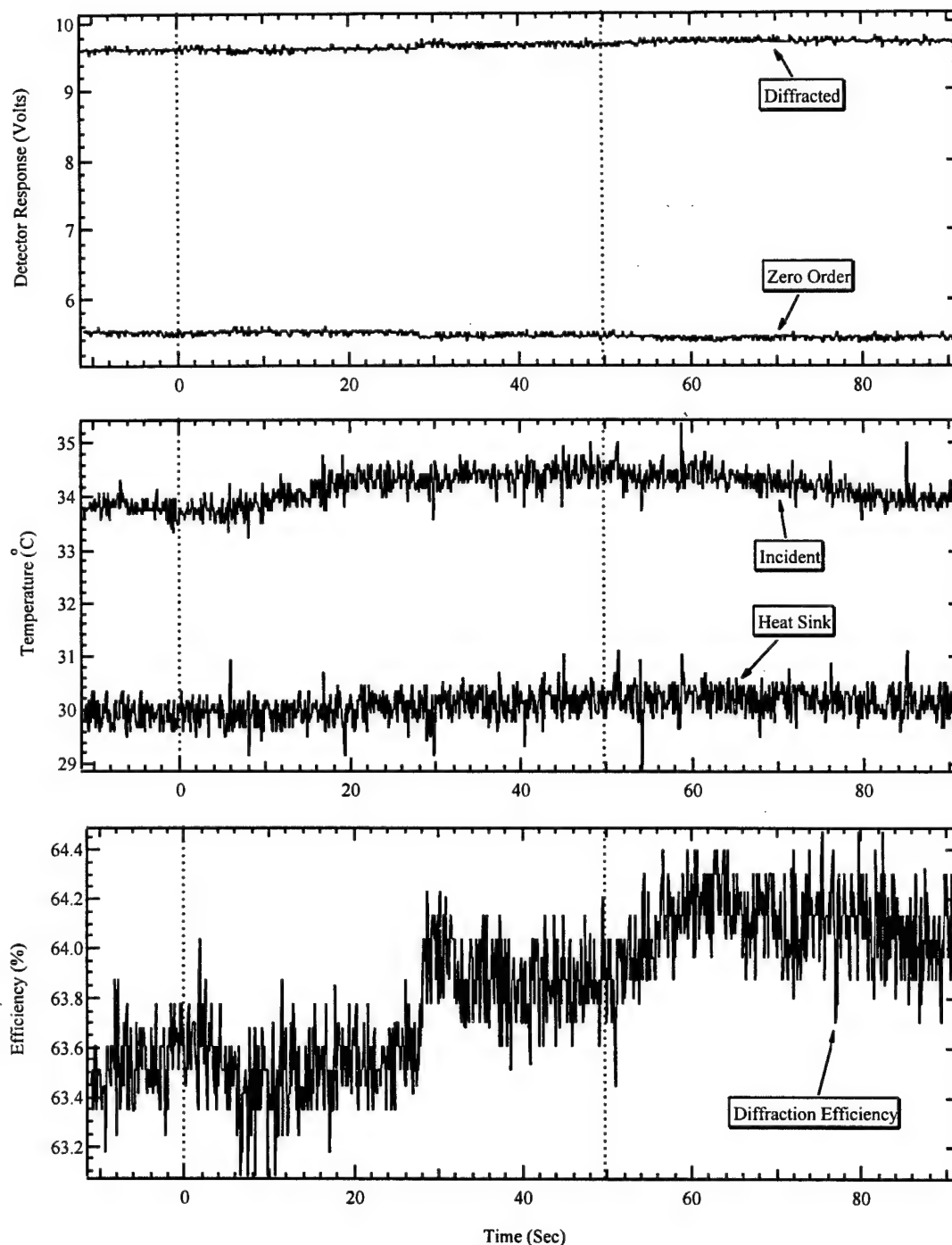


Figure A-72. Three plots showing the measured AO-cell response before, during and after an ion beam exposure #a13. The dashed lines indicate the duration of the ion beam. Refer to Table A-3 for the precise beam location. The upper plot shows the power of the diffracted and zero order laser beam exiting the AO-cell and the center plot shows the temperature of the crystal face being struck by the ion beam as well as the temperature of the heat sink. The bottom plot shows the calculated diffraction efficiency.

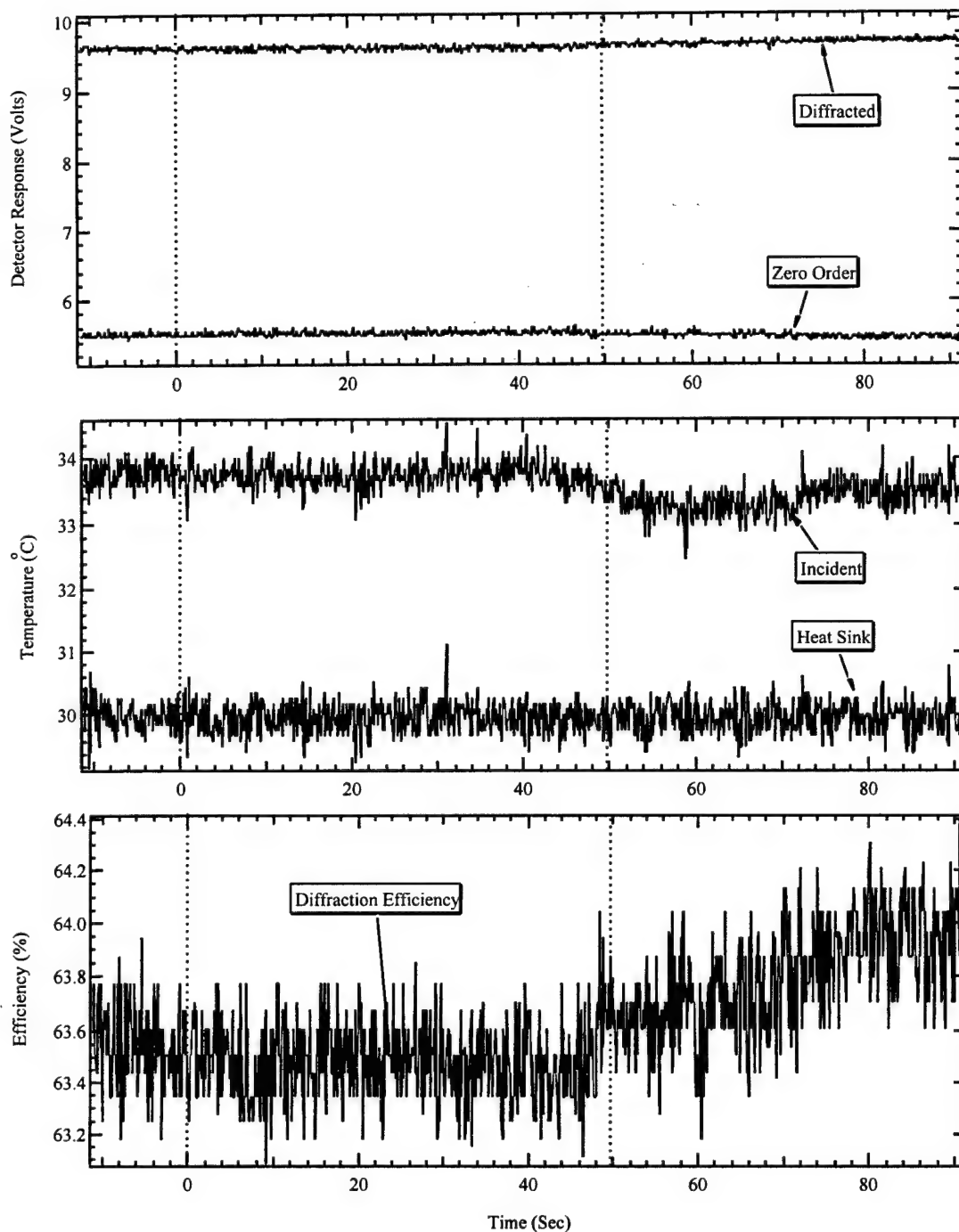


Figure A-73. Three plots showing the measured AO-cell response before, during and after an ion beam exposure #a14. The dashed lines indicate the duration of the ion beam. Refer to Table A-3 for the precise beam location. The upper plot shows the power of the diffracted and zero order laser beam exiting the AO-cell and the center plot shows the temperature of the crystal face being struck by the ion beam as well as the temperature of the heat sink. The bottom plot shows the calculated diffraction efficiency.

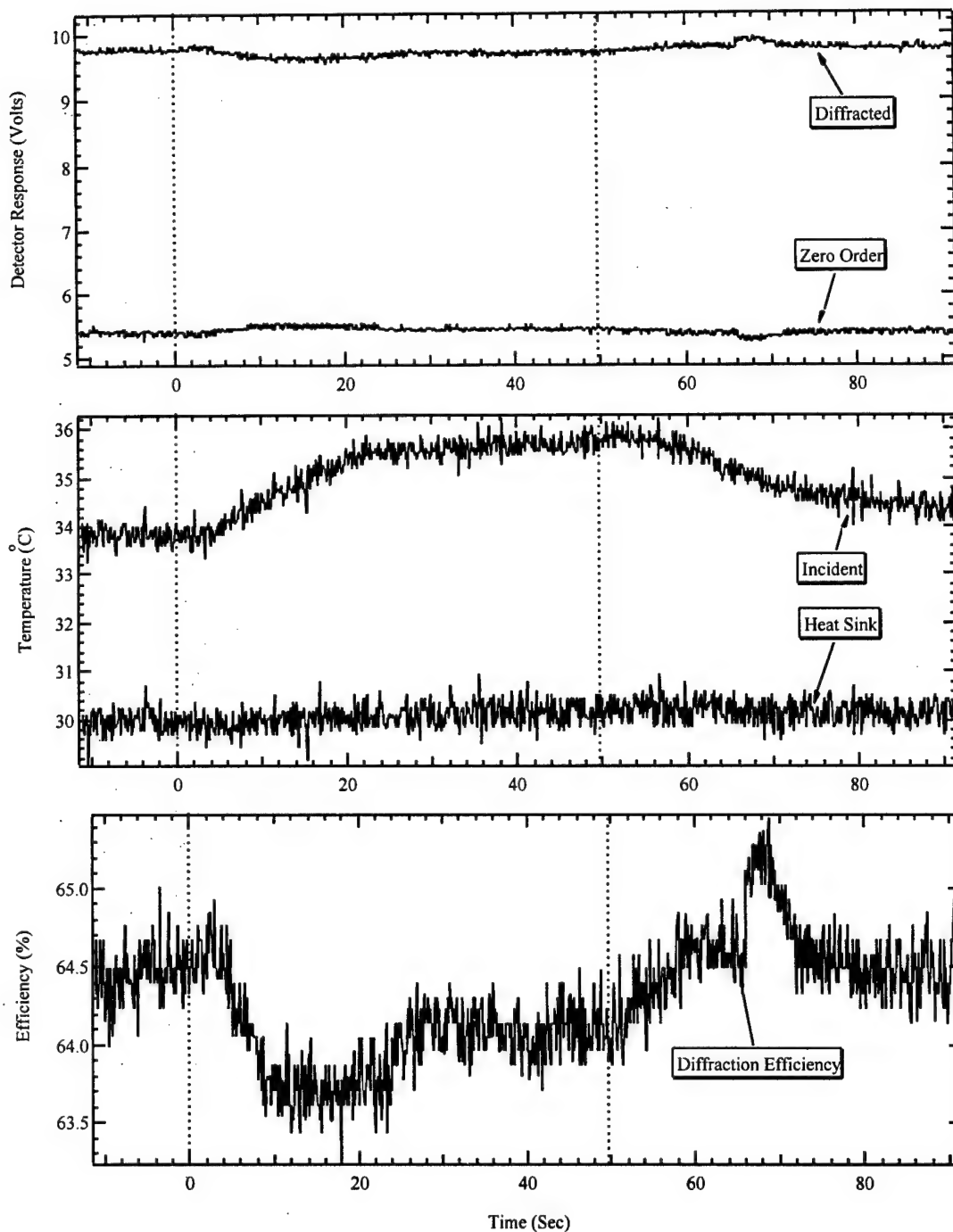


Figure A-74. Three plots showing the measured AO-cell response before, during and after an ion beam exposure #a15. The dashed lines indicate the duration of the ion beam. Refer to Table A-3 for the precise beam location. The upper plot shows the power of the diffracted and zero order laser beam exiting the AO-cell and the center plot shows the temperature of the crystal face being struck by the ion beam as well as the temperature of the heat sink. The bottom plot shows the calculated diffraction efficiency.

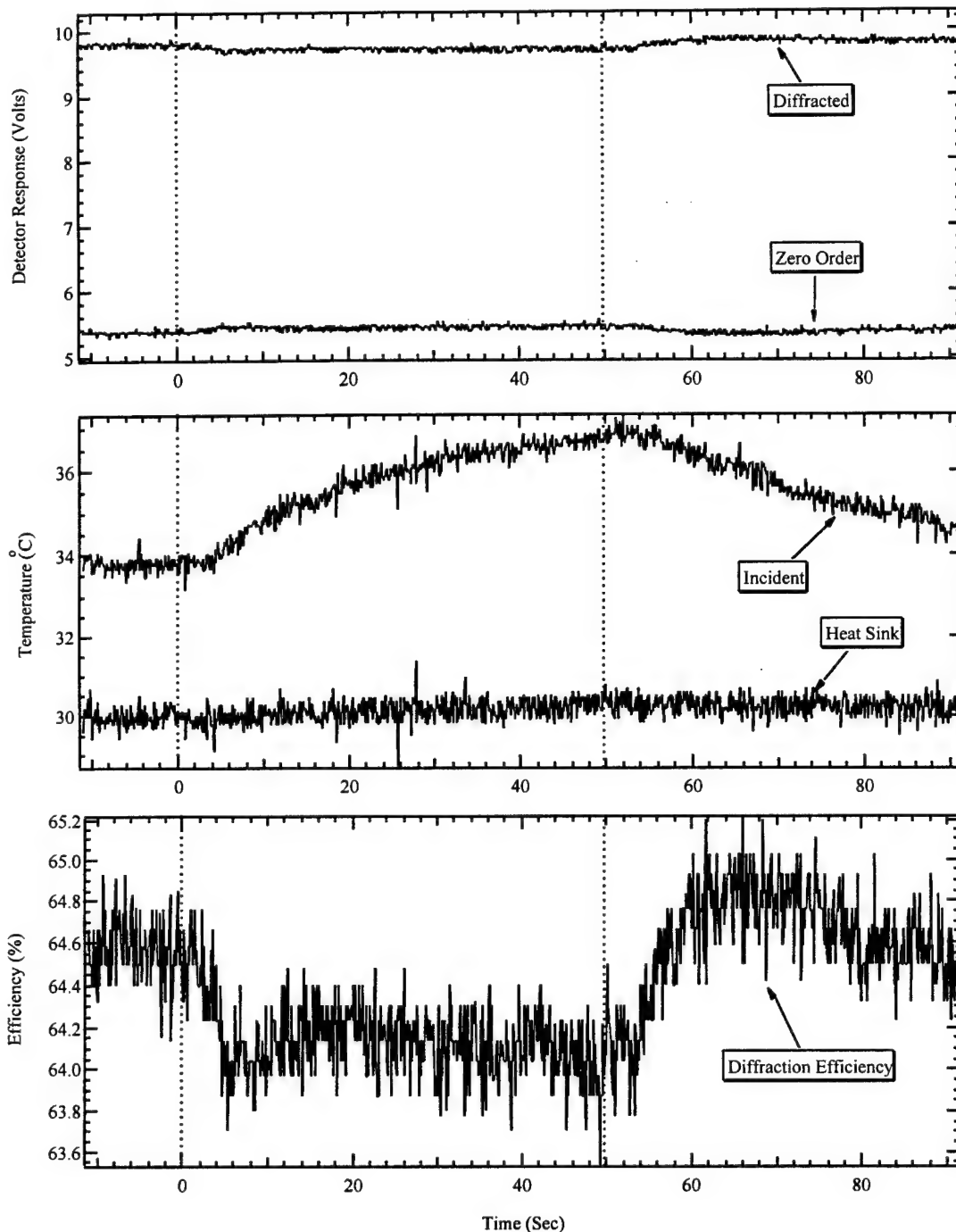


Figure A-75. Three plots showing the measured AO-cell response before, during and after an ion beam exposure #a16. The dashed lines indicate the duration of the ion beam. Refer to Table A-3 for the precise beam location. The upper plot shows the power of the diffracted and zero order laser beam exiting the AO-cell and the center plot shows the temperature of the crystal face being struck by the ion beam as well as the temperature of the heat sink. The bottom plot shows the calculated diffraction efficiency.

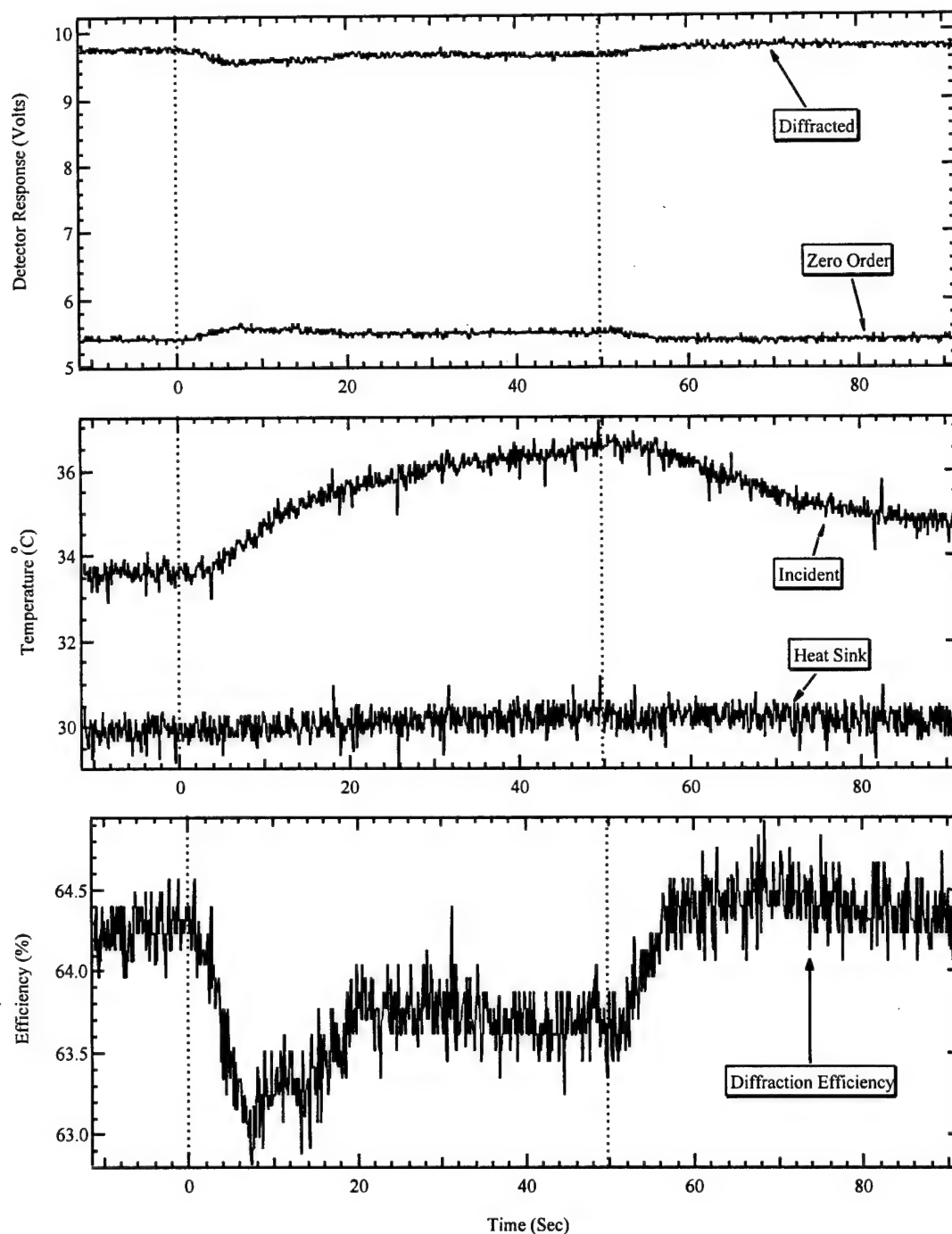


Figure A-76. Three plots showing the measured AO-cell response before, during and after an ion beam exposure #a17. The dashed lines indicate the duration of the ion beam. Refer to Table A-3 for the precise beam location. The upper plot shows the power of the diffracted and zero order laser beam exiting the AO-cell and the center plot shows the temperature of the crystal face being struck by the ion beam as well as the temperature of the heat sink. The bottom plot shows the calculated diffraction efficiency.

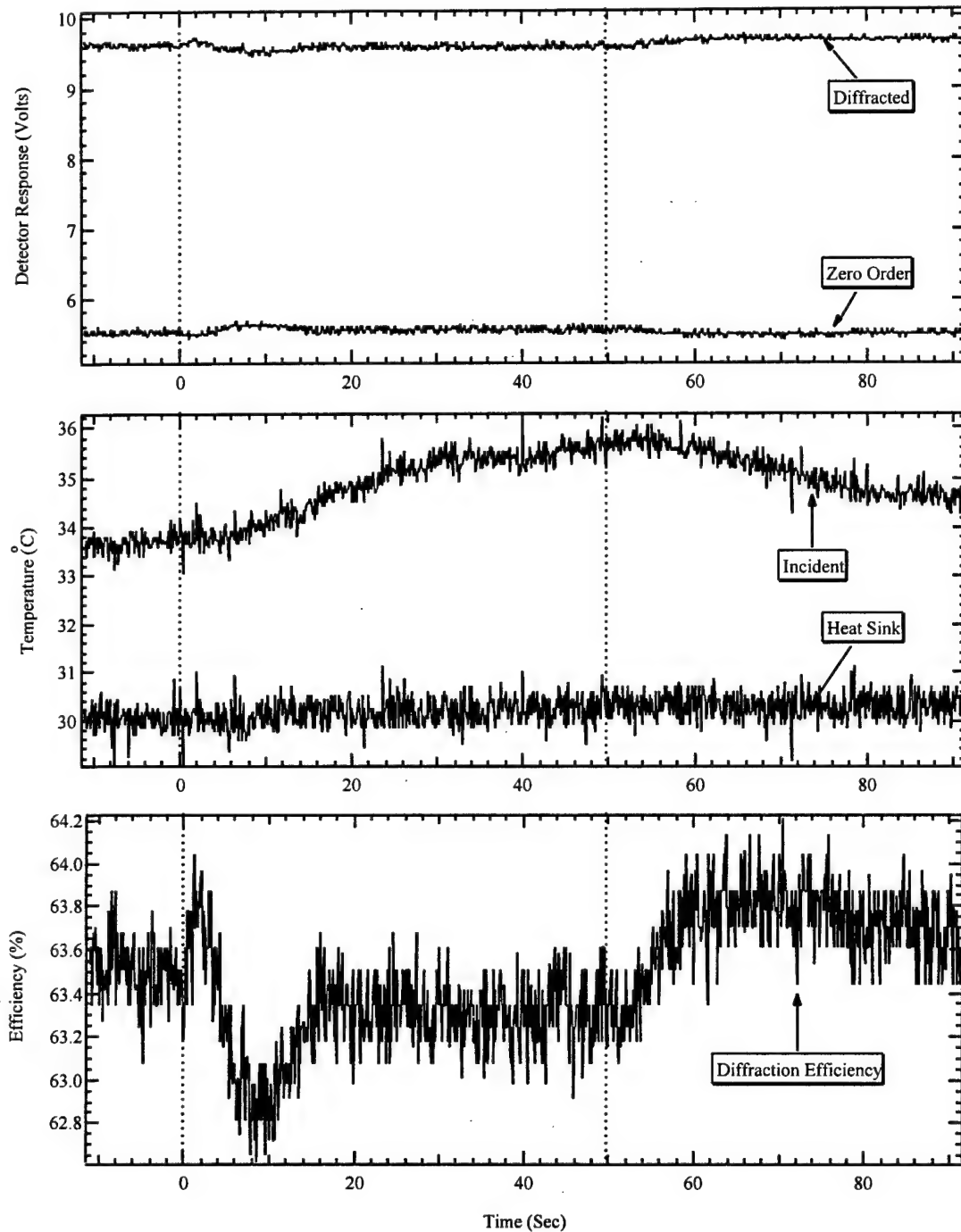


Figure A-77. Three plots showing the measured AO-cell response before, during and after an ion beam exposure #a18. The dashed lines indicate the duration of the ion beam. Refer to Table A-3 for the precise beam location. The upper plot shows the power of the diffracted and zero order laser beam exiting the AO-cell and the center plot shows the temperature of the crystal face being struck by the ion beam as well as the temperature of the heat sink. The bottom plot shows the calculated diffraction efficiency.

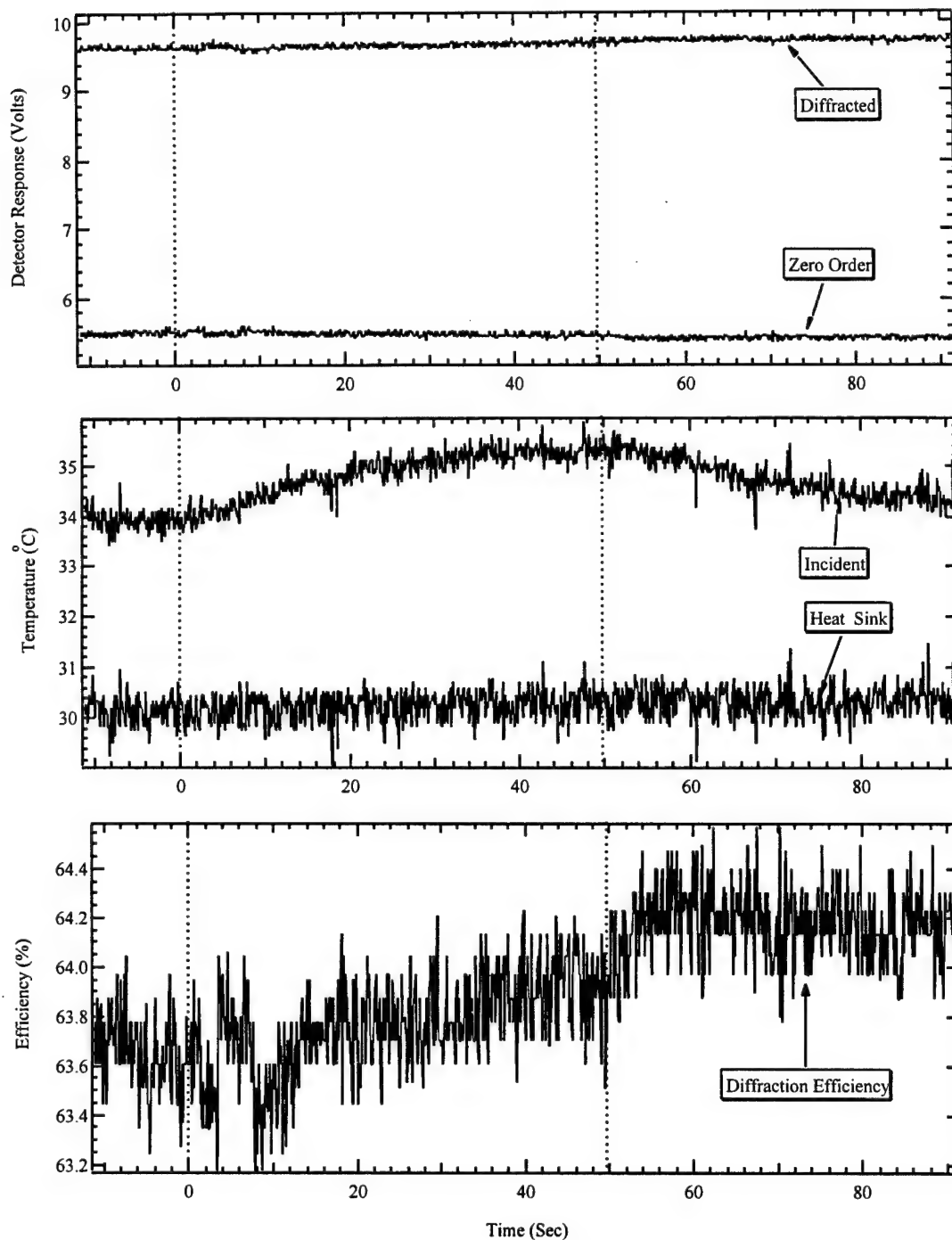


Figure A-78. Three plots showing the measured AO-cell response before, during and after an ion beam exposure #a19. The dashed lines indicate the duration of the ion beam. Refer to Table A-3 for the precise beam location. The upper plot shows the power of the diffracted and zero order laser beam exiting the AO-cell and the center plot shows the temperature of the crystal face being struck by the ion beam as well as the temperature of the heat sink. The bottom plot shows the calculated diffraction efficiency.

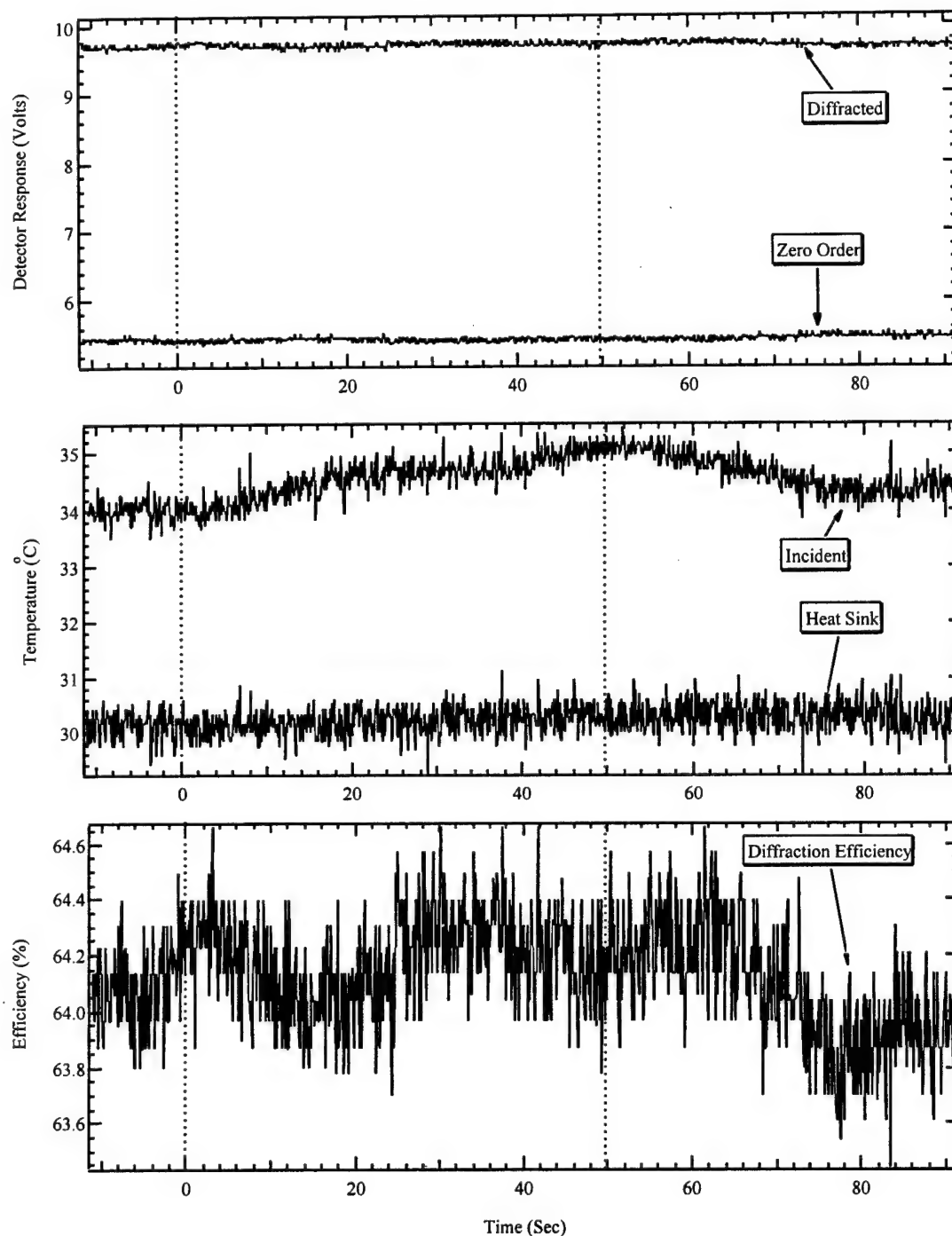


Figure A-79. Three plots showing the measured AO-cell response before, during and after an ion beam exposure #a20. The dashed lines indicate the duration of the ion beam. Refer to Table A-3 for the precise beam location. The upper plot shows the power of the diffracted and zero order laser beam exiting the AO-cell and the center plot shows the temperature of the crystal face being struck by the ion beam as well as the temperature of the heat sink. The bottom plot shows the calculated diffraction efficiency.

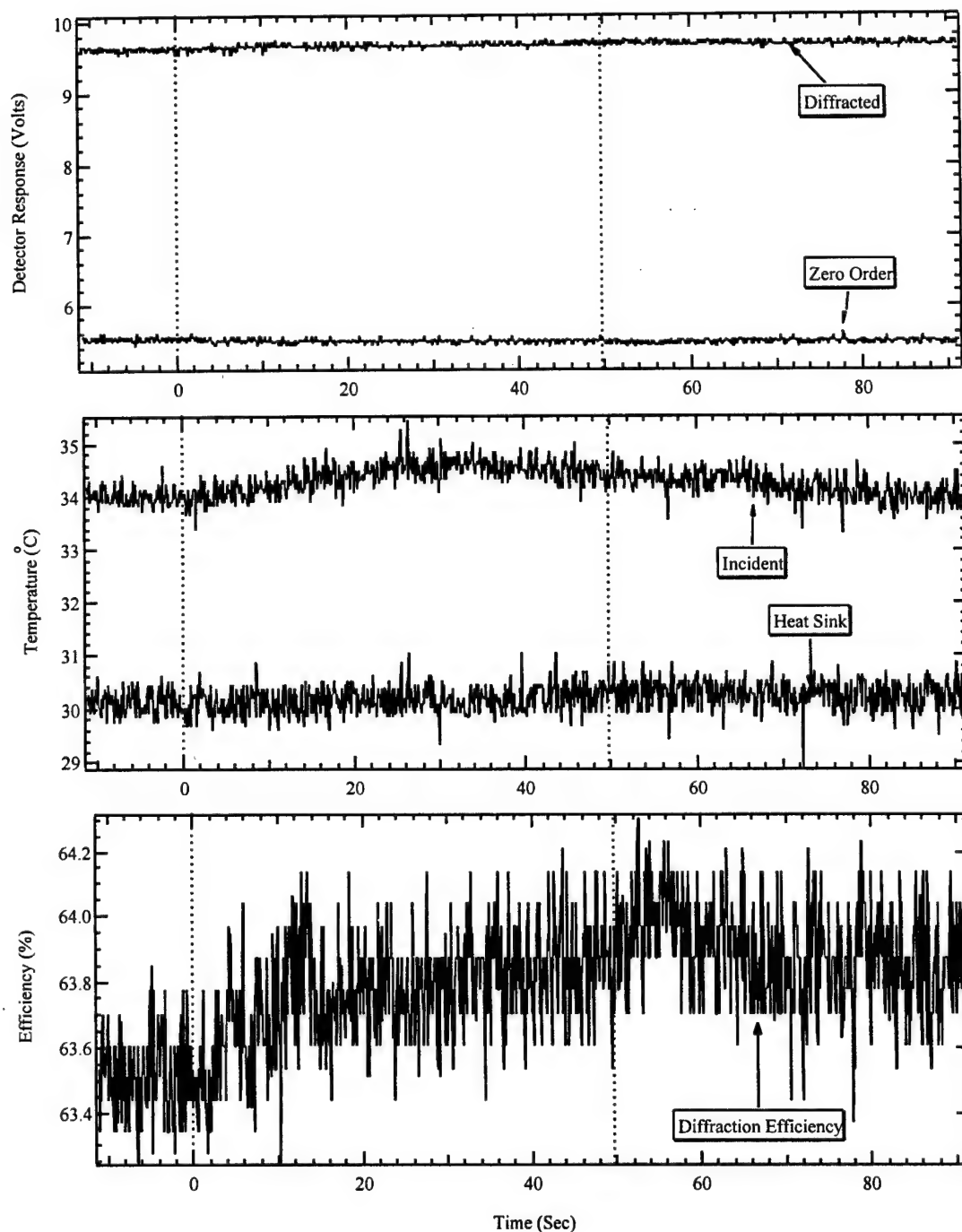


Figure A-80. Three plots showing the measured AO-cell response before, during and after an ion beam exposure #a21. The dashed lines indicate the duration of the ion beam. Refer to Table A-3 for the precise beam location. The upper plot shows the power of the diffracted and zero order laser beam exiting the AO-cell and the center plot shows the temperature of the crystal face being struck by the ion beam as well as the temperature of the heat sink. The bottom plot shows the calculated diffraction efficiency.

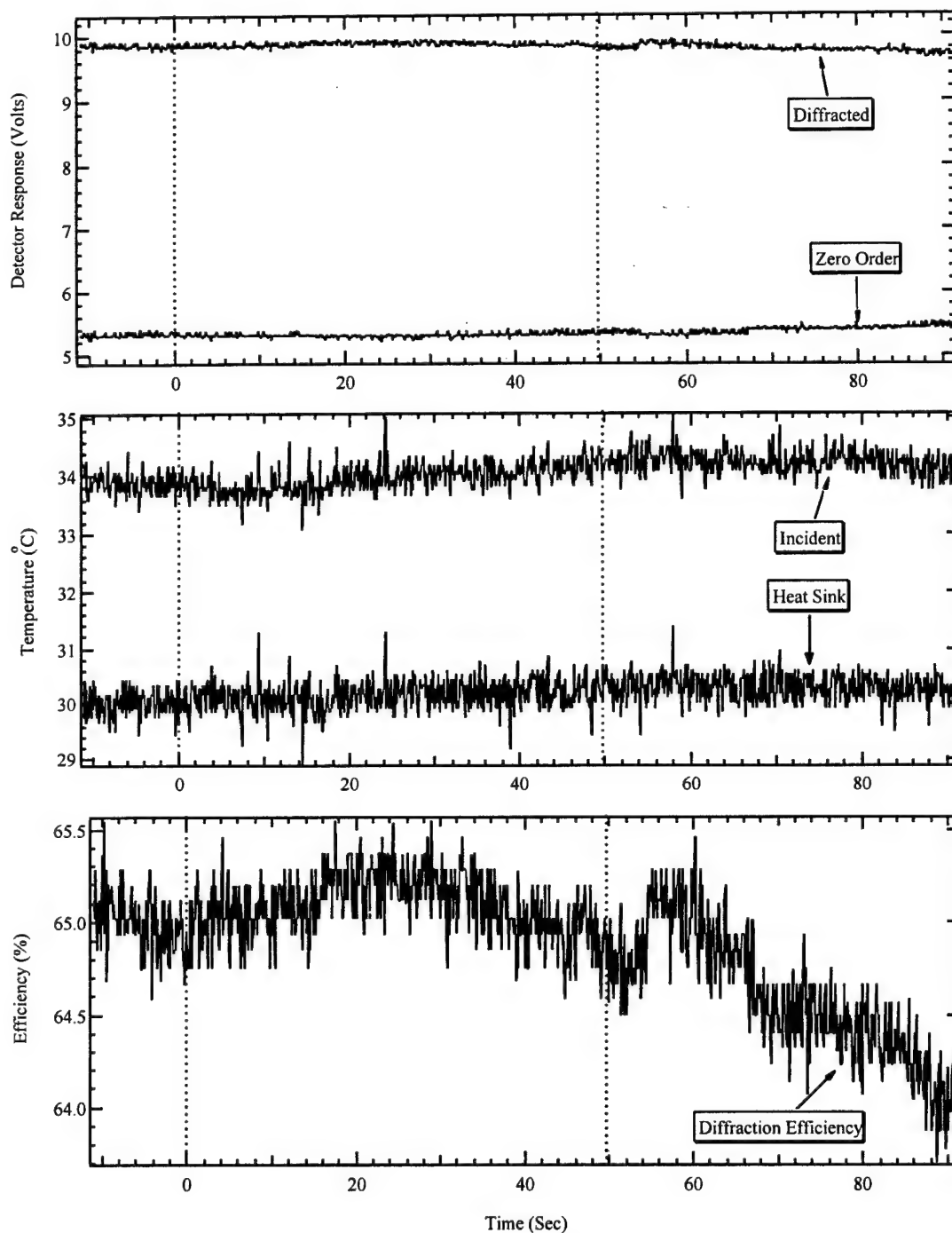


Figure A-81. Three plots showing the measured AO-cell response before, during and after an ion beam exposure #a22. The dashed lines indicate the duration of the ion beam. Refer to Table A-3 for the precise beam location. The upper plot shows the power of the diffracted and zero order laser beam exiting the AO-cell and the center plot shows the temperature of the crystal face being struck by the ion beam as well as the temperature of the heat sink. The bottom plot shows the calculated diffraction efficiency.

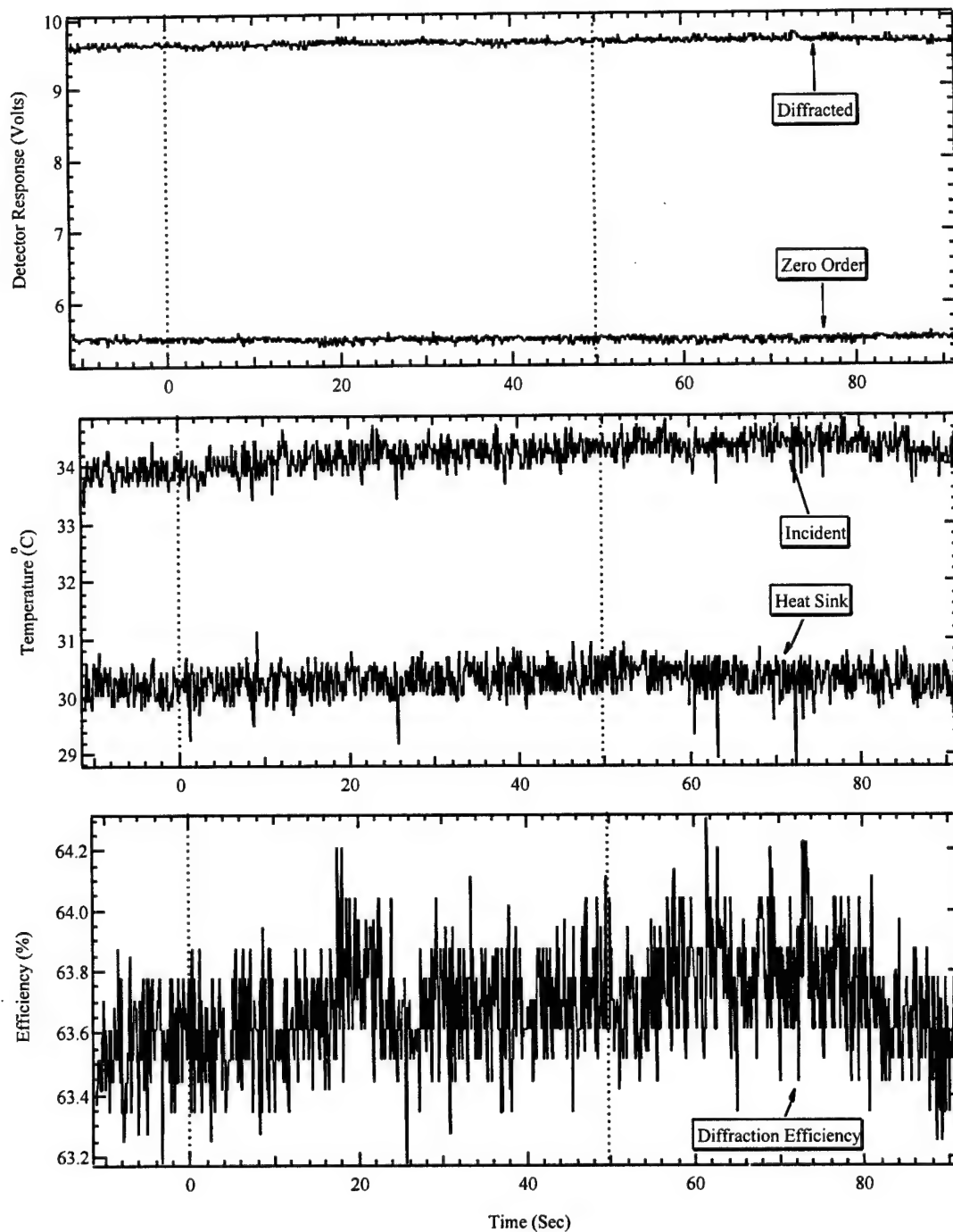


Figure A-82. Three plots showing the measured AO-cell response before, during and after an ion beam exposure #a23. The dashed lines indicate the duration of the ion beam. Refer to Table A-3 for the precise beam location. The upper plot shows the power of the diffracted and zero order laser beam exiting the AO-cell and the center plot shows the temperature of the crystal face being struck by the ion beam as well as the temperature of the heat sink. The bottom plot shows the calculated diffraction efficiency.

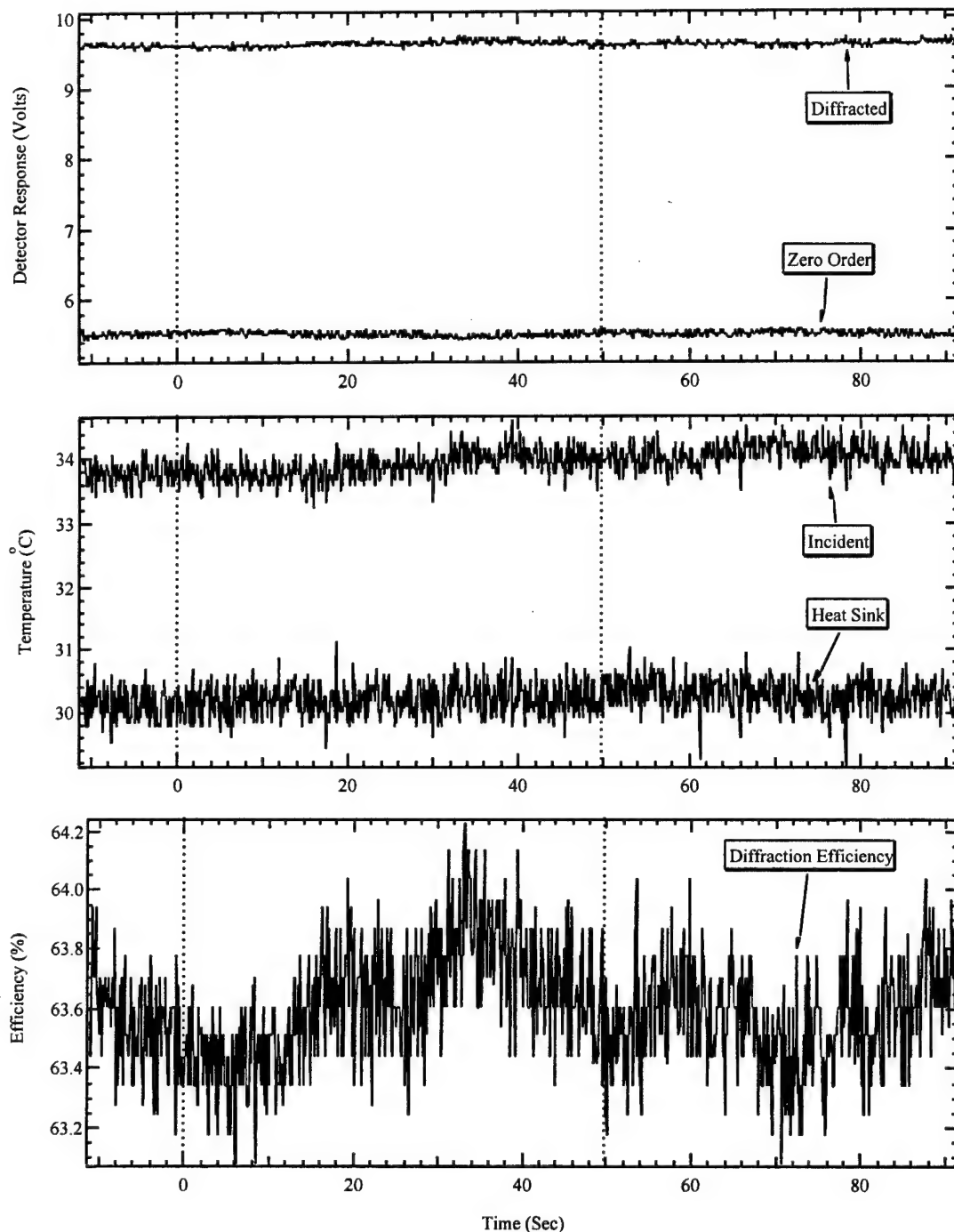


Figure A-83. Three plots showing the measured AO-cell response before, during and after an ion beam exposure #a24. The dashed lines indicate the duration of the ion beam. Refer to Table A-3 for the precise beam location. The upper plot shows the power of the diffracted and zero order laser beam exiting the AO-cell and the center plot shows the temperature of the crystal face being struck by the ion beam as well as the temperature of the heat sink. The bottom plot shows the calculated diffraction efficiency.

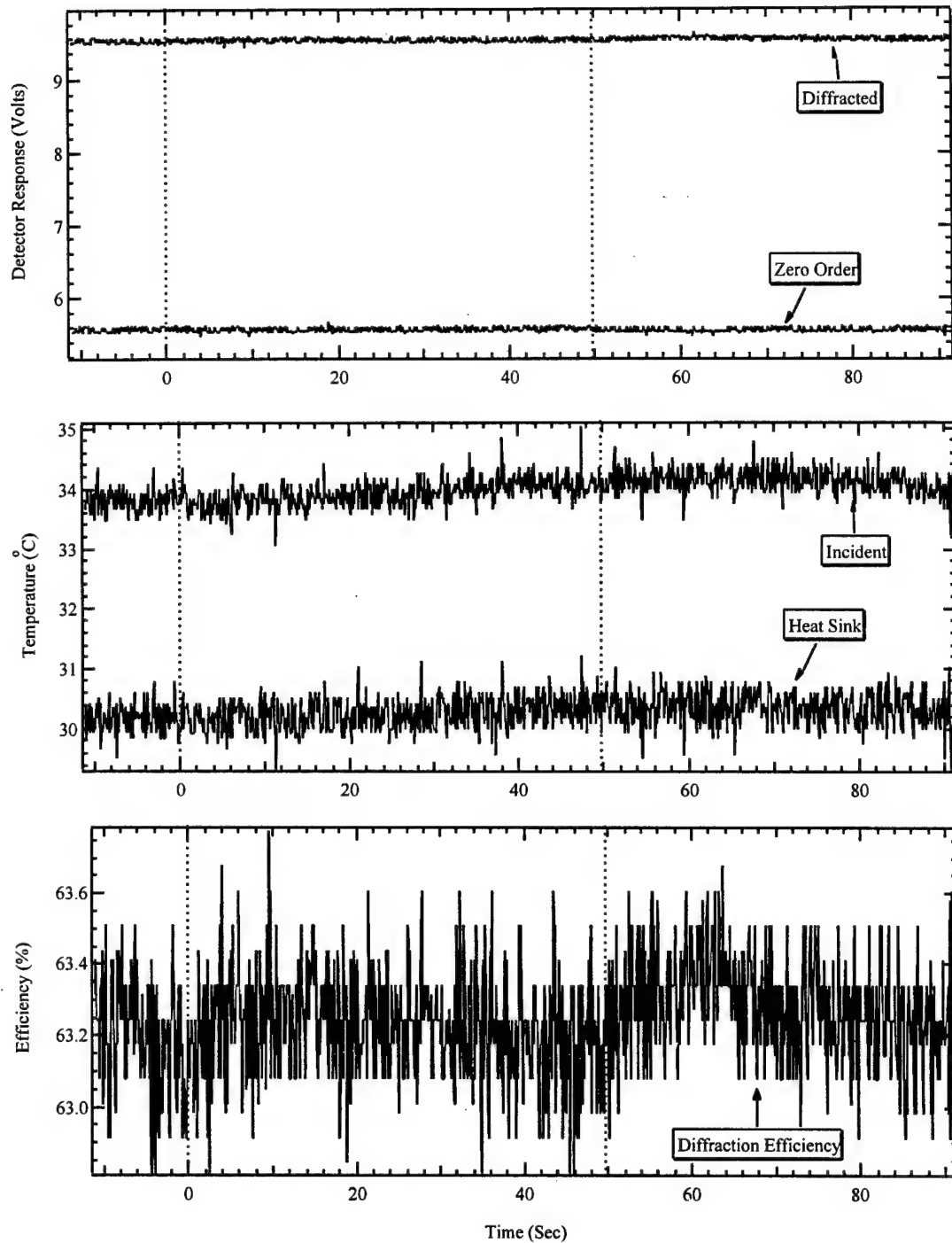


Figure A-84. Three plots showing the measured AO-cell response before, during and after an ion beam exposure #a25. The dashed lines indicate the duration of the ion beam. Refer to Table A-3 for the precise beam location. The upper plot shows the power of the diffracted and zero order laser beam exiting the AO-cell and the center plot shows the temperature of the crystal face being struck by the ion beam as well as the temperature of the heat sink. The bottom plot shows the calculated diffraction efficiency.

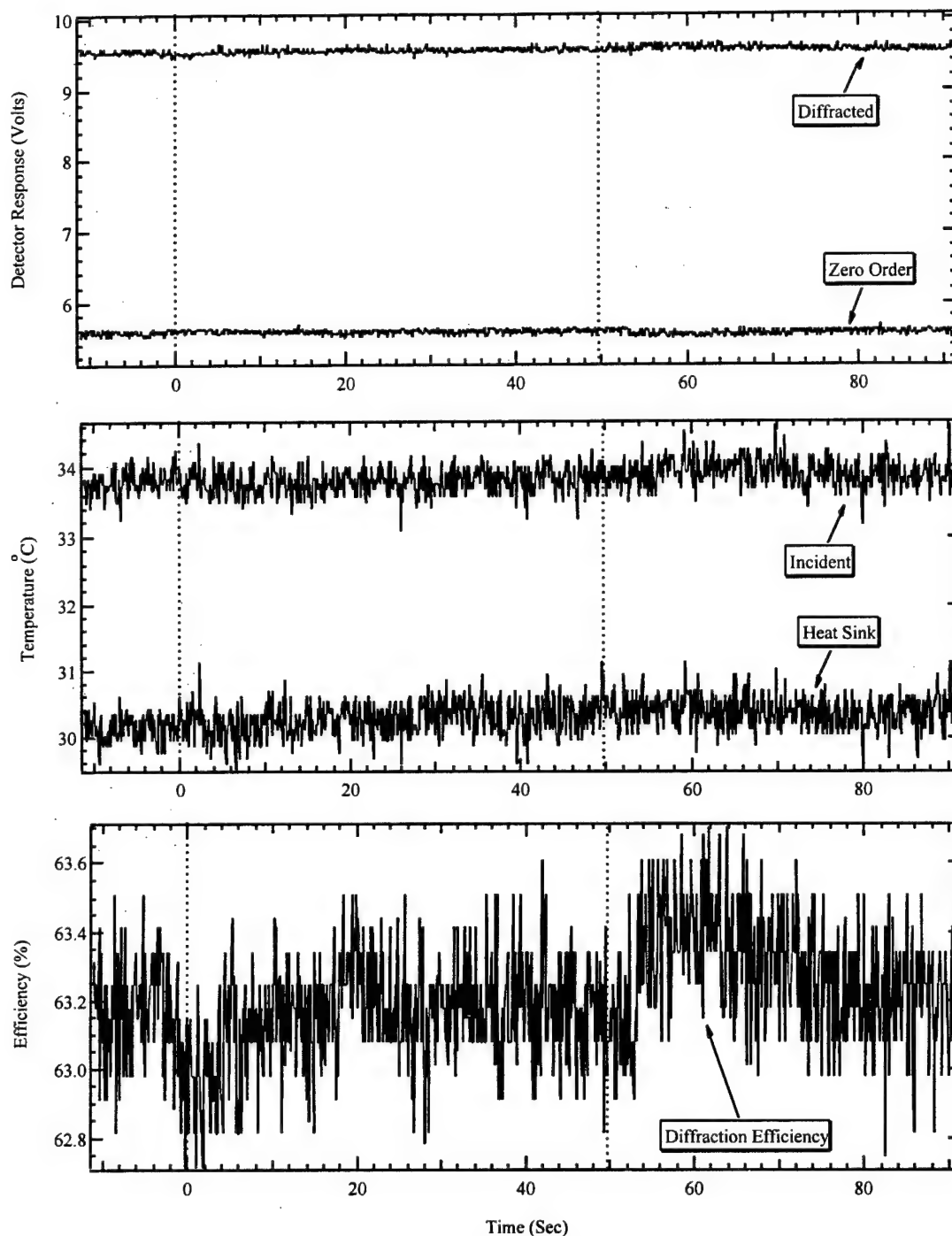


Figure A-85. Three plots showing the measured AO-cell response before, during and after an ion beam exposure #a26. The dashed lines indicate the duration of the ion beam. Refer to Table A-3 for the precise beam location. The upper plot shows the power of the diffracted and zero order laser beam exiting the AO-cell and the center plot shows the temperature of the crystal face being struck by the ion beam as well as the temperature of the heat sink. The bottom plot shows the calculated diffraction efficiency.

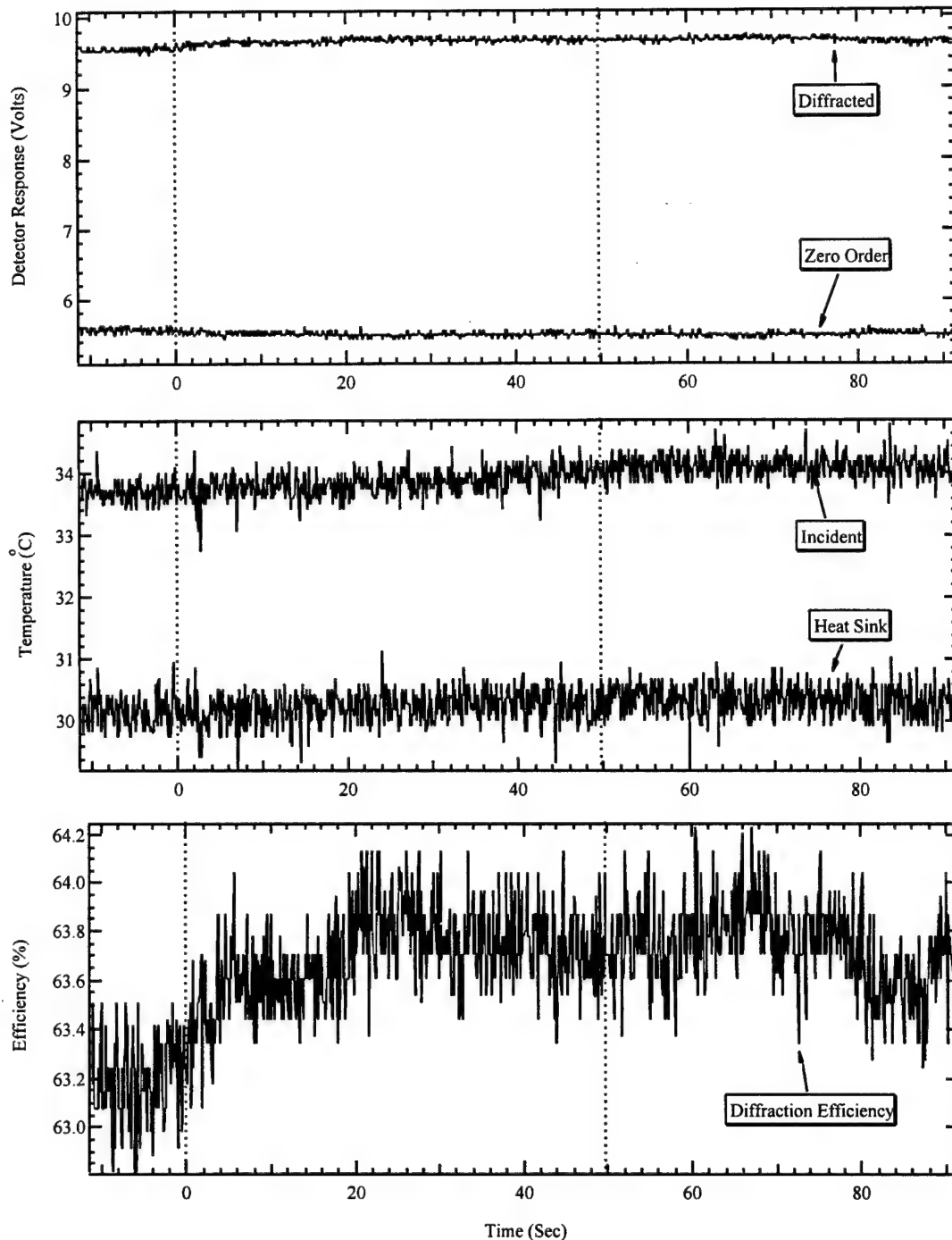


Figure A-86. Three plots showing the measured AO-cell response before, during and after an ion beam exposure #a27. The dashed lines indicate the duration of the ion beam. Refer to Table A-3 for the precise beam location. The upper plot shows the power of the diffracted and zero order laser beam exiting the AO-cell and the center plot shows the temperature of the crystal face being struck by the ion beam as well as the temperature of the heat sink. The bottom plot shows the calculated diffraction efficiency.

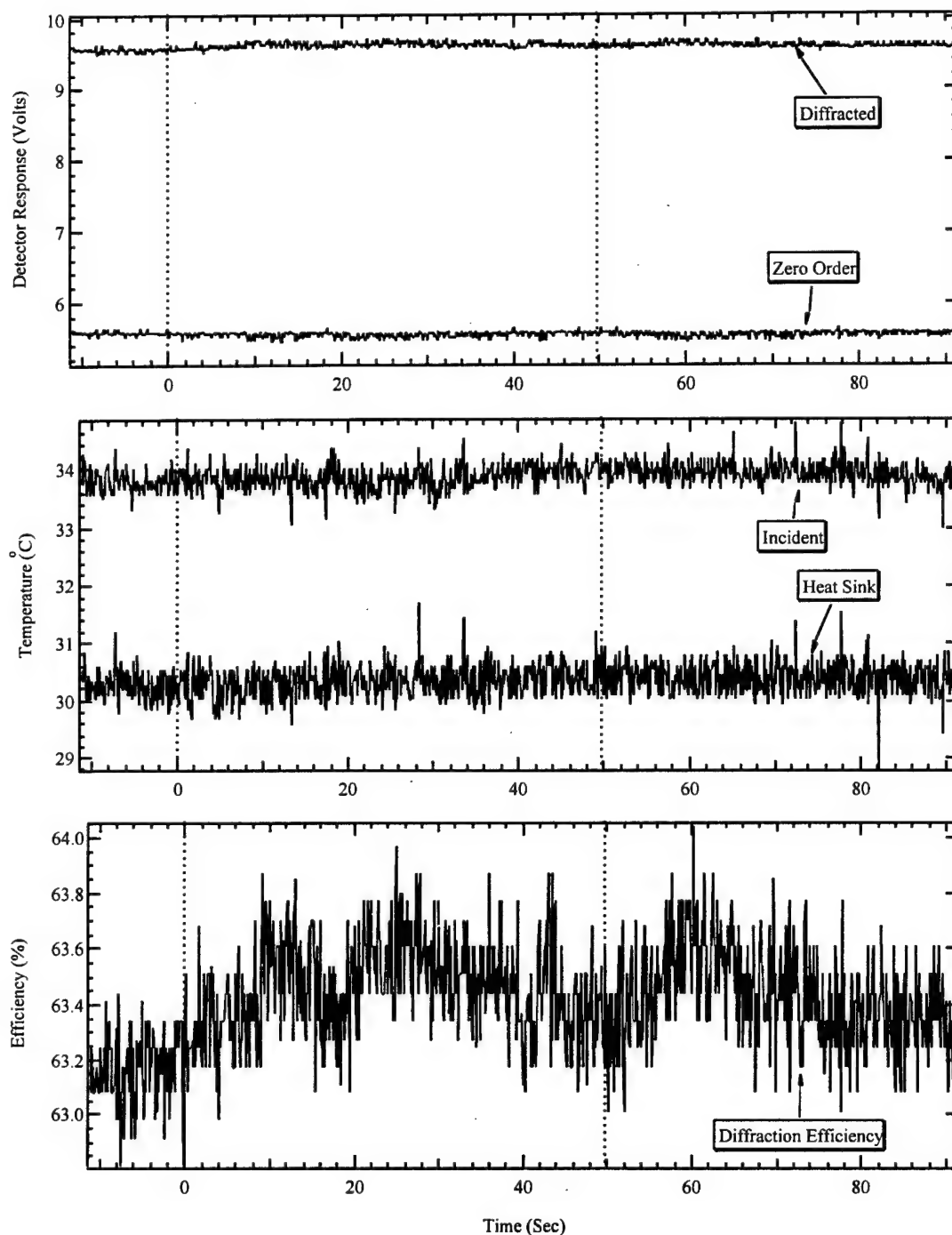


Figure A-87. Three plots showing the measured AO-cell response before, during and after an ion beam exposure #a28. The dashed lines indicate the duration of the ion beam. Refer to Table A-3 for the precise beam location. The upper plot shows the power of the diffracted and zero order laser beam exiting the AO-cell and the center plot shows the temperature of the crystal face being struck by the ion beam as well as the temperature of the heat sink. The bottom plot shows the calculated diffraction efficiency.

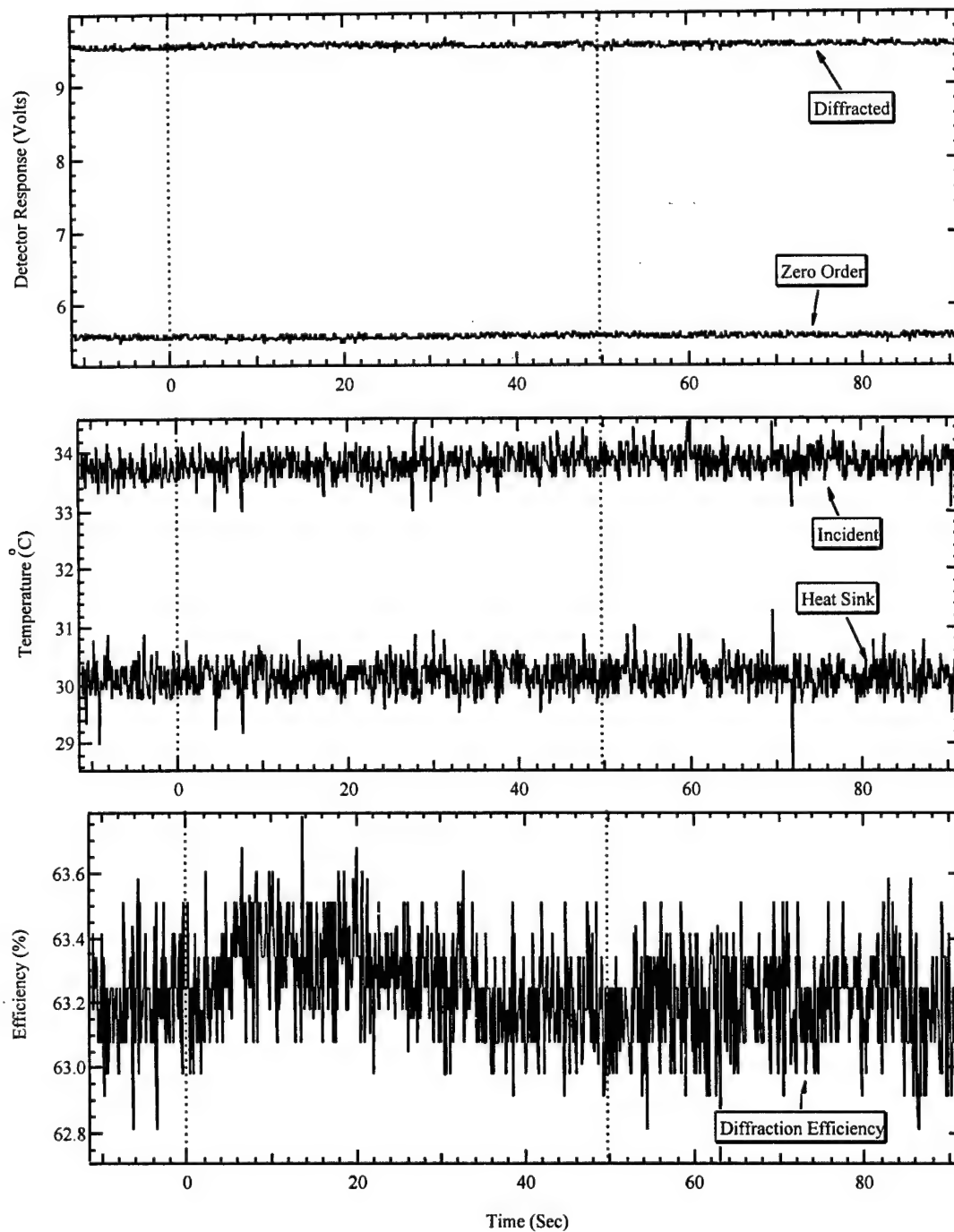


Figure A-88. Three plots showing the measured AO-cell response before, during and after an ion beam exposure #a29. The dashed lines indicate the duration of the ion beam. Refer to Table A-3 for the precise beam location. The upper plot shows the power of the diffracted and zero order laser beam exiting the AO-cell and the center plot shows the temperature of the crystal face being struck by the ion beam as well as the temperature of the heat sink. The bottom plot shows the calculated diffraction efficiency.

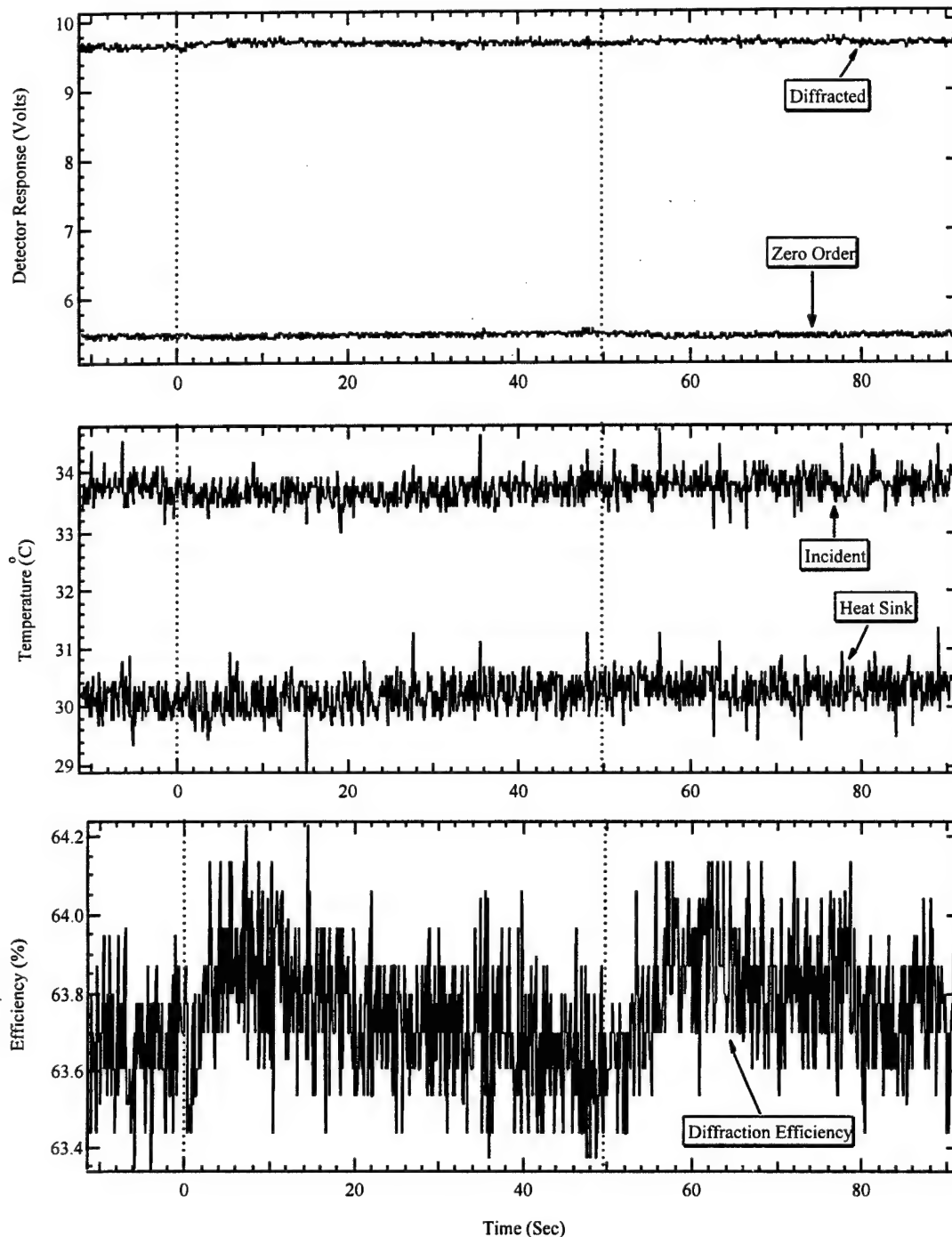


Figure A-89. Three plots showing the measured AO-cell response before, during and after an ion beam exposure #a30. The dashed lines indicate the duration of the ion beam. Refer to Table A-3 for the precise beam location. The upper plot shows the power of the diffracted and zero order laser beam exiting the AO-cell and the center plot shows the temperature of the crystal face being struck by the ion beam as well as the temperature of the heat sink. The bottom plot shows the calculated diffraction efficiency.

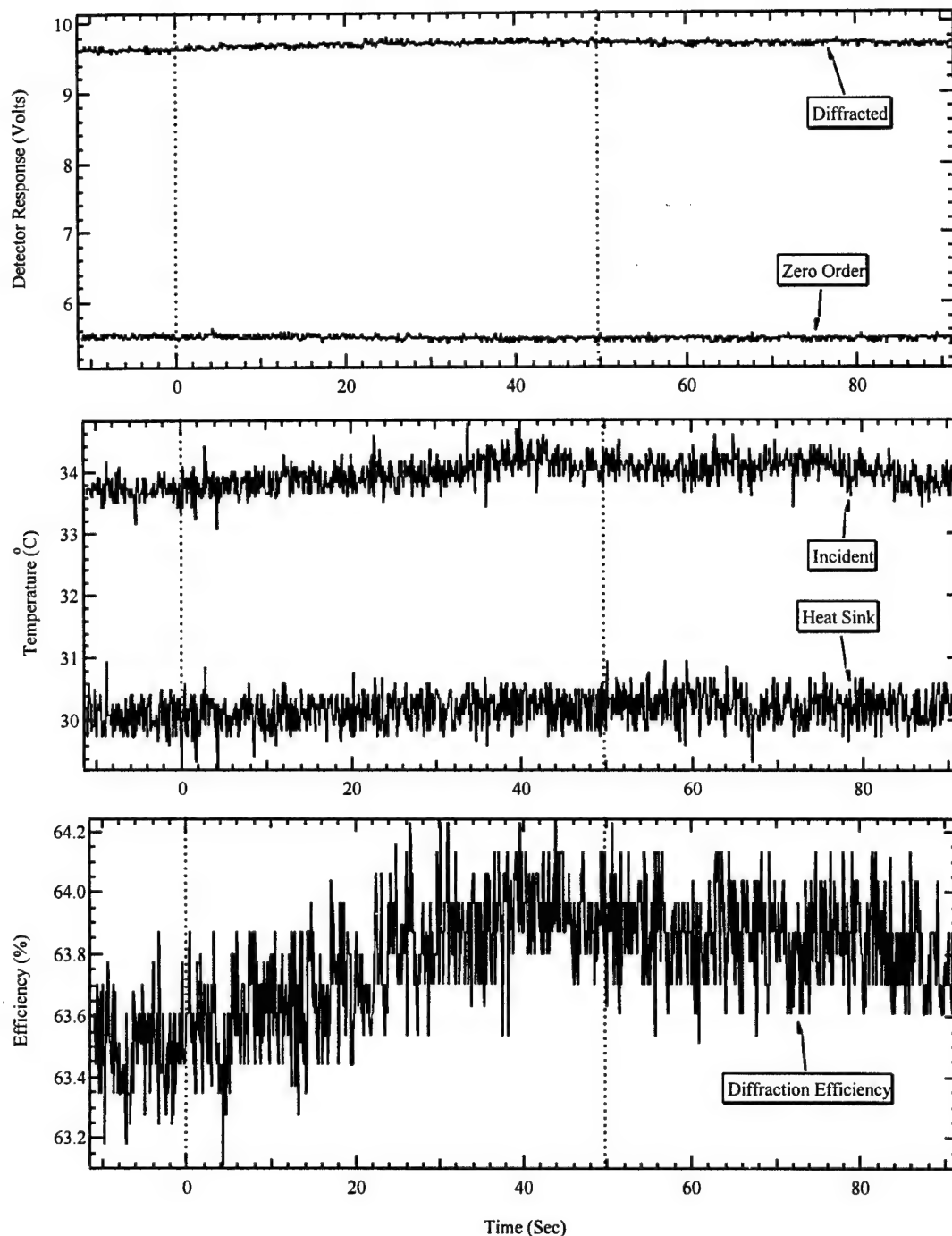


Figure A-90. Three plots showing the measured AO-cell response before, during and after an ion beam exposure #a31. The dashed lines indicate the duration of the ion beam. Refer to Table A-3 for the precise beam location. The upper plot shows the power of the diffracted and zero order laser beam exiting the AO-cell and the center plot shows the temperature of the crystal face being struck by the ion beam as well as the temperature of the heat sink. The bottom plot shows the calculated diffraction efficiency.

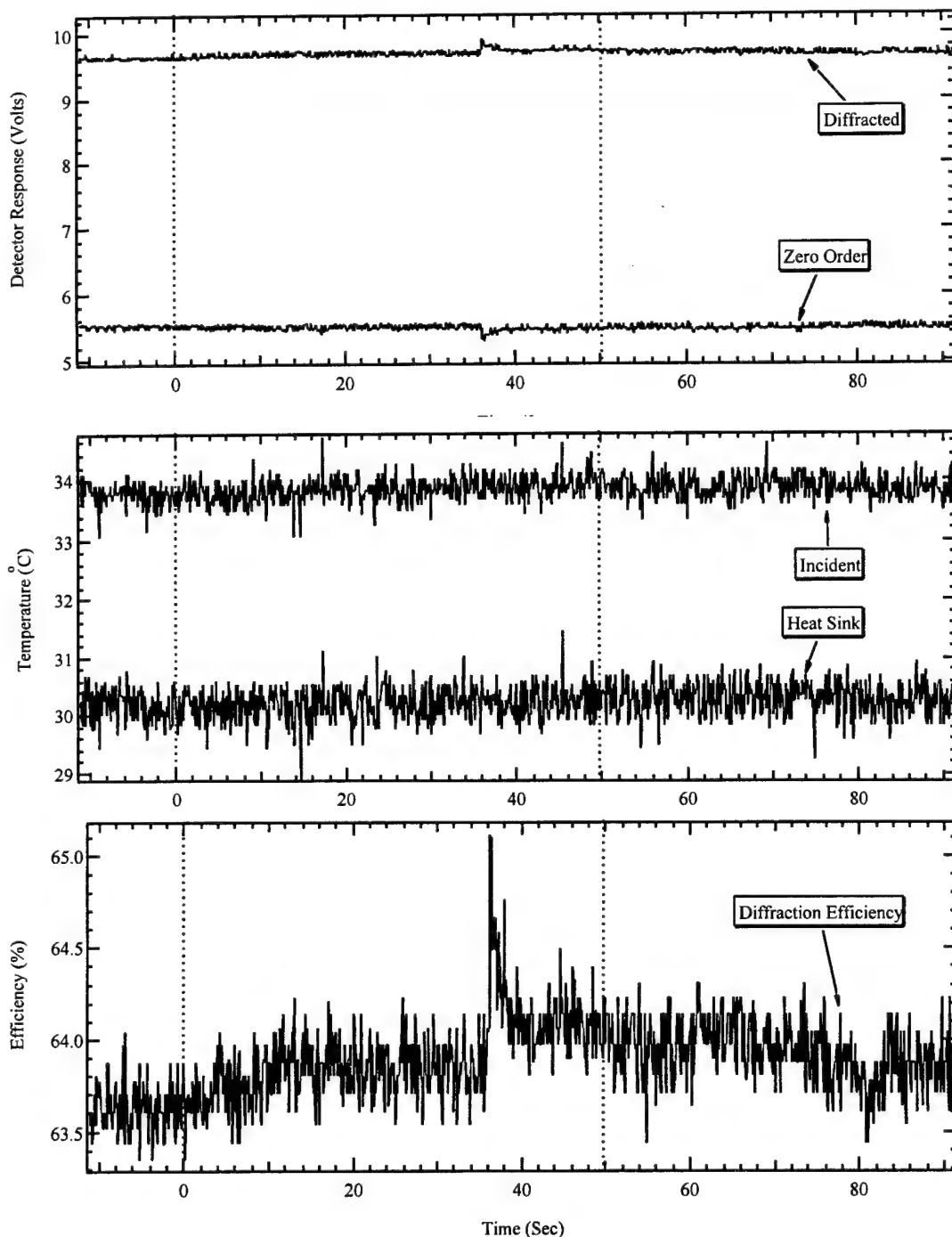


Figure A-91. Three plots showing the measured AO-cell response before, during and after an ion beam exposure #a32. The dashed lines indicate the duration of the ion beam. Refer to Table A-3 for the precise beam location. The upper plot shows the power of the diffracted and zero order laser beam exiting the AO-cell and the center plot shows the temperature of the crystal face being struck by the ion beam as well as the temperature of the heat sink. The bottom plot shows the calculated diffraction efficiency.

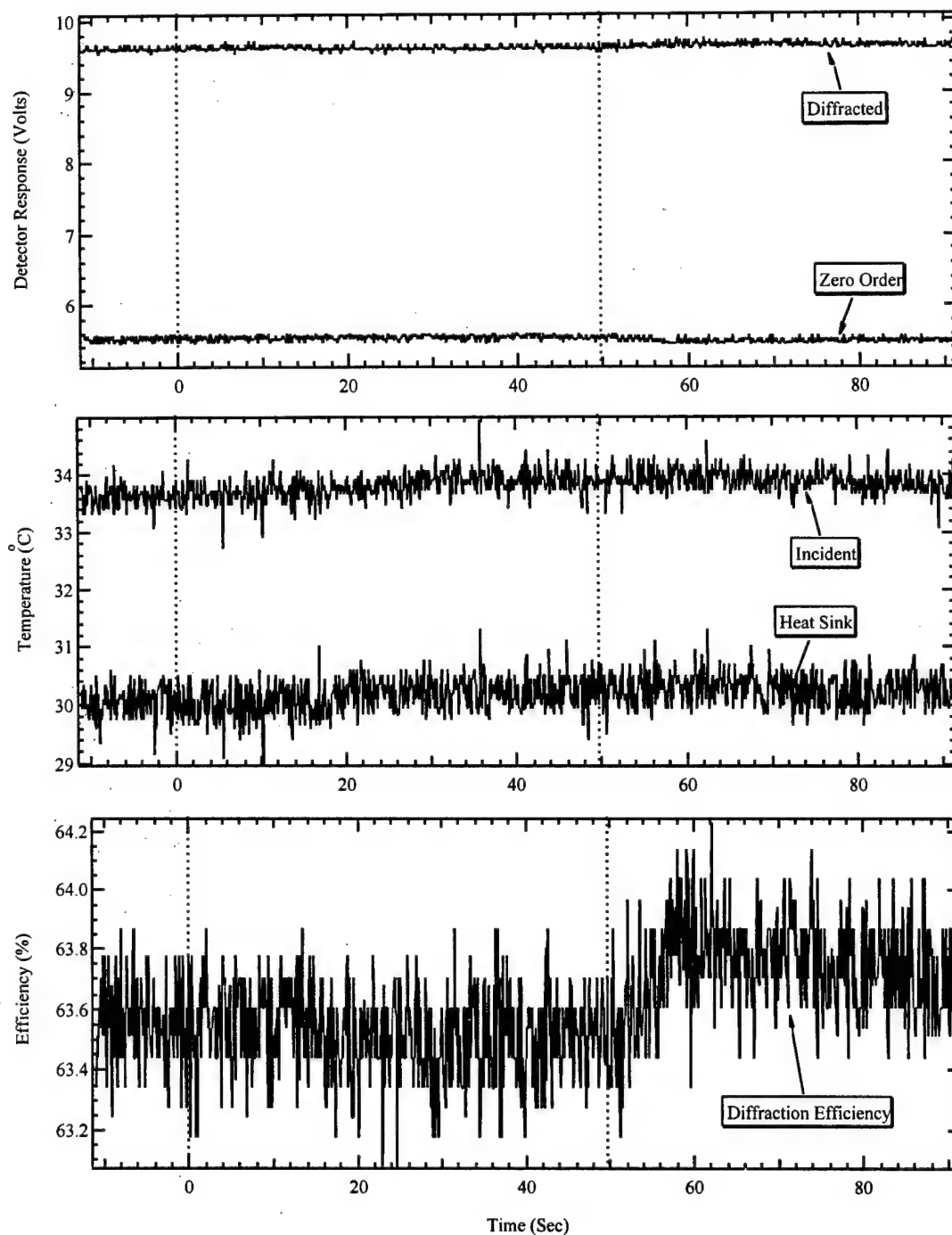


Figure A-92. Three plots showing the measured AO-cell response before, during and after an ion beam exposure #a33. The dashed lines indicate the duration of the ion beam. Refer to Table A-3 for the precise beam location. The upper plot shows the power of the diffracted and zero order laser beam exiting the AO-cell and the center plot shows the temperature of the crystal face being struck by the ion beam as well as the temperature of the heat sink. The bottom plot shows the calculated diffraction efficiency.

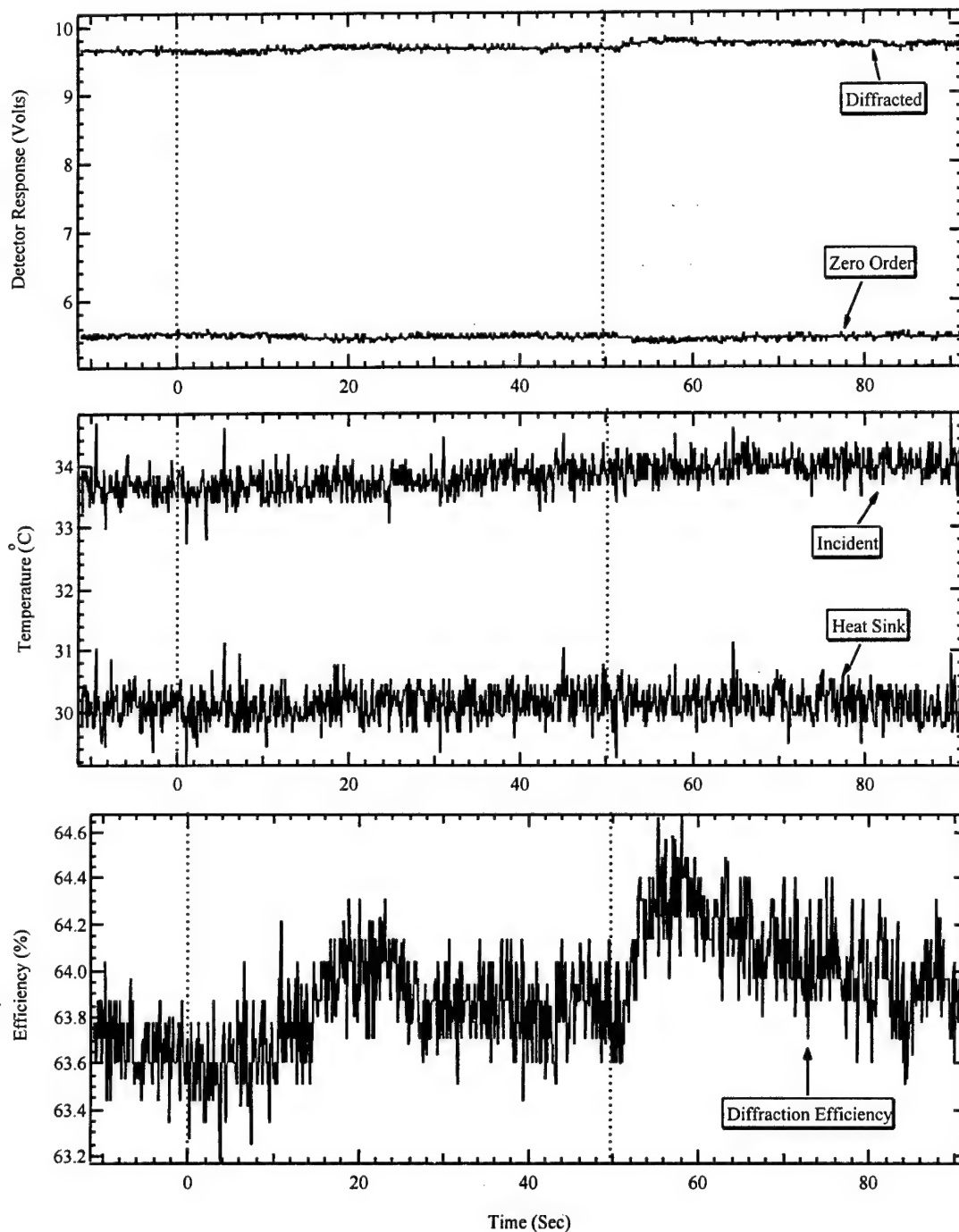


Figure A-93. Three plots showing the measured AO-cell response before, during and after an ion beam exposure #a35. The dashed lines indicate the duration of the ion beam. Refer to Table A-3 for the precise beam location. The upper plot shows the power of the diffracted and zero order laser beam exiting the AO-cell and the center plot shows the temperature of the crystal face being struck by the ion beam as well as the temperature of the heat sink. The bottom plot shows the calculated diffraction efficiency.

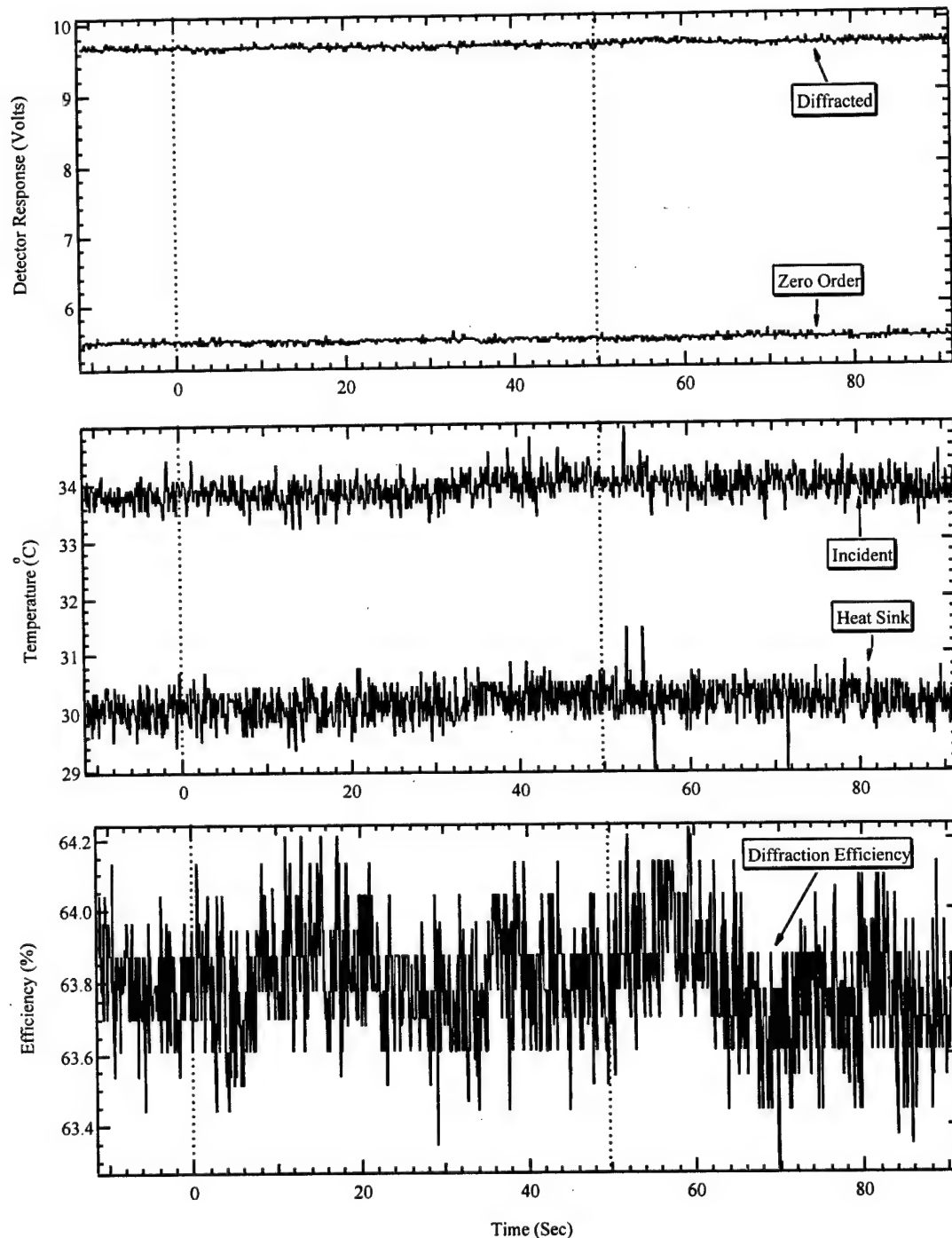


Figure A-94. Three plots showing the measured AO-cell response before, during and after an ion beam exposure #a36. The dashed lines indicate the duration of the ion beam. Refer to Table A-3 for the precise beam location. The upper plot shows the power of the diffracted and zero order laser beam exiting the AO-cell and the center plot shows the temperature of the crystal face being struck by the ion beam as well as the temperature of the heat sink. The bottom plot shows the calculated diffraction efficiency.

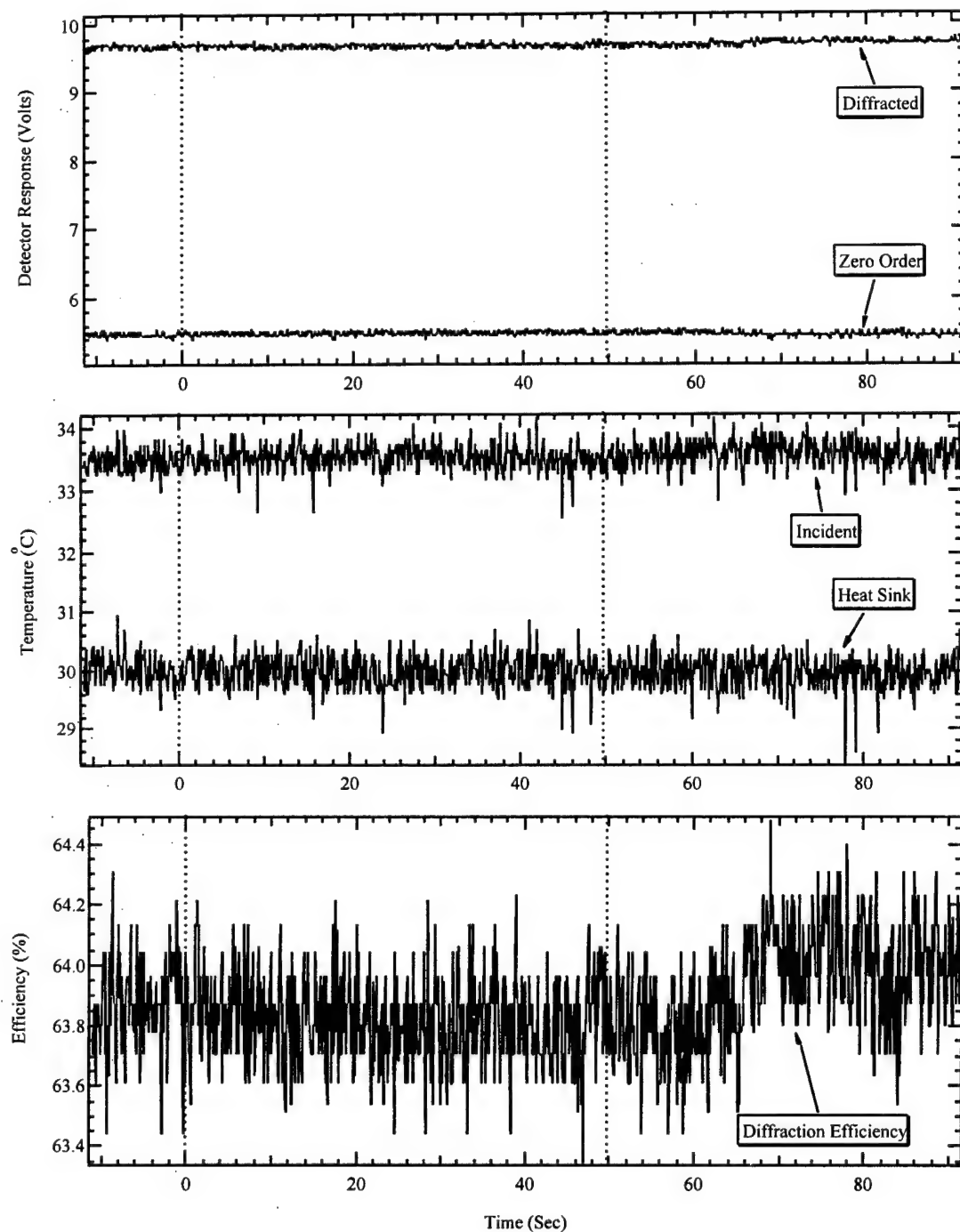


Figure A-95. Three plots showing the measured AO-cell response before, during and after an ion beam exposure #a37. The dashed lines indicate the duration of the ion beam. Refer to Table A-3 for the precise beam location. The upper plot shows the power of the diffracted and zero order laser beam exiting the AO-cell and the center plot shows the temperature of the crystal face being struck by the ion beam as well as the temperature of the heat sink. The bottom plot shows the calculated diffraction efficiency.

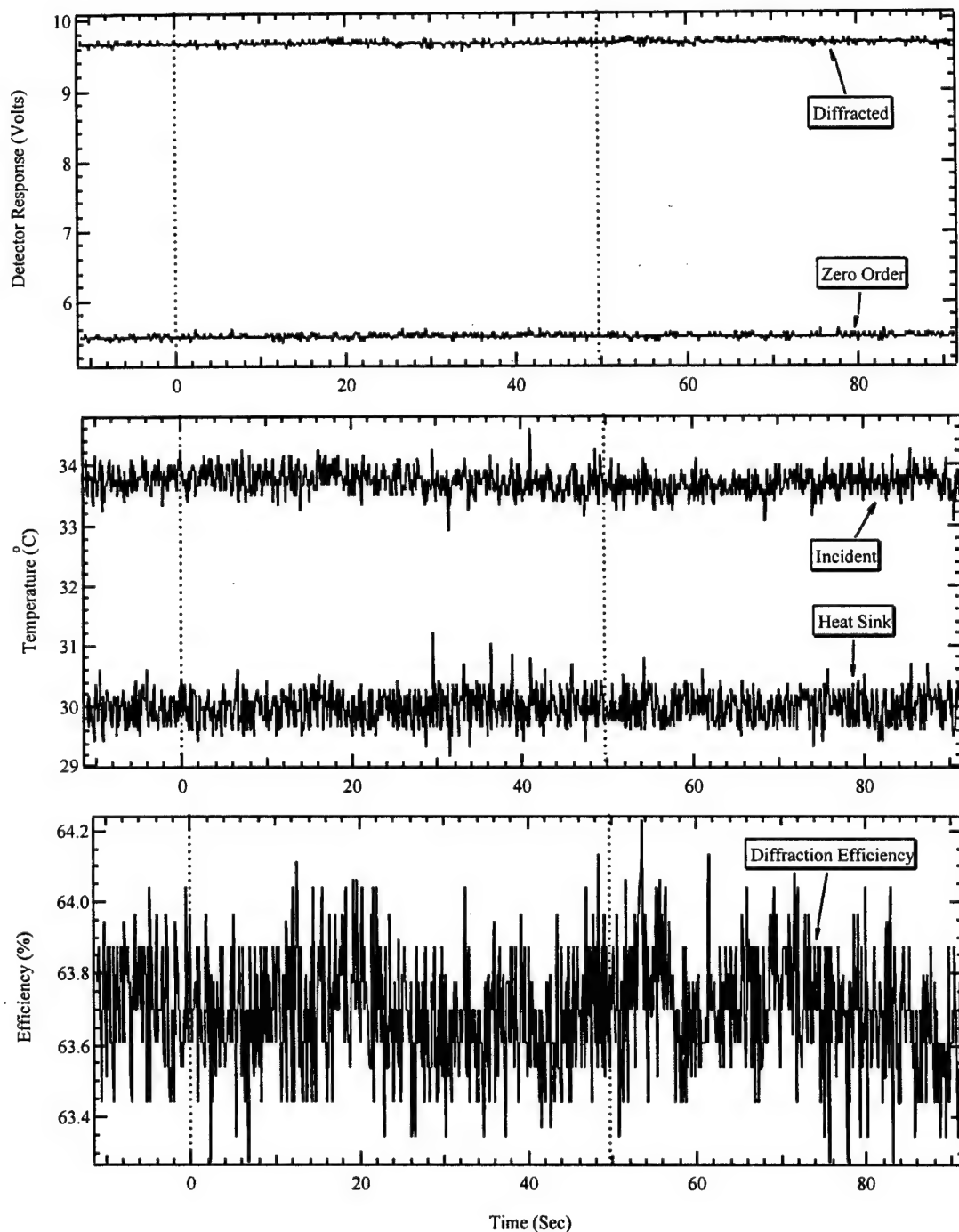


Figure A-96. Three plots showing the measured AO-cell response before, during and after an ion beam exposure #a38. The dashed lines indicate the duration of the ion beam. Refer to Table A-3 for the precise beam location. The upper plot shows the power of the diffracted and zero order laser beam exiting the AO-cell and the center plot shows the temperature of the crystal face being struck by the ion beam as well as the temperature of the heat sink. The bottom plot shows the calculated diffraction efficiency.

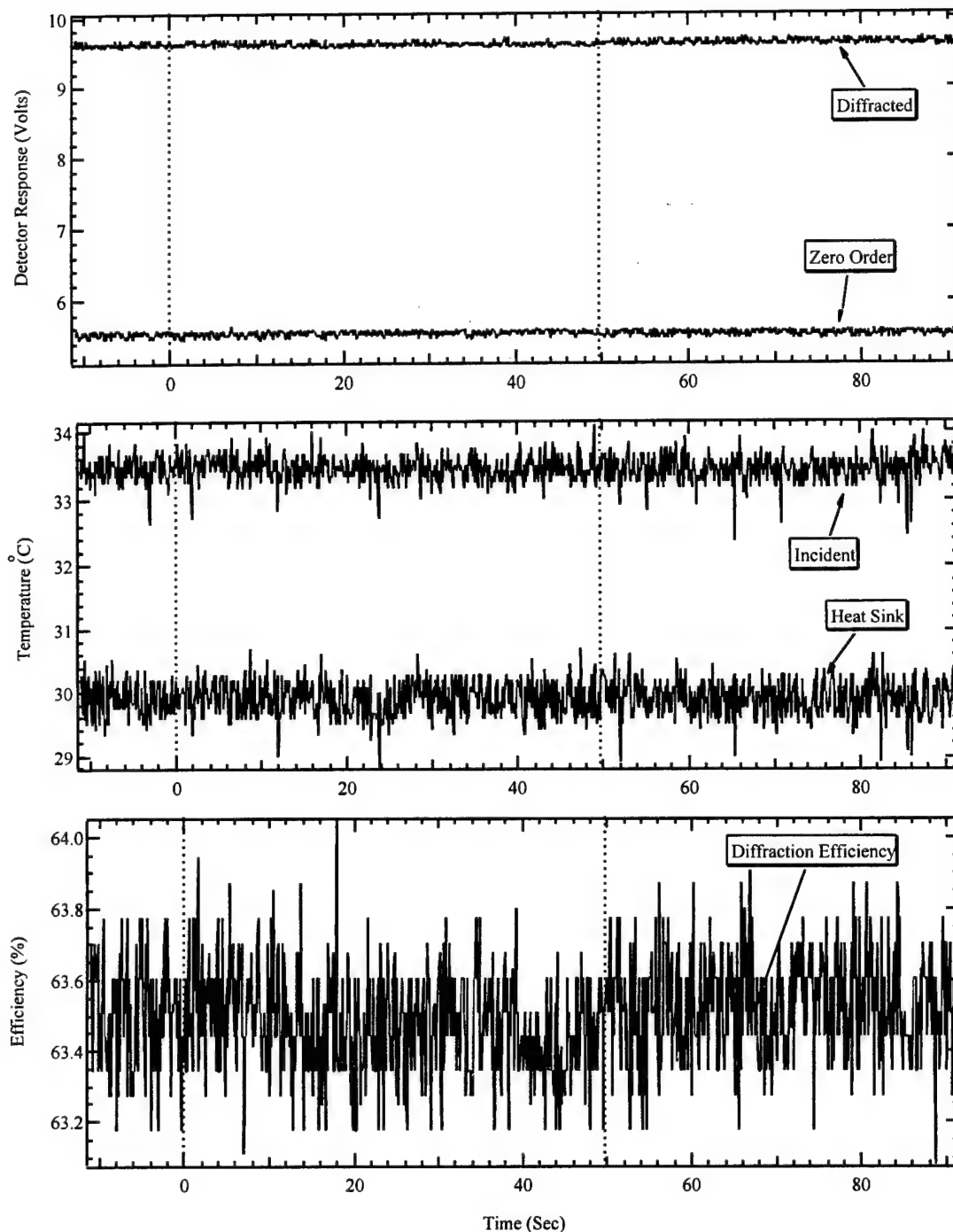


Figure A-97. Three plots showing the measured AO-cell response before, during and after an ion beam exposure #a39. The dashed lines indicate the duration of the ion beam. Refer to Table A-3 for the precise beam location. The upper plot shows the power of the diffracted and zero order laser beam exiting the AO-cell and the center plot shows the temperature of the crystal face being struck by the ion beam as well as the temperature of the heat sink. The bottom plot shows the calculated diffraction efficiency.

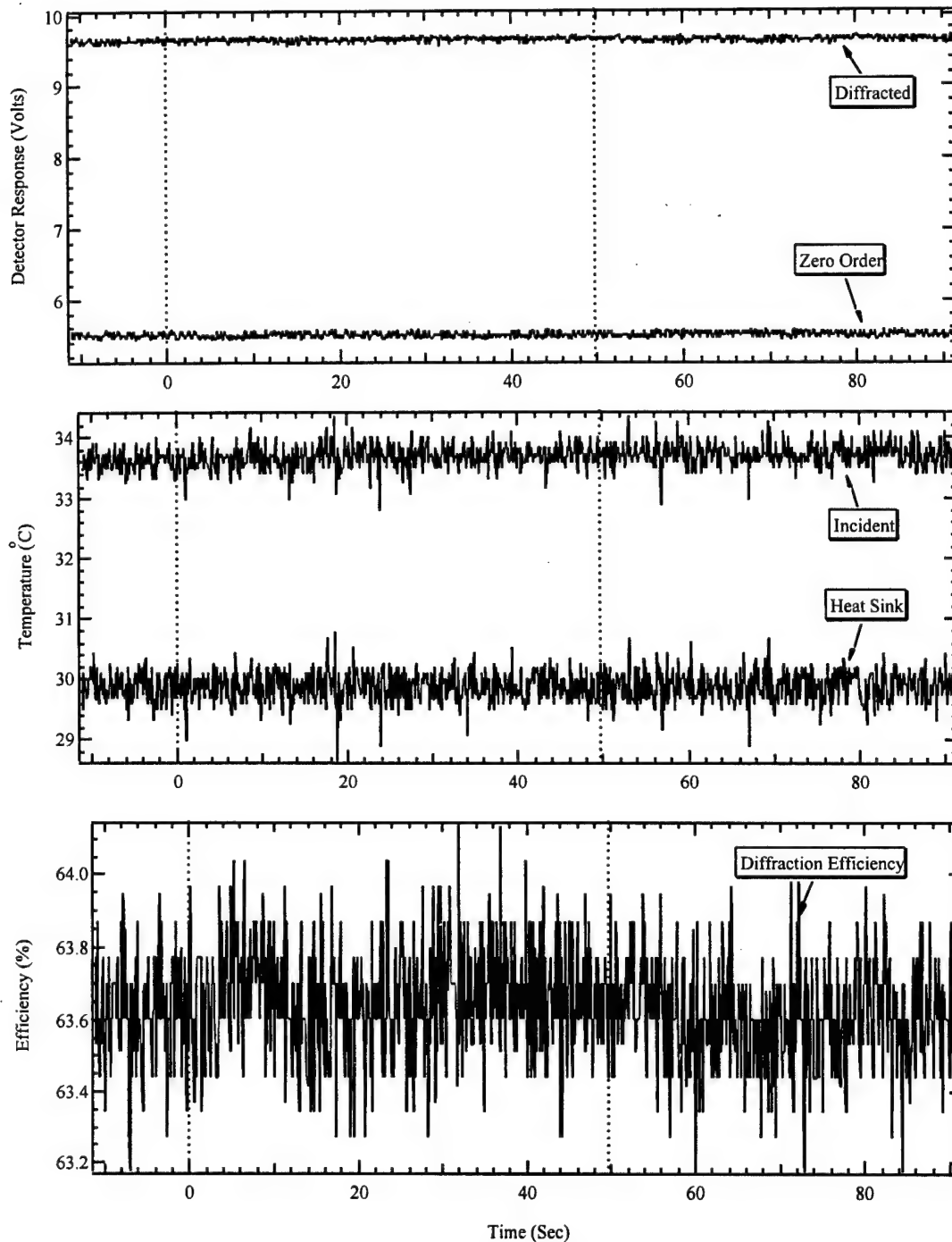


Figure A-98. Three plots showing the measured AO-cell response before, during and after an ion beam exposure #a40. The dashed lines indicate the duration of the ion beam. Refer to Table A-3 for the precise beam location. The upper plot shows the power of the diffracted and zero order laser beam exiting the AO-cell and the center plot shows the temperature of the crystal face being struck by the ion beam as well as the temperature of the heat sink. The bottom plot shows the calculated diffraction efficiency.

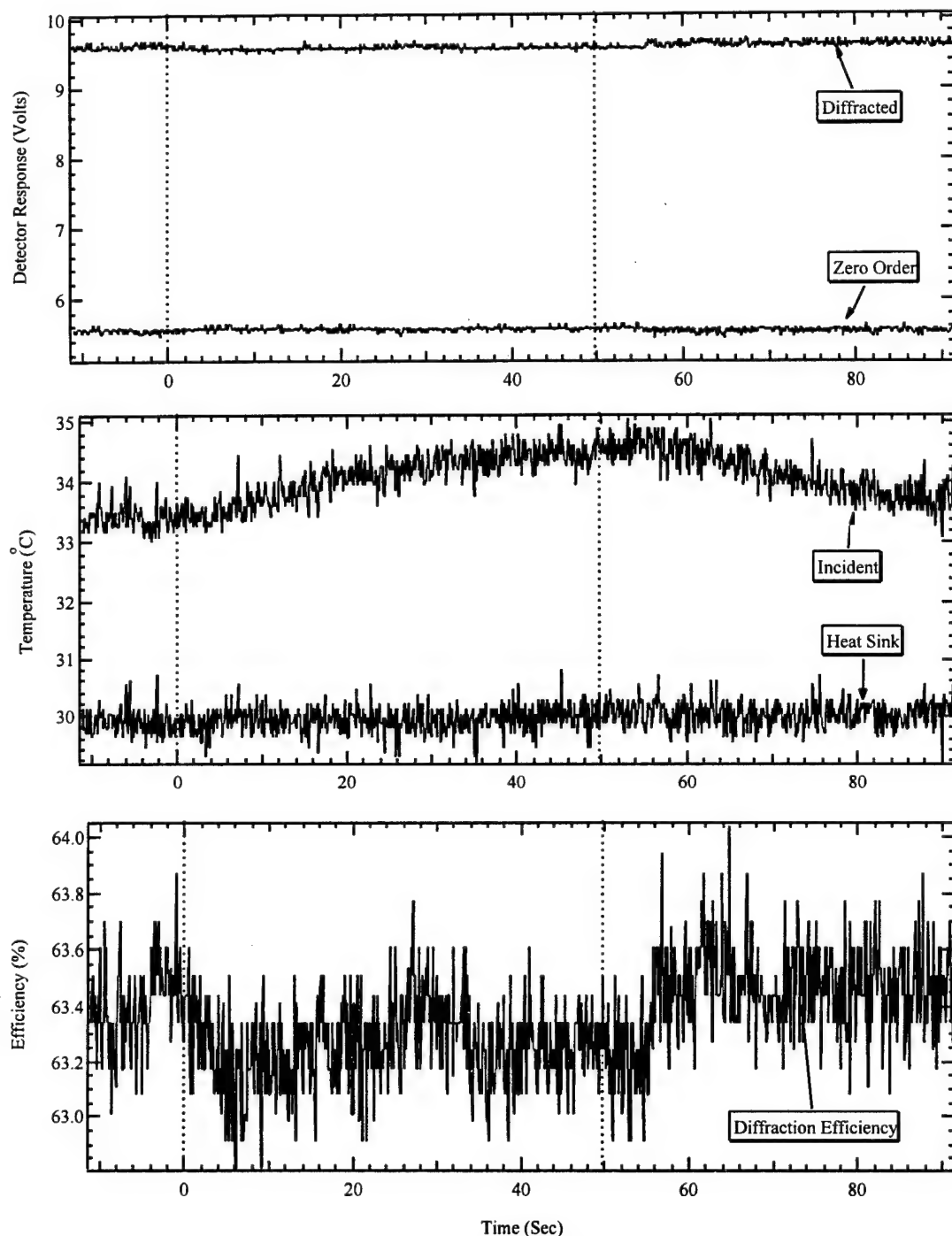


Figure A-99. Three plots showing the measured AO-cell response before, during and after an ion beam exposure #a41. The dashed lines indicate the duration of the ion beam. Refer to Table A-3 for the precise beam location. The upper plot shows the power of the diffracted and zero order laser beam exiting the AO-cell and the center plot shows the temperature of the crystal face being struck by the ion beam as well as the temperature of the heat sink. The bottom plot shows the calculated diffraction efficiency.

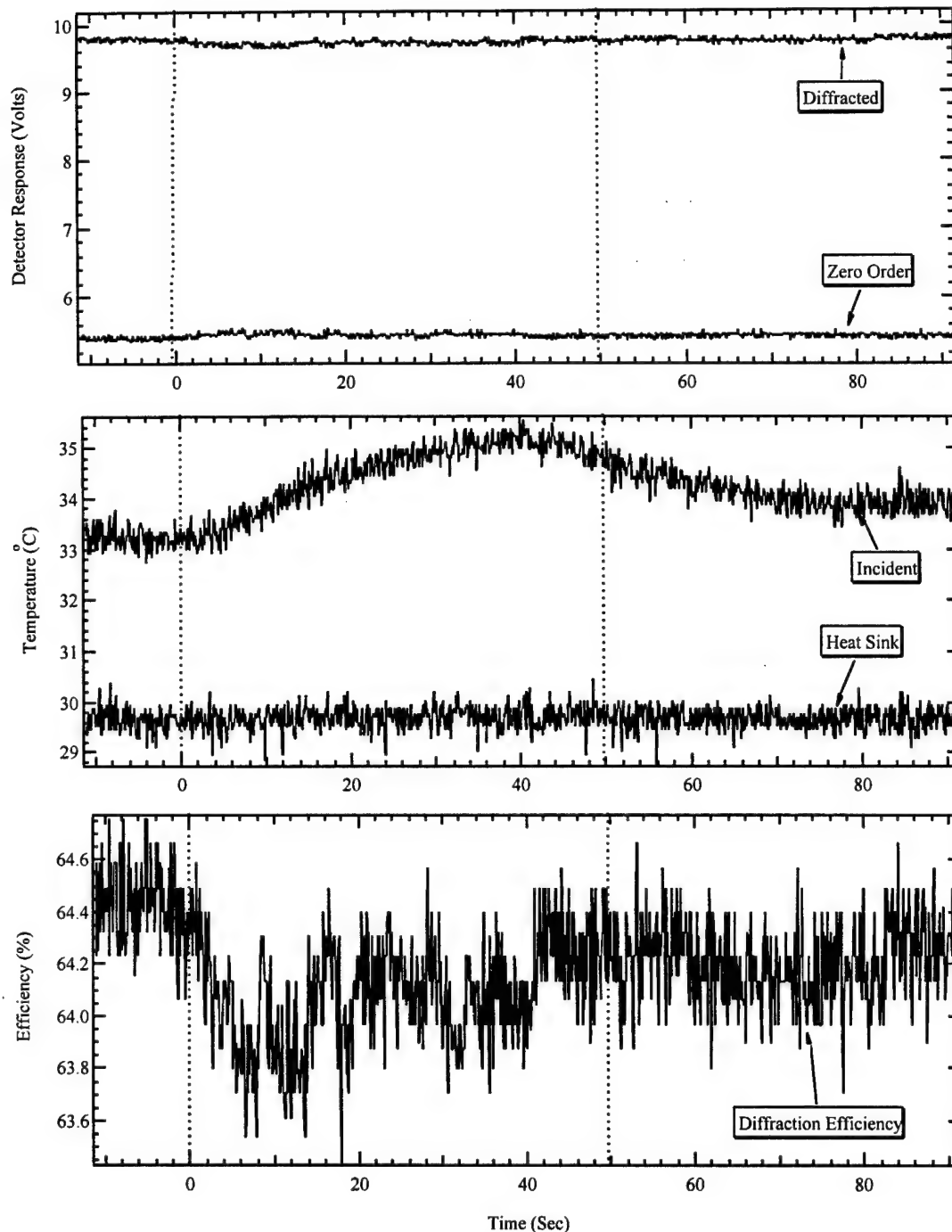


Figure A-100. Three plots showing the measured AO-cell response before, during and after an ion beam exposure #a42. The dashed lines indicate the duration of the ion beam. Refer to Table A-3 for the precise beam location. The upper plot shows the power of the diffracted and zero order laser beam exiting the AO-cell and the center plot shows the temperature of the crystal face being struck by the ion beam as well as the temperature of the heat sink. The bottom plot shows the calculated diffraction efficiency.

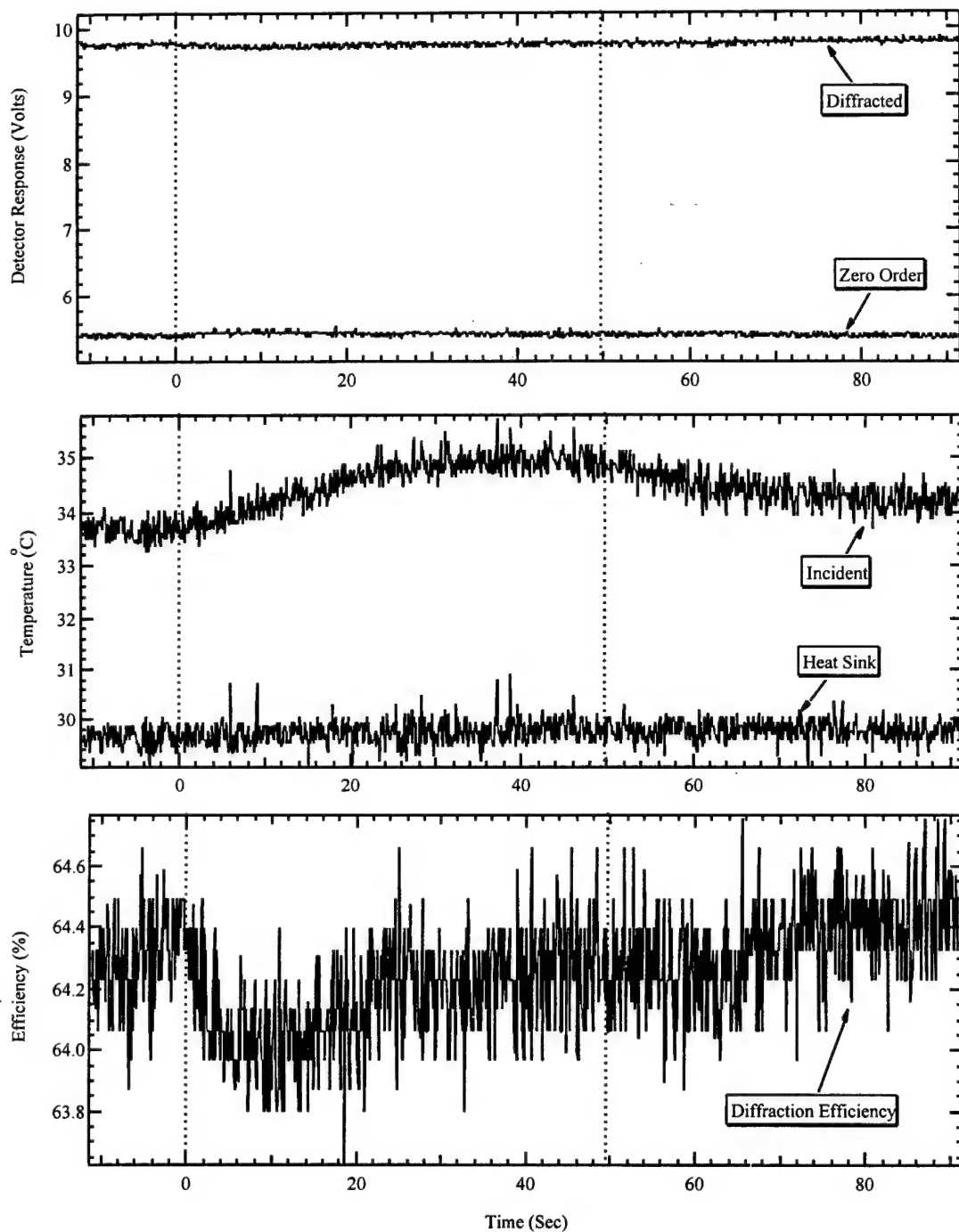


Figure A-101. Three plots showing the measured AO-cell response before, during and after an ion beam exposure #a43. The dashed lines indicate the duration of the ion beam. Refer to Table A-3 for the precise beam location. The upper plot shows the power of the diffracted and zero order laser beam exiting the AO-cell and the center plot shows the temperature of the crystal face being struck by the ion beam as well as the temperature of the heat sink. The bottom plot shows the calculated diffraction efficiency.

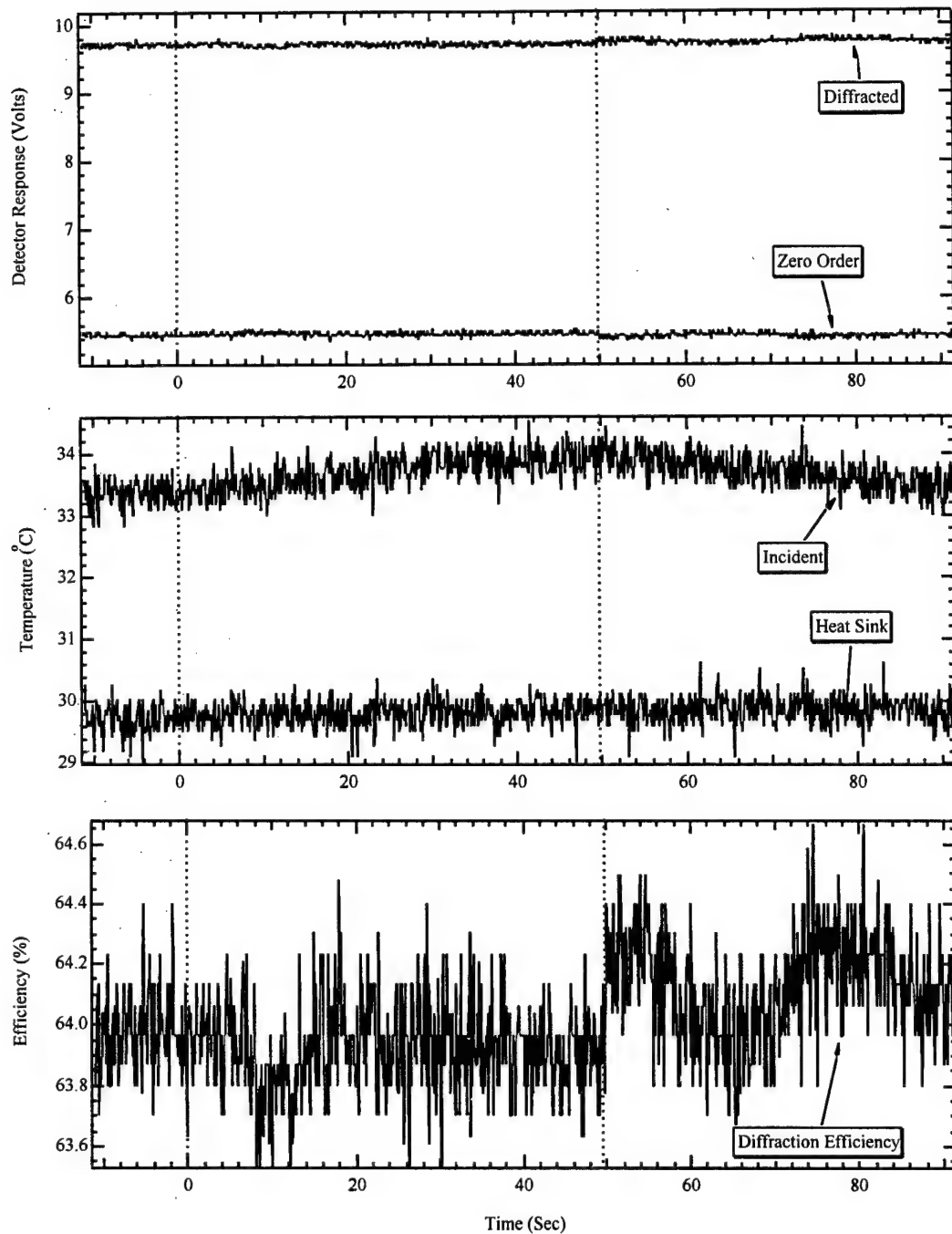


Figure A-102. Three plots showing the measured AO-cell response before, during and after an ion beam exposure #a44. The dashed lines indicate the duration of the ion beam. Refer to Table A-3 for the precise beam location. The upper plot shows the power of the diffracted and zero order laser beam exiting the AO-cell and the center plot shows the temperature of the crystal face being struck by the ion beam as well as the temperature of the heat sink. The bottom plot shows the calculated diffraction efficiency.

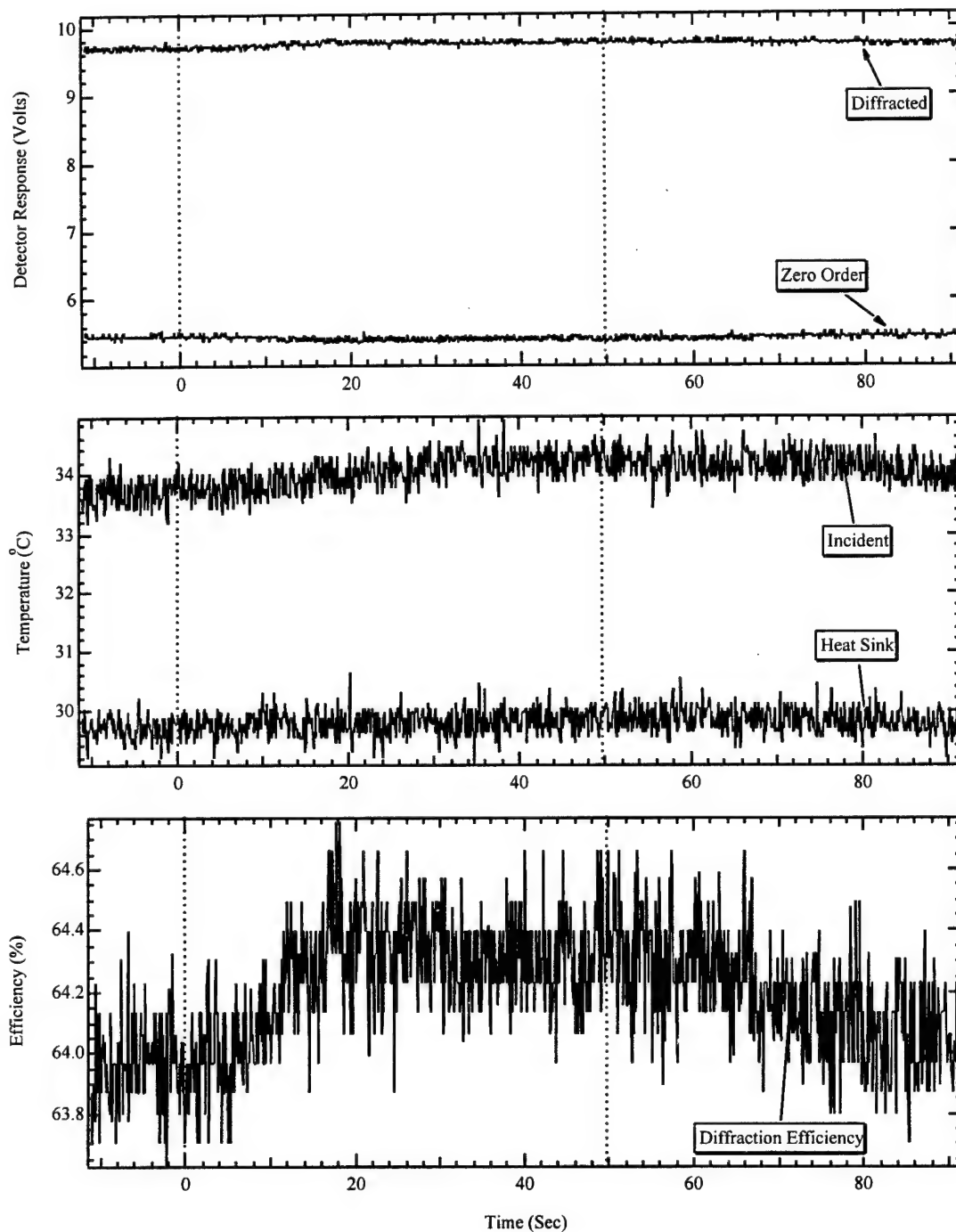


Figure A-103. Three plots showing the measured AO-cell response before, during and after an ion beam exposure #a45. The dashed lines indicate the duration of the ion beam. Refer to Table A-3 for the precise beam location. The upper plot shows the power of the diffracted and zero order laser beam exiting the AO-cell and the center plot shows the temperature of the crystal face being struck by the ion beam as well as the temperature of the heat sink. The bottom plot shows the calculated diffraction efficiency.

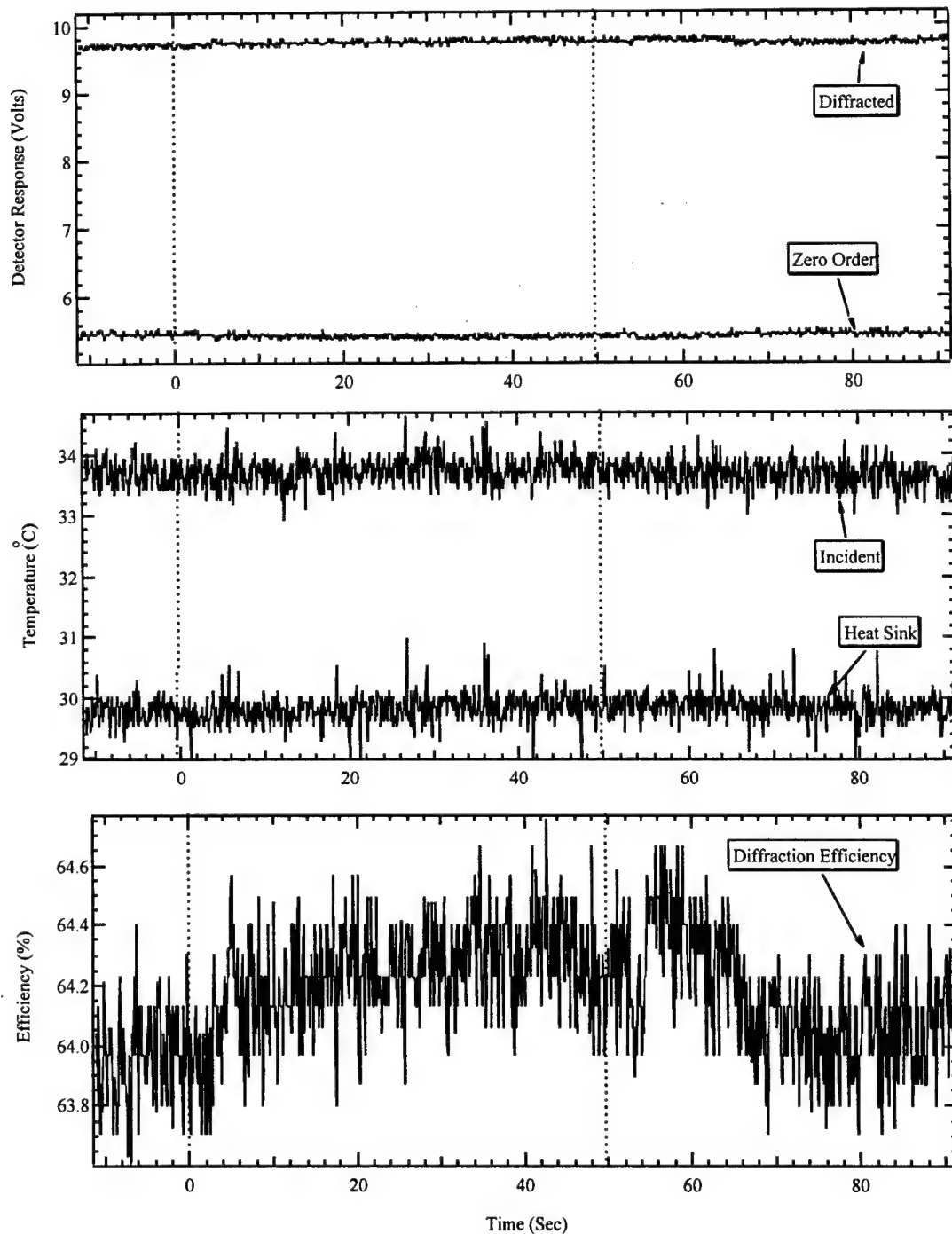


Figure A-104. Three plots showing the measured AO-cell response before, during and after an ion beam exposure #a46. The dashed lines indicate the duration of the ion beam. Refer to Table A-3 for the precise beam location. The upper plot shows the power of the diffracted and zero order laser beam exiting the AO-cell and the center plot shows the temperature of the crystal face being struck by the ion beam as well as the temperature of the heat sink. The bottom plot shows the calculated diffraction efficiency.

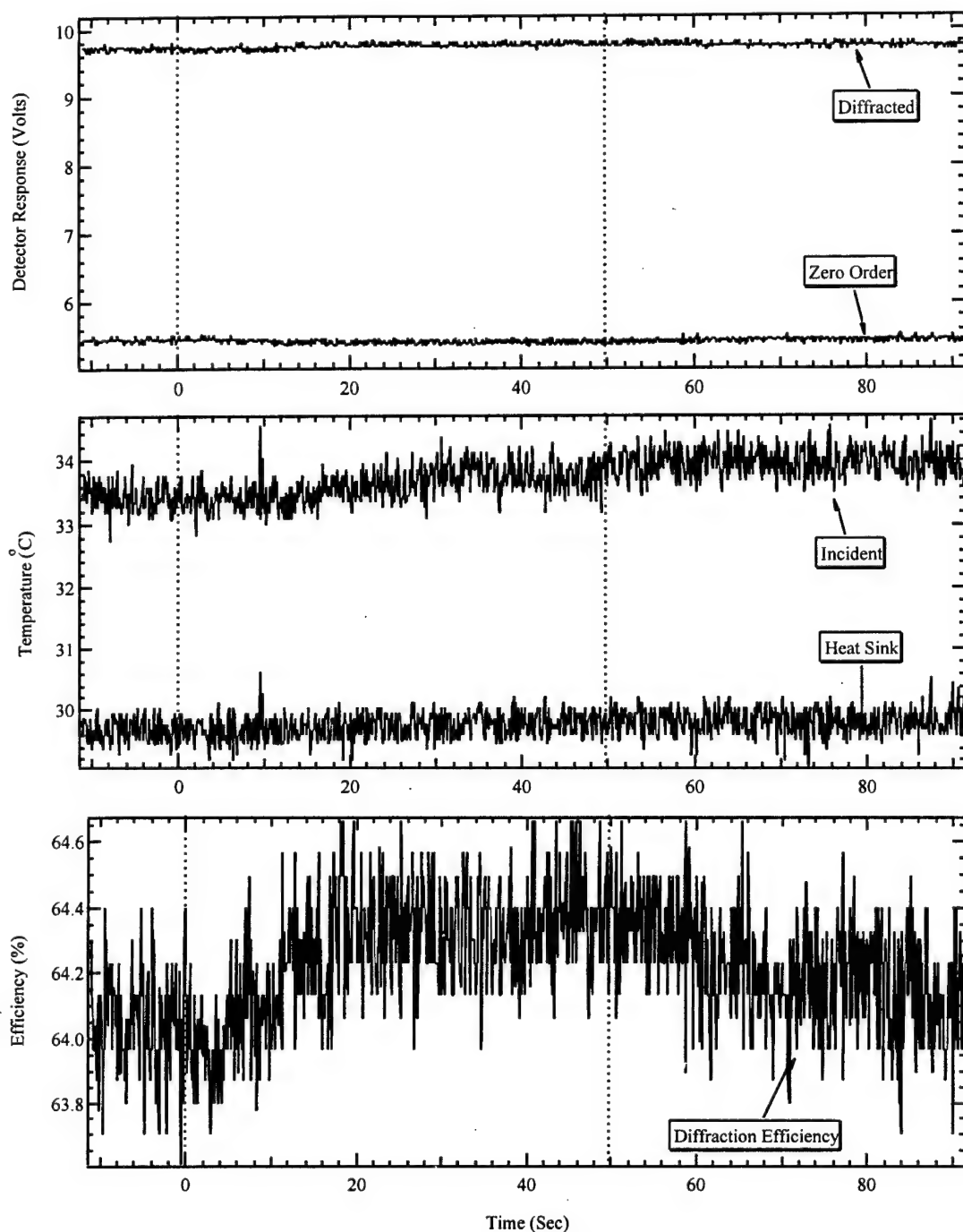


Figure A-105. Three plots showing the measured AO-cell response before, during and after an ion beam exposure #a47. The dashed lines indicate the duration of the ion beam. Refer to Table A-3 for the precise beam location. The upper plot shows the power of the diffracted and zero order laser beam exiting the AO-cell and the center plot shows the temperature of the crystal face being struck by the ion beam as well as the temperature of the heat sink. The bottom plot shows the calculated diffraction efficiency.

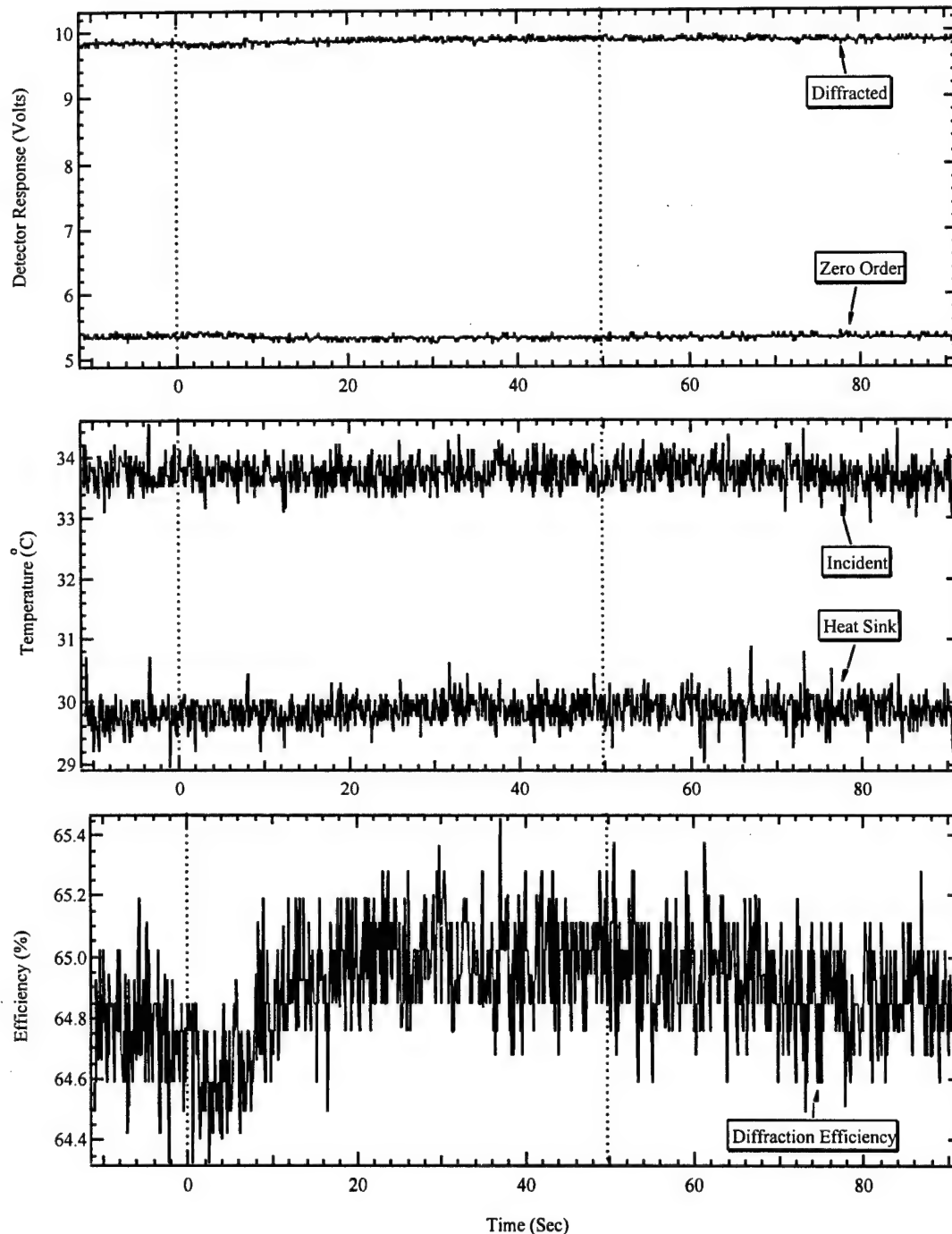


Figure A-106. Three plots showing the measured AO-cell response before, during and after an ion beam exposure #a48. The dashed lines indicate the duration of the ion beam. Refer to Table A-3 for the precise beam location. The upper plot shows the power of the diffracted and zero order laser beam exiting the AO-cell and the center plot shows the temperature of the crystal face being struck by the ion beam as well as the temperature of the heat sink. The bottom plot shows the calculated diffraction efficiency.

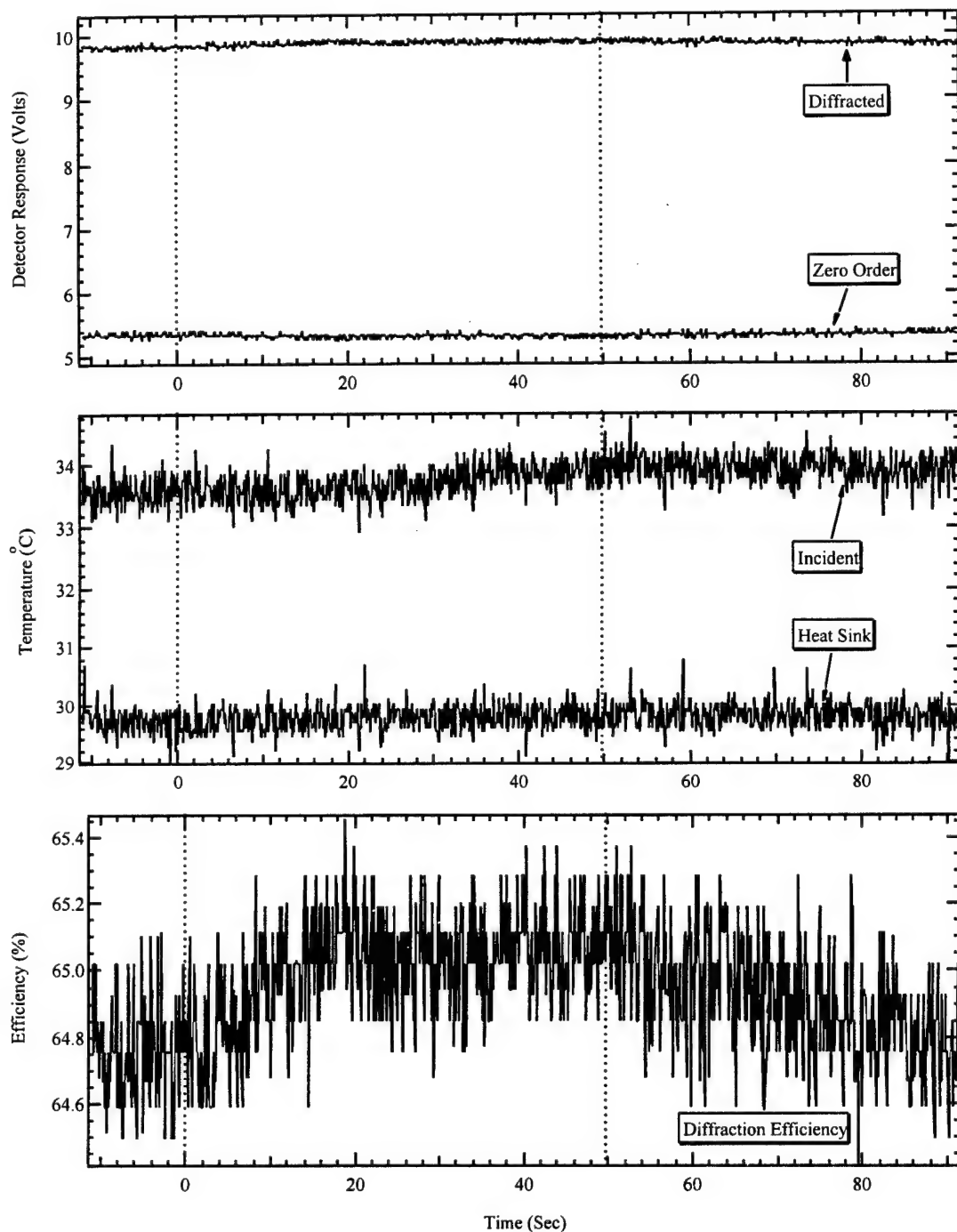


Figure A-107. Three plots showing the measured AO-cell response before, during and after an ion beam exposure #a49. The dashed lines indicate the duration of the ion beam. Refer to Table A-3 for the precise beam location. The upper plot shows the power of the diffracted and zero order laser beam exiting the AO-cell and the center plot shows the temperature of the crystal face being struck by the ion beam as well as the temperature of the heat sink. The bottom plot shows the calculated diffraction efficiency.

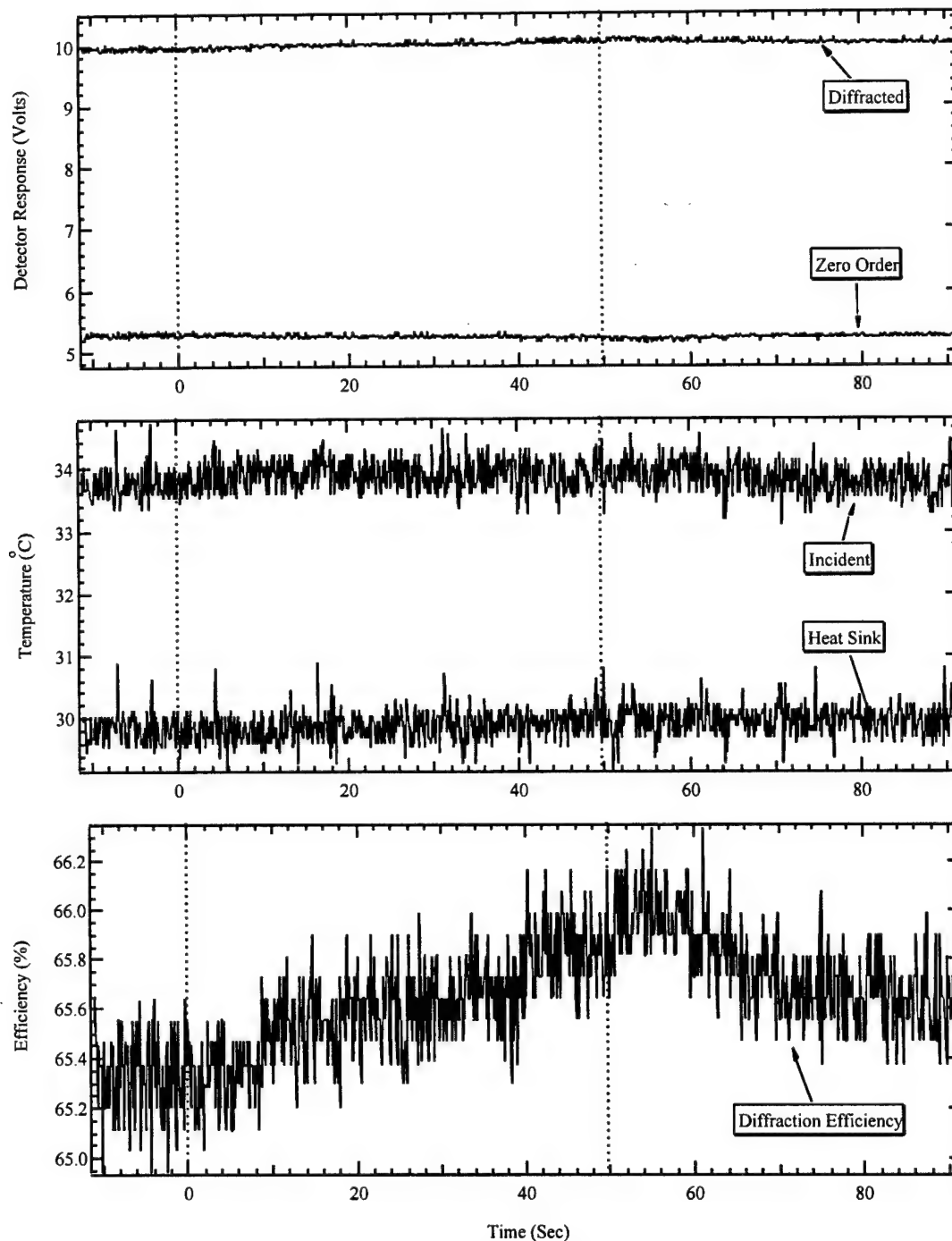


Figure A-108. Three plots showing the measured AO-cell response before, during and after an ion beam exposure #a50. The dashed lines indicate the duration of the ion beam. Refer to Table A-3 for the precise beam location. The upper plot shows the power of the diffracted and zero order laser beam exiting the AO-cell and the center plot shows the temperature of the crystal face being struck by the ion beam as well as the temperature of the heat sink. The bottom plot shows the calculated diffraction efficiency.

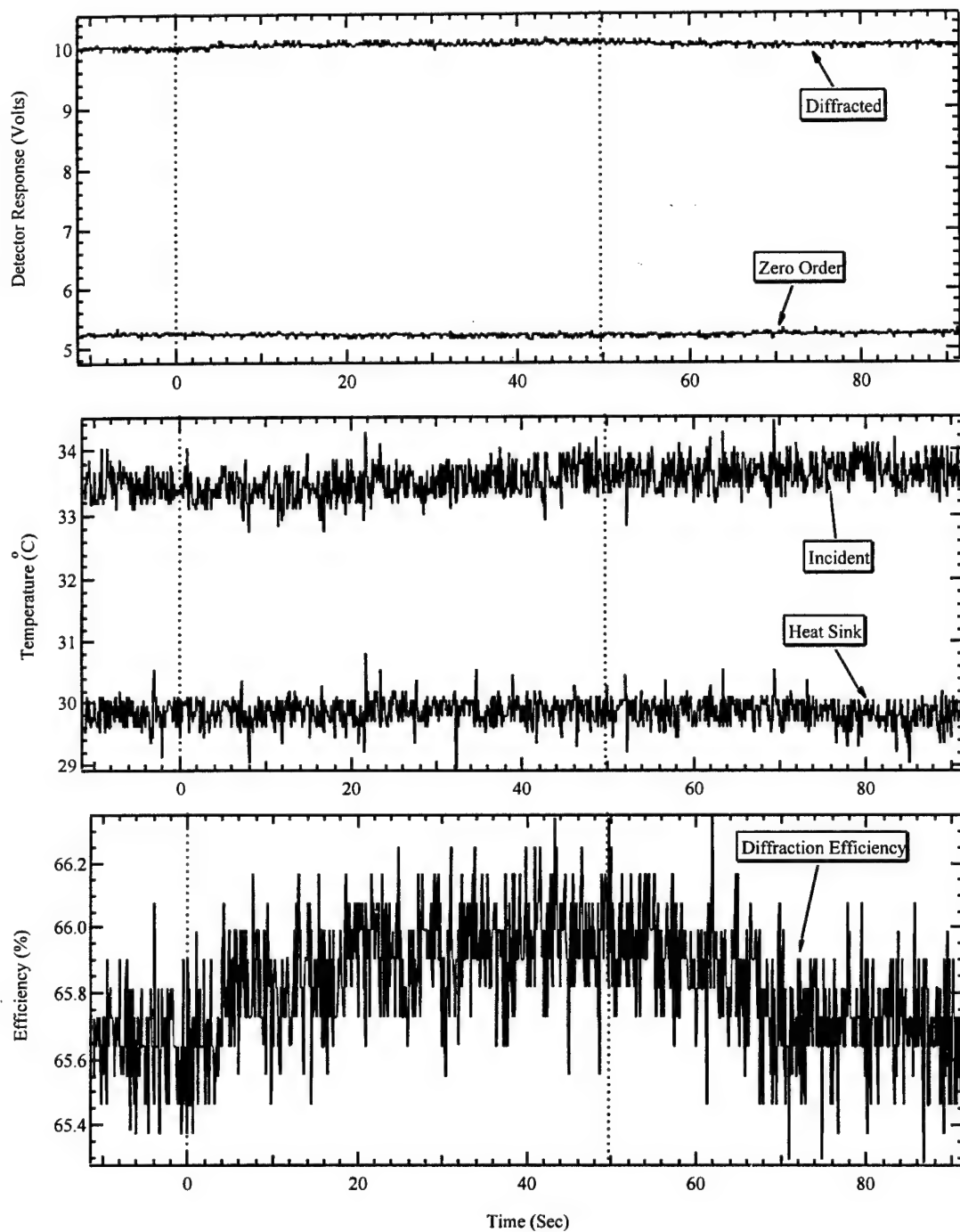


Figure A-109. Three plots showing the measured AO-cell response before, during and after an ion beam exposure #1. The dashed lines indicate the duration of the ion beam. Refer to Table A-3 for the precise beam location. The upper plot shows the power of the diffracted and zero order laser beam exiting the AO-cell and the center plot shows the temperature of the crystal face being struck by the ion beam as well as the temperature of the heat sink. The bottom plot shows the calculated diffraction efficiency.

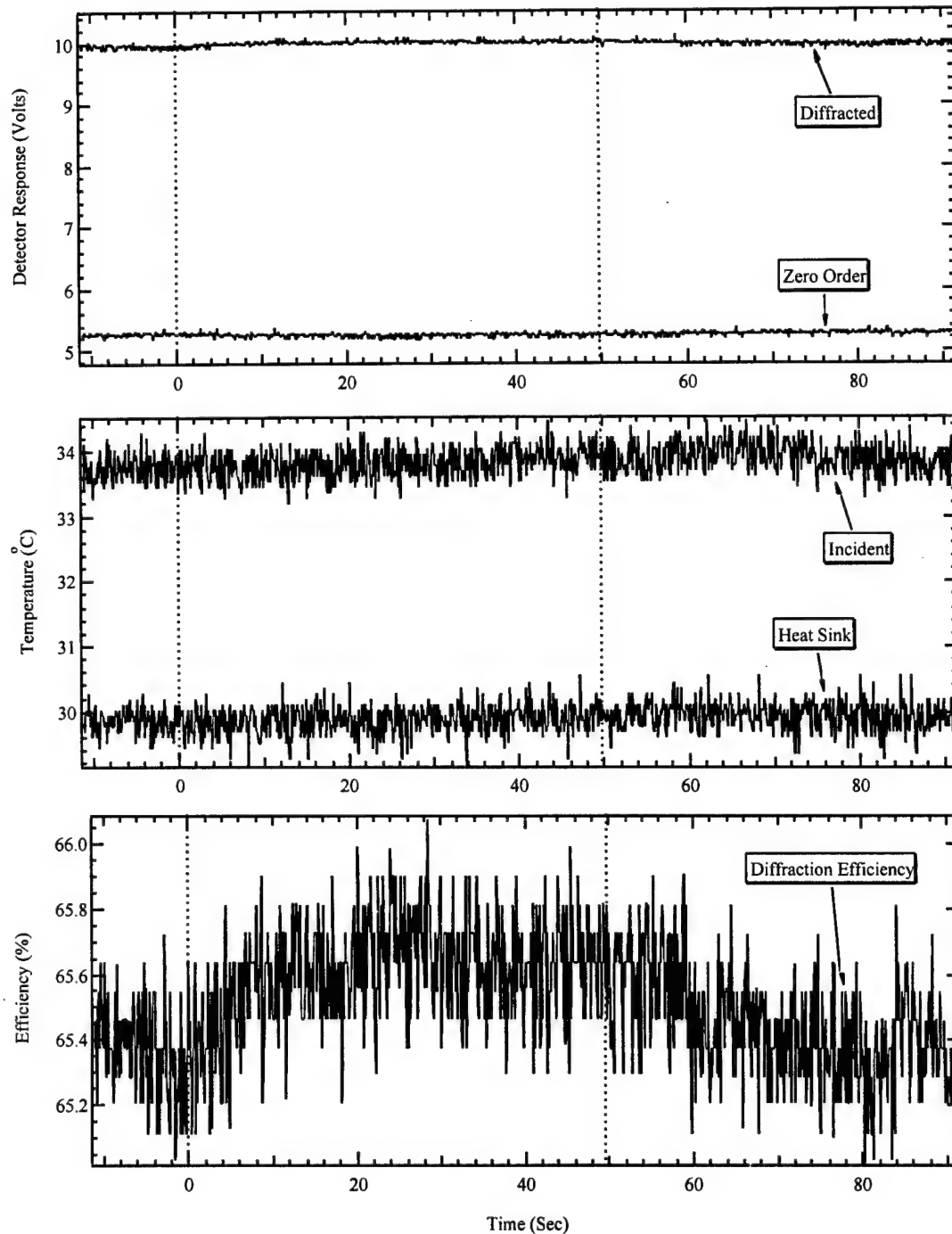


Figure A-110. Three plots showing the measured AO-cell response before, during and after an ion beam exposure #2. The dashed lines indicate the duration of the ion beam. Refer to Table A-3 for the precise beam location. The upper plot shows the power of the diffracted and zero order laser beam exiting the AO-cell and the center plot shows the temperature of the crystal face being struck by the ion beam as well as the temperature of the heat sink. The bottom plot shows the calculated diffraction efficiency.

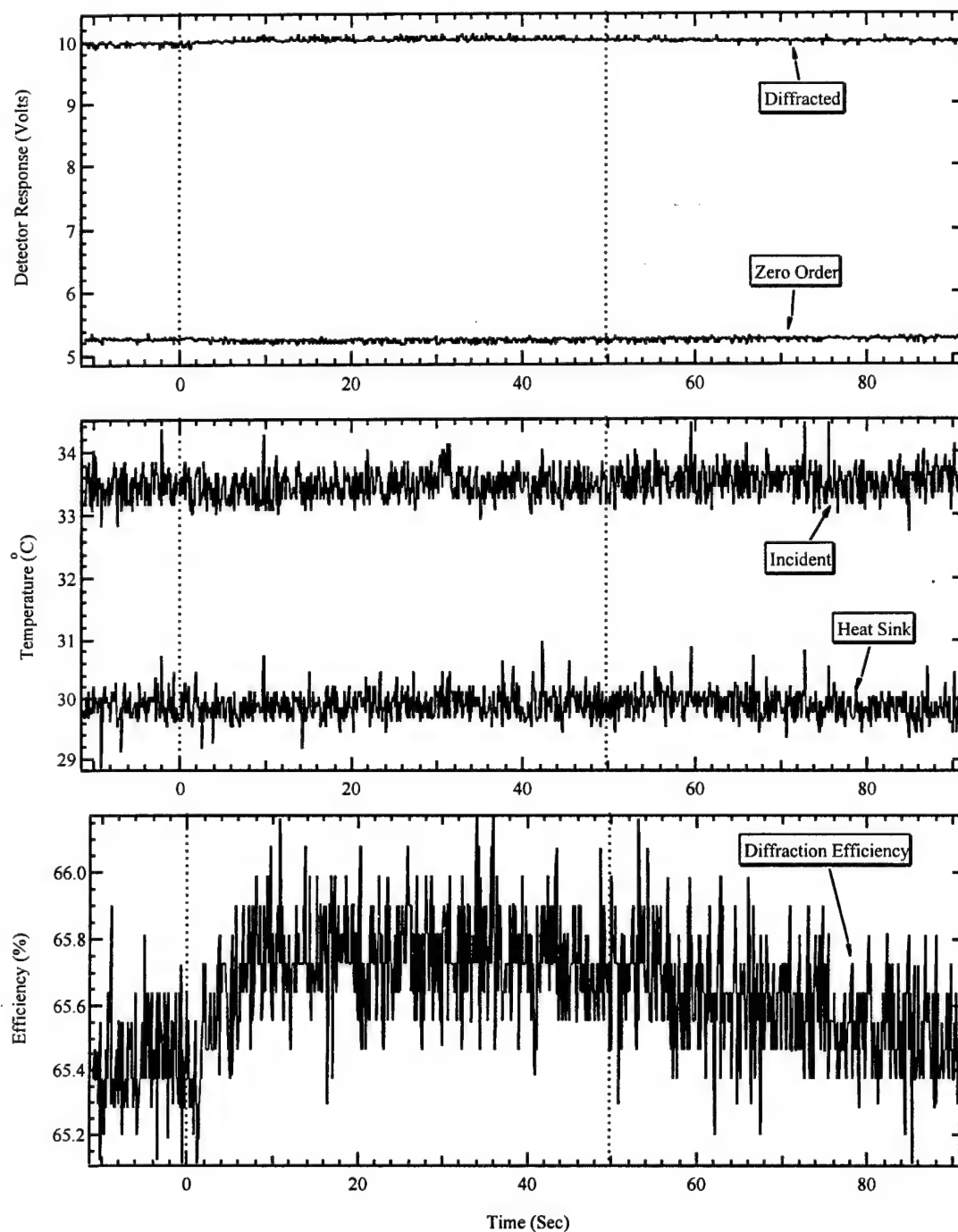


Figure A-111. Three plots showing the measured AO-cell response before, during and after an ion beam exposure #3. The dashed lines indicate the duration of the ion beam. Refer to Table A-3 for the precise beam location. The upper plot shows the power of the diffracted and zero order laser beam exiting the AO-cell and the center plot shows the temperature of the crystal face being struck by the ion beam as well as the temperature of the heat sink. The bottom plot shows the calculated diffraction efficiency.

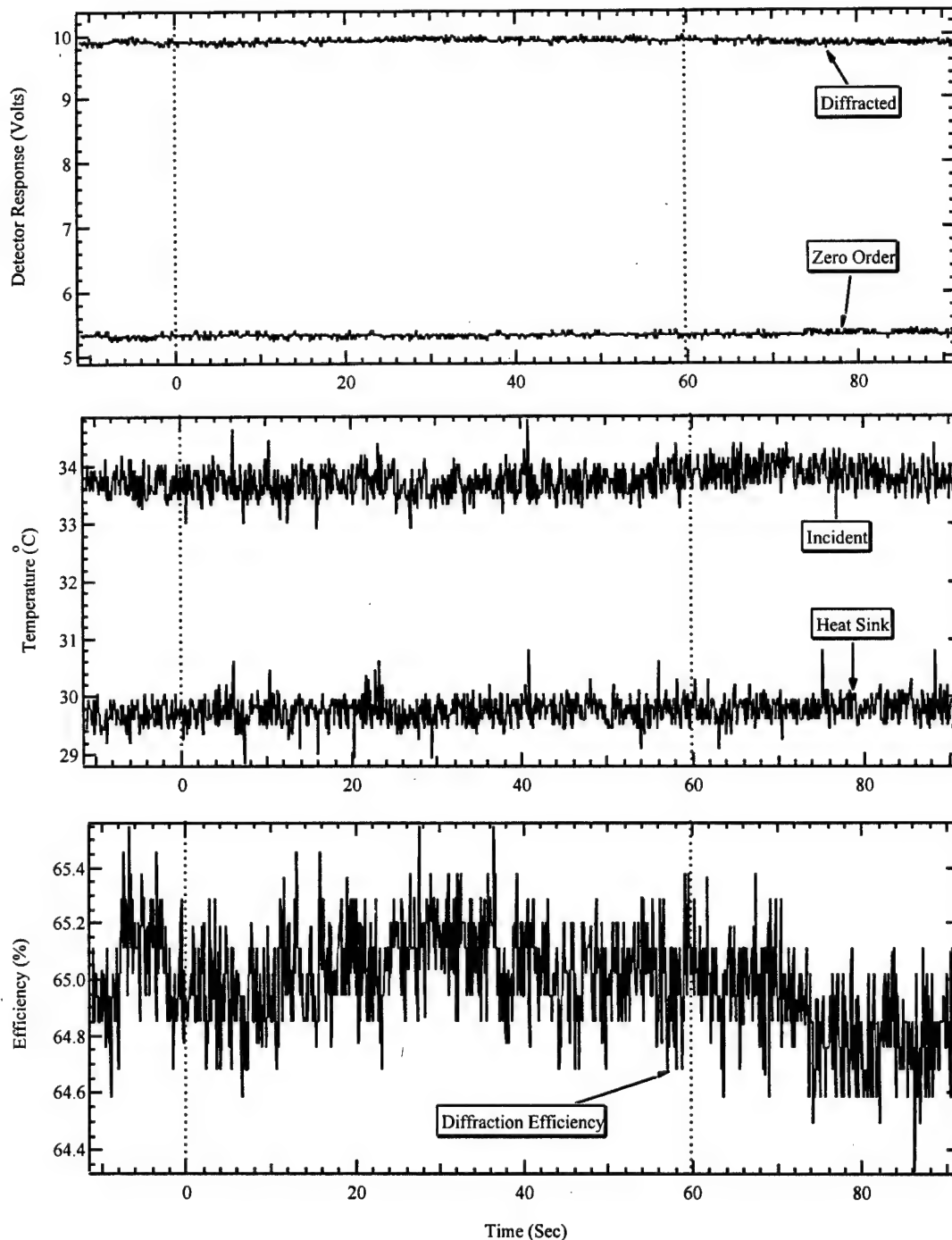


Figure A-112. Three plots showing the measured AO-cell response before, during and after an ion beam exposure #4. The dashed lines indicate the duration of the ion beam. Refer to Table A-3 for the precise beam location. The upper plot shows the power of the diffracted and zero order laser beam exiting the AO-cell and the center plot shows the temperature of the crystal face being struck by the ion beam as well as the temperature of the heat sink. The bottom plot shows the calculated diffraction efficiency.

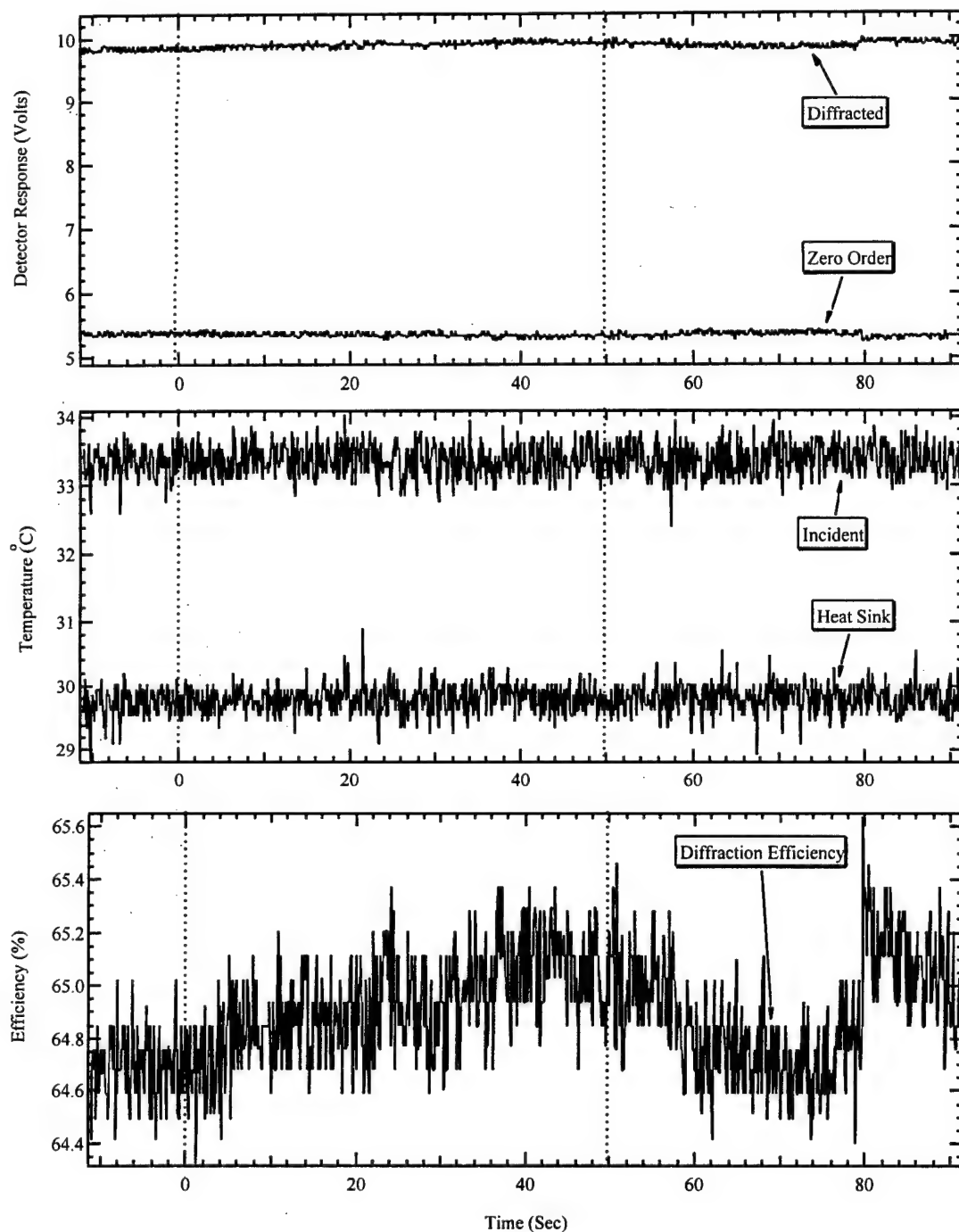


Figure A-113. Three plots showing the measured AO-cell response before, during and after an ion beam exposure #5. The dashed lines indicate the duration of the ion beam. Refer to Table A-3 for the precise beam location. The upper plot shows the power of the diffracted and zero order laser beam exiting the AO-cell and the center plot shows the temperature of the crystal face being struck by the ion beam as well as the temperature of the heat sink. The bottom plot shows the calculated diffraction efficiency.

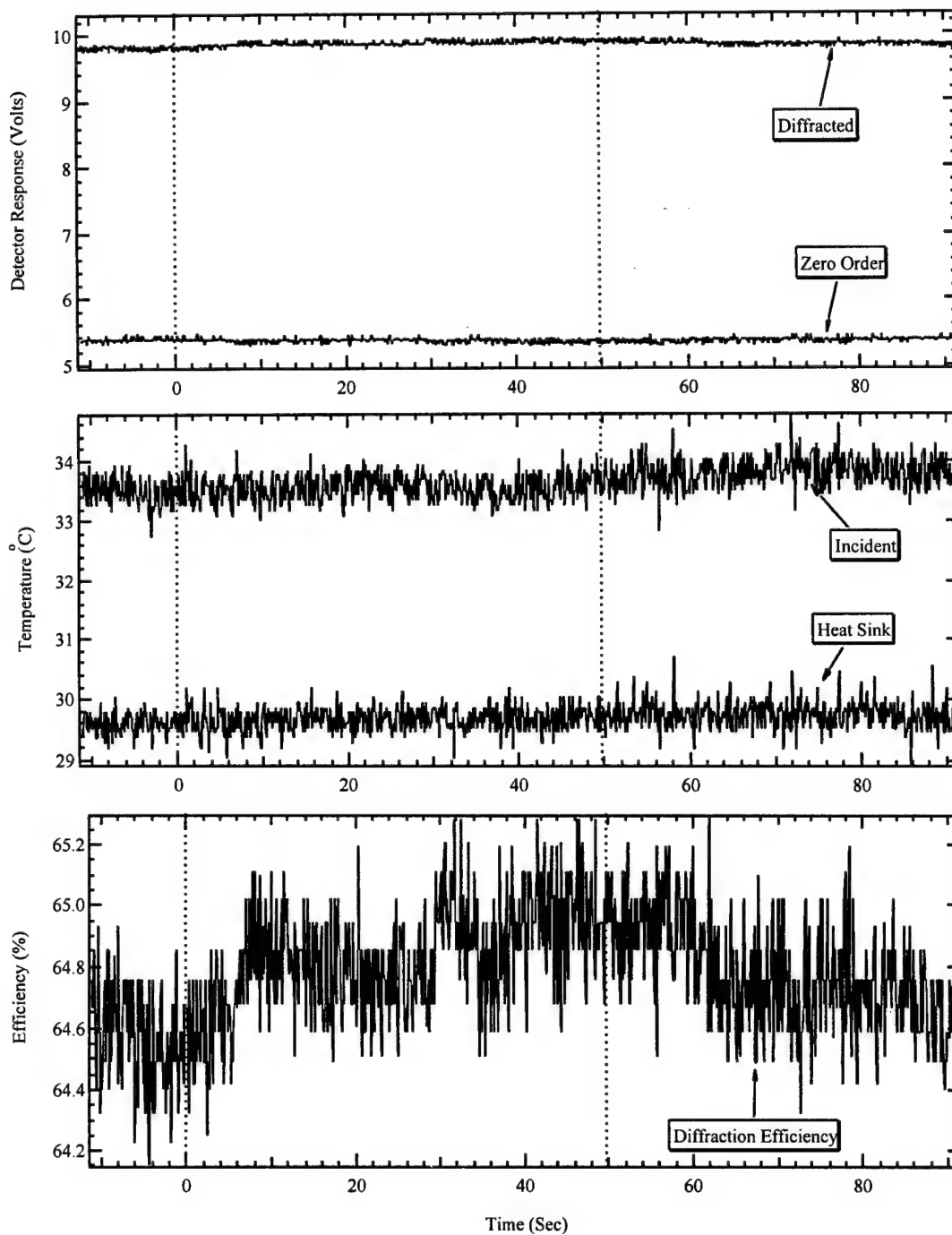


Figure A-114. Three plots showing the measured AO-cell response before, during and after an ion beam exposure #6. The dashed lines indicate the duration of the ion beam. Refer to Table A-3 for the precise beam location. The upper plot shows the power of the diffracted and zero order laser beam exiting the AO-cell and the center plot shows the temperature of the crystal face being struck by the ion beam as well as the temperature of the heat sink. The bottom plot shows the calculated diffraction efficiency.

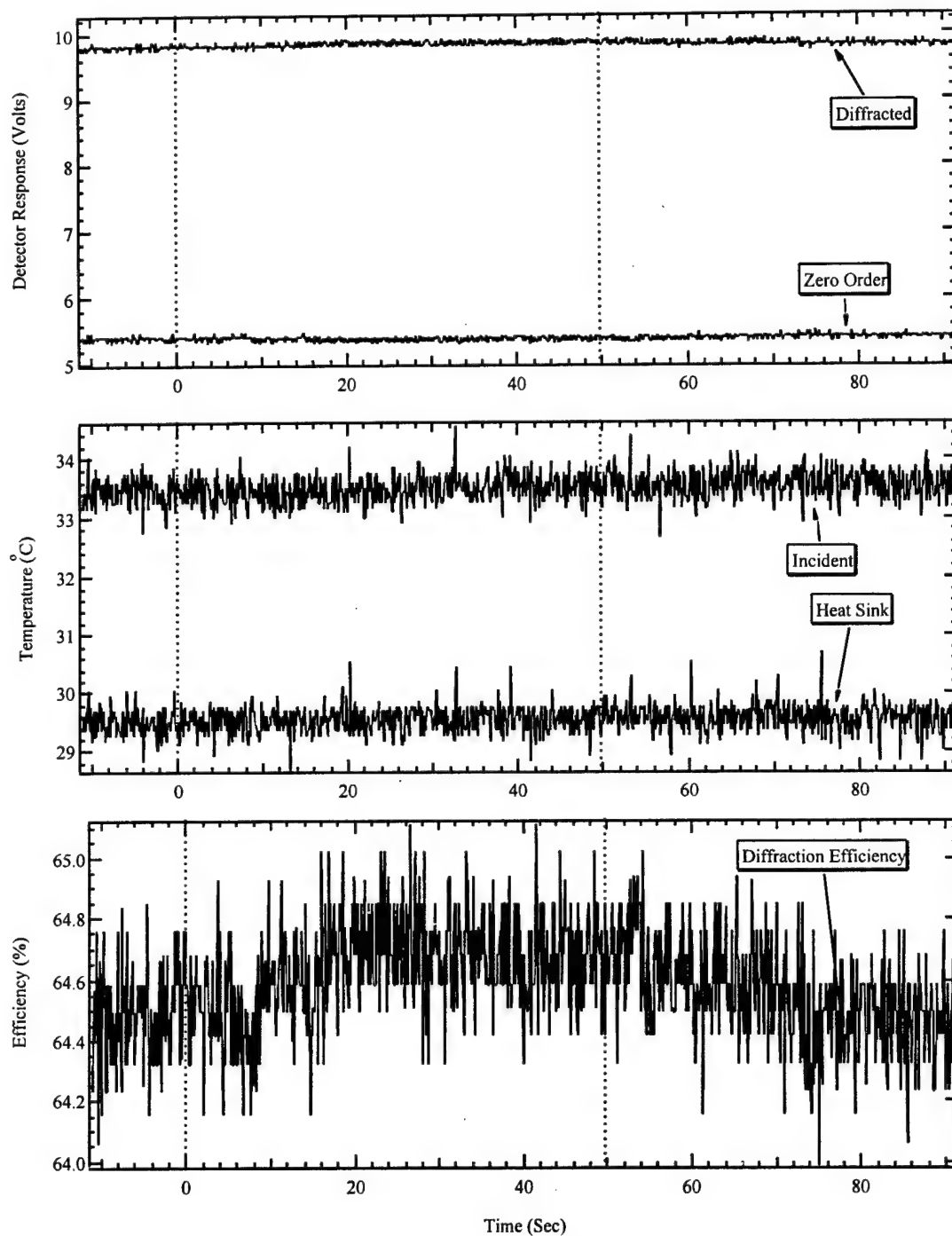


Figure A-115. Three plots showing the measured AO-cell response before, during and after an ion beam exposure #7. The dashed lines indicate the duration of the ion beam. Refer to Table A-3 for the precise beam location. The upper plot shows the power of the diffracted and zero order laser beam exiting the AO-cell and the center plot shows the temperature of the crystal face being struck by the ion beam as well as the temperature of the heat sink. The bottom plot shows the calculated diffraction efficiency.

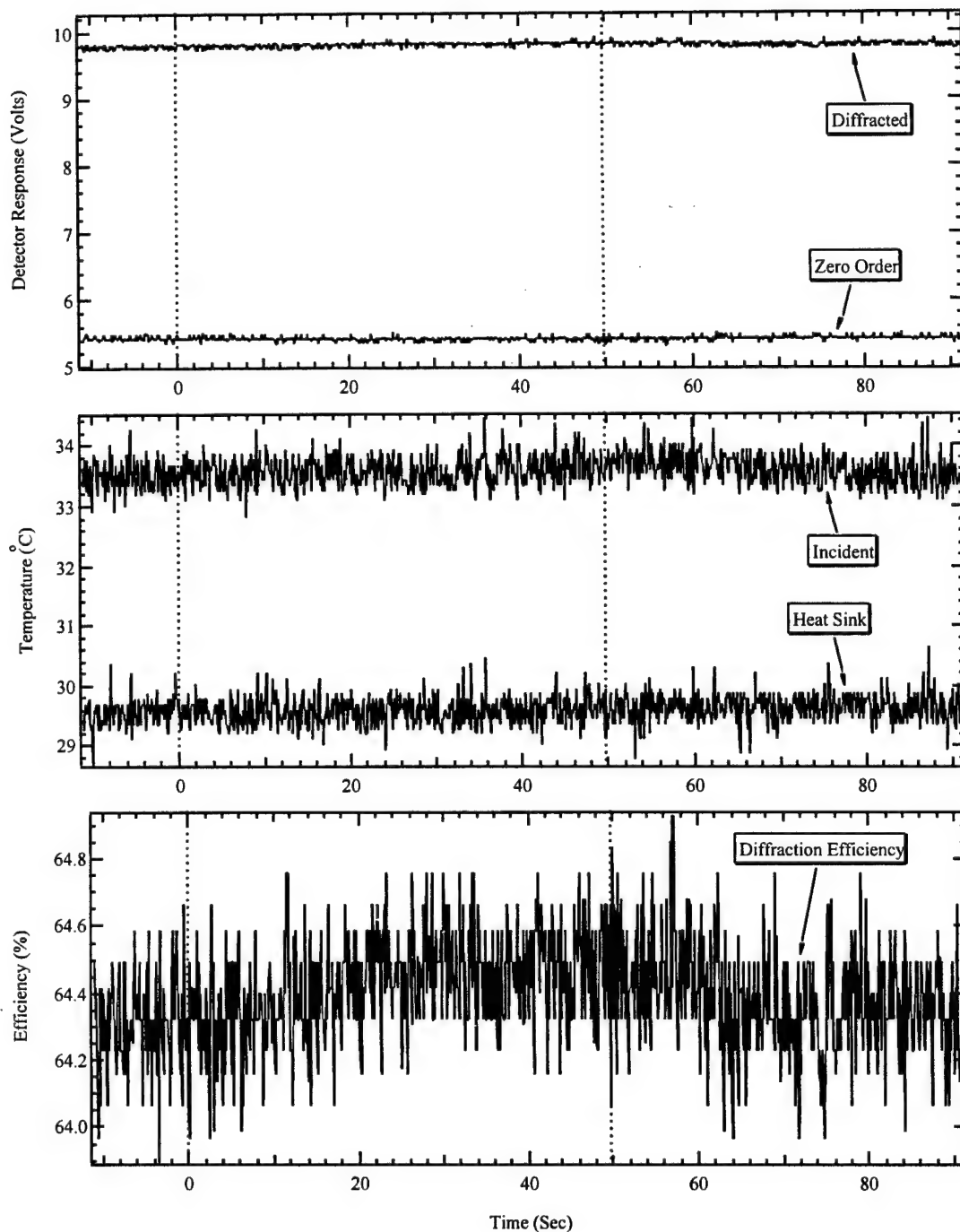


Figure A-116. Three plots showing the measured AO-cell response before, during and after an ion beam exposure #8. The dashed lines indicate the duration of the ion beam. Refer to Table A-3 for the precise beam location. The upper plot shows the power of the diffracted and zero order laser beam exiting the AO-cell and the center plot shows the temperature of the crystal face being struck by the ion beam as well as the temperature of the heat sink. The bottom plot shows the calculated diffraction efficiency.

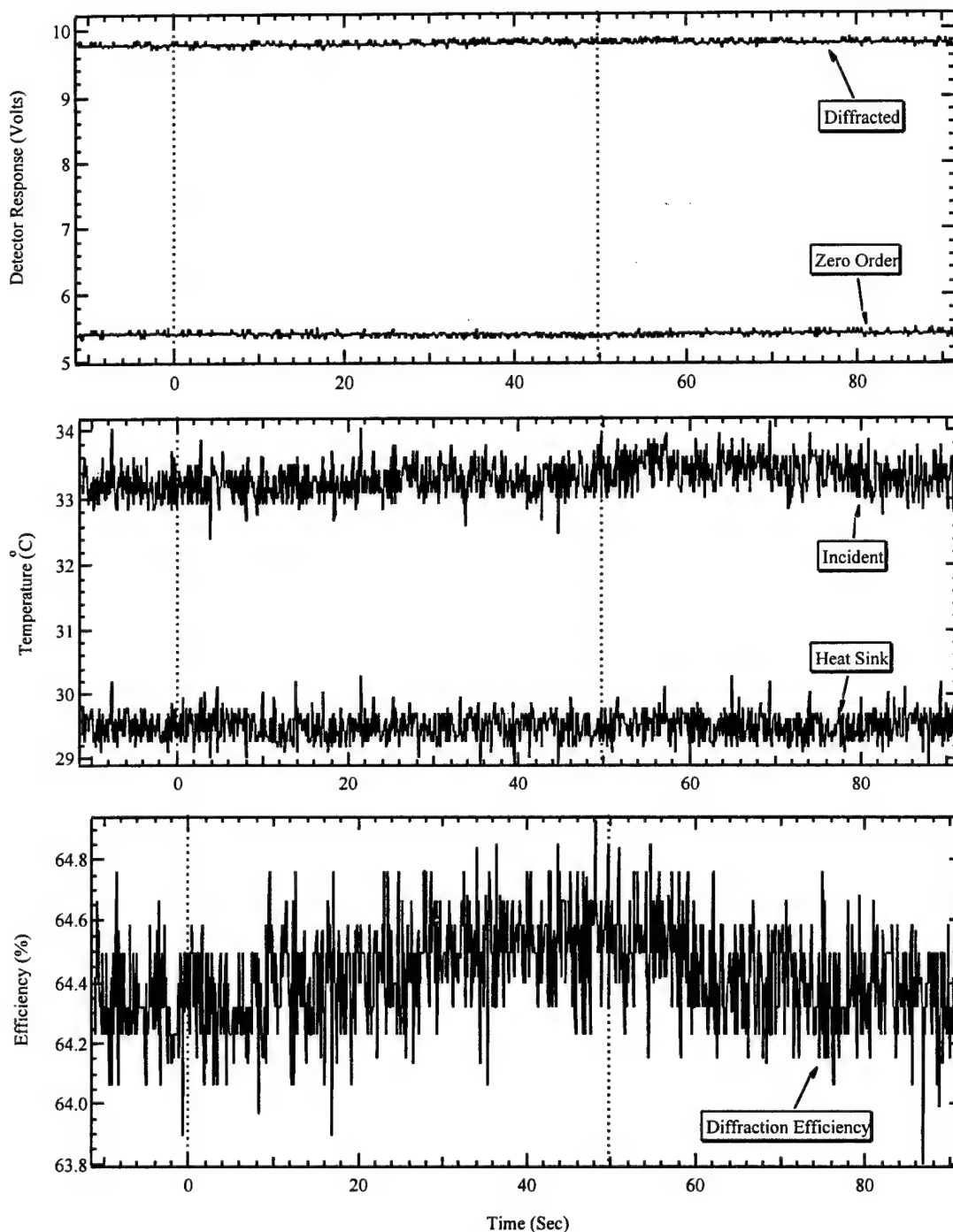


Figure A-117. Three plots showing the measured AO-cell response before, during and after an ion beam exposure #9. The dashed lines indicate the duration of the ion beam. Refer to Table A-3 for the precise beam location. The upper plot shows the power of the diffracted and zero order laser beam exiting the AO-cell and the center plot shows the temperature of the crystal face being struck by the ion beam as well as the temperature of the heat sink. The bottom plot shows the calculated diffraction efficiency.

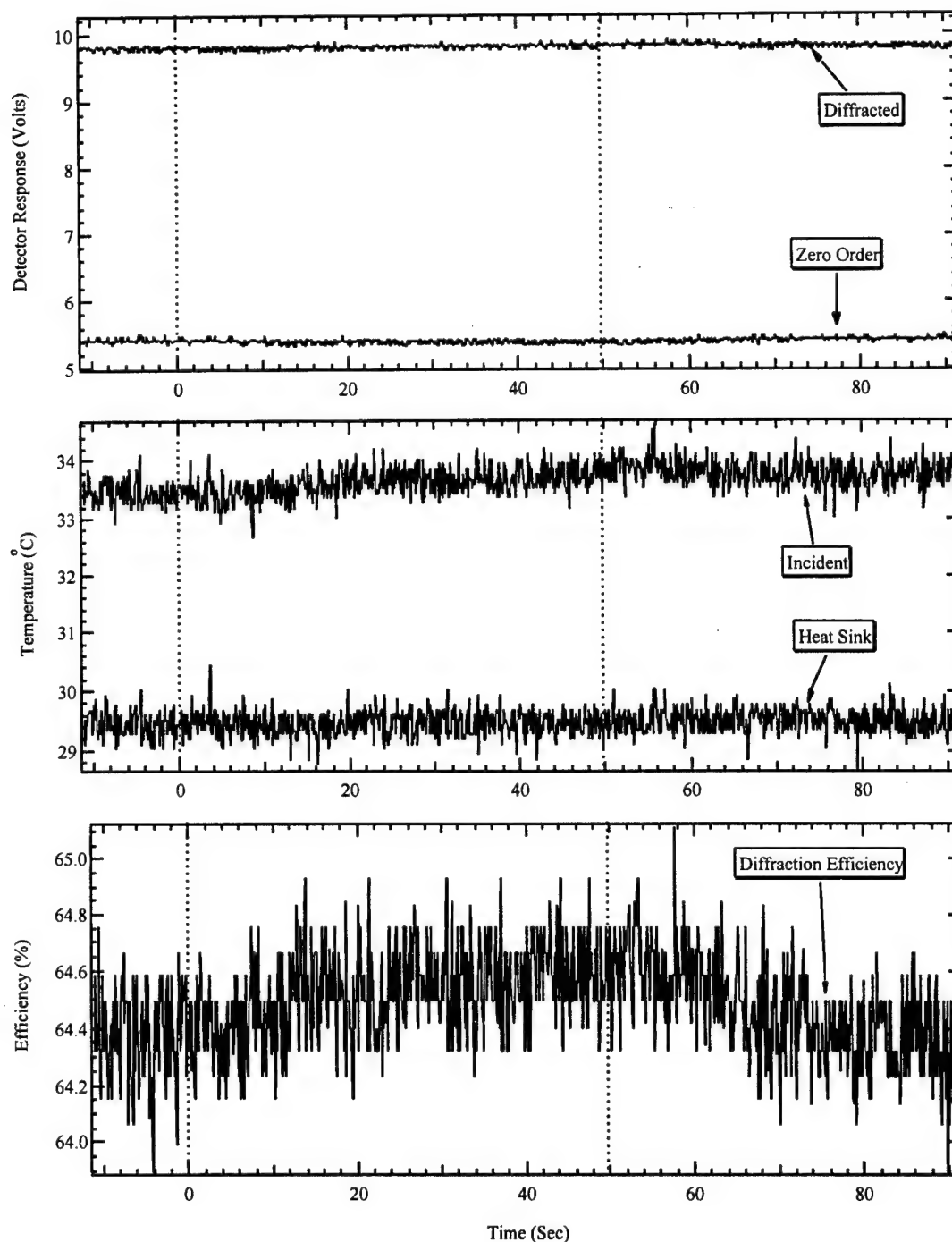


Figure A-118. Three plots showing the measured AO-cell response before, during and after an ion beam exposure #10. The dashed lines indicate the duration of the ion beam. Refer to Table A-3 for the precise beam location. The upper plot shows the power of the diffracted and zero order laser beam exiting the AO-cell and the center plot shows the temperature of the crystal face being struck by the ion beam as well as the temperature of the heat sink. The bottom plot shows the calculated diffraction efficiency.

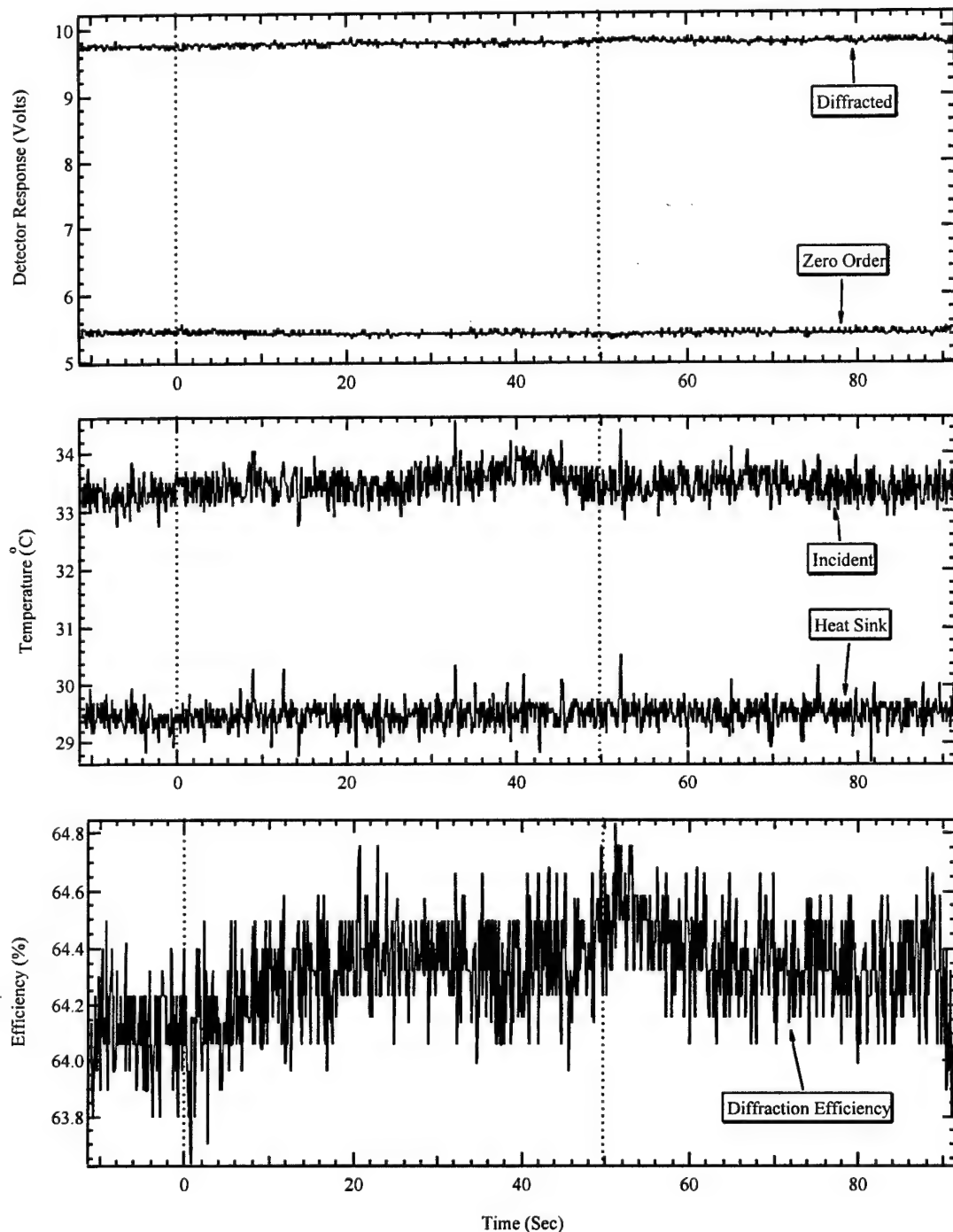


Figure A-119. Three plots showing the measured AO-cell response before, during and after an ion beam exposure #11. The dashed lines indicate the duration of the ion beam. Refer to Table A-3 for the precise beam location. The upper plot shows the power of the diffracted and zero order laser beam exiting the AO-cell and the center plot shows the temperature of the crystal face being struck by the ion beam as well as the temperature of the heat sink. The bottom plot shows the calculated diffraction efficiency.

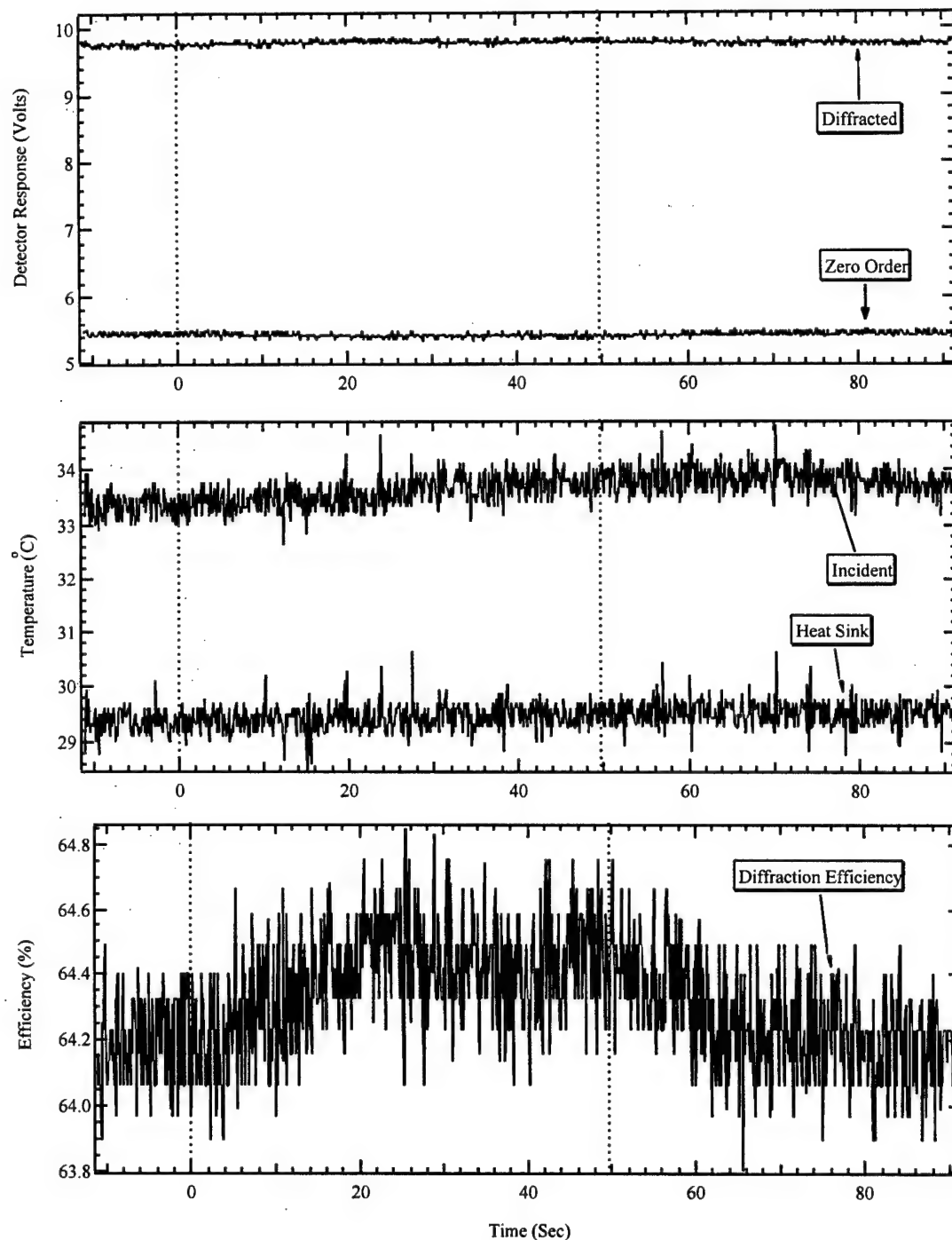


Figure A-120. Three plots showing the measured AO-cell response before, during and after an ion beam exposure #12. The dashed lines indicate the duration of the ion beam. Refer to Table A-3 for the precise beam location. The upper plot shows the power of the diffracted and zero order laser beam exiting the AO-cell and the center plot shows the temperature of the crystal face being struck by the ion beam as well as the temperature of the heat sink. The bottom plot shows the calculated diffraction efficiency.

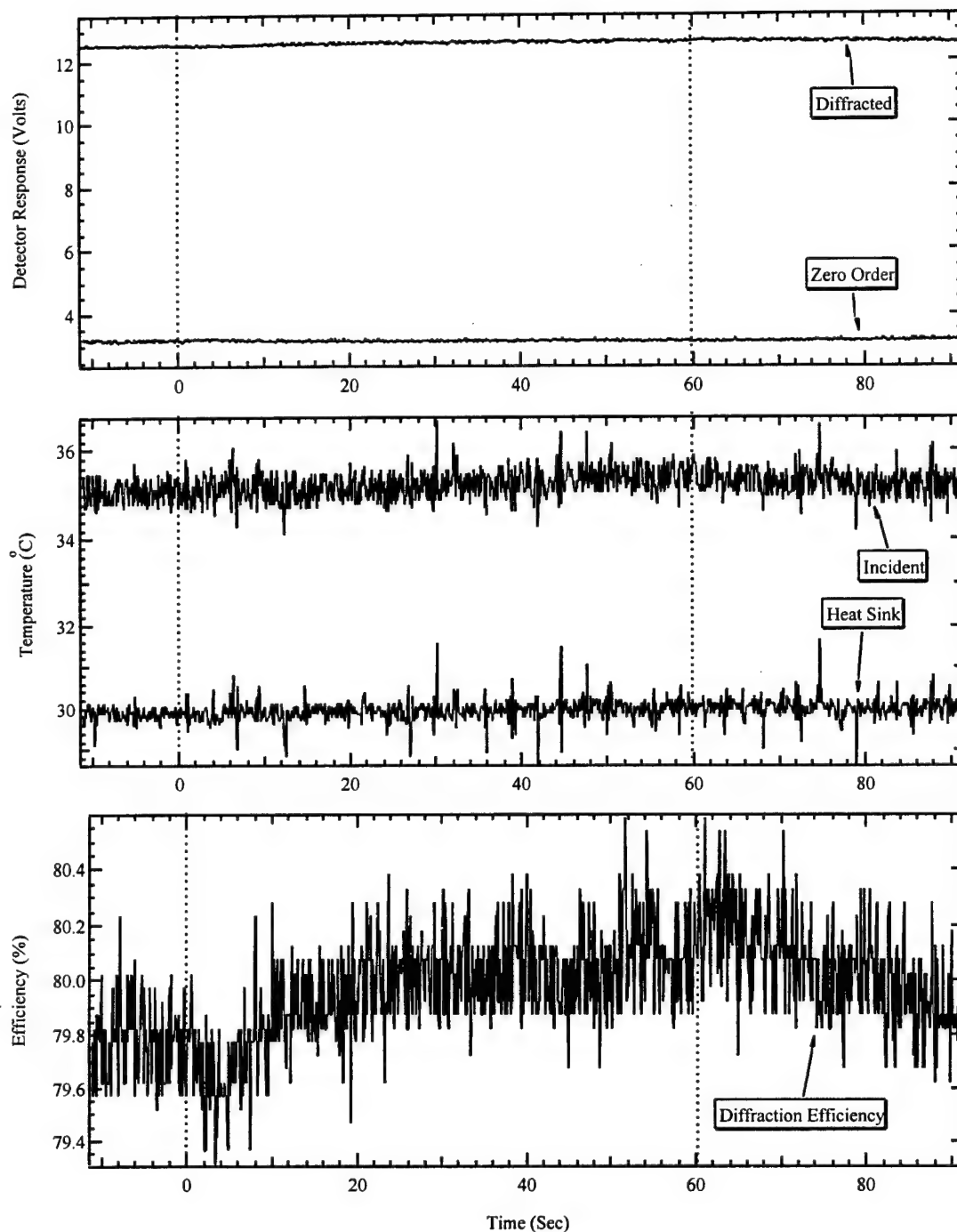


Figure A-121. Three plots showing the measured AO-cell response before, during and after an ion beam exposure #13. The dashed lines indicate the duration of the ion beam. Refer to Table A-3 for the precise beam location. The upper plot shows the power of the diffracted and zero order laser beam exiting the AO-cell and the center plot shows the temperature of the crystal face being struck by the ion beam as well as the temperature of the heat sink. The bottom plot shows the calculated diffraction efficiency.

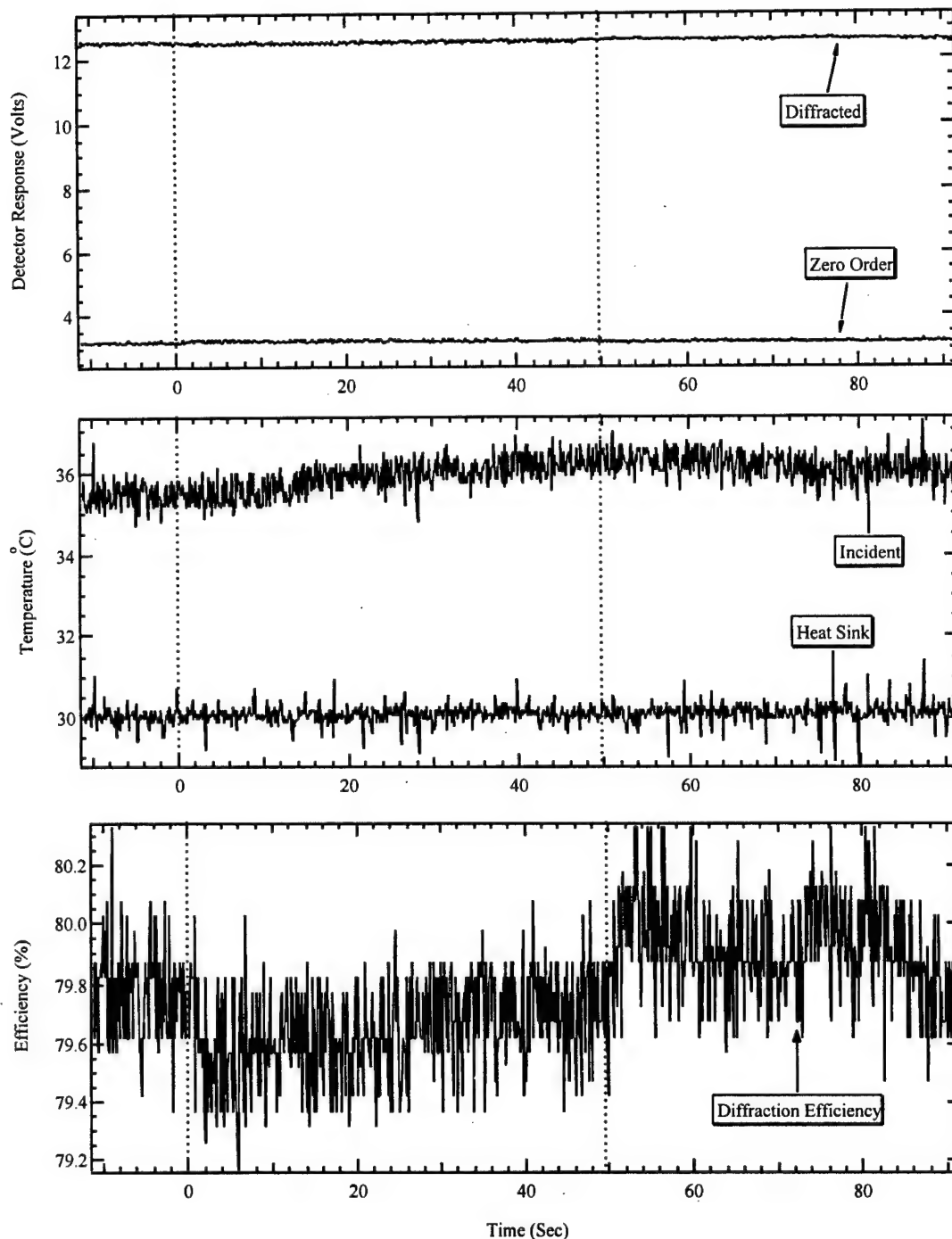


Figure A-122. Three plots showing the measured AO-cell response before, during and after an ion beam exposure #14. The dashed lines indicate the duration of the ion beam. Refer to Table A-3 for the precise beam location. The upper plot shows the power of the diffracted and zero order laser beam exiting the AO-cell and the center plot shows the temperature of the crystal face being struck by the ion beam as well as the temperature of the heat sink. The bottom plot shows the calculated diffraction efficiency.

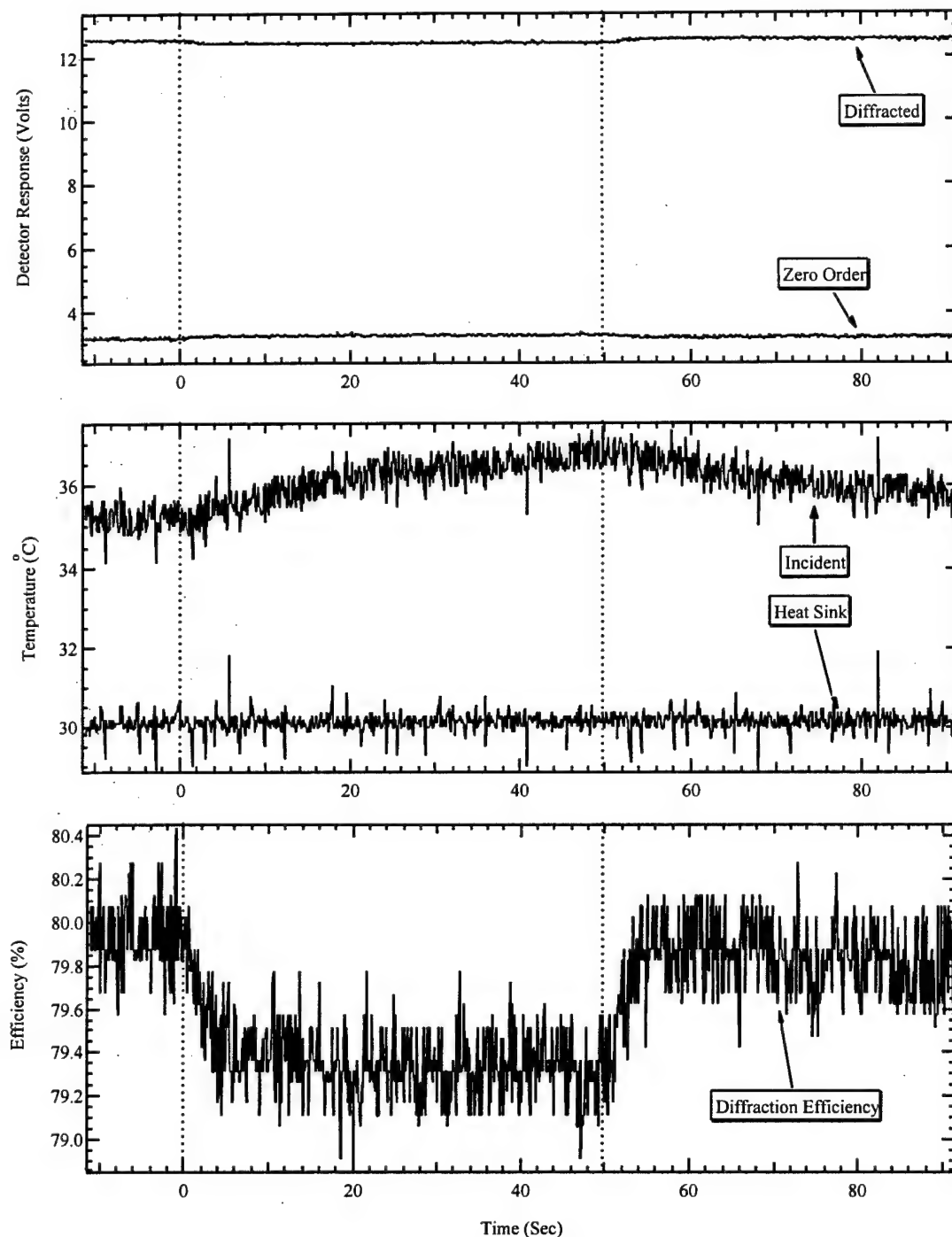


Figure A-123. Three plots showing the measured AO-cell response before, during and after an ion beam exposure #15. The dashed lines indicate the duration of the ion beam. Refer to Table A-3 for the precise beam location. The upper plot shows the power of the diffracted and zero order laser beam exiting the AO-cell and the center plot shows the temperature of the crystal face being struck by the ion beam as well as the temperature of the heat sink. The bottom plot shows the calculated diffraction efficiency.

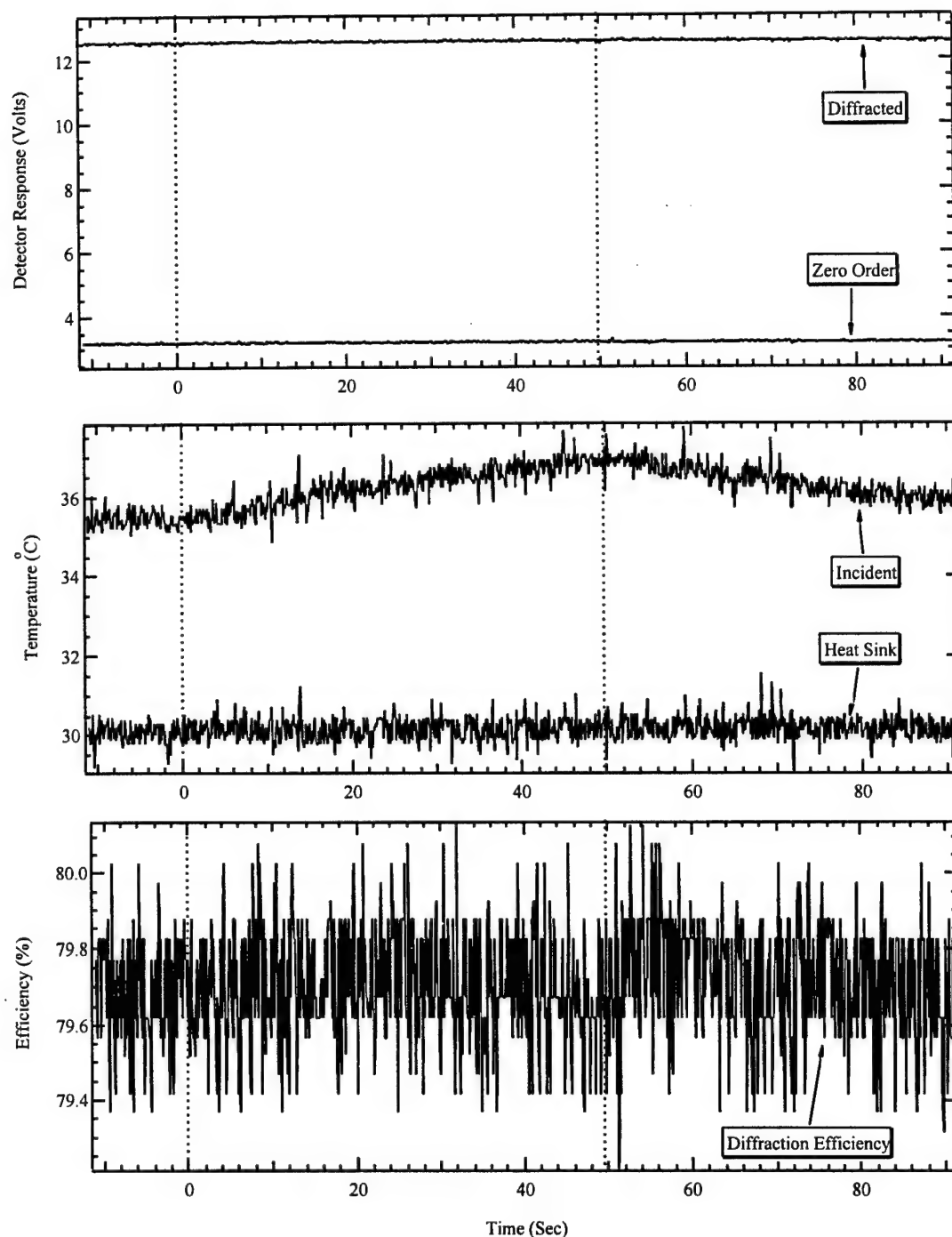


Figure A-124. Three plots showing the measured AO-cell response before, during and after an ion beam exposure #16. The dashed lines indicate the duration of the ion beam. Refer to Table A-3 for the precise beam location. The upper plot shows the power of the diffracted and zero order laser beam exiting the AO-cell and the center plot shows the temperature of the crystal face being struck by the ion beam as well as the temperature of the heat sink. The bottom plot shows the calculated diffraction efficiency.

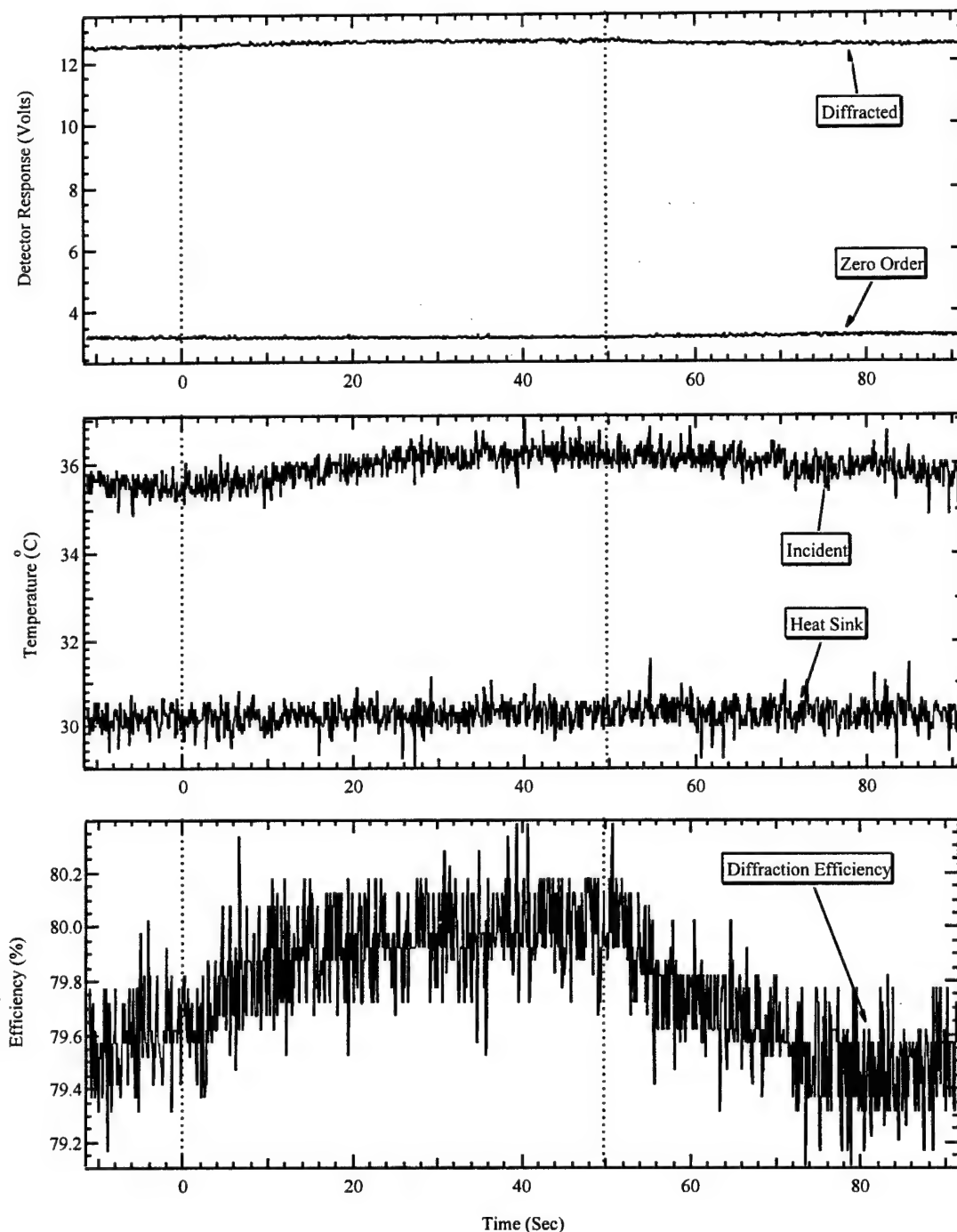


Figure A-125. Three plots showing the measured AO-cell response before, during and after an ion beam exposure #17. The dashed lines indicate the duration of the ion beam. Refer to Table A-3 for the precise beam location. The upper plot shows the power of the diffracted and zero order laser beam exiting the AO-cell and the center plot shows the temperature of the crystal face being struck by the ion beam as well as the temperature of the heat sink. The bottom plot shows the calculated diffraction efficiency.

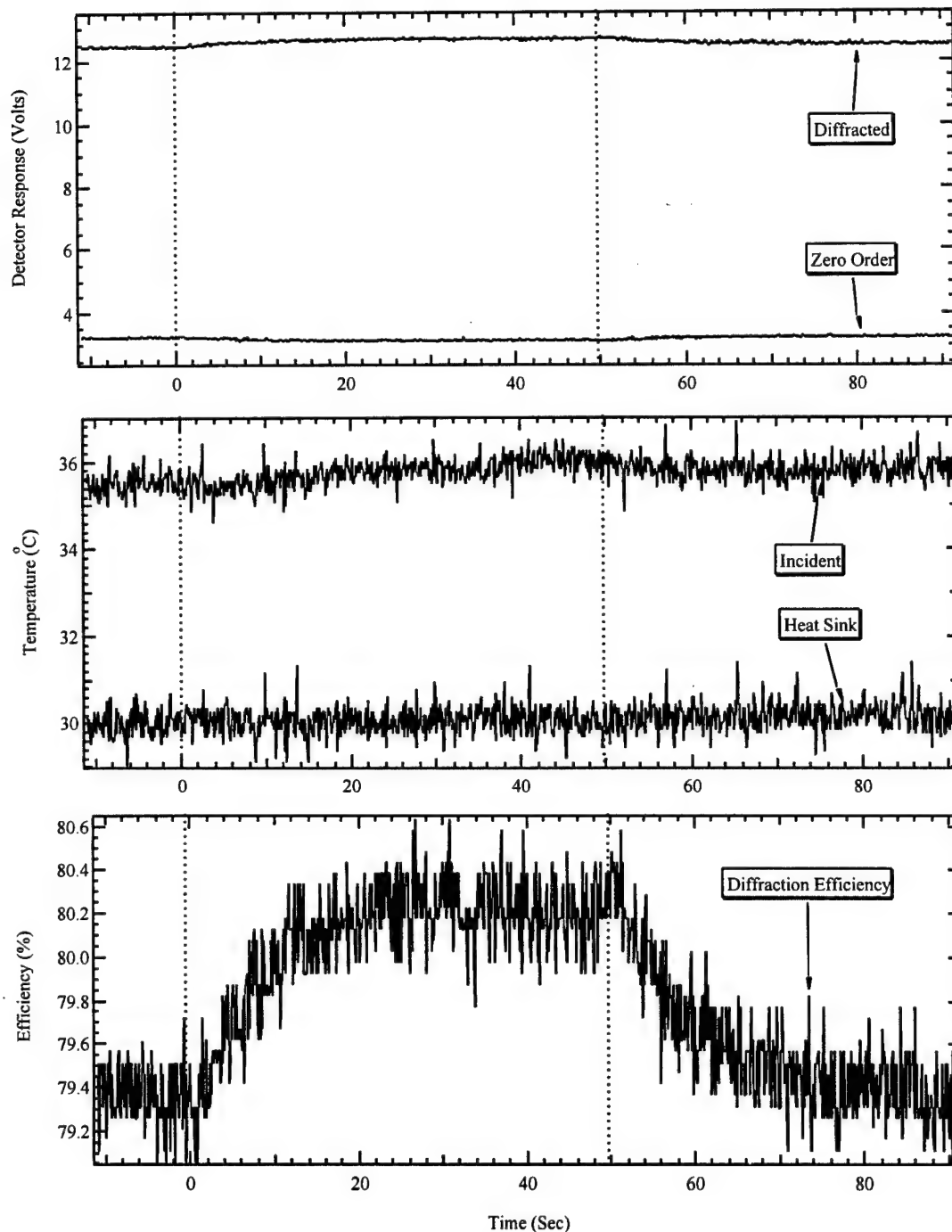


Figure A-126. Three plots showing the measured AO-cell response before, during and after an ion beam exposure #18. The dashed lines indicate the duration of the ion beam. Refer to Table A-3 for the precise beam location. The upper plot shows the power of the diffracted and zero order laser beam exiting the AO-cell and the center plot shows the temperature of the crystal face being struck by the ion beam as well as the temperature of the heat sink. The bottom plot shows the calculated diffraction efficiency.

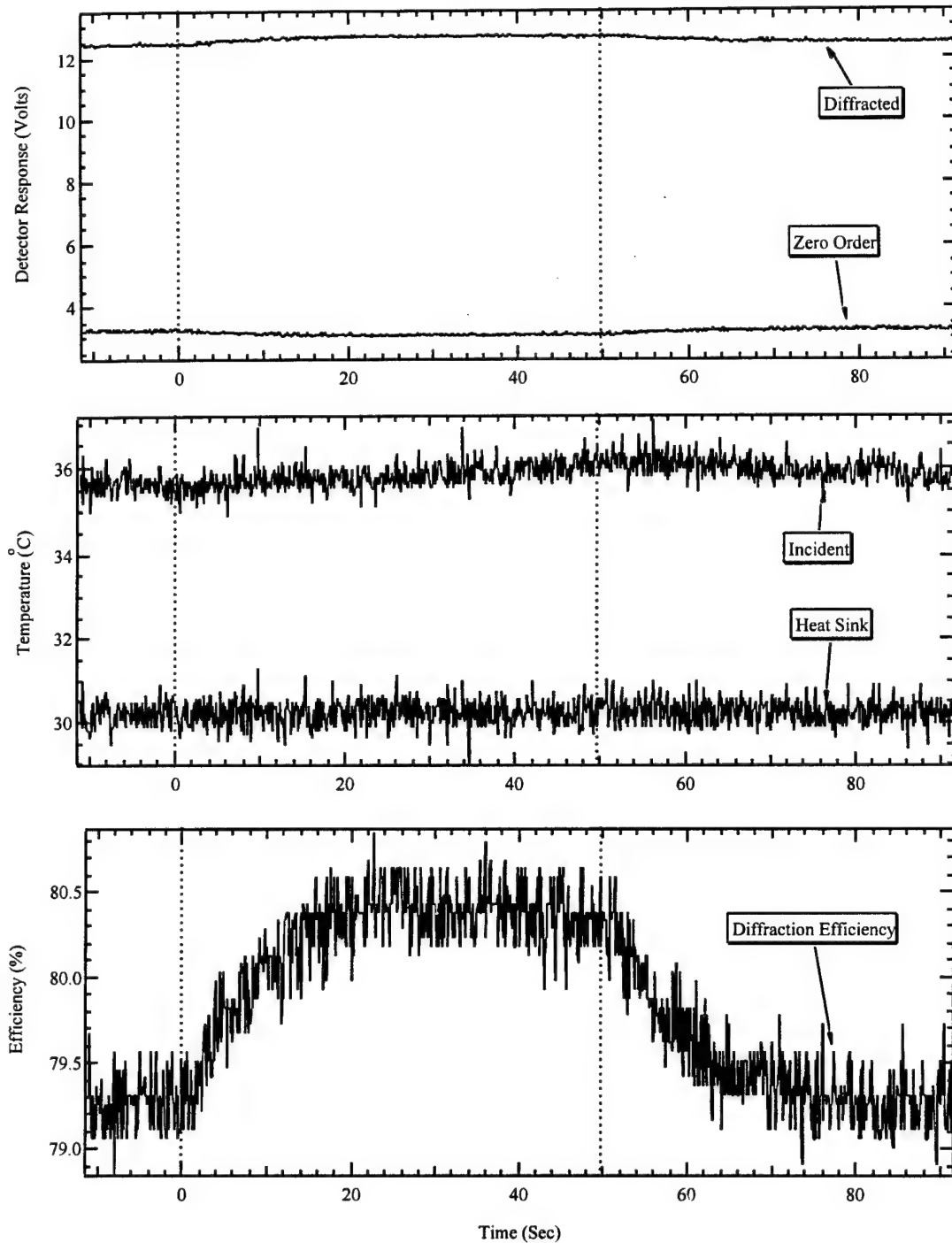


Figure A-127. Three plots showing the measured AO-cell response before, during and after an ion beam exposure #19. The dashed lines indicate the duration of the ion beam. Refer to Table A-3 for the precise beam location. The upper plot shows the power of the diffracted and zero order laser beam exiting the AO-cell and the center plot shows the temperature of the crystal face being struck by the ion beam as well as the temperature of the heat sink. The bottom plot shows the calculated diffraction efficiency.

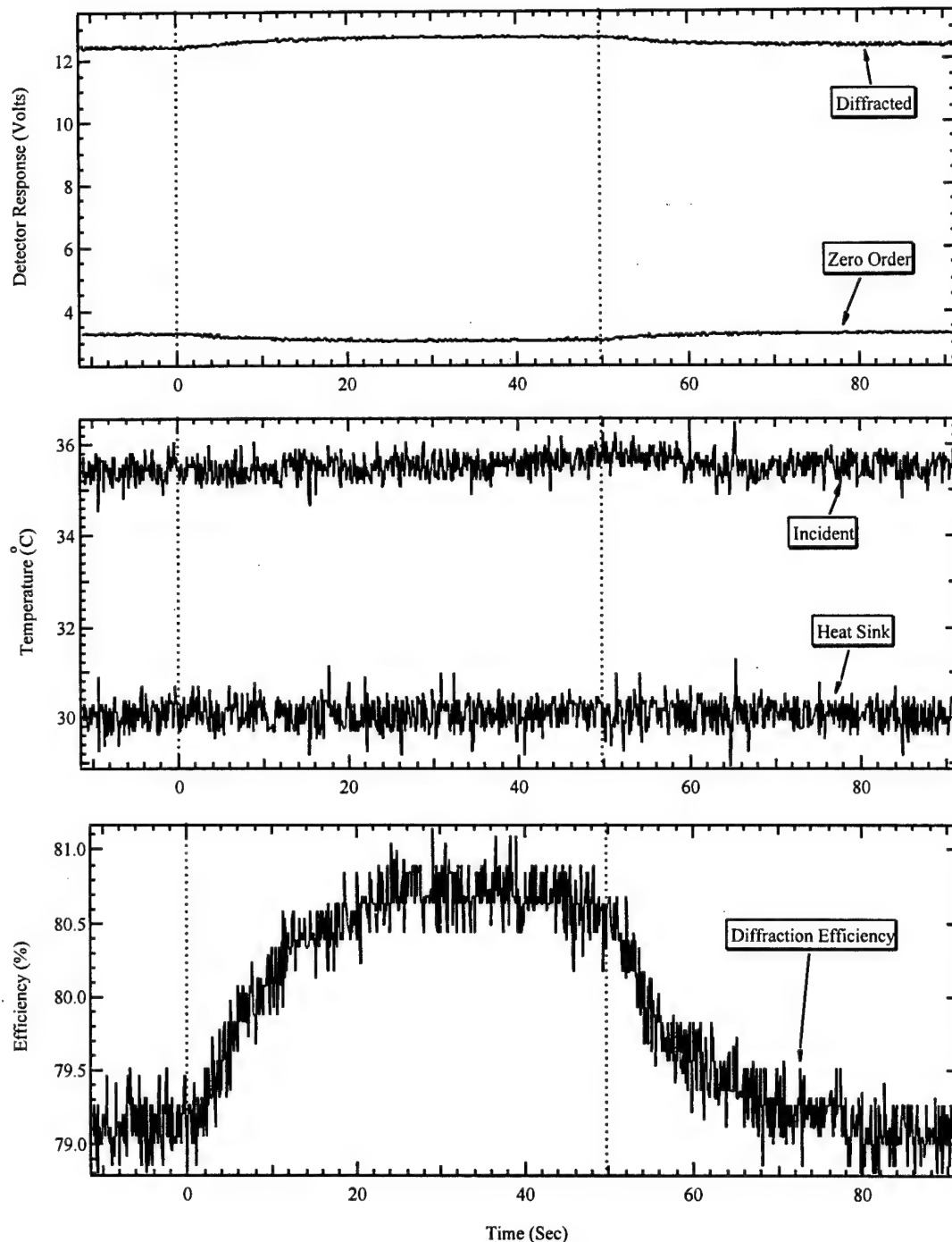


Figure A-128. Three plots showing the measured AO-cell response before, during and after an ion beam exposure #20. The dashed lines indicate the duration of the ion beam. Refer to Table A-3 for the precise beam location. The upper plot shows the power of the diffracted and zero order laser beam exiting the AO-cell and the center plot shows the temperature of the crystal face being struck by the ion beam as well as the temperature of the heat sink. The bottom plot shows the calculated diffraction efficiency.

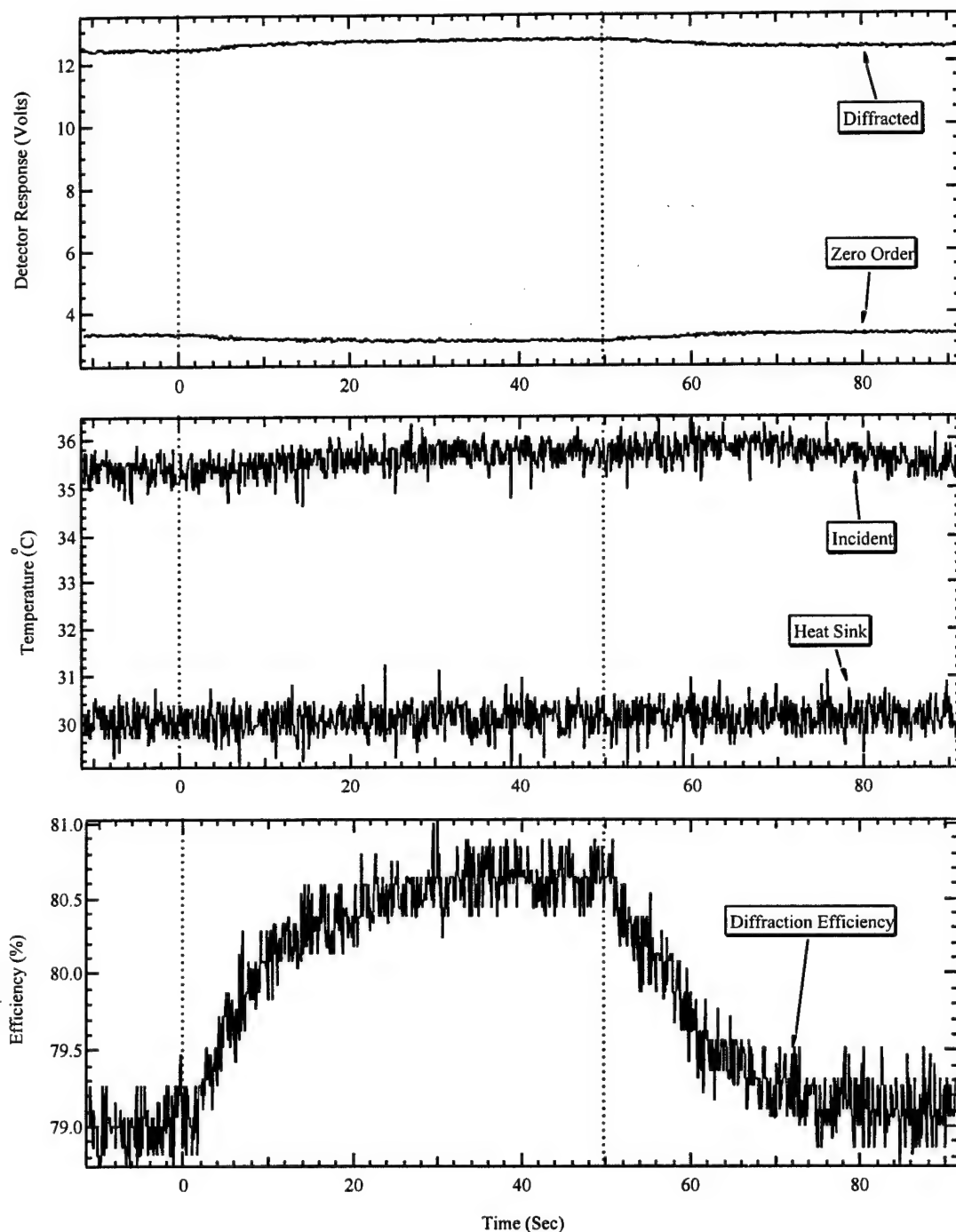


Figure A-129. Three plots showing the measured AO-cell response before, during and after an ion beam exposure #21. The dashed lines indicate the duration of the ion beam. Refer to Table A-3 for the precise beam location. The upper plot shows the power of the diffracted and zero order laser beam exiting the AO-cell and the center plot shows the temperature of the crystal face being struck by the ion beam as well as the temperature of the heat sink. The bottom plot shows the calculated diffraction efficiency.

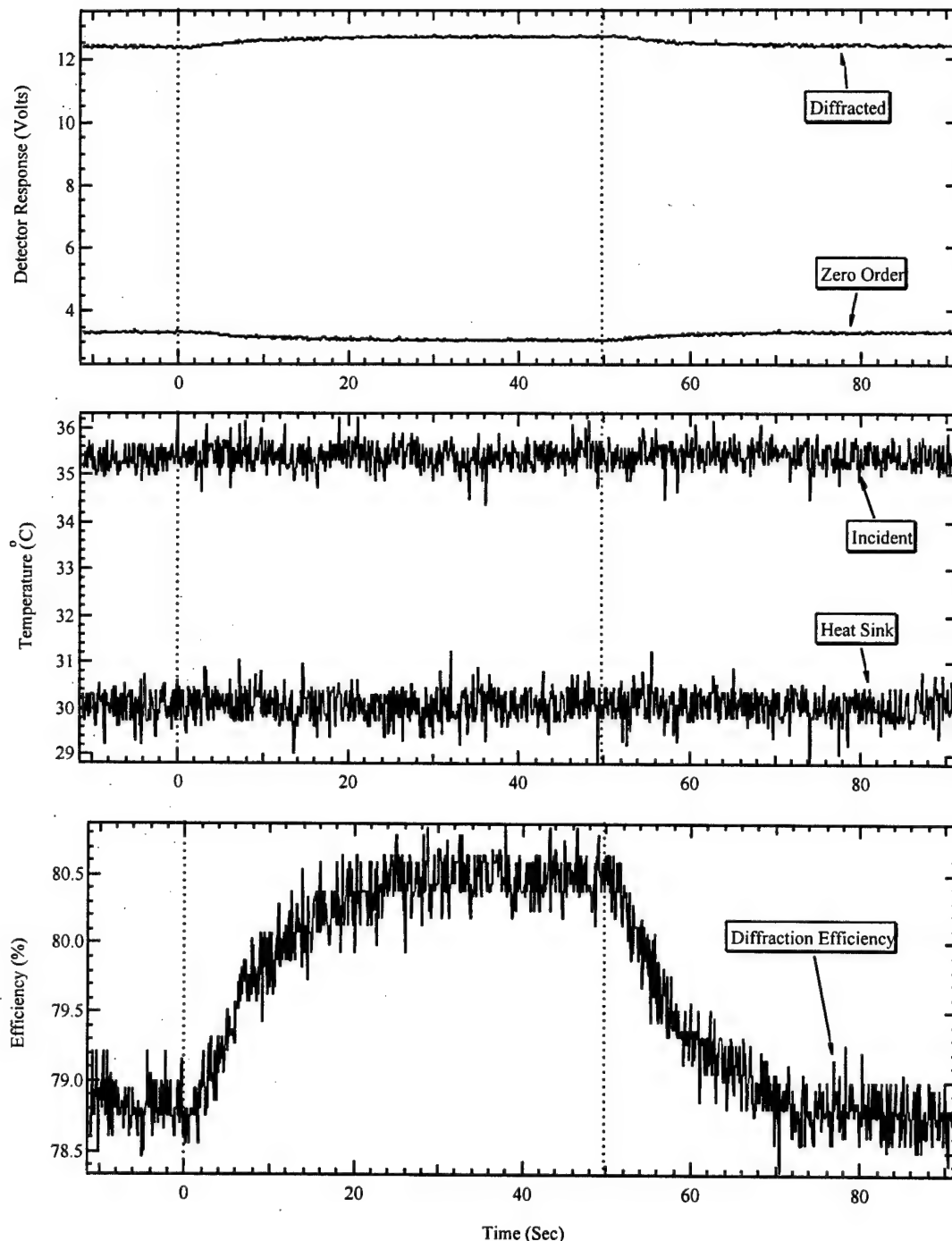


Figure A-130. Three plots showing the measured AO-cell response before, during and after an ion beam exposure #22. The dashed lines indicate the duration of the ion beam. Refer to Table A-3 for the precise beam location. The upper plot shows the power of the diffracted and zero order laser beam exiting the AO-cell and the center plot shows the temperature of the crystal face being struck by the ion beam as well as the temperature of the heat sink. The bottom plot shows the calculated diffraction efficiency.

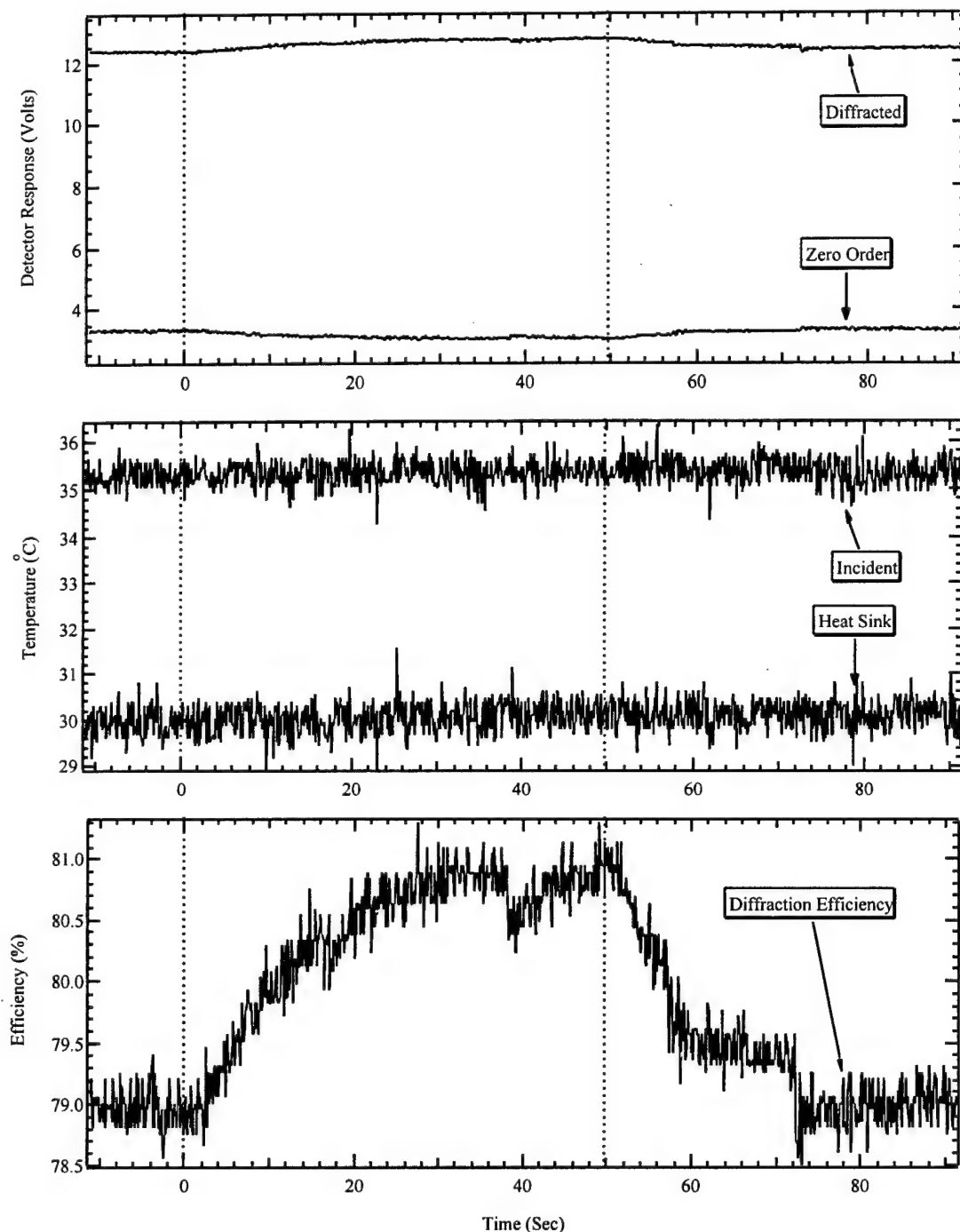


Figure A-131. Three plots showing the measured AO-cell response before, during and after an ion beam exposure #23. The dashed lines indicate the duration of the ion beam. Refer to Table A-3 for the precise beam location. The upper plot shows the power of the diffracted and zero order laser beam exiting the AO-cell and the center plot shows the temperature of the crystal face being struck by the ion beam as well as the temperature of the heat sink. The bottom plot shows the calculated diffraction efficiency.

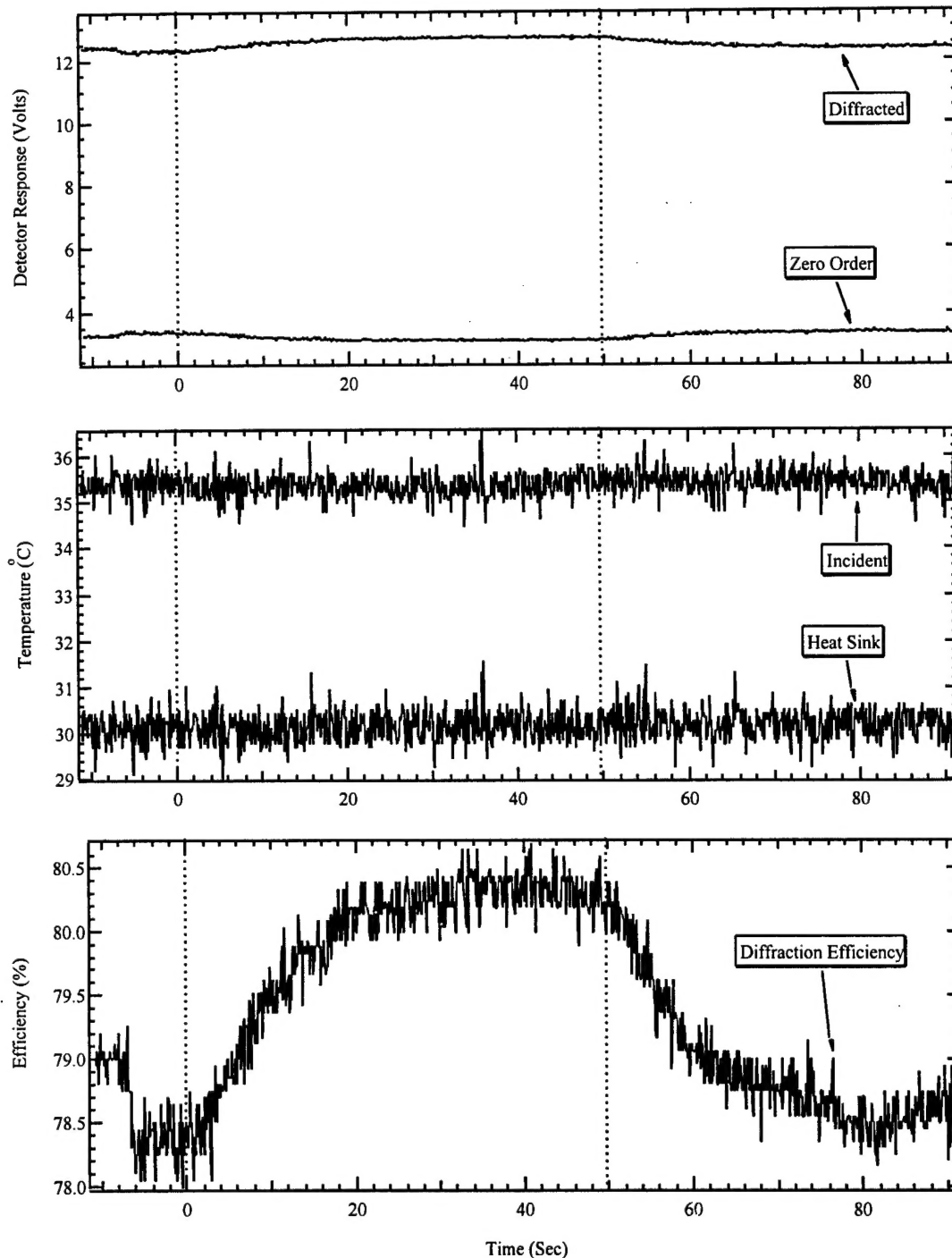


Figure A-132. Three plots showing the measured AO-cell response before, during and after an ion beam exposure #24. The dashed lines indicate the duration of the ion beam. Refer to Table A-3 for the precise beam location. The upper plot shows the power of the diffracted and zero order laser beam exiting the AO-cell and the center plot shows the temperature of the crystal face being struck by the ion beam as well as the temperature of the heat sink. The bottom plot shows the calculated diffraction efficiency.

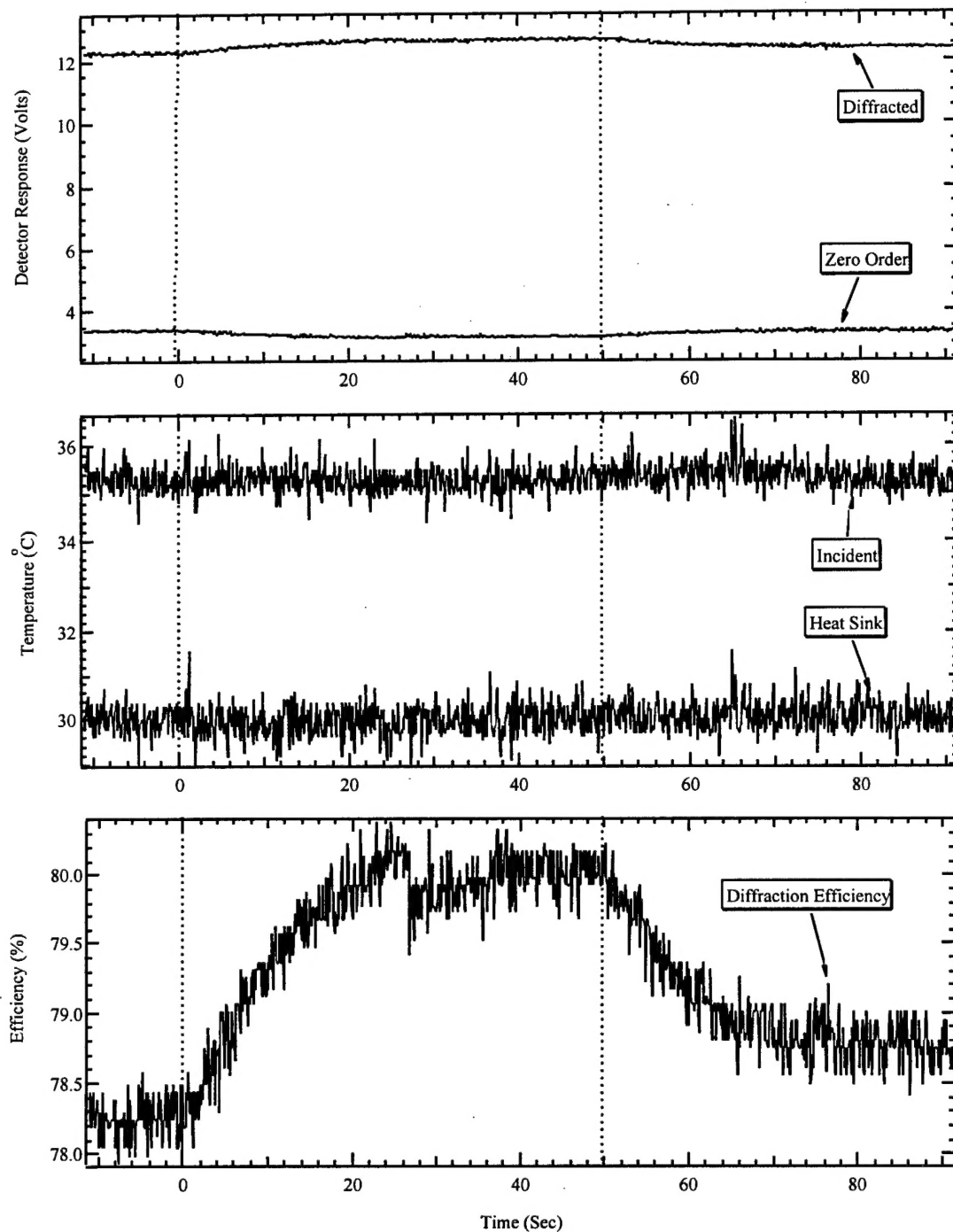


Figure A-133. Three plots showing the measured AO-cell response before, during and after an ion beam exposure #25. The dashed lines indicate the duration of the ion beam. Refer to Table A-3 for the precise beam location. The upper plot shows the power of the diffracted and zero order laser beam exiting the AO-cell and the center plot shows the temperature of the crystal face being struck by the ion beam as well as the temperature of the heat sink. The bottom plot shows the calculated diffraction efficiency.

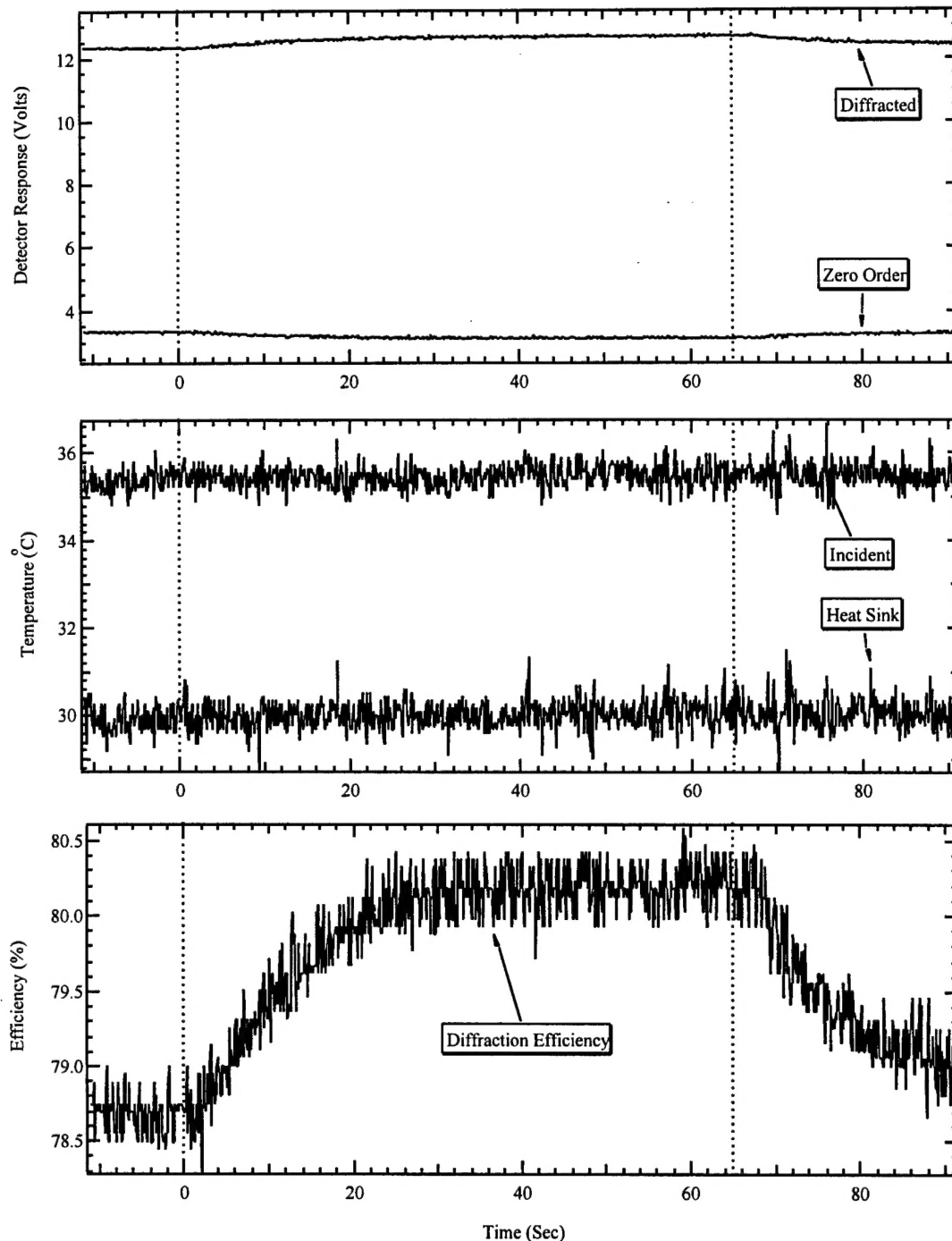


Figure A-134. Three plots showing the measured AO-cell response before, during and after an ion beam exposure #26. The dashed lines indicate the duration of the ion beam. Refer to Table A-3 for the precise beam location. The upper plot shows the power of the diffracted and zero order laser beam exiting the AO-cell and the center plot shows the temperature of the crystal face being struck by the ion beam as well as the temperature of the heat sink. The bottom plot shows the calculated diffraction efficiency.

DISTRIBUTION LIST

AUL/LSE Bldg 1405 - 600 Chennault Circle Maxwell AFB, AL 36112-6424	1 cy
DTIC/OCP 8725 John J. Kingman Rd, Suite 0944 Ft Belvoir, VA 22060-6218	2 cys
AFSAA/SAI 1580 Air Force Pentagon Washington, DC 20330-1580	1 cy
AFRL/PSOTL Kirtland AFB, NM 87117-5776	2 cys
AFRL/PSOTH Kirtland AFB, NM 87117-5776	1 cy
DSWA/Director/Attn: ESE 6801 Telegraph Road Alexandria, Virginia, 22310-3398	1 cy
DSWA/Lou Cohn 6801 Telegraph Road Alexandria, Virginia, 22310-3398	10 cys
AFRL/VS/Dr. Fender Kirtland AFB, NM 87117-5776	1 cy
AFRL/VSSE/Anthony D. Sanchez Kirtland AFB, NM 87117-5776	10 cys
AFRL/VSSE/James E. Winter Kirtland AFB, NM 87117-5776	10 cys
AFRL/VSSE/Stanley J. McKinney Kirtland AFB, NM 87117-5776	10 cys
AFRL/VSSE/Alan H. Paxton Kirtland AFB, NM 87117-5776	10 cys
AFRL/VSSE/Harald Schone Kirtland AFB, NM 87117-5776	10 cys
AFRL/VSSE/Douglas M. Craig Kirtland AFB, NM 87117-5776	10 cys
Official Record Copy AFRL/VSSE/Edward W. Taylor Kirtland AFB, NM 87117-5776	10 cys